

# **Discerning halokinetic from autocyclic sequences in deep-water sedimentary systems**

A thesis submitted to The University of Manchester  
for the degree of Doctor of Philosophy  
in the Faculty of Science and Engineering

**2021**

**Zoë Adele Cumberpatch**

School of Natural Sciences  
Department of Earth and Environmental Sciences

## Table of Contents

<i>List of Figures</i> .....	5
<i>List of Tables</i> .....	9
<i>Abstract</i> .....	10
<i>Declaration</i> .....	11
<i>Acknowledgments</i> .....	12
<b>Chapter 1: Rationale</b> .....	15
1.1 What are halokinetically-influenced deep-water systems and why are they important? ...	15
1.2 How does an integrated approach help to understand halokinetically-influenced deep-water systems? .....	17
1.3 Thesis aims.....	18
1.4 Thesis objectives .....	19
1.5 Thesis outline .....	19
1.6 List of publications.....	23
<b>Chapter 2: Halokinetically-influenced deep-water sedimentary systems: processes, products, interactions and implications</b> .....	25
2.1 Introduction.....	25
2.2 Deep-water processes and products .....	30
2.3 Components of deep-water depositional systems.....	39
2.4 Salt properties and tectonics .....	45
2.5 Salt diapirs.....	55
2.6 Halokinetic growth stratigraphy .....	60
2.7 Examples of halokinetically-influenced environments.....	67
2.8 Topographic controls on deep-water sedimentary systems.....	75
2.9 Halokinetic controls on deep-water sedimentary systems .....	84
2.10 Subsurface Energy Implications .....	95
2.11 Summary .....	99
<b>Chapter 3: Interactions between deep-water gravity flows and active salt tectonics</b> .	101
3.1 <i>Abstract</i> .....	101
3.2 Introduction .....	101
3.3 Geological setting.....	103
3.4 Methods and data.....	111
3.5 Lithofacies.....	111
3.6 Interpretation of depositional elements .....	120
3.7 Stratigraphic Evolution .....	128
3.8 Evidence for seafloor topography .....	135
3.9 Discussion.....	142

3.10	Conclusions .....	151
<b>Chapter 4: External signal preservation in halokinetic stratigraphy: A discrete element modelling approach..... 153</b>		
4.1	Abstract .....	153
4.2	Introduction .....	153
4.3	Numerical modelling of salt tectonics .....	155
4.4	Data and Methods.....	160
4.5	Results.....	165
4.6	Summary of halokinetic influence .....	174
4.7	Discussion.....	178
4.8	Future work.....	191
4.9	Conclusions.....	192
<b>Chapter 5: How confined is confined? An investigation into the effect of diapir-induced topographic spacing on deep-water sediment dispersal in the Paleocene Eastern Central Graben (ECG), UK..... 193</b>		
5.1	Abstract .....	193
5.2	Introduction .....	193
5.3	Geological Setting .....	196
5.4	Methods and data.....	200
5.5	Results: Paleocene Facies Distribution .....	205
5.6	Results: Effects of lateral spacing in subsurface and models .....	217
5.7	Discussion.....	226
5.8	Conclusions.....	234
<b>Chapter 6: Synthesis.....235</b>		
6.1	How do deep-water facies and architecture vary around salt structures?.....	235
6.2	How does this modulation of stratigraphic architectures vary laterally and temporally? 247	
6.3	Criteria for the recognition of halokinetically-influenced deep-water systems .....	252
6.4	The importance of integrated workflows .....	262
6.5	Comparison to other depositional settings .....	267
6.6	Reducing facies uncertainty in the subsurface .....	280
6.7	Subsurface energy implications .....	285
6.8	Future research directions.....	290
<b>Chapter 7: Conclusions .....</b>		
7.1	Interactions between deep-water gravity flows and active salt tectonics: an exposed example from the Bakio Diapir, Basque-Cantabrian Basin, Northern Spain.....	299
7.2	External signal preservation in halokinetic stratigraphy: A discrete element modelling approach .....	300
7.3	How confined is confined? An investigation into the effect of diapir-induced topographic spacing on deep-water sediment dispersal in the Eastern Central Graben, UK .....	300

7.4	Controls on halokinetically-influenced deep-water successions .....	301
7.5	Lateral and temporal variations in halokinetic modulation of stratigraphic architectures .....	302
7.6	Criterion for the recognition of halokinetically-influenced deep-water systems .....	302
7.7	Comparison to other salt, or topographically influenced basins .....	302
7.8	Summary .....	303
<i>References.....</i>		<i>304</i>
<i>Appendix A: External signal preservation in halokinetic stratigraphy: A discrete element modelling approach.....</i>		<i>377</i>
<i>Appendix B: Halokinetic modulation of sedimentary thickness and architecture: a numerical modelling approach.....</i>		<i>385</i>
<i>Appendix C: Evolution of a mixed siliciclastic-carbonate deep-marine system on an unstable margin: the Cretaceous of the Eastern Greater Caucasus .....</i>		<i>424</i>
<i>Appendix D: The Influence of Confining Topography Orientation on Experimental Turbidity Currents and Geological Implications.....</i>		<i>461</i>

## List of Figures

Figure 2.1: Conceptual model of a source-to-sink sedimentary system (Ferguson et al. 2020). ...	26
Figure 2.2: Main controls on deep-water sedimentary depositional systems .....	27
Figure 2.3: Distribution of global salt basins across geological time (Warren 2016) .....	28
Figure 2.4: Giant hydrocarbon discoveries between 2000 and 2012.....	30
Figure 2.5: The range of different sediment gravity flow types from laminar to turbulent.....	31
Figure 2.6: Classification of sediment gravity flows based on their rheological properties illustrating different flow types, deposits, textures and implications for subsurface energy reservoir quality. ....	31
Figure 2.7: Cross-section of a turbidity current observed in a laboratory experiment, .....	32
Figure 2.8: Summary of low- and high- density turbidity currents.....	32
Figure 2.9: Idealised vertical profile (Bouma sequence) through a turbidite .....	33
Figure 2.10: Examples of debrites and mass transport deposits from outcropping and subsurface stratigraphy.....	36
Figure 2.11: Model for the longitudinal rheological flow evolution of a single event from a fully turbulent flow to a laminar flow and the resultant deposits.....	38
Figure 2.12: A) Plan view down-current flow transformation of a turbulent flow to a transitional-laminar flow .....	39
Figure 2.13: Bathymetric map view of part of the Monterey Canyon, offshore central California. ....	40
Figure 2.14: Schematic depiction of facies heterogeneities within different hierarchical scales of channel complex systems.....	41
Figure 2.15: A map surface and stratigraphic vertical expression of a channel-lobe transition zone .....	42
Figure 2.16: A) Plan view of submarine lobe sub-environments.....	43
Figure 2.17: Hierarchy of compensational stacking of submarine lobes. ....	44
Figure 2.18: Hierarchical scheme for the Fan 3 lobe complex of the Tanqua depocenter, Karoo Basin, South Africa (Prélat et al. 2009). ....	45
Figure 2.19: Idealised evaporitic basin in cross-section and plan view showing the order and different types of salt precipitated in a radial nature from brines (Warren 2006). ....	46
Figure 2.20: End-member models for the deposition of ancient salt sequences.....	48
Figure 2.21: Depth versus strength plot for overburden, salt and basement.....	49
Figure 2.22: Depth versus density plot for salt and siliciclastic rocks (sandstone and mudstone). ....	50
Figure 2.23: Comparison of tensional and compressional strengths of dry and wet salt with equivalent dry and wet sedimentary rocks and sediments. ....	50
Figure 2.24: Physical properties of rock salt (halite) compared to other lithologies.....	51
Figure 2.25: Processes driving salt flow inferred from hydraulic heads. ....	53
Figure 2.26: Salt structures, after Fossen (2010).....	55
Figure 2.27: Classical evolutionary stages of diapirs. ....	56
Figure 2.28: The cross-sectional shapes of diapirs.....	59
Figure 2.29: End member models for diapir growth and overburden deformation (Poprawski et al. 2014) .....	61
Figure 2.30: End member models of halokinetic sequences showing the characteristic features of hook and wedge halokinetic sequences .....	62
Figure 2.31: End member models for composite halokinetic sequences (CHS).....	63
Figure 2.32: Genetic model for formation of tabular and tapered CHS (Giles and Rowan 2012)65	
Figure 2.33: Geometric patterns of stacked CHS .....	66
Figure 2.34: Map view and cross-section of halokinetic sequences in the 500-1,000 m wide contact zone around El Papalote and El Gordo diapirs (La Popa basin, Mexico) .....	70

Figure 2.35: Halokinetic (HS), and composite halokinetic (CHS) and depositional sequence stratigraphy of the Upper Cretaceous- Lower Palaeogene stratigraphy exposed on the east side of El Papalote Diapir and the north side of the La Popa Weld, La Popa Basin, Mexico (Giles and Rowan 2012).....	73
Figure 2.36: Schematic block diagram reconstructions of depositional environments and local paleogeography in the Mt. Frome area.....	74
Figure 2.37: Different scales of topography in deep-water depositional systems.....	76
Figure 2.38: Topographic interaction model of different flow types.....	77
Figure 2.39: Example of the reflected facies that may be produced as turbulent flow interacts with topography (Tinterri et al. 2016).....	79
Figure 2.40: Possible deep-water termination styles close to topographic highs.....	81
Figure 2.41: Different method of confinement that a deep-water system, or individual SGF, may be characterised by (from Southern et al. 2015).....	82
Figure 2.42: The fill-spill model, showing vertical stratigraphic evolution of a confined basin sequence generated by episodic uplift of basin topography.....	83
Figure 2.43: Sketch summarising the structural controls, with respect to gravity-driven processes, on depositional systems from the shelf to basin floor.....	85
Figure 2.44: Summary of sedimentary facies distribution and stacking patterns observed in a variety of deep-water halokinetically-influenced settings (Bouma 1997; DeVay et al. 2002; Kendall 2012).....	86
Figure 2.45: The distribution of late Pliocene sediments in the Auger minibasin.....	87
Figure 2.46: Schematic cross-section of reservoir facies and architectures between salt walls in the Auger minibasin.....	88
Figure 2.47: Summary of the relationships between deep-water depositional systems and salt-related structures in the Lower Congo Basin.....	90
Figure 2.48: Example of a detailed spectral decomposition analysis used to interpret the seismic geomorphology of unit 4.....	92
Figure 2.49: Summary graph of the major observed influences of salt-cored structures on deep-water sedimentary systems (Howlett et al. 2020).....	93
Figure 2.50: Dynamic evolution of submarine channel-lobe systems and salt-cored structures within the contractional salt domain developed from the Miocene stratigraphy of the Kwanza Basin.....	94
Figure 2.51: Schematic showing elements of the petroleum system which are influenced by salt presence or halokinesis (Jackson and Hudec 2017).....	95
Figure 2.52: Subsurface energy traps that may be expected to form in halokinetically-influenced basins.....	96
Figure 2.53: Seismic reflection cross-section from the Pierce diapirs, Eastern Central Graben, UK North Sea, highlighting some of the key questions and uncertainties of subsurface interpretations in salt-influenced basins.....	98
Figure 2.54: Conceptual model illustrating porosity, permeability and quartz-cement development with burial for HDTs (yellow), hybrid beds (green) and LDTs (brown).....	99
Figure 3.1: Sketch summarising the structural controls, with respect to gravity-driven processes, on depositional systems from the shelf to basin floor.....	103
Figure 3.2: Simplified geological map, stratigraphy, and cross-section of the Basque–Cantabrian Basin (BCB),.....	107
Figure 3.3: A) Geological map located in Figure 3.2 and B) stratigraphic column for the study area.....	109
Figure 3.4: Schematic structural–stratigraphic cross-section through the Bakio and Guernica diapirs.....	110
Figure 3.5: Photograph of carbonate facies, supporting observations in Table 3.1.....	114
Figure 3.6: Siliciclastic facies photographs.....	119

Figure 3.7: Type examples of the seven documented facies associations in this study (Table 3.3). .....	125
Figure 3.8: Photographs showcasing the variety of geometries observed in the study area. ....	128
Figure 3.9: Sedimentological log through the Black Flysch Group at Gaztelugatxe Island. ....	130
Figure 3.10: Variability of facies and architectures within large-scale depositional elements at Bakio West Bay .....	132
Figure 3.11: Sedimentary log through Cabo Matxitxako Beach.....	134
Figure 3.12: Evidence for topography and paleoflow direction. ....	136
Figure 3.13: Schematic depositional models showing the geological evolution of the system through time, specifically detailing deep-water sub-environments and their interactions with salt-induced topography. ....	142
Figure 3.14: Schematic deep-water facies and architectural elements observed on both flanks of the Bakio diapir showing the sub-seismic-scale heterogeneity that can be associated with these systems and diapir flank plays .....	144
Figure 3.15: Simplified comparison between lobes in unconfined and A–C) confined settings and D–F) progradation style in these settings.....	146
Figure 3.16: Thought experiment comparing the effects of variable topography in the evolution of deep-water systems. ....	150
Figure 4.1: Seismic reflection cross-section from the Pierce diapirs, Eastern Central Graben, UK North Sea (located in Figure 4.12) highlighting some of the key questions and uncertainties of subsurface interpretation in salt-influenced basins. ....	155
Figure 4.2: Recent examples of Finite Element Model (FEM) used in salt tectonics.....	158
Figure 4.3: Example of the relationships that can exist between a particle i (white) and a neighbouring particle j (purple). x and y are the midpoints of the respective particles.....	161
Figure 4.4: Initial set up of the DEM (T=0) and key parameters.....	163
Figure 4.5: Model 3, the intermediate aggradation experiment with a sedimentation rate of 0.3mm/year.....	165
Figure 4.6: M1, the model with no sedimentary fill, after 4.6 Myr. ....	167
Figure 4.7: Uninterpreted and interpreted static images of the DEM for M2-M4 (constant sedimentation rate models) after 4.6 Myr.....	168
Figure 4.8: Uninterpreted and interpreted static image of the DEM with variable sedimentation (M5 and M6) after 4.6 Myr. ....	169
Figure 4.9: (A) Interpretation of M5 based on Figure 4.7. ....	173
Figure 4.10: Diagrammatic comparison of static 4.6 Myr DEM across all models. ....	175
Figure 4.11: Comparison of the flank section stratigraphy across all models with sediment (M2-M6). ....	178
Figure 4.12: Schematic interpretations of M2-M6, focussed on the central 2000 m of the syn-kinematic stratigraphy .....	181
Figure 4.13: Tectonic framework of the North Sea rift system .....	184
Figure 4.14: Subsurface example of model application comparing some of the modelled results to stratigraphy from the Pierce Field, Eastern Central Graben, UK North Sea .....	186
Figure 4.15: Conceptual facies diagram for a deep-water succession based on integration of field-based facies analysis around the Bakio diapir, Basque Cantabrian Basin Northern Spain .....	188
Figure 4.16: Halokinetic zonation scheme shown for M3.....	191
Figure 5.1: Sketch summarising the structural controls, with respect to gravity-driven processes, on depositional systems from the shelf to the basins floor .....	196
Figure 5.2: A) Tectonic framework of the North Sea rift system, B) Structural map of the Central Graben showing distribution of salt diapirs related to major basin faults and Jurassic salt-withdrawal basins .....	198
Figure 5.3: Subsurface dataset map .....	201
Figure 5.4: Initial set up of DEM (T=0) with two diapirs, showing key parameters.....	204

Figure 5.5: Photographs of type examples of facies from core.....	209
Figure 5.6: Summary figure showing the anticipated observations across different types of data and scales in different depositional environments within the study area. ....	213
Figure 5.7: A) Spectral Frequency Decomposition map for the Top Lista Formation.....	216
Figure 5.8: Uninterpreted and interpreted two-way travel-time seismic reflection cross-sections across the Eastern Central Graben .....	224
Figure 5.9: Interpreted static images of the DEM for M1-M6 after 4.6 Myr .....	225
Figure 5.10: Comparative diagram showing examples of different spaced diapirs in subsurface and model datasets used in this study, and the key observations associated with those different amounts of diapir spacing.....	230
Figure 5.11: A) Halokinetic zonation scheme shown for M1, M2 and M3.....	232
Figure 6.1: Stratigraphic architectural panel through the Black Flysch Group at Cabo Matxixako, Bakio, Spain .....	236
Figure 6.2: Conceptual model for locally-derived MTDs in salt-controlled basin (Poprawski et al. 2021) .....	240
Figure 6.3: Spectral decomposition of a horizon slice within the Halibut Slide.....	242
Figure 6.4: Two-dimensional difference maps for the flume tank experiments.....	245
Figure 6.5: Schematic charts plotting sedimentation rate and diapir rise rate evolution through time .....	251
Figure 6.6: Sedimentological evidence for topography during deposition of deep-water successions .....	255
Figure 6.7: Some of the criteria used to identify halokinetically-influenced stratigraphy in two dimensions .....	258
Figure 6.8: Analysis of halokinetically-influenced deep-water depositional elements across different data sets.....	260
Figure 6.9: Characteristic stratigraphic geometry plots for confined and unconfined lobes from Prélat et al. (2010) .....	261
Figure 6.10: Workflow diagram showing the different types of data in this study .....	265
Figure 6.11: Observations of onlap and pinch out across multiple scales and datasets.....	266
Figure 6.12: Evidence for palaeotopography in the Eastern Greater Caucasus .....	272
Figure 6.13: Evidence for allochthonous block model as the most likely for the generation of Cretaceous topography in the Eastern Greater Caucasus of Azerbaijan.....	273
Figure 6.14: Evolutionary model for the Cretaceous of the Eastern Greater Caucasus of Azerbaijan. ....	274
Figure 6.15: Comparison of different types of topography that influence deep-water depositional systems, under increasing deformation rates .....	276
Figure 6.16: Summary diagram showing how diapir topography can influence facies distribution throughout all depositional environments (after Hudec and Jackson 2017).....	280
Figure 6.17: Four of the potential models proposed for the structural configuration of Gaztelugatxe Island. ....	293
Figure 6.18: Expected result of a three-dimensional DEM based on the two-dimensional models used within this study. ....	294
Figure 6.19: Examples of seismic data from in the Bay of Biscay which is suggested to be used alongside outcrop observations to better understand along strike variability for salt structures and halokinetic sequences. ....	297



## List of Tables

Table 2.1: Expected evaporite mineral crystallisation sequence in increasingly concentrated hypersaline solutions. ....	46
Table 2.2: Various physical properties of halite (rock salt) compared to quartz and ice (Hudec and Jackson 2017).....	49
Table 2.3: Characteristics of hook and wedge halokinetic sequences (Giles et al. 2004; Giles and Rowan 2012).....	63
Table 2.4: Summary of halokinetically-influenced stratigraphy studies in published literature.....	68
Table 3.1: Table of carbonate facies detailing the major observations of the six facies which constitute the early Albian Bakio Marls and early middle Albian Bakio Breccias formations.....	111
Table 3.2: Table of siliciclastic facies detailing the ten facies that comprise the Black Flysch Group. ....	114
Table 3.3: Table of facies association detailing the assemblages that constitute the Black Flysch Group. ....	121
Table 3.4: Table describing geometrical configurations observed in the Black Flysch Group. ..	125
Table 4.1: Details of the different sedimentation patterns and rates used in the six experiments. S1-3 refer to sedimentation intervals. ....	163
Table 4.2: Comparison of diapir growth and overburden anticline width across all six experiments at T=4.6 Myr.....	170
Table 4.3: Comparison of stratigraphic thinning across M2-M6.....	172
Table 5.1: Core data used for facies analysis across the study area.. ....	202
Table 5.2: Details of the different spacing distances between diapirs (measured from crest to crest) used in each model.....	202
Table 5.3: Siliciclastic facies table based on core observations. ....	205
Table 5.4: Summary of characteristics of subsurface facies observed in the Paleocene across a number of different data types and scales of data.....	210
Table 5.5: Variably spaced diapirs used in this study.....	217

**Total Words (main text): 92,831**

## Abstract

Halokinetic stratigraphy refers to sedimentary deposits affected by the growth or retreat of salt-cored topography. Deep-water sediment gravity flows can be influenced by seafloor topography associated with salt structures, and the interaction between the two ultimately controls the depositional architecture of their successive deposits. Where these deposits onlap salt diapirs they can form reservoirs with combined structural-stratigraphic traps. Typically, these halokinetic sequences are poorly-imaged in seismic data due to steep dips, salt overhangs and near-diapir deformation. In addition, they are not well represented in outcrop, largely due to dissolution of the associated halites. Therefore, the facies and architecture of these halokinetically-influenced deep-water successions are challenging to investigate, but are anticipated to differ from those in unconfined basins, or those where topography is generated by non-halokinetic processes.

This study aims to understand how and why halokinetically-influenced deep-water systems differ from those in unconfined settings, using a multi-scalar and multi-method approach. Outcrop data from the Cretaceous Basque-Cantabrian Basin are compared with subsurface data from the Paleocene North Sea Central Graben. The results of these studies are compared to two-dimensional Discrete Element Models of different sedimentation patterns influenced by salt growth.

Key insights derived from this approach include: 1) salt-related, active topography, and the degree of confinement are shown to be important modifiers of depositional systems, affecting the degree of flow confinement which results in predictable facies variability and remobilisation of deposits; 2) facies analysis reveals that channels and lobes are influenced (re-routed and confined) by salt growth at a range of scales, from centimetre-scale sedimentological characteristics identified in core and outcrop, to kilometre-scale geomorphological attributes visible in seismic; 3) axially-derived deep-water depositional systems are heavily modified by laterally impinging mass transport deposits formed in response to salt-controlled topographic growth of the sea bed; 4) recognition criteria for deep-water halokinetically-influenced settings include: multiple directions of ripple lamination, injectites, fluidisation structures, presence of hybrid beds, range of MTD types, stratigraphic thickness variations, onlap of deposits against halokinetically-deformed substrate, and abrupt juxtaposition of deep-water depositional facies and MTDs; 5) modelled thinning rates are up to six times greater within 350 metres of a salt diapir, compared to further afield, and typically decrease upwards (with time) and laterally (with distance) from the diapir; and 6) in both subsurface and modelled scenarios, stratigraphy deposited between closely-spaced diapirs (<3 km) is deformed by diapirism. Conversely, in widely-spaced diapirs (>3 km), a flat, plateau-like zone is developed between the deformation zones, where halokinetic-modulation is reduced. Salt basins are complex, due to: the presence and variability of the top and base salt; early diapiric stratigraphy; non-piercing diapirs; and salt-related faults, therefore, even these 'minimal modulation' zones are unlikely to contain stratigraphy which is completely undeformed by halokinesis.

The integration of these diverse techniques allows for the spatial and temporal distribution of deep-water facies and architectures in salt-influenced basins to be recognised. These characteristics are compared to their halokinetically-influenced counterparts from different depositional environments, and unconfined, or non-halokinetic topographically-confined deep-water basins. In most deep-water successions the dominant controls are allocyclic (external), but these successions are heavily influenced by halokinesis (salt growth) which drives autocyclic (internal) modulation of the primary depositional signal. Supplementing subsurface data with modelled stratal architectures and global outcrop observations from exhumed halokinetically-influenced settings aids the prediction of sedimentary unit thickness, facies, architectures, deformation, halokinetic alteration and thinning rates. This combined approach can be used to test interpretations arising from incomplete or low-resolution subsurface and outcrop data when building geological models. When applied to petroleum exploration and development, geothermal energy extraction, and to carbon and hydrogen storage industries in salt basins globally, this approach enables better prediction of trap geometry, and reservoir quality and distribution.

## Declaration

University of Manchester PhD by published work Candidate Declaration

Candidate Name: Zoë Adele Cumberpatch

Faculty: Science and Engineering

Thesis Title: Discerning halokinetic from autocyclic sequences in deep-water sedimentary systems

I declare that this thesis has been composed by myself and that the work has not be submitted for any other degree or professional qualification. I confirm that the work submitted is my own, except where work which has formed part of jointly-authored publications has been included. My contributions and those of the other authors have been explicitly within. I confirm that appropriate credit has been given within this thesis where reference has been made to the work of others. All work included in this thesis was completed whilst at The University of Manchester.

## Copyright Statement

- i. The author of this thesis (including any appendices and/or schedules to this thesis) owns certain copyright or related rights in it (the “Copyright”) and s/he has given The University of Manchester certain rights to use such Copyright, including for administrative purposes.
- ii. Copies of this thesis, either in full or in extracts and whether in hard or electronic copy, may be made only in accordance with the Copyright, Designs and Patents Act 1988 (as amended) and regulations issued under it or, where appropriate, in accordance with licensing agreements which the University has from time to time. This page must form part of any such copies made.
- iii. The ownership of certain Copyright, patents, designs, trademarks and other intellectual property (the “Intellectual Property”) and any reproductions of copyright works in the thesis, for example graphs and tables (“Reproductions”), which may be described in this thesis, may not be owned by the author and may be owned by third parties. Such Intellectual Property and Reproductions cannot and must not be made available for use without the prior written permission of the owner(s) of the relevant Intellectual Property and/or Reproductions.
- iv. Further information on the conditions under which disclosure, publication and commercialisation of this thesis, the Copyright and any Intellectual Property and/or Reproductions described in it may take place is available in the University IP Policy (see <http://documents.manchester.ac.uk/DocuInfo.aspx?DocID=24420>), in any relevant Thesis restriction declarations deposited in the University Library, The University Library’s regulations (see <http://www.library.manchester.ac.uk/about/regulations/>) and in The University’s policy on Presentation of Theses.

## Acknowledgments

Embarking on a PhD whilst fighting against a little voice, routed in years of trauma and neglect, telling me I wasn't good enough, and a global pandemic that flipped our world upside down has been no easy task. I wish to thank everyone who has made this possible, and dare I say, enjoyable. In true Zoë style, this will not be brief, and will be raw.

Firstly, my supervisory team. Although I have not hidden my annoyance at many rounds of revisions due to the sheer number of you, I am so very grateful for your guidance, wisdom, humour, patience and encouragement.

Ian Kane, thank you for believing in me from day 0, supporting me through all my crazy ideas and meltdowns, cutting literally thousands of words of waffle and for pushing me to achieve more than I ever thought possible in four years. SedResQ is such a positive and kick-ass research group to be part of, and that starts and ends with you.

Dave Hodgson, Chris Jackson, Ben Kilhams, Emma Finch and Mads Huuse thanks for ensuring that Ian didn't have to endure supervising me alone.

Dave, you have an eye for detail, and terminology that I will never truly appreciate. Thanks for translating my manuscripts from Zoë speak into Science and trusting me to run the Lobe3 sponsors trip so early on.

Chris, your insights into salt basins have been eye opening. A 10 minute conversation with you can genuinely teach me more than reading 60 papers. Your efforts to promote diversity and equality in Geoscience, and life, continually inspire me to be a better human.

Ben, you really are the living breathing Paleocene volume of the Millennium Atlas, thanks for helping me to keep the implications of my research at the forefront. You've shown its possible to straddle industry and academia, and I'm hoping to follow in your footsteps there.

Emma, I know you never signed up to this 'minion' but I cannot thank you enough for being a mentor, supervisor and friend. I knew nothing about numerical modelling before you took me under your wing. After a few trips down the rabbit hole with Alice, and a few papers, I still think you're an absolute mathematical magician. The last year would have been impossible without you.

Mads, thank you for making sure I don't inadvertently break any confidentially agreements.

Secondly, funders. Thank you to the National Environment Research Council (NERC) Centre of Doctoral Training (CDT) in Oil and Gas for funding this research. The CDT has provided an excellent array of training courses which have broadened my knowledge of subsurface Geoscience, and helped me keep my research relevant. I'm grateful to have been a part of the amazing CDT community, a ship that wouldn't sail without Anna Clark, Lorna Morrow and John Underhill. Thank you to the entirety of my wonderful cohort for 4 years of fun, especially Edoardo Fiordalisi, Chris Lloyd, Claire McGhee, Claudia Haindl, Olivia Walker, Louis Howell and Chris Brennan. You're champions. We've survived this together.

I'm very grateful to have received (or have received as part of a group) the following grants: the Presidents Doctoral Scholar Award (UoM), the Presidents Award (Geological Society), a TNO to EPOS grant, a CASP Fieldwork Grant, the Norman H. Foster Memorial Grant and the Gustavus E. Archie Memorial Grant (AAPG Grants in Aid). These awards have helped me to broaden and deepen my research and keep my fingers in so many pies (and publications!).

My research has benefitted from the affiliation with the Lobe 3 joint industry programme, thank you to the sponsors for insightful discussions in the field and at meetings, particularly to Tyler Foster at BHP for showing me the true application of my research. Thanks to fellow Lobe 3-ers: Tim Wigan, Ander Martínez-doñate, Dave Lee and Damjan Ostrelc, and our up-dip friends Max Bouwmeester and Will Taylor. It's been nice to have some sense of stability and accountability during our weekly lockdown meetings.

Thank you to PGS for providing the subsurface data used in this project, the British Geological Survey for core viewings, and Schlumberger and Geoteric and FMB (TGS) for providing academic licenses to software.

Next up, the amazing research group at Manchester. It has been a dream (and at times a nightmare of self-doubt) to be involved with the forces of nature that are SedResQ and the Basins Group. Thank you to SedResQ past, present and future (Daniel Bell, Arne Fuhrmann, Ross Ferguson, Euan Soutter, Jefferson Nwoko, Ander, Lauren Clarehugh, Ashley Ayckbourne, and Max) for being an absolute power house. Dan, thank you for all your initial support helping me get this PhD project and for always being game for 6 G&Ts at Big Hands on a random Tuesday following a Dominoes 2FT. Ross, thanks for literally being a shoulder to cry on, you're such a genuine hero, I really enjoyed all our chats whilst grain size separating and your interview help was beyond helpful. Extra special thanks to Euan for all in the in-field discussions, showing me how to log effectively, putting up with my driving (Azerbaijan fine, Man U line up. I'll say no more) and teaching me in a few weeks, more than I'd learnt about deep water sedimentology in my undergrad and masters. It's been a pleasure to tour the best deep-water rocks in Europe with you, I've gained a lot more than you've lost (tape measures, notebooks, camera, car keys....)

Thanks to Ander, Ash, Lauren, Dan, Max, Eoin Dunlevy, Kévin Boulesteix and Jorge Lajo Yanez for sharing the super office over the years. I remember our whiteboard discussions of what is a bed and what is a lamination, and who will die and who will live in game of thrones, fondly.

Manchester Basins Group are known globally for being at the forefront of research and fun. I'm grateful to have been part of such a great, dynamic research group who are always game for a pint. In particular, Leonardo Muniz-Pichel, Chris Lloyd, Arkadyuti Sarkar, Jack Stacey, David Cox, and Max Casson. I think I've made enough speeches declaring how important and inspirational you all are to me – I really do mean it ☺. Edoardo Fiordalisi and Gustavo Pereira thanks for being my rocks, and keeping me sane with coffee and cake breaks.

MANchester wouldn't be what it is without the amazing women in the group. Lucy Manifold, Aude Duval-Arnould, Nawwar Al-Sinawi, Lauren and Hannah Rawson have certainly helped prevent me from turning into a 'lad lad lad'. Cathy Hollis, thanks for being an unsung hero and for keeping Basins ticking over, even during lockdown. Kofi Owusu saved my computers (and the plotters) life every time I messed it up, thank you so so much for the stress avoidance. Extra special thanks to Hannah, Lauren, Max, Emma, Ander, Ben, Tim, Ash, Will and Ross for proof reading chapters of this thesis, for very reasonable rates!

Thank you to Yvonne Spychala, Domenico Chiarella, Hilary Corlett, Gemma Doughty-Jones, Evey Gannaway Dalton, Chris Brennan, Jürgen Adam, Bruce Trudgill, Frank Peel and Mike Hudec for insightful reviews of the publications that form the basis of this work, and Atle Rotevatn, Gary Hampson, James Schmitt and Craig Magee for their editorial handling of those manuscripts. Thanks to Yohann Poprawski and Mark Rowan for great discussions on Bakio and Steve Vincent and Chris Van Baak for discussions in Azerbaijan. Cheers to the GeoTwitter community for providing so much joy and support. It's been fun bumbling through the highs and lows of academia with two of my oldest Geology friends, Billy Andrews and Samantha Bell- we've come a long way since Geofformation. Thanks to Yvonne, Anna, Kirsty Wright, Rachelle Kernan and Gillian Apps for being supportive research friends/colleagues/fan girls and to Clara Rodriguez for being my Geo Mumma and fellow salt queen.

As an advocate for work life balance, my pals outside of the research group/life have kept me grounded, sane and reminded me there is a life outside of the PhD. Special thanks to my nearest and dearest: Harry Bramhall, Emily Hawthorne, Chloe Bennet, Elena Hamilton, Eleanor Pritcher, Alex Redford, Lauren Mayhew, Samantha Marshall and Claerwen Snell - you're the family I never had. Buying into the 'Grant Clan' of structural Geologist in oil companies has given me some very

nosey ‘in laws’, thanks Colin and Neil for your genuine interest. I look forward to years of family discussions about stratigraphic traps and fault seals over dinner and glorious wine.

Rachel Scully, my wonderful mentor, thanks for helping me to prioritise and always being positive. Thank you to Becky Parry, Sophie Hollands, Amy Stutz, Guy Garson, Lauren Mallia, Dayna Evans and Adam Turner for being great housemates over the years in Manchester. Thanks to Cloud Aerial Arts (especially Zoey Gritto) and Manchester Aquatics Centre (especially Heather Sherwood and Katie Bexley) for keeping my positive endorphins flowing. Setting up Phoenix support group has been the proudest achievement of my life to date, that not even a Geology paper could trump, I thank every one of our members for making me feel supported and strong despite all of the difficulties. *We survived because the fire within us, burnt brighter than the fire around us.*

I’m incredibly grateful to have had motivation to finish my PhD in the form of a job offer, with my dream company. Thank you to ex Manchester Basins student Chris Leppard for seeing something in me a looong time ago, which ultimately financially allowed me to do an MSc, which led to the PhD. Thanks to Cath Allsop, Ophélie Phillet, Hannah Jones and Anna Belan for acting as role models, disguised as friends, and to Tony Doré for initially teaching me to question the literature. I’m so grateful to Equinor for seeing something in me once again, during these crazy times. The motivation to help solve tomorrow’s energy challenges, alongside so many inspirational, incredible, caring colleagues has dragged me over the finish line. I’ve been lucky enough to get to know many of them already over the last year whilst writing up in northern Norway. Becca McCann, Alicia Murphy, Floriane Mortier Ivy Becker, Emily Crowder, Izzy Edmundson, and Alana Kent I really appreciate being involved in your girl gang during the dark days (literally and metaphorically). Thanks also to Alex Rowland, Tobias Müller, Ricardo Fasolo, Fabian Tilhams, Andrew Robinson, Inge Stømsøyen, Cyrus Gillet and Audun Brandsæter for all the fun trips, times and chats. Special thanks to Cauê Hess for being unbelievable. I look forward to lots of future adventures in the Arctic Circle with this wonderful team.

Finally, and most importantly to my better half, biggest fan, future colleague and future husband, Ross Grant. Thank you from the bottom of my heart for being there through every single ‘I want to quit this PhD, I’m a failure, It’s too hard’ and every ‘I won an international award I’m a superstar’, and all of the chaos in between. Watching you complete your PhD, and start your career with such enthusiasm and excellence has inspired me, more than I’ll ever let on. You were always there when things got tough, providing me an all-important escape, Adobe Tech Support, ears for ranting to and happiness. Sharing a desk with you was hard, keeping up with you in the gym harder and trying to produce figures half as good as your near on impossible. I know I’ve been an absolute nightmare at times, but we managed and it is an absolute pleasure to have you by my side, quite frankly you deserve another PhD in ‘crazy zobes studies’. Thanks for setting the pace, and letting me keep up, and sometimes even sprint past. I can’t wait for all our future adventures (and that hot tub you promised....).

## Chapter 1: Rationale

The interaction of sediment gravity flows with seafloor topography (such as salt-cored structures) strongly influences the evolution of the individual flows, and hence the development of the entire sedimentary system that they build. These sedimentary bodies may act as reservoirs for hydrocarbons, or potential sites for carbon sequestration, and additionally, their post-depositional remobilisation can present a geohazard in terms of seafloor infrastructure (Hodgson et al. 1992; Jackson and Hudec 2017; Maia da Costa et al. 2018; Roelofse et al. 2019; Pichel and Jackson 2020). Correspondingly, understanding the way that sediment gravity flows interact with topography can be of considerable commercial importance. The evolution of such flows, and ultimately systems, in settings affected by topography is hypothesised to significantly differ from those deposited in settings absent in topography (Kneller et al. 1991; McCaffrey and Kneller 2001; Sinclair and Tomasso 2002; Amy et al. 2004; Hodgson and Haughton 2004; Cullen et al. 2019; Soutter et al. 2019; Cumberpatch et al. 2021a; b). Stratigraphy deposited in basins with active, quickly-growing topography (e.g., salt diapirs) is also speculated to differ from that deposited adjacent to static or slowly-moving topography (such as mass transport deposits (e.g., Ortiz-Karpp et al. 2015; 2015) or slowly deforming fold and thrust belts (e.g., Hodgson and Haughton 2004; Kane et al. 2010; Bakke et al. 2013; Soutter et al. 2019)). Much of our understanding of deep-water depositional processes, stacking patterns and system evolution is derived from settings without significant topography, or those influenced by static topography, and therefore may be redundant, or require alteration to be fit for purpose in salt-influenced deep-water settings (e.g., Mayall et al. 2006; 2010; Oluboyo et al. 2014; Doughty-Jones et al. 2017; 2019; Soutter et al. 2019; Cumberpatch et al. 2021b). For consistency in this thesis and associated manuscripts, sedimentary systems, below storm wave base that have been affected by active salt growth are termed ‘halokinetically-influenced deep-water systems’.

### **1.1 What are halokinetically-influenced deep-water systems and why are they important?**

Deformation by salt-tectonics influences over 120 sedimentary basins globally (e.g., Hudec and Jackson 2007). These basins include some of the world’s largest subsurface energy-producing provinces, such as the Gulf of Mexico (e.g., Booth et al. 2003; Hudec et al. 2013), the North Sea (e.g., Mannie et al. 2014; Charles and Ryzhikov 2015; Stricker et al. 2018), offshore Angola (e.g., Oluboyo et al. 2014; Doughty-Jones et al. 2017; Howlett et al. 2020), offshore Brazil (e.g., Rodriguez et al., 2018; 2020; Pichel et al., 2019), and the Precaspian Basin (e.g. Duffy et al., 2017; Pichel and Jackson 2020). Subsurface studies have shown that salt structures deforming the seafloor can exert substantial control on the location, pathway, and architecture of lobe, channel-fill, levee, and mass-transport deposits (e.g., Mayall et al. 2006, 2010; Jones et al. 2012; Wu et al. 2020; Howlett et al. 2020), with evidence for sediment gravity flows being ponded, diverted, deflected, and confined by salt structures (Jones et al. 2012; Oluboyo et al. 2014; Howlett et al. 2020; Cumberpatch et al. 2021b). However, questions remain regarding: the temporal and lateral extent of such salt-influence; the variability of deep-water facies and architectures around salt structures; how halokinetically-influenced deep-water settings can be identified across multiple scales in different types of data; and what ultimately controls the amount, type and extent of influence that a salt structure has on a deep-water depositional system.

In order to address these questions, and others, there is a need to better understand the interactions of sedimentary processes interacting with topographic relief associated with salt tectonics, to provide insight into sediment routing patterns around topography (e.g., Giles and Lawton 2002; Rowan et al. 2003; Ribes et al. 2015; Pichel and Jackson 2020; Cumberpatch et al. 2021b). As a consequence, this can improve predictions of reservoir distribution and trap geometry and style for carbon storage (e.g., Maia da Costa et al. 2018; Roelofse et al. 2019), geothermal energy (e.g., Harms

2015; Daniilidis and Herber 2017; Andrews et al. 2020), and hydrocarbons (e.g., Hodgson et al. 1992; Jackson and Hudec 2017; Pichel and Jackson 2020).

The sedimentology and stratigraphic architecture of deep-water systems deposited in unconfined basins (e.g., Johnson et al. 2001; Baas 2004; Hodgson 2009; Pr elat et al. 2009; Hodgson et al. 2011; Spychala et al. 2017), or in basins with static or relatively static topography (e.g., Kneller et al. 1991; McCaffrey and Kneller 2001; Sinclair and Tomasso 2002; Amy et al. 2004; Soutter et al. 2019), are reasonably well-established compared to those in basins influenced by active topography (e.g., Hodgson and Haughton 2004; Cullen et al. 2019; Cumberpatch et al. 2021a;b). Due to the breadth and depth of research in unconfined deep-water settings, numerous concepts, models and phenomenon are proposed which are often taken to be directly analogous for deep-water systems influenced by salt tectonics (Pratson and Ryan 1994; Booth et al. 2003; Madof et al. 2009). For example, reservoir models for the Gulf of Mexico (a salt-influenced setting e.g., Jackson and Hudec 2017), often use deep-water facies and architectures derived from the Karoo Basin, South Africa (a well-studied exposed, unconfined deep-water setting e.g., Hodgson 2009; Pr elat et al. 2009; Spychala et al. 2017). However, facies and architecture are likely to be more variable over the same length scale when influenced by salt topography, systems are likely to experience more tectonic deformation; depositional elements will exploit topographic lows created by salt-growth, vary spatially and temporarily, and be influenced by a mixture of allogenic, autogenic and halokinetic controls (Cumberpatch et al. 2021 b;c;d). Therefore, the preconception that understanding from unconfined settings can be directly applied to confined settings is an oversimplification, that will not capture the stratigraphic complexity, variability and modulation caused by salt growth, from the flow to the sedimentary environment scale.

On the other hand, halokinetically-influenced stratigraphy is well documented in outcrop and sub-surface studies (Giles and Lawton 2002; Rowan et al. 2003; Madof et al. 2009; Giles and Rowan 2012; Rowan and Giles 2021), for different depositional environments (Giles and Lawton 2002; Banham and Mountney 2013a; b; 2014; Poprawski et al. 2014; 2016; Ribes et al. 2015; 2017; Counts and Amos 2016; Counts et al. 2019; Cumberpatch et al. 2021b). Successions of genetically related growth strata influenced by near-surface diapiric or extrusive salt form unconformity-bounded packages of thinned and folded strata termed ‘halokinetic sequences’, which become composite when stacked (Giles and Rowan 2012; Rowan and Giles 2021). The geometry and stacking of composite sequences are dependent on the interplay between sediment accumulation rate and diapir rise rate. Giles and Rowan (2012) recognize two end-member stacking patterns; tapered (stacked wedge) and tabular (stacked hook). The scale of these sequences (<1500 m) suggests they typically modify and complicate stratigraphic traps adjacent to salt structures (Rowan and Giles 2021). These generic stratigraphic models are not representative of any particular sedimentary environment, and thus show the amount of upturn and pinch-out of stratigraphy that may be expected regardless of specific depositional environment controls. Detailed depositional facies models can be developed using these conceptual stratigraphic models by integrating subsurface (e.g., Madof et al. 2009; Rodriguez et al. 2020) and outcrop datasets (e.g., Banham and Mountney 2013a; b; 2014; Cumberpatch et al. 2021b) providing a useful framework to be more predictive about the distributions of depositional elements that can be applied to salt-influenced basins globally. Such combined stratigraphic-depositional element models exist for shallow- (Giles and Lawton 2002; Giles and Rowan 2012), and non- marine (Banham and Mountney 2013a; b; 2014; Ribes et al. 2015; 2017) siliciclastic and carbonate environments (Poprawski et al. 2014; 2016). However, prior to this study, such information was limited for deep-water siliciclastic settings due to the rarity of outcropping halokinetically-influenced deep-water stratigraphy (Cumberpatch et al. 2021b). This often resulted in generic halokinetic sequence models, being used in combination with facies distributions from different environments (which differ in depositional processes and evolution to deep-water environments), or from unconfined deep-water environments (which do not take into



account lateral facies variability approaching salt diapirs) (Cumberpatch et al. 2021b;c;d). Therefore, the preconception that understanding of one halokinetically-influenced environment can be directly applied to all others is an underestimate of the complexity of salt-basins, that does not capture: the different depositional flow processes acting in deep-water settings; the different architectures and stacking patterns associated with deep-water environments, the lack of sub-aerial exposure of salt structures and the prolonged periods of quiescence (suspension fall out) between gravity flow deposition in deep-water settings (Giles and Rowan 2012; Rowan and Giles 2021; Roca et al. 2021; Cumberpatch et al. 2021b).

In short, there is a necessity to understand halokinetically-influenced deep-water systems, across multiple-scales and techniques, rather than representing them using a combination of the unfocussed models and understanding described above. This will help to reduce uncertainty associated with salt-influenced deep-water settings, in order to accurately capture complexity when visualising subsurface energy prospects.

## **1.2 How does an integrated approach help to understand halokinetically-influenced deep-water systems?**

Constraining the dynamic evolution of the depositional systems around salt topography through time and space is challenging, especially using just one method. Despite advances in the quantity and quality of 3D seismic reflection data, the salt-sediment interface remains difficult to image due to ray path distortion at the salt-sediment interface, poor velocity control, steep to overturned bedding and near-diapir deformation associated with salt rise (Jones and Davison 2014). Resolution issues caused by variable lithological distributions, both within the salt and its overburden further complicate seismic reflection-based, subsurface analysis (Davison et al. 2000; Jones and Davison 2014). This leads to difficulties deciphering salt from stratigraphy in reflection data and various attributes, and leads to uncertainty in prediction of facies and thicknesses via seismic methods (e.g., Berton and Vesely 2016; Hossain 2019). Therefore, halokinetically-influenced depositional systems (or portions of such systems) benefit from calibration with outcrop analogues (e.g., Lerche and Petersen 1995; Jackson and Hudec 2017).

Exposed examples are often limited in the rock record, largely due to dissolution of halite forming the core of the salt (Jackson and Hudec 2017). Often, halokinetically-influenced stratigraphy has been subject to subsequent erosion, inversion and uplift, making it difficult to decipher if stratigraphic deformation is salt-related or a later overprint (e.g., Soto et al. 2017). Outcropping examples are often incomplete, without full source-to-sink coverage, making interpreting interplaying controls difficult, and outcrops often do not have adequate three-dimensional coverage, making correlations difficult and extrapolations required. Deep-water facies often vary as they approach salt structures, and therefore the very nature of these deposits (i.e., not consistent lithofacies for numerous kilometres) makes it difficult to correlate with confidence in the absence of a detailed biostratigraphic framework (Agirrezabala and López-Horgue 2017). Many outcrop examples are small in size compared to subsurface basins and therefore provide only small-scale details of, for example, sedimentary structures and stratal stacking patterns, rather than the larger, basin-scale tectonostratigraphic context of salt-sediment interactions provided by integrated subsurface datasets.

While valuable, each subsurface or outcrop example represents a unique record of the ratio of salt rise and sedimentation rate, and therefore concepts created using just one example are not directly transferable to all settings. Also, subsurface and outcrop examples provide only one 'snapshot' in time of a complicated evolution controlled by a dynamic interplay of parameters (sedimentation rate, salt supply etc.). Models enable multiple scenarios to be tested, and end members to be created, providing the ability to isolate and study one specific controlling variable to understand its

influence on system evolution, which is impossible in nature. However, all models are based on lots of assumptions, most notably regarding scaling (Davison et al. 1993; Dooley et al. 2013; 2015; 2020; Ferrer et al. 2017; Soutter et al. 2021), and are simplified (often two-dimensional) compared to natural examples (Finch et al. 2003; 2004; Gaullier and Vendeville 2005; Dooley and Hudec 2017; Pichel et al. 2017; 2019; Cumberpatch et al. 2021b). Physical models have an advantage in recreating the evolution of specific subsurface analogues (Dooley et al. 2013; 2015; 2020; Dooley and Hudec, 2017; Ferrer et al. 2017; Roma et al. 2018) and studying sedimentary gravity-currents flow distribution and evolution adjacent to salt topography (Gaullier and Vendeville, 2005; Sellier and Vendeville, 2009; Soutter et al. 2021). Numerical models make it possible to quickly and inexpensively isolate and investigate the influence of a specific variable. Finite Element Models (FEM) are advantageous for studying ductile deformation and salt flow dynamics (Albertz and Ings 2012), conditions required for initiation and development of diapirism (Poliakov et al. 1993; Gemmer et al., 2004; 2005; Chemia et al. 2008; Fuchs et al. 2011; Fernandez and Kaus 2015; Nikolinakou et al. 2017; Hamilton-Wright et al. 2019; Peel et al. 2020) and salt-related stress and strain analysis (Luo et al. 2012; 2017; Nikolinakou et al. 2012; 2014a; b; 2018; Heidari et al. 2017). Discrete Element Models (DEM) replicate spontaneous, realistic, localised fault nucleation and growth (Finch et al. 2003; 2004; Imber et al. 2004; Hardy and Finch 2005; 2006; Abe and Urai 2012; Katz et al. 2014; Pichel et al. 2017; 2019; Cumberpatch et al. 2021b) and are therefore appropriate for studying regional-scale compressional salt tectonics (Pichel et al. 2017), the effects of base salt relief on salt flow and overburden deformation styles (Pichel et al. 2019), and the interactions between salt-related topography, sedimentation and stratigraphic evolution (Cumberpatch et al. 2021c;d).

Overall, it is imperative to integrate multiple data types and scales of observations, interpretations and understanding in order to get the most complete picture of the processes operating in deep-water halokinetically-influenced settings. Subsurface data commonly enhances understanding of: mega-sequence scale salt-stratigraphy relationships; minibasin evolution; variation in relative sedimentation rate versus diapir rise rate through halokinetic sequence analysis; source-to-sink relationships enabling inferences about local and regional controls; stratigraphic architecture and termination analysis; and lateral and temporal variability in three-dimensions (incorporating well, seismic and core data). Outcrop analysis typically allows better comprehension of small-scale details, such as: bed-scale flow processes and facies variability; sedimentary structures providing evidence for reflection and deflection of flows; interaction of halokinetically-derived and alloctonically-derived depositional elements; stacking patterns; geometrical configurations of stratal terminations; thickness variations and reservoir quality deterioration. This often provides two-dimensional stratal panels, below the scale of seismic-resolution, which may act as lateral analogues to one-dimensional core data; and aid prediction of physical properties of subsurface. Numerical and physical models enable halokinetic-stratigraphic relationships to be studied through time, and provide the unique opportunity to isolate and test a number of controls (e.g., sedimentation rate, diapir geometry, salt density) in order to generate end members quickly. This thesis integrates subsurface, field and numerical modelling data to better comprehend the processes operating, controlling and influencing the evolution of deep-water halokinetically-influenced environments across multiple scales.

### **1.3 Thesis aims**

The fundamental aim of this thesis is to decipher halokinetic (salt) from allocyclic (external) and autocyclic (internal) controls in deep-water systems. Put simply, this thesis aims to investigate how and why salt-influenced deep-water systems differ from those where no salt topography is present.

More specifically this thesis aims to:

- Understand how sediment gravity flows and their subsequent deposits are distributed around active topography

- Investigate how halokinesis can modulate stratigraphy and mask allocyclic signals
- Explain how sedimentation rates and variable confinement impact halokinetic modulation.

Furthermore, this work will document an exposed example of a halokinetically-influenced deep-water system to complement the global atlases of other halokinetically-influenced environments, and deep-water settings influenced by static, relatively static or absent in, topography. This will be a useful analogue for subsurface energy exploration and production in salt basins globally.

#### 1.4 Thesis objectives

In order to achieve the above, this thesis has the following objectives:

- 1) **Document deep-water facies and architecture variability around salt structures** across different scales and data types, with different amounts of salt-induced confinement, recording the development of a coeval deep-water axial and debrite rich lateral depositional system and characterising distribution in terms of halokinetically or allocyclically controlled.
- 2) **Analyse lateral and temporal variations in halokinetic modulation of stratigraphic architectures** in response to different sedimentation rates and amount of diapiric confinement, quantify near-diapir thinning rates and pinch-out geometries, compare modelled results to subsurface and field analogues to test their validity.
- 3) **Distinguish criteria for the recognition of halokinetically-influenced deep-water systems** across different scales and datasets, for comparison to other salt influenced environments and basins effected by different types of, or no topography, in order to better predict reservoir properties in subsurface energy exploration.

#### 1.5 Thesis outline

This thesis has been prepared in journal format in accordance with the standards set forth by The University of Manchester. This thesis consists of seven chapters and associated appendix material. Chapters 3, 4, and 5 have been written in a format suitable for publication in a peer-reviewed journal.

**Chapter 2:** An overview of existing literature on halokinetically-influenced deep-water systems is presented within the context of how deep-water sediment gravity flows, and their associated depositional products are influenced by salt related topography. The different approaches to studying salt-sediment interactions are outlined, and a number of case studies are used to highlight these different approaches, current understanding and industrial application. This serves as a foundation for the research presented in Chapters 3, 4 and 5.

**Chapter 3:** Interactions between deep-water gravity flows and active salt tectonics: an exposed example from the Bakio Diapir, Basque-Cantabrian Basin, Northern Spain

**Status:** Published in Journal of Sedimentary Research

*Cumberpatch, Z.A., Kane, I.A., Soutter, E.L., Hodgson, D.M., Jackson, C. A-L., Kilhams, B.A., and Poprawski, Y., 2021, Interactions of deep-water gravity flows and active salt tectonics, Journal of Sedimentary Research, v. 91, p. 34-65.*

**Author contributions:** Zoë Cumberpatch (Lead Author, data collection, processing, and analysis, writing manuscript and preparing figures), Ian Kane (field assistance, supervision, discussion, manuscript editing), Euan Soutter (field assistance, discussion, manuscript editing), David Hodgson (supervision, discussion, manuscript editing), Christopher Jackson (supervision, discussion, manuscript editing), Ben Kilhams (supervision, discussion, manuscript editing), Yohan Poprawski (discussion, manuscript editing).

**Summary:** This study uses a rare exposed example of halokinetically-influenced deep-water stratigraphy to: 1) document lateral and vertical changes in deep-water facies and architecture with variable amounts of salt-induced confinement; 2) document the evolution of coeval deep-water

axial and debrite-rich lateral depositional systems; and 3) distinguish criteria for the recognition of halokinetically-influenced deep-water systems.

**Highlights:**

- Stratigraphic variability and juxtaposition of architectural elements in the studied basins is high and controlled by the interplay of halokinetic, autocyclic, and allocyclic processes.
- Confinement against topography increases the effects of allocyclic progradation.
- Indicators of active topography include: hybrid beds; remobilised strata; lateral thickness changes over short distances; reversal in ripple cross-lamination in beds; and intercalation of debrites throughout the stratigraphy. These indicators individually are not diagnostic of salt-influenced topography, but collectively they provide a set of features that support interpretation of halokinetic modulation of a deep-water setting.
- Following the cessation of diapir growth, topography does not heal instantly, and the “passive” paleotopography continues to confine subsequent depositional systems despite diapir inactivity.
- Closely related depositional systems can be highly variable depending on their complete or partial confinement. Stacked, amalgamated sandstones are observed between two confining barriers, whereas more variable architectures are observed where only partial confinement is present. These observations are due to the modulation of a broadly progradational system by halokinetically-influenced lateral barriers and the coeval development of axial allocyclic and lateral debrite-rich depositional systems.

**Chapter 4:** External signal preservation in halokinetic stratigraphy: A discrete element modelling approach

**Status:** Part published in *Geology* and part published with *Basin Research*

*Cumberpatch, Z.A., Finch, E., and Kane, I. A., 2021, External signal preservation in halokinetic stratigraphy: A discrete element modelling approach: Geology, v. 49 (6), p.687-692. (Appendix A)*

*Cumberpatch, Z. A., Finch, E., Kane, I.A., Pichel, L.M., Jackson, C.A-L., Kilhams, B.A., Hodgson, D.M., and Huuse, M., accepted, Halokinetic modulation of sedimentary thickness and architecture: a numerical modelling approach: Basin Research, accepted, in press, available online (Appendix B).*

**Author contributions:** Zoë Cumberpatch (Lead Author, data collection, processing, and analysis, writing manuscript and preparing figures), Emma Finch (model design, discussion, supervision, manuscript review), Ian Kane (discussion, supervision, manuscript review), Leonardo Pichel (discussion, manuscript review), Christopher Jackson (discussion, supervision, manuscript review), Ben Kilhams (discussion, supervision, manuscript review), David Hodgson (discussion, supervision, manuscript review), Mads Huuse (discussion, manuscript review).

**Summary:** A discrete element model (DEM) is used to understand how sedimentation rate effects stratal geometries in salt basins experiencing diapirism, and to test the hypothesis that halokinesis can modulate stratigraphy and mask allocyclic signals. The study aims to: 1) identify and quantify thickness variations and pinch-out geometries in a salt-influenced depositional system; 2) investigate how halokinetic modulation of stratigraphic architectures changes with variable syn-kinematic sedimentation rates adjacent to a dynamic salt diapir; and 3) compare the results to subsurface and field analogues to test the validity of our model predictions.

**Highlights:**

- Laterally, we observe a zone of ~1150 m to either side of the diapir that is influenced by halokinesis, and beyond this zone, strata are undeformed.
- The models generate realistic salt-related faults. In all models, structural deformation and extent of halokinetic influence are similar, and syn-kinematic strata, at least initially, are isolated to either side of the diapir, thinning and onlapping towards the high.
- In all models, thinning is about six times greater between the salt flank and crest, compared to the undeformed section and the salt flank, indicating more intense deformation close to the diapir.

- Thinning rate decreases through time (up stratigraphy), showing a reduction of halokinetic modulation with increased sediment thickness, as halokinetic bathymetry is ‘healed’.
- While the overall modulation style close to the diapir is stratigraphic thinning, stratigraphic thickening is observed in the salt-withdrawal basins.

**Chapter 5:** How confined is confined? An investigation into the effect of diapir-induced topographic spacing on Paleocene deep-water sediment dispersal in the Eastern Central Graben, UK

**Status:** In preparation for submission to Petroleum Geoscience

*Cumberpatch, Z.A., Kilhams, B.A., Kane, I.A., Finch, E., Jackson, C., A-L., Hodgson, D.M., Huuse, M., and Grant, R.J., in preparation, How confined is confined? An investigation into the effect of diapir-induced topographic spacing on deep-water sediment dispersal: in preparation for submission to Petroleum Geoscience.*

**Author contributions:** Zoë Cumberpatch (Lead Author, data collection, processing, and analysis, writing manuscript and preparing figures), Ben Kilhams (supervision, discussion, manuscript review), Ian Kane (supervision, discussion, manuscript review), Emma Finch (model design, supervision, discussion, manuscript review), Christopher Jackson (supervision, discussion, manuscript review), David Hodgson (supervision, discussion, manuscript review), Mads Huuse (discussion, manuscript review), Ross Grant (discussion, manuscript review).

**Summary:** This study uses a wealth of subsurface data and understanding from the well-studied salt-influenced Paleocene basin floor system in the Eastern Central Graben of the UK North Sea, to study deep-water facies and architecture distribution around diapirs, and the effects of lateral spacing of salt diapirs on halokinetic modulation. This study compares modification of deep-water stratigraphy between subsurface spaced diapirs to the results of a simple two-dimensional discrete element model (DEM) with variably spaced diapirs, aiming to: 1) Analyse salt-influenced deep-water facies and characterise their distribution in terms of halokinetic or allocyclically controlled; 2) compare stratigraphic architectures between variably spaced salt structures; and 3) describe the extent of halokinetically modified stratigraphy between different distances of confinement.

**Highlights:**

- Facies analysis in the Paleocene of the Eastern Central Graben, UK North Sea, reveals that channels and lobes are influenced (re-routed and confined) by salt growth on a number of different scales (from centimetre-scale sedimentological character in core, to kilometre-scale geomorphological attributes in seismic).
- Stratigraphic thickness variations are common regardless of diapir spacing; thickening is observed in subsurface and models in the salt withdrawal basin, with thickening being most common above areas of autochthonous thinned salt.
- In closely spaced diapirs (<3km) a synclinal shaped minibasin develops with steeply rotated flanks, reflecting diapir growth. In more widely spaced diapirs (>4km) there is a zone between the diapirs where stratigraphy is relatively flat, forming a broad plateau.
- Between closely spaced diapirs (<3 km) the zone of halokinetic influence of one diapir is laterally connected to the halokinetic influence of another diapir, such that the zone between the diapirs is influenced by both structures. When diapirs are more than 4 km apart there is a zone of minimal deformation that develops between the diapirs.
- Due to the complexity of salt basins, and therefore the presence and variability in the early diapiric stratigraphy and salt-related faults, even these ‘minimal modulation’ zones are unlikely to contain stratigraphy which is completely undeformed. Subsurface energy prospects are likely to be influenced by subtle salt-related topography even far away from diapirs.

**Chapter 6:** A synthesis of the results, discussions, conclusions and applications of the previous chapters is presented within the contexts of the three broad research aims outlined in Chapter 1. An outlook on future work is presented.

**Chapter 7:** The key conclusions, learnings and recommendations arising from this thesis are summarised.

**Appendix A:** Manuscript associated with **Chapter 4**

Cumberpatch, Z.A., Finch, E., and Kane, I. A., 2021, *External signal preservation in halokinetic stratigraphy: A discrete element modelling approach: Geology*, v. 49 (6), p.687-692.

**Appendix B:** Manuscript associated with **Chapter 4**

Cumberpatch, Z. A., Finch, E., Kane, I.A., Pichel, L.M., Jackson, C.A-L., Kilhams, B.A., Hodgson, D.M., and Huuse, M., accepted, *Halokinetic modulation of sedimentary thickness and architecture: a numerical modelling approach: Basin Research*, accepted, in press, available online.

**Appendix C:** Supplementary manuscript used in **Chapter 6**

Cumberpatch, Z.A., Soutter, E.L., Kane, I.A., Casson, M., and Vincent, S.J., 2020, *Evolution of a mixed siliciclastic-carbonate deep-marine system on an unstable margin: the Cretaceous of the Eastern Greater Caucasus, Azerbaijan. Basin Research*, v. 33 (1), p. 612-647.

**Author contributions:** Zoë Cumberpatch (Lead Author, data collection, processing, and analysis, writing manuscript and preparing figures), Euan Soutter (data collecting, processing and analysis, writing manuscript and preparing figures), Ian Kane (supervision, discussion, manuscript review), Max Casson (discussion, manuscript review), Steve Vincent (discussion, manuscript review).

**Summary:** This study addresses how exportable depositional models (documenting sub-seismic scale facies variability, stacking patterns and hierarchies) developed in deep-water siliciclastic environments are to mixed deep-water carbonate-siliciclastic systems. The study aims to: 1) document characteristics of mixed lobes; 2) discuss processes that govern their deposition; 3) compare mixed lobes with their siliciclastic counterparts; 4) describe the sedimentological evolution of the Eastern Greater Caucasus throughout the Cretaceous; and 5) provide insights into depocentres characterised by unstable margins.

**Highlights:**

- For the first time a mixed siliciclastic-carbonate deep-water system is documented in the Eastern Greater Caucasus of Azerbaijan.
- A siliciclastic submarine channel complex abruptly transitions into an overlying mixed siliciclastic-carbonate lobe succession.
- Deep-marine depositional systems were affected by submarine landslide topography during deposition.
- Interaction between the two contemporaneous systems makes typical lobe stacking patterns difficult to decipher.
- The evolution of a mixed siliciclastic-carbonate deep-marine system offshore The Gambia, NW Africa is suggested as an offshore analogue.

**Appendix D:** Supplementary manuscript used in **Chapter 6**

Soutter, E.L., Bell, D. Cumberpatch, Z.A., Ferguson, R.A., Kane, I.A., Spychala, Y.T., and Eggenhuisen, J. 2021, *The Influence of Confining Topography Orientation on Experimental Turbidity Currents and Geological Implications: Frontiers in Earth Science*, v. 8.

**Author contributions:** Euan Soutter (Lead Author, data collection, processing, and analysis, writing manuscript and preparing figures), Daniel Bell (data collection, processing, and analysis, discussion, manuscript review), Zoë Cumberpatch (data collection, processing, and analysis, discussion, manuscript review), Ross Ferguson (data collection, discussion, manuscript review), Ian Kane (supervision, data collection, discussion, manuscript review), Yvonne Spychala (supervision, data collection, discussion, manuscript review), Joris Eggenhuisen (discussion, manuscript review).

**Summary:** This study documents scaled physical models of turbidity currents interacting with basin-floor topography and has three main aims: 1) to assess the effect of confining topography orientation (0, 45, and 90°) on turbidity currents and their deposits; 2) to explore the effect of topography on flow criticality and associated depositional features; and 3) to use these findings to aid in the stratigraphic interpretation of deep-water basins.

**Highlights:**

- Unconfined turbidity currents are able to spread radially over the slope, forming a lobate deposit that thickens, then thins distally.
- Laterally confined turbidity currents are prevented from spreading on one side, forming an asymmetric deposit. Down-dip thinning rates are also reduced in a laterally confined setting, allowing flows to deposit farther into the basin.
- Oblique confinement resulted in an upstream deflected deposit and a downstream deposit, which has implications for deposit correlation in deep-water outcrop and subsurface datasets.
- Frontal confinement caused lateral spreading, with inferred trapping of coarse grains higher on the slope, compared to unconfined deposits.
- Two styles of topographically-forced hydraulic jump are inferred from these experiments. Upstream jumps are formed when flows rapidly decelerate upstream of slope topography, resulting in the deposition of thick sandstones up-dip of topography. Downstream jumps are formed downstream of topography and are caused by rapid deceleration of flows at the foot of the barrier, with slope erosion occurring at the foot of the barrier as the flow impacts the slope.

## 1.6 List of publications

### *Manuscripts that form the basis of this thesis*

**Cumberpatch, Z.A.**, Kane, I.A., Soutter, E.L., Hodgson, D.M., Jackson, C. A-L., Kilhams, B.A., and Poprawski, Y., 2021, Interactions of deep-water gravity flows and active salt tectonics, *Journal of Sedimentary Research*, v. 91, p. 34-65.

**Cumberpatch, Z.A.**, Finch, E., and Kane, I. A., 2021, External signal preservation in halokinetic stratigraphy: A discrete element modelling approach: *Geology*, v. 49 (6), p.687-692.

**Cumberpatch, Z.A.**, Finch, E., Kane, I.A., Pichel, L.M., Jackson, C.A-L., Kilhams, B.A., Hodgson, D.M., and Huuse, M., in press, Halokinetic modulation of sedimentary thickness and architecture: a numerical modelling approach: *Basin Research*, accepted, in press, available online.

**Cumberpatch, Z.A.**, Kilhams, B.A., Kane, I.A., Finch, E., Jackson, C., A-L., Hodgson, D.M., Huuse, M., and Grant, R.J., in preparation, How confined is confined? An investigation into the effect of diapir-induced topographic spacing on paleocene deep-water sediment dispersal: in preparation for submission to *Petroleum Geoscience*.

### *Additional manuscript contributions within deep water sedimentology*

Bell, D., Soutter, E.L., **Cumberpatch, Z.A.**, Ferguson, R.A., Sychala, Y., Kane, I.A., and Eggenhuisen, J., 2021, Flow process controls on grain-type distribution in an experimental turbidity current deposit: Implications for signal-preservation and microplastic distribution in submarine fans: *The Depositional Record*, accepted, available online.

**Cumberpatch, Z.A.**, Soutter, E.L., Kane, I.A., Casson, M., and Vincent, S.J., 2021, Evolution of a mixed siliciclastic-carbonate deep-marine system on an unstable margin: the Cretaceous of the Eastern Greater Caucasus, Azerbaijan. *Basin Research*, v. 33 (1), p. 612-647.

Kane, I. A., Ayckbourn, A., Bell, D., **Cumberpatch, Z.A.**, Ferguson, R., Fuhrmann, A., Martínez-doñate, A., and Soutter, E.L., in preparation, Bed-scale indicators of sediment gravity flow sedimentation against topography. in preparation for submission to *Frontiers in Earth Science*.

Poprawski, Y., Basile, C., **Cumberpatch, Z.**, and Eude, A., 2021, Mass transport deposits in deep-water minibasins: outcropping examples from the minibasins adjacent to the Bakio salt wall (Basque Country), Northern Spain: *Marine and Petroleum Geology*, accepted, in press, available online.

Soutter, E.L., Kane, I.A., Fuhrmann, A., **Cumberpatch, Z.A.**, and Huuse, M. 2019. The Stratigraphic Evolution of Onlap in Clastic Deep-marine Systems: Autogenic Modulation of Allogenic Signals. *Journal of Sedimentary Research*, 89 (10), 890-917.

Soutter, E.L., Bell, D. **Cumberpatch, Z.A.**, Ferguson, R.A., Kane, I.A., Sychala, Y.T., and Eggenhuisen, J. 2021, The Influence of Confining Topography Orientation on Experimental Turbidity Currents and Geological Implications: *Frontiers in Earth Science*, v. 8.

### ***Additional research***

Andrews, B.J., **Cumberpatch, Z.A.**, Shipton, Z.K., and Lord, R. 2020, Collapse processes in abandoned pillar and stall coal mines: Implications for shallow mine geothermal energy: *Geothermics*, v. 88, 101904.

Andrews, B.J., **Cumberpatch, Z.A.**, Shipton, Z.K., and Lord, R., in preparation, Small scale sedimentary heterogeneity controls large scale fracture network geometry: in preparation for submission to *Journal of the Geological Society*.



## Chapter 2: Halokinetically-influenced deep-water sedimentary systems: processes, products, interactions and implications

### 2.1 Introduction

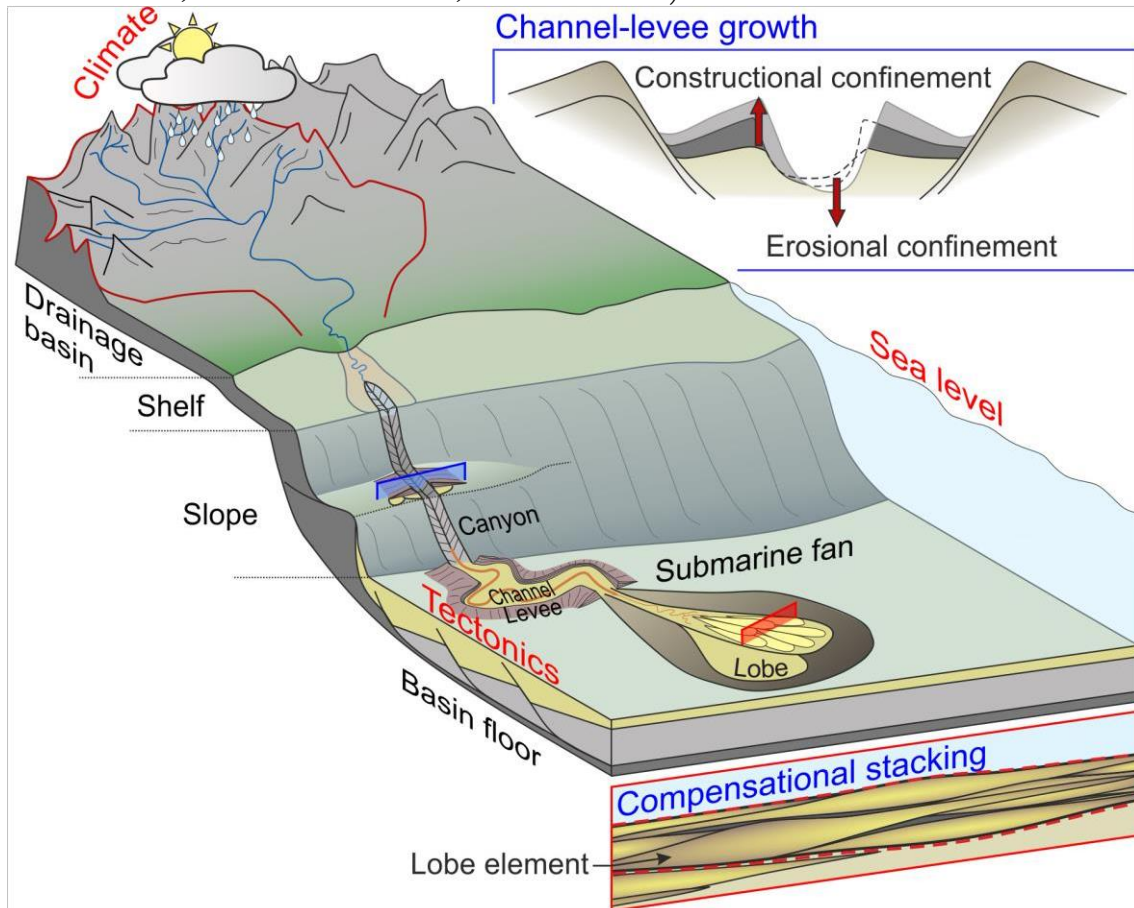
#### *Deep-water depositional systems*

Deep-water sedimentary systems are amongst the most volumetrically and economically significant sedimentary deposits on the Earth, and are often the ultimate sink of sediment and pollutants transported to the ocean. Consequently, they have been well studied for over 70 years and continue to be studied today (e.g., Kuenen and Migliorini 1950; Bouma et al. 1962; Hampton 1972; Mutti 1977; Lowe 1982; Hiscott 1994; Clark and Pickering 1996; Baas and Best 2002; Kneller 2003; Mayall et al. 2006; Kane et al. 2007; Haughton et al. 2009; Prélat et al. 2009; Kane and Hodgson 2011; Kane and Pontén 2012; Bakke et al. 2013; Hodgson et al. 2016; Jobe et al. 2017; Southern et al. 2017; Spychala et al. 2017; Bell et al. 2018 a;b; Soutter et al. 2018; 2019; 2021; Ferguson et al. 2020; Fuhrmann et al. 2020).

Deep-water sedimentary systems, formed predominantly by sediment gravity flows, are typically characterised by canyon- or delta-fed submarine slope channels, which act as sediment conduits for deposition in the deep-marine environment (Burke 1972; Normark 1978; Normark and Piper 1991). Fundamentally, sediment can be sourced for delivery to deep-water environments in one of two ways. Usually, sediment is eroded from the hinterland and transported to continental margins via rivers; this can provide direct sediment supply to the deep ocean when deep-water systems are directly connected to fluvial drainage systems (Blum and Hattier-Womack 2009). Alternatively, littoral drift along coastlines can feed sediment into submarine canyons that are incised through continental shelves to the shoreline (Normark 1970; McArthur and McCaffrey 2019). Both of these mechanisms can result in build-up of sediment, that eventually becomes unstable, on the continental shelf and upper slope. This instability, and commonly an external trigger mechanism (e.g., sea level change (Weaver and Kuipers 1983), earthquakes or storms (Fine et al. 2005; Prior and Coleman 1982) or changes in continental slope physiography (Assier-Rzadkiewicz et al. 2000)) can result in the collapse of the unstable sediment, forming a range of sediment gravity flows (Masson et al. 2006; Clare et al. 2016). The submarine gravity flows that feed these deep-water depositional systems are amongst the largest sediment transport agents on Earth, with individual flows transporting up to an order of magnitude more sediment than the annual global sediment flux of all rivers (Milliman and Syvitski 1992; Talling et al. 2007).

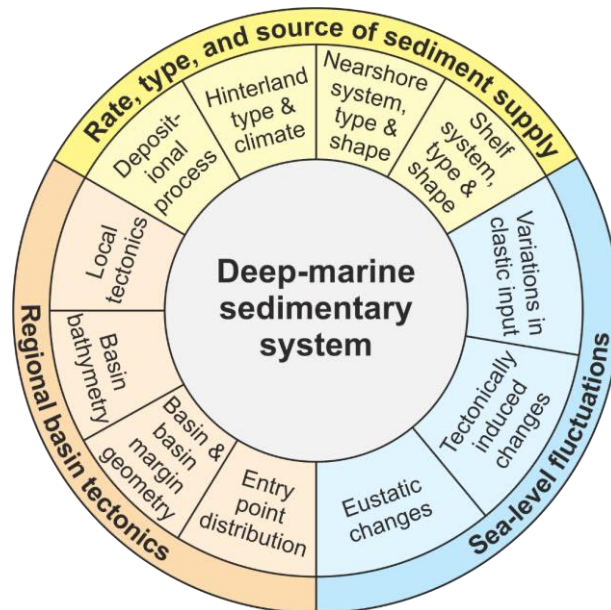
The basinal expression of these conduit-fed sediment gravity flows is a broadly fan-shaped geometry (referred to as ‘submarine fans’), consisting of individual lobe-shaped deposits (Walker 1978; Normark and Piper 1991). From proximal to distal, submarine fan systems generally comprise: a large feeder canyon or channel, which may significantly cut back into the continental slope (Figure 2.1; e.g., Burke 1972; Normark 1978; Walker 1992; Millington and Clark, 1995; Kolla et al., 2001; Prather 2003; Wynn et al. 2007; Jegou et al. 2008; Di Celma et al. 2014); a slope channel-levee system, which may prograde far from the continental slope (Figure 2.1; e.g., Normark 1978; Reading and Richards 1994; Bouma 2001; Posamentier 2003; Mayall et al. 2006; Kane et al. 2007; Jegou et al. 2008; Janocko et al. 2013; Morris et al. 2014; Peakall and Sumner 2015; Hodgson et al. 2016; Ferguson et al. 2020); and lobes at the end of the system (Figure 2.1; Walker, 1966; Mutti and Ricci-Lucchi, 1972; Mutti, 1977; Walker 1978; Reading and Richards, 1994; Johnson et al., 2001; Gervais et al., 2006; Deptuck et al., 2008; Prélat et al., 2009; Grundvåg et al., 2014; Picot et al., 2016; Dodd et al., 2019; Boulesteix et al. 2021; Privat et al. 2021).

Due to their occurrence on the deep seafloor these submarine fans and the sediment gravity flows that form them are difficult to observe directly and therefore knowledge of these deep-water depositional processes is not as advanced as their terrestrial or shallow-water counterparts (Prior et al. 1987; Hughes Clarke 2016). However, understanding the flow processes in deep-water systems and their associated deposits, is important for: the assessment of seafloor geohazards, submarine fibre optic cable placement, the prediction of reservoir quality distribution in the subsurface and prediction of sediment and pollutant dispersal into the deep-oceans (e.g., Pettingill 1998; Heinrich and Piatanesi 2000; McSaveney et al. 2000; Ward 2001; Bondevik et al. 2003; Lien et al. 2006; Hsu et al. 2006; Saller et al. 2008; Kilhams et al. 2012; Hunt et al. 2014; Talling et al. 2014; Woodall et al. 2014; Gwiazda et al. 2015; Marchand et al. 2015; McKie et al. 2015; Hughes Clarke et al. 2016; Dodd et al. 2019; Kane and Clare 2019; Kane et al. 2020).



**Figure 2.1:** Conceptual model of a source-to-sink sedimentary system (Ferguson et al. 2020). Common external and internal controls on submarine fans are highlighted by red and blue text respectively. Cross-section locations are indicated on the model. The typical sub-environments of a submarine fan: feeder channel, levees, and lobes, are labelled. Compensational stacking image modified from Prélat et al. (2009) and source-to-sink cartoon modified from Somme et al. (2009).

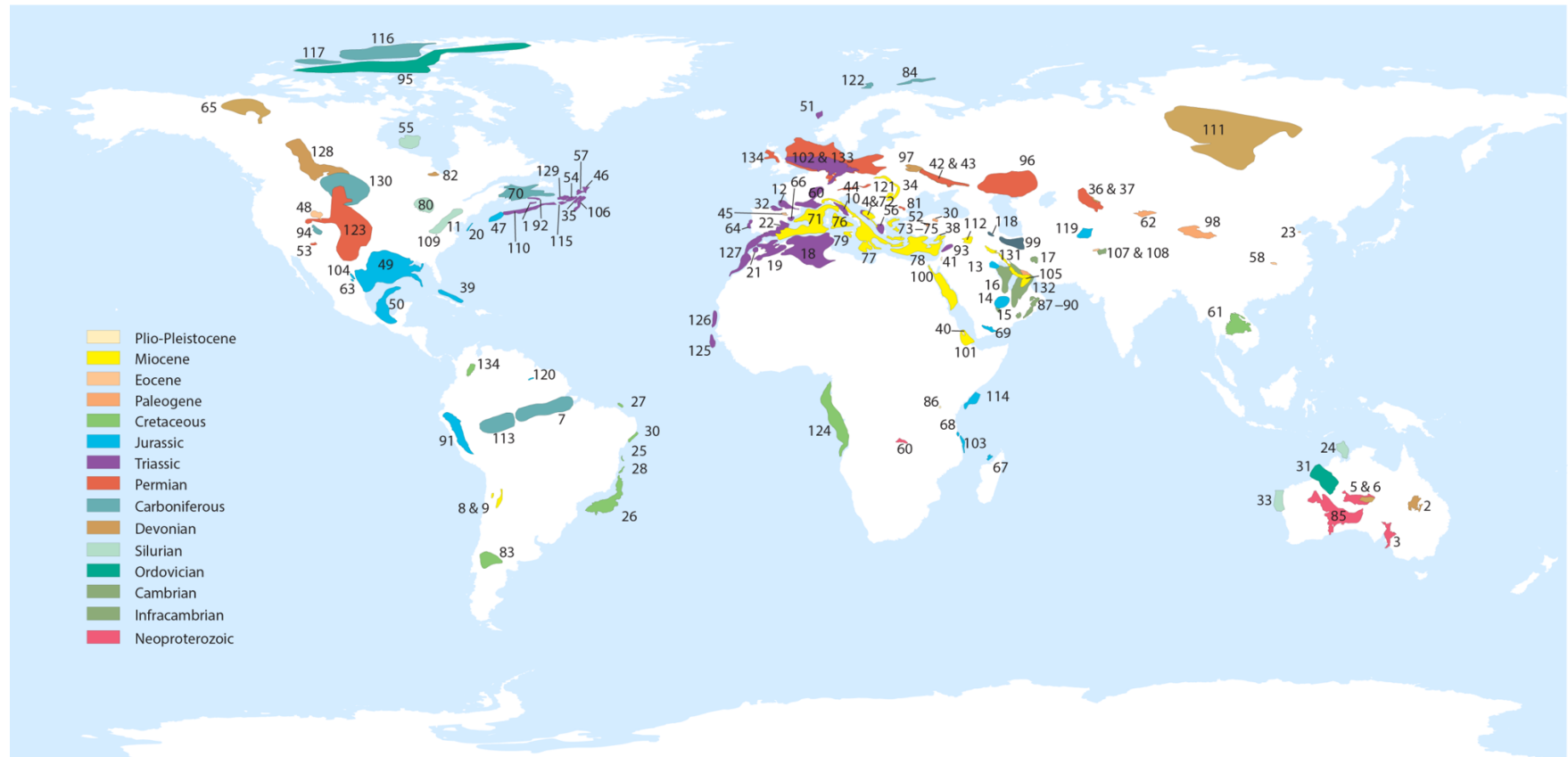
The morphology, evolution and ultimately economic significance of deep-water sedimentary systems is dependent upon several external (allogenic) variables including sea level, climate, tectonics and sediment supply (Figures 2.1 and 2.2; Posamentier et al. 1991; Reading 1991; Baas et al. 2005). The combination of these variables with internal (autogenic) processes such as lobe switching and channel avulsion, results in unique system-specific depositional environments. These systems are further complicated where they are influenced by either static (Kneller et al. 1991; McCaffrey and Kneller 2001; Sinclair and Tomasso 2002; Amy et al. 2004; Soutter et al. 2019; Cumberpatch et al. 2021a) or active (Hodgson and Haughton 2004; Cullen et al. 2019; Muravchik et al. 2020; Howlett et al. 2020; Tilhams et al. 2021; Cumberpatch et al. 2021b;c) topography. This thesis focusses on the interaction of deep-water sedimentary systems with active, salt related topography.



**Figure 2.2:** Main controls on deep-water sedimentary depositional systems (Stow et al. 1996; Baas et al. 2005).

### **Salt basins**

Basins containing appreciable volumes of evaporites display tectonic complexity and the structural styles of deformation and sedimentary facies patterns are fundamentally different from those in basins that lack evaporites (Jackson and Hudec 2017). This difference stems from the over-arching fact that evaporites have mechanical and physical properties different from most siliciclastic and carbonate rocks (Jackson and Hudec 2017). Such basins, often referred to as ‘salt giants’, consist of hundreds to several thousand metres-thick evaporite-dominated successions deposited in isolated sedimentary basins (Figure 2.3). Well-documented examples include: the Jurassic Louann salt in the Gulf of Mexico, (e.g., Bird et al. 2005); the Messinian salt in the Mediterranean sea, (e.g., Cartwright et al. 2012); the Permian Zechstein Supergroup in Europe, (e.g., Hodgson et al. 1992; Stewart and Clark 1999; Davison et al. 2002; Charles and Ryzhikov 2015; Grant et al. 2019 a;b; 2020); the Pennsylvanian Paradox Formation (Trudgill 2011) and the circum-South Atlantic salt basins offshore west Africa and offshore east Brazil (e.g., Jackson et al. 2000; Davison 2007; Oluboyo et al. 2014).

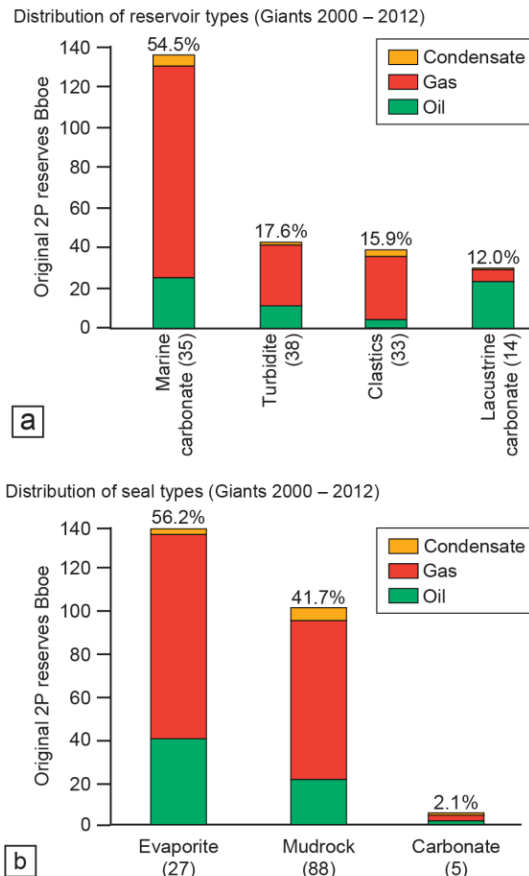


- |  |  |  |                                      |  |                                    |  |  |
|--|--|--|--------------------------------------|--|------------------------------------|--|--|
| 1. Abenaki (N. Scotian)                  | 18. Atlas (Algerian – Tunisian)              | 35. Carson Basin (Grand Banks)               | 52. Haymana-Polatli                  | 69. Ma'Rib-Al Jawf/Shabwah (Hadramaut) | 86. Olduvai depression             | 103. Ruvuma Basin                                  | 119. Tadjik Basin                      |
| 2. Adelaide foldbelt                     | 19. Atlas (Moroccan)                         | 36. Chu-Sarysu (Devonian)                    | 53. Holbrook Basin                   | 70. Maritimes Basin                    | 87. Oman (Fahud Salt Basin)        | 104. Sabinas Basin                                 | 120. Takutu Salt Basin                 |
| 3. Adriatic-Albanian foredeep            | 20. Baltimore Canyon                         | 37. Chu-Sarysu (Permian)                     | 54. Horseshoe Basin (Grand Banks)    | 71. Mediterranean–Western              | 88. Oman (Ghaba Salt Basin)        | 105. Sachun Basin                                  | 121. Transylvanian                     |
| 4. Amadeus Basin                         | 21. Berrechid                                | 38. Cicia-Latakia                            | 55. Hudson Bay                       | 72. Mediterranean–Adriatic             | 89. Oman (Ghudun Salt Basin)       | 106. Salar Basin (Grand Banks)                     | 122. Tromso Basin                      |
| 5. Amadeus Basin (Chandler)              | 22. Betic-Guadalquivir Basin                 | 39. Cuban                                    | 56. Ionian                           | 73. Mediterranean–Andros Basin         | 90. Oman (South Oman Salt Basin)   | 107. Salt Range (Hormuz – Punjab region)           | 123. USA Midcontinent                  |
| 6. Amadeus Basin (Chandler)              | 23. Bohai Basin                              | 40. Danakil                                  | 57. Jeanne d'Arc Basin (Grand Banks) | 74. Mediterranean–Cretean Basin        | 91. Oriente-Ucayali (Pucara) Basin | 108. Salt Range (Kohat Plateau)                    | 124. West Africa (Angola-Gabon)        |
| 7. Amazonas                              | 24. Bonaparte (Petrel)                       | 41. Dead Sea                                 | 58. Jiangnan Basin                   | 75. Mediterranean – Samothraki Basin   | 92. Orpheus graben                 | 109. Saltville (Appalachian)                       | 125. West Africa (Gambia-Guine Bissau) |
| 8. Andean                                | 25. Brazilian Aptian Basin (Camamu)          | 42. Dniepr-Donets                            | 59. Jura/Rhodanian                   | 76. Mediterranean–Tyrrhenian           | 93. Palmyra                        | 110. Scotian Basin                                 | 126. West Africa (Mauritania-Senegal)  |
| 9. Andean                                | 26. Brazilian Aptian Basin (Campos-Santos)   | 43. Dniepr-Donets                            | 60. Katangan                         | 77. Mediterranean–Central              | 94. Paradox Basin                  | 111. Siberia, East                                 | 127. West Africa (Morocco-S. Spain)    |
| 10. Apennine                             | 27. Brazilian Aptian Basin (Ceara)           | 44. Eastern Alps                             | 61. Khorat Basin                     | 78. Mediterranean–Eastern              | 95. Parry Islands Foldbelt         | 112. Sirjan Trough                                 | 128. Western Canada (Alberta Basin)    |
| 11. Appalachian                          | 28. Brazilian Aptian Basin (Cumuruxatiba)    | 45. Ebro Basin                               | 62. Kuqa Foreland (Tarim Basin)      | 79. Mediterranean–Sicilian             | 96. Pricaspian Basin               | 113. Solimoes                                      | 129. Whale Basin (Grand Banks)         |
| 12. Aquitaine                            | 29. Brazilian Aptian Basin (Sergipe-Alagoas) | 46. Flemish Pass Basin (Grand Banks)         | 63. La Popa (Monterrey) Basin        | 80. Michigan Basin                     | 97. Pripyat Basin                  | 114. Somalia-Kenya                                 | 130. Williston Basin                   |
| 13. Arabian Basin (Gotnia Salt Basin)    | 30. Cankiri-Corum                            | 47. Georges Bank                             | 64. Lusitanian                       | 81. Moesian                            | 98. Qaidam Basin                   | 115. South Whale Basin (Grand Banks)               | 131. Zagros (Mesopotamian Basin)       |
| 14. Arabian Basin (Hitt Salt Basin)      | 31. Carrington Basin                         | 48. Green River Basin                        | 65. Mackenzie Basin                  | 82. Moose River Basin                  | 99. Qom-Kalut                      | 116. Sverdrup Basin (Eller Ringnes – NW Ellesmere) | 132. Zagros (Mesopotamian Basin)       |
| 15. Arabian Basin (Hormuz central Saudi) | 32. Cantabrian-West Pyrenees                 | 49. Gulf of Mexico (Northern Gulf coast)     | 66. Maestrat                         | 83. Neuvquen Basin                     | 100. Red Sea (North)               | 117. Sverdrup Basin (Melville Is)                  | 133. Zechstein (NW Europe)             |
| 16. Arabian Basin (Hormuz Gulf region)   | 33. Carnarvon Basin (Yaringa)                | 50. Gulf of Mexico (Southern Salina-Sigsbee) | 67. Majunga Basin                    | 84. Nordkapp Basin                     | 101. Red Sea (South)               | 118. Tabriz Salt Basin                             | 134. Zechstein (onshore UK)            |
| 17. Arabian Basin (Hormuz-Kerman region) | 34. Carpathian foredeep                      | 51. Haltenbanken                             | 68. Mandawa Basin                    | 85. Officer Basin                      | 102. Rot Salt Basin                | 135. Zapaquia Basin                                |  |

Figure 2.3: Distribution of global salt basins across geological time (Warren 2016).

Evaporite deformation by salt tectonics has received significant interest and study over the last 40 years (Talbot 1978; 1995; Davis and Engelder 1987; Vendeville and Jackson 1992 a;b; Jackson and Talbot 1991; Weijermars et al. 1993; Jackson and Vendeville 1994; Jackson et al. 1994; Jackson 1995; 1997; Coward and Stewart 1995; Peel et al. 1995; 2020; Nilsen et al. 1995; Rowan et al. 1999; 2003; 2004; Giles and Lawton 2002; Hudec and Jackson 2004; 2006; 2007; Gaullier and Vendeville 2005; Sellier and Vendeville 2009; Fuchs et al. 2011; Giles and Rowan 2012; Dooley et al. 2013; 2015; 2020; Rowan 2014; 2020 Rowan et al. 2016; Jackson and Hudec 2017; Duffy et al. 2017; Ferrer et al. 2017; Pichel et al. 2017; 2018; 2019; 2020; Hamilton-Wright et al. 2019; Peel et al. 2020). This has been driven mainly by advancements in 3-D seismic acquisition and processing, especially 3-D pre-stack depth migration, and the realisation that salt tectonics is best modelled as a layer of pressurised fluid overlain by brittle sediment (Hale et al. 1992; Hodgkins and O'Brien 1994; Ratcliff and Weber 1997; Dooley et al. 2013; 2015; 2020; Warren 2016). Understanding salt tectonics can help in mineral exploration and extraction. Faults can concentrate hot brines which may transport dissolved metals, thus evaporites can concentrate metal deposits (Hudec and Jackson 2007; Jackson and Hudec 2017). Evaporites may also offer trap and seal potential for carbon storage projects (Maia da Costa et al. 2018; Roelofse et al. 2019; Lloyd et al. 2021), and provide numerous important economic resources including fertilizers, salts and other minerals (Woods 1979).

Significantly, evaporites affect all aspects of the petroleum system (Figure 2.4). Salt flow works to create structural traps, influence reservoir facies distribution and seal hydrocarbon traps (Hudec and Jackson 2007; Jackson and Hudec 2017). Evaporites are powerful heat conductors and large salt-bodies can alter heat flow patterns, thus maturity above, adjacent to and below salt structures (Harms 2015; Daniilidis and Herber 2017). Furthermore, salt can cause drilling hazards due to stress changes (Luo et al. 2012; Nikolinakou et al. 2012; 2014), pore-pressure variations, salt creep, rubble zones, intercalated strata and bitumen associated with many salt structures (Jackson and Hudec 2017). Complex evaporite structures are difficult to image in reflection seismic data because of their generally high rock velocities and the steep dips and overhangs that can form (Jones and Davison 2014). In addition, salt structures have a significant effect on stratigraphic thicknesses, adjacent facies distributions and association with faults in nearby successions (Giles and Rowan 2012; Mannie et al. 2014; Ribes et al. 2015; 2017; Pichel and Jackson 2020). The geometries of salt structures must be accurately modelled during processing before seismic data can be reliably used to interpret stratigraphy below (Jones and Davison 2014).


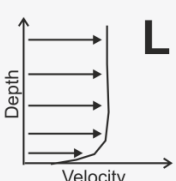

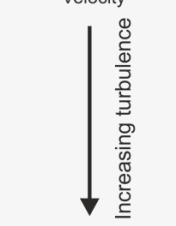


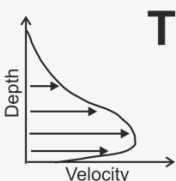



**Figure 2.4:** Giant hydrocarbon discoveries between 2000 and 2012 divided by A) dominant reservoir type, note 17.6% deep-water reservoir (turbidite), having the greatest reserves out of all siliciclastic settings and B) seal type, note 56.2% salt seals (evaporite). A giant field is defined as one containing 500 million barrels or more recoverable oil or 3.5 Tcf or more recoverable gas. Numbers in brackets are number of fields (Warren 2016).

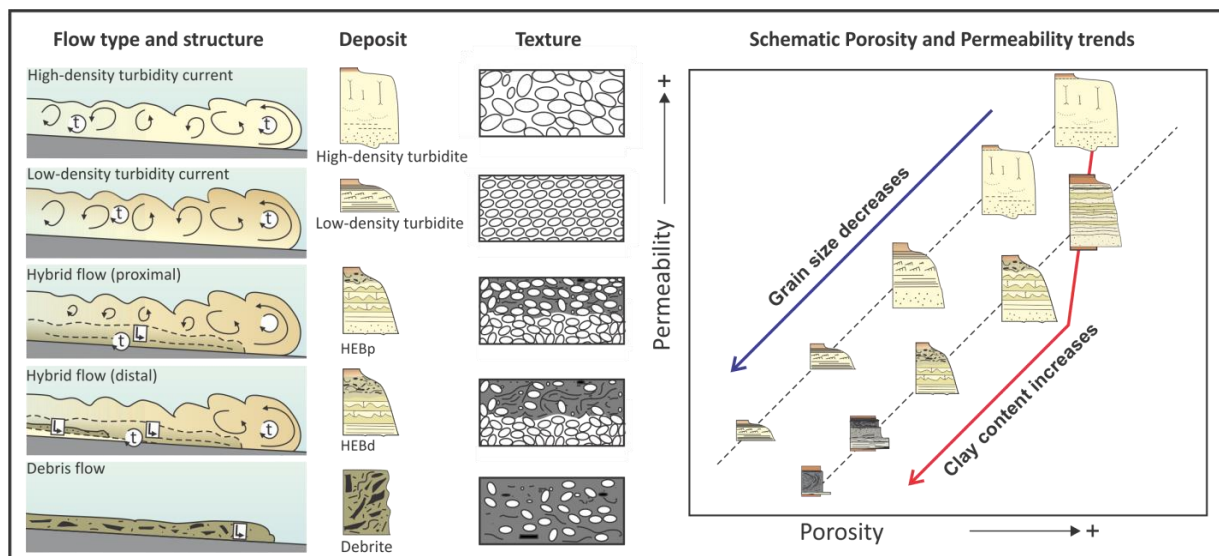
## 2.2 Deep-water processes and products

Sediment is transported to deep-water (below storm wave-base) by sediment gravity flows (SGFs) (Figures 2.5 and 2.6; Daly 1936; Kuenen and Migliorini 1950; Middleton and Hampton 1973; Lowe 1982; Mulder and Alexander 2001; Talling et al. 2012). SGFs form due to the action of gravity on the density contrast between sediment-laden fluid and ambient fluid (seawater or freshwater) (e.g., Middleton and Hampton 1973; Lowe 1979). A spectrum of SGF types, in a continuum from turbulent to laminar, has been identified and differentiated based on their particle support mechanism (Figures 2.5 and 2.6), which is controlled by: sediment concentration, flow thickness, slope gradient, matrix strength, grain-size, basin topography buoyancy, pore pressure, grain-to-grain interaction, turbulence, flow confinement and bed support (Fisher 1971; Hiscott 1994; Mulder and Alexander 2001; Joseph and Lomas 2004; Straub et al. 2008; Talling et al. 2012).

SGFs can be classified into three main sediment transport mechanisms (Figures 2.5 and 2.6): 1) Turbulent flows (Figures 2.7, 2.8 and 2.9; Kuenen and Migliorini 1950; Middleton 1967; Lowe 1982; McCaffrey and Kneller 2001; Baas et al. 2009); 2) laminar, or debris flows (Figure 2.10; Hampton 1972; Nardin et al. 1979; Ilstad et al. 2004; Pickering and Corregidor 2005; Baas et al. 2009), and; 3) hybrid, or transitional flows (Figures 2.11 and 2.12; Haughton et al. 2003; 2009; Sylvester and Lowe 2004; Talling et al. 2007; Baas et al. 2009; Kane and Pontén 2012; Kane et al. 2017).

EVENT TYPE	L = Laminar T = Turbulent	DEPOSIT	BEHAVIOUR
DEBRIS FLOW		 Debrite	
CO-GENETIC FLOWS		 Linked debris (HEB)	
SLURRY FLOW		 Banded sandstone	
HIGH DENSITY TURBIDITY CURRENT		 High density turbidite	
LOW DENSITY TURBIDITY CURRENT		 Low density turbidite	

**Figure 2.5:** The range of different sediment gravity flow types from laminar to turbulent, and their associated deposits and schematic velocity-depth profiles (modified from Haughton et al. 2009).



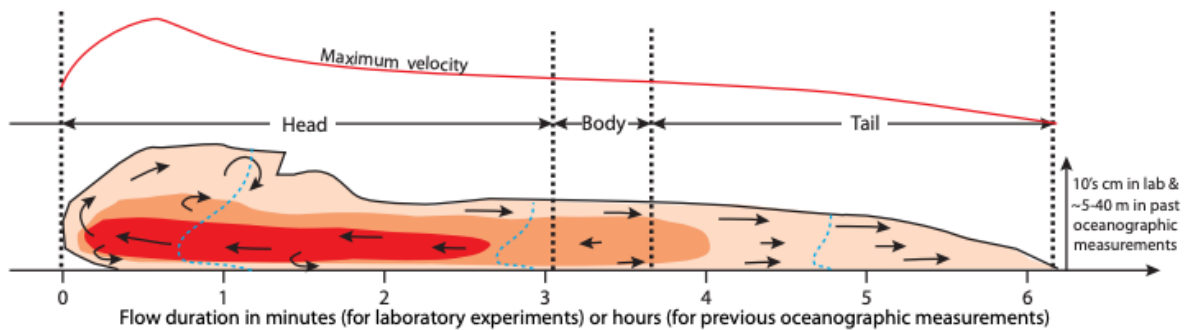
**Figure 2.6:** Classification of sediment gravity flows based on their rheological properties illustrating different flow types, deposits, textures and implications for subsurface energy reservoir quality. Both porosity and permeability decrease with grain size reduction and clay content increase (Haughton et al. 2009; Porten et al. 2016).

### Turbidity currents

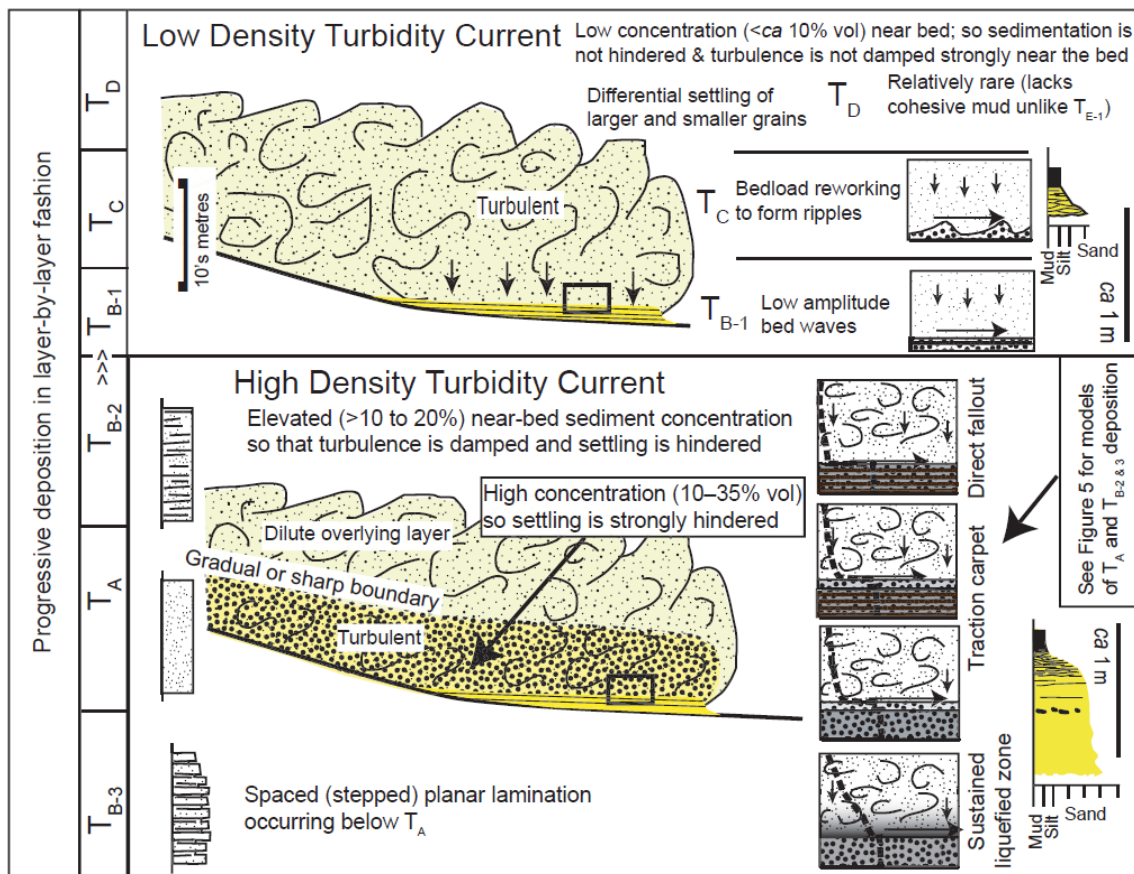
Turbulence is characteristic of a low-viscosity flow, whereby inertial forces dominate over viscous forces (Middleton 1967). Turbidity currents are SGFs in which fluid turbulence plays a major role in sustaining the sediment load (Middleton and Hampton 1973). Turbulence is generated in these currents by shear stress acting on the boundary between the flow and the ambient fluid, and the underlying substrate (Buckee et al. 2001).

Turbulent SFGs have a general structure comprising a head, body and tail (Figure 2.7). The mean velocity and sediment concentration is highest in the body of the flow, because the head of the flow interacts with and entrains the ambient fluid (e.g., Middleton 1967; Kneller and Buckee 2000; Azpiroz-Zabala et al. 2017). The mean velocity and sediment concentration then decreases toward

the tail (Figure 2.7). Turbulent flows can be sub-divided based on their sediment concentration into low- and high- density flows (Figure 2.8; e.g., Lowe 1982; Kneller and Branney 1995). Low-density flows have lower sediment concentrations (<10%) and are entirely supported by fluid turbulence (e.g., Baas et al. 2011). High-density flows have higher sediment concentrations (>10%), which suppresses turbulence close to the bed (Lowe 1982; Talling et al. 2012). High-density flows are therefore supported by a combination of fluid turbulence and grain-to-grain interaction (Mulder and Alexander 2001).



**Figure 2.7:** Cross-section of a turbidity current observed in a laboratory experiment, showing the head of the flow being fed with sediment by the body. The velocity profile decreases towards the tail (Aşpıroç-Zabala et al. 2017).



**Figure 2.8:** Summary of low- and high- density turbidity currents and their associated depositional processes, sedimentary structures and depositional products (Talling et al. 2012).

**Low-density turbidity currents:** Low-density turbidity currents (LDTs) are dilute flows that have sediment concentrations low enough (<10%) that the flow can be fully turbulent throughout the entire vertical profile of the turbidity current and sedimentation is not hindered by grain-to-grain interactions (Figure 2.8; Buckee et al. 2001; Talling et al. 2012). Lowe (1982) defines LDTs as turbidity currents which form tractional divisions only (structures such as ripple cross-



lamination, planar-laminations and flutes), providing evidence for near bed turbulence (Elliot 2000). These sedimentary structures are preserved in deposits known as low-density turbidites (LDTs; Figure 2.8; Sumner et al. 2008; Baas et al. 2011). The vertical profile of a LDT is commonly normally-graded, indicative of a waning flow (Lowe 1982), reflecting preferential settling of larger grains within the flows due to vertical density stratification (Garcia 1994; Baas et al. 2005; Eggenhuisen et al. 2019). A LDT typically has characteristics of all, or part, of the Tb-e divisions of the idealised sequence through a turbidite (Figure 2.9; Bouma 1962). As LDTs wane only fine particles are transported, resulting in beds being capped by laminated to homogeneous muds or silts (Te, Figures 2.8 and 2.9; Bouma 1962). The basal part may show planar laminations which transition up into cross laminations as a result of bed reworking due to near-bed turbulence and concurrent waning flow velocity (Tb-Tc, Figure 2.9; Bouma 1962; Mulder and Alexander 2001).

LDTs are typically thin (<30 cm) (Ricci Lucchi 1967; Talling 2001) and commonly observed in distal or marginal environments as flows become more dilute because of entrainment of water and loss of sediment downslope, or away from the flow axis (e.g., Walker 1966; Mutti 1977; Hiscott et al. 1997; Boulesteix et al. 2019; 2020), or where flows spill over from confining channels (e.g., Mutti 1977; Hansen et al. 2015; Jobe et al. 2017; Eggenhuisen et al. 2019), forming levees (e.g., Normark et al. 1983; Kane et al. 2007; Kane and Hodgson 2011).

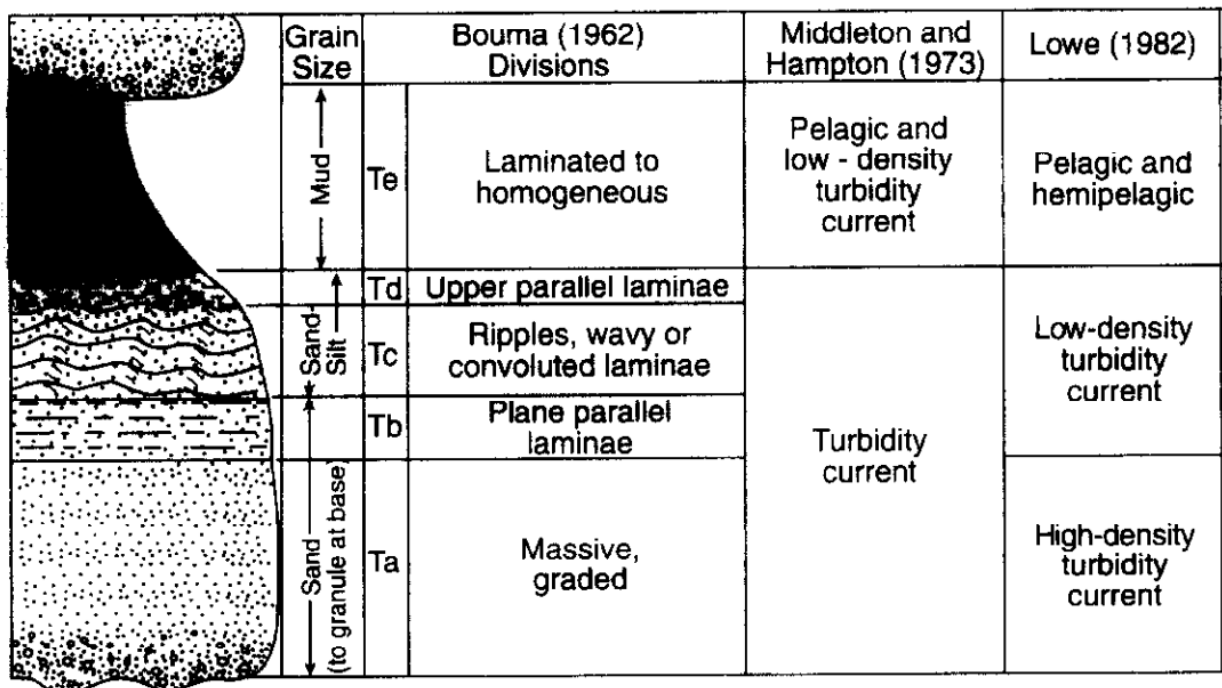


Figure 2.9: Idealised vertical profile (Bouma sequence) through a turbidite, including interpretations from Middleton and Hampton (1973), and Lowe (1982), (Shanmugam 1997).

**High-density turbidity currents:** High-density turbidity currents (HDTCs) are turbidity currents which feature a sediment concentration high enough (>10%) for grain-to-grain interaction to significantly dampen turbulence and hinder grain settling (Figure 2.8; Lowe 1982; Talling et al. 2012). HDTCs differ from LDTs in that they have been recorded to have a two-layer structure with a gradual or sharp boundary between the basal high-concentration, non-Newtonian plastic flow phase, with a constant or weakly decreasing concentration, and the upper, low-concentration Newtonian turbulent flow phase, with exponentially decreasing concentration (Figure 2.8; Kuenen and Migliorini 1950; Middleton 1967; 1993; Azpiroz-Zabala et al. 2017; Paull et al. 2018; Stevenson et al. 2018). Processes other than fluid turbulence may act to support particles in the lower boundary

layer (e.g., grain-grain interactions, excess pore pressure, increased fluid velocity and reduced density differences between particles and fluid (Kuenen 1951; Lowe 1982; Talling et al. 2012)).

If the turbidity current has capacity to transport its large volume of sediment it will be capable of bypassing material and potentially eroding the substrate (Kneller and Branney 1995). However, if sediment volume exceeds the flows' capacity, the flow will rapidly decelerate and deposition will occur 'en masse' (Hiscott 1994), resulting in a massive, occasionally graded sandstone deposit known as a high density turbidite (HDT; Figure 2.8; Kuenen 1957; Middleton and Hampton 1973; Lowe 1982). HDTs may also be deposited in a layer-by-layer fashion rather than en-masse (Kneller and Branney 1995), but at higher bed aggradation rates compared to LDTCs (Talling et al. 2012). The high volume of sediment transported by HDTCs can often result in sediment being concentrated at the base of the flow in a 'traction carpet' (Figures 2.8 and 2.9; Dzulynski and Sanders 1962; Hiscott and Middleton 1980; Lowe 1982; Sohn 1997; Sumner et al. 2008; Talling et al. 2012).

HDTs tend to be relatively thick (50 cm +), poorly-sorted, ungraded and structureless sandstones (Middleton and Hampton 1973; Talling et al. 2012). Planar laminations, grain-size breaks and internal erosional surfaces and scour fills are often preserved within HTDs (Lowe 1982; Postma 1986; Talling et al. 2012; Stevenson et al. 2015; 2020). HDTs are typically deposited in proximal areas where high-energy flows capable of transporting high volumes of sediment are most prevalent, or at points of rapid deceleration e.g., due to a reduction in confinement or slope gradient (Middleton and Hampton 1973). HDTs are therefore characteristic of both channel (Hubbard et al. 2016; Jobe et al. 2017; Bell et al. 2018) and lobe (Hodgson et al. 2006; Grundvåg et al. 2014; Spychala et al. 2017; Bell et al. 2018 a; b; Hansen et al. 2019) axis deposition.

Planar laminations are observed in both HDTs and LDTCs and therefore the transition between HDTC and LDTC is interpreted to be within the planar laminated division of the Bouma idealised sedimentary sequence (Tb; Figure 2.9; Bouma 1962; Shanmugam 1997; Talling et al. 2012; Stevenson et al. 2020).

### ***Debris flows***

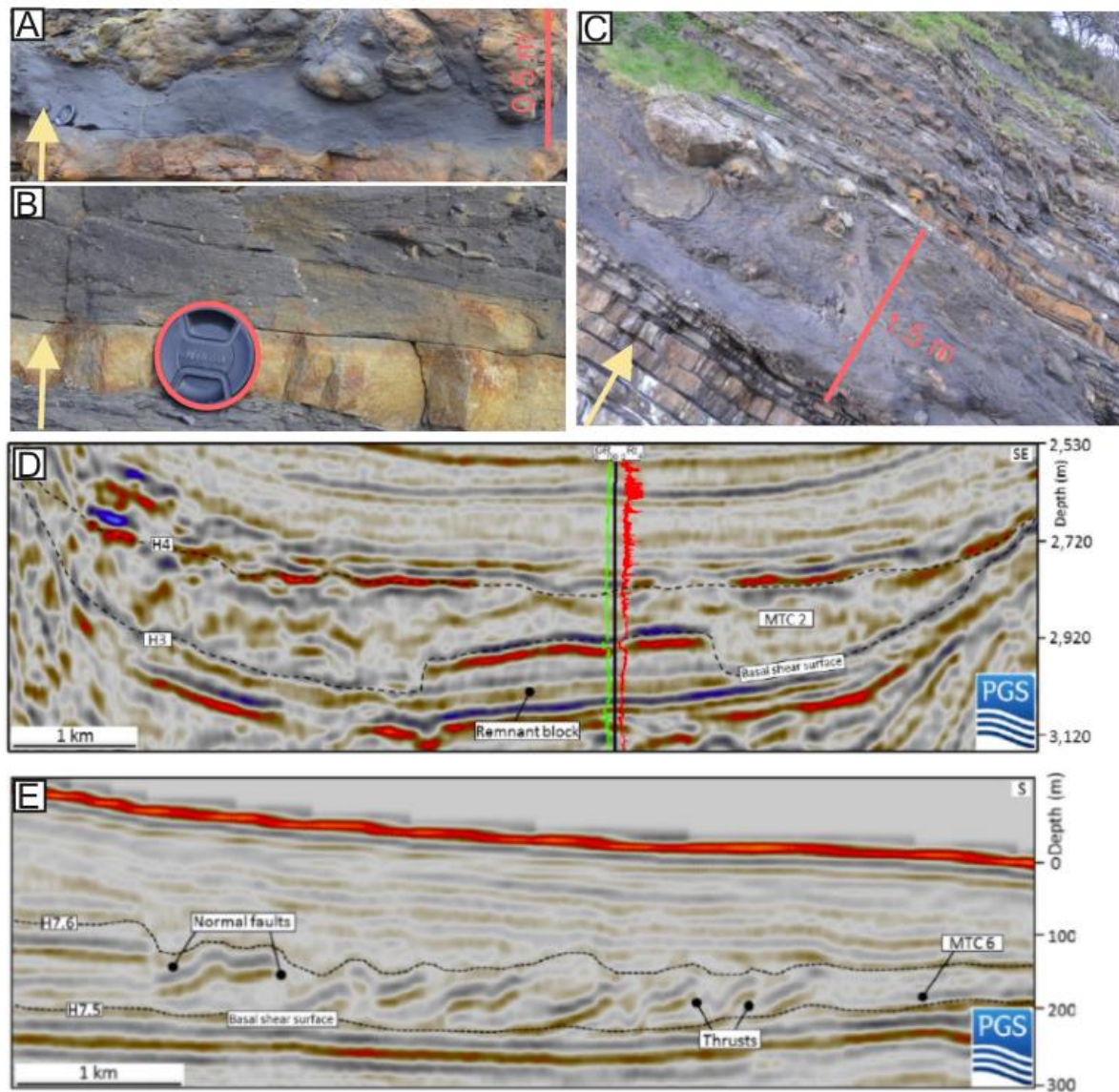
In contrast to turbulent flows, laminar (or debris) flows are highly viscous and the sediment within them is supported not by turbulence, but by a matrix of high yield-strength fluid: a mixture of interstitial fluid and cohesive fine sediment (mud) (e.g., Vanoni 1946; Hampton 1972; Middleton and Hampton 1973; Nardin et al. 1979; Wang and Plate 1996; Iverson et al. 1997; 2010; Sohn 2000; Iltad et al. 2004; Baas et al. 2009). Laminar flow conditions typically arise when electrostatic bonds between clay minerals cause the suppression of turbulence, resulting in non-Newtonian flow (e.g., Wang and Larsen 1994; Coussot and Meunier 1996). Laminar conditions may also arise in cohesionless (mud-poor) flows if grain concentrations are high enough for grains to interlock and give the flow frictional strength (Shanmugam and Moiola 1995; Amy et al. 2005). Rapid 'en-masse' deposition of the flow occurs when the shear stress (Middleton and Hampton 1973) applied to the flow cannot overcome the yield or frictional strength of the flow (Lowe 1982; Postma 1986; Amy et al. 2005), often due to rapid flow deceleration (Figures 2.5 and 2.6; Amy et al. 2005).

The behaviour of a debris flow, and thus the characteristics of its deposit, is controlled by the internal mixture of solids and fluids, and their interaction with each other (Sohn 2000). Therefore, debris flow processes are dependent on the properties of the grains and clasts (size, density and volume fraction) and of the interstitial fluids (density, viscosity and volume fraction), all of which are dependent on the matrix mud-content (Sohn 2000; Iverson et al. 2010). Debris flows are capable of transporting poorly-sorted material, with a wide grain-size range, including oversized clasts, for long distances (e.g., Nardin et al. 1979; Hampton et al. 1996; Iverson 1997; Masson et al. 1997; Sohn 2000; Pickering and Corregidor 2005; Hodgson et al. 2019), and tend to deposit en

masse abruptly due to ‘freezing’ (Nardin et al. 1979; Talling et al., 2012). These oversized clasts may accumulate at the base of the flow if mud content is low (Baas and Best 2002).

Debrites are the depositional products of debris flows, and are typically thickly-bedded, matrix-supported, poorly-sorted and lacking of any internal grading or structuration (Figure 2.10; Middleton and Hampton 1973; Prior et al. 1984). However, they also often feature rafts or blocks of interbedded sandstone and mudstone and ‘floating’ clasts (Figure 2.10; Talling et al. 2012). Debrites often have a ‘chaotic’ appearance due to syn-depositional fluid escape and shearing at the base and margins of the flow (Figure 2.10; Amy et al. 2005) and pinch out abruptly at their edges (Talling et al. 2012; 2013; 2014). The cohesive nature of debris flows makes them prone to deformation during transport (e.g., Jackson 2011; Soutter et al. 2018). This often results in the preservation of deformational structures, such as folding (e.g., Poprawski et al. 2014; 2016; 2021; Sobesiak et al. 2016) and faulting (e.g., Bull et al. 2009), within debrites. Debrite thickness and clast-size depends on the yield strength of the parent debris flow. High-strength debrites are characterised by thick deposits capable of transporting km-scale clasts (e.g., Soutter et al. 2018; Hodgson et al. 2019), and low-strength deposits characterised by thinner debrites capable of transporting sand-grade clasts (Figure 2.10; Talling et al. 2013).

Large-scale slope failure can cause the deposition of large masses of lithified and unlithified sediment hundreds of kilometres into the basin (Hampton et al. 1996; Locat and Lee 2002; Moscardelli and Wood 2008; Nwoko et al. 2020 a; b), forming some of the largest depositional events on Earth (Talling et al. 2007; Georgiopoulou et al. 2010; Calvès et al. 2015). The deposits of these failures are generally referred to as submarine landslides (Hampton et al. 1996; Masson et al. 2006) or mass-transport deposits (MTDs), and can vary from debrites and slides, to slumps and relatively dilute flows, depending on source material and the degree of disaggregation (Nardin et al. 1979). MTDs often transport ‘megaclasts’ into deep-water, and are internally deformed, typically by up-dip extension (represented by normal faults) and down-dip compression (represented by thrust faults) and have ‘megascours’ at their base (Moscardelli et al. 2006; Jackson 2011; Soutter et al. 2018; Hodgson et al. 2019; Nwoko et al. 2020 a;b). Therefore, MTDs are associated with widely varying lithology and depositional relief (Bryn et al. 2005; Kneller et al. 2016; Fallgatter et al. 2017; Soutter et al. 2018; Cumberpatch et al. 2021a; Nwoko et al. 2020 a;b). Mass transport deposits can be triggered by volcanic activity (e.g., Chadwick Jr et al. 2012), excess pore pressures (Urlaub et al. 2018), glacial activity (Bryn et al. 2005), and most relevantly to this work, tectonic activity (Ortiz-Karpf et al. 2015; 2016), specifically salt tectonics (Doughty-Jones et al. 2019; Wu et al. 2020).



**Figure 2.10:** Examples of debris and mass transport deposits from outcropping and subsurface stratigraphy. A-C) Photographs of laminar flow deposits from the Black Flysch Group at Cabo Matxixako, Basque-Cantabrian Basin, Northern Spain. Yellow arrow indicates way up, peach highlights scale, lens cap is 52mm. A) Poorly-sorted mudstone foundered in to by a thick-bedded muddy sandstone; B) Poorly-sorted sandy mudstone with stary night (floating clast) texture, containing sporadic granules and rafts blocks; C) Chaotic clast-rich matrix-supported deposit encased between units of thin-to-medium-bedded sandstones (Cumberpatch et al. 2021b). D and E are seismic sections from the northern Gulf of Mexico salt walled minibasins (Wu et al. 2020). D) Seismic section across mass transport complex (MTC) 2 showing a highly sheared basal surface; E) Seismic section across MTC 6 showing syn-depositional up-dip extensional faulting and down-dip compressional faulting.

### **Transitional flows**

Individual SGFs can transform longitudinally from turbulent to laminar, or vice-versa. Flows which exhibit characteristics of both flow states are termed transitional flows (Figures 2.11 and 2.12; Baas et al. 2009; 2011; Hodgson, 2009; Kane and Pontén 2012; Kane et al. 2017; Southern et al. 2017). Transitional flows are those in which sediment is transported through a continuum of processes between fully turbulent and fully laminar (e.g., Wang and Plate 1996; Baas and Best 2002; Sumner et al. 2009; Baas et al. 2009) and typically arise when fully turbulent flows increase their relative concentration of mud as they flow down-dip (Figure 2.11), either by deposition of coarse grains up-dip and/or erosion and entrainment of mud (e.g., Marr et al. 2001; Haughton et al. 2003; Kane and Pontén 2012).

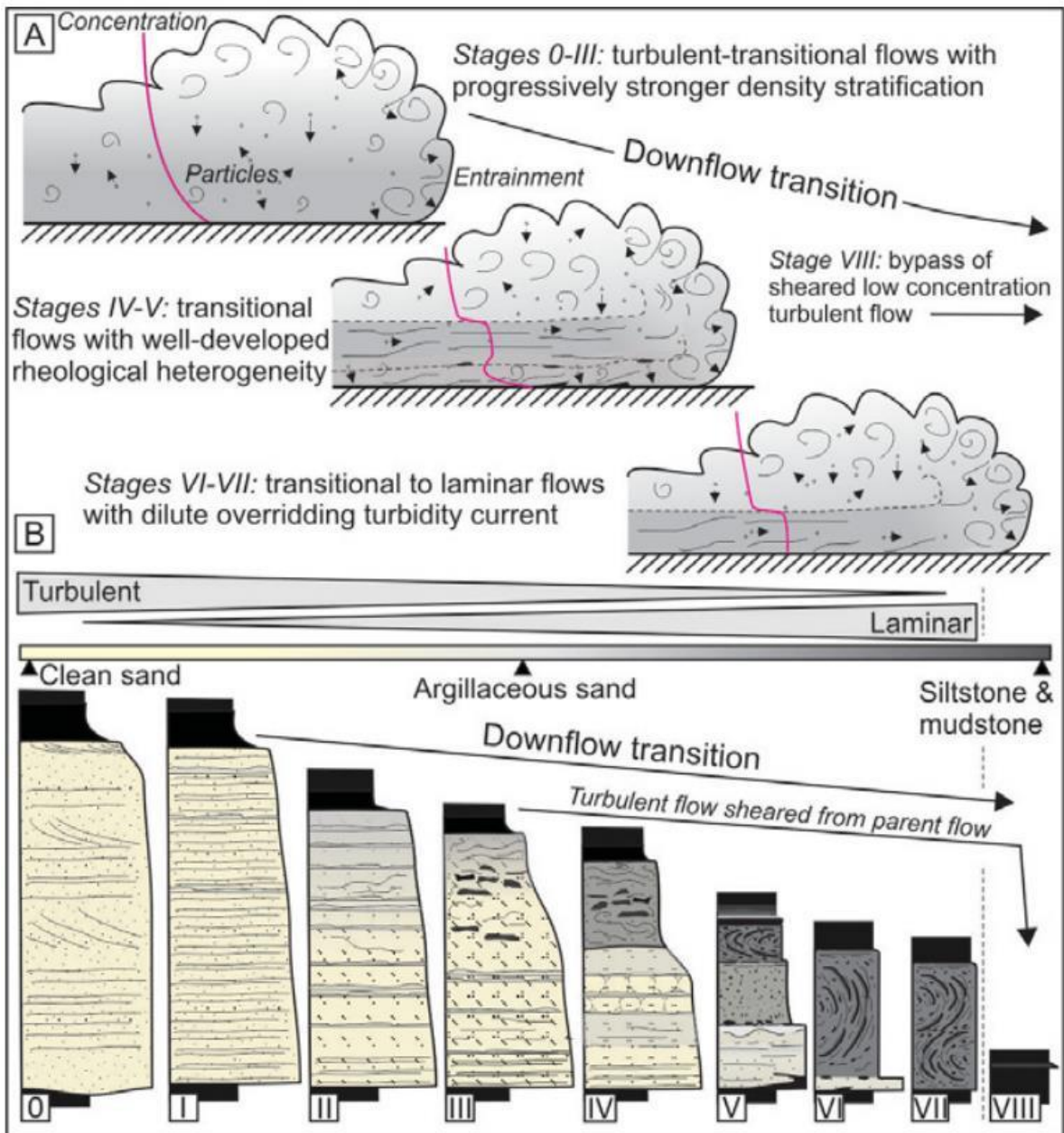
Hybrid flows tend to initiate within marginal and distal locations of submarine fans (Haughton et al. 2003; Barker et al. 2008; Spychala et al. 2017), where they are often initiated by flow transformation due to extended flow run-out, or by substrate entrainment (Hodgson 2009; Kane and Pontén 2012; Kane et al. 2017). Therefore, a flow that was initially fully turbulent can become partially cohesive, resulting in deposits that are vertically segregated, representing the flows down-slope evolution (Figure 2.11; Lowe and Guy 2000; Kane and Pontén 2012). Transitional flows are also recorded proximally due to confining topography (Patacci et al. 2014; Soutter et al. 2019).

Turbidity currents can transform into transitional flows by entraining substrate into the flow, which increases the sediment and clay concentrations of the flow, acting to 'bulk' it up, which in turn dampens turbulence and increases flow cohesion, promoting the development of a laminar flow (Figures 2.5, 2.6, 2.11 and 2.12; Piper and Aksu 1987; Mulder et al. 1997; Baas and Best 2002; Sumner et al. 2009; Baas et al. 2009; 2011; Kane et al. 2017). The deposit of such a flow will show turbidite characteristics proximally, and hybrid bed characteristics distally, a pattern commonly observed in submarine lobes (Figures 2.11 and 2.12; Talling et al. 2004; Hodgson 2009; Kane and Pontén, 2012; Grundvåg et al. 2014; Kane et al. 2017; Spychala et al. 2017; Fonnesu et al. 2018). A decelerating turbidity current can also transition into a transitional flow, due to an increase in clay content (Figure 2.11; Baas and Best 2002; Baas et al. 2009). As turbulence decreases coarser grains fall from suspension and the flow collapses, effectively increasing clay-concentration in a positive feedback relationship, promoting transitional flow conditions. Such a relationship is interpreted to develop in distal parts of systems (Hodgson 2009; Kane and Pontén 2012; Kane et al. 2017) and adjacent to topography, where flows interact with, and are forced to decelerate against a counter-slope (Muzzi Magalhaes and Tinterri 2010; Patacci and Haughton 2014; Southern et al. 2015; Tinterri et al. 2016; Soutter et al. 2019).

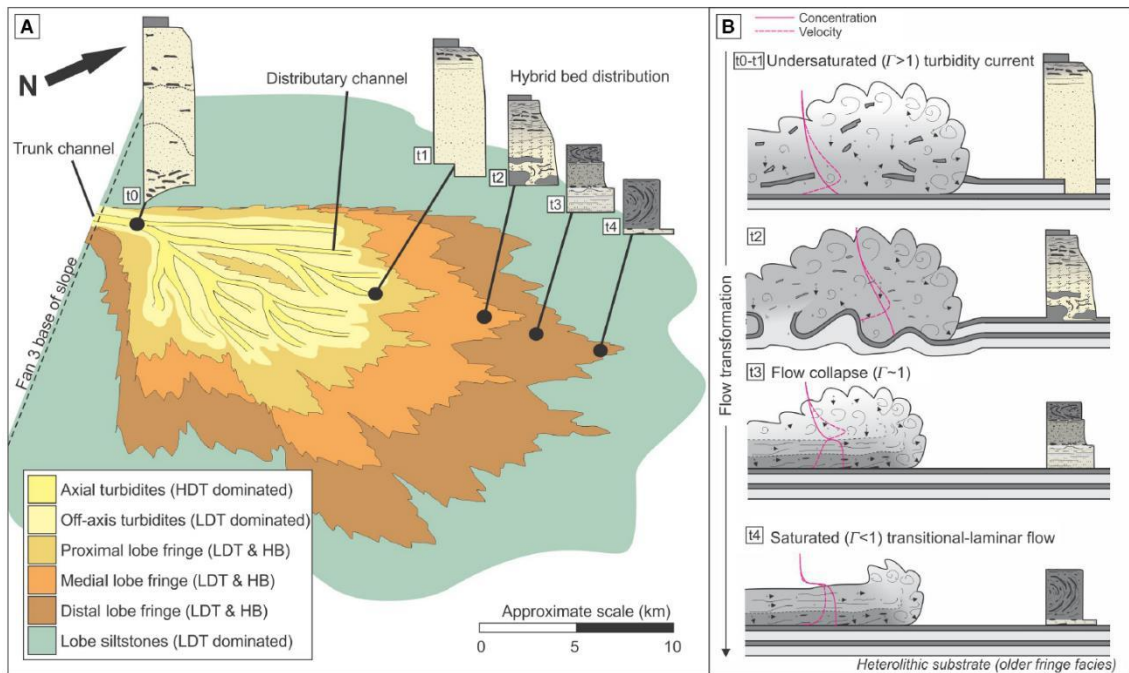
The generation of a turbidity current from a debris flow (e.g., Hampton 1972) is facilitated by the entrainment of ambient fluid into the debris flow. This sufficiently dilutes the flow to the point where fluid turbulence becomes the dominant transport mechanism (Figures 2.5, 2.6, 2.11 and 2.12; Mohrig et al. 1998; Piper et al. 1999; Marr et al. 2001; Baas and Best 2002).

Hybrid beds, one of the deposits of transitional flows, are typically observed as single event beds comprising a basal sandstone (turbidite) capped by, or associated with, a co-genetic debrite (Wood and Smith 1958; Talling et al. 2004; Jackson et al. 2009; Haughton et al., 2009; Baas et al. 2011; Talling et al. 2013; Southern et al. 2017). The upper debrite is sometimes termed a 'linked-debrite' (Haughton et al. 2003; Sumner et al. 2009; Jackson et al. 2009). Hybrid beds often show variable spatial heterogeneity (e.g., Haughton et al. 2003; Talling et al. 2004; Haughton et al. 2009; Hodgson 2009; Fonnesu et al. 2015; 2018; Spychala et al. 2017; Soutter et al. 2019) and typically have a distinct boundary between the turbulent and laminar flow deposits (e.g., Haughton et al. 2003; 2009; Fonnesu et al. 2015; 2018). If the defined separation is lacking, the deposit is usually referred to as a transitional flow deposit rather than a hybrid bed (Talling et al. 2012).

Hybrid bed deposition typically requires long run-out distances to allow flow segregation and elevated mud concentrations, therefore hybrid beds are often found in the distal extents of deep-water systems, supporting the longitudinal flow transformation from turbulent to transitional or laminar flow conditions (Figure 2.12; Davis et al. 2009; Hodgson 2009; Pyles and Jenette 2009; Kane and Pontén 2012; Grundvåg et al. 2014; Kane et al. 2017; Spychala et al. 2017; Fonnesu et al. 2018). It has also been observed that flow deceleration due to basinal topography (Tinterri and Magalhaes 2011; Patacci et al. 2014; Southern et al. 2015; Soutter et al. 2019) and enhanced erosion at channel-lobe transitions (e.g., Mueller et al. 2017) may cause the deposition of relatively proximal hybrid beds.



**Figure 2.11:** Model for the longitudinal rheological flow evolution of a single event from a fully turbulent flow to a laminar flow and the resultant deposits (a down-dip transition from clean turbidites, to linked turbidite-debrites, to deformed debritic homogeneous silty mudstones) (Kane and Pontén 2012).



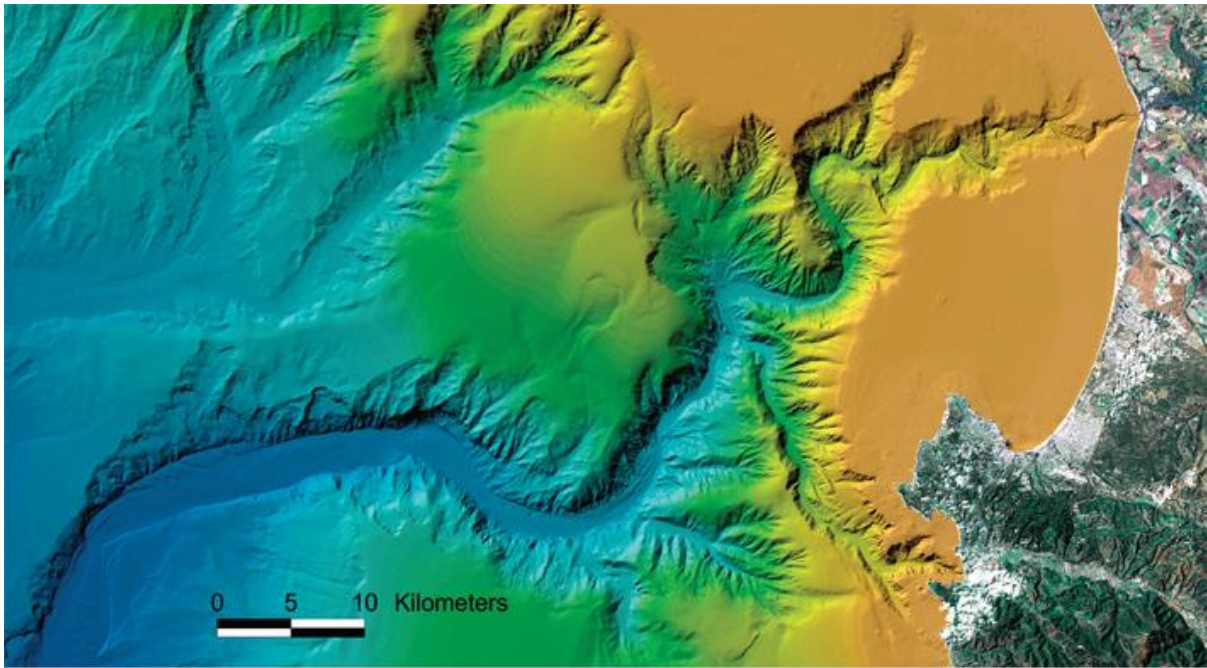
**Figure 2.12:** A) Plan view down-current flow transformation of a turbulent flow to a transitional-laminar flow, demonstrating the spatial distribution of hybrid beds within a submarine lobe (note distribution is concentrated to lobe fringe sub-environments). This is interpreted to form due to flow deceleration and entrainment of the substrate. B) Summary diagram of flow evolution and deposit type for flows in the lobe fringe (Kane et al. 2017).

### 2.3 Components of deep-water depositional systems

Modern and ancient deep-water fan systems are linked by common components that evolve in response to SGF erosion and deposition through time (e.g., Walker 1967; 1978; Normark 1978; Normark et al. 1979; 1983; Deptuck et al. 2007; Prather et al. 2012). These elements can be broadly sub-divided into canyons, channels, channel-lobe transition zones and lobes.

#### *Canyons*

Canyons are the main conduits for sediment transport from the continental shelf to the deep ocean basin and represent erosional and predominantly linear features that are incised into the slope or shelf, providing a long-term point-source for deep-water systems (Figure 2.13; Daly et al. 1936; Farre et al. 1983; Pratson and Coakley 1996; Talling 1998). They typically occur as long (100s km), narrow (10s km) and deep (several kms) v-shaped valleys with steep walls that can be connected to onshore river mouths (Figure 2.13; Harris and Whiteway 2011). Submarine canyons are formed by a combination of submarine erosion beneath successive SGFs, retrogressive slope failure, and subaerial erosion during low sea-levels (e.g., Daly et al. 1936; Farre et al. 1983; Pratson and Coakley 1996; Talling 1998; Popescu et al. 2004; Krastel et al 2001; Harris and Whiteway 2011). Flows that enter submarine canyons are often not of high enough magnitude to flow through the entirety of the canyon (Howell and Normark 1982), with only rare high-magnitude events passing through the canyon, eroding the canyon floor and depositing further down-slope (Jobe et al. 2018). When exhumed, canyon fills are characterised by coarse-grained HDTs in a canyon axis confined by a slump-dominated inner-canyon margin (Anderson et al. 2006).



**Figure 2.13:** Bathymetric map view of part of the Monterey Canyon, offshore central California. Blue-orange represents deep-shallow, from Monterey Bay Aquarium Research Institute.

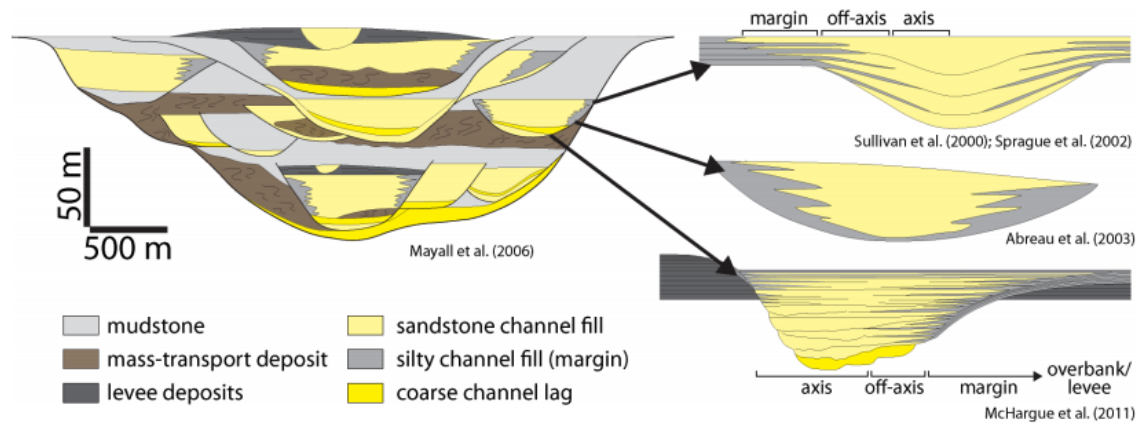
### **Channels**

Submarine channels are long-lived erosional or depositional features on the seafloor that act as conduits for SGFs carrying vast quantities of sediment down-dip (e.g., Normark et al. 1983; Mutti and Normark 1987; Clark and Pickering 1996; Peakall et al. 2000; Abreu et al. 2003; Deptuck et al. 2007; Straub et al. 2008; Kane et al. 2010; 2011; Mayall et al. 2010; Hodgson et al. 2011; Sylvester et al. 2011; Figueiredo et al. 2013; Hubbard et al. 2014; Hansen et al. 2015; Jobe et al. 2017; McArthur et al. 2019; Kneller et al. 2020) and often evolve from canyons up-dip (e.g., Normark 1978; Covault et al. 2011; 2012). Submarine channels tend to initiate during a period of erosion and bypass (Elliott 2000; Fildani et al. 2013; Stevenson et al. 2015) and multiple phases of incision often mean they become embedded on the slope (Sylvester et al. 2011; Hodgson et al. 2016). They often decrease in size basinwards, and commonly develop branching networks of distributary channels. Channels are composed of an axis and margin (Figure 2.14; Kneller et al. 2020). Channel belts are highly confined features and can be erosionally confined within a canyon or by external levees (Winn and Dott 1979; Millington and Clark 1995; Beaubouef 2004; Kane et al. 2009; 2012; Kane and Hodgson 2011; McHargue et al. 2011; Sylvester et al. 2011; Janocko et al. 2013; Morris et al. 2014; Hansen et al., 2017; Kneller et al. 2020). Channels are often also confined internally, within their bounding erosional surfaces, by internal levees, terraces or debrites (Figure 2.14; Kane and Hodgson 2011; Ortiz-Karppf et al. 2015; Morris et al. 2016; Hansen et al. 2017).

As aggradation rates increase, driven by sediment supply or sea-level changes (e.g., Kneller 2003; Sylvester et al. 2011), or a decreased slope angle (Kneller 2003; Sylvester et al. 2011; McHargue et al. 2011) channel-fills migrate vertically (McHargue et al. 2011; Covault et al. 2016). Aggradation will continue until the accommodation space within the channel is filled and avulsion occurs (e.g., Clark and Pickering 1996; Maier et al. 2013; 2018), or deformation re-routes flows (e.g., Sylvester et al. 2011), resulting in channel abandonment (e.g., Figueiredo et al. 2013). Through time, channel sinuosity is also shown to increase (Peakall et al. 2000; Kane et al. 2008; Sylvester et al. 2011, Maier et al. 2013). This inherent complexity in parameters controlling submarine channel-fills makes subsurface prediction of their architecture and reservoir quality challenging (Figure 12.14; Kolla et al. 2001; Falivene et al. 2006; Mayall et al. 2006; Bakke et al. 2008; Barton et al. 2010; McHargue et al. 2011; Zhang et al. 2015).



The large variation in channels identified in the subsurface and at outcrop has led to the development of hierarchical models that attempt to normalise descriptions across different deep-water systems (e.g., Sprague et al. 2002; 2005; Campion et al. 2003; McHargue et al. 2011; Maier et al. 2013). The primary architectural component is the channel element (Sprague et al. 2002; McHargue et al. 2011; Macauley and Hubbard 2013). Genetically related channel elements stack together to form an individual channel complex (McHargue et al. 2011), which in turn stack to form a channel complex set (Campion et al. 2003; McHargue et al. 2011). In general, a submarine channel system is composed of one or more complex sets that can be tied to a sequence stratigraphic framework, with multiple complex sets typically representing a 3<sup>rd</sup> order sea-level cycle (1 – 10 My) and a single complex set representing higher-order cycles (< 1 My) (McHargue et al. 2011).

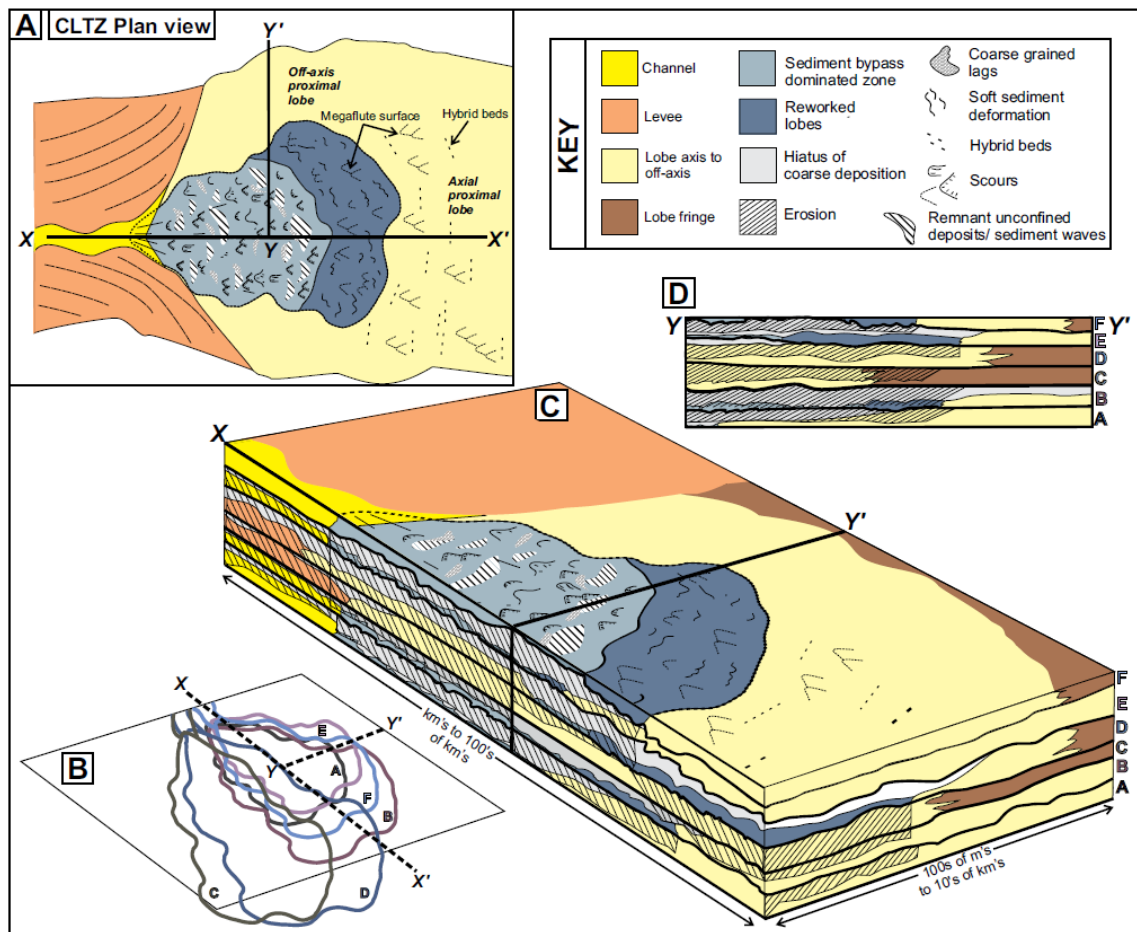


**Figure 2.14:** Schematic depiction of facies heterogeneities within different hierarchical scales of channel complex systems. Highlighting the variation in facies and architectures observed within channel elements (Sullivan et al. 2000; Sprague et al. 2002; Abreau et al. 2003; Mayall et al. 2006; McHargue et al. 2011; Romans et al. 2013).

### Channel-lobe transition zone

The channel-lobe transition zone (CLTZ) of a deep-water system is the geographical area between well-defined channels and levees up-dip, and lobes down-dip (Figure 2.15; Mutti and Normark 1987; Palanques et al. 1995; Wynn et al. 2002; Hofstra et al. 2015; Stevenson et al. 2015; Carvajal et al. 2017; Brooks et al. 2018; Maier et al. 2018; Pohl et al. 2019; 2020). CLTZs are typically located both where flows become relatively unconfined, and at the base-of-slope (Mutti and Normark 1987; Wynn et al. 2002; Brooks et al. 2018), and as such are dominated by erosion and bypass (Garcia and Parker 1989; Wynn et al. 2002; Brooks et al. 2018). Such conditions have been attributed to enhanced turbulence as rapidly decelerating flows undergo a hydraulic jump (Garcia and Parker 1989; Kenyon et al. 1995; Dorrel et al. 2016) or flow ‘relaxation’ as flows thin upon loss of channel confinement, resulting in a lowering of the maximum velocity (Pohl et al. 2019).

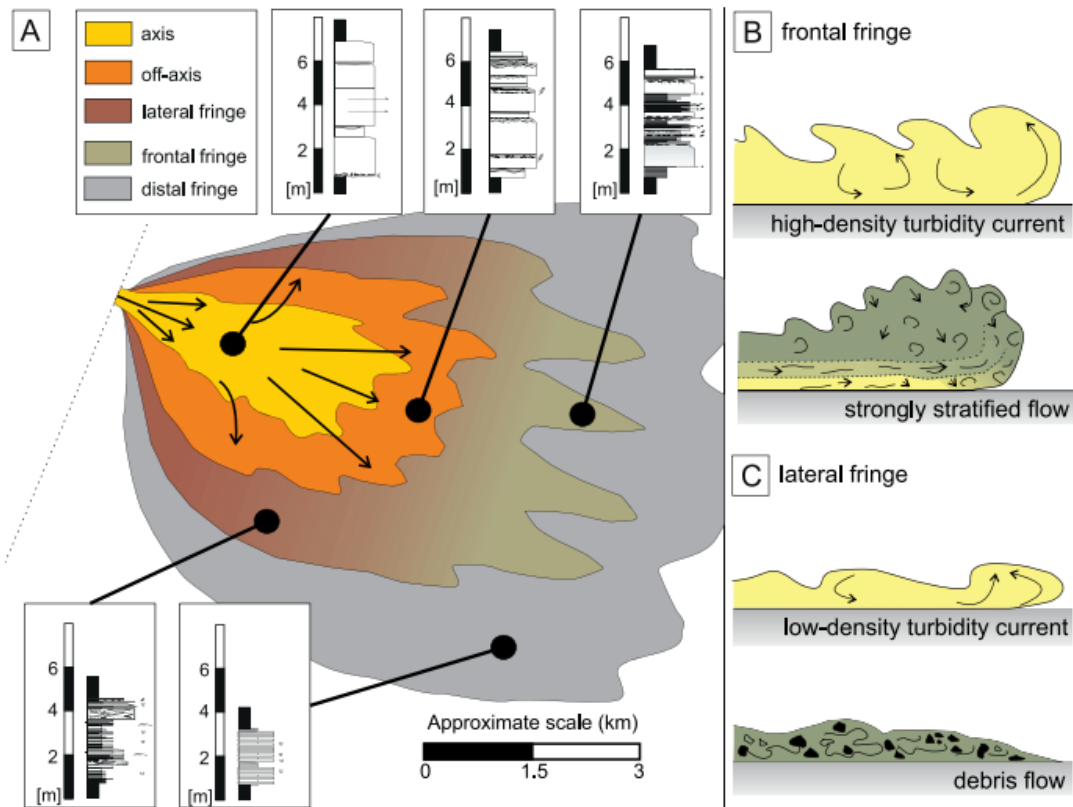
CLTZs are characterised by an array of erosional and depositional features, including: isolated and amalgamated scours (Figure 2.15; Wynn et al. 2002; Hofstra et al. 2015; Brooks et al. 2018; Maier et al. 2018); headless channels (Maier et al. 2018); upstream migrating bedforms (Postma et al. 2016); banded sandstones (Hofstra et al. 2018); coarse-grained lag deposits (Brooks et al. 2018); mounds down-dip of scours (Wynn et al. 2002); sediment waves (Wynn et al. 2002; Brooks et al. 2018; Hofstra et al. 2018; Maier et al. 2018) and hybrid beds developed downstream of erosion (Brooks et al. 2018). CLTZs are typically poorly-preserved (or recognised) in the rock record because they are subject to repeated periods of erosion and aggradation as flow axes migrate laterally and longitudinally at the mouth of feeder channels (e.g., Hofstra et al. 2018), thus CLTZs tend to require channel avulsion or enhanced aggradation to be preserved (Figure 2.15; Pemberton et al. 2016; Brooks et al. 2018).



**Figure 2.15:** A map surface and stratigraphic vertical expression of a channel-lobe transition zone highlighting the key depositional features and their spatial distribution. Note: area of mixed depositional and erosional features, area of reworked and scoured lobe and axial- and off-axis proximal lobe deposits. Study based on the Fort Brown Formation, South Africa (Brooks et al. 2018).

### Lobes

Submarine lobes are convex-up, lobate deposits of gravity flows typically deposited down-dip of where flows exit confinement on the basin-floor; or within intraslope basins created by salt diapirism, faulting, or mass-transport deposits (Figures 2.12 and 2.16; Ricci-Lucchi 1975; Mutti 1977; Normark 1978; Normark et al. 1979; 1983; Shanmugam and Moiola 1988; Mutti 1992; Postma et al. 1993; Bouma and Wickens 1994; Booth et al. 2003; Deptuck et al. 2008; Jegou et al. 2008; Prélat et al. 2009; 2010; Grundvåg et al. 2014; Marini et al. 2015; Oluboyo et al. 2014; Spychala et al. 2015; 2017a;b;c; Picot et al. 2016; Kane et al. 2017; Doughty-Jones et al. 2017; 2019; Dodd et al. 2019; Rabouille et al. 2019; Cumberpatch et al. 2021a). Lobe deposition occurs in response to flows spreading radially and decelerating as they exit the confines of a channel (e.g., Normark 1978; Mutti 1992; Kneller and Branney 1995; Kane et al. 2017). As flows spread, they progressively lose energy, depositing sand-rich HTDs in proximal locations, and mud-dominated LDTs and hybrid beds in distal lobe environment (Figure 2.16; Kane et al. 2017; Spychala et al. 2017b; Fonnesu et al. 2018). Lobes often thicken from the channel and through the CLTZ to an apex (e.g., Brooks et al. 2018; Pohl et al. 2019; 2020), and thin distally and laterally (Figures 2.12 and 2.16; Deptuck et al. 2008; Spychala et al. 2017; Hansen et al. 2018). This depositional thickness variation generates positive seafloor topography resulting in compensational stacking of successive lobes (Figure 2.17; e.g., Groenenburg et al. 2010; Straub and Pyles 2012; Jobe et al. 2017).



**Figure 2.16:** A) Plan view of submarine lobe sub-environments, showing representative facies associations related to each sub-environment, reflecting the longitudinal evolution of flows across a lobe. B, C) Flow process changes in the frontal fringe and the distal fringe (Spychala et al. 2017b).

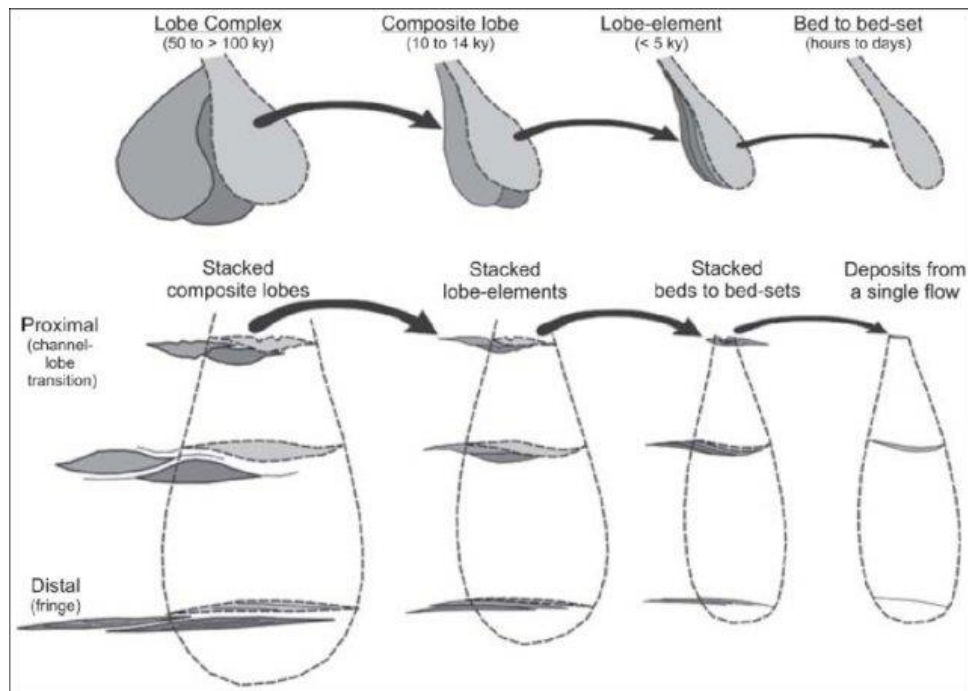
Traditionally, lobes were thought to be relatively simple, lobate features with ‘halo like’ facies associations, distributed in sheet-like architectures (Hesse 1964; Ricci-Lucchi and Valmori 1980; Tinterri et al. 2003; Remacha et al. 2005; Amy et al. 2007; Marini et al. 2015). The advent of high-resolution seismic imaging, and detailed field studies has demonstrated that in fact lobes can exhibit complex geometries and facies distributions (Figure 2.16).

Lobes can be divided into sub-environments (axis, off-axis, fringe) based on the proximal-distal and proximal-lateral evolution of the flows that build them (e.g., Walker 1966; Mutti 1977; 1992; Chen and Hiscott 1999; Grundvåg et al. 2014; Spychala et al. 2015; 2017b; Kane et al. 2017; Bell et al. 2018a; Fonnesu et al. 2018; Hansen et al. 2019). High- and medium- density turbidites of the lobe axis and off-axis, transition down-dip to transitional flow deposits, hybrid beds and LDTs of the lobe fringe (Figure 2.16; e.g., Walker 1966; Haughton 2003; Kane and Pontén 2012; Spychala et al. 2017; 2019; Boulesteix et al. 2019; 2020).

Lobe axis deposits, which are found towards the centre of the lobe, are characterised by relatively thick, often structureless and amalgamated packages of high net-to-gross HDTs (Figure 2.16; Prélat et al. 2009; Grundvåg et al. 2014; Terlaky et al. 2016; Spychala et al. 2017; Kuswandar et al. 2018; Dodd et al. 2019). Scouring and localised channelisation (small feeder channels) are common in the proximal part of a lobe axis (Bouma 2000; Hodgson et al. 2006; Burgreen and Graham 2014; Grundvåg et al. 2014; Stevenson et al. 2015; Terlaky et al. 2016). High-levels of erosion and entrainment of substrate result in large numbers of mudstone clasts, which may be aligned along ‘mudstone amalgamation surfaces’ or distributed throughout beds (Prélat et al. 2009; Burgreen and Graham 2014; Grundvåg et al. 2014; Terlaky et al. 2016).

Lobe off-axis positions are typically characterised by packages of structured sandstones, with localised structureless sandstones, and lower net-to-gross compared to the lobe axis (Figure 2.16; Prélat et al. 2009; Grundvåg et al. 2014; Sychala et al. 2017b; Dodd et al. 2019).

Lobe fringe deposits are the outer-most deposits of a lobe and contain the highest proportion of thin-bedded mud-rich LDTs and hybrid beds (Figure 2.16; Marini et al. 2015; Nagatomo and Archer 2015; Sychala et al. 2017 a; b; Hansen et al. 2019). The lobe fringe can be further subdivided into lateral, frontal and distal fringe (Figure 2.16; Sychala et al. 2017). Lateral fringes are characterised by thin-bedded, rippled LDTs (Figure 2.16; Prélat et al. 2009; Marini et al. 2015; Sychala et al. 2017b). Frontal fringes are hybrid bed prone (Figure 2.16; Hodgson 2009; Kane and Pontén 2012; Kane et al. 2017; Sychala et al. 2017 a; b; Fonnesu et al. 2018); because flows within the axis of lobes are more erosive, and therefore more capable of incorporating mud and rheologically transforming (Sychala et al. 2017a;b). The distal fringe is typically dominated by mud-rich deposits, with very minor thin-beds of siltstone and sandstone. These mudstones have previously been thought to represent ‘background’ deposition but have recently been shown to be heterogeneous and represent mud-rich LTDs which may extend for 10’s-100’s of kilometres into basins (Boulestex et al. 2019; 2020).

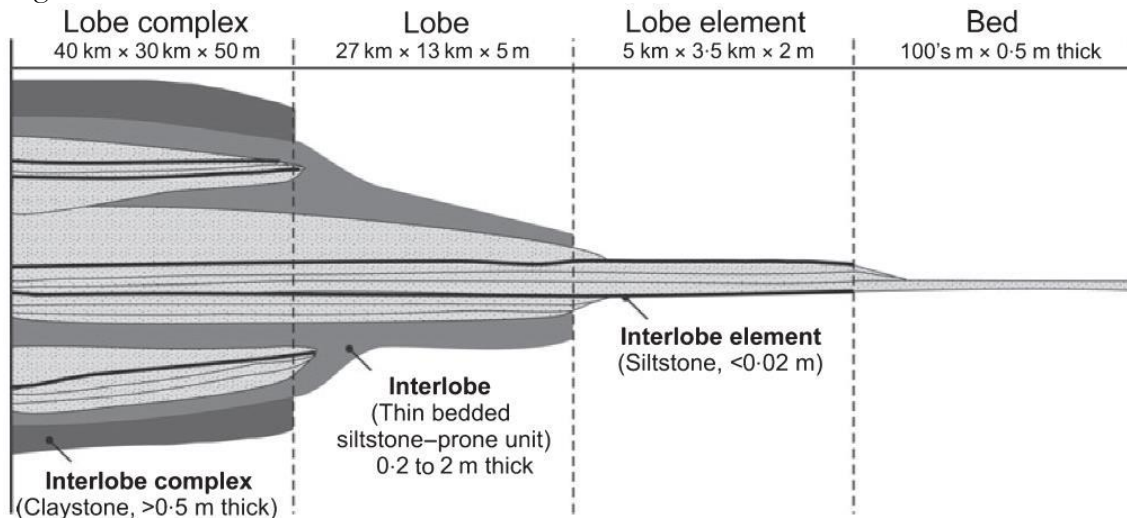


**Figure 2.17:** Hierarchy of compensational stacking of submarine lobes. Note: duration of each hierarchy from hours (bed) to 100,000s years (lobe complex), from Deptuck et al. (2008).

As with all components of deep-water systems, lobe development is system specific and controlled by: sediment supply rates (Jervey 1988; Kneller et al. 2016), sea-level, accommodation and underlying seafloor topography (Amy et al. 2004; Smith and Joseph 2004). In unconfined basins, lobes spread laterally, preferentially depositing in topographic lows adjacent to earlier lobe deposits; stacking compensationally (Figure 2.17; Deptuck et al. 2008; Prélat et al. 2009; 2010; Marini et al. 2015). If sedimentation rates are high, and maintained, lobes will grow and prograde basinward (Morris et al. 2014). If sediment supply begins to reduce, the system will retreat and back-step antecedent lobe deposits (Prélat and Hodgson 2013; Ferguson et al. 2020). Once sediment supply has been cut-off, lobe development will cease and lobe deposits will be subsequently overlain by hemipelagic deposits (Prélat et al. 2010). This could be either due to an internal (autogenic) event such as an up-dip avulsion, or an external (allogenic) event such as reduced hinterland erosion (Ferguson et al. 2020).

Multiple different hierarchical frameworks can be applied to lobes (Figures 2.17 and 2.18; Gervais et al. 2006; Pyles et al. 2007; Pr elat et al. 2009; Deptuck et al. 2008; MacDonald et al. 2011; Flint et al. 2011; Straub and Pyles 2012; Cullis et al. 2018; 2019; Sweet et al. 2020). This thesis uses the outcrop-based lobe-stacking hierarchy of Pr elat et al. (2009) from the Skoorsteenberg Formation of the Tanqua depocenter, Karoo Basin, South Africa (Figure 2.18). This work defined the hierarchy of architectural elements by characterising both sandstone-prone successions and their bounding silt- and mudstone-rich intervals, and seems to be the most widely adopted hierarchal scheme (e.g., Macdonald et al. 2011; Burgreen and Graham 2014; Grundv ag et al. 2014; Rotzien and Lowe 2014; Collins et al. 2015; Eldrett et al. 2015; Le Heron et al. 2016). Pr elat et al. (2009) describe the most fundamental building block of this scheme as the ‘bed’ which represents a single flow event. Stacks of individual event-beds are interpreted to form a lobe element (Figure 2.18). Lobe elements in turn stack to form lobes, with a sequence of genetically related lobes making up a lobe complex (Pr elat et al. 2009).

Using interlobe (mudstone rich intervals) observations Pr elat et al. (2009) suggested lobe elements were controlled by autogenic compensation and lobe complexes controlled by allogenic sediment supply shut-off. However, Boulesteix et al. (2019; 2020) shows that interlobes are composed of mm-scale event beds, and are in fact the distal or lateral extents of lobes, rather than reflecting ‘background’ conditions.



**Figure 2.18:** Hierarchical scheme for the Fan 3 lobe complex of the Tanqua depocenter, Karoo Basin, South Africa (Pr elat et al. 2009). Four main elements are presented: beds which stack into lobe elements, which make up lobes, which in turn are the building blocks of lobe complexes. The sand-rich lobe components are separated by mud-rich ‘interlobe’ components.

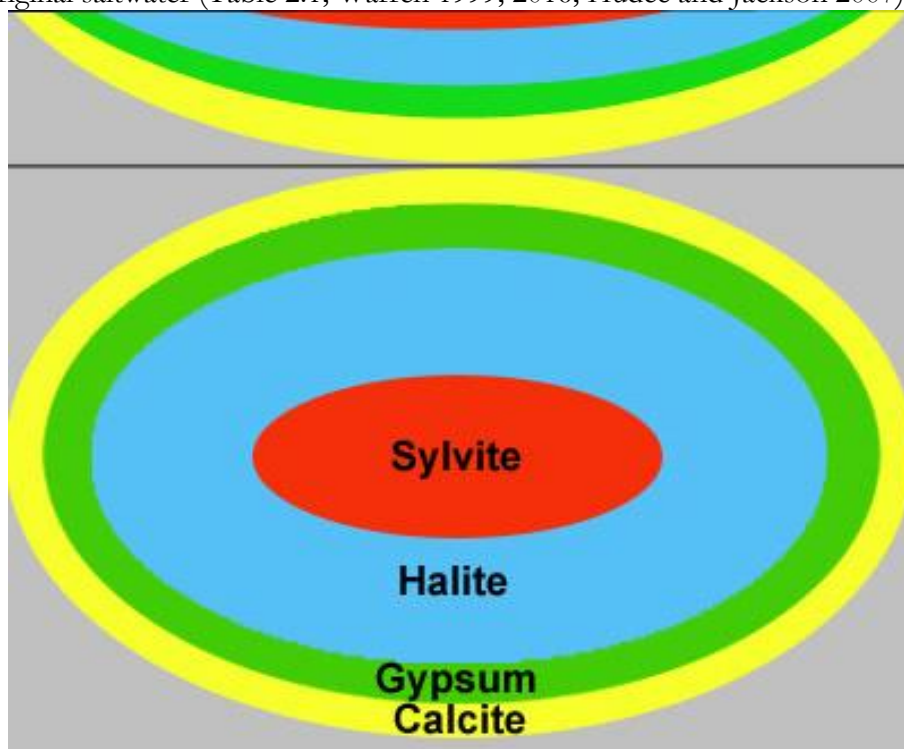
## 2.4 Salt properties and tectonics

Rock salt is a crystalline aggregate of the mineral halite (sodium chloride, NaCl) (Jackson 1997a;b). Given the rareness of ‘pure’ halite sequences in nature, most salt-tectonic literature uses “salt” for all rocks composed mostly of halite, with varying amounts of other evaporitic minerals (especially anhydrite or its hydrated form, gypsum, and K-Mg-rich salts), as well as non-evaporite rocks (e.g., carbonates or igneous clasts; Hudec and Jackson 2007).

### *Evaporitic sequences*

Evaporitic sequences are precipitated from saturated surface brines due to evaporation (Warren 1999) and are deposited in restricted basins, where outflow of water due to evaporation exceeds inflow, due to lack of sea level connection (Usiglio 1849; Clarke 1924; Warren 2006; Hudec and Jackson 2007). As such, these deposits are common in arid – semi-arid environments, at roughly 30° latitude, where cold, dry, high-pressure air descends in Hadley circulation cells (Clarke 1924; Warren 1999; Hudec and Jackson 2007).

Evaporitic facies vary laterally and are controlled by the solubility and crystallisation sequence from increasingly concentrated hypersaline waters (Table 2.1; Figure 2.19; Usiglio 1849; Clarke 1924; Valyashko 1956; Richter-Bernburg 1973; Warren 2006; 2010; Mohriak and Szatmari 2008; Babel and Schreiber 2014; Warren 2016). This typically produces a rim of evaporitic carbonates (mesohaline) which becomes increasingly magnesium-rich with increasing salinity and surrounds a rim of gypsum (penesaline), which in turn, encases a rim of halite (supersaline), which surrounds a central zone of potassium or magnesium sulphates and chlorides (Bittern salts, e.g., sylvite, carnallite, polyhalite, and tachyhydrite; Table 2.1; Figure 2.19). Halite begins to precipitate at seawater concentrations of 340-360‰ and bittern salts finally precipitate from brines concentrated to 70-90 times the original saltwater (Table 2.1; Warren 1999; 2016; Hudec and Jackson 2007).



**Figure 2.19:** Idealised evaporitic basin in cross-section and plan view showing the order and different types of salt precipitated in a radial nature from brines (Warren 2006).

**Table 2.1:** Expected evaporite mineral crystallisation sequence in increasingly concentrated hypersaline solutions, responsible for the radial nature of evaporitic mineral precipitation from what was originally seawater (Warren 2006; 2010).

	Brine stage	Mineral precipitate	Salinity (%) (onset of precipitation)	Degree of Evaporation
Hypersaline (>35% salinity)	Mesohaline	Alkaline earth carbonates	> 60%	1.5-3x
	Penesaline	Gypsum/Anhydrite(CaSO <sub>4</sub> )		
		CaSO <sub>4</sub> (+- Halite)	>150%	5-6x
	Supersaline	Halite (NaCl)	>350%	10-11x
Bittern Salts (K-Mg salts)		Extreme and variable	> 60-70x	

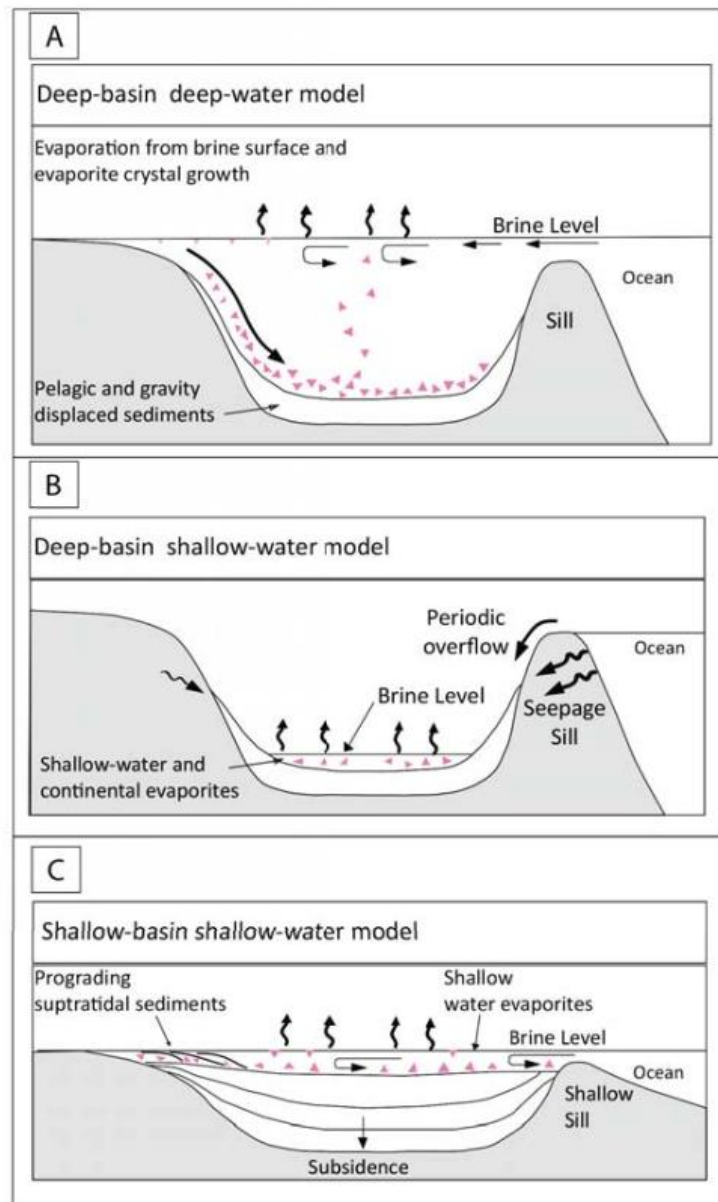
There are three end-member models (Figure 2.20) for the deposition of ancient salt sequences, which now form global salt basins (Figure 2.3). These models (Figure 2.20) highlight the role of basin configuration and depth, and require specific conditions over geological time scales (i.e.,

long-lived periods with an arid climate and isolation from the open ocean, where outflow exceeds inflow (Schmalz 1969; Hsü 1972; Taylor 1990; Warren 2006; Jackson and Hudec 2017).

The deep-basin deep-water model (Figure 2.20A) assumes an isolated deep basin largely filled with brine, which is separated from the ocean by a substantial topographic barrier (10s-100s m tall), preventing free flow of sea water between the open ocean and the basin (Warren 2006). The brine level is above the topography (sill) and thick deposits of certain minerals (e.g., gypsum) occur due to seaward escape of some of the brine, allowing the specific concentration of brine to be maintained for evaporite precipitation.

The deep-basin shallow-water model (Figure 2.20B) assumes that evaporative drawdown occurs when brine level is reduced below the level of the topographic barrier (sill), 100s–1000s m below sea level (Warren 2006). Water interchange with the open ocean occurs by seepage through the barrier or by periodic flow over it. Thick evaporite basins can accumulate in these settings due to continued subsidence (Jackson and Hudec 2017).

The shallow-basin shallow-water model (Figure 2.20C) assumes that the thick accumulations of evaporites occur in a shallow, restricted basin with little topographic relief due to continued subsidence on the basin floor (Warren 2006; Jackson and Hudec 2017). This can occur within shallow bodies of brine or within saline mudflats (Warren 2006).



**Figure 2.20:** End-member models for the deposition of ancient salt sequences, such as the Louann (Gulf of Mexico) and the Zechstein (NW Europe). From Warren (2006).

### **Properties of salt**

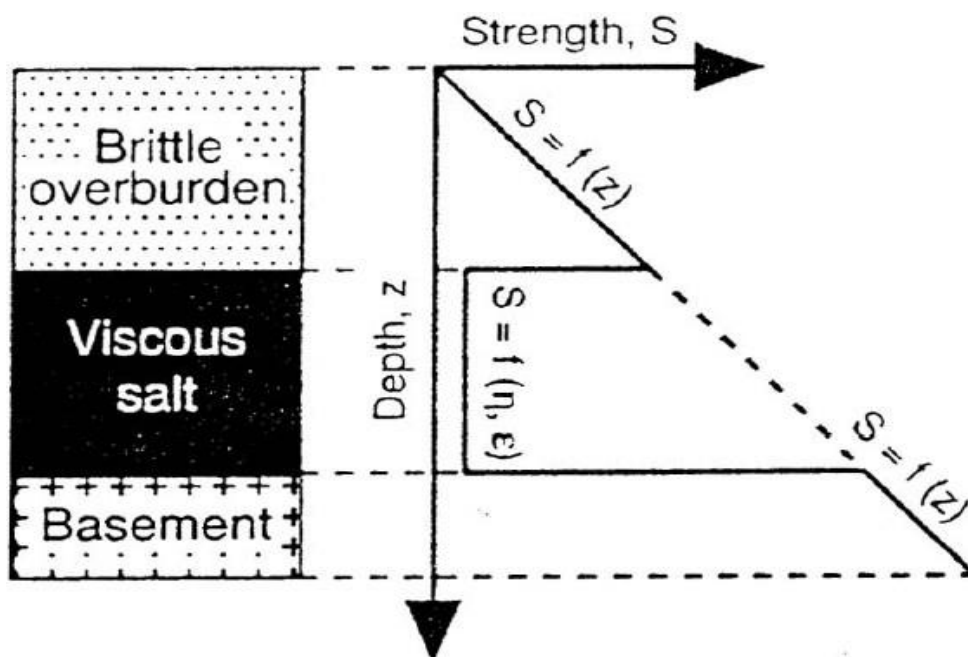
The physical properties of evaporites make them fundamentally different from other sedimentary rocks, and give rise to their growth and evolution via ‘salt tectonics’ (Table 2.2; Figures 2.21 – 2.24; Jackson and Hudec 2017). Salt is mechanically weak and unstable and tends to flow like a viscous fluid (at geologically rapid strain rates) under gravitational forces when it experiences slopes with  $<0.5^\circ$  dip, due to its low density ( $2.16 \text{ g/cm}^3$ ; halite) and negligible yield strength (Warren 2006; Hudec and Jackson 2007; Archer et al. 2012; Jackson and Hudec 2017). Salt behaves as a non-Newtonian fluid (viscosity varies with stress; Figure 2.24), such that there is no minimum stress below which it will not flow (Jackson and Talbot 1986). Therefore, there is no critical minimum overburden or minimum salt thickness necessary for salt to move, although these factors will impact the rate at which salt will move.



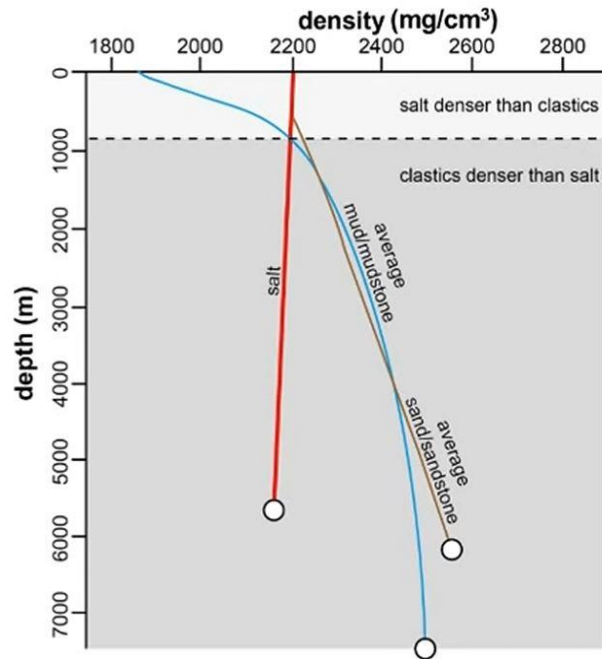
Being crystalline, salt is virtually incompressible, meaning that it does not change density with depth when it is compressed by the overburden, and that the shear strength of salt remains constant with depth (Figure 2.21; Vendeville and Jackson 1992 a; b). Therefore, it is less dense than most carbonates and all moderately to fully compacted siliciclastic rocks once buried beneath an overburden of at least 1000 m (Figures 2.22 and 2.24A). This buoyancy contrast, driven by the density inversion between the salt and overburden, can trigger upwards movement of salt into structures (Rommelts 1995; 1996; Taylor 1990; 1998; Hudec and Jackson 2007; Jackson and Hudec 2017). Due to its rheology and incompressibility salt is much weaker than other lithologies under both tension and compression (Figure 2.23; Jackson and Vendeville 1994), it can flow at low temperatures, for long periods and it is thermally conductive (Figure 2.24; Jackson and Hudec 2017).

**Table 2.2:** Various physical properties of halite (rock salt) compared to quartz and ice (Hudec and Jackson 2017).

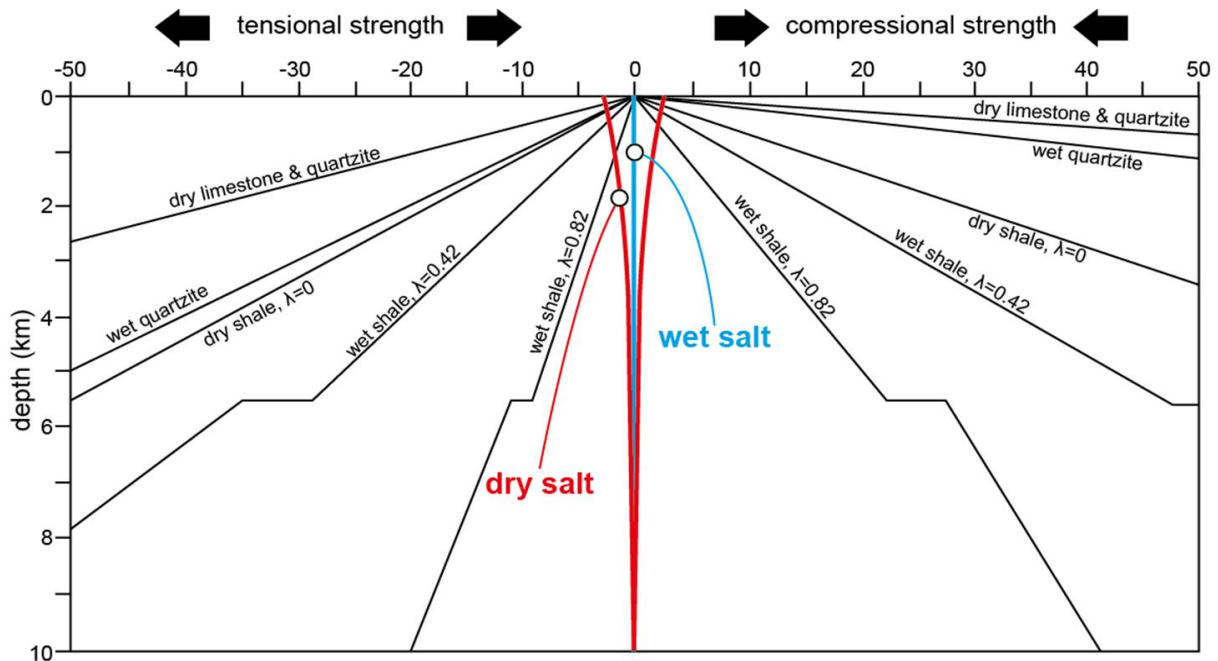
Property	Halite	Quartz	Ice
Density	2,160 kg/m <sup>3</sup>	2,650 kg/m <sup>3</sup>	920 kg/m <sup>3</sup>
Bulk modulus	22 GPa	37 GPa	9 GPa
Young's modulus	29 GPa	72 GPa	9 GPa
Rigidity (shear) modulus	11 GPa	38 GPa	4 GPa
Poisson's ratio	0.31	0.17	0.33
Compressive strength	24 MPa	1,100 MPa	4 MPa
Tensile strength	2 MPa	50 MPa	1 MPa
P-wave acoustic velocity	4,200 m/s	5,800 m/s	3,800 m/s
S-wave acoustic velocity	2,400 m/s	3,750 m/s	3,100 m/s
Thermal conductivity	6.7 W/m.K	1.4 W/m.K	2.2 W/m.K
Thermal diffusivity	$3.6 \times 10^{-6}$ m <sup>2</sup> /s	$0.9 \times 10^{-6}$ m <sup>2</sup> /s	$1.3 \times 10^{-6}$ m <sup>2</sup> /s
Thermal expansivity (linear)	$42 \times 10^{-6}$ /K	$0.6 \times 10^{-6}$ /K	$23 \times 10^{-6}$ /K
Melting point	801 °C	1,670 °C	0 °C
Boiling point	1,466 °C	2,230 °C	100 °C



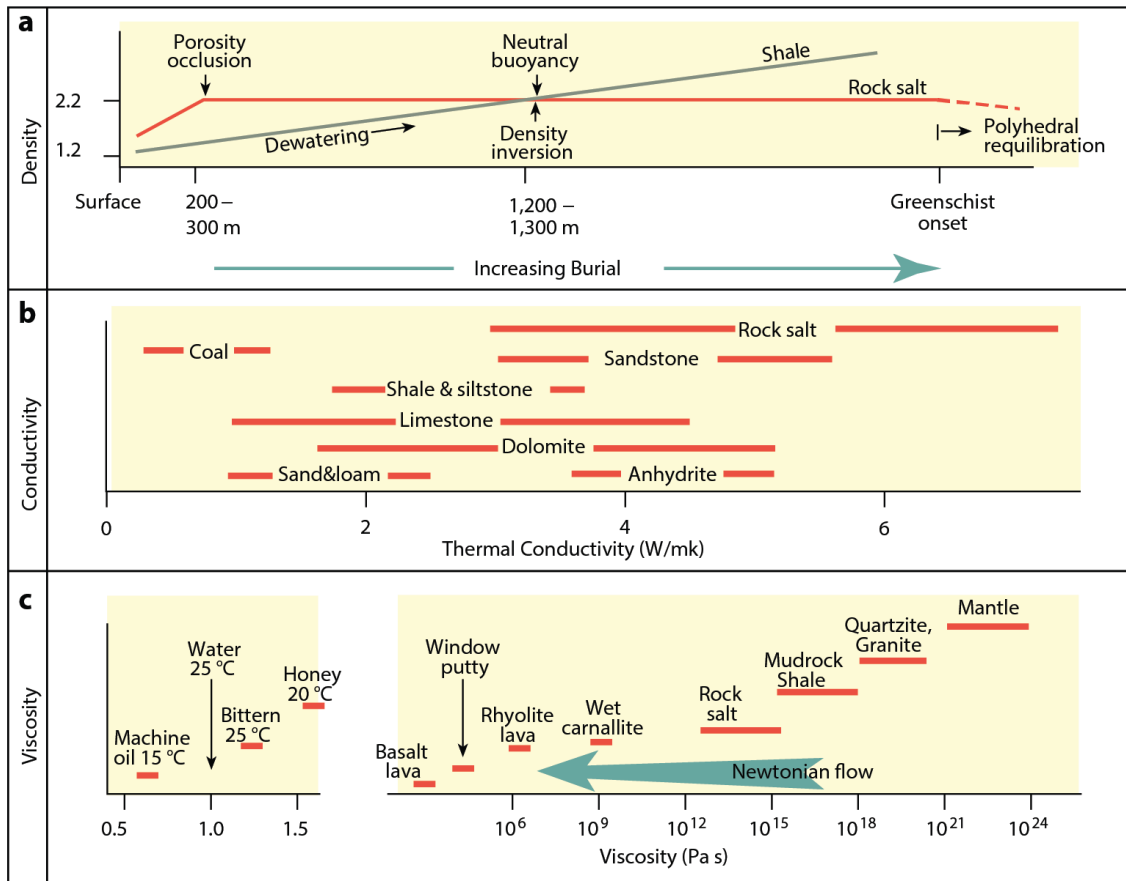
**Figure 2.21:** Depth versus strength plot for overburden, salt and basement. Note: in the overburden and basement strength increases with depth due to compression and reduction of porosity. Due to salt's crystalline nature it remains at a constant strength (very weak) with increased depth (Vendeville and Jackson 1992a;b; Hudec and Jackson 2007).



**Figure 2.22:** Depth versus density plot for salt and siliciclastic rocks (sandstone and mudstone). Due to its relative incompressibility, salt is higher density than uncompacted siliciclastic units (sand and mud) until it is buried beneath ~1000 m overburden, when the siliciclastic rocks become denser due to compaction with depth and salt remains a consistent density due to its incompressibility (Jackson and Hudec 2017).



**Figure 2.23:** Comparison of tensional and compressional strengths of dry and wet salt with equivalent dry and wet sedimentary rocks and sediments. Note dry salt is slightly stronger than wet salt, which has a negligible strength of ~0.01 MPa (Jackson and Vendeville 1994).

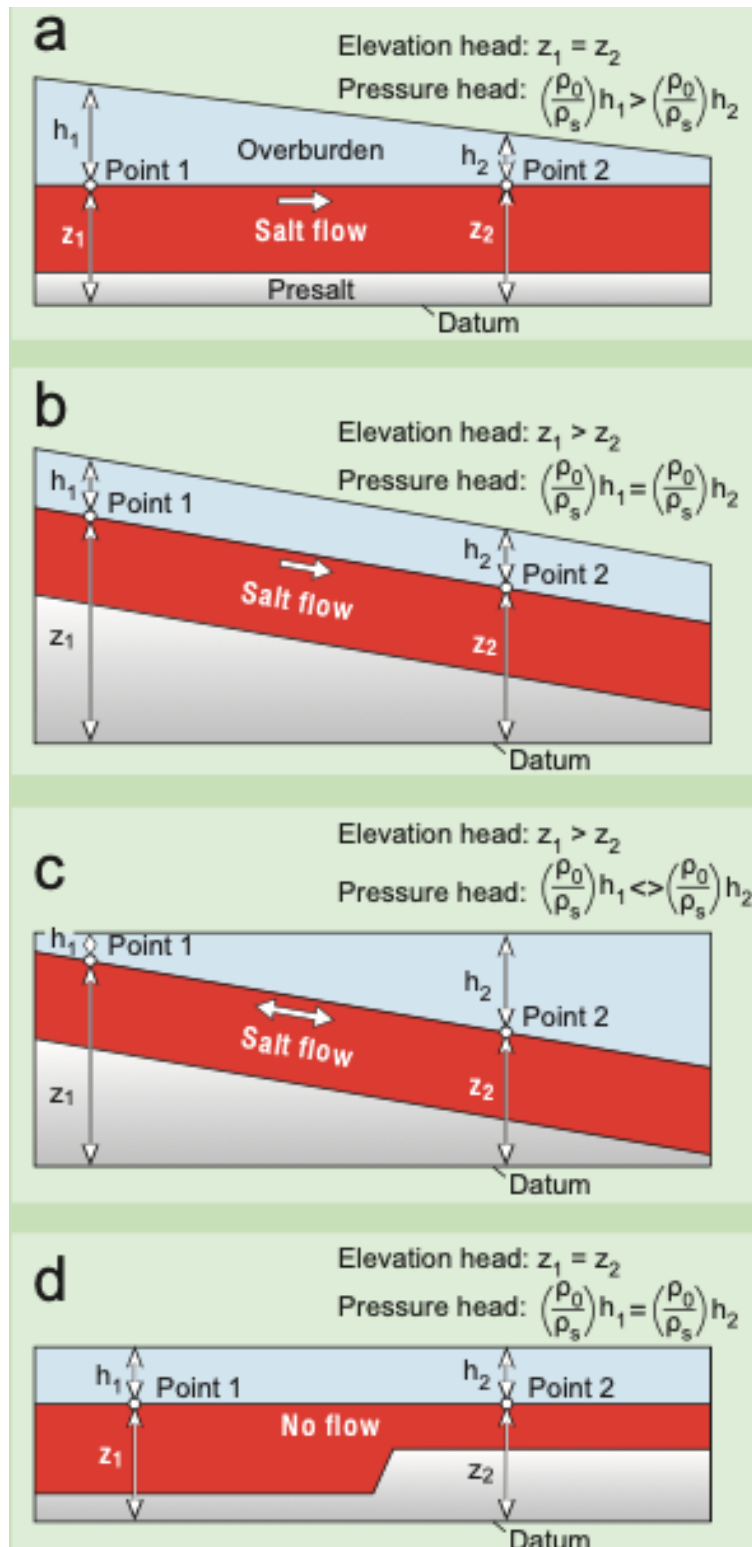


**Figure 2.24:** Physical properties of rock salt (halite) compared to other lithologies. A) Density changes with burial, note the density inversion between shale and rock salt at 1200-1300 m. B) Thermal conductivity, note the broad range dependent on mineralogy but overall high conductivity compared to other sedimentary rocks. C) Viscosity (Warren (2016)).

### Salt tectonics

“Salt tectonics” is the term used to describe tectonic deformation involving bodies of halite or other evaporites (Hudec and Jackson 2007; Warren 2016). Deformation in salt tectonics includes lateral and vertical flow, trans-stratal movement, pillowing and diapirism of evaporites, which create complex and variable structures (Mrazec 1907; 1910; Talbot 1978; 1995; Davis and Engelder 1987; Vendeville and Jackson 1992a;b; Jackson and Talbot 1991; Weijermars et al. 1993; Jackson and Vendeville 1994; Jackson et al. 1994; Jackson 1995; 1997; Coward and Stewart 1995; Peel et al. 1995; 2020 Nilsen et al. 1995; Rowan et al. 1999; 2003; 2004; Giles and Lawton 2002; Hudec and Jackson 2004; 2006; 2007; Gaullier and Vendeville, 2005; Sellier and Vendeville, 2009; Fuchs et al. 2011; Giles and Rowan 2012; Dooley et al. 2013; 2015; 2020; Rowan 2014; 2020 Rowan et al. 2016; Jackson and Hudec 2017; Duffy et al. 2017; Ferrer et al. 2017; Pichel et al. 2017; 2018; 2019; 2020; Hamilton-Wright et al. 2019). Two principles summarise salt tectonics: 1) salt is very weak and incompetent in the subsurface and; 2) it is driven by differential loading (Figure 2.25), making it a relatively passive process (Jackson and Vendeville 1994; Rowan et al. 1999; Hudec and Jackson 2007). Differential loading (Figure 2.25) drives salt flow, whilst the overburden strength and boundary friction within the salt layer resist salt flow (Hudec and Jackson 2007). Generally, it does not matter whether the overburden is of lesser, equal or greater density than the salt; if driving forces are sufficient to overcome resisting forces, then salt will flow. The flow of salt from areas of high load is termed “salt expulsion” (Hudec and Jackson 2007).

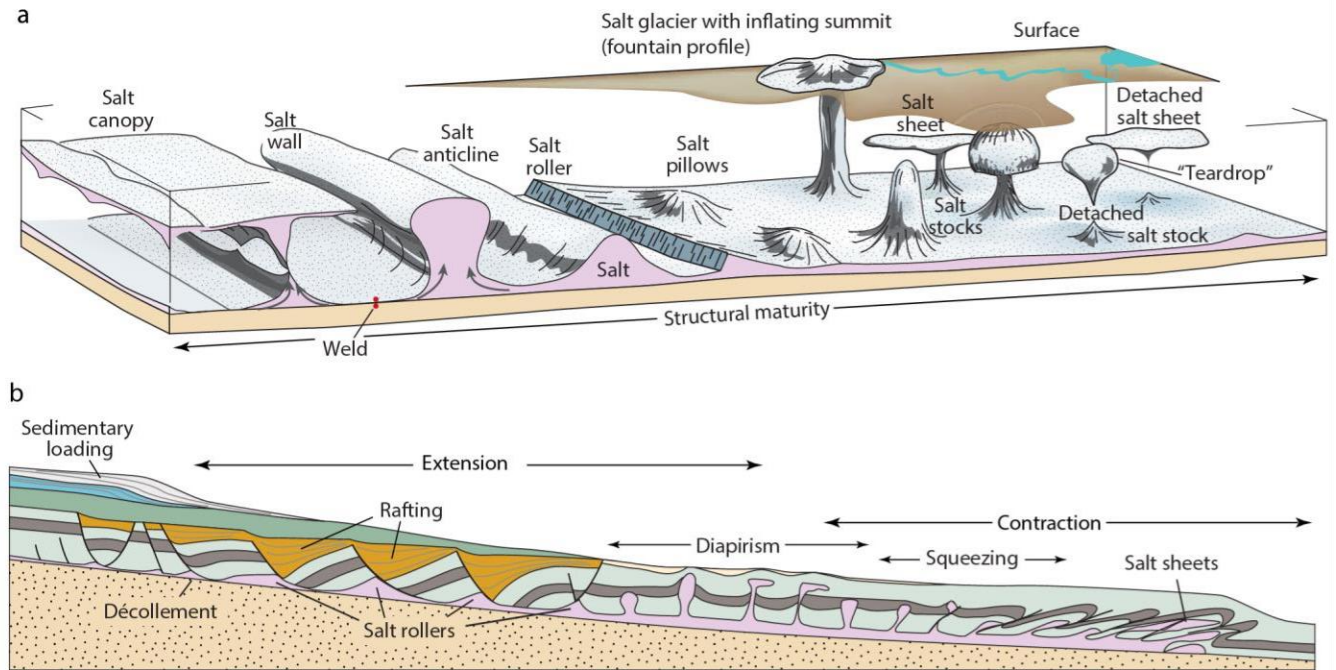
Three types of loading can drive salt flow: gravitational loading, displacement loading and thermal loading (Figure 2.25). These are driven by differences in pressure head and/or elevation head (Figure 2.25). Depth of salt burial, geometry of the salt body, geologic setting and thermal conditions of the salt determine which of the three types of loading is most likely to occur (Hudec and Jackson 2007). Gravitational loading is produced by a combination of the weight of rocks overlying the salt and the gravitational body forces within the salt. Salt flows in response to hydraulic head gradients, from areas of high head to low head (Kehle 1970; 1988). Conversely, if the hydraulic head is constant everywhere the salt remains at rest. Displacement loading results from the forced displacement of one boundary of a rock body relative to another (e.g., Suppe 1985). In salt tectonics, this type of loading occurs when the flanks of a salt body move toward or away from one another during regional shortening or extension. This type of displacement is common where basins with pre-existing salt structures are deformed because the weak salt structures typically focus regional strain (Hudec and Jackson 2007). Thermal loading results from volume changes caused by changes in temperature. Hot salt expands and becomes buoyant, producing intra-salt convection (Talbot 1978; Talbot et al. 1982; Jackson et al. 1990).



**Figure 2.25:** Processes driving salt flow inferred from hydraulic heads. A) A laterally varying overburden thickness above a horizontal, tabular salt layer produces a pressure head gradient from Point 1 to Point 2 but no elevation head gradient. Salt will flow from left to right along the pressure head gradient. The load variation may be produced by sedimentation (e.g., a river delta) or deformation (a stack of thrust slices at the left end of the section) or by erosion. B) A uniform overburden thickness above an inclined, tabular salt layer produces an elevation head gradient from Point 1 to Point 2 but no pressure head gradient. Salt will flow from left to right down the elevation head gradient. C) Salt that could be driven either way, depending on whether the elevation head gradient is more or less than (denoted by “<>”) the pressure head gradient. D) A uniform overburden thickness above a flat-lying salt layer produces neither elevation nor head gradients, even though the salt thickness varies. Salt remains at rest because there is no hydraulic head gradient (Hudec and Jackson 2007; Jackson and Hudec 2017).

Salt tectonic deformation is fundamentally governed by regional (plate) tectonics (Vendeville and Jackson 1992a; 1992b; Davison et al. 2000; Fossen 2010). During extension, salt's lateral flow and sliding carries along its overburden, whereas in compression, salt acts as a décollement (detachment) (Figure 2.26; Vendeville and Jackson 1992a; 1992b; Davison et al. 2000). The dynamic nature of salt tectonic systems (salt presence, salt thickness, basement involvement, overburden thickness) and the rock properties inherent to evaporites result in a complex suite of controls on structural styles of deformation which operate locally to basin-wide (Jackson and Talbot 1991; Weijermars et al. 1993; Jackson and Vendeville 1994; Jackson et al. 1994; Jackson 1995; 1997; Coward and Stewart 1995; Peel et al. 1995; Hudec and Jackson 2004; 2006; 2007; Pichel et al. 2017; 2018; 2019; 2020; Grant et al. 2019 a;b; 2020). Hence, deformation and structural styles that characterise one domain (i.e., up-dip margin) may differ to those elsewhere (i.e., down-dip basin) or even more locally within the domain itself (i.e., along the same margin; Figure 2.26; Rowan et al. 2004; Hudec and Jackson 2007; Fossen 2010; Jackson and Hudec 2017).

Salt movement driven by gravity is referred to halokinesis (Trusheim 1957; 1960). Sedimentary loading (rates and sediment type), tectonic strain and salt flow rate form some of the important controls on halokinesis. Halokinesis requires initiation, typically a disturbance (differential loading or localised faulting) above or at the base of salt (Geluk et al. 2007; Fossen 2010). Movement can also be retarded or accelerated by regional tangential forces (Jackson and Talbot 1986). In a typical gravity-driven, salt tectonic passive margin, within the updip “extensional domain” thin-skinned extension occurs, with salt rollers forming in the footwalls of listric normal growth faults, and rafts, turtleback anticlines and triangular-shaped salt walls also being common (Figure 2.26; Mrazec 1907; Demercian et al. 1993; Fort et al. 2004; Rowan et al. 2004; Hudec and Jackson 2007; Fossen 2010; Mohriak et al. 2009; 2012; Oluboyo et al. 2014; Jackson and Hudec 2017). Salt welds form where salt is thin or absent (Jackson et al. 2019). In the central, or “translational domain” salt pillows, salt diapirs, salt welds and salt withdrawal minibasins occur (Figure 2.26; Jackson 2012; Mohriak et al. 2012; Jackson et al. 2014). In the downdip “compressional domain” thin-skinned shortening occurs, the salt is relatively thick and characterised by salt-cored folds and anticlines, asymmetric salt walls, intra-salt thrusts, salt nappes and allochthonous salt tongues and canopies (Figure 2.26; Cobbold and Szatmari 1991; Demercian et al. 1993; Brun and Fort 2004; 2011; Fort et al. 2004; Mohriak et al. 2009; Fiduck and Rowan 2012; Adam et al. 2012; Jackson et al. 2014; 2015). This thesis focusses on how deep water SGFs and their deposits interact with salt diapirs, salt walls and salt stocks. Such structures have discordant interactive contacts with their encasing sedimentary strata, often displaying geometries that are a response to salts' inherent mechanical weakness (Jackson and Hudec 2007).

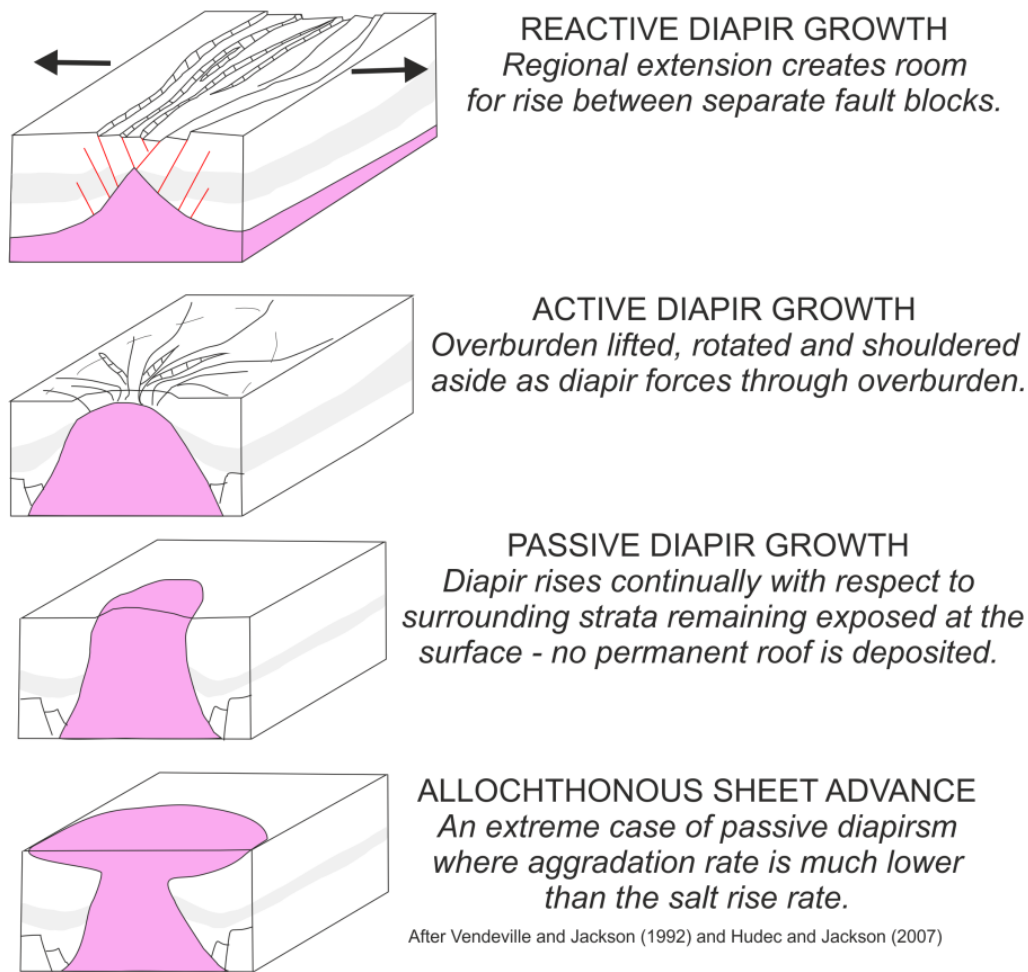


**Figure 2.26:** Salt structures, after Fossen (2010). A) Morphological classification of the different structures, derived from cross-sectional shape and map view geometry, and deformation styles that define salt distribution in salt basins (Jackson and Talbot (1986)). Structural maturity of features increases left and right from the central part of the diagram. Linear structures on the left commonly form by regional extension or shortening. Equant or vertical (plug) structures tend to form by *balokinesis* (driven by gravity). B) Salt morphologies placed in the typical evolutionary framework of salt structures in a halokinetically deforming passive-margin setting, typified by updip extension and downdip compression, and a central translational domain characterised by diapirism (Jackson and Hudec 2017).

## 2.5 Salt diapirs

Salt stocks and salt walls are the most classic of salt structures. They rise as subterranean mountains from the basin floor and are remarkable for their size: some stocks are more than 10 km tall, and some walls are more than 100 km long (Jackson and Hudec 2017). In the Precaspian basin alone there are 1,800 named stocks and walls (Pichel and Jackson 2020). These structures are all “diapirs”, which are often vertical, geological structures that consists of mobile, ductile material that was forced into brittle surrounding rocks (piercing or appearing to pierce their overburden) usually by the upward flow of salt from a source layer (Jackson and Hudec 2017). The term “salt diapir”, first proposed in the Romanian Carpathians by Mrazec (1907) is widely used to describe all salt structures with discordant contacts with their overburden, regardless of processes of initiation and growth (Harris and Veatch 1899). Salt diapirs can be subdivided into salt domes, salt stocks and salt walls (Harris and Veatch 1899). Salt domes have rounded planforms and can be cored by either a diapir or a salt pillow (Figure 2.26; Harris and Veatch 1899; Stewart 2006; Yin and Groshong 2007). Salt stocks are plug-like bodies with equant planforms, whilst salt walls are more elongate; the usage of stocks and wall is somewhat gradational (Hudec and Jackson 2011; Jackson and Hudec 2017). In order for buried salt to be emplaced into its overburden as a diapir, the rock previously occupying that space must be removed or displaced (Vendeville and Jackson 1992 a; b; Hudec and Jackson 2007); this typically occurs via a combination of reactive, active and passive diapirism (Figure 2.27; Vendeville and Jackson 1992 a; b; Jackson and Hudec 2017). Viscous evaporites cannot pierce through thick overburden and therefore diapiric growth can initiate in two ways: either shortly after deposition when the overburden is thin and unconsolidated or later in evolution due to tectonics triggering diapir growth through thinning of the overburden (Jackson and Vendeville 1994; Jackson et al. 1994). Many diapirs initiated first by regional compression or extension (reac-

tive diapirism), subsequently experienced a rapid stage of active diapirism which permitted piercement of the roof, allowing the diapir to evolve passively (Nettleton 1934; Jackson et al. 1990; Talbot et al. 1992; Jackson and Vendeville 1994; Jackson et al. 1994; Hudec and Jackson 2007; Rowan and Giles 2021). If salt reaches the surface, it can continue to rise by passive diapirism, in which the diapir grows as sediments accumulate around it by ‘downbuilding’, whereby the diapir top remains at a fixed level with respect to flanking strata, which sink as more sediment is added (Barton 1933; Jackson and Talbot 1986; 1991; Jackson et al. 1988; Rowan and Giles 2021). A rapidly rising passive diapir may spread over the sediment surface to form an allochthonous salt sheet (Figure 2.27; Jackson and Talbot 1989 a; b; Hudec and Jackson 2007; 2011; Dooley et al. 2013; Jackson and Hudec 2017; Rowan 2020).



**Figure 2.27:** Classical evolutionary stages of diapirs. Diapirs do not necessarily progress through all of these stages. Structural maturity depends on salt availability, total amount of extension and relative ratio of extension and sedimentation (Vendeville and Jackson 1992a; Hudec and Jackson 2007).

### **Reactive diapirism**

Regardless of overburden density, diapirs commonly initially pierce their overburden “reactively” in response to regional extension (Vendeville and Jackson 1992a). During regional extension, the overburden is thinned and fractured, creating grabens and half-grabens above salt layers. Analogue modelling has shown that the locations of salt diapirs in extensional settings are governed by the location of cover fault systems (Vendeville and Jackson 1992b), demonstrating that an extension of at least 20% of the cover ( $\beta = 1.2$ ) via normal faulting is needed for diapirs to be initiated. This, often heterogeneous, thinning creates a differential load and weakens the overburden by fracturing and faulting (Vendeville and Jackson 1992a). Salt walls pressurised by overburden



load on adjoining areas begin to rise below the thinned overburden and salt fills the space created by extensional thinning and separation of overlying fault blocks (Figure 2.27; Link 1930; Cloos 1939; Parker and McDowell 1951;1955; Withjack and Scheiner 1982; Withjack and Callaway 2000; Sims et al. 2013; Jackson and Hudec 2017). The hanging wall of an initial fault sinks into the source layer until it is resisted by increasing pressure forces and bending resistance. New faults form repeatedly nearer the axis of the graben. The dwindling central fault block sinks while the diapir rises below it (Vendeville and Jackson 1992a). In this way, as faults slice up the graben, the underlying salt begins to rise up the axis of the graben, filling the space created by thinning of sediment and separation of fault blocks, and rising as a triangular diapir (Figure 2.27; Bowie 1927; Vendeville and Jackson 1992 a; b). This type of salt upwelling is termed reactive diapirism, and is fundamentally controlled by regional extension (Vendeville and Jackson 1991). For the geological timescales and temperatures of the buried salt in sedimentary basins, Price and Cosgrove (1990) calculate that lateral salt movement sufficient to feed reactive and active diapirs will occur if the salt layer is in excess of 500 m thick. Most diapir provinces worldwide initiated during phases of basement-involved or detached extension (Jackson and Vendeville 1994). This fact suggests that regional extension is the primary trigger for salt diapirism (Jackson and Vendeville 1994; Hudec and Jackson 2007). Swarms of normal faults adjoin the deep flanks of many diapirs, reflecting their early extensional histories (Vendeville and Jackson 1991; 1992a; b; Jackson and Vendeville 1994; Hudec and Jackson 2007; 2011). The width of a reactive diapir's base records the amount of extension. At the base, extension is accommodated entirely by flow of salt. Midway up the diapir, extension is partly by flow of salt and partly by faulting. Above the diapir, extension is entirely by faulting (Bally 1981;1982; Jackson and Hudec 2017).

The key diagnostic features of reactive diapiric walls are: a triangular shape, pointed crest and a crestal graben or half-graben, which dominate the map view. An axial trench in the floor of the graben is bounded by fault terraces that step upward and outward to the upwardly flexed margins of the graben. Faults are subparallel but may anastomose (Cloos 1955; 1968; Withjack and Scheiner 1982; Vendeville and Jackson 1992; Hudec and Jackson 2007; Sims et al. 2013; Jackson and Hudec 2017). Reactive diapirism stops whenever regional extension stops, and continues again whenever extension recommences (Jackson and Vendeville 1994). Rapid extension with low sedimentation rates leads to progressive thinning of the diapir roof, allowing the transition into active and then passive diapiric growth. Low extension and high sedimentation rates lead to diapir burial (Figure 2.28; Vendeville and Jackson 1991; 1992a; b; Giles and Lawton 2002).

### ***Active diapirism***

“Active diapirism” corresponds to intrusion of salt through the overburden which triggers doming and faulting of the diapir roof (Nelson 1989; 1991; Jackson and Talbot 1991; Vendeville and Jackson 1992 a; b; Schultz-Ela et al. 1993; Hudec and Jackson 2011; Jackson and Hudec 2017). If the diapir becomes tall enough, its roof sufficiently thinned and the graben trough deep enough, a diapir can pierce actively by lifting and shouldering aside its roof to emerge rapidly at the surface (Vendeville and Jackson 1992a). As reactive diapirism thins and weakens the overburden; eventually the roof may weaken to the point where it can be uplifted and shouldered aside by forcible rise of the underlying diapir (i.e., active diapirism; Figure 2.27). In extensional settings, this forcible rise is driven by salt buoyancy, so active diapirism will occur only if the salt is less dense than its overburden (Figure 2.22). Because active diapirism is controlled by gravitational forces acting on the salt, it continues even if regional extension stops (Vendeville and Jackson 1992a; Hudec and Jackson 2007; 2011; Jackson and Hudec 2017; Rowan 2020). Active diapirs typically break through their remaining roofs quickly and rise to the sediment surface, becoming passive diapirs (Figure 2.27).

Halokinetic active rise is influenced most strongly by sediment density, roof strength and anisotropy, and salt geometry (Schultz-Ela et al. 1993). Active rise is promoted by increasing the average density and thickness of sediments overlying the source layer, which increases the driving force by decreasing thickness and density of sediments above the salt structure, which decreases the resisting force (Schultz-Ela et al. 1993; Jackson and Hudec 2017). Active rise is also promoted by weak roofs, especially in faulted or unconsolidated sediment (Schultz-Ela et al. 1993; Jackson and Hudec 2017). Active rise forms two types of structures: arched roofs and upturned collars. Arched roofs result where the salt has not pierced to the surface, whereas upturned collars are evidence that a formerly active diapir once broke through to the surface (Link 1930; Cloos 1939; Parker and McDowell 1951; 1955; Hanna 1953; Cloos 1955; Atwater and Forman 1959; Bornhauser 1969; Withjack and Scheiner 1982; Davison et al. 2000; Schultz-Ela and Walsh 2002; Schultz-Ela 2003; Sims et al. 2013; Jackson and Hudec 2017).

Due to the almost synonymous usage of active and passive diapirism in the literature, Rowan and Giles (2021) proposed two specific scenarios for which active diapir rise should be used; 1) transitional active diapirism; the single, short-lived stage when the salt in a precursor structure (e.g., reactive diapir, contractional fold or thrust or salt pillow) is pressurised enough to arch, rotate aside and breakthrough its covering strata, subsequently rising by passive diapirism and; 2) contractional active diapirism (Jackson and Hudec 2017), which occurs when an inactive diapir, buried beneath a relatively thick roof is squeezed during shortening, thereby uplifting (and possibly breaking through) the roof as salt rise is rejuvenated (Vendeville and Nilsen 1995; Jackson and Hudec 2017; Rowan and Giles 2021).

### ***Passive diapirism***

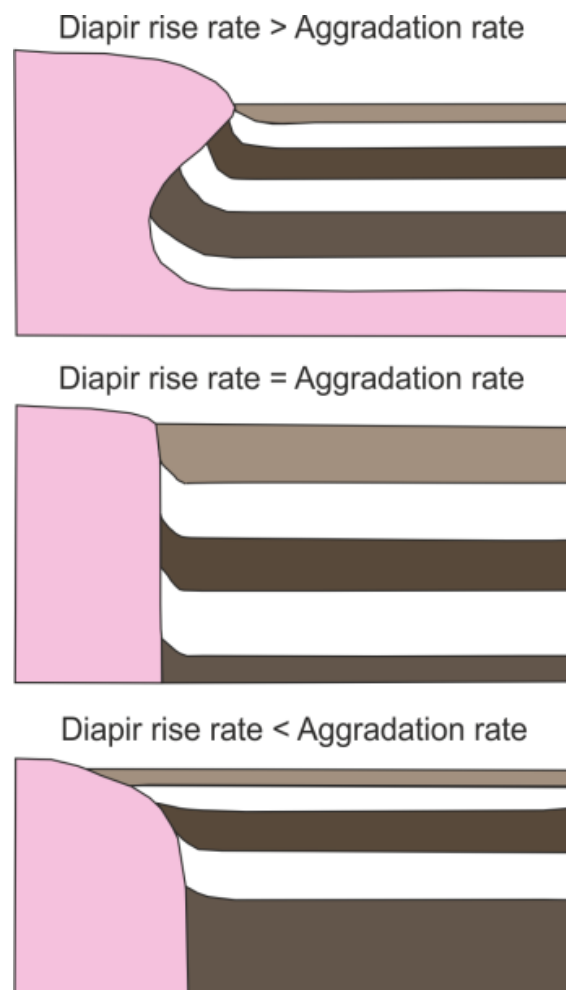
During subsequent passive piercement, a diapir widens by regional extension and increases in relief by downbuilding during concurrent sedimentation (Figure 2.27; Barton 1933; Jackson and Talbot 1991; Hossack 1995; Hudec and Jackson 2007; Jackson and Hudec 2017; Rowan and Giles 2021). In passive diapirism, salt may rise through thousands of meters of section without ever having to forcibly break through anything more than transient sedimentary layers (Hudec and Jackson 2007).

Most of the worlds tall salt domes and walls spent the majority of their evolution as passive diapirs (Hudec and Jackson 2011; Rowan and Giles 2021). Diapirs can bypass the reactive and active modes of growth, and commence with passive diapirism if the overburden is thin and uneven (Vendeville and Jackson 1992a). Passive diapirism may occur in any tectonic setting (Hudec and Jackson 2011); however, for passive diapirism to begin, either part of the salt layer must remain exposed during initial burial of surrounding areas, or the salt must break through its overburden to reach the surface. This is usually achieved by earlier active diapirism and is especially likely after a long phase of reactive diapirism, where extension has established a load gradient and weakened the roof (Vendeville and Jackson 1992a). In order for a passive diapir to grow, salt within it must be pressurised enough to flow upward at the sediment surface. This pressure may be generated in at least three ways. First, if the average density of the overburden above the source layer is greater than that of salt, salt will be forced to the surface. Second, the salt diapir may be laterally shortened, causing salt to rise at the surface by displacement loading. Third, salt may be loaded by sedimentary topography, for example, near the toe of a continental slope or within a graben which has topographic relief (Vendeville and Jackson 1992; Jackson and Vendeville 1994; Hudec and Jackson 2007; 2011; Giles and Rowan 2012; Jackson and Hudec 2017; Rowan and Giles 2021).

In most depositional environments, sedimentation, and thus sedimentary loading, is episodic, so the diapir is periodically buried beneath a sedimentary veneer during rapid sedimentation. Passive diapirs thus have three growth modes: 1) true passive diapirism, when the salt is emergent; 2)

temporary diapir burial after sediments aggrade faster than the diapir crest rises; and 3) active piercing as aggradation is outpaced by diapiric rise (Jackson et al. 1988; 1994). These three processes are repeated as cycles that keep the crest of the diapir at or near the sediment surface during growth (Nelson 1989; 1991; Jackson and Talbot 1991; Rowan et al. 2003; Giles and Rowan 2012; Jackson and Hudec 2017).

Sedimentary deposits accumulate around, and wedge out above diapirs (Figure 2.28; Giles and Lawton 2002; Rowan et al. 2003). The geometry of the overburden is therefore determined by the ratio of sediment accumulation rate and diapir rise (Figure 2.28; Vendeville and Jackson 1991; Jackson et al. 1994; Talbot 1995; Giles and Lawton 2002; Rowan et al. 2003; Karam and Mitra 2016). Where rates are equal, diapirs and their deposits grow vertically; when the diapir rises are faster than the surrounding sediment, salt may reach the basin floor and spread laterally and when sedimentation rate outpaces diapir rise, successions onlap and progressively cover the outcropping salt, which may become completely buried (Figure 2.28; Giles and Lawton 2002).



**Figure 2.28:** The cross-sectional shapes of diapirs, particularly passive diapirs, are controlled by the relative rates of net diapir rise (salt rise minus erosion and dissolution) and sediment aggradation. Where diapir rise rate exceeds aggradation rate, diapirs widen upward and may ultimately form extrusive sheets. Where diapir rise rate is equal to aggradation rate, diapirs have vertical walls. Where diapir rise rate is less than aggradation rate, diapirs narrow upward and may ultimately become completely buried. Modified from Giles and Lawton (2002).

Once the salt source layer is exhausted, diapirs may fall if extension continues as they widen (Vendeville and Jackson 1992b; Hudec and Jackson 2007; Jackson and Hudec 2017). Subsequent thinned salt layers typically act as a detachment in both gravity-driven and basement-involved extension (Hudec and Jackson 2007; Fossen 2010; Dooley et al. 2013; 2015; 2020; Rowan 2020).

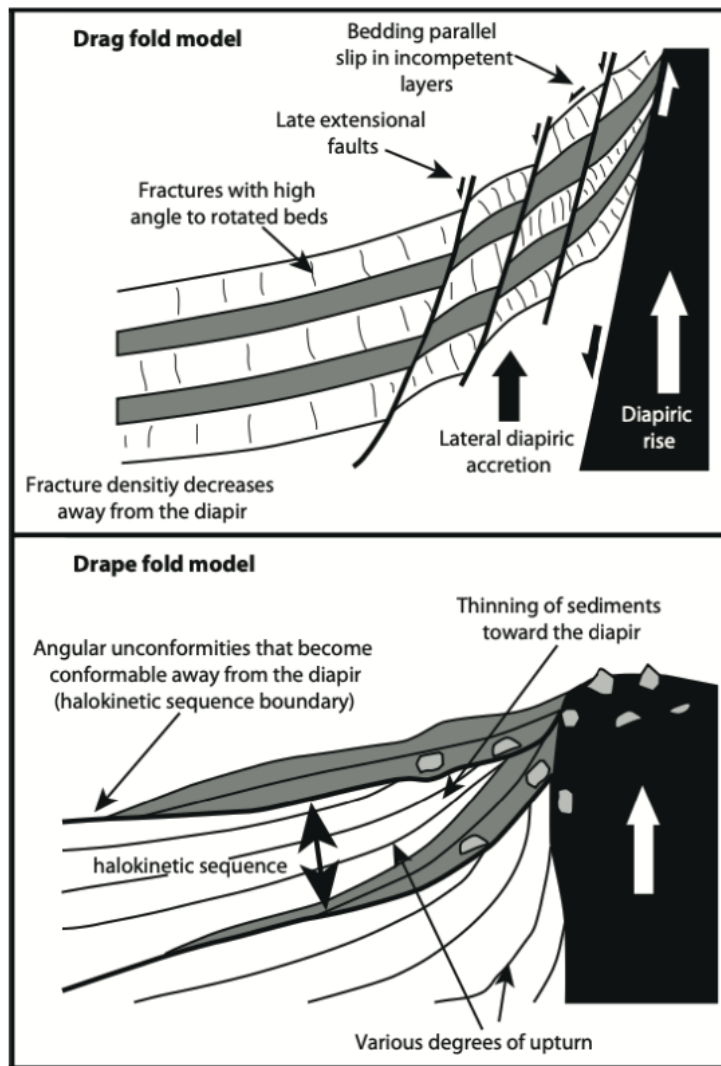
During lateral shortening, the salt's overburden may buckle. Flow of underlying salt into the lower-pressure core of a rising anticline creates a salt-cored anticline (Figure 2.26). Anticlines can form above previously undeformed salt (Bally 1981; Jones 1959; Coward and Stewart 1995) but they are especially common above pre-existing salt structures (Jones 1959; Nilsen et al. 1995; Vendeville and Nilsen 1995; Hudec and Jackson 2007; Cámara 2020). Shortening can also amplify pre-existing structures by arching their roofs (Bally 1981; 1982; Schultz-Ela et al. 1993; Hudec and Jackson 2007; Rowan 2020). During the amplification of a diapir by compression, salt may pierce its roof by some combination of crestal normal faulting, erosion, active diapirism and buoyancy.

Where pre-existing salt structures are shortened, a common structure formed is the teardrop diapir, whose upper part becomes largely detached from its source layer (Figure 2.26; Hudec and Jackson 2007; Ferrer et al. 2012; Schorn and Neubauer 2014; Pichel et al. 2017). The original ascent zone of the salt is marked only by a steep salt weld in the former 'waist' (which was pinched off during shortening), of an originally hourglass-shaped diapir (Hudec and Jackson 2007; Fossen 2010; Ferrer et al. 2012; Schorn and Neubauer 2014; Pichel et al. 2017). Most of the salt in the waist is expelled upward to promote rise of the upper part of the diapir and the arching of its roof. The lower part of the diapir remains, forming a salt pedestal in the original position of the salt diapir (Fossen 2010; Schorn and Neubauer 2014; Pichel et al. 2017; Jackson and Hudec 2017).

## **2.6 Halokinetic growth stratigraphy**

During passive diapirism the geometry of the diapir and the overlying syn-kinematic stratigraphy is much dependent on the ratio between sedimentation rate and diapir rise rate (Figure 2.28; Giles and Lawton 2002). As such, overburden deformation along diapir flanks has been widely reported (e.g., Alsop et al. 1995; 2000; Rowan et al. 2003; Stewart 2006; Hudec and Jackson 2007; 2011; Coleman et al. 2018; Cumberpatch et al. 2021b;c). Characteristics of such deformation are: steep, vertical or overturned strata; rapid thinning towards the diapir; and concentric and radial faults on diapir flanks (Alsop et al. 2000; Stewart 2006; Hudec and Jackson 2007; Carruthers et al. 2013; Poprawski et al. 2014; 2016; 2021; Coleman et al. 2018; Cumberpatch et al. 2021b;c).

Two models exist for diapir-induced overburden deformation; drag and drape folds (Figure 2.29). Drag folds involve shearing and deformation of consolidated sediments along the diapir edges and are sometimes referred to as external shear zones (Figure 2.29; Jackson and Talbot 1991; Alsop 1996; Alsop et al. 2000; 2016; Schultz-Ela 2003; Hudec and Jackson 2007; Rowan et al. 2019). Drape folds are related to deformation of unconsolidated sediment, where folding is explained by differential uplift of the diapir roof and subsidence of diapir flanks. Older strata undergo more deformation than younger strata which explains the shallowing and thickening of deposits away from the diapir as well as unconformities and slumps, which are seen to develop on diapir flanks due to gravitational instability (Figure 2.29; Giles and Lawton 2002; Rowan et al. 2003; Giles and Rowan 2012; Carruthers et al. 2013; Jackson and Hudec 2017; Pichel and Jackson 2020; Rowan and Giles 2021; Roca et al. 2021).



**Figure 2.29:** End member models for diapir growth and overburden deformation (Poprawski et al. 2014). Drag fold model (Alsop et al. 2000) and drape fold model (Giles and Lawton 2002).

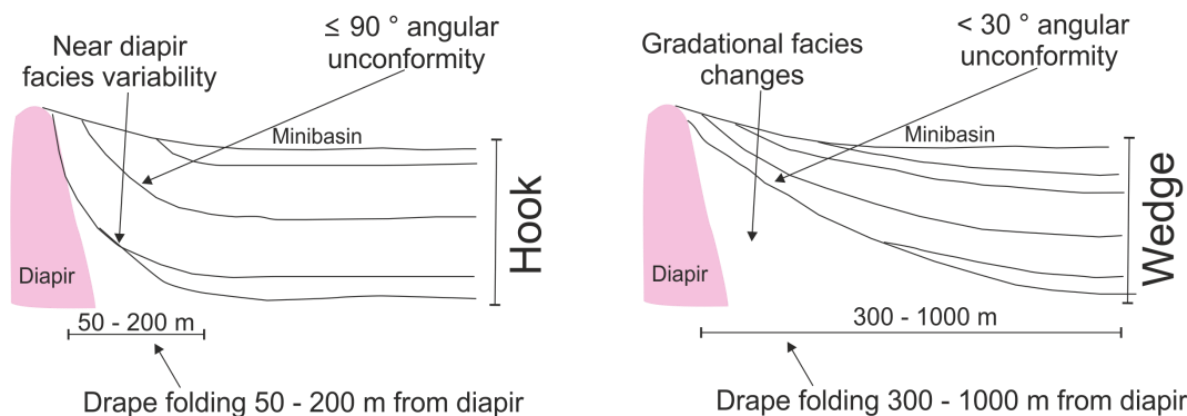
### **Halokinetic Sequences**

Drape folding controls the development of halokinetic sequences (Figures 2.30, 2.31, 2.32 and 2.33; Table 2.3; Giles and Lawton 2002; Rowan et al. 2003; Giles and Rowan 2012; Saura et al. 2014; Poprawski et al. 2014; 2016; Martín-Martín et al. 2017; Jackson and Hudec 2017; Rojo and Escalona 2018; Snidero et al. 2019; Escosa et al. 2019; Rowan and Giles 2021). Halokinetic sequences were first recognised around the El Papalote Diapir, Mexico, by Giles and Lawton (2002) who defined them as “unconformity-bound packages of thinned and deformed strata adjacent to passive diapirs”. Halokinetic sequences represent cycles of passive diapirism and minor active diapirism (more recently referred to as transitional active diapirism; Jackson and Hudec 2017; Rowan and Giles 2021) when salt periodically rises and pierces the diapir roof (Rowan et al. 2003). Halokinetic sequences are different from ‘traditional’ depositional sequences in scale and mechanisms of formation. Depositional sequences are typically basin wide whilst halokinetic sequences are localised to the area directly surrounding a diapir (they could not be traced further than 1 km at El Papalote). Depositional sequences form as the accommodation rate varies relative to the regional rate of sediment accumulation, while halokinetic sequences form as the rate of net vertical diapiric rise varies relative to the local rate of sediment accumulation (Figure 2.28; McGuinness and Hosack 1993; Jackson et al. 1994; Talbot 1995; Koyi 1998; Giles and Lawton 2002). Two end members of halokinetic sequences (Hook and Wedge; Figure 2.30; Table 2.3) are described by Giles and Rowan (2012). Hook sequences have narrow zones of deformation, high angle unconformities

and abrupt facies changes. Hook halokinetic sequences are observed when diapir rise rate exceeds sedimentation rate. Wedge halokinetic sequences occur when diapiric rise is less than sedimentation rate and are characterised by broad zones of folding, low-angle unconformities and gradual facies changes (Figure 2.30; Table 2.3). Halokinetic sequences have thicknesses and time scales equivalent to parasequence sets (Giles and Rowan 2012).

Angular unconformities form when net diapiric rise rate exceeds local sediment accumulation rate, allowing the diapir to rise to the surface and generate a steep, unstable slope. This slope commonly fails, forming a mass transport deposit (slump) overlying the sequence-bounding unconformity (Giles and Lawton 2002). If uplift and roof destabilisation are sufficient the diapir may pierce the basin floor. Increasing the sediment accumulation rate relative to diapiric rise suppresses the diapiric surface topography and is preserved as onlap and overlap surfaces (Giles and Lawton 2002). When sedimentation rate exceeds diapiric rise rate the diapir becomes buried (Figure 2.32; Giles and Lawton 2002; Rowan et al. 2003; Giles and Rowan 2012; Rowan and Giles 2021).

Perhaps confusingly, wedge-shaped stratal packages are also common at larger (multi-km) scales, and are due to variable uplift and/or subsidence associated with salt-related deformation within minibasins (e.g., Rowan and Weimer 1998; Jackson and Hudec 2017; Mianaekere and Adam 2020). These are termed “minibasin tectonostratigraphic packages” (Rowan and Giles 2021), and are explicitly different from halokinetic sequences (widths of <1 km) in that they can be multiple kilometers wide and include megaflaps (panels of deep minibasin strata extending far up the sides of steep-sided diapirs; e.g., Rowan et al. 2016; Kergaravat et al. 2017; Martín-Martín et al. 2017; Asl et al. 2019; Espurt et al. 2019). Minibasin tectonostratigraphic packages are typically independent of deformation adjacent to bounding diapirs and can be related to any combination of extension, contraction, or differential loading and subsidence (Jackson et al. 2019; Rowan and Giles 2021).



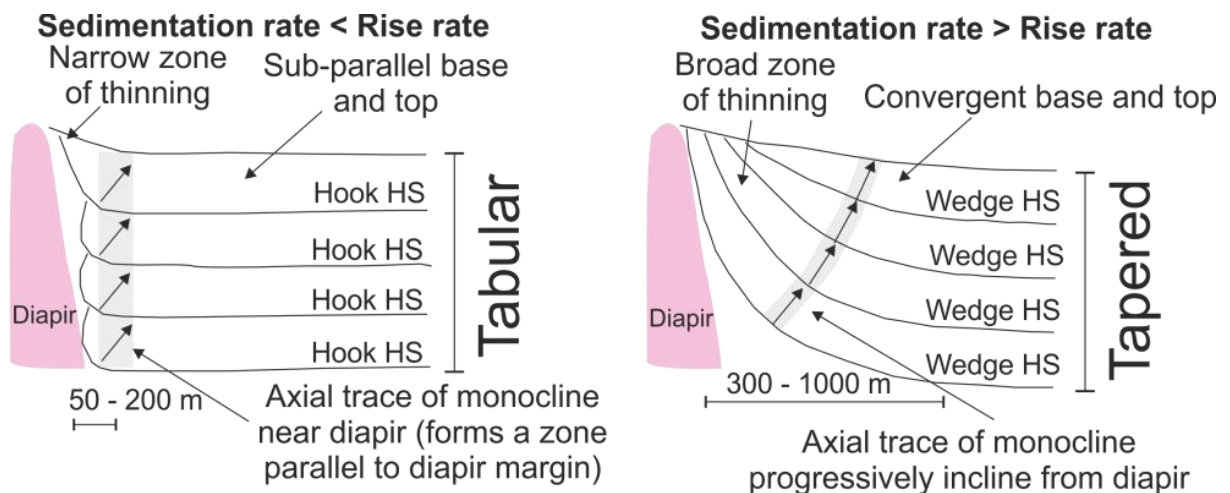
**Figure 2.30:** End member models of halokinetic sequences showing the characteristic features of hook and wedge halokinetic sequences. Hooks represent diapir rise rates greater than sedimentation rate and wedges represent diapir rise rates less than sedimentation rates (Giles and Rowan 2012).

**Table 2.3:** Characteristics of hook and wedge halokinetic sequences (Giles et al. 2004; Giles and Rowan 2012).

Feature	Hook sequence	Wedge sequence
Facies in a single halokinetic sequence	Outer-shelf black shale (top) Middle-lower shoreface Outer-shelf black shale Subaqueous debris flow (base)	Middle-shelf shale (top) Tidal or lagoonal sandstone Upper-shoreface sandstone Lower-shoreface sandstone/shale Middle-shelf shale (base)
Internal folding	Folding common J-hook unconformities, salt cusps Truncation angles <90°	Folding rare Truncation angles <15°
Slip on sequence-bounding unconformity	Significant slip Abundant brittle shear	Negligible slip
Relative aggradation rate	Very low, during transgression	Moderately high, during regression
Termination of halokinetic sequence	Terminates directly against diapir	Terminates against older, folded halokinetic sequences; diapir averages 250 m from truncation
Width of upturn	Up to 200 m	Up to 800 m

**Composite Halokinetic Sequences (CHS)**

Cycles of salt diapirism and onlap lead to the deposition of stacked (or composite) halokinetic sequences (CHS; Figure 2.31), bounded by angular unconformities, which are scale-equivalent to third-order depositional cycles (Giles and Lawton 2002; Rowan et al. 2003; Giles and Rowan 2012; Rowan and Giles 2021). Hook sequences stack into tabular composite sequences which are characterised by sub-parallel boundaries, thin roofs and local deformation (Figure 2.31; Table 2.3). Wedge sequences stack into tapered composite sequences with folded, convergent boundaries, thicker roofs and broad zones of deformation (Figure 2.31; Table 2.3). Composite halokinetic sequence style is determined by the ratio of sediment-accumulation rate to diapiric rise rate; low ratios (i.e., sedimentation rate < diapir rise rate) lead to tabular sequences and high ratios (i.e., sedimentation rate > diapir rise rate) result in tapered sequences (Figure 2.31; Giles and Rowan 2012; Rowan and Giles 2021).



**Figure 2.31:** End member models for composite halokinetic sequences (CHS). CHS are stacked halokinetic sequences. In tabular (stacked hook) CHS net sedimentation rate is less than net diapiric rise rate, whilst in tapered (stacked wedge) CHS net sedimentation rate is more than net diapiric rise rate (Giles and Rowan 2012).

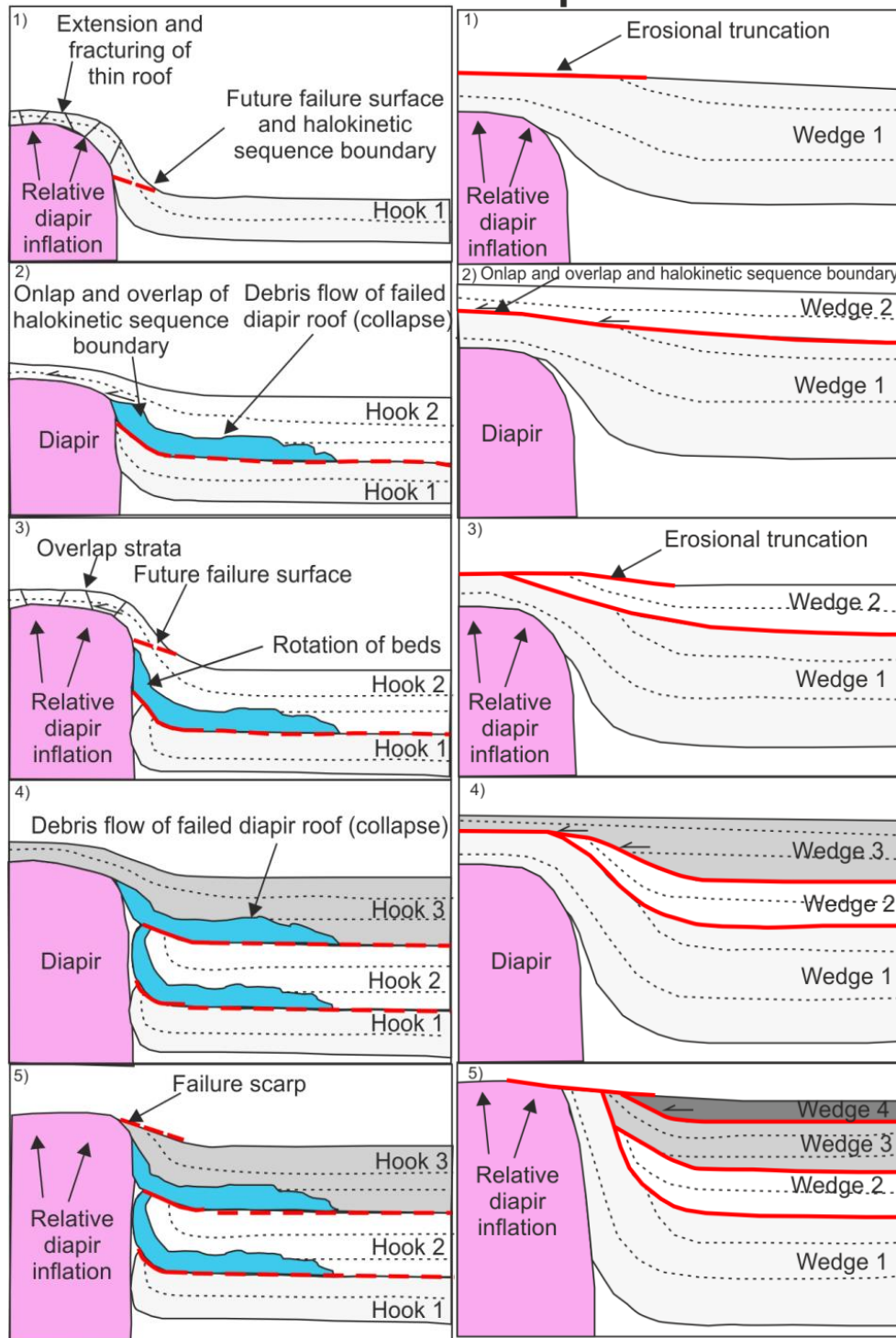
In tabular CHS (Figures 2.31 and 2.32), long term diapir rise rate outpaces deposition, which results in a particularly thin roof due to the topographic relief of the salt diapir. The roof panel is particularly thin and prone to failure and mass wasting, especially if the roof is extended and fractured during folding (1, Figure 2.32). Failure along a steep scarp creates a high angled unconformity with overlying mass transport deposits that downlap the basin floor (2, Figure 2.32). Short lived periods

of rapid deposition result in stratigraphy that onlap and overlap the topography caused by the mass transport deposit and subsequent slower deposition leads to the generation of increased topography (3, Figure 2.32). Onlapping and overlapping strata become the next roof strata which get progressively folded and the CHS development continues (4, 5, Figure 2.32; Giles and Rowan 2012; Jackson and Hudec 2017; Rowan and Giles 2021).

In tapered CHS (Figures 2.31 and 2.32) topographic relief is minor because sedimentation keeps up with the local accommodation created by diapiric rise. During minor decreases in sedimentation rate the diapir continues to rise, creating an area of slight topographic relief that may become a zone of sedimentary bypass or erosion, thereby producing a low-angle truncation surface (1, Figure 2.32). The resumption of increased sedimentation rates results in onlap and progressive overlap of the low-angle unconformity and the diapir roof strata (2, Figure 2.32), with continued rotation of underlying wedges due to diapiric rise. The onlapping and overlapping strata form the next wedge (3, Figure 2.32), with repetition of the process creating the tapered CHS (4, 5, Figure 2.32) (Giles and Rowan 2012; Jackson and Hudec 2017; Rowan and Giles 2021).



# Tabular CHS      Tapered CHS



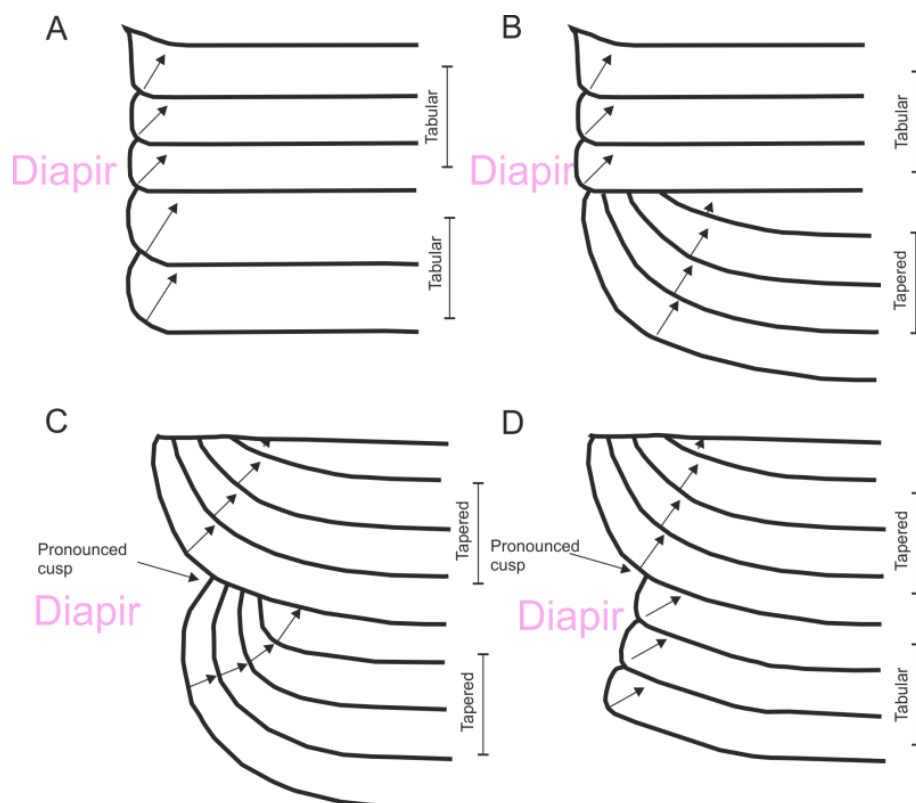
**Figure 2.32:** Genetic model for formation of tabular and tapered CHS (Giles and Rowan 2012). Tabular evolution comprises: 1) inflated diapir with a folded thin roof (Hook 1); 2) failure of roof forming unconformity overlain by debris flow (blue) and onlap/ overlap of diapir (Hook 2); 3) relative diapir inflation and drape folding of Hooks 1 and 2; 4) failure of roof panel with onlap/ overlap forming Hook 3; and 5) failure of Hook 3 roof panel. Tapered evolution comprises: 1) thick roof panel over diapir, which inflates resulting in erosional truncation of roof panel and Wedge 1; 2) overlap by Wedge 2; 3) erosional truncation of Wedge 2 over the inflating diapir; 4) onlap and overlap of Wedge 3; and 5) erosional truncation of Wedge 3 and onlap of Wedge 4.

## Factors influencing halokinetic sequences

It is specifically the interaction between salt rise and sediment accumulation (or preservation if

there is erosional stripping of the roof) that controls the topographic relief, roof thickness, and style of drape folding and thus halokinetic sequence type (Rowan and Giles 2021). It is important to note that halokinetic sequences, in similarity with drape folds, are not characterised by faulting (Figure 2.29; Rowan and Giles 2021).

CHS can stack together in a variety of geometries to form pronounced cusps adjacent to diapirs (Figure 2.33), dependent on variability in the parameters controlling sedimentation rate and diapir rise rate. As the diapir and minibasin both grow, rise rate and subsidence rate will increase. Even if average sedimentation rates (and sand percentage) stay constant, there will be an upwards transition from tapered CHS to tabular CHS, a commonly observed pattern around deep-water diapirs. In addition, pulses of shortening will increase salt-rise rate, making tabular CHS more likely even if plenty of sand is in the system. Any extension will have the opposite effect, with tapered CHS more common (Giles and Rowan 2012; Jackson and Hudec 2017; Rowan and Giles 2021).



**Figure 2.33:** Geometric patterns of stacked CHS, arrows show axial trace of monocline (Giles and Rowan 2012). A) Tabular CHS over tabular CHS; B) Tabular CHS over tapered CHS; C) Tapered CHS over tapered CHS; and D) tapered CHS over tabular CHS.

Similar halokinetic styles are seen across all depositional environments, but how halokinetic sequence boundaries correlate to sequence stratigraphic systems tracts depends on depositional setting (Giles and Rowan 2012). In deep-water settings, composite halokinetic sequence boundaries typically develop due to slow deposition (suspension fallout) during the transgressive and highstand systems tracts. In contrast, the slowest deposition on the shelf is during the lowstand to transgressive systems tracts, so that CHS boundaries usually fall somewhere within the transgressive to earliest highstand systems tracts. In sub-aerial depositional settings, erosional unroofing of the diapir may lead to gradual thinning of the roof (even during relatively rapid sedimentation) so that the zone of folding in a tapered composite halokinetic sequence narrows upward.

The presence and thickness of a roof above a near surface diapir influences the evolution of halokinetic sequences. Thin roofs generate narrow zones of drape folding (hook halokinetic sequences

that stack into tabular CHS), whilst thick roofs form wider collars of upturned strata (wedge halokinetic sequences that stack into tapered CHS; Figures 2.30, 2.31, 2.32; Giles and Rowan 2012; Rowan and Giles 2021).

Analysis of thickness patterns of growth strata over salt diapirs suggests that passively growing diapirs can have up to 300 m (Schultz-Ela and Jackson 1996) of drape-folded roof; whilst diapirs with thicker roofs are no longer growing (Jackson and Hudec 2017). Schultz-Ela et al. (1993) stated that diapir height must be more than 66-75% (i.e., the roof should be less than 25-34%) of the surrounding overburden for growth to occur. This value should not be taken too rigidly as it may depend on such factors as: diapir width and thus salt flux (Rowan 2017), the shape of the diapir top (Schulz-Ela et al. 1993), depositional environment and whether or not shortening is involved (which can lift thicker roofs due to added pressure on the salt, Jackson and Hudec 2017).

The width of a deformation halo around a diapir is expected to correlate loosely with lithology and aggradation rate; the latter affects the thickness of the halokinetic wedge (Rowan et al. 2003; Rowan and Giles 2021). Slow, mud-dominated sedimentation is likely to result in halokinetic aureoles about 200 to 300 m wide, where sands thin from regional thickness only near the diapir. Fast sedimentation should be associated with halokinetic aureoles about 600 to 800 m wide, where sands onlap and eventually cover the diapir. Diapirs growing along contractional anticlines could have deformation aureoles as much as 3 km wide (Rowan et al. 2003; Jackson and Hudec 2017; Rowan and Giles 2021).

Depositional environment has a strong control on the development of a roof. In deep-water and many shallow-water settings, there is always a hemipelagic fall-out of fine-grained sediment that blankets even the topographic highs of growing salt stocks and walls (e.g., Prather et al. 1998; Giles and Rowan 2012; Rowan and Giles 2021). In other shallow-water environments, there may be thick, aggrading carbonate platforms that keep pace with or even outpace salt rise (e.g., Giles et al. 2008; Giles and Rowan 2012; Poprawski et al. 2014; 2016) and in nonmarine settings, the presence and thickness of a roof depends on the magnitude of the freeboard (height of the diapir top above the floor of the adjacent minibasins; Talbot 1993) relative to the sediment accumulation rate at the diapir margin. If sedimentation rate is too low, the diapir remains emergent, with onlap onto its flanks (e.g., Pichel and Jackson 2020), but if the freeboard is small and the sedimentation rate is great enough, the diapir will get buried (Figure 2.28).

Of course, as with any sedimentary system, emergence and burial can fluctuate over time. Erosion of any sort will also impact roof thickness; this may be caused by local sedimentary processes such as wave-base erosion, channelised flow, bottom currents, and gravity-flows incorporating surficial sediment or mass wasting of roof scarps at the edges of diapirs. Roof erosion could also be regional erosion related to base-level changes or climatic shifts. All erosional and depositional systems may act asymmetrically with respect to the margin of the diapir, occurring on one flank and not another, and varying over time (e.g., Giles and Lawton 2002; Rowan et al. 2003; Giles and Rowan 2012; Poprawski et al. 2014; 2016; Jackson and Hudec 2017; Pichel and Jackson 2020; Rowan and Giles 2021; Roca et al. 2021; Cumberpatch et al. 2021b).

## **2.7 Examples of halokinetically-influenced environments**

Halokinetically-influenced stratigraphy has been studied in outcrop across a multitude of different depositional environments (Table 2.4), however prior to this thesis deep-water halokinetically-influenced settings were not well documented in outcrop (Cumberpatch et al. 2021b). Below, two case studies of halokinetically-influenced environments are presented; firstly, the stratigraphic ar-

chitecture and facies of the shallow marine stratigraphy around diapirs in the La Popa Basin, Mexico; and secondly, the evolution of a mixed depositional system surrounding the Mt. Frome diapir, Adelaide Rift Complex, South Australia.

**Table 2.4:** Summary of halokinetically-influenced stratigraphy studies in published literature, focussing on studies that describe some component of sedimentology or stratigraphy. Ordered by stratigraphic age. Several examples encompass many different depositional settings. Updated from Counts and Amos (2016).

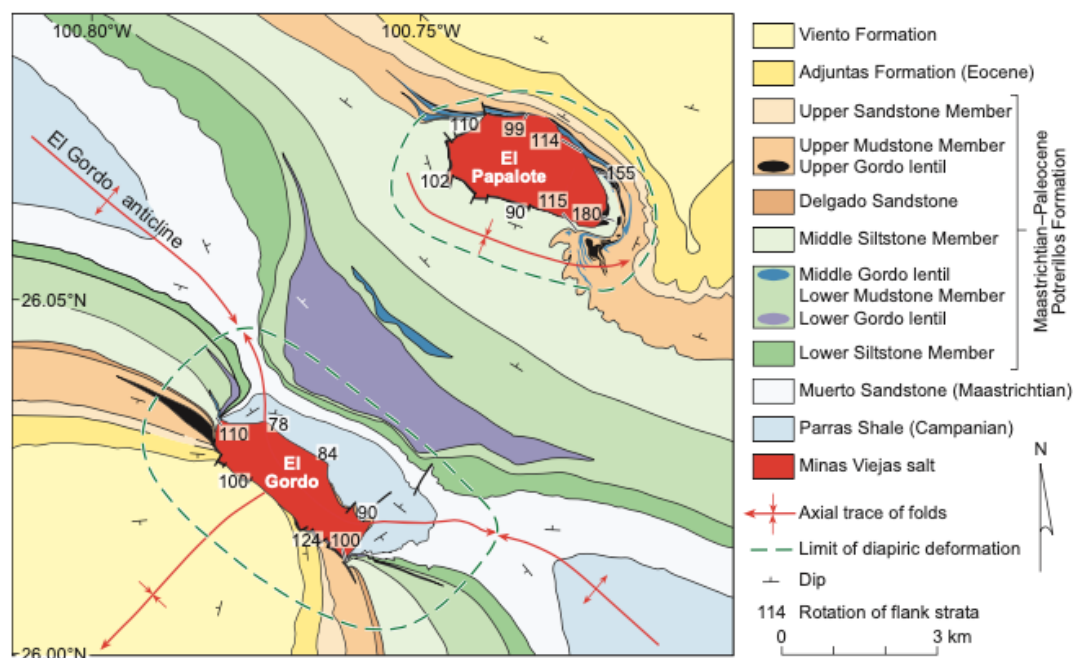
Study area	Location	Age of surrounding stratigraphy	Depositional environment	Studies
Mt. Frome diapir, Witchelina diapir, Patawarta salt sheet	Adelaide Rift Complex, Flinders Ranges, South Australia	Ediacaran-Cambrian	Mixed (shallow marine, carbonate shelves, reefs, mounds, subaerially exposed tidal flats, slope, deep-water and alluvial fans).	Lemon 1985; 2000; Dyson 1996; 1999; 2001; 2004 a; b; 2005; Reilly 2001; Dyson and Rowan 2004; Dyson and Marshall 2007; Collie and Giles 2011; Kernan et al. 2012; 2020; Hearon et al. 2015; Counts and Amos 2016; Counts et al. 2019; Gannaway Dalton et al. 2020.
Paradox Basin	Utah, USA	Carboniferous-Triassic	Fluvial-lacustrine, aeolian, shallow marine, alluvial.	Trudgill et al. 2004; Matthews et al. 2007; Tudgill and Paz 2009; Trudgill 2011; Banham and Mountney 2013 a; b; 2014; Venus et al. 2015.
Salt canopy on Axel Heiberg Island	Sverdrup Basin, Arctic Canada	Carboniferous-Eocene	Fluvial-deltaic.	Jackson and Harrison 2006.
Saraktash diapir	Ural Mountains, Russia	Permian-Triassic	Fluvio-lacustrine, terrestrial.	Newell et al. 2012.
Moussa diapir, Tazaoult salt wall	Atlas Mountains, Morocco	Jurassic	Slope-shelf, mixed platform.	Saura et al. 2014.
Santa Cruz, São Pedro de Moel, Caldas da Rainha-Óbidos and Rio Maior-Porto de Mós diapirs	Lusitanian Basin, Portugal	Jurassic-Cretaceous	Shallow marine, lacustrine.	Kullberg 2000; Alves et al. 2002; Kullberg et al. 2006, 2013; Kullberg and Kullberg 2017; Pimentel and Pena dos Reis 2016; Pena dos Reis et al. 2017; Davison and Barreto 2020.
Bakio diapir	Basque-Cantabrian Basin, Spain	Cretaceous	Carbonate shelf-slope, deep-water.	Arbués et al. 2012; Ferrer et al. 2014; Poprawski et al. 2014; 2016; 2021; Cumberpatch et al. 2021b; Roca et al. 2021.
El Chingue Bluff	Magellanes Basin, southern Chile	Cretaceous	Slope.	Shultz and Hubbard 2005.
Fars Province	Persian Gulf, Iran	Cretaceous-Neogene	Shallow marine.	Ala 1974; Jahani et al. 2007.
El Papalote, El Godo and La Popa diapirs	La Popa Basin, Mexico	Cretaceous-Palaeogene	Shallow marine-shelf-shoreface.	Laudon 1984; Giles and Lawton 2002; Rowan et al. 2003; Aschoff and Giles 2005;

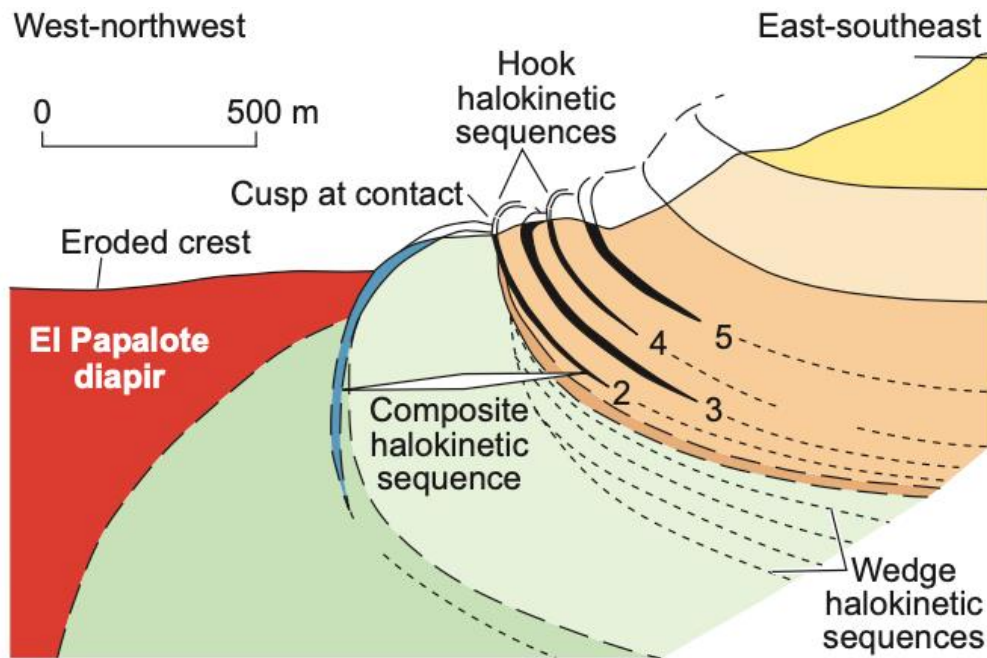
				Giles et al. 2008; Giles and Rowan 2012.
Emirhan mini-basin	Sivas Basin, Turkey	Oligocene - Miocene	Fluvial, braided stream, playa-lake, lacustrine, sabkha, shallow marine.	Ringenbach et al. 2013; Callot et al. 2014; Ribes et al. 2015; 2017.
Clovelly, Cote Blanche, Lake Washington, Napoleonville, Weeks Island and White Castle salt domes	South Louisiana, USA	Miocene	Shallow marine.	Johnson and Bredeson 1971.
Al Salif and Jabal al Milh diapirs	Red Sea, North-west Yemen	Miocene	Alluvial, lacustrine, shallow marine, arid.	Davison et al. 1996.

### Case Study: La Popa Basin, Mexico

La Popa Basin contains an estimated 7000 m of Lower Cretaceous to Palaeogene strata, all of which form halokinetic sequences adjacent to three exposed salt diapirs (El Gordo, El Papalote and La Popa Weld, formerly a salt wall; Figures 2.34 and 2.35; Giles and Rowan 2012).

The presence of halokinetic sequences indicates ongoing passive diapirism throughout deposition of the strata. The salt diapirs arise from the Jurassic (Oxfordian) Minas Viejas Formation. The bulk of exposed strata in the basin comprise the Parras Shale and the overlying Difunta Group (containing, in ascending order, the Muerto, Potrerillos, Adjuntas, Viento and Carroza formations; Figures 2.34 and 2.35). These marine to non-marine, dominantly siliciclastic units were deposited within the distal part of the Upper Cretaceous to Palaeogene Laramide foreland basin system, such that the uppermost Cretaceous and Palaeogene part of the basin fill was deposited whilst contraction was ongoing (Dickinson and Lawton 2001; Lawton et al. 2001; Rowan et al. 2003; 2012).





**Figure 2.34:** Map view and cross-section of halokinetic sequences in the 500-1,000 m wide contact zone around El Papalote and El Gordo diapirs (La Popa basin, Mexico). Strata are locally overturned in hook halokinetic sequences; angular unconformities bounding the sequences are subvertical and grade into correlative conformities within about 250 m of the diapirs' contact (Rowan et al. 2003; Jackson and Hudc 2017).

Hook halokinetic sequences are well developed in both the Lower Mudstone and Upper Mudstone members of the Potrerillos Formation at all three diapirs and within the Middle Siltstone Member at La Popa Weld (Figure 2.35). The mudstones represent the deepest-water facies in the La Popa Basin (outer-shelf hemipelagic black shales) and presumably the slowest overall sediment-accumulation rates. The Middle Siltstone Member comprises pro-deltaic mudstone and siltstone deposited in a middle-shelf setting, and represents slightly shallow-water conditions and presumably slightly higher sedimentation rates (Druke 2005).

Internally, hook halokinetic sequences follow a repetitive upwards facies progression. Near-diapir basal deposits, above the halokinetic sequence boundaries, comprise carbonate debris-flow facies that contain evaporite and non-evaporite clasts in a silty to sandy carbonate matrix (Hunnicut 1998; Garrison and McMillan 1999; Mercer 2002; Druke 2005). These diapir-derived debris flows are thickest near the diapir and thin away from it but typically do not extend more than a few hundred metres away from the diapir. The debris flows are commonly overlain by or interbedded with packstones and grainstones that represents carbonate grain and turbidity flows (Giles et al. 2008). This facies association of carbonate SGF deposits are collectively referred to as carbonate lentils (Laudon 1975) because of their diapir-centric distribution.

Open-shelf and lower-shelf fine-grained sandstones sometimes thin and onlap onto the basal carbonate facies, but generally do not overlap the diapir (Figures 2.34 and 2.35; Druke and Giles 2008). In all cases, the sequence finishes with middle- to outer-shelf black shale or siltstone that thins onto and overlaps the diapir.

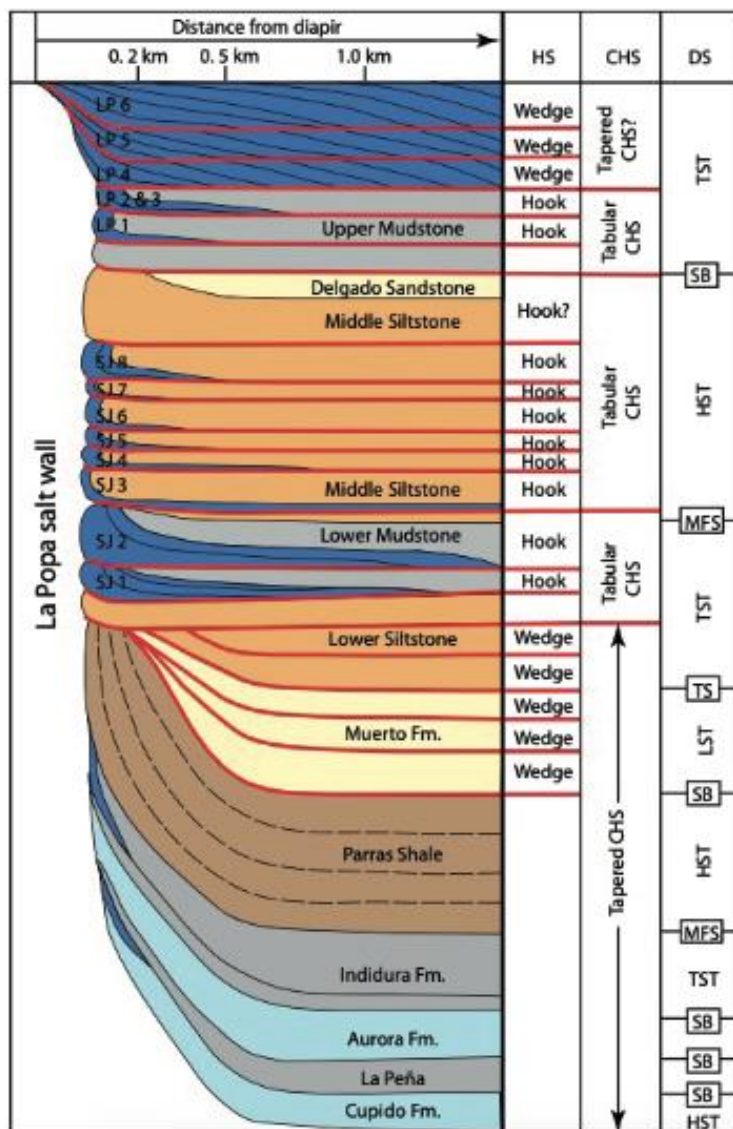
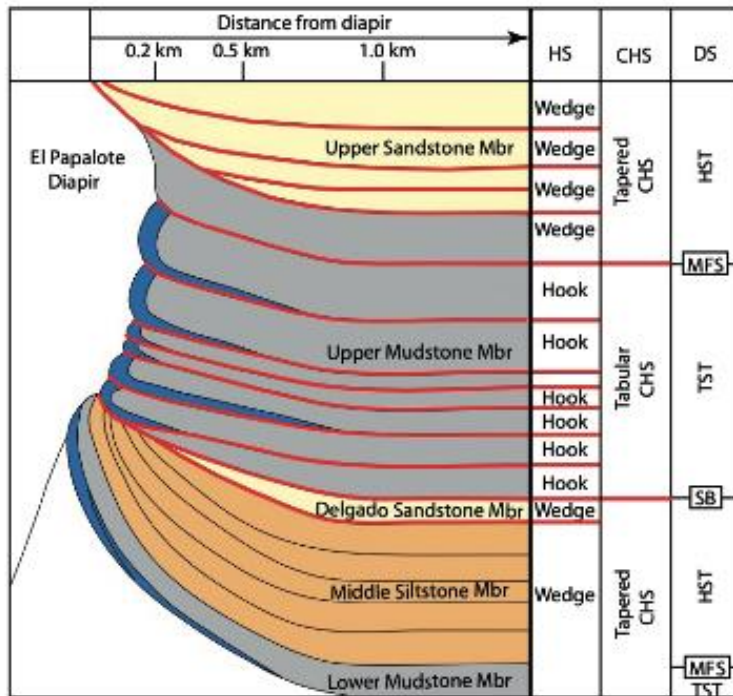
Hook sequences typically range in thickness from 25 m to a little over 100 m, with folding and thinning in a narrow zone 50–200 m wide. Giles and Rowan (2012) infer that topographic relief built up during prolonged, slow deposition of the black-shale facies, formed steep unstable slopes

that eventually failed and produced debris flows. The failure scarp formed an angular unconformity commonly directly overlain by mass-wasting deposits, that forms the base of the next hook halokinetic sequence (Druke and Giles 2008; Giles et al. 2008).

Wedge halokinetic sequences are well developed within the Muerto Formation at the La Popa Weld. The Muerto Formation comprises siltstone to medium-grained sandstone with rare chert-pebble conglomerates deposited within a prograding deltaic system (Hon 2001; Weislogel 2001). The siliciclastic strata represent shallow-shelf/ pro-deltaic siltstones and lower-shoreface to fore-shore or tidal sandstones organised into progradational-parasequence sets that suggest relatively high sediment-accumulation rates. The repetition of facies within an individual wedge halokinetic sequence starts within lower- to middle-shoreface sandstone parasequences that onlap the halokinetic sequence boundary. The parasequences display a progradational stacking pattern shallowing up to upper-shoreface and tidal/coastal-plain parasequences at the top of the parasequence set. These are capped by major flooding surfaces that are in turn overlain by shallow shelf/prodeltaic siltstones (Figure 2.35; Giles and Rowan 2012).

Muerto Formation wedge halokinetic sequences typically range from 50 to 100 m in thickness and thin over a distance of 400 – 600 m. Muerto Formation wedge successions lack the debris-flow conglomerates containing diapir-derived detritus that are a common component of hook halokinetic sequences, suggesting the diapir was buried beneath a roof comprising mostly Parras Shale (Giles and Rowan 2012). Erosional unconformities are nevertheless present. Topographic relief over the diapir probably built-up during periods of slower deposition of the shallow-shelf/pro-deltaic siltstone so that near-diapir strata may have been elevated into a shoreface environment. Shoreface wave erosion over the slightly inflated diapir likely cut the angular unconformity surfaces that were then onlapped by lower- to upper-shoreface sandstones of the next wedge halokinetic sequence (Hon 2001; Giles and Lawton 2002; Giles and Rowan 2012).

Individual hook and wedge halokinetic sequences stack into tabular and tapered composite halokinetic sequences respectively at La Popa Weld and El Papalote Diapir. In the shelf setting of La Popa Basin, tapered CHS generally formed during the highstand systems tract and (if present) the lowstand systems tract, when siliciclastic sediment influx to the shelf increased due to shoreline regression. Examples include the Parras and Muerto formations at the La Popa Weld and the Middle Siltstone to Delgado members and the Upper Sandstone Member of the Potrerillos Formation at El Papalote Diapir. Tabular composite halokinetic sequences primarily formed in the transgressive systems tract in the shallow-water setting of La Popa basin, when siliciclastic sediment influx to the shelf decreased due to shoreline transgression. The prime examples are the Lower Mudstone Member of the Potrerillos Formation at La Popa Weld and the Upper Mudstone Member at El Papalote Diapir (Figure 2.35; Rowan et al. 2003; Giles and Rowan 2012).





**Figure 2.35:** Halokinetic (HS), and composite halokinetic (CHS) and depositional sequence stratigraphy of the Upper Cretaceous–Lower Palaeogene stratigraphy exposed on the east side of El Papalote Diapir and the north side of the La Popa Weld, La Popa Basin, Mexico (Giles and Rowan 2012). Colours indicate dominant lithology of the unit: dark blue, carbonate lentil; light blue, regional carbonate unit; grey, outer-shelf mudstone; brown, pro-deltaic shale; orange, lower-shelf to middle-shelf siltstone; yellow, deltaic sandstone. LST: lowstand systems tract; TST: transgressive systems tract; HST: highstand systems tract; SB: sequence boundary; TS: transgressive surface; MFS: maximum flooding surface (Giles and Rowan 2012).

### **Case Study: Mt. Frome diapir, Adelaide Rift Complex, South Australia**

In the Adelaide Rift Complex of South Australia, diapirs intersected the seafloor and land surface during the Ediacaran–Cambrian at the same time as sediment was being deposited, giving rise to excellent exposures of these diapirs, including the Mt. Frome diapir, and their associated minibasins (Counts and Amos 2016; Counts et al. 2019).

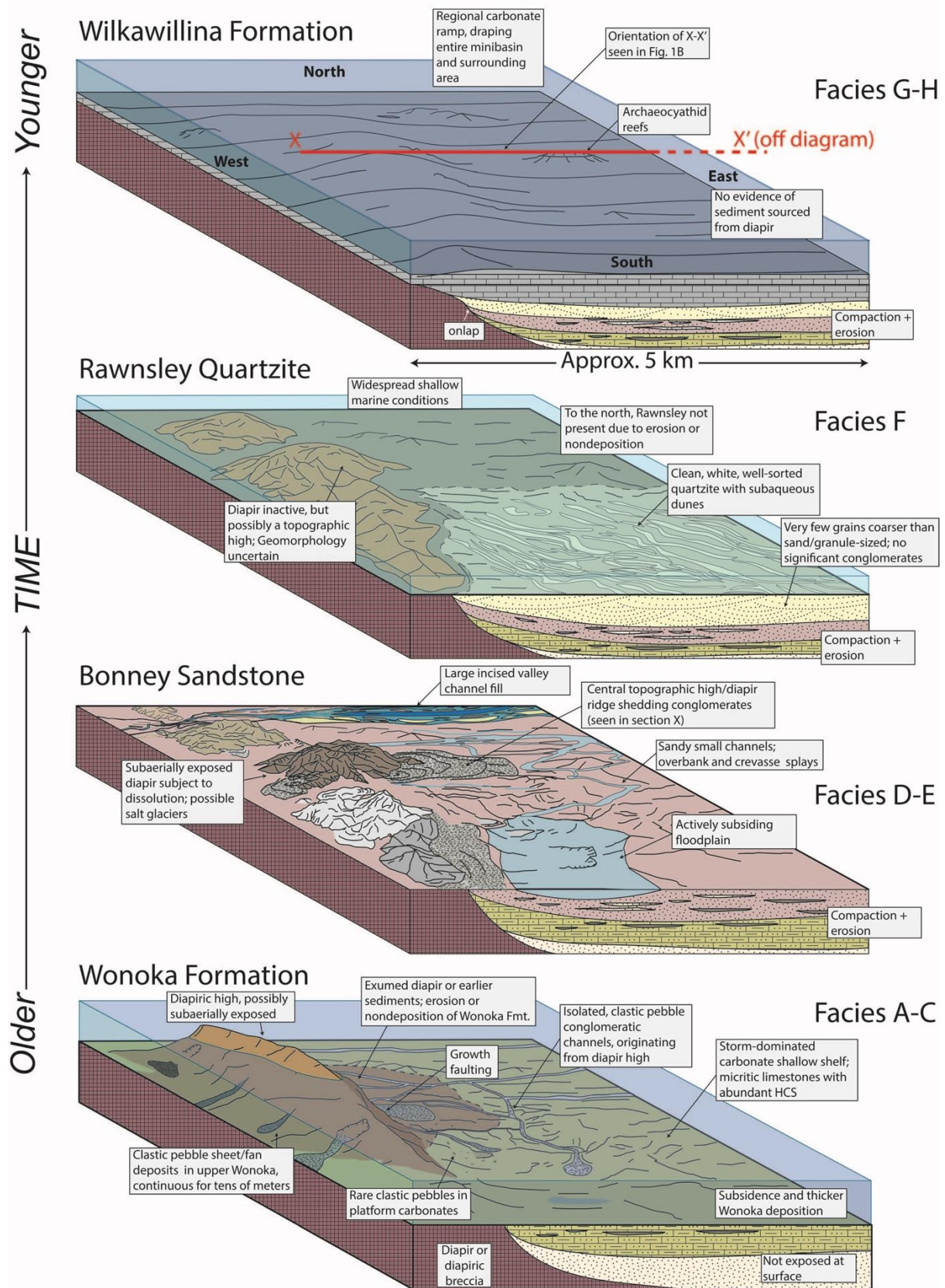
Deposits in the Mt. Frome minibasin were deposited in a variety of shallow-marine and continental environments that were influenced by proximity to an extrusive diapir body (Figure 2.36). The exposure and uplift of the diapir body and the erosion of allochthonous clasts from within the diapir created a unique depositional setting and resulted in processes and products dissimilar to those found in the same formations elsewhere in the basin. Diapir-related features in the minibasin deposits include depositional thinning and onlap, rotational growth faulting, abundant pebble conglomerates deposited in debrites and turbidites and channelisation. Conglomerates are sourced from growth-fault scarps that expose diapir matrix, leading to the deposition of diapir-derived pebble beds in lower shoreface, shallow marine, intertidal and alluvial-fan environments. Below, the evolution of the halokinetically-influenced environments adjacent to the Mt. Frome diapir throughout the Ediacaran and Cambrian is summarised (Figure 2.36; Counts et al. 2019).

The Ediacaran Wonoka formation is dominated by calcareous shales and resistant limestones and clastic pebble conglomerates of shallow marine origin. During this time Mt. Frome was possibly subaerially exposed, with growth faulting and diapir exposure resulting in siliciclastic pebble sheet fans which were continuous across 10s of metres. Pebble conglomerates were also deposited by isolated channels which originated from the diapir high and appear to have re-routed to exploit topographic lows. Stratigraphic thickness increases away from the diapir (Figure 2.36; Counts et al. 2019).

The Bonney Sandstone comprises shales, fine-grained sandstones and pebble conglomerate deposited in a paralic environment by intertidal and marginal marine processes. Pebble conglomerates are deposited by intermittent gravity flows due to diapir instability along the central ridge. At this time, it is thought that parts of the subaerially exposed diapir were subject to dissolution, forming extensive salt glaciers. Actively subsiding topographic lows adjacent to salt structures were dominated by flood plain facies, and small channels re-routed to avoid positive diapir topography; channelised facies are more common with distance from the diapir than on the flanks (Figure 2.36; Counts et al. 2019).

The Rawnsley Quartzite is the first unit to contain no diapirically-derived material. Instead, it comprises cross-stratified and planar-laminated clean quartz-rich sandstones deposited under wave and current processes in a shallow marine environment, possibly by intertidal dunes. By this stage, the diapir was inactive, but likely remained a topographic high, influencing subsequent deposition, and controlling the architecture of Rawnsley quartzite deposition, which thins towards the remnant diapir (Figure 2.36; Counts et al. 2019).

## Environmental Controls on Facies Change



**Figure 2.36:** Schematic block diagram reconstructions of depositional environments and local paleogeography in the Mt. Frome area over a series of time slices corresponding to each formation. Blocks are vertically exaggerated and not to scale (Counts et al. 2019).

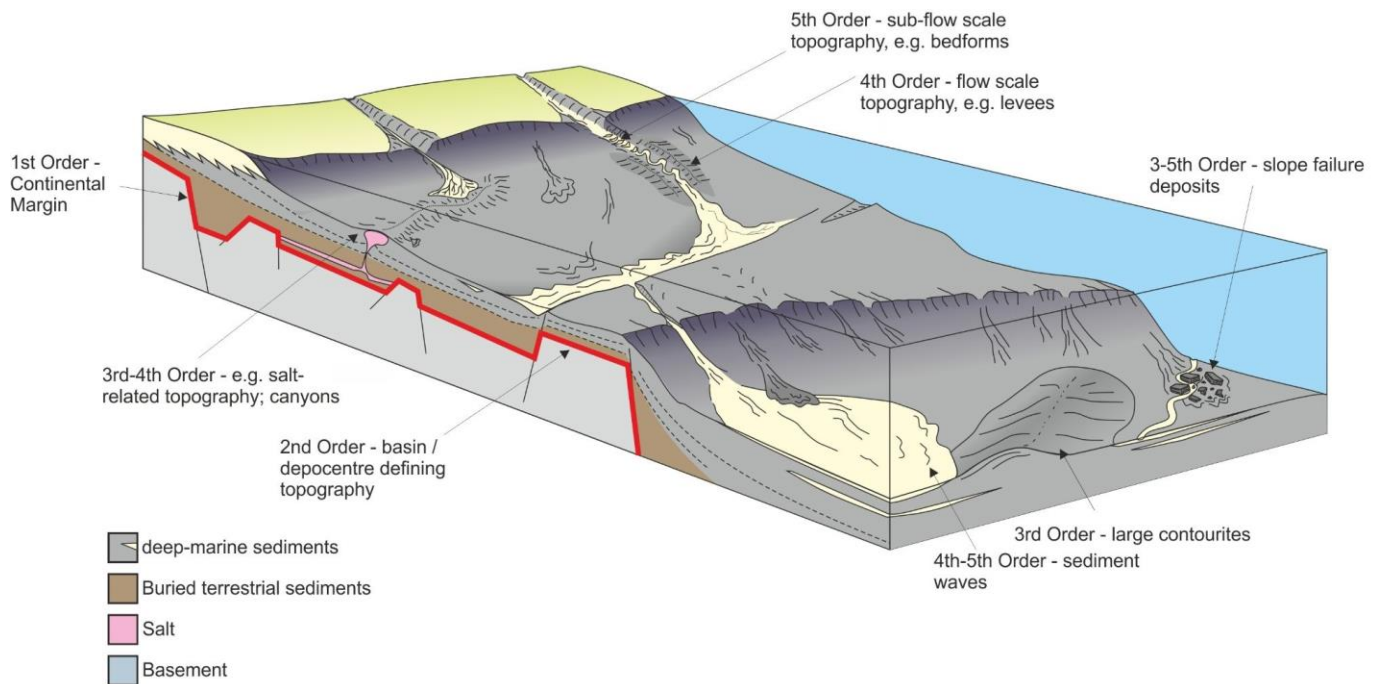
The Cambrian Wilkawillina Formation is dominated by massive grey micritic limestone and occasional white sandy limestone, deposited in a low energy sub-tidal depositional setting, dominated by gravity settling. By this point, there is no diapir-derived material, no evidence for sediment sourced from the diapir, and the remnant diapir topography is almost completely buried, with a regional carbonate ramp draping the entire minibasin (Figure 2.36; Counts et al. 2019).

## **2.8 Topographic controls on deep-water sedimentary systems**

### ***Types of topography***

Different types (static and dynamic), scales and orientations of topography ultimately influence the evolution of the depositional system, and how this will differ from unconfined settings (Figure 2.37). Static topography is topography which does not move on the time scale of the sedimentary system. Even the most dynamic slopes, e.g., salt-related topography, may be largely static during the development of sedimentary systems (e.g., during quiescence). In these static, or largely static settings, typically, individual flows will not experience the effects of slope movement (such as mass transport deposits), but they will be manifested between flows, or following deposition on the slope. Static topography includes pre-existing structural features, carbonate platforms, and other palaeotopography. Dynamic topography is typically considered as allogenic in origin (e.g., salt growth or tectonism) but may also be generated autogenically at the flow- to system-scale, e.g., lobes and levees (Kane et al. in prep). A further category is that of static topography transported within or from outside the system, i.e., mass transport deposits, although such deposits commonly undergo deformation during the history of the system (Figure 6.16). The reaction of sedimentary systems to static or dynamic topography may be very different; for example, growing or retreating structures may repulse or attract channel systems respectively (e.g., Mayall et al. 2010; Kane et al. 2010; 2012).

Kane et al. (in prep) described five scales of topography from the largest to smallest scale (Figure 2.37). 1st order topography is the continental margin, which largely defines the sediment entry points to deep-marine basins and the systems which develop downdip as a consequence. 2nd order topography can loosely be defined as depocentre scale and may define individual basins or include several distinct basins. 3rd order intrabasinal scale topography includes surface expressions of faults and salt-related topography, which may form discrete ‘minibasins’. 4th order is broadly flow scale topography, inducing much autogenic relief (e.g., erosional channels, levees, terraces and convex-up lobe bodies). Finally, 5th order, sub-flow-scale, includes seafloor roughness, and bed-forms, from which sediment is entrained. It is implicit in this scheme that 1st order topography may be superimposed by each lower level of topography. 1st order topography is largely independent of depositional systems; 2nd order can experience feedback from the sedimentary system through loading and subsidence, and all orders below (3-5) are subject to depositional and erosional feedback, and may entirely be a product of the depositional system itself (autogenic topography, e.g., levees).

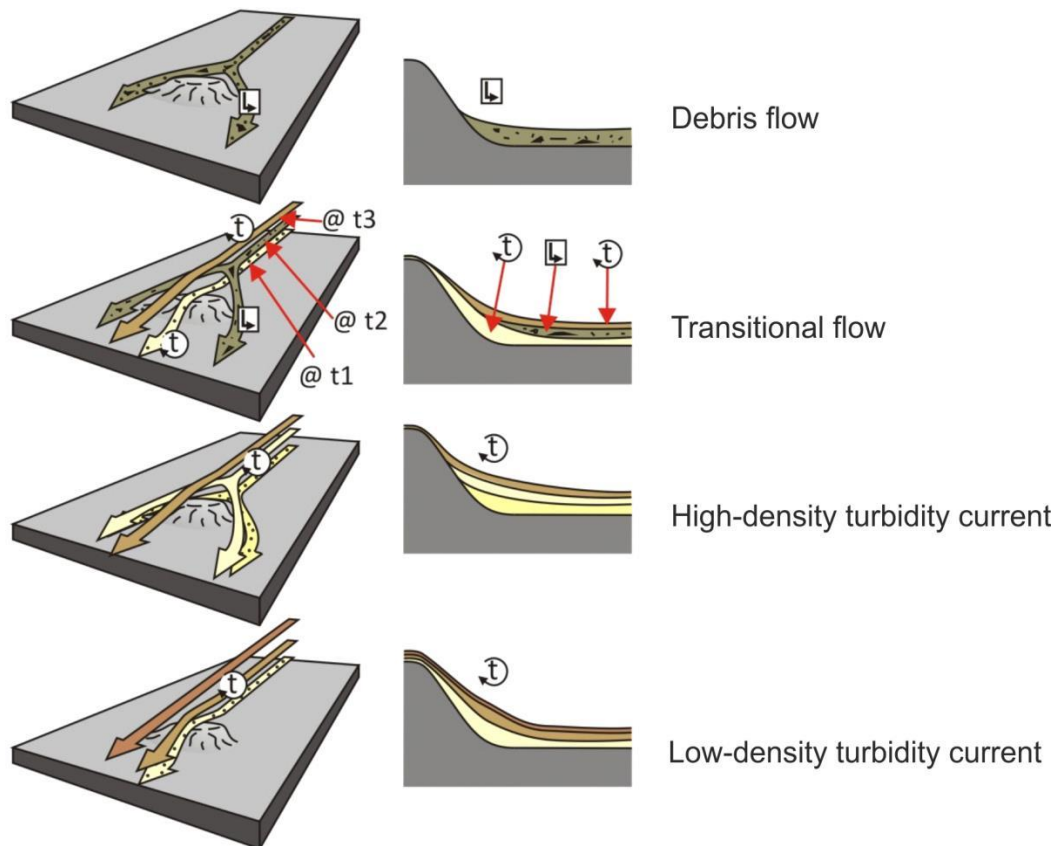


**Figure 2.37:** Different scales of topography in deep-water depositional systems, from 1<sup>st</sup> order, continental margin scale, to 5<sup>th</sup> order, sub-flow scale topography (Kane et al. in prep).

### **Sediment gravity flow interaction with topography**

Basin topography has a substantial effect on the routing of sediment gravity flows and subsequent architecture of associated channel and lobe deposits (Booth et al. 2003). It has been almost 70 years since the first observations of SGFs being affected by topography, and the seafloor being partitioned into a series of confined sub-basins were proposed (Menard 1955; Gorsline and Emery 1959; Van Andel and Komar 1969; Allen 1985; Muck and Underwood 1990). This topography can be generated by mud or salt diapirism (Fusi and Kenyon 1996; Gee and Gawthorpe 2006; 2007; Doughty-Jones et al. 2017), tectonic events (Hodgson and Haughton 2004; McArthur et al. 2019; Cullen et al. 2019; Tilhams et al. 2021) and depositional and erosional relief (Normark et al. 1979; Ortiz-Karppf et al. 2015; 2016; Sychala et al. 2015; Soutter et al. 2018; Cumberpatch et al. 2021a). Flow interaction with this topography can result in highly heterogeneous and complex onlap geometries as flows can be redirected, transform, or run up-topography to variable degrees (Al Ja'aidi 2000; Al Ja'aidi et al. 2004; Bakke et al. 2013; Bell et al. 2018a; Soutter et al. 2019). A relatively restricted basin may confine flows to the point where deposits are generally thick and amalgamated, stacking aggradationally (Marini et al. 2015).

SGFs are driven down-slope by the force of gravity acting upon them (e.g., Daly 1936). The shape of this slope dictates the direction and speed of these flows, which will affect the location and character of their deposits (e.g., Pickering and Hiscott 1985; Kneller et al. 1991; Edwards et al. 1994; Kneller 1995; Davis et al. 2009; Kane et al. 2010; 2012) and therefore directly impacts their potential as hydrocarbon reservoirs. The deposits of SGFs can therefore be used to infer the shape of the topography that the flow interacted with, and the nature of flows themselves. The different flow processes responsible for SGFs respond to topography in different ways (e.g., Middleton and Hampton 1973; Mulder and Alexander 2001; Talling et al. 2015). Kneller and McCaffrey (1999) suggested that the basal and denser part of an individual flow will respond differently to topography than the upper and more dilute part of the same flow, which will affect deposition adjacent to topography. Higher density regions of flows will be more affected by topography than lower-density regions of flows; deposits from these flows will consequently be differentially distributed around topography, resulting in deep-water facies arrangements that may be considered indicative of topographic interaction (Figure 2.38).



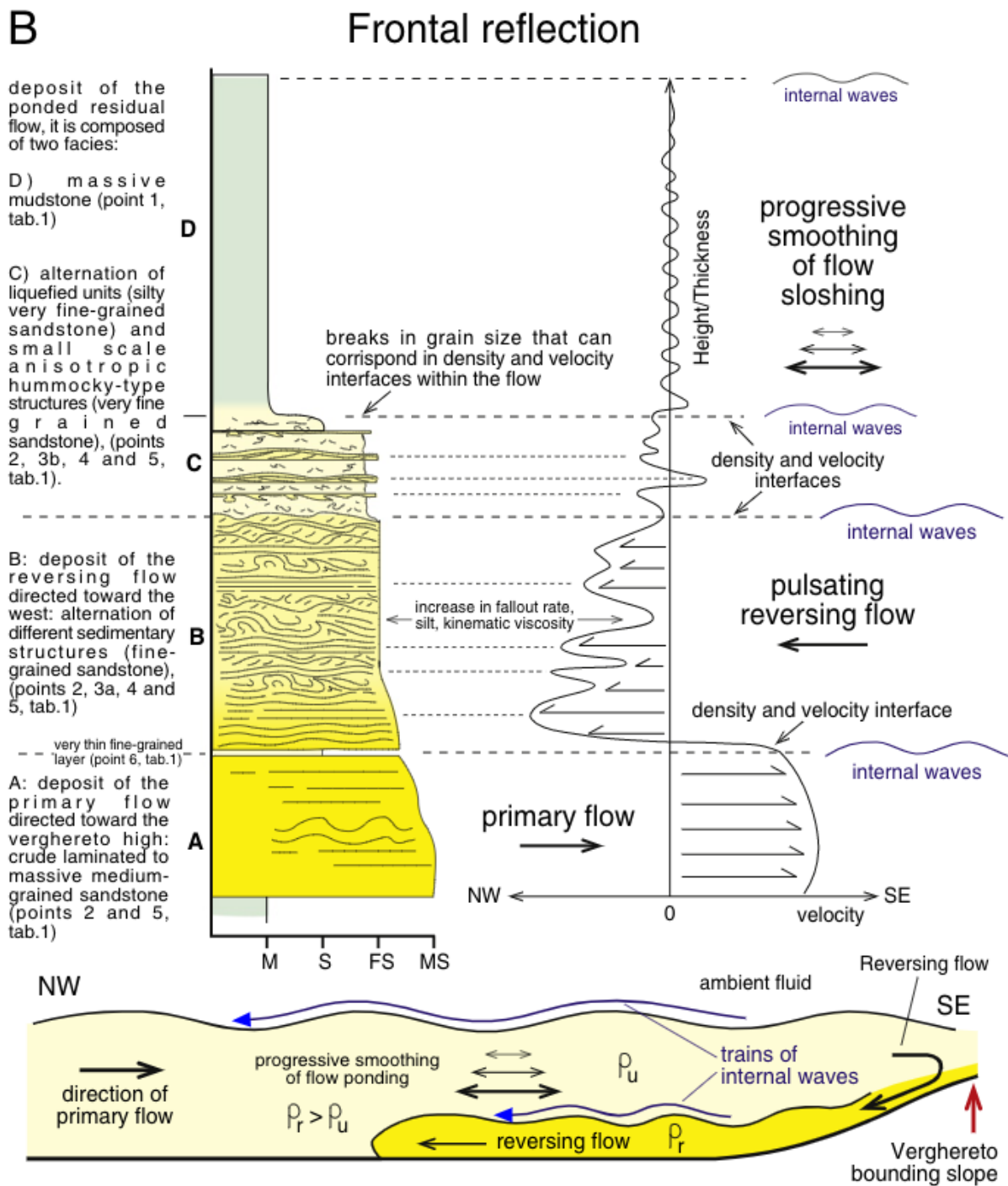
**Figure 2.38:** Topographic interaction model of different flow types. Note how laminar flows have a tendency to follow topographic obstructions, whereas turbidity currents may be able to surmount significant topography (Al Ja'aidi 2000; Bakke et al. 2013).

As high-concentration mixtures of fluid and sediment, where particles are supported by grain-to-grain interaction and the matrix strength of the flow (Lowe 1982; Sohn 1997), debris flows are strongly influenced by topography and will tend to be steered around obstructions; their deposits are typically found in topographic lows (Figure 2.38). Turbidity currents have lower concentrations than debris flows, and the particles are maintained in suspension by fluid turbulence; accordingly, because much of the load is carried above the bed, these flows can override significant topography (Figure 2.38; e.g., Dolan et al. 1989; Muck and Underwood 1990; Lucchi and Camerlenghi 1993). HDTCs will tend to be strongly density stratified flows and are thus more strongly affected by topographic interaction than weakly stratified or near homogeneously mixed flows, such as low-density turbidity currents (Al Ja'aidi 2000; Gladstone et al. 2004). The interaction of strongly stratified sand-rich turbidity currents with a slope may result in deflection and/or the relatively abrupt deposition of the high-density lower part of the flow, whereas the more dilute, well-mixed, and finer-grained upper part may overcome the topography (Figure 2.38; e.g., Normark et al. 1983). Kneller and McCaffrey (1999) explain the abrupt transition from massive coarse sandstones up into structured fine sandstones with variable paleocurrent directions as a consequence of density stratification within ponded turbidity currents. In their interpretation, the stratigraphically lower, higher-density portion of the flow decelerates, resulting in rapid sediment fallout; in contrast, the overlying, lower density portion is reflected and deflected by the bounding topography. In hybrid event beds the forerunning turbidity current will run up the slope much further than the trailing debris flow (Figure 2.38; Haughton et al 2009). Interaction of sediment gravity flows with confining slopes may also drive flow transformations, for example, by decelerating a turbidity current and thus driving an increase in the near-bed sediment concentration to develop transitional flow deposits (Kane and Pontén 2012).

### ***Facies indicative of topographic influence***

Flow interaction with topography has been shown to result in a range of facies variations that are characteristic of deposition adjacent to slopes (Figure 2.39; Pickering and Hiscott 1985; Sinclair 1994; Kneller and McCaffrey 1999; McCaffrey and Kneller 2001; Felletti 2002; Al Ja'Aidi et al. 2004; Lomas and Joseph 2004; Bersezio et al. 2005; Pyles et al. 2007; Pyles and Jennette 2009; Stevenson and Peakall 2010; Bakke et al. 2013; Patacci et al. 2014; Spsychala et al. 2017c; Southern et al. 2017; Tinterri et al. 2016; Cunha et al. 2017; Bell et al. 2018a; Soutter et al. 2019; 2021; Cullen et al. 2020; Howlett et al. 2020; Cumberpatch et al. 2021 a;b; Tilhams et al. 2021).

Topographic interaction has been used to explain the deposition of thick, sand-rich turbidites adjacent to paleo-slopes (e.g., Alexander and Morris 1994; Kneller and McCaffrey 1995; Puigdefàbregas et al. 2004; Bersezio et al. 2005; Stevenson and Peakall 2010; Tinterri and Magalhaes 2011). Topographic interaction may also cause flow deflection (Figure 2.39), which can result in: 1) remobilisation and re-deposition of sand deposited higher on the slope at the foot of the slope (e.g., McCaffrey and Kneller 2001; Puigdefàbregas et al. 2004); 2) run-up and collapse of the high-velocity base of a flow into its more dilute cloud (Haughton 1994; Hodgson and Haughton 2004); or 3) pulsing and repetition of turbidite divisions (i.e., Bouma divisions) (e.g., Edwards et al. 1994). Topographic interaction may also result in laminae-scale soft-sediment deformation (e.g., Tinterri et al. 2016) and complex tractional structures (e.g., Pickering and Hiscott 1985) as flows deflect off a counter-slope and re-work their aggrading deposit (Figure 2.39; Allen 1985; Pantin and Leeder 1987; Muck and Underwood 1990; Patacci et al. 2014; Bell et al. 2018a; Soutter et al. 2019; Cumberpatch et al. 2021a;b). This re-working can also result in paleocurrent divergence adjacent to topography, which can be used to reconstruct the geometry and orientation of the topography (Pickering and Hiscott 1985; Kneller et al. 1991; Sinclair 1994; Marini et al. 2015). High-aggradation rates adjacent to topography and consequent deposition of sand-grade sediment has also been shown to relatively enrich flows in mud, resulting in short length-scale (10s – 100 m) rheological flow transformation and hybrid bed deposition (Lowe and Guy 2000; Patacci et al. 2014; Southern et al. 2015; 2017; Bell et al. 2018a; Soutter et al. 2019) which may affect depositional architectures adjacent to slopes (Figure 2.38). Hybrid beds have also been hypothesised to form next to topography due to incoming flows inducing slope failure and the emplacement of a debrite within an aggrading turbidite (McCaffrey and Kneller 2001), with thicker debrites indicating proximity to the slope.



**Figure 2.39:** Example of the reflected facies that may be produced as turbulent flow interacts with topography (Tinterri et al. 2016).

Lateral tracing of individual sandstone beds away from their termination reveals a characteristic change in facies that is below the resolution of most seismic data, but can be seen in outcrop in the Ordovician – Silurian Welsh Basin (Smith 2004) and the Eocene-Oligocene Annot Sandstones (Sinclair 1994; Sinclair and Tomasso 2002; Soutter et al. 2019). Thin-bedded, non-graded, fine-grained sandstones with upper-flow regime planar laminations pass downslope into medium-bedded, partially graded sandstones with ripple lamination and planar lamination. At the base of the slope turbidites are thick-bedded and fully-graded coarse sandstones. Slumping and liquefaction are commonly associated with upslope amalgamation on beds (Sinclair 1994).

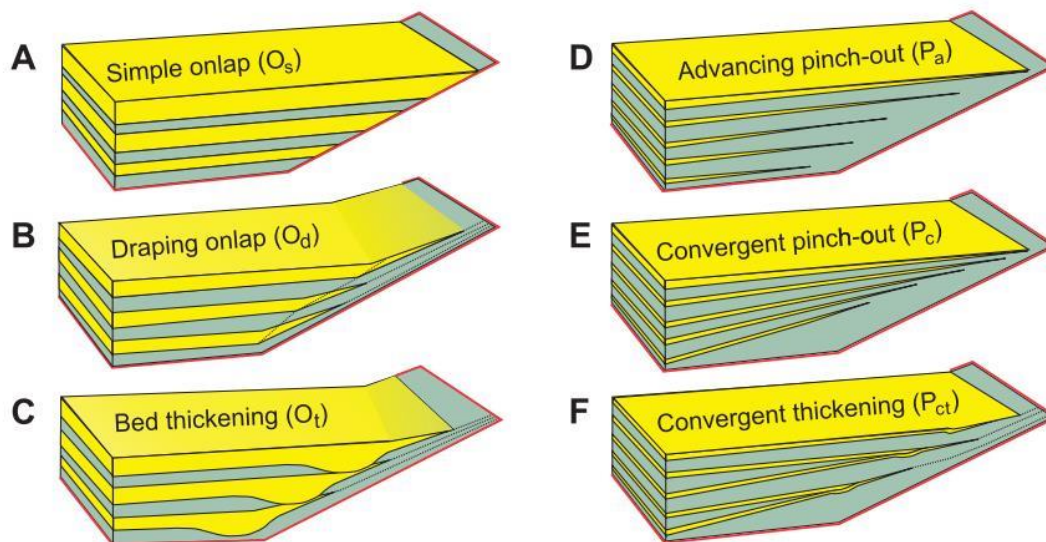
The notable characteristics of “contained turbidites” (Pickering and Hiscott 1985) include: 1) the presence of thick mudstone caps overlying sandstone beds; 2) complex palaeocurrent directions; 3) dominance of thick beds; 4) complex grading patterns; 5) evidence of dewatering; and 6) onlap of sheet-like bed geometries (Sinclair and Tomasso 2002). Evidence for syn-depositional uplift of the basin topography (active as opposed to static topography) can be identifiable from growth strata and onlap–offlap relationships towards the margins of the basin. Increased slumping, debris flows and soft-sediment deformation are also commonly associated with active topography (Holman and Robertson 1994). While none of these features alone are diagnostic of the presence of evolving seafloor topography, the combination and repetitive patterns described can give some indication of seafloor deformation.

### ***Stratal onlap***

Onlap is defined by Mitchum et al (1977) as “a base-discordant relation in which initially horizontal strata terminate progressively against an initially inclined surface, or in which initially inclined strata terminate progressively up-dip against a surface of greater initial inclination”. A number of different schemes to classify onlap trajectories based on amounts of slope aggradation (Smith and Joseph 2004), significance of draping turbidites (Pickering and Hilton 1998) and parent flow magnitude (large flows will thicken at topography while smaller flows will thin; McCaffrey and Kneller 2001), have been proposed. In attempt to unify these schemes, Bakke et al. (2013) integrated their own subsurface and outcrop observations with results from other studies (McCaffrey and Kneller 2001; Gardiner 2006) to propose six different styles of seismically-resolvable deep-water stratal termination: simple onlap, draping onlap, bed thickening, advancing pinch-out, convergent pinch-out and converging thickening (Figure 2.40). Preferential formation of each of these onlap styles is controlled by various factors, such as: flow concentration, flow magnitude, slope angle and slope stability (Bakke et al. 2013).

The slope angle and flow characteristics are critical: for the same flow, a low-angled slope may drive flow transformation so that its deposit evolves from a clean sandstone in a downslope setting into a progressively muddy poorly-sorted sandstone toward the pinch-out; conversely, the same flow interacting with a steep slope may decelerate relatively rapidly, leading to deposition across the available grain-size spectrum, and the deposition of a thick poorly-sorted sandstone with little draping of the slope (Bakke et al. 2013). An additional factor when considering deposition against slopes is deformation induced by the incoming flows (e.g., Puigdefàbregas et al. 2004) and post depositional remobilisation associated with slope instability, both of which have the potential to impart more complexity on the deposits and their stratigraphic architecture.



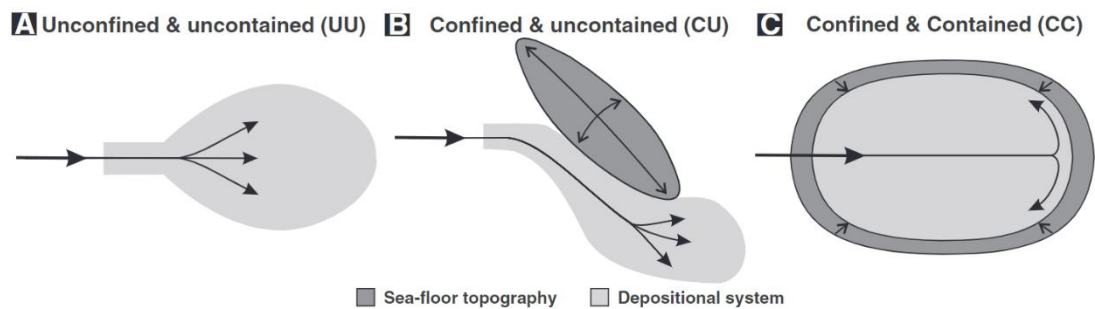


**Figure 2.40:** Possible deep-water termination styles close to topographic highs. A-C show relatively sand-prone (yellow) stratigraphic units while heterolithic (green) pinch outs are shown in D-F (Bakke et al. 2013).

Termination geometries (Figure 2.40) are difficult to detect seismically but are critical to assess in deep-water topographically-influenced settings, because they may be indicative of stratigraphic traps or hydrocarbon leakage points. Understanding stratal terminations (Figure 2.40) can help understand the slope gradient during deposition and if bathymetry was static or active, allowing a better understanding of the type of reservoir architectures (Bakke et al. 2013). Draping onlap and heterolithic pinch-out terminations are likely on low-gradient confining slopes and have higher risk of containing laterally extensive thief sandstones below seismic resolution, due to their increased chance of being detached and lower reservoir quality (Figure 2.40; Bakke et al. 2013). Simple and bed thickening onlaps occur in higher gradient confining slopes and are associated with higher reservoir quality and increased sandstone connectivity (Figure 2.40; Hadler-Jacobsen et al. 2005; Bakke et al. 2013).

### ***Stratigraphic evolution of confined basins***

Confined basins are those in which SGF routing and depositional patterns are controlled by the topography of the basin (e.g., Gorsline and Emery 1959; Van Andel and Komar 1969; Ricci-Lucchi and Valmori 1980; Hiscott et al. 1986; Winker 1996; Gervais et al. 2004; Lomas and Joseph 2004; Bersezio et al. 2005; Covault and Romans 2009; Marini et al. 2015; 2016; Cunha et al. 2017; Dodd et al. 2019). Southern et al (2015) classified confined systems based on whether they are confined and/or contained (Figure 2.41). Confined flows are affected by topography, while contained flows are entirely encircled and retained within a depositional low (Southern et al. 2015). Contained deposition is analogous to flow ‘ponding’ which is used superfluously in the literature but typically describes flows entirely confined by their basin margins (Van Andel and Komar 1969).



**Figure 2.41:** Different method of confinement that a deep-water system, or individual SGF, may be characterised by (from Southern *et al.* 2015).

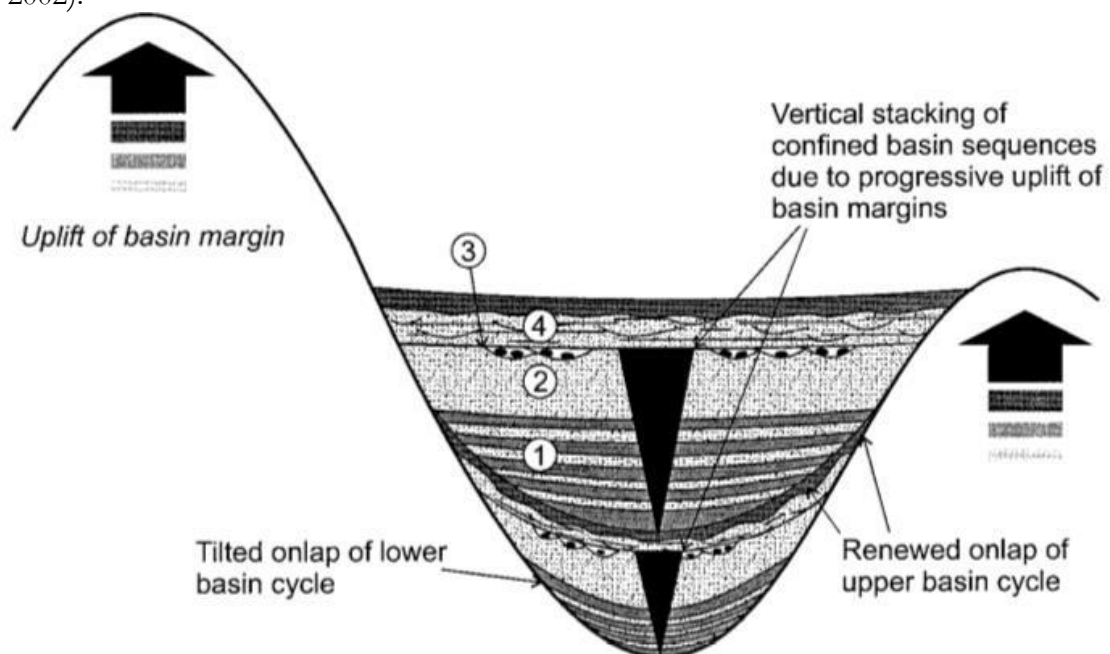
Ponded flows generate limited positive relief as the full sediment load is trapped within the basin, thus developing a ‘flat-topped cloud’ that spreads over the whole basin (Hickson 2000; Toniolo *et al.* 2006; Marini *et al.* 2015), which results in ‘sheet-like’ deposition and simple vertical stacking patterns (e.g., Pickering and Hiscott 1985; Haughton 1994; Talling *et al.* 2007). Ponded turbidite systems are common in a range of different geodynamic contexts (e.g., salt-withdrawal minibasins of continental slopes in passive margins, structurally-confined basins of rifted margins and fore-land basin systems (Smith 2004)). When relative confinement is reduced, stacking patterns become more complex as beds are able to thin distally and thus stack with varying degrees of compensation (e.g., Marini *et al.* 2015; Bell *et al.* 2018a; Liu *et al.* 2018). Relative confinement has also been inferred through the stratigraphic trend of the mud-to-sand ratio within individual event beds (e.g., Felletti 2002; Sinclair and Cowie 2003; Bersezio *et al.* 2005; Marini *et al.* 2015). The absence of a mud-cap indicates that the confining topographical relief was not sufficient to prevent bypass of the finer, upper region of the flow (e.g., Haughton 1994), resulting in ‘flow stripping’ (e.g., Sinclair and Tomasso 2002; Sinclair and Cowie 2003; Toniolo *et al.* 2006; Patacci *et al.* 2014). Thick mud-caps may indicate flows were fully confined by their basin margins (e.g., Haughton 1994; Marini *et al.* 2015).

Sinclair and Tomasso (2002), integrated outcrop (e.g., Sinclair 1994) and subsurface (e.g., Prather *et al.* 1998; Prather 2000) data to describe a generic four-fold depositional evolution model for the fill of a confined basin (Figure 2.42). The “fill-spill” model comprises: 1) flow ponding, where flows are entirely confined by the basin margins; 2) flow stripping, where the upper parts of flows are able to ‘escape’ the basin; 3) flow bypass, where the majority of the incoming flow is able to deposit down-dip; and 4) blanketing or abandonment (Figure 2.42).

‘Flow ponding’ occurs where incoming flows are totally trapped, depositing thick, sheet-like sandstone- mudstone couplets. In order for flow ponding to take place, the confining basin must be surrounded by topographic barriers that are sufficient to prevent turbidity currents surmounting them (Figure 2.42; Sinclair and Tomasso 2002). ‘Flow stripping’ occurs where the finer, more dilute portion of the flow is able to overtop the confining basin topography and be deposited elsewhere, causing an increased sandstone: mudstone ratio within the basin as much of the fines have been displaced. The coarse, dense core of the turbidity current remains constrained, and thus preferentially infills the confined basin, while the upper, dilute part of the flow can be stripped off and transported over the topographic barrier, often into a lower basin (Figure 2.42; Alexander and Morris 1994; Sinclair and Tomasso 2002).

When the upper basin is sufficiently filled with sediment, the break of slope that defined the margin of the upper basin becomes healed (Prather *et al.* 1998) and the opposing intrabasinal high is predominantly buried. ‘Flow bypass’ occurs where accommodation space is limited either by flows traversing over the filled basin resulting in incision, or by switching of feeder channels away from the basin resulting in abandonment. The transition from sheet sandstone bodies towards more

channelised geometries within the healed basin is characterised by incision (Figure 2.42; Satterfield and Behrens 1990). An alternative response to the decrease in accommodation space following flow stripping is the switching of the sediment routing system away from the healed basin. In this case the confined basin will be abandoned, resulting in fine-grained, condensed, overbank sediments being deposited (Sinclair and Tomasso 2002). During flow bypass, the bulk of sediment deposition will occur downslope of the buried topography, often in a lower basin. This is typically associated with a reduction in gradient at the base of the intrabasinal high, which leads to rapid deceleration of turbidity currents, typically resulting in the deposition of amalgamated and de-watered toe-of-slope deposits (Figure 2.42; Garcia 1994; Sinclair and Tomasso 2002). ‘Blanketing’ of the basin and surrounding topography due to base-level rise is the final stage of confined basin evolution. Where bypass has occurred by incision, the canyon will become partly or wholly back-filled by sediment accumulation in the lower basin, and so the local base level for the upper basin will rise, leading to renewed sediment accumulation. This usually takes the form of meandering channel-levee complexes with low sandstone-to-mudstone ratios (Figure 2.42; Sinclair and Tomasso 2002).



**Figure 2.42:** The fill-spill model, showing vertical stratigraphic evolution of a confined basin sequence generated by episodic uplift of basin topography (Sinclair and Tomasso 2002). Evolutionary steps 1: ponding, 2: flow stripping 3: flow bypass and 4: blanketing (described in text).

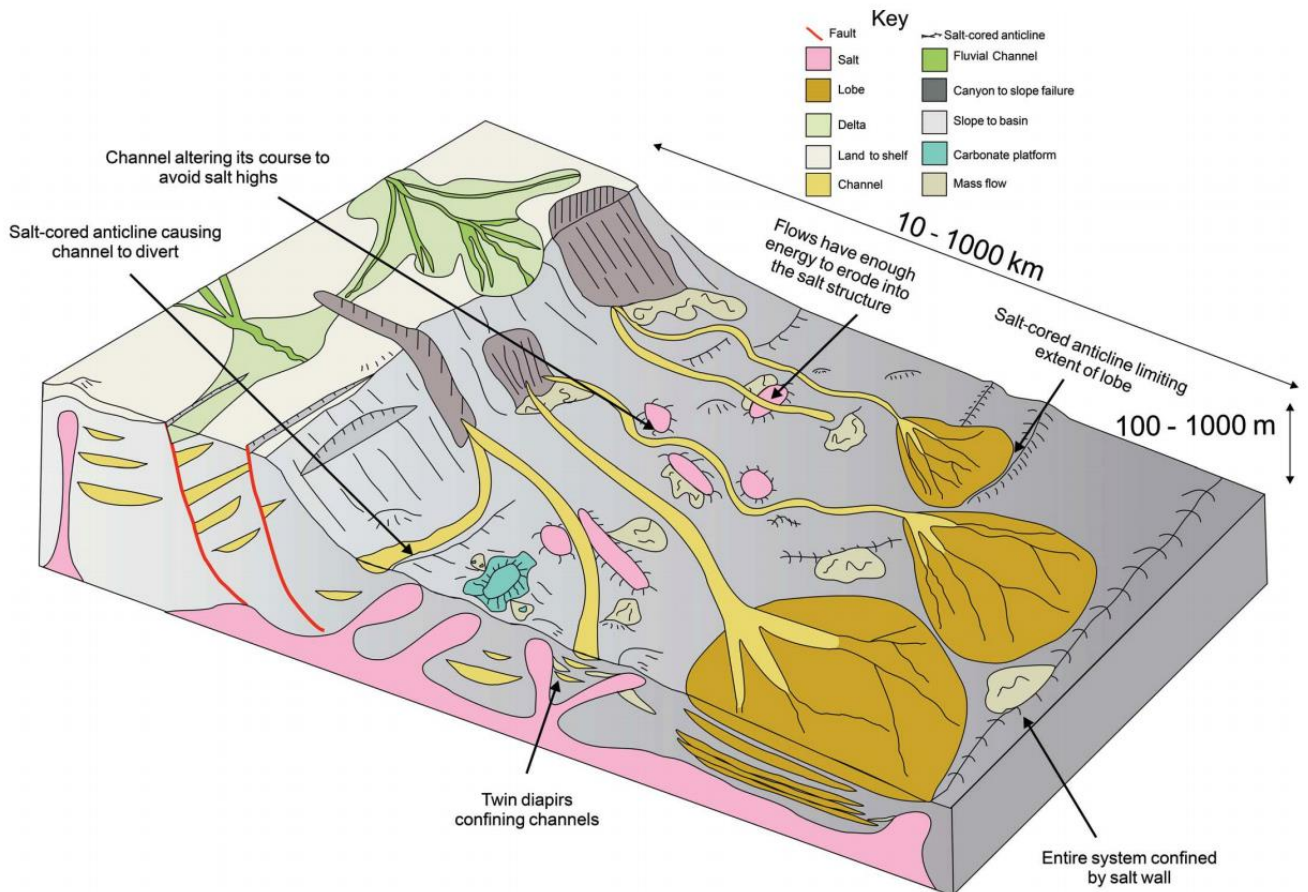
The fill-spill model is an end member for confined basins, with the other end member being termed a ‘connected tortuous corridor’ (Smith 2004). In the tortuous corridor model flows are laterally confined down-dip, but not frontally confined, and follow a ‘tortuous’ topographically-controlled path down-dip. This style of deposition has since been observed on the modern seafloor (Bourget et al. 2011), in the subsurface (e.g., Hay and Prather 2012) and at outcrop (e.g., Vinnels et al. 2010; Pinter et al. 2018; Cumberpatch et al. 2021b). Outcrop observations (Amy et al. 2007) and numerical modelling (Wang et al. 2017) have shown that, contrary to the ‘fill-spill’ model, confined minibasins often fill retrogradationally with deposition concentrated in the basin centre and counter slope due to a hydraulic jump as incoming flows decelerate upon impact with the basin floor.

## 2.9 Halokinetic controls on deep-water sedimentary systems

Processes of flow deflection, reflection and ponding of turbidity currents in response to basinal topography have been widely recognised (e.g., Van Andel and Komar 1969; Pickering and Hiscott 1985; Haughton 1994). Extreme examples of these effects are recorded in the salt-withdrawal minibasins of the Gulf of Mexico (Winker 1996; Prather et al. 1998; Beaubouef and Friedmann 2000) where, in addition to the effects of flow confinement, abrupt gradient changes at the base-of-slope strongly influence depositional patterns (Pirmez et al. 2000; Sinclair and Cowie 2003). Flow velocities of turbidity current can decrease across obstacles (e.g., ramps, diapirs or intra-basinal horsts) and the flow state may alter to waning and depletive flow (Kneller 1995).

Owing to their importance in hydrocarbon exploration, halokinetically-influenced deep-water sedimentary systems have predominantly been studied in subsurface datasets. Such subsurface studies have shown that salt structures deforming the seafloor can exert substantial control on the location, pathway, and architecture of lobe, channel-fill, levee and mass-transport deposits (e.g., Cronin 1995; Rowan and Weimer 1998; Mayall and Stewart 2000; Gee and Gawthorpe 2006; 2007; Mayall et al. 2006; 2010; Heinio and Davies 2007; Clark and Cartwright 2009; Jones et al. 2012; Wu et al. 2020; Howlett et al. in 2020). When the erosive power of SGF is enough to overcome the rate of diapiric growth channels, or less commonly lobes, can flow across, but do not erode into, the growing structure. Examples exist where channels appear to cross active structures such as folds, salt walls or diapirs and thus behave counterintuitively (Figure 2.43; e.g., Morgan 2004, Saller et al. 2004; Mitchell et al. 2020).

Turbidity currents that were ponded, diverted, deflected and confined by salt structures (Figures 2.43 and 2.44) are well documented in the eastern Mediterranean (e.g., Clark and Cartwright 2009; 2011), offshore Angola (e.g., Gee and Gawthorpe 2006; 2007; Mayall et al. 2006; 2010; Jones et al. 2012; Oluboyo et al. 2014; Doughty-Jones et al. 2017; 2019; Howlett et al. 2020), the Gulf of Mexico (e.g., Booth et al. 2000; 2003; Winker and Booth 2000; Prather 2003; Giles and Rowan 2012), offshore Brazil (e.g., Rodriguez et al. 2018; in press), the North Sea (e.g., Mannie et al. 2014) and the Precaspian Basin (e.g., Pichel and Jackson 2020).



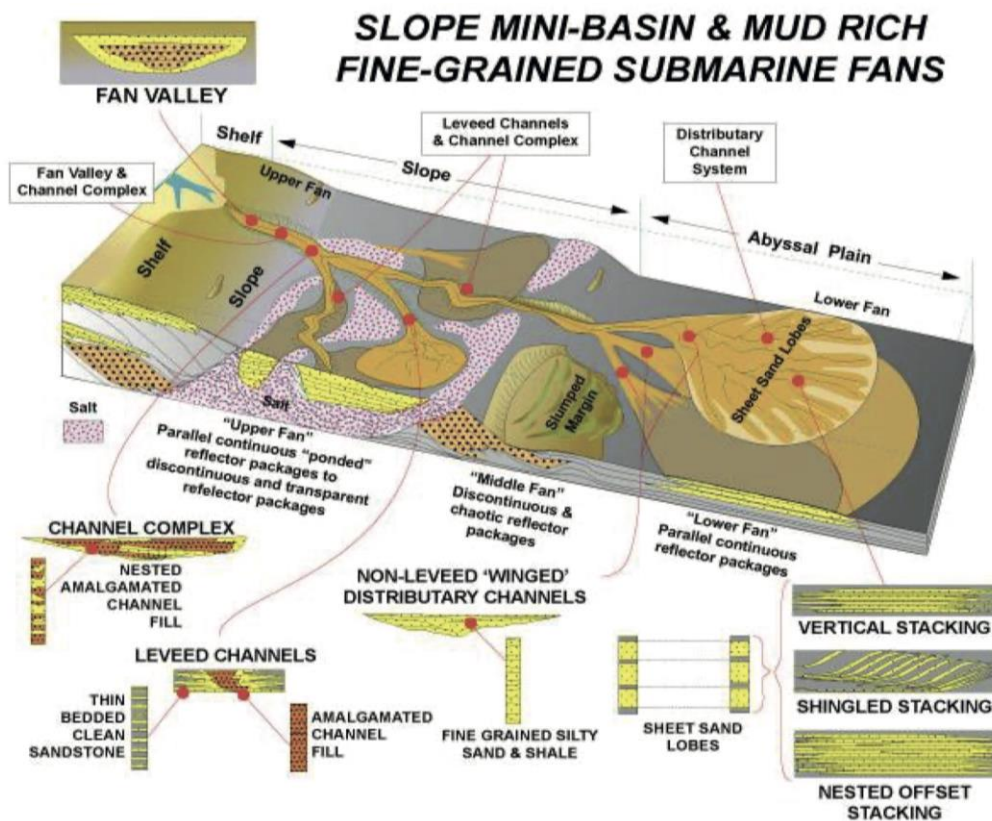
**Figure 2.43:** Sketch summarising the structural controls, with respect to gravity-driven processes, on depositional systems from the shelf to basin floor. Note the complex and sinuous paths taken by slope channels around salt structures (Modified from Mayall et al. 2010; Cumberpatch et al. 2021b).

Salt-induced topography can cause confinement on a variety of scales from depositional element (e.g., individual lobes, 5<sup>th</sup> order topography) to entire system (e.g., 2<sup>nd</sup> – 3<sup>rd</sup> order topography). In many submarine slope systems, turbidite channels commonly have complex routes to traverse salt-influenced slope topography (Figures 2.43 and 2.44). Salt and shale diapirism (e.g., Morley and Guerin 1996; Rowan et al. 1999; Hudec and Jackson 2007) can complicate the bathymetric relief at the seabed. If the rate of growth of the salt structure increases, the deep-water sedimentary system shifts systematically sideways to avoid rising topography (Mayall et al. 2010; Kane et al. 2012). Growth-fault-related basins, turtle structures, crestal-collapse basins, minibasins on salt canopies, piggyback basins behind folds and thrusts all provide areas where sediments can pond and stack (Figures 2.43 and 2.44). In a completely enclosed minibasin, once accommodation space is filled, basins will overflow and depocenters will move seaward, in agreement with the ‘fill-spill’ model (Prather et al. 1998; Booth et al. 2000; Winker and Booth 2000; Sinclair and Tomasso 2002; Prather 2003). The pattern of lobe or channel response to induced topography is dictated by the timing of structural growth, the size, shape and orientation of the structures and the erosional power of the gravity flows (Mayall et al 2010; Doughty-Jones et al. 2017).

Features forming positive relief such as tilted fault-block crests, rollover anticlines, salt or shale diapirs, salt walls, folds and thrusts form obstacles to gravity flows and frequently cause channels to deflect or be diverted over tens of kilometres. Smaller scale structures (4<sup>th</sup> order topography) with a topographic expression of less than 5 km generally just deflect channels locally from their downslope pathway, whereas larger structures (3<sup>rd</sup> order topography) of tens of kilometers scale can cause large diversion of channel systems forcing them to travel near parallel to the slope for

significant distances (Figures 2.43 and 2.44; Mayall et al. 2006; 2010; Oluboyo et al. 2014; Doughty-Jones et al. 2017; 2019).

Another process that can affect reservoir facies distribution in salt-basins is the shedding of debris from salt-cored topographic highs. These redeposited sediments may comprise a wide range of compositions and depositional fabrics. The sediments may be relatively fine grained if they are reworked by turbidity currents, or they can be composed of much larger blocks if sediment transport is primarily by sliding or slumping. Source material can be from the roof of the diapir or from the salt itself if the diapir is exposed. In many cases, diapir-sourced reservoirs are likely to have poor reservoir quality (Poprawski et al. 2014; 2016; 2021 Jackson and Hudec 2017; Doughty-Jones et al. 2019; Wu et al. 2020). Such mass transport deposits can also be derived from up-dip failure of the regional slope, but may be compositionally different (Figure 2.44; Soutter et al. 2018; Doughty-Jones et al. 2019).



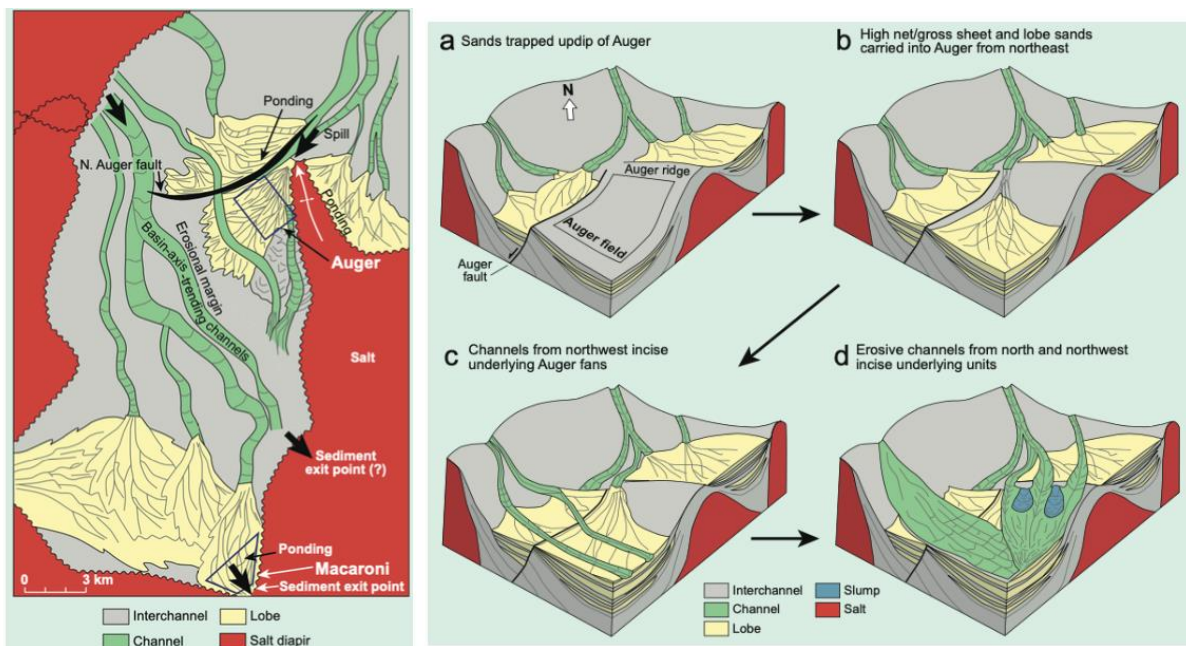
**Figure 2.44:** Summary of sedimentary facies distribution and stacking patterns observed in a variety of deep-water halokinetically-influenced settings (Bouma 1997; DeVay et al. 2002; Kendall 2012).

Prior to this study the majority of our knowledge of deep-water halokinetically-influenced systems was from subsurface studies. Below, two of these subsurface case studies are used to document recent advances in the understanding of halokinetically-influenced deep-water systems; firstly, the Auger minibasin, Gulf of Mexico and secondly, the Lower Congo and Kwanza Basins, offshore Angola. Chapters 3, 4 and 5 build on these ideas and concepts using outcrop, modelling and subsurface data respectively.

### **Case study: Auger minibasin, Gulf of Mexico**

The Auger minibasin is an intraslope minibasin located in the northern Gulf of Mexico (Booth et al. 2000; 2003; Winker and Booth 2000; Prather 2003). Sediment pathways, routing and distribution of the Pliocene reservoir are well known due to numerous discoveries in the basin, including

the Auger and Macaroni fields. Pliocene sediments were transported into the Auger Basin from multiple sources (northeast, north, northwest and west) and either deposited within the Auger minibasin or spilled into the neighbouring Tampa minibasin through a southerly exit point (Figure 2.45). Facies distribution and depositional reservoir quality within the minibasin were strongly influenced by salt-induced topography, position within the sediment transport system (autocyclic controls) and changes in sediment supply and basin subsidence (allocyclic controls). The Auger and Macaroni fields are at different points within the transport system, close to a sediment entry and exit point respectively and therefore very different depositional characteristics are observed (Figure 2.45; Booth et al. 2003; Jackson and Hudec 2017).



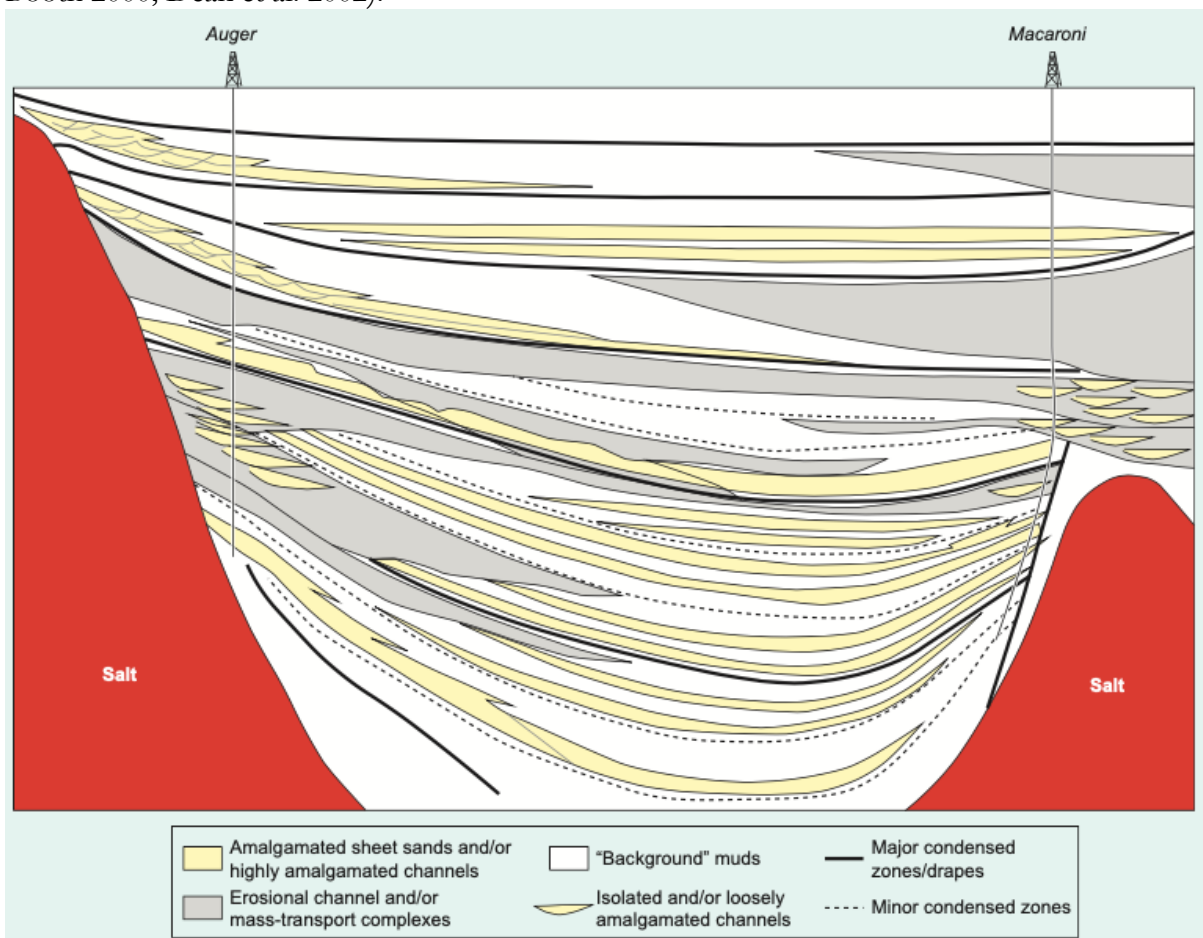
**Figure 2.45:** The distribution of late Pliocene sediments in the Auger minibasin. A-D highlights the evolution of the Auger field in four main stages: A) Turbidites are ponded to the northeast of the Auger ridge and on the downthrown side of Auger fault, trapping the bulk of sand-sized sediment before it can reach the minibasin; B) Sediments spill into the Auger minibasin, depositing high net-to-gross sheet and lobe deposits in the Auger field area; C) and D) Erosive channels cut across the Auger field area, incising many of the previously deposited reservoir sands (Booth et al. 2003; Jackson and Hudec 2017).

Sediments of the Auger Field were deposited on a slope just below the northeastern entry point (Figure 2.45). The lack of an intraslope salt sill resulted in slow sediment accumulation at the Auger Field because much of the sediment was deposited further basinward (Winker and Booth 2000). Sediment was often ponded in updip topographic depressions and turbidity currents at the sediment entry point were often erosional rather than depositional, furthering the slow accumulation rates at Auger (Booth et al. 2000). Submarine fan, variably amalgamated channel complexes and over-bank deposits are all complexly distributed at the Auger Field as a direct result of its location down-dip of a major salt-cored anticline (Winker and Booth 2000). Erosion of older channel deposits by younger channels has a particularly important control on reservoir stacking (Booth et al. 2003).

The Macaroni Field records progressive infilling of salt-induced bathymetry. The southern salt body originally provided large relief and trapped both LDTs and HDTs (Figure 2.45). Thin sandstones are seen to pinch-out towards the edge of the basin and the sequence has an overall low net-to-gross (Kendrick 2000). Rapid aggradation caused by ponding of gravity flow deposits soon lowered the apparent height of the salt induced topography and flow stripping of the turbidity currents trapped HDTs in the Auger minibasin while much of the low-density tail of the turbidite

was deposited into the neighbouring Tampa minibasin (Dean et al. 2002). This led to a sandstone dominated succession with sandstones not terminating before minibasin margins. Continued aggradation built the system to a stable, in grade profile which allowed for the formation of incisional channels and led to the bypass of turbidity currents into the Tampa minibasin. The upper minibasin fill at Macaroni is dominated by amalgamated erosional channels and mass transport complexes (Figure 2.46; Booth et al. 2000; 2003).

Sedimentation patterns in the Auger minibasin shows the effects of salt-induced topography on subsurface energy reservoir deposition. Active minibasin topography can change depositional style from ponded to bypass, and up-dip salt topography can reduce sediment accumulation in down-dip intra-slope basins (Kendrick 2000). The difference in reservoir facies distribution between the Auger and Macaroni fields are largely a function of the different bathymetric settings of the fields, the geometry of the salt structures and the proximity of sediment input and exit points to the fields, which partially controls sediment accumulation rate (Figure 2.46; Booth et al. 2000; Winker and Booth 2000; Dean et al. 2002).



**Figure 2.46:** Schematic cross-section of reservoir facies and architectures between salt walls in the Auger minibasin, showing how salt topography can influence reservoir type and distribution (Booth et al. 2003; Jackson and Hudec 2017).

### **Case study: Lower Congo and Kwanza Basins, offshore Angola**

The Lower Congo and Kwanza basins, offshore Angola, provide excellent opportunities to use spectral frequency decomposition techniques to study salt-tectonic controls on a deep-water depositional system that span several millions of years (Mayall et al. 2006; 2010; Oluboyo et al. 2014; Doughty-Jones et al. 2017; 2019; Howlett et al. 2020).

Up to 1 km of Barremian-Aptian aged salt was deposited and halokinesis began in the Albian with the evolution of large growth faults and continues today with a range of salt-cored structures that rapidly deform the sea floor (Duval et al. 1992; Valle et al. 2001; Serié et al. 2017). The Miocene

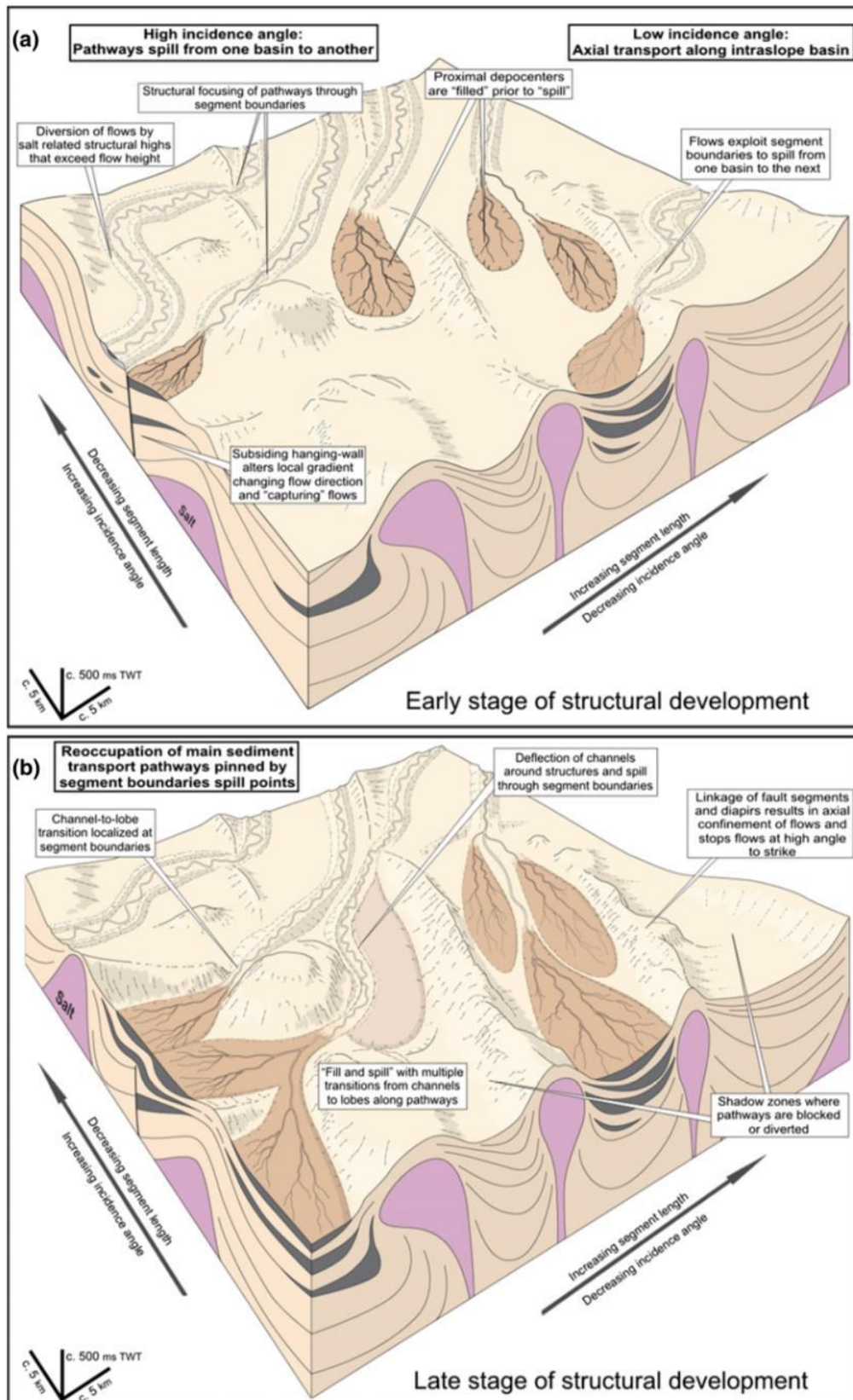


turbidites are attributed to uplift and westward tilting of the African margin which resulted in enhanced sediment supply from the ancestral Congo River (Anderson et al. 2000; Jackson et al. 2005; Seranne and Anka 2005).

In the Lower Congo Basin, Oluboyo et al. (2014) show that the importance of structural lows (segment boundaries) which have the potential to act as spill points, allowing flows to pass from one intra-slope basin to another (Figure 2.47). Channelised lobes are located down-flow of structural depressions between diapirs and segment boundaries along salt walls and normal faults (Figure 2.47). Major sediment transport pathways that pass through structurally complex slope topography may repeatedly occupy the same transport routes, resulting in vertical stacking of deep-water sedimentary systems. Shadow zones (with no coarse siliciclastic deposition) develop in areas that are either bypassed by channel-levee complexes as a result of diversion or are isolated from sediment transport pathways by laterally continuous structures (Oluboyo et al. 2014). Longer salt structures lead to large deflections or diversions and occasional blockages of sediment transport (Mayall et al. 2006; 2010).

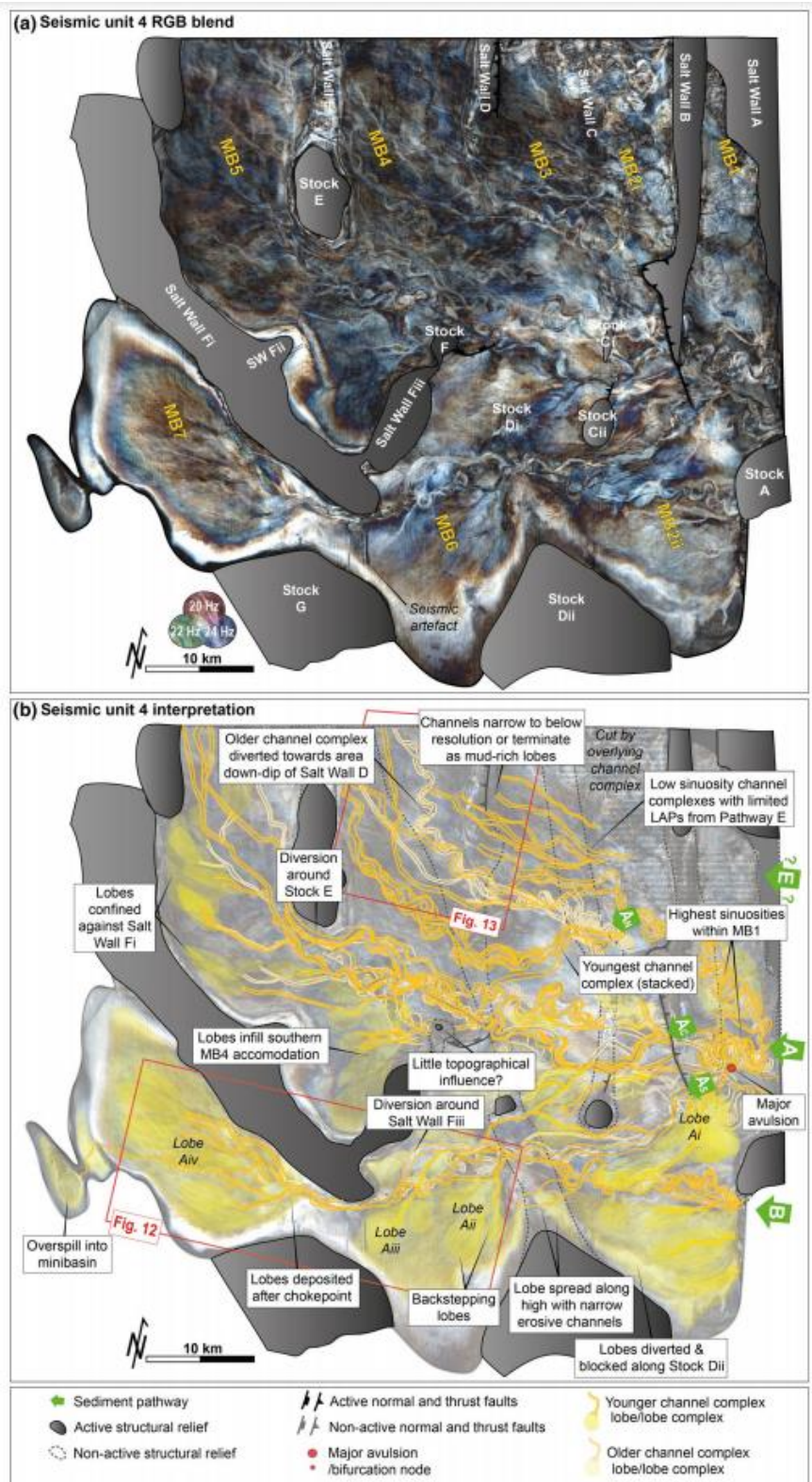
Oluboyo et al. (2014) highlight that incidence angle of the sediment transport direction with respect to strike of the salt structures exhibits a fundamentally important control on deep-water facies distribution. Where the regional flow direction is at a high angle (left hand side of Figure 2.47) to structural strike, segment boundary-controlled spill points allow sediment transport pathways to pass through multiple intraslope basins in a fill and spill manner. Local diversion around normal faults, diapirs and salt walls is controlled by the length of individual structures and the location of segment boundaries. Channel-lobe transitions are commonly located at spill points, with channelised lobes deposited down-flow of segment boundaries, where flows expand and enter depocentres (Oluboyo et al. 2014). Many previous studies have documented global examples of deep-water facies distributions where transport direction is perpendicular to salt structure strike (e.g., Sinclair 1994; Prather et al. 1998; Sinclair and Tomasso 2002).

Gravity flow deposit distribution is less well documented in scenarios where regional flow is at a lower angle to structural strike. Where these conditions occur (right hand side of Figure 2.47) the dominant style of interaction is confinement, in parallel to the 'connected tortuous corridor' of Smith (2004). Depositional systems tend to develop axially along intraslope basins. Long-distance confinement is aided by the presence of elongate salt walls or linked normal fault zones that do not have well-developed segment boundaries. These structural settings also promote the development of large and long-lived shadow zones in areas where intraslope basins are structurally isolated from the main sediment transport pathways (Oluboyo et al. 2014).

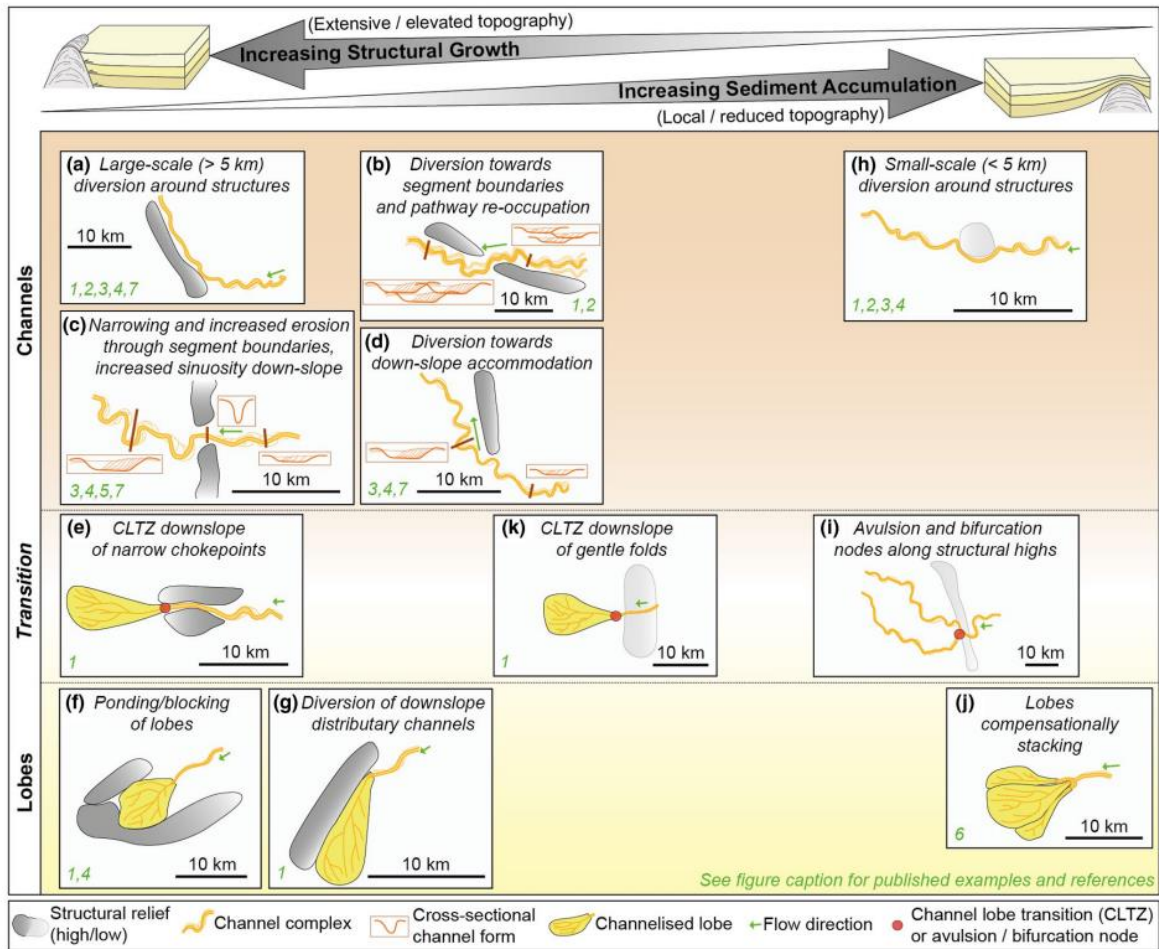


**Figure 2.47:** Summary of the relationships between deep-water depositional systems and salt-related structures in the Lower Congo Basin. A) Early phase of tectono-sedimentary development with highly segmented salt-related structures, note the control of incidence angle on sediment dispersal. B) Later phase of tectono-sedimentary development when salt-related structures have localised and linked to form more laterally continuous salt walls and elongate intra-slope basins (Oluboyo et al. 2014).

In the Kwanza Basin, Howlett et al. (2020) used advanced attribute mapping to document depositional evolution in response to topography through a 6 Myr interval of the Upper Miocene (e.g., Figure 2.48). They showed that initially, high-relief salt-cored structures confine deep-water systems to the up-dip minibasins through large-scale diversion of transverse-to-structure channel complexes, with segment boundaries localising sediment transport pathways between adjacent minibasins. Major salt-cored structures control the location of channel-lobe transition zones to immediately down-dip of segment boundaries, chokepoints and structural gradient changes across salt wall crests. The youngest units only display subtle structural topography and the expression of the salt-cored structures diminishes with time. Low-relief structures still influence turbidite systems through small-scale diversion and by controlling the location of avulsion above remnant structural highs (Howlett et al. 2020). Gradual channel diversion through lateral migration is observed during times of relatively high structural growth rate, whilst abrupt channel movement via avulsion nodes is documented during times of relatively high sediment accumulation rate (Figure 2.49; Mayall and Stewart 2000; Gee and Gawthorpe 2006; 2007; Clark and Cartwright 2009; 2011; Mayall et al. 2006; 2010; Jones et al. 2012; Hay 2012; Anderson et al. 2012; Oluboyo et al. 2014; Doughty-Jones et al. 2017; 2019; Howlett et al. 2020). Observations from the Kwanza Basin highlight complications due to strong local structural gradients and the varying angle of incidence between the deep-water system and structural strike, in agreement with observations from the Lower Congo Basin (Oluboyo et al. 2014). This drastically impacts the degree of blocking and diversion, as well as the tendency of sediment routing systems to be orientated transverse or axial to structure (Mayall et al. 2006; 2010; Jones et al. 2012; Doughty-Jones et al. 2017; 2019).

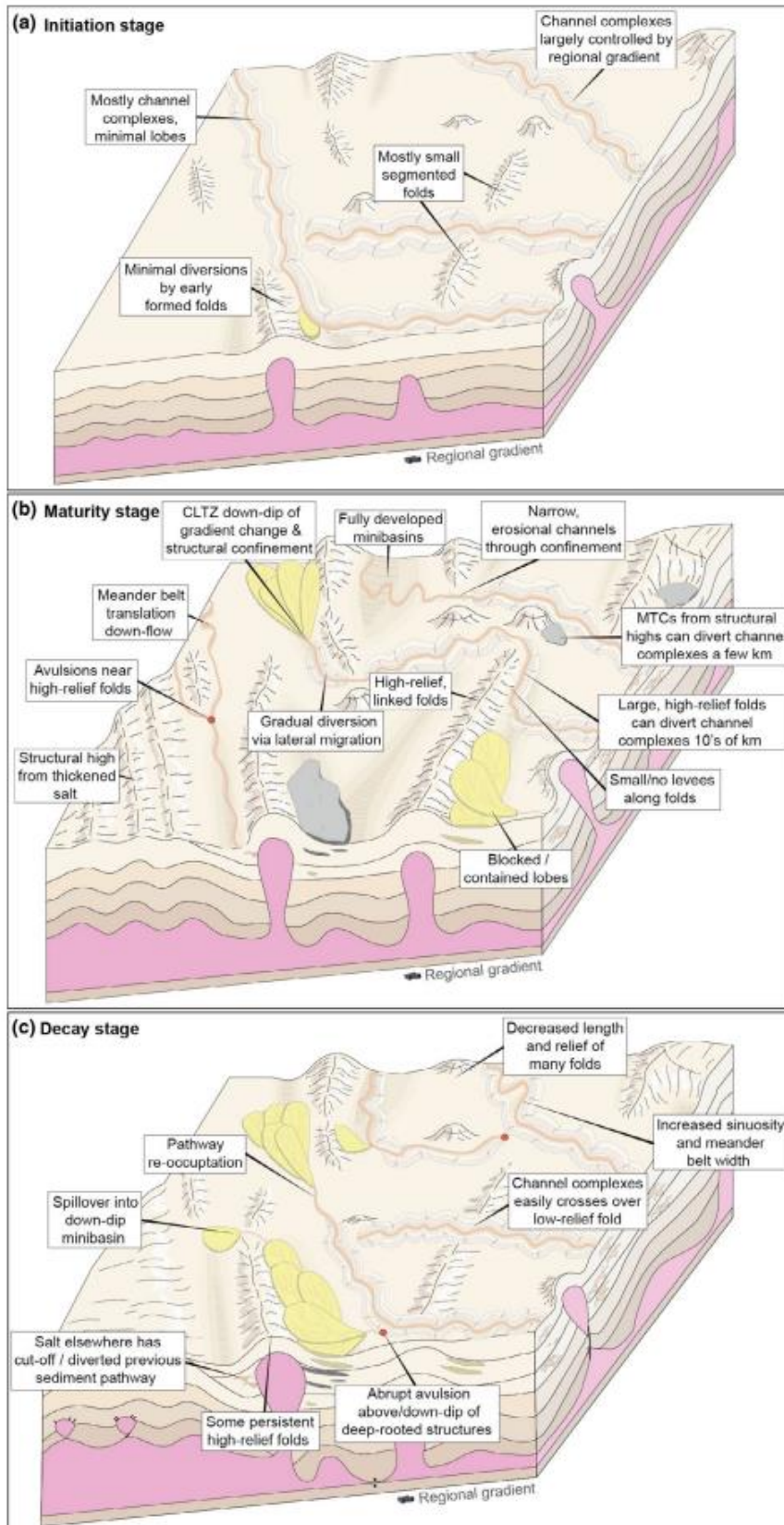


**Figure 2.48:** Example of a detailed spectral decomposition analysis used to interpret the seismic geomorphology of unit 4. A) Highlights the main salt structures and minibasins. B) Interpretation showing the main submarine channels and lobes. Active/positive topographic relief of salt structures is displayed in solid grey and the inactive/negligible topographic relief is outlined with dashed lines. Major sediment input pathways are marked with green arrows. Figure 12 and 13 of Howlett et al. (2020) are highlighted.



**Figure 2.49:** Summary graph of the major observed influences of salt-cored structures on deep-water sedimentary systems (Howlett et al. 2020). The x-axis varies sediment accumulation rate and structural growth rate relative to each other. The y-axis is separated into different depositional elements, from proximal to distal. Each sketch box contains selected subsurface examples. 1) Oluboyo et al. 2014; 2) Mayall et al. 2010; 3) Gee and Gawthorpe 2006; 4) Clark and Cartwright 2009, 2011; 5) Hay 2012; 6) Doughty-Jones et al. 2017; 7) Anderson et al. 2012.

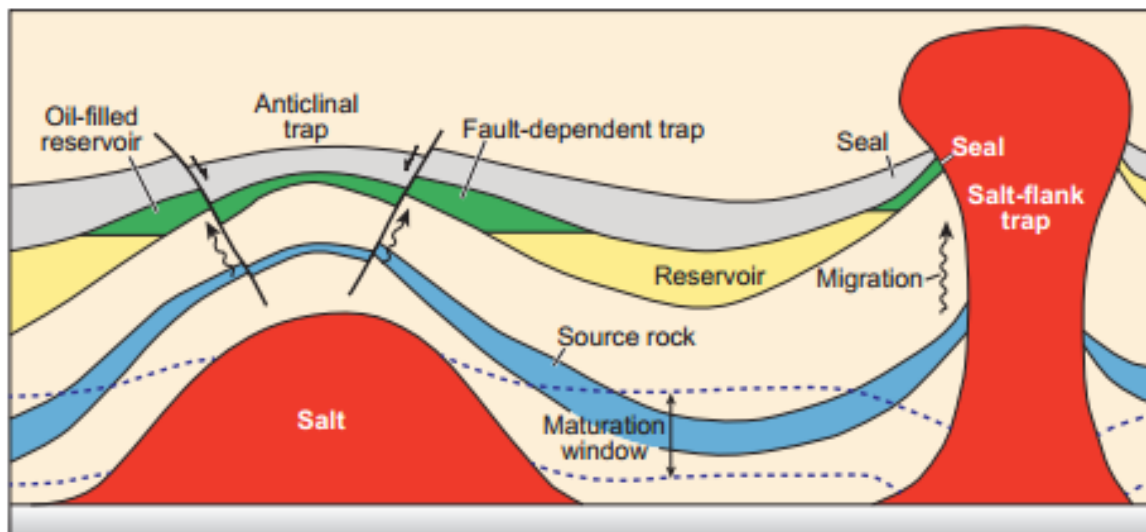
Howlett et al. (2020) use the results from Kwanza, alongside observations in other salt-influenced margins globally, to develop a generic model for the tectono-sedimentary response of deep-water systems in contractional salt domains in terms of: initiation, maturity and decay (Figure 2.50). The initiation stage is characterised by low-relief, segmented salt-cored structures and poorly defined minibasins, allowing channel complexes to largely follow the regional margin gradient with minimal diversions or ponding of unconfined flows (Figure 2.50). The maturity stage is characterised by elongate, high-relief salt-cored highs expressed as folds on the sea-floor, leading to large-scale axial diversion of channel complexes along structural strike and funnelling of depositional systems through segment boundaries and chokepoints. Diapirically-derived MTDs from local fold flanks and ponded channel-lobe systems are commonly deposited in well-developed minibasins (Figures 2.48 and 2.50). During the decay stage, structural relief is gradually subdued as sediment accumulation begins to outpace structural growth. This leads to a more complicated array of depositional elements, the evolution of which is still influenced by bypass, diversion and ponding. During the decay stage, remnant structures still exert a subtle but key control on the development and positioning of avulsion nodes within deep-water depositional environments (Figures 2.48, 2.49 and 2.50).



**Figure 2.50:** Dynamic evolution of submarine channel-lobe systems and salt-cored structures within the contractional salt domain developed from the Miocene stratigraphy of the Kwanza Basin. A) Initiation or development stage, largely controlled by the regional margin gradient and consisting of low-relief, segmented salt-cored structures. B) Maturity stage, comprised of linked, high relief salt-cored structures and well-defined minibasins. C) Decay stage, where many structures have substantially diminished in length and relief relative to sedimentation rate (Howlett et al. 2020).

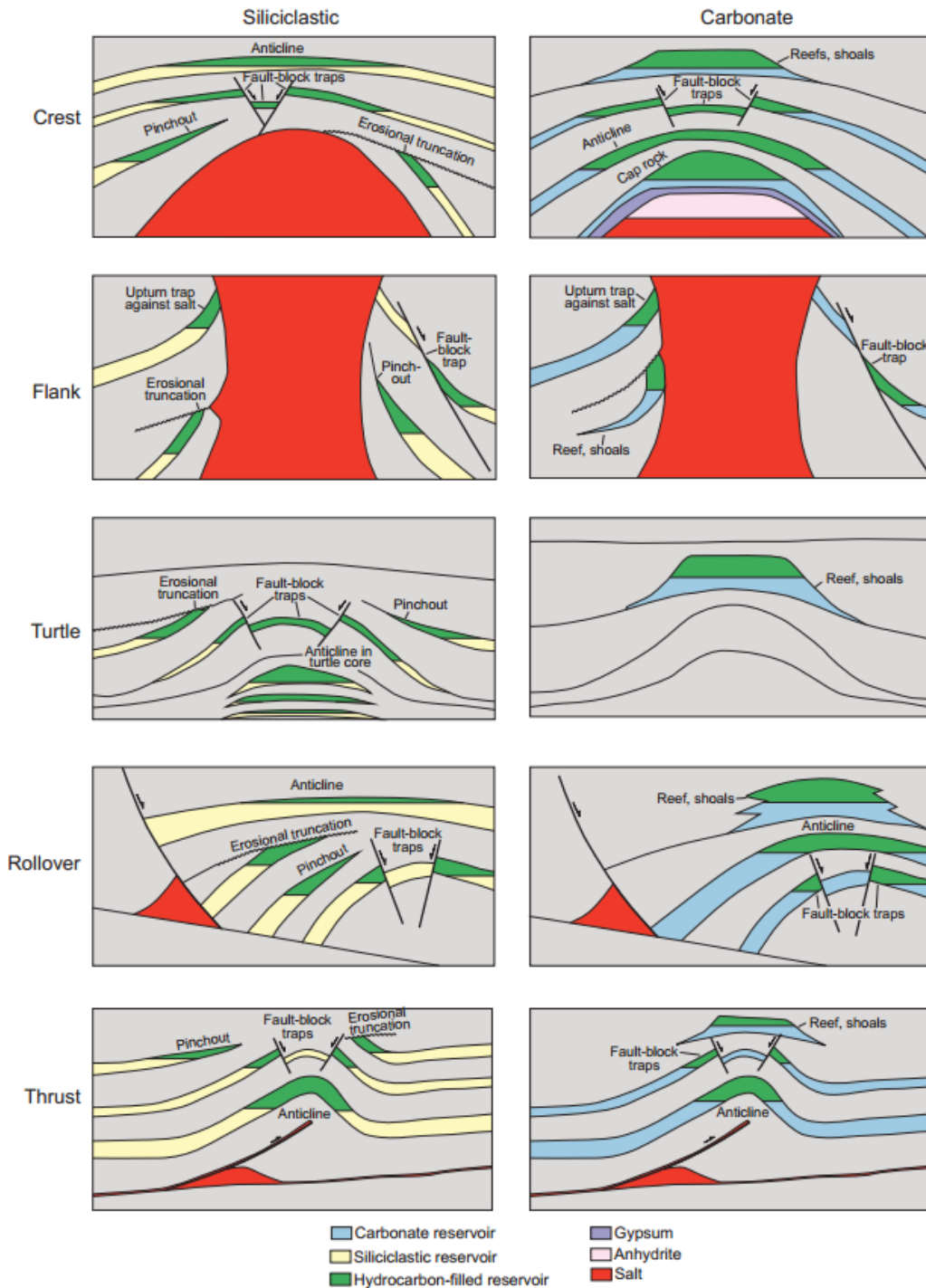
## 2.10 Subsurface Energy Implications

Historically, salt has played an important role in petroleum exploration since the Spindletop Dome discovery in Beaumont, Texas in 1906. Today, much of the prime interest in salt tectonics still derives from the petroleum industry because many of the world's largest hydrocarbon provinces reside in salt-related sedimentary basins (e.g., Gulf of Mexico, North Sea, Campos Basin, Lower Congo Basin, Santos Basin and Zagros; Figure 2.3). An understanding of salt and how it influences tectonics and sedimentation are therefore critical to effective and efficient petroleum exploration and development because salt influences all components of the hydrocarbon play (Figure 2.51; Archer et al. 2012; Jackson and Hudec 2017). Salt may also offer trap and seal potential for carbon storage projects (Archer et al. 2012; Maia da Costa et al. 2018; Roelofse et al. 2019; Lloyd et al. 2021), potential storage sites for nuclear waste (Bonin 2010; Archer et al. 2012) and areas of enhanced heat flow suitable for geothermal exploration (Harms 2015; Daniilidis and Herber 2017; Andrews et al. 2020).



**Figure 2.51:** Schematic showing elements of the petroleum system which are influenced by salt presence or halokinesis (Jackson and Hudec 2017).

The relative timing of salt movement and its impact on all components of the hydrocarbon system often governs the prospectivity of salt basins. Halokinesis controls syn- and post-kinematic sediment dispersal patterns and thus reservoir distribution (Figures 2.47, 2.48, 2.50 and 2.51). The interaction between sedimentation, salt growth and structuration are also important in understanding and predicting different types of traps. A variety of structural, stratigraphic and combined trapping mechanisms are recognised in salt basins (Figure 2.52; Jackson and Hudec 2017). Salt also provides an effective top and side seal to hydrocarbon prospects as well as carbon and hydrogen storage accumulations, acting to seal fluid migrations (Figure 2.51). In geothermal systems, as well as for source rocks in hydrocarbon systems, salt may dramatically affect the thermal evolution of sediment due to its high thermal conductivity (Figure 2.51). A thick layer of salt cools sediments that lie below it while heating sediments above it; this helps to provide favourable conditions for source rock maturation beneath thick sedimentary overburdens in the deep-water Gulf of Mexico and offshore Brazil (Jackson and Hudec 2017).



**Figure 2.52:** Subsurface energy traps that may be expected to form in halokinetically-influenced basins. Not specific to deep-water environments. Note the difference in trap geometry between siliciclastic and carbonate systems (Jackson and Hudec 2017).

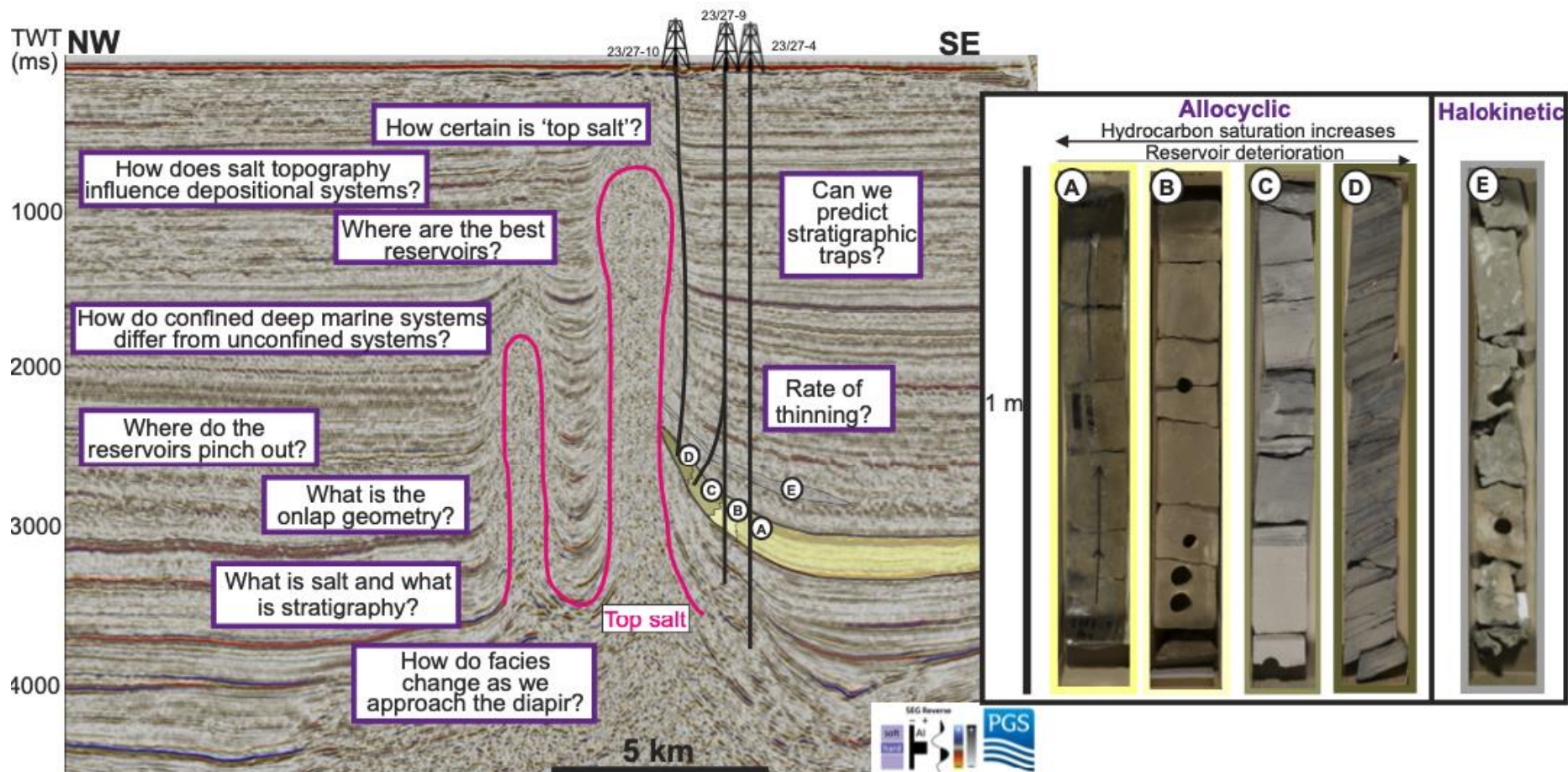
Being able to delineate the salt-sediment interface is essential for subsurface energy exploration and production but often difficult in subsurface data alone because of the well-known “shadowing” effect of salt, especially if the diapirs have developed overhangs (Jones and Davison 2014). Seismic imaging of diapir flank reservoirs is poor due to a combination of steeply-dipping beds, intensely-fractured strata, extreme stratigraphic thickness variations, overlying gas clouds and poor velocity control (Davison et al. 2000). The combined evolution of salt and surrounding sediments, including their mutual interaction, remains one of the major problems in understanding salt-dominated basins (Figure 2.53; Lerche and Petersen 1995; Jackson and Hudec 2017). Seismic data alone



cannot indicate the exact location of reservoir sandstone terminations against topography, and therefore incorporation of well data and other data sets (e.g., outcrop, modelling) is imperative to properly characterise stratigraphic pinch-outs adjacent to salt structures (Jones and Davison 2014; Nagatomo and Archer 2015; Jackson and Hudec 2017).

The variable distribution of depositional facies also impacts potential seal against salt or steep welds since some of the sandstones will be in contact with the salt/weld and others will be encased in shales some distance away. In CHS, Giles and Rowan (2012) suggest sandstones at lower (deeper) levels in tapered (stacked wedges) will be steep-overtuned such that pressures might be high and only a small, local column will be contained (Figures 2.30, 2.31, 2.32 and 2.33). Sandstones in upper levels of tapered CHS might have lower pressure, due to shallower nature, allowing for the build-up of larger hydrocarbon column height and greater lateral extent (Giles and Rowan 2012).

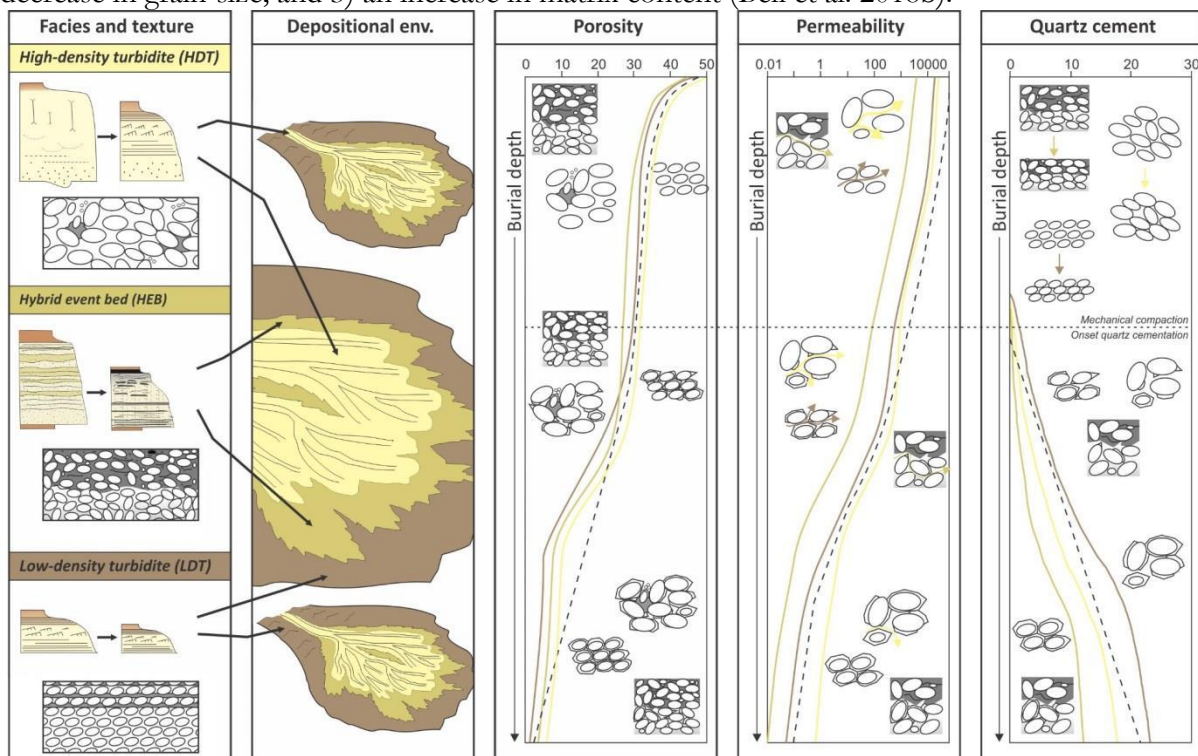
Reservoir geometries might impact which sandstones are hydrocarbon charged: if migration is only along the salt-sediment interface reservoirs isolated away from the diapir flanks (e.g., channels and lobes confined between two structures) may remain water wet (Giles and Rowan 2012). If hydrocarbons migrate towards the diapir from elsewhere (e.g., more basinal positions) these diapirically isolated sandstones may be hydrocarbon charged and therefore make the best hydrocarbon targets, especially where these channels or lobes are well-stacked due to confinement between the diapirs (Figure 2.53; Giles and Rowan 2012; Jackson and Hudec 2017).



**Figure 2.53:** Seismic reflection cross-section from the Pierce diapirs, Eastern Central Graben, UK North Sea, highlighting some of the key questions and uncertainties of subsurface interpretations in salt-influenced basins. Confidently mapping top salt, visualising pinch-outs and onlap geometries in areas of lower-quality data adjacent to the salt, and studying lateral and vertical extent of syn-kinematic deformation and sedimentation are challenging. Seismic data courtesy of PGS (MegaSurvey Plus 3D seismic data). Drape fold model (modified from Giles and Lawton 2002) shows the importance of understanding diapir onlaps for reservoir quality prediction and hydrocarbon saturation estimations. Shading schematically indicates reservoir quality, yellow indicating good reservoir quality and brown showing reservoir deterioration. Core sticks A-E are representative of halokinetically-influenced stratigraphy on the diapirs flanks of the Pierce Diapirs. Core images publicly available from the British Geological Survey.

Flows transforming from HDTs at the base of slope to LDTs, transitional flow deposits or laminar flow deposits upslope, generally decrease in reservoir quality (Figure 2.53). Therefore, reservoir quality typically deteriorates, mudstone percentage increases and bed thickness decreases as the diapir is approached (Figure 2.53; Nagatomo and Archer 2015; Porten et al. 2016; Bell et al. 2018b). Porosity, permeability and cementation have been studied for deposits of different SGF (Figure 2.54; Porten et al. 2016; Bell et al. 2018b). Porosity is greater in HDTs compared to LDTs and hybrid beds (Figure 2.54). Permeability trends show that consistently, regardless of depth, HDTs have the highest permeability, followed by LDTs and then hybrid beds (Figure 2.54). Quartz cementation is most abundant in LDTs followed by HDTs, and hybrid beds are less cemented (Porten et al. 2016).

Within a deep-water sedimentary system, a sharp decrease in depositional reservoir quality between the lobe off-axis and lobe fringe occurs due to: 1) an abrupt increase in matrix content; 2) an abrupt decrease in sandstone amalgamation; and 3) a decrease in grain-size (Figures 2.53 and 2.54; Porten et al. 2016). There is also a sharp decrease in depositional reservoir quality between channel axis and channel margin due to: 1) a decrease in total sandstone thickness and amalgamation; 2) a decrease in grain-size; and 3) an increase in matrix content (Bell et al. 2018b).



**Figure 2.54:** Conceptual model illustrating porosity, permeability and quartz-cement development with burial for HDTs (yellow), hybrid beds (green) and LDTs (brown). The dashed line represents typical previously published depth trends for reservoir sandstones (e.g., Bjørlykke et al. 1998; Ehrenberg 1990; Ramm 2000). Variability in evolution of reservoir properties with burial is controlled by depositional character (especially grain size, sorting, detrital-clay content and proportion of ductile grains) and quartz cementation (function of temperature history, quartz grain volume, grain size and degree of quartz grain coating by clays etc.) (Porten et al. 2016).

## 2.11 Summary

Understanding of halokinetically-influenced deep-water systems has advanced substantially since Menard (1955) first proposed the idea that the basin floor was sub-divided into confined pockets or ‘minibasins’. This has mainly been driven by an increase in subsurface data quantity and quality, reflecting the commercial interest in salt-basins from the hydrocarbon industry (Jackson and Hudec 2017). Outcrop, numerical modelling and integrated studies of halokinetically-influenced

deep-water settings remain rare and therefore the evolution, controlling variables and sub-seismic scale heterogeneities of these systems remain poorly understood. This chapter has introduced the key aspects of deep-water depositional systems, salt tectonics and the interactions of the two, which provides a foundation of historic understanding and recent advancements, on which subsequent chapters build.

## Chapter 3: Interactions between deep-water gravity flows and active salt tectonics

Zoë A. Cumberpatch<sup>1</sup>, Ian A. Kane<sup>1</sup>, Euan L. Soutter<sup>1</sup>, David M. Hodgson<sup>2</sup>, Christopher A-L. Jackson<sup>1</sup>, Ben A. Kilbams<sup>3</sup>, and Yohann Poprawski<sup>4</sup>.

<sup>1</sup>*SedRESQ, Department of Earth and Environmental Sciences, University of Manchester, Oxford Road, Manchester M13 9PL, U.K.*

<sup>2</sup>*The Stratigraphy Group, School of Earth and Environment, University of Leeds, Leeds LS2 9JT, U.K.*

<sup>3</sup>*Shell Upstream International, York Road, London SE1 7LZ, U.K.*

<sup>4</sup>*LPG-BIAF UMR-CNRS 6112, UNIV Angers, CNRS, UFR Sciences, 2 bd Lavoisier 49045, Angers CEDEX 01, France.*

**Status:** Published in Journal of Sedimentary Research

*Cumberpatch, Z.A., Kane, I.A., Soutter, E.L., Hodgson, D.M., Jackson, C. A-L., Kilbams, B.A., and Poprawski, Y., 2021, Interactions of deep-water gravity flows and active salt tectonics, Journal of Sedimentary Research, v. 91, p. 34-65.*

### 3.1 Abstract

Behaviour of sediment gravity flows can be influenced by seafloor topography associated with salt structures; this can modify the depositional architecture of deep-water sedimentary systems. Typically, salt-influenced deep-water successions are poorly imaged in seismic reflection data, and exhumed systems are rare, hence the detailed sedimentology and stratigraphic architecture of these systems remains poorly understood. The exhumed Triassic (Keuper) Bakio and Guernica salt bodies in the Basque–Cantabrian Basin, Spain, were active during deep-water sedimentation. The salt diapirs grew reactively, then passively, during the Aptian–Albian, and are flanked by deep-water carbonate (Aptian–earliest Albian Urgonian Group) and siliciclastic (middle Albian–Cenomanian Black Flysch Group) successions. The study compares the depositional systems in two salt-influenced minibasins, confined (Sollube basin) and partially confined (Jata basin) by actively growing salt diapirs, comparable to salt-influenced minibasins in the subsurface. The presence of a well-exposed halokinetic sequence, with progressive rotation of bedding, beds that pinch out towards topography, soft-sediment deformation, variable paleocurrents, and intercalated debrites indicate that salt grew during deposition. Overall, the Black Flysch Group coarsens and thickens upwards in response to regional axial progradation, which is modulated by laterally derived debrites from halokinetic slopes. The variation in type and number of debrites in the Sollube and Jata basins indicates that the basins had different tectonostratigraphic histories despite their proximity. In the Sollube basin, the routing systems were confined between the two salt structures, eventually depositing amalgamated sandstones in the basin axis. Different facies and architectures are observed in the Jata basin due to partial confinement. Exposed minibasins are individualised, and facies vary both spatially and temporally in agreement with observations from subsurface salt-influenced basins. Salt-related, active topography and the degree of confinement are shown to be important modifiers of depositional systems, resulting in facies variability, remobilisation of deposits, and channelisation of flows. The findings are directly applicable to the exploration and development of subsurface energy reservoirs in salt basins globally, enabling better prediction of depositional architecture in areas where seismic imaging is challenging.

### 3.2 Introduction

The sedimentology and stratigraphic architecture of deep-water systems deposited in unconfined basins (e.g., Johnson et al. 2001; Baas 2004; Hodgson 2009; Prélat et al. 2009; Hodgson et al. 2011; Sychala et al. 2017), or in basins with static or relatively static topography (e.g., Kneller et al. 1991;

Haughton 1994; McCaffrey and Kneller 2001; Sinclair and Tomasso 2002; Amy et al. 2004; Soutter et al. 2019), are reasonably well established compared to those in basins influenced by active topography (e.g., Hodgson and Haughton 2004; Cullen et al. 2019).

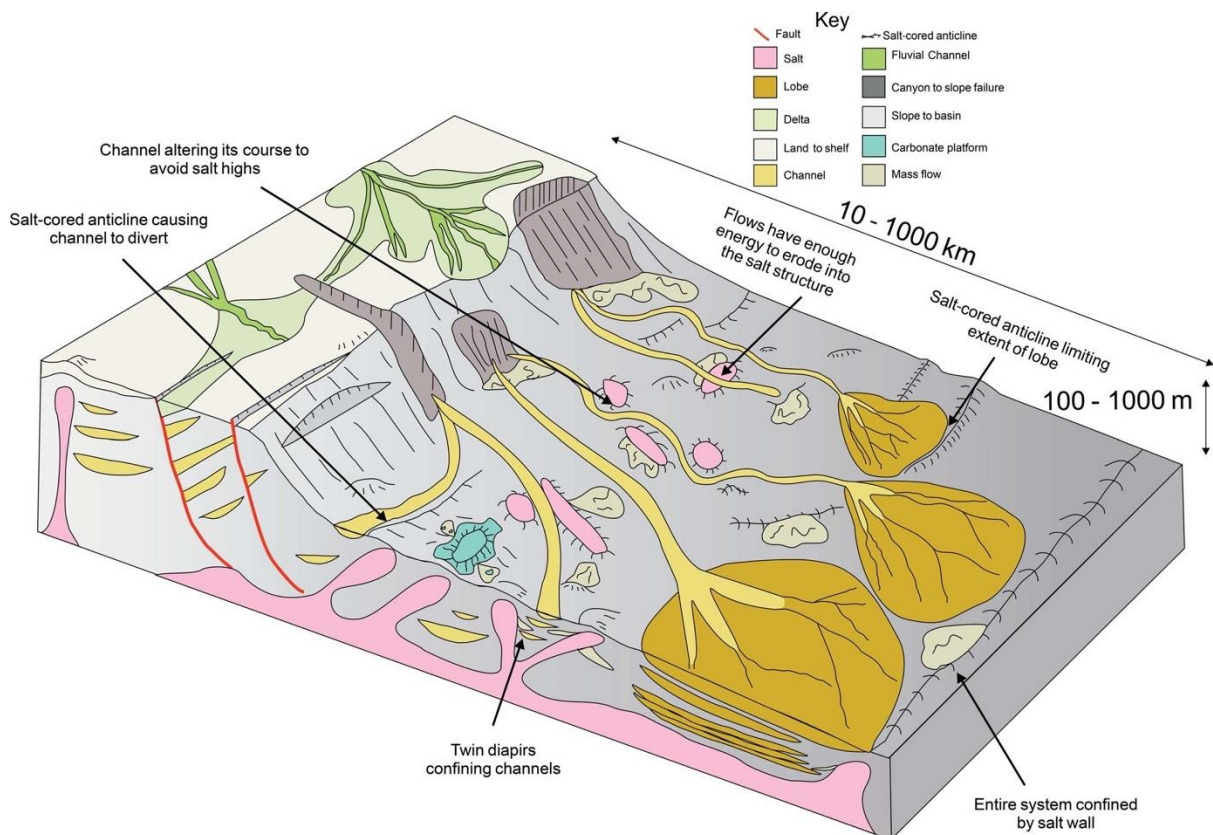
Seafloor topography is generated by a variety of geological processes, including relief above mass-transport deposits (MTDs) (e.g., Ortiz-Karppf et al. 2015; 2016; Soutter et al. 2018; Cumberpatch et al. 2021), syn-depositional tectonic deformation (e.g., Hodgson and Haughton 2004; Kane et al. 2010) and salt diapirism (Figure 3.1; e.g., Hodgson et al. 1992; Kane et al. 2012; Prather et al. 2012; Oluboyo et al. 2014). Salt-tectonic deformation influences over 120 basins globally (Hudec and Jackson 2007), including some of the world's largest petroleum-producing provinces (e.g., Booth et al. 2003; Oluboyo et al. 2014; Charles and Ryzhikov 2015; Rodriguez et al. 2018; 2020; Grant et al. 2019; 2020a; 2020b; Pichel et al. 2020).

Subsurface studies have shown that salt structures deforming the seafloor can exert substantial control on the location, pathway, and architecture of lobe, channel-fill, levee, and mass-transport deposits (Figure 3.1; e.g., Mayall et al. 2006; 2010; Jones et al. 2012; Wu et al. 2020; Howlett et al. 2020). Turbidity currents that were ponded, diverted, deflected, and confined by salt structures (Figure 3.1) are well documented in the eastern Mediterranean (e.g., Clark and Cartwright 2009; 2011), offshore Angola (e.g., Gee and Gawthorpe 2006, 2007), the Gulf of Mexico (e.g., Booth et al. 2003) offshore Brazil (e.g., Rodriguez et al. 2018; 2020), the North Sea (e.g., Mannie et al. 2014), and the Precaspian Basin (e.g., Pichel and Jackson 2020). Successions of genetically related growth strata influenced by near-surface diapiric or extrusive salt form unconformity-bounded packages of thinned and folded strata termed halokinetic sequences, which become composite when stacked (Giles and Rowan 2012; Rowan and Giles 2021). The geometry and stacking of composite sequences are dependent on the interplay between sediment accumulation rate and diapir rise rate. Giles and Rowan (2012) recognise two end-member stacking patterns; tapered (stacked wedge) or tabular (stacked hook).

Typically, salt-influenced successions are poorly imaged in seismic reflection data due to ray path distortion at the salt–sediment interface, steep stratigraphic dips, and deformation associated with salt rise (Davison et al. 2000; Jones and Davison 2014). Due to these complications, our understanding of subsurface salt-influenced systems benefits from their calibration to outcrop analogues (Lerche and Petersen 1995). Exposed examples are rare, largely due to dissolution of associated halites (Jackson and Hudec 2017). Exhumed systems typically contain shallow-marine (e.g., Laudon 1975; Giles and Lawton 2002; Giles and Rowan 2012) or nonmarine (e.g., Banham and Mountney 2013a, 2013b, 2014; Ribes et al. 2015) strata. The Bakio diapir in the Basque–Cantabrian Basin (BCB), northern Spain, provides a rare exhumed example of deep-water strata deposited in a syn-halokinetic setting (Figures 3.2 and 3.3; Lotze 1953; Robles et al. 1988; Rowan et al. 2012; Ferrer et al. 2014). The overburden displays well-exposed, unconformity-bounded sedimentary wedges that thin towards and upturn against the diapir, supporting the interpretation of syn-halokinetic growth strata (Poprawski et al. 2014; 2016).

Previous studies in the area have focused on carbonate halokinetic sequences in the middle Albian overburden (Poprawski et al. 2014, 2016), hence the salt-influenced deep-water succession remains poorly understood. This study aims to use large-scale outcrops exposed along the Bakio–Guernica coastline to study the bed-scale flow-topography interactions, deep-water facies distribution, and depositional architecture in salt-controlled minibasins. The objectives of this study are to: 1) reappraise the stratigraphy of the study area using specific deep-water sub-environments; 2) document lateral and vertical changes in deep-water facies and architecture with variable amounts of salt-induced confinement; 3) document the evolution of coeval deep-water axial and debrite-rich lateral

depositional systems; and 4) distinguish criteria for the recognition of halokinetically-influenced deep-water systems.



**Figure 3.1:** Sketch summarising the structural controls, with respect to gravity-driven processes, on depositional systems from the shelf to basin floor. Note the complex and sinuous paths taken by slope channels around salt structures (Modified from Mayall et al. 2010).

### 3.3 Geological setting

#### ***Evolution of the Basque-Cantabrian Basin (BCB)***

The BCB is a peri-cratonic rift basin in northern Spain, inverted during the Campanian–Eocene western Pyrenean Orogeny (Figure 3.2; Gómez et al. 2002; Ferrer et al. 2008). The basin is located between the Iberian and Eurasian plates and is associated with hyper-extensive rifting and mantle exhumation during the opening of the North Atlantic and the Bay of Biscay (Van der Voo 1969; Brunet 1994; Jammes et al. 2009; DeFelipe et al. 2017; Teixell et al. 2018). The BCB is a magma-poor hyper-extended rift with extremely thin crust and locally exhumed mantle (Jammes et al. 2009; Teixell et al. 2018). The stratigraphy of the BCB is mainly of Mesozoic to Cenozoic age, sourced from a punctuated rift system that existed from Permian–Triassic to Late Cretaceous times (Cámara 2017).

The Mesozoic evolution of the BCB began with the development of a rift system in the Permian–Triassic. During the Carnian–Norian, a thick sequence of mudstones, sabkha evaporites and carbonates accumulated in an arid, restricted environment (Keuper Group; Geluk et al. 2018). The Keuper Group in the BCB varies in thickness from 10 to <3000 m (Pinto et al. 2005) with increased thickness associated with zones of intense diapirism (Cámara 2017). The Jurassic to Early Cretaceous was characterised by limited subsidence and shallow-water and terrestrial deposition (Martín-Chivelet et al. 2002; García-Mondéjar et al. 2004). Extensional thin-skinned tectonics, controlled by basement faulting, in the Early Cretaceous initiated reactive diapirism across the basin (Bodego and Agirrezabala 2013; Agirrezabala and Dinarés-Turell 2013; Teixell et al. 2018).

As rifting continued, the Lower Cretaceous succession preferentially accumulated over down-thrown blocks, forming a differential load that triggered a transition into passive diapirism (Agirrezabala and García-Mondéjar 1989; Agirrezabala and López-Horgue 2017). During the Barremian–Albian the flanking minibasins were filled with c. 500 m of mixed carbonates and siliciclastics (García-Mondéjar 1990; 1996). Aptian–middle Albian shallow-water carbonate platforms of Urgonian limestone (García-Mondéjar et al. 2004) formed on the footwalls of tilted normal-fault blocks; these limestones pass abruptly into deeper-water marlstones and mudstones deposited in hanging-wall depocenters (Rosales and Pérez-García 2010). The Urgonian platforms of the BCB evolved in four major stages of platform development: carbonate ramp (early Aptian), distally-steeped ramp (late Aptian), progradational-aggradational steep-sloping platform (earliest Albian) and carbonate bank (mid-late Albian). These stacked major platform intervals are separated by unconformities that represent platform exposure and karstification (Type 1 sequence boundaries) and/or drowning and/or increased terrestrially derived siliciclastic influx (García-Mondéjar 1990; Fernández-Mendiola et al. 1993; Rosales 1999; Gómez-Pérez et al. 1999; Rosales and Pérez-García 2010).

From the late Albian to the early Cenomanian, subsidence combined with early Albian global sea-level rise (Vail et al. 1977; Haq et al. 1987; Robles et al. 1988; Haq 2014) was concurrent with the development of siliciclastic turbidites and redeposited carbonates of the Black Flysch Group (BFG), which are the focus of this study. Pillow-lavas and submarine volcanoclastic deposits, related to seafloor spreading in the Bay of Biscay, are intercalated in the upper part of the Black Flysch Group in some locations across the BCB allowing for a paleontologically constrained late middle Albian age ((c. 102 Ma representing the base of the *Hysterocheras varicosum* Zone (Castañares et al. 2001; Castañares and Robles 2004; López-Horgue et al. 2009)).

As rifting waned, passive diapirs continued to grow at the paleo-seafloor due to minibasin subsidence (Zamora et al. 2017). During the Late Cretaceous to the early Paleogene, subsidence continued and calci-turbidites and basin wide mudstones were deposited (Mathey 1987; Pujalte et al. 1994; 1998). Lower Palaeocene to Eocene stratigraphy records a gradual transition from mainly calcareous to siliciclastic deposition, with an increase in deposition of siliciclastic turbidites. This change is associated with erosion of the emerging Pyrenean Mountain belt (Crimes 1973; Pujalte et al. 1998). Pyrenean NE–SW-oriented compression in Eocene to Oligocene times reactivated Mesozoic–Cenozoic normal faults (Ábalos 2016) and squeezed pre-existing diapirs (Pujalte et al. 1998).

### ***Diapirs in the BCB***

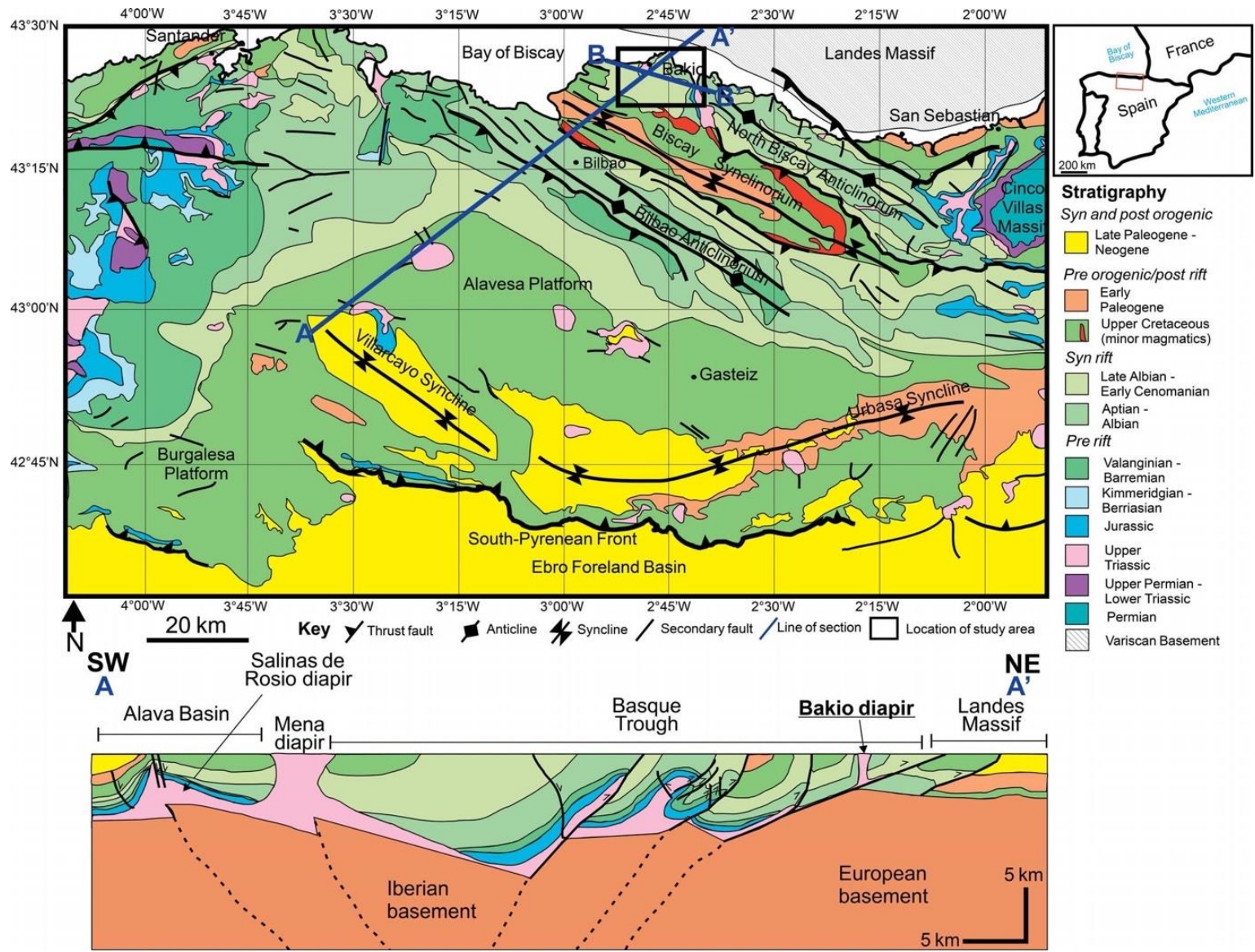
The Triassic Keuper Group outcrops in several diapirs across the Basque Cantabrian Basin; some of these diapirs have been documented for over 70 years (Lotze 1953). The Estella-Lizarrá, Salinas de Oro, Gulina and Mena diapirs (García-Mondéjar 1996), Pondra and Laredo Bay diapirs (López-Horgue et al. 2009), Guernica Diapir (García-Mondéjar and Robador 1987) and Bakio Diapir (Poprawski et al. 2014; 2016) were growing during the Albian, due to regional extension and subsequent subsidence. Several of these diapirs are located at the intersection between major Hercynian Basement faults (García-Mondéjar 1996), reactivated during the opening of the BCB. Basement faulting controlled the distribution of halokinetic structures during middle-late Albian times (Bodego and Agirrezabala 2013). The diapirs of Bakio, Guernica and Lequeitio were at or close to the seabed during the middle Albian creating highs which were capped by isolated Urgonian carbonate platforms (Cámara 2017).

The Bakio diapir is a NE–SW-trending (c. 1 km by 4 km) salt wall of Keuper Group evaporites. Partial exposure of the salt wall occurs at Bakio beach; in other locations the evaporites are easily eroded, typically marked by topographic depressions and/or coastal embayments (e.g., Figure



3.3A; the Guernica structure, located c. 9 km to the east). At Bakio beach, the Keuper Group consists of red clays, gypsum, and carbonate, with Triassic- age tholeiitic ophitic inclusions (see Robles et al. 1988; Poprawski et al. 2014). From the middle Albian, the Bakio diapir grew rapidly and reactively in response to regional hyper-extension (Teixell et al. 2018). The diapir then grew passively during the late Albian due to sediment loading, at around 500 m Myr<sup>-1</sup> (Poprawski et al. 2014).

The Guernica structure is poorly understood due to limited exposure, and hence is referred to as a “salt structure” rather than a salt diapir like Bakio. The Guernica structure has previously been interpreted as a salt-cored anticline (Poprawski and Basile 2018). Vintage onshore seismic reflection data suggest that the basal salt layer is present at depth connecting the Bakio and Guernica structures (Figure 3.4; Robles et al. 1988; Poprawski and Basile 2018). The structures were close to the seafloor during the middle Albian creating highs that were capped by isolated carbonate platforms and influenced the deposition of the BFG (Vicente Bravo and Robles 1991a, 1991b; Pujalte et al. 1986; Cámara 2017; Roca et al. 2021). Slope apron facies, deposited at the platform edge, and subsequent stratigraphy formed tapered halokinetic sequences against the west of the Bakio diapir (Figure 3.4; García-Mondéjar and Robador 1987; Soto et al. 2017; Roca et al. 2021).



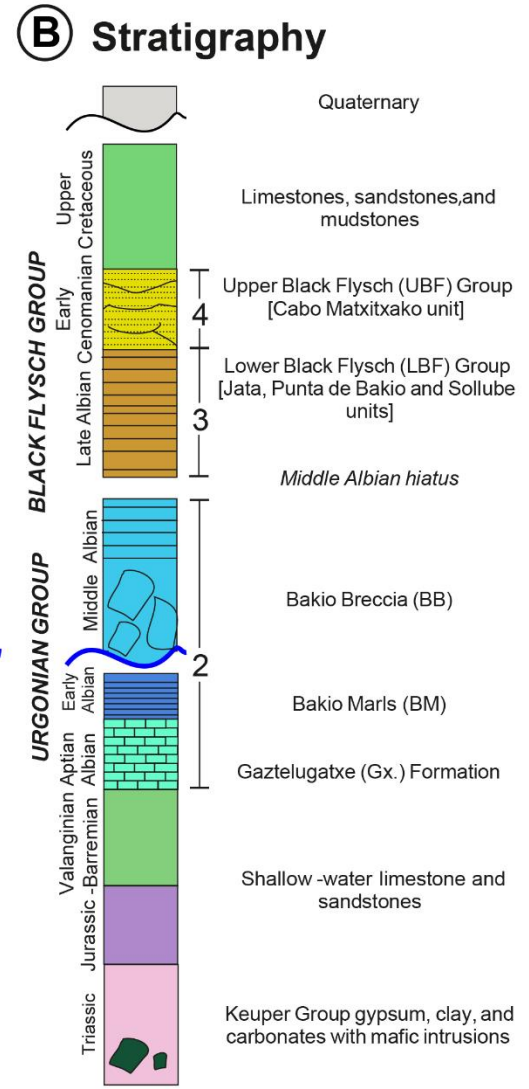
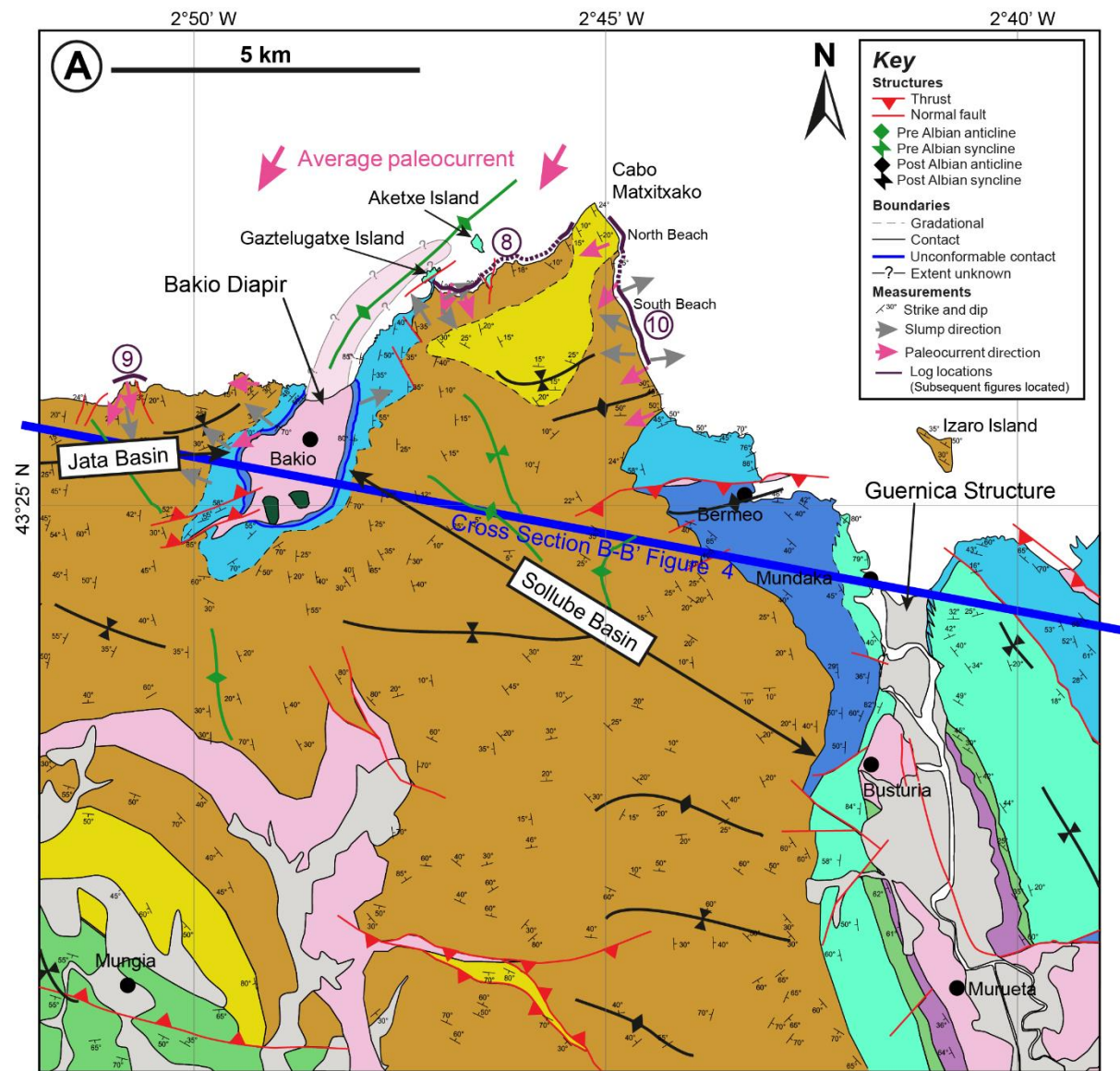
**Figure 3.2:** Simplified geological map, stratigraphy, and cross-section of the Basque–Cantabrian Basin (BCB), highlighting numerous present-day surface exposures of NE–SW-oriented diapirs (including the Bakio diapir, the focus of this study), commonly flanked by Cretaceous strata. The inset map shows the location of the BCB in northern Spain. Line A–A' locates cross section and line B–B' locates Figure 3.4. Black box locates Figure 3.3. Stratigraphy indicates mega sequences that can be used to group basin fill (after Abalos 2016). Cross section is modified from Poprawski et al. (2016).

### **Bakio Stratigraphy**

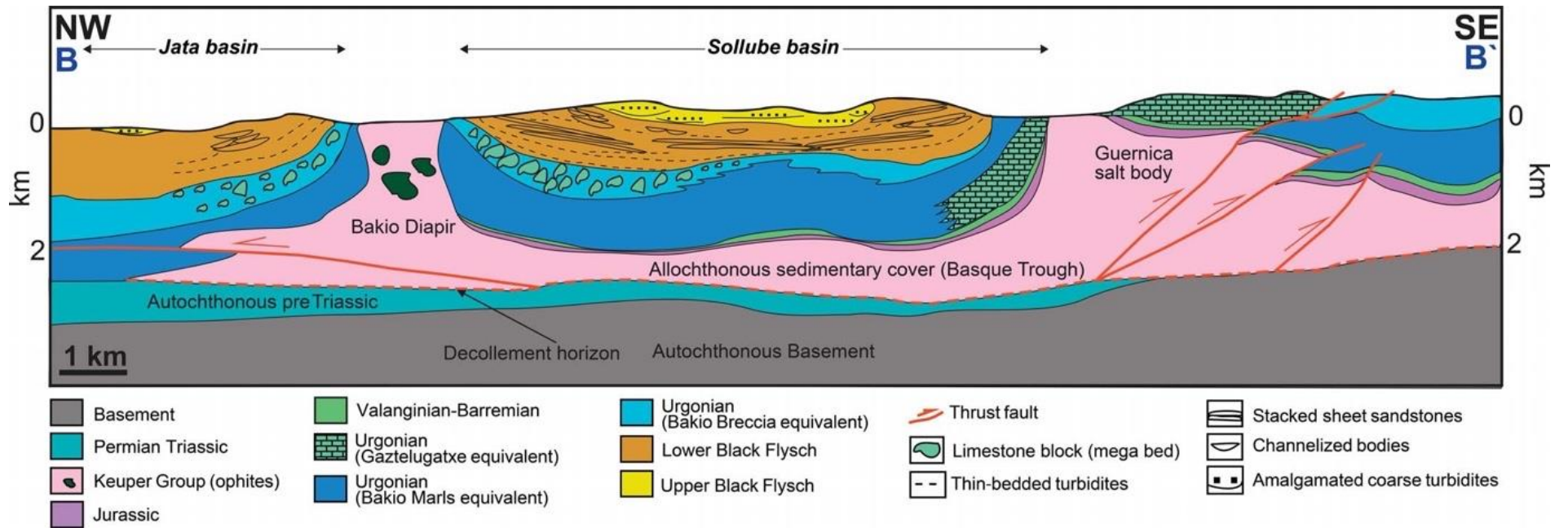
Studies of magnetic anisotropy in the Bakio–Guernica area demonstrate a minimal Pyrenean compressional overprint to the stratigraphy (Soto et al. 2017), as the tholeiitic ophitic inclusions in the diapir acted as buttresses forming shadow areas protected from the compression. Hence the area is used to study syn-halokinetic deposition without a regional tectonic-deformation overprint.

The Aptian–middle Albian Urgonian stratigraphy (middle Albian Sequence 2: *H. dentatus* Zone of Agirrezabala and López-Horgue 2017) comprises the Gaztelugatxe, Bakio Marls, and Bakio Breccias formations (Figure 3.3B). The Gaztelugatxe Formation (GZF) is a massive-brecciated limestone, interpreted as a karstified platform carbonate (García-Mondéjar and Robador 1987; Robles et al. 1988). The Bakio Marls Formation (BMF) (minimum 60 m thick: Poprawski et al. 2016) comprises thin-bedded calci-debrites deposited in a low-energy mud-dominated environment intermittently punctuated by catastrophic debris flows sourced from local, carbonate-capped highs (García-Mondéjar and Robador 1987; Poprawski et al. 2014). The Bakio Breccias Formation (BBF) is up to 550 m thick and unconformably overlies the BMF (Figures 3.3B and 3.4; Table 3.1). The BBF is primarily composed of poorly sorted, carbonate breccia beds tens of metres thick (Table 3.1; García-Mondéjar and Robador 1987; Poprawski et al. 2014; 2016) that are interpreted as earliest middle Albian mass failures from carbonate platforms developed on top of salt structures (Poprawski et al. 2014). The abrupt change from carbonate-dominated to siliciclastic-dominated stratigraphy is associated with a middle Albian hiatus (López-Horgue et al. 2009).

The Urgonian section is overlain by the upper Albian–early Cenomanian BFG, which has been subdivided into a lower and upper unit (Figure 3.3B). The Lower Black Flysch Group (LBF) corresponds to the upper Albian Sequence 3 (*D. cristatum*–*M. inflatum* zones; Agirrezabala and López-Horgue 2017), including the Sollube, Punta de Bakio, and Jata units (Poprawski et al. 2014). This group consists of thin-bedded siliciclastic turbidites, marls, and debrites, and is interpreted to represent a submarine fan system (Robles et al. 1988; Vincente Bravo and Robles 1991; 1995; Poprawski et al. 2014; Roca et al. 2021). The Upper Black Flysch Group (UBF) corresponds to the upper Albian–Cenomanian Sequence 4 (*M. fallax* zone; Agirrezabala and López-Horgue 2017), and the Cabo Matxitxako unit of Poprawski et al. (2014), which consists of thick-bedded, coarse-grained, siliciclastic turbidites deposited in a submarine fan system (Robles et al. 1988; 1989). Provenance studies indicate that BFG sediment was sourced from the northerly Landes Massif, of the Amorrican Platform, a c. 100 km by 40 km granitic basement block, presently located c. 10 km offshore in the Bay of Biscay (Figure 3.2; García-Mondéjar 1996; Puelles et al. 2014).



**Figure 3.3:** A) Geological map located in Figure 3.2 and B) stratigraphic column for the study area. A) Compiled from Espejo and Pastor (1973), Espejo (1973), Garrote-Ruiz et al. (1991, 1992, 1993a, 1993b), Pujalte et al. (1986), García-Mondéjar and Robador (1987), Robles et al. (1988; 1989), Vicente Bravo and Robles (1991a, 1991b), Poprawski et al. (2014; 2016), Ábalos (2016), and fieldwork observations. Lateral facies changes in carbonates around the salt outcrop at Guernica are modified from García-Mondéjar and Robador (1987). The Guernica structure has been weathered away and forms a present-day estuary. Orange lines show locations of stratigraphic logs shown in subsequent figures, dashed lines indicate missing section, and numbers refer to subsequent figures where logs are presented. B) Abbreviations for stratigraphic units are shown in ( ) and formation names of Poprawski et al. (2014; 2016), where they differ from those used in this study, are shown in [ ]. Numbers adjacent to the stratigraphy refer to regional sequences of Agirrezabala and López-Horgue (2017), based on biostratigraphy. Line of section is shown for Figure 3.4; for full extent see Figure 3.2.



**Figure 3.4:** Schematic structural–stratigraphic cross-section through the Bakio and Guernica diapirs. Full extent is located using B–B' in Figure 3.2, partial extent is also shown in Figure 3.3. The section combines Poprawski and Basile (2018), Robles et al. (1988), field observations, and publicly available vintage onshore seismic lines from IGME. Facies are indicated where known or inferred from the literature but are left blank where they cannot be inferred. Two times vertical exaggeration for clarity.

### 3.4 Methods and data

The dataset comprises 28 sedimentary logs (totalling 821 m of stratigraphy) collected along the Bakio–Guernica coastline. The logs were collected at a 1:25 scale, with 1:10 scale used locally to capture additional detail. Halokinesis during BFG deposition (García-Mondéjar 1996; Poprawski et al. 2014; 2016; Roca et al. 2021) generated syn-depositional basin-floor relief and led to the development of multiple discrete depocenters (Vicente Bravo and Robles 1991a; 1991b; 1995; Agirrezabala 1996). As such, correlating stratal surfaces in and between depocenters is difficult and uncrewed-aerial-vehicle (UAV) photography was used to aid stratigraphic correlations (Hodgetts 2013). Paleocurrent, bedding, and structural data were collected in the field to determine the influence of syn-depositional basin-floor relief and to quality-control the pre-existing geological map of Poprawski et al. (2014; 2016). Paleocurrent readings were taken where sedimentary structures were clear enough to permit unambiguous data collection. Sparse biostratigraphic data (Agirrezabala and López-Horgue 2017) hinders correlation across the structures; hence we refer to the Lower (LBF) and Upper (UBF) Black Flysch group only, to avoid further subdivisions based on geographic location (e.g., Robles et al. 1988; Vicente-Bravo and Robles 1991a, 1991b, 1995; Poprawski et al. 2014).

#### ***Basin subdivision***

To aid comparison, the study area has been divided into two depocenters: the Jata and Sollube basins (Figures 3.3 and 3.4). These are analogous to subsurface minibasins, defined as relatively small (5–30 km) syn-kinematic depocenters subsiding into thick salt (Hudec and Jackson 2007; Jackson and Hudec 2017). The Jata basin is confined to the east by the Bakio diapir. The Sollube basin is confined on both its western and eastern sides by the Bakio and Guernica structures, respectively (Figure 3.3), and hence is more confined than the Jata basin.

### 3.5 Lithofacies

This study focuses primarily on the facies variability in the siliciclastic BFG. A description and discussion of the carbonate facies of the BMF and BBF is provided in Poprawski et al. (2016). Here, the carbonate facies are tabulated for reference in Figure 3.5 and Table 3.1, where their depositional process are interpreted. The BFG lithofacies presented in Table 3.2 and in Figure 3.6 represent “event beds” and are classified based on outcrop observations. “Mud” is used here as a general term, for mixtures of clay, silt, and organic fragments. Where individual facies are heterogeneous, multiple photographs are shown to illustrate this lithological and sedimentological variability (Figure 3.6).

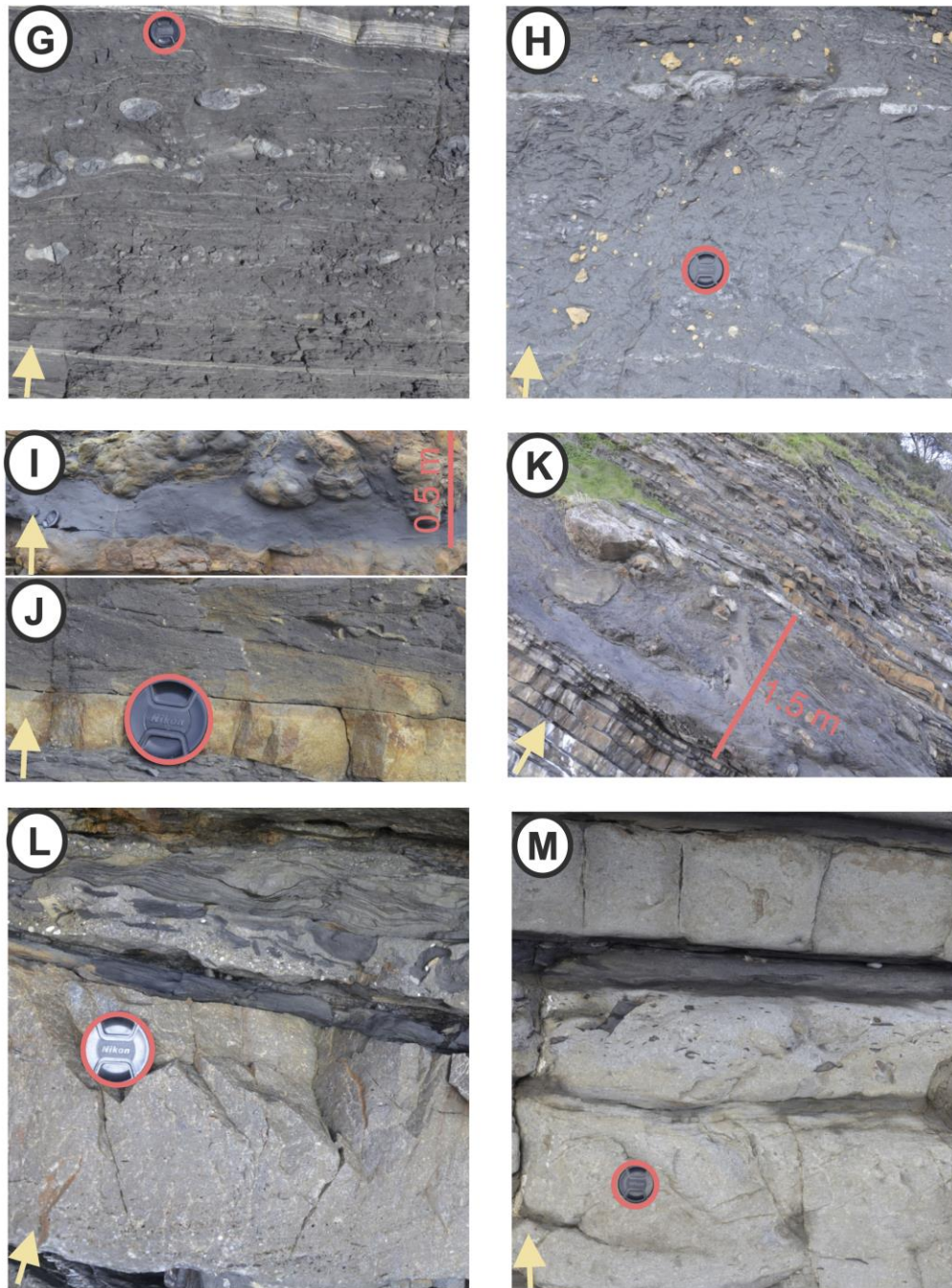
**Table 3.1:** Table of carbonate facies detailing the major observations of the six facies which constitute the early Albian Bakio Marls and early middle Albian Bakio Breccias formations. For further discussion see Poprawski et al. (2014; 2016). Supporting facies photographs are provided in Figure 3.5.

Facies name	Description	Interpretation
Thin-bedded calcareous sandstone	0.01-0.1-m-thick beds of bioclastic (corals and shell fragments) very fine-fine grained sandstones. Commonly normally graded with flat tops and flat bases. Weak planar, ripple, and convolute lamination.	<b>Low-density calci-turbidites:</b> Thin-bedded structured sandstones deposited from dilute turbidity currents.

Medium-bedded calcareous sandstone	0.1-0.3-m-thick very fine to medium-grained normally graded sandstones, with flat bases and flat tops. Planar, ripple, and convolute lamination observed. Mud clasts and intense dewatering also present.	<b>Medium to high-density turbidites:</b> Presence of tractional structures suggests deposition from a dilute turbidity current. High mud-clast percentage could suggest imminent flow transformation (Barker et al. 2008).
Limestone breccia	10+-m-thick beds of matrix- or clast-supported limestone breccia, with erosional bases and undulating tops. Poorly sorted beds consisting of subangular to angular limestone megaclasts, which can be normally, inversely or non-graded. Megaclasts commonly contain entire rudists and fragmented corals.	<b>Mass-transport deposit:</b> Poorly sorted clasts suggest deposition from “flow freezing” of a flow with yield strength (Iverson et al. 2010). Limestone clasts are similar in composition to the Gaztelugatxe Limestone, suggesting that it is their source (Poprawski et al. 2014; 2016).
Fossiliferous poorly sorted carbonate wackestone	0.03-0.2-m-thick poorly sorted, non-graded carbonate wackestone with fossil fragments. Beds are laterally discontinuous, with undulose, gradational beds and tops. Cm-to-dm-size bioclasts of urchins, brachiopods, bryozoans bivalves, corals, crinoid stems, and rarer mollusc shell fragments.	<b>Debris flow:</b> Fragmented bioclasts, poor sorting, and undulose contacts suggest deposition from a laminar flow (Nardin et al. 1979). Fossils are fragmented, indicating reworking, but are not lithified, indicating direct reworking from an active platform or reef.
Remobilised carbonates	5+-m-thick packages consisting of a combination of the above facies that have been slightly remobilized but maintain bedding planes. Contacts are erosional, scalloped, or smooth, and underlying mudstone units often appear sheared. Convolute lamination and soft-sediment deformation are present.	<b>Slide deposits:</b> The remobilisation but maintenance of individual bedding planes and sheared basal contacts indicates that these are slide deposits. Lack of internal deformation suggest these deposits have been remobilized post lithification, conceivably due to halokinetic movements (Ferrer et al. 2014; Poprawski et al. 2016).
Clast-rich poorly-sorted carbonate wackestone	0.1-1 + m thick poorly sorted beds with angular limestone clasts in a mud-silt matrix. Clasts can be cm to m scale, generally 1-12 cm, and are rich in mollusc fragments. Rare lithics and organics are observed. Undulose tops reflect clast topography and, bases are flat, weakly-erosional or undulose. Weak normal grading and rarer reverse grading are observed.	<b>Carbonate-clast-rich debrites:</b> Poor-sorting and large clast size indicates en-masse deposition from a laminar flow (Nardin et al. 1979; Iverson 1997; Sohn 2000) Weak normal grading suggests that some turbulence was influencing the flow. Clast angularity suggests proximity to source area. Lack of unconsolidated fossil debris suggests that lithification has occurred before reworking into the flow.







**Figure 3.5:** Photograph of carbonate facies, supporting observations in Table 3.1. Yellow arrow indicates way up. Peach highlights scale, either lens cap (52 mm), or indicated. For further discussion see Poprawski et al. (2014; 2016). A) Thin-bedded calcareous sandstone. B) Medium-bedded calcareous sandstone. C) Limestone breccia. D) Fossiliferous poorly sorted carbonate wackestone. E) Remobilised carbonates. F) Clast-rich poorly sorted carbonate wackestone.

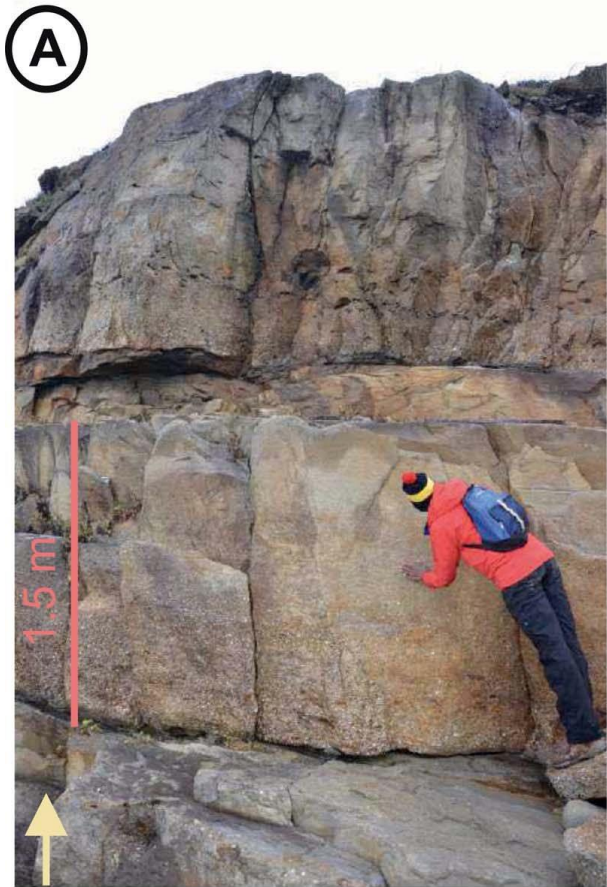
**Table 3.2:** Table of siliciclastic facies detailing the ten facies that comprise the Black Flysch Group.

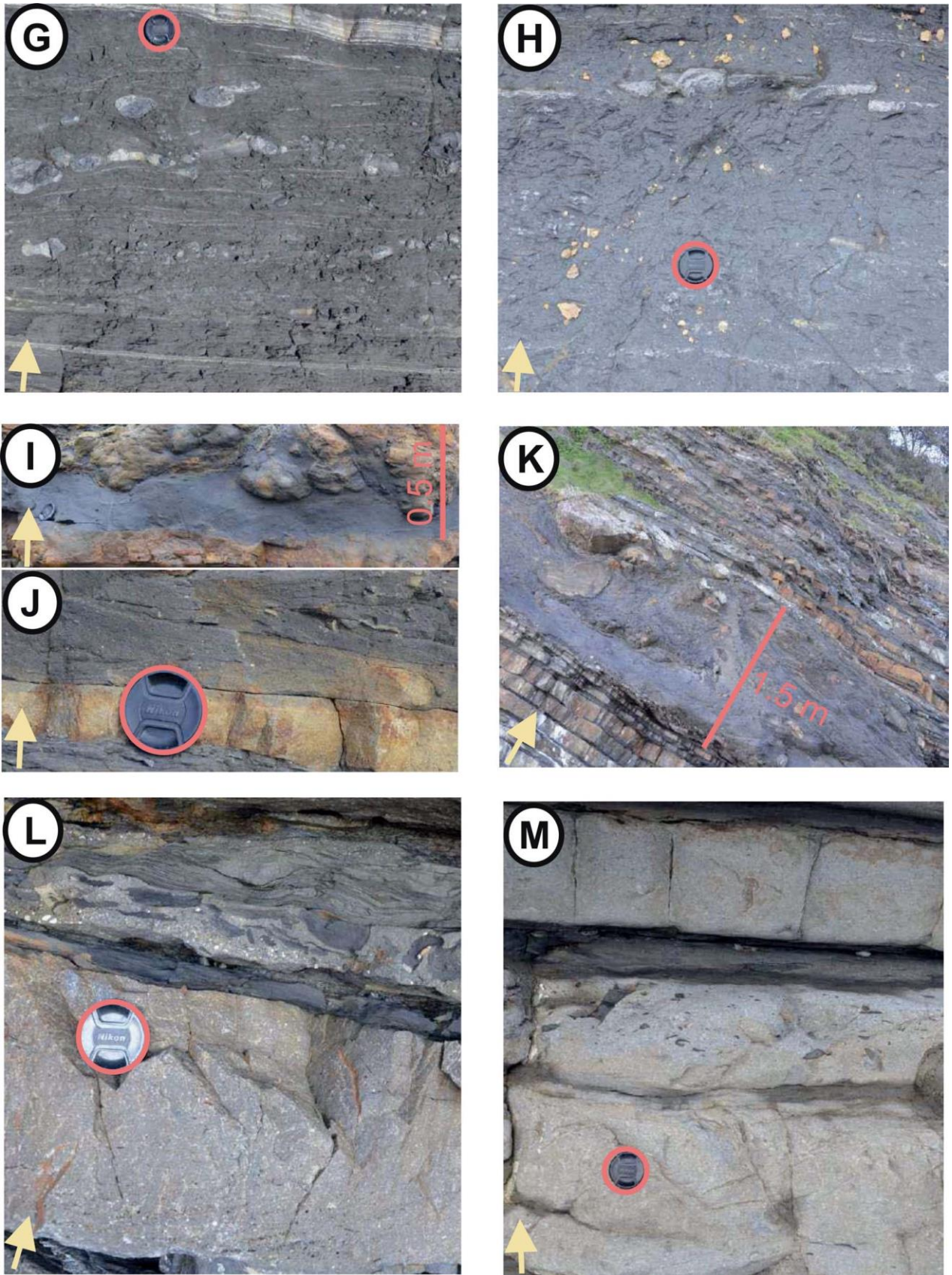
Facies name	Description	Interpretation
<b>Granular-cobbly sandstones</b>	0.1-1.5+-m thick beds of granular-cobble sandstones (Fig. 3.6A, B), with subangular (Fig. 3.6B) to well-rounded, moderately sorted clasts. Weak cross-	<b>High-density turbidites:</b> The coarse grain size, thick beds, and amalgamation surfaces suggest deposition from a highly concentrated turbulent flow, indicating that these

	stratification (Fig. 3.6A), pebble imbrication, amalgamation, mud clasts and erosional surfaces (Fig. 3.6A, B) are observed. Dish structuration is pervasive (Fig. 3.6A).	beds are turbidites. Weak stratification indicates traction-carpet deposition (Lowe 1982), suggesting high-density turbidites.
<b>Thick-bedded sandstones</b>	0.5-1+-m-thick beds of very-fine-to coarse-grained normally graded sandstones, which lack primary depositional structures and are commonly dewatered (Fig. 3.6C). Bases can be sharp, erosional, stepped, or amalgamated, commonly along a mudstone amalgamation surface with a subtle grain-size break (Fig. 3.6C), and tops are often flat. Plane-parallel lamination, mud clasts, and soft-sediment deformation are occasionally observed.	<b>High-density turbidites:</b> The general massive structuration of these deposits suggests that they represent rapid aggradation beneath a highly concentrated flow (Lowe 1982).
<b>Medium-bedded sandstones</b>	0.1-0.5 m thick beds of very fine-medium grained, normally graded sandstones. Beds are rich in tractional structures, particularly plane parallel laminations (Fig. 3.6D). Ripple laminations is observed in bed tops, and beds are more frequently structureless towards bases. Bed bases are flat with tool marks or loaded, and tops are flat or convolute and often rich in mud clasts (Fig. 3.6D). Occasionally amalgamated.	<b>Medium-density turbidites:</b> Based on their tractional structures and normal grading, beds of this lithofacies are interpreted as deposition from a dilute turbidity current. These beds are interpreted as medium-density turbidites due to their bed thickness and common lack of structures in the lower part of the bed.
<b>Thin-bedded sandstones</b>	0.01-0.1-m-thick beds of very fine-fine, normally graded sandstones. Rich in tractional structures, particularly plane-parallel lamination (Fig. 3.6E, F). Banding on a sub-cm scale (Fig. 3.6E, F) and convolute lamination are common. Bases are flat (Fig. 3.6F), undulose, loaded (Fig. 3.6E, F), or weakly erosional and tops are flat to undulose and rich in mud clasts. Starved, climbing, and opposing paleoflow ripples are observed (Fig. 3.6E).	<b>Low-density turbidites:</b> Tractional structures and normal grading indicate deposition from a dilute turbidity current and are therefore interpreted as low-density turbidites. Common banding may reflect some periodic suppression of turbulence associated with flow deceleration or increased concentration (Lowe and Guy 2000; Barker et al. 2008). Ripples with opposing paleoflow suggests topographic interference.
<b>Siltstone and very thin-bedded sandstones</b>	Packages of 0.1 m composed of individual fine siltstone to fine sandstone events less than 0.01 m. Beds form discontinuous drapes within mudstone (Fig. 3.6G), with flat bases and flat tops. Parallel and ripple lamination and diagenetic phosphate nodules are observed (Fig. 3.6G).	<b>Low-density turbidites:</b> Fine grain size and thin bed thickness suggest that this unit represents deposition from dilute turbidity currents (Boulestex et al. 2019), representing lower-energy conditions than thin-bedded sandstones.
<b>Mudstone</b>	0.01-5-m-thick mudstone to fine siltstone beds of carbonate or siliciclastic mudstone (Fig. 3.6H). Weakly planar-laminated, friable packages (Fig. 3.6H) with drapes and discontinuous lenses of	<b>Background sedimentation:</b> Fine grain size indicates low-energy conditions, representative of background sedimentation via suspension

	siltstone (Fig. 3.6H). <i>Nereites</i> bioturbation and diagenetic spherical cm-scale phosphate nodules present.	fallout. Discontinuous siltstones suggest that lamination may be present below the scale visible in outcrop, representing deposition from a dilute turbidity current (Boulesteix et al. 2019).
<b>Poorly-sorted mudstone</b>	0.1-1+-m-thick siltstone to fine-sandstone rich mudstones (Fig. 3.6I). Poorly sorted, matrix-supported, clast-rich deposit with starry-night texture. Granules, organic fragments, mud clasts and rare shelly fragments present, often with subtle alignment. Bases are flat or undulose, tops flat or loaded (Fig. 3.6I).	<b>Mud-rich debrites:</b> The poorly sorted matrix and clast-rich nature indicates en-masse deposition from a laminar flow (Nardin et al. 1979).
<b>Poorly-sorted muddy sandstone</b>	0.1-1+-m-thick, mud-rich poorly sorted matrix-supported, fine to medium grained sandstones with starry-night texture (Fig. 3.6J). Organised mudstone clasts and sporadic granules to pebbles are observed. Flat-undulose tops and flat-graded base are common (Fig. 3.6J). Rare normal grading and grain-size segregation and infrequent sheared layers present.	<b>Sand-rich debrites:</b> En-masse deposition from a laminar flow (Nardin et al. 1979; Iverson 1997; Sohn 2000). Weak normal-grading suggests that some turbulence was influencing the flow and therefore deposition from a transitional flow regime is interpreted (Baas et al. 2009; 2013; Sumner et al. 2013).
<b>Chaotic clast-rich matrix supported deposit</b>	0.5-3-m-thick, poorly sorted deposit with a poorly sorted matrix of mudstone to fine sandstone. Clasts include: cm-to-m scale sandstone balls (Fig. 3.6K), showing internal lamination and soft-sediment deformation, dm – m scale sandstone and heterolithic subangular rafts, deformed siderite nodules, limestone clasts, gastropod and sponge fragments, mud clasts and phosphate nodules. Beds are flat-topped, and bases are weakly loaded (Fig. 3.6K).	<b>Mega-debrites:</b> The poorly sorted matrix and large clast size are suggestive of “flow freezing” indicating deposition in a debris-flow regime (Iverson et al. 2010). These deposits are interpreted as mega-debrites due to their large clast size (rafts), suggesting they are derived from localised mass failure.
<b>Bipartite or tripartite beds</b>	0.1-1.5-m-thick beds that contain multiple parts (Fig. 3.6L, M). Typically consisting of a lower fine-medium sandstone (division 1) overlain by a poorly sorted, muddy siltstone-sandstone (division 2) with a flat to slightly undulose base (Fig. 3.6L, M). Division 3 is sometimes present, consisting of cleaner siltstone or fine-grained sandstone loaded into division 2 (Fig. 3.6L). Division 1 can contain planar lamination and weak cross-stratification (Fig. 3.6L) but is often massive with sporadic-slightly organised mud clasts (Fig. 3.6M). Division 2 is organic-rich, highly deformed, and can contain sporadic granules or pebbles (Fig. 3.6L, M). “Starry night” tex-	<b>Hybrid beds:</b> Tractional structures in division 1 and 3 suggest that these deposits formed under turbulent flows. Starry-night texture, poor sorting, and mud content suggest that division 2 was deposited under a transitional-laminar flow regime (Haughton et al. 2009). Flow transformation from turbulent to laminar can occur through flow decelerations (Barker et al. 2008; Patacci et al. 2014) or by an increase in concentration of fines during flow run-out (Kane et al. 2017).

	ture is observed in this division. Division 3 is more frequently planar laminated than division 1 but can be highly chaotic (Fig. 3.6L).	
--	--	--





**Figure 3.6:** Siliciclastic facies photographs. Yellow arrow indicates way up. Peach outline highlights scale, either lens cap (52 mm), or indicated. A) Granular-cobbly laterally extensive thick sandstone beds. B) Granular-cobbly sandstone with medium-thickness beds exhibiting lateral facies variations. C) Stacked, amalgamated thick-bedded sandstones. D) Medium-bedded sandstones interspersed with mudstones and poorly sorted mudstones and sandstones. E) Thin-bedded sandstone showing ripples, planar lamination, and loading. F) Succession of stacked thin-bedded sandstones. G) Siltstone and very-thin-bedded sandstones; phosphate nodules are

*common in this facies, likely diagenetic in origin. H) Mudstone with occasional, rare drapes of siltstone. I) Poorly sorted mudstone, founded into by a thick-bedded sandstone. J) Poorly sorted muddy sandstone, containing sporadic granules and raft blocks. K) Chaotic clast-rich matrix-supported deposit encased between units of thin-to-medium-bedded sandstones. L) Tripartite bed consisting of lower medium-bedded sandstone with weak cross-lamination, middle poorly sorted mudstone and upper poorly sorted sandstone. M) Bipartite bed consisting of lower thick-bedded sandstone which becomes mud-clast rich upwards overlain by a poorly sorted mudstone above.*

### **3.6 Interpretation of depositional elements**

Facies associations (Table 3.3; Figure 3.7) and architectures (Table 3.4; Figure 3.8) are integrated to support interpretation of depositional environment. Facies associations are interpreted based on dominant lithofacies (Table 3.2; Figure 3.6) and use lobe (Prélat et al. 2009; Sychala et al. 2017) and channel–levee (Kane and Hodgson 2011; Hubbard et al. 2014) nomenclature that best fit field observations. Facies associations and geometries are described separately, because architecture alone is not diagnostic of the depositional sub-environment, and multiple facies associations can form a similar architecture.



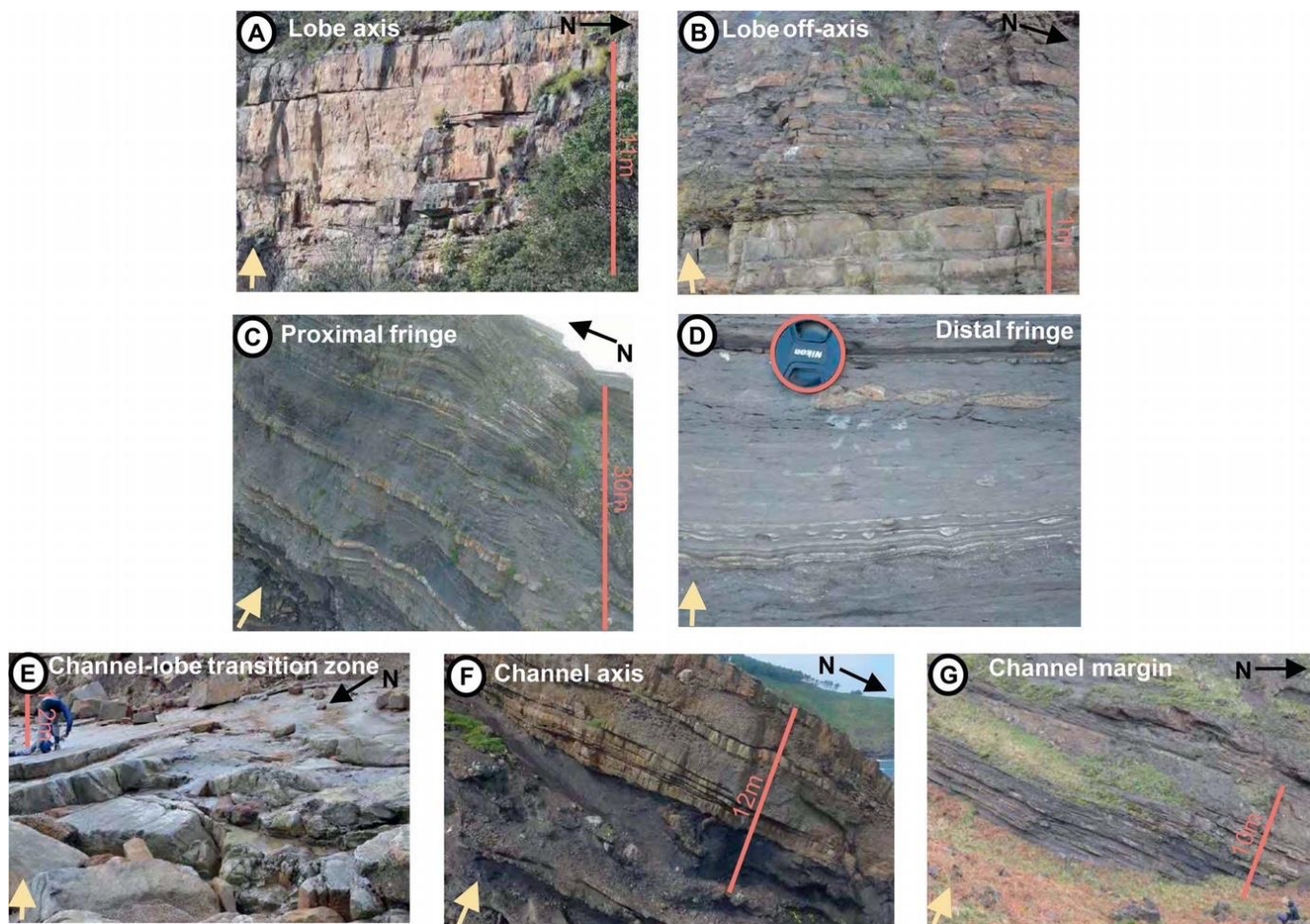
**Table 3.3:** Table of facies association detailing the assemblages that constitute the Black Flysch Group.

Facies association name	Description	Interpretation	Architecture (Table 3.4; Fig. 3.8)
<b>Lobe axis</b>	Dominantly thick-bedded sandstones (Fig. 3.7, 3.8C) with subordinate medium-bedded (Fig. 3.6D), thin-bedded (Fig. 3.6E, F), and granular-cobbly sandstones (Fig. 3.7). Beds are often massive and amalgamated (Fig. 3.7) with pervasive dewatering, frequent mud clasts and subtle normal grading (Fig. 3.6C). Thin-bedded granular-cobbly sandstones can underlie thick-bedded sandstones or form isolated lenticular geometries (Fig. 3.6B).	Thick-bedded nature suggests deposition from high concentration turbidity currents with relatively high rates of aggradation preventing the development of tractional sedimentary structures (Kneller and Bramney 1995; Talling et al. 2012). Common amalgamation, and entrainment of mudstones clasts in thick-bedded sandstones, indicate that the parent flows were highly energetic and capable of eroding, entraining, and bypassing sediment during the passage of flow (Lowe 1982; Mutti 1992; Stevenson et al. 2015). Similar deposits elsewhere have been interpreted as lobe-axis deposition (Walker 1978; Pr��lat et al. 2009; Kane et al. 2017). Thin-bedded granular-cobbly sandstones are associated with overlying and adjacent amalgamated thick-bedded sandstones and are thought to represent a mostly bypassing equivalent of the depositional thick-bedded sandstones within the lobe axes (Kane et al. 2009).	Pinching out upslope (Fig. 3.8C) or convex up (Fig. 3.7)
<b>Lobe off-axis</b>	Composed principally of normally graded structured to structureless medium-bedded sandstones (Fig. 3.6D) with less common thin-bedded (Fig. 3.6F) and thick-bedded sandstones (Fig. 3.6C). Ripples at the tops of beds commonly show paleoflow directions opposite to those that are measured from flutes and grooves on bed bases. Mudstones, poorly sorted mudstones, sand-rich mudstones, and rarer chaotic clast-rich matrix-supported deposits are periodically or randomly interspersed in this facies association (Fig. 3.7).	A medium-density turbidite interpretation is given for these units based on the preservation of both structured and structureless sandstones. Similar preservation of both deposit types has been interpreted as off-axis lobe environments, deposited by decelerating turbidity currents (Pr��lat et al. 2009; Spsychala et al. 2017; Soutter et al. 2019). Opposing paleocurrent directions in event beds is characteristic of topographically influenced flows (Kneller et al. 1991; Bakke et al. 2013). Periodic deposition of mudstones suggests episodic system shutdown. Poorly sorted mudstones, sand-rich mudstones, and chaotic clast-rich matrix supported deposit occurrence indicate periodic laminar flows which could indicate nearby active topography (Kneller et al. 1991; Mayall et al. 2010).	Pinching out upslope (Fig. 3.8C) or convex up (Fig. 3.7)

<b>Proximal fringe</b>	Consists principally of thin-bedded sandstones (Fig. 3.6 E, F) and bipartite or tripartite event beds (Fig. 3.6L, M). Siltstone and very-thin-bedded sandstones and medium-bedded-sandstones (Fig. 3.7) are infrequently observed. Poorly sorted mudstones, sand-rich mudstones, and rarer chaotic clast-rich matrix-supported deposits are periodically or randomly interspersed in the otherwise organised thin-bedded sandstones and bipartite or tripartite beds (Fig. 3.7).	Thin-bedded, structured sandstones are interpreted to be deposited from low-concentration turbidity currents (Mutti 1992; Jobe et al. 2012, Talling et al. 2012). Bipartite and tripartite event beds are interpreted as hybrid beds (Haughton et al. 2009). The transformation of flows in hybrid beds observed here document a change in flow process from high-medium- concentration turbulent to laminar or transitional, to low-concentration turbulent (Remacha et al. 2005; Baas et al. 2011). Thin-bedded sandstones and hybrid beds underlie lobe and lobe-axis facies associations and are therefore interpreted to be deposited adjacent to such deposits. Abundant hybrid beds and thin beds indicate lobe-fringe deposition elsewhere (Hodgson 2009; Jackson and Johnson 2009; Kane et al. 2017; Soutter et al. 2019), specifically in the proximal fringe (Sypchala et al. 2017). In tectonically confined settings, flow types are highly variable and the frontal and lateral fringe can be difficult to decipher because flow transformation is influenced by topography so hybrid beds can be common in the lateral and frontal fringe (Barker et al. 2008; Soutter et al. 2019) termed “proximal fringe”.	Tabular (Fig. 3.8A) or pinching out up slope (Fig. 3.8C).
<b>Distal fringe</b>	Dominated by siltstone and very-thin-bedded sandstones (Fig. 3.6G) and mudstones (Fig. 3.6H) with secondary thin-bedded sandstones, bipartite and tripartite beds and thin-bedded poorly sorted mudstones (Fig. 3.7). Mudstones separating individual events are often slightly deformed or sheared and show drapes of discontinuous siltstone (Fig. 3.7).	The fine grain size, thin-bedded character, and low stratigraphic position of these beds is consistent with lobe-fringe deposition. The relative lack of hybrid beds in this facies association support a distal-lobe-fringe interpretation (Hodgson 2009; Jackson et al. 2009; Kane et al. 2017; Soutter et al. 2019), specifically in the proximal fringe (Sypchala et al. 2017).	Tabular (Fig. 3.8A)
<b>Channel-lobe transition zone</b>	Consists of granular-cobbly sandstones (Fig. 3.6A) and intensely dewatered thick-bedded sandstones up to 5 m thick (Fig. 3.6C). Erosional bases, megaflutes, stepped amalgamation surfaces, and mudclast abundance are common (Fig. 3.7). Granular-cobbly sandstone lenses infilling lensoid, spoon-shaped depressions are observed (Fig. 3.7). Weakly	Erosionally based geobodies infilled with coarser clasts indicate active erosion and deposition. Common amalgamation, and entrainment of mudstones clasts in thick-bedded sandstones, indicate that the parent flows were highly energetic and capable of eroding, entraining, and bypassing sediment during the passage of flow (Lowe 1982; Mutti	Tabular amalgamated beds (Fig. 3.8G)

	stratified cross-lamination of gravels in sandstone matrix and pebble imbrication is also observed (Fig. 3.6A, 3.8). Low-wavelength hummock-like structures are observed (Fig. 3.7) (Vincente Bravo and Robles 1991).	1992; Stevenson et al. 2015), while weak cross-stratification, slight grading, and pebble imbrication are more typical of depositional conditions (Mutti and Normark 1987). This juxtaposition of depositional and erosional elements has been observed elsewhere in channel-lobe transition zones (Mutti and Normark 1987; Wynn et al. 2002; Pemberton et al. 2016; Brooks et al. 2018). The presence of cross-stratified gravels supports the facies association proposed by previous work (Vincente Bravo and Robles 1991a; 1991b; 1995).	
<b>Channel-axis</b>	Thick-bedded sandstones (Fig. 3.6C), granular-cobbly sandstones (Fig. 3.6A), poorly sorted muddy sandstones, (Fig. 3.6I) and chaotic clast-rich matrix-supported deposits (Fig. 3.6K). Thick-bedded sandstones typically gradationally overlie granular-cobbly sandstones, which are commonly grooved on the base, showing normal grading (Fig. 3.7). These successions are erosional into the underlying poorly sorted muddy sandstones or chaotic clast-rich matrix supported deposits, which exhibit some deformation and shearing (Fig. 3.7). Sandstone beds either erode into each other, are amalgamated, or less commonly are separated by thin beds of mudstone (Fig. 3.7). Low-angle cross-stratification is observed (Fig. 3.6A). The sandy mudstones and chaotic units contain subangular to angular poorly sorted clasts of up to boulder size. The composition of these clasts includes limestone fragments, organics, siliciclastic fragments, slumped and reworked thin-bedded heterolithics, clasts of granite, deformed and reworked siderite, mud clasts, and fossil fragments (Fig. 3.7).	Common amalgamation, erosion, and entrainment of clasts in the sandstones indicate that the parent flows were highly energetic and capable of eroding, entraining, and bypassing sediment (Mutti 1992; Stevenson et al. 2015; Soutter et al. 2019). The coarse grain size and basal location of granular-cobbly sandstones suggests that these beds were deposited as a coarse-grained lag in a bypass-dominated regime (Hubbard et al. 2014). Erosionally based lenticular sandstones and their grading from cobbly–fine sandstone is consistent with deposition in a submarine channel described elsewhere (Hubbard et al. 2008; Romans et al. 2011; McArthur et al. 2020). Weak low-angle lamination in sandstone beds could indicate lateral accretion (Kane et al. 2010; Jobe et al. 2016). Poorly sorted muddy sandstones and chaotic units could represent channel collapse and margin failure (Flint and Hodgson, 2005; Pringle et al. 2010; Jobe et al. 2017). The wide variation in clast composition, more diverse than that observed in any other facies association, indicates broader catchment area for these debris flows, which may indicate an extrabasinal provenance (Stevenson et al. 2015).	Concave upward (Fig. 3.7, 3.8B)
<b>Channel-margin</b>	Thin-bedded sandstones (Fig. 3.7E, F) and poorly sorted mudstones with secondary medium-bedded sandstones and chaotic clast-rich matrix-supported	The supercritical bedforms and thin-bedded nature of these deposits is similar to those described as channel-margin facies by others (Kane and Hodgson 2011; Hodgson et al. 2011; Hubbard et al. 2014; Jobe et al. 2017; McArthur	Tabular (Fig. 7, 8A)

	<p>deposits (Fig. 3.7). Thin- and medium- bedded sandstones are planar and ripple laminated (Fig. 3.6E). Poorly sorted mudstones and chaotic clast-rich matrix-supported deposits include angular to rounded clasts of limestone, siliciclastic fragments, and mud clasts. Medium-bedded sandstones erode into the tops of chaotic clast-rich matrix-supported deposits, and thin-bedded sandstones show loaded, flat and weakly erosional bases. This facies association appears beneath the channel-axis facies associations (Fig. 3.7).</p>	<p>et al. 2020). The location of this facies association beneath channel-axis deposits suggests that they were deposited adjacent to them, and this indicates they represent channel-margin facies association.</p>	
--	--	---	--



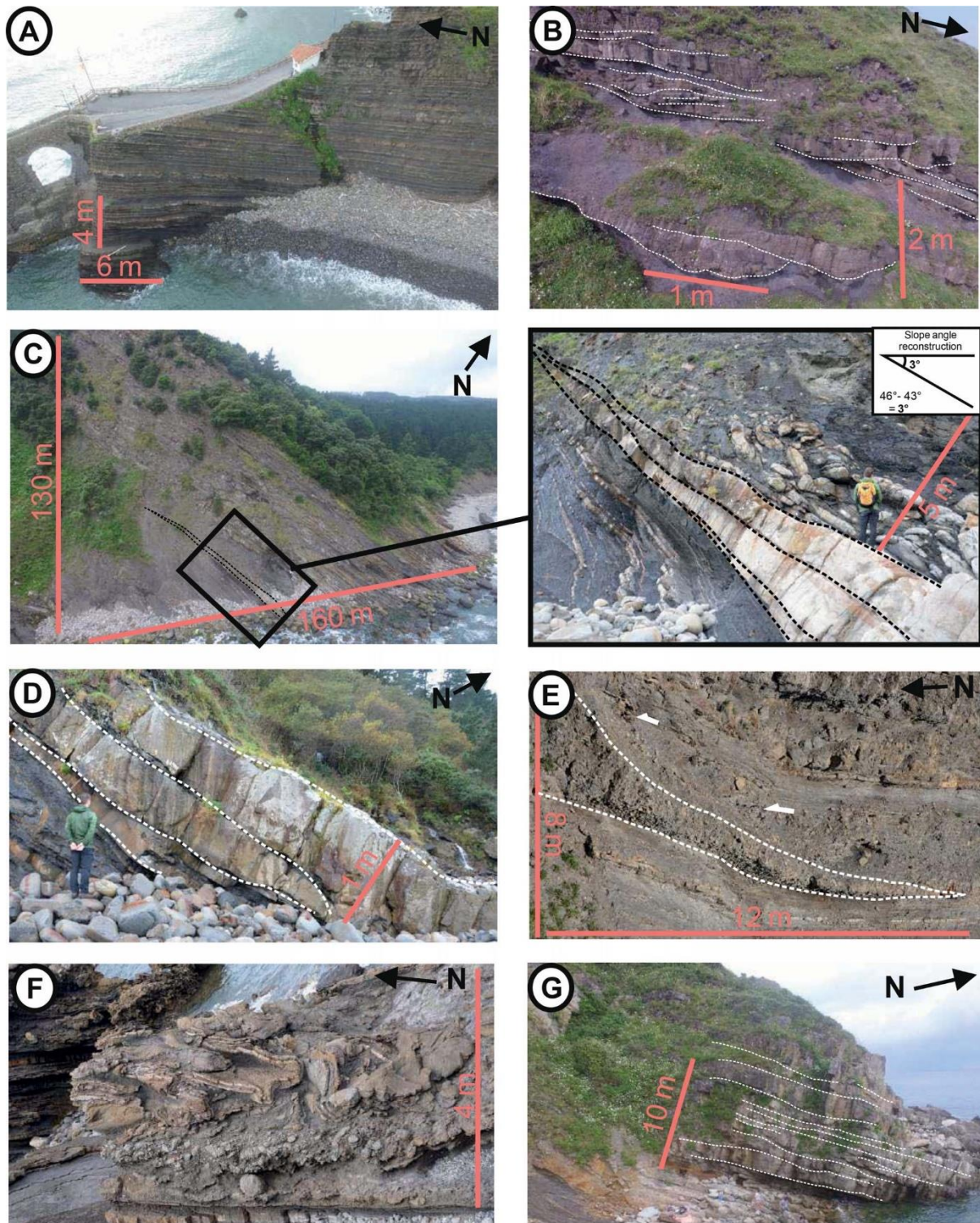
**Figure 3.7:** Type examples of the seven documented facies associations in this study (Table 3.3). Peach highlights scale, either lens cap (52 mm), or indicated. Black arrow points to the north, and yellow shows the way up. A) Thick-bedded sandstones of the lobe axis. B) Interbedded sandstones and mudstones of the lobe off-axis. C) Thin-bedded sandstones interbedded with mudstones of the proximal fringe. D) Mudstones and very thin-bedded sandstones and siltstones of the distal fringe. E) Thick-bedded granular sandstones of the channel-lobe transition zone. F) Sandstones and poorly-sorted mudstones of the channel axis. G) Thin-bedded sandstones interbedded with mudstones of the channel margin.

**Table 3.4:** Table describing geometrical configurations observed in the Black Flysch Group.

Architecture name	Description	Interpretation	Facies association (Table 3.3; Figure 3.7)
<i>Tabular bedded</i>	A package of stacked beds which show a continuous thickness laterally for 10s to 100s m, occasionally with some subtle thickness changes (Fig. 3.8A). Post depositional faulting and tectonic and halokinetic tilt prevent these geometries from being traced on a 100s m-km-scale. Common in thin-bedded (Fig. 3.8A) and medium-bedded sandstones (Fig. 3.6D). Tabular geometries are observed >500 m away from diapiric influence.	This continuous, stacked geometry suggests constant depositional energy. Tabular architectures appear to be uninfluenced by topography, and are similar to unconfined settings (Prélat et al. 2009). Low-density turbidites are less affected by topography than more cohesive flow (Al-Ja'aidi 2000; Bakke et al. 2013) and therefore can run up topography for greater distances, without becoming ponded.	Distal fringe (Fig. 3.7), proximal fringe (Fig. 3.8A), channel margin (Fig. 3.7G).

<i>Concave upward (erosionally based)</i>	Curvilinear geobodies with variable thickness that are concave upward, consisting of a centroid and two margins, toward which the centroid thins, sometimes by up to 80%. (Fig. 3.8B). Erosionally based granular sandstones are present in the centroid of the geobody, often overlain by high-density turbidites, which become thinner-bedded towards the margins. The thickness of these geobodies is typically decimetre to metre scale, and thickness to width ratios can range between 1:10 and 1:50. The geobodies commonly erode and amalgamate with each other, and stack above the previous deposit.	Each geobody represents at least one event; the coarse-grained basal lag could represent a bypass event before the high-density turbulent flow which filled the geometry. These multipart geobodies, which are attributed to deep-water channels based on their geometries, stack on top of and erode into each other, suggesting increasing confinement (Mayall et al. 2010).	Channel axis (Fig. 3.7, 3.8B).
<i>Pinching out upslope</i>	Elements that change in thickness, but only in one direction (Fig. 3.8C). Commonly these geometries are amalgamated, with individual events displaying a convex-up geometry. Thinning rate is approximately 10cm/m in Figure 3.8C.	Thinning of deposits indicates flow deceleration related to topography, which ultimately lowers flow concentration (Baas et al. 2011; Teles et al. 2016). The eventual pinch-out of the sandstone is due to the inability of the flow to run up the entirety of the topography.	Proximal fringe (Fig. 3.7, Fig. 3.8C), lobe off-axis, lobe axis (Fig. 3.8C).
<i>Convex up</i>	Packages are generally continuous in thicknesses on the scale of the outcrop, with beds thinning slightly to either side (Fig. 3.8E). The centroid is typically decimetres to metres thick. The upper surface of each deposit is commonly undulose with an overall, often subtle, convex-upward geometry (Fig. 3.8E). High-density turbidites dominate these architectures and are commonly stacked or amalgamated.	The upwards curvature and slight thinning of this geometry lead to their interpretation as lobate geometries (Prélat et al. 2009; Hodgson 2009; Sypchala et al. 2017). Shifting of the centroid of the lobe axis indicates that compensational stacking is influencing these deposits similar to that observed in unconfined settings (Prélat et al. 2009; Sypchala et al. 2017).	Lobe off-axis (Fig. 3.7), Lobe axis (Fig. 3.6C, 3.7).
<i>Pinching out downslope</i>	Packages are triangular in geometry and pinch out gradually. These architectures are very common at Gaztelugatxe Island (Fig. 3.3, 3.5), where they consist of limestone breccia (Table 3.1) and have thinning rates of 6.7–10 cm/ m downslope (Fig. 3.8E). Towards the top of Gaztelugatxe Island (closer to the contact with Gaztelugatxe Limestone) these architectures are amalgamated, whilst farther	These deposits are interpreted as talus deposits, common around diapiric highs (Giles and Lawton 2002; Giles and Rowan 2012) and on fault scarps (Poprawski et al. 2014, 2016). The similarity in facies and geometry to “carbonate lentils” described elsewhere (McBride et al. 1974; Hunnicutt 1998; Kernén et al. 2012, 2018) and the likely close to the offshore Bakio diapir (Poprawski et al.	Limestone breccia (Table 3.1; Fig 3.5).

	away from the limestone they are interspersed within tabular architectures. Successive thin-bedded, tabular deposits appear to onlap onto the topography formed by these downslope-thinning geobodies (Fig. 3.8E).	2016) suggest that these geometries are halokinetically driven. The source of this talus is interpreted to be the Gaztelugatxe Limestone due to its proximity and geometrical relationships. Onlap of successive deposits suggest that diapiric collapse was coeval with deep-marine deposition.	
<i>Undulose</i>	Packages have an undulose, heterogeneous geometry (Fig. 3.8F). Individual beds vary in thickness and facies, and include thin beds, chaotic mud-rich debrites, and limestone breccias (Fig. 3.8F), but overall architecture maintains a broadly consistent thickness. The base of these architectures can be composed of limestone breccias (Fig. 3.8F; Table 3.1).	These remobilised units represent slump deposits. Ranging paleoflow directions, and both carbonate and siliciclastic inclusions, suggest they are derived from the diapir roof and flanks (Poprawski et al. 2014). The undulose geometries could overlie carbonate “lentils” or may reflect the reworking of “lentils” in these deposits (Fig. 3.8F).	Mass-failure deposits; limestone breccia (Table 3.1), chaotic debrites (Fig. 3.6J, 3.6K), remobilized proximal-distal fringe (Fig. 3.8F).
<i>Tabular amalgamated beds</i>	Packages appear tabular and consist of beds which remain relatively consistent in thickness, with minor deviations related to previous topography (Fig. 3.8G). This architecture is principally composed of the channel-lobe transition zone facies association (Fig. 3.7). Concave depressions, which are spoon-shaped and metre scale in width, can be seen on bed tops and bed bases and are associated with undulations at bed scale (Fig. 3.8G). Overall, the geometry is slightly concave up, with the center of each deposit thinning slightly on either side at the scale of the outcrop (Fig. 3.8G).	The dominance of channel-lobe-transition zone facies associations leads to an interpretation of a stacked, scoured, broad channel-lobe transition zone where erosional and depositional processes were active (Vicente Bravo and Robles 1991; Robles et al. 1995; Brooks et al. 2018). Spoon-shaped depressions are representative of megafutes and scours (Robles et al. 1995). These cause a variable depositional topography which influenced subsequent flows, resulting in slight compensational stacking.	Channel-lobe transition zone (Fig. 3.6A, 3.7)



**Figure 3.8:** Photographs showcasing the variety of geometries observed in the study area. North is indicated. Peach highlights scale. A) Tabular bedded. B) Concave upward; white lines highlight individual architectural elements. C) Pinching out upslope; black lines highlight pinch-out geometry, black box locates zoom in which was used for reconstruction of the slope angle. D) Convex upwards; white lines highlight each element. E) Pinching out downslope; white lines outline triangular geometries, and white arrows indicate onlap (also in Figure 3.6C). F) Undulose. G) Tabular amalgamated beds; white lines outline individual beds.

### 3.7 Stratigraphic Evolution

Extensive exposures permit detailed lithostratigraphic analysis (Figures 3.3, 3.9, 3.10 and 3.11), allowing investigation of the role of salt-induced relief on depositional patterns (Figures 3.12, 3.13 and 3.14). The following sections describe the exposures from oldest to youngest, first focusing



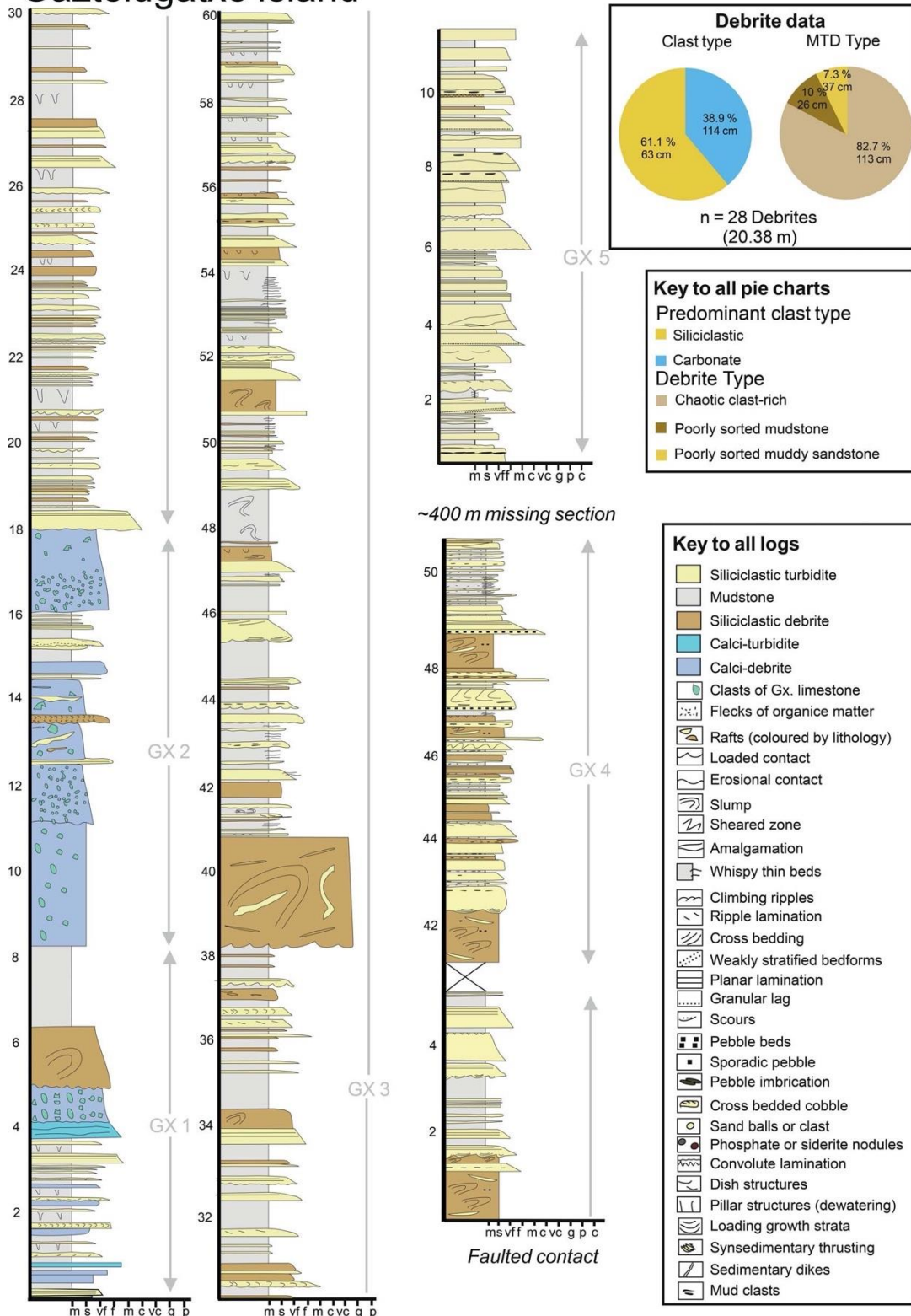
on the flanks of the Sollube and Jata basins (Gaztelugatxe Island and Bakio West Bay, respectively) and then the axis of the Sollube basin (Cabo Matxitxako).

### ***Gaztelugatxe Island***

**Description:** GX1 is 8 m thick and consists of bioturbated mudstones, calci-debrites, calci-turbidites, thin-bedded turbidites, and mud-rich debrites. It shows an overall coarsening- and thickening-upwards from centimetre-to metre-scale interbeds of each facies. GX2 is 10 m thick and dominated by carbonate–clastic debrites, with angular clasts of the Gaztelugatxe Limestone, up to 1 m in diameter. GX2 pinches out downslope, forming a triangular geometry (Table 3.4; Figure 3.9E). GX3, has a minimum thickness of 42 m, onlaps GX2 and is recognised as the first purely siliciclastic succession; comprising thin- to medium- bedded turbidites, debrites, hybrid beds, and bioturbated mudstones. GX4 has a minimum thickness of 9 m, and its base is marked by a metre-thick slump, overlain by interbeds (centimetre to decimetre scale) of turbidites, debrites, slumps, slides, hybrid beds, and mudstones. GX5 is identified on the western side of Cabo Matxitxako (Figure 3.9), having a minimum thickness of 30 m. There is approximately 400 metres of missing stratigraphy between GX4 and 5 (Robles et al. 1988), but GX5 is projected to lie stratigraphically above GX4. GX5 comprises predominantly amalgamated medium- to high-density turbidites showing evidence of soft-sediment deformation.

**Interpretation:** The presence of siliciclastic and calci-turbidite deposits and debrites in GX1 (Figure 3.9) suggests a transition from the upper BBF to the LBF (Figure 3.13C: Poprawski et al. 2014; 2016). The carbonate deposits could have been remobilised from previous BBF deposits or remnant carbonate highs (Poprawski et al. 2014; 2016). GX2 represents a period of increased mass failure, which is interpreted to be halokinetically driven due to the lentil-shape and diapir-centric distribution of these limestone breccias (Table 3.4; Figure 3.8E; e.g., McBride et al. 1974; Huncutt 1998; Giles and Lawton 2002). The thin-bedded nature and presence of hybrid beds in GX3 suggests early BFG deposition in a proximal lobe-fringe environment (Spychala et al. 2017; Soutter et al. 2019). Thin-bedded debrites are interpreted to be delivered axially, based on their association with thin-bedded turbidites that show regional paleocurrents. Thick-bedded, chaotic, clast-rich units are interpreted to be halokinetically-driven based on variable slump-axis paleocurrent readings (Poprawski et al. 2014). At the base of GX4, a metre-scale debrite overlies 30 m of missing section (Figure 3.9), which given the low-lying geomorphology is likely mud- rich. The overlying turbidites and debrites suggest deposition in a lobe off-axis setting (Prélat et al. 2009; Sychala et al. 2017) where the seafloor was, at least periodically, unstable (Figure 3.13E). Metre-thick beds that stack into 30-metre-thick packages suggest that GX5 represents deposition in the axis of a lobe complex (Figure 3.13F: Prélat et al. 2009; Soutter et al. 2019). The absence of debrites or slumps in GX5 (Figure 3.9) suggests minimal halokinetic influence, either due to diapir inactivity or sediment accumulation, due to uplift and erosion from the Landes Massif (Agirrezabala 1996), outpacing the rate of seafloor deformation. The presence of amalgamated, laterally extensive medium- and high-density turbidites in GX5 supports deposition in a channel-lobe transition zone (Vincente Bravo and Robles 1991a; 1991b; 1995) or lobe-axis setting.

# Gaztelugatxe Island



**Figure 3.9:** Sedimentological log through the Black Flysch Group at Gaztelugatxe Island. Location is on Figure 3.3. Transects of individual logs are separated by missing sections as highlighted, and are therefore not continuous. Similar sedimentary facies on either side of the fault suggest that GX3 continues on both sides of the structure, and therefore the impact of the structure is minor. Key for all the logs and pie charts shown. Thicknesses are in metres. GX# relate to stratigraphic units discussed in the text. Pie chart shows debris data divided by predominant clast type and debris type (Table 3.2), and relative proportions of all debris at this section, and average thickness of each type is shown.

### ***Bakio West Bay***

The coastal cliff section at Bakio West Bay (Figure 3.10) exposes c. 150 m of the BFG above its basal contact with the BBF (Robles et al. 1988), c. 1 km west of the Bakio diapir. This section is divided lithostratigraphically into three units (BW1–3), and is further divided by halokinetically driven unconformities into sub-units (Figure 3.10; Poprawski et al. 2014).

**Description:** BW1 is 6-metre-thick, consists of calciturbidites and siliciclastic turbidites, debrites, and mudstones, and is overlain by BW2 across an angular unconformity (U2; Figure 3.10A; Poprawski et al. 2014). BW2 is principally siliciclastic, comprising predominantly turbidites, with minor debrites and mudstones. A 10-metre-thick package of fine sand- to pebble- grade turbidites with lenticular geometries and scoured-amalgamated bases is observed to overlie a 2-metre-thick debrite (Figure 3.10A). BW3 consists of interbedded metre-scale siliciclastic turbidites and debrites (Figure 3.10B). Unconformities 5 and 6 are intra-BW3, and thus BW3 is subdivided into three sub-units (BW3a, b, and c).

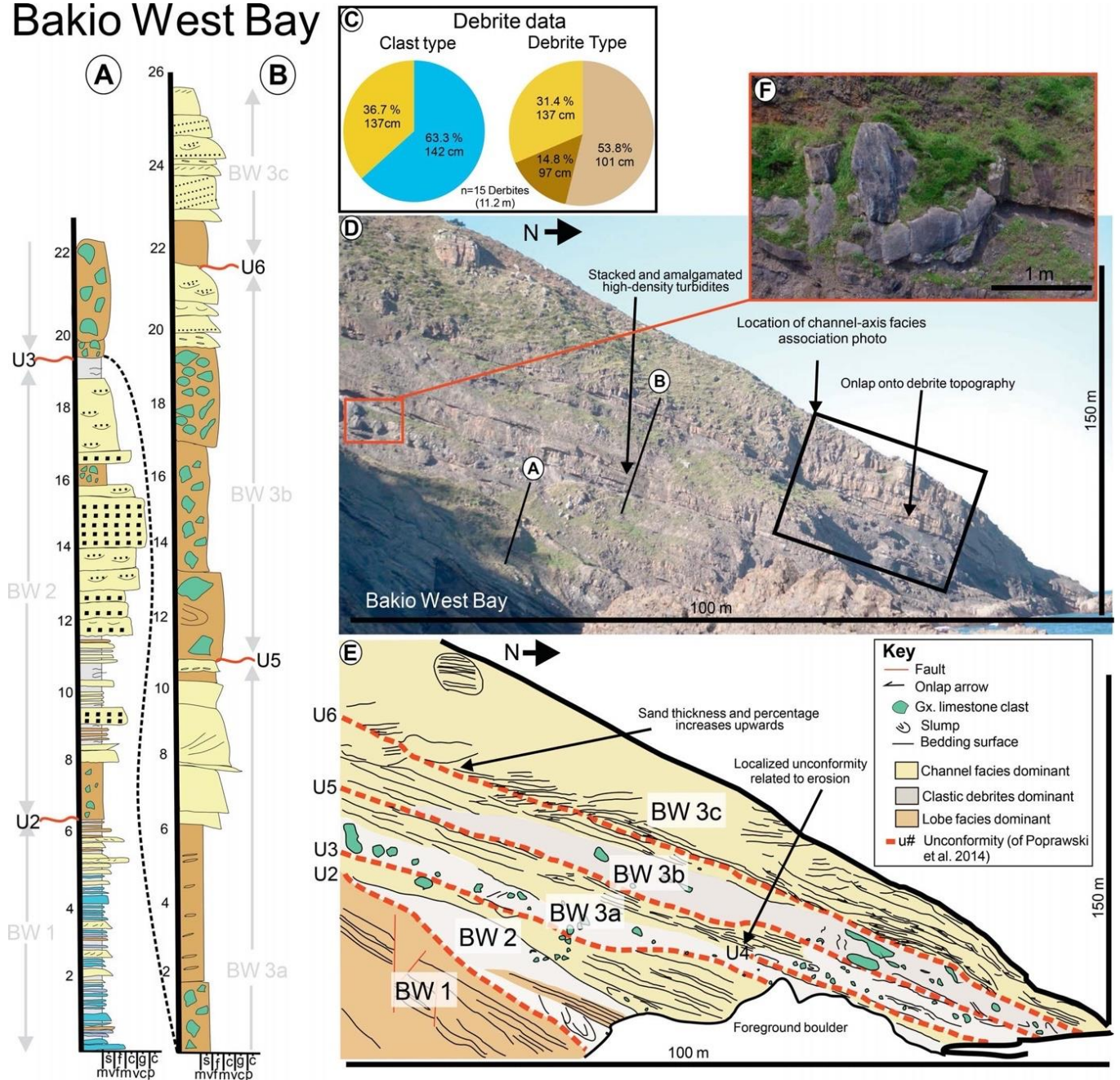
At the bases of BW3a, BW3b, and BW3c, 1–12-metre-thick debrites with variable thickness across the exposure overlie the angular unconformity (Figure 3.10). Grain-size varies from medium sand to boulders and clasts vary from rounded to angular. A more diverse range of clast rock types than elsewhere in the study area are observed, including limestone, sandstone, mudstone, organics, heterolithics, siderite, mafic material, granite, and siderite (Table 3.3). An undulose contact exists between the debrites and the 2–4-metre-thick amalgamated turbidites which overlie them (Figure 3.10). These medium sand- to pebble-grade turbidites are lenticular in geometry, can be divided into metre-scale fining-upwards successions, and contain inclined stratification (Figure 3.10).

**Interpretation:** The angular unconformities are interpreted to be related to salt-diapir movements, and are interpreted as part of a tapered halokinetic sequence (Giles and Rowan 2012; Poprawski et al. 2014). Unit BW1 marks the transition from BBF to BFG, and is interpreted as representing deposition at the base of slope of the carbonate platform, which was growing on the Bakio diapir (Figure 3.13D; Poprawski et al. 2014). Coarse-grained sandstones with lenticular geometries, scoured bases, and normal grading, such as those observed in BW2, indicate deposition in a channelised or scoured setting (Figures 3.7F, 3.10 and 3.13E; e.g., Hubbard et al. 2014; Hofstra et al. 2015). The debrites capping unconformities could be halokinetically-derived or related to channel-margin collapse induced by diapir movement (Rodriguez et al. 2020). The wide range of clast rock types in these debrites suggests that they are dissimilar to other halokinetically-derived debrites and could indicate a different set of mass flows sourced up-dip of the depositional system (Figure 3.10C; e.g., Doughty-Jones et al. 2019; Wu et al. 2020).

The deepest point of each lenticular geometry in BW3 appears to step eastward towards the Bakio diapir (Figures 3.7F and 3.8A); this could indicate lateral-accretion deposits from a meandering submarine channel (e.g., Peakall et al. 2007; Kane et al. 2010; Janocko et al. 2013). The concave-upward geometry of the turbidites and the undulose contact with the debrite below (Figures 3.7F, 3.8B and 3.10) could represent channel fills or scour fills influenced by previous debrite topography (e.g., Cronin et al. 1998; Jackson and Johnson 2009; Kneller et al. 2016). The thick beds, concave-upward geometry, erosional bases, and coarse grain size suggests that these deposits are channel fills rather than scour fills (Hubbard et al. 2008; Romans et al. 2011; McArthur et al. 2020).

The repeated facies change between pebbly chaotic debrites and channelised turbidites is interpreted to represent periods of rapid diapir growth, evidenced by debrites overlying halokinetic unconformities (Giles and Rowan 2012). This is suggested to have been followed by periods of relative diapir quiescence, which permitted submarine channels to infill debrite topography and migrate around the diapir due to reduced seafloor topography (Kane et al. 2012).

# Bakio West Bay



**Figure 3.10:** Variability of facies and architectures within large-scale depositional elements at Bakio West Bay, located in Figure 3.3. A, B) Stratigraphic logs, which are located in part D and blown up for clarity. Thickness is in metres. Key is in Figure 3.9. BW# refers to stratigraphic unit discussed in the text. Dashed lines between logs highlight correlation. C) Pie chart showing debrite data divided by predominant clast type and debrite type (Table 3.2), and relative proportions of all debrites at this section, and average thickness of each type is shown. D) Uninterpreted and E) Interpreted large-scale architectures and facies details at Bakio West Bay. Unconformities are from Poprawski et al. (2014), and are highlighted in red where they divide packages of stratigraphy. U4 of Poprawski et al. (2014) is not laterally-extensive and appears to represent an isolated, erosionally-based depositional element (Figure 3.10E). Based on these observations and the presence of channel-axis facies associations we suggest that U4 represents the base of a channel cut and not a halokinetic angular unconformity (sensu Giles and Rowan 2012). The black box locates the channel-axis facies association photograph (Figure 3.6F). F) Clasts of Gaztelugatxe Limestone which form out-runner blocks forming sea-floor topography.

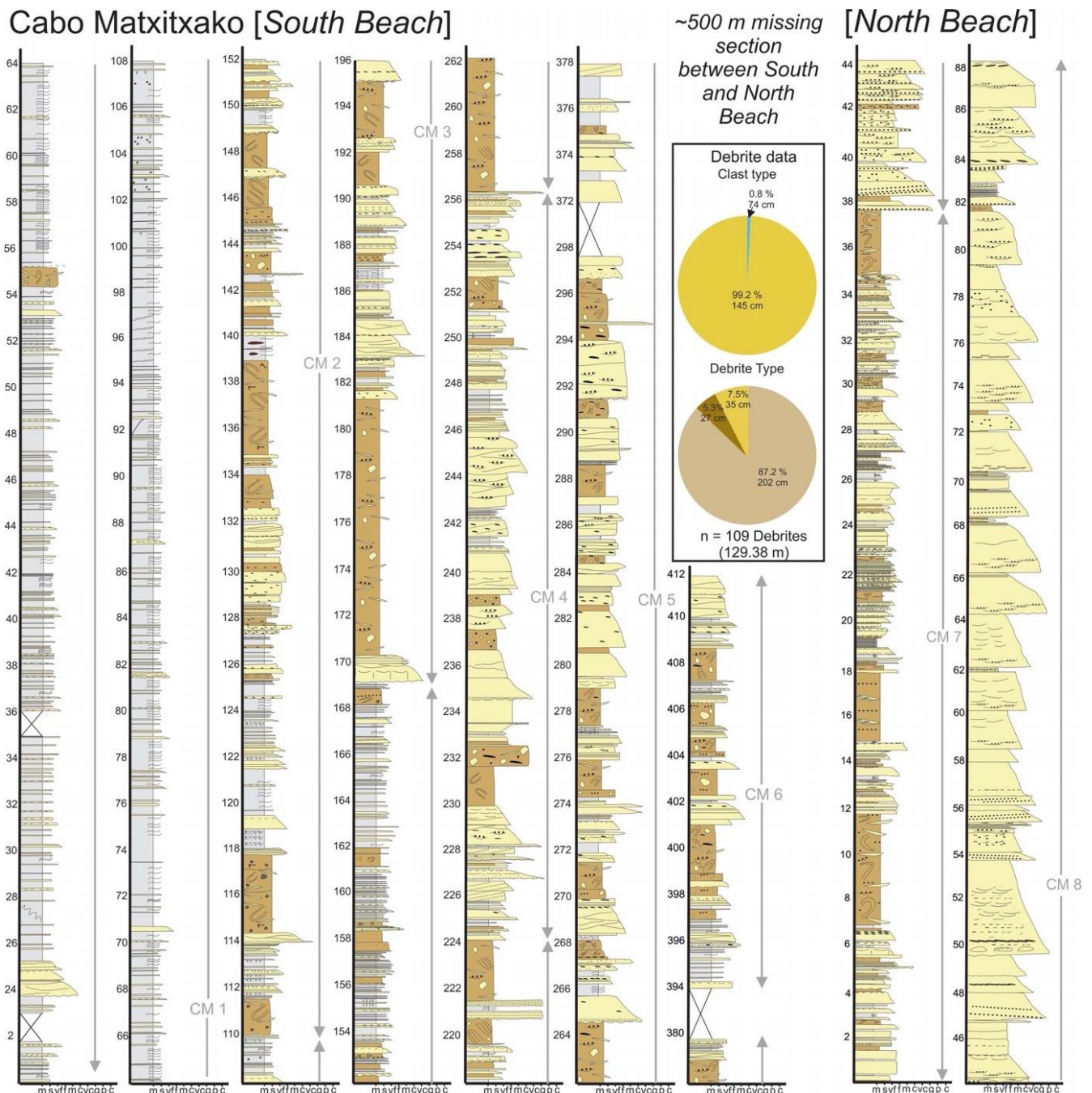
## ***Cabo Matxitxako***

Cabo Matxitxako provides an extensive section (c. 600 m) through the BFG. In this locality, we subdivide the group into eight lithostratigraphic units (CM1–8; Figure 3.11). There is c. 500 m of missing section between Cabo Matxitxako North and South Beach (Figure 3.3). Cabo Matxitxako is located in the Sollube basin, c. 4.5 km northeast and c. 5 km northwest of the Bakio and Guernica salt structures, respectively.

**Description:** CM1 is a 110-metre-thick package of mudstones, with minor thin- to medium-bedded siliciclastic turbidites and debrites. CM2 is 60 m thick and is dominated by metre-scale debrites with subordinate thin- to medium-bedded turbidites, hybrid beds, and mudstones (Figure 3.11). Slump axes, where present, indicate a range of paleoflow directions (forming two clusters: 80–160° and 280–320°; Figure 3.3). CM3 is 50 m thick and contains metre-thick packages of stacked medium to thick bedded, dewatered turbidites and slumps, metre to tens of metres thick containing rafts of thin-bedded turbidites. Two beds of granular sandstone (27 and 19 cm thick) with lenticular geometries are observed at the top of CM3. CM4 is 32 m thick, is distinguished from CM3 as it is debrite-poor and mostly comprises thick-bedded, amalgamated high-density turbidites that stack into 3 to 6-metre packages. CM5 is 124 m thick and consists of roughly equal proportions of 1 to 3-metres-thick amalgamated turbidites, which are normally-graded on a bed scale, and metre-scale slumps and debrites, which occur every 2–10 m and contain rafts of thin-bedded turbidites. CM6 has a minimum thickness of 18 m, is observed at the northern part of South Beach, and is composed of 1 to 3 m debrites and 1 to 80 cm turbidites and mudstones (Figures 3.3 and 3.11). CM7 has a minimum thickness of 38 m, similar to CM6; however, the units are separated by c. 500 m of missing stratigraphy, much of which is assumed to have been removed due to Pyrenean deformation and recent landslides (Vicente Bravo and Robles 1995), so have been separated. CM8 is 40 m thick and consists of predominantly metre-scale, normally graded thick-bedded turbidites with erosional bases, cross-stratification, amalgamation, mud-clasts, and dewatering structures common throughout (Figure 3.11).

**Interpretation:** The Cabo Matxitxako succession (Figure 3.11) suggests a broadly basinward-shifting (i.e., progradational) system from CM1 to CM4 due to overall coarsening and thickening of beds, followed by a slight back-step (i.e., retrogradational) or lateral shift in CM5 to CM7 representing by thinner beds and muddier facies, followed by a further basinward shift in CM8 indicated by significant coarsening and thickening of sandstone beds and reduction of mudstone facies (Figure 3.13). Debrites and slumps with clasts of thin- and medium-bedded stratigraphy are present throughout CM2, 3, 5, 6, and 7 suggesting that the seafloor was periodically unstable, possibly due to relatively high rates of diapir rise and related seafloor deformation. CM1 is dominated by background suspension fallout and dilute low-density turbidites in a lobe-complex distal fringe setting (Figure 3.13D). CM2 represents higher-energy, more proximal lobe conditions compared to CM1, based on facies, hybrid beds, geometry, stacking patterns, and thickness and is interpreted as proximal lobe fringe deposition (Spychala et al. 2017). The depositional sub-environment of CM3 is interpreted as an off-axis lobe complex, based on facies and bed thicknesses, with small distributive channel fills, evidenced by lenticular granular sandstones (Normark et al. 1979; Deptuck and Sylvester 2017). CM4 is dominated by stacked, amalgamated, high-density turbidites (Figure 3.11) and is interpreted to represent deposition in the axis of a lobe complex (Figure 3.13F; Prélat et al. 2009; Spychala et al. 2017). CM5 contains distributions of facies similar to those of CM3, so is interpreted to represent lobe-complex off-axis deposition with some distributive channel fills (Normark et al. 1979; Deptuck and Sylvester 2017). Debrite dominance in CM6 and CM7 suggests remobilisation due to diapir growth throughout deposition (Figure 3.13F). These deposits are interpreted to represent proximal-fringe to lobe-off-axis deposition (Spychala et al. 2017), which is highly modulated by halokinetic debrites. The coarse grain size, cross-stratification, thick beds, and lack of debrites

and mudstones (Figures 3.7E and 3.11), suggests that CM8 was deposited in either a lobe-axis or channel-lobe transition zone. This unit has previously been interpreted as a channel-lobe transition zone (Vincente Bravo and Robles1995) and shares characteristics similar to channel-lobe transition zones reported elsewhere (e.g., Brooks et al. 2018). This unit shows little evidence for active topography, suggesting that the sedimentation rate had increased with respect to the diapir rise rate, possibly associated with uplift of the Landes Massif (Rat 1988; Martín-Chivelet et al. 2002), or welding of the salt source layer. Any remaining seafloor topography was filled by CM8 (Figure 3.13G).



**Figure 3.11:** Sedimentary log through Cabo Matxitxako Beach. Location in Figure 3.3. Missing sections are indicated; thickness is in metres. Key for all logs is provided in Figure 3.9. CM# indicate stratigraphic units discussed in the text. Roughly 500 m of missing section separates South and North Cabo Matxitxako. The pie chart shows debrite data divided by predominant clast type and debrite type (Table 3.2), and relative proportions of all debrites at this section, and average thickness of each type is shown.

### ***Stratigraphic Correlation***

The BW, GX, and CM lithostratigraphic units represent different depositional systems despite their close proximity. Poor biostratigraphic calibration renders stratigraphic correlations between the areas challenging (Agirrezabala and López-Horgue 2017). Using lithostratigraphy, BW1 is correlated to GX1–2, BW2–3 are correlated to GX3–4 and CM1–7, and GX5 is correlated to CM8 (Figures 3.9, 3.10 and 3.11).

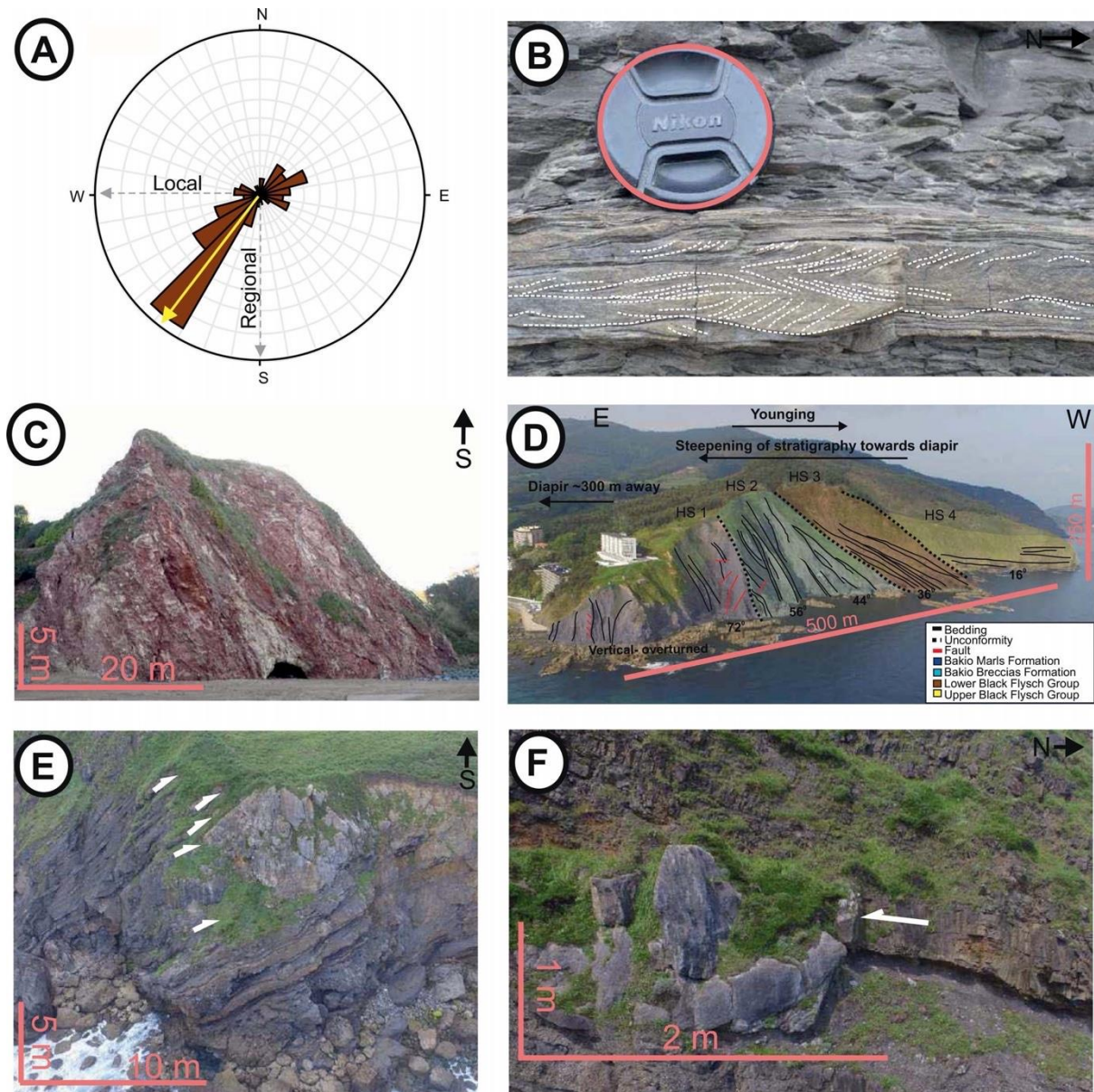
### **3.8 Evidence for seafloor topography**

There is widespread sedimentological evidence for seafloor topography during deposition of the BFG, which as we discuss below reflects the interplay between active salt growth and depositional processes controlling the available accommodation.

Ripple cross-lamination, cross-stratification, and sole marks indicate a regional south-westward paleoflow direction (Figure 3.12). This direction is consistent with a northward source for the BFG, supporting the Landes Massif as a potential regional source area (Rat 1988; Robles et al. 1988; Ferrer et al. 2008; Puelles et al. 2014). At Cabo Matxiatxako, a secondary westward paleoflow orientation (Figure 3.12A) is comparable to findings by Robles et al. (1988), who suggest that this reflects the passage of gravity flows that spilled across the Guernica structure into the Sollube basin. Therefore, paleocurrent data (Figure 3.12A) suggest modulation of a regional (primarily south-trending) paleoflow by salt-induced topography (west-trending flows off east-facing slopes) (Figure 3.13). Analogously, a west–south- westward paleoflow observed at Bakio West Bay (Figure 3.3) may reflect the passage of gravity flows that spilled from the Sollube basin, across the Bakio structure into the Jata basin. This west–south-westward paleoflow could alternatively represent the westward deflection of regional paleoflow around the Bakio diapir.

Ripple lamination in opposing directions is common in individual thin-bedded turbidites (Figure 3.12B). Such features have been attributed to flow reflection or deflection from seafloor topography (e.g., Kneller et al. 1991; McCaffrey and Kneller 2001; Barr et al. 2004; Hodgson and Haughton 2004). Moreover, hybrid beds seen throughout the distal fringe (Figures 3.6L, M, 3.9, 3.10 and 3.11) indicate that topography had influenced a transformation of flow from turbulent to laminar (Figure 3.15; e.g., Barker et al. 2008; Soutter et al. 2019).

Distal terminations of turbidity flows that pinch out up depositional slope (Figure 3.8C) reflect thinning towards topography (e.g., Ericson et al. 1952; Gorsline and Emery 1959) as the low-density part of the turbidity current ran up the topography farther than the high-density component (e.g., Al-Ja'aidi 2000; Bakke et al. 2013). Hence, thicker sandstones are more likely to be confined to localised salt-withdrawal minibasins (Figures 3.13, 3.14 and 3.15), whereas thinner sandstones may drape halokinetically influenced slopes (Figures 3.13, 3.14 and 3.15; Straub et al. 2008; Soutter et al. 2019). Based on a bed-scale thinning rate of 10 cm/m at Cabo Matxiatxako (Figures 3.3 and 3.11), we calculate the slope angle to be 2–3° (Figure 3.8C). Due to the distance (c. 5 km) from the present-day Bakio diapir, it is unlikely that this slope is solely related to diapir growth, but rather caused by a combination of salt withdrawal or welding from the salt source layer at depth, and salt-structure growth, as observed in similar-sized subsurface examples (e.g., Doughty-Jones et al. 2017). Multiple paleoflow directions, hybrid beds, and abrupt pinch-out of beds can suggest the presence of (static) topography. However, the number of debrites intercalated with lobes, and the tapered composite halokinetic sequence observed at Bakio West Bay (Figure 3.12D) suggest that this topography and salt growth was active at the time of deposition.



**Figure 3.12:** Evidence for topography and paleoflow direction. Black arrow shows orientation and peach indicates scale, and lens cap is 52 mm. A) Rose diagram for 284 paleocurrent indicators (ripples, sole marks, cross-stratification) from the Black Flysch Group. Readings have been corrected for tectonic tilt yellow arrow indicates dominant paleoflow direction some radial spread is due to ripple reflection. Grey arrows indicate regional (to the south) and local (to the west) paleoflow directions, discussed in the text. B) Evidence for opposing-direction ripples suggesting ripple reflection. C) Triassic-age Keuper Group outcrop of clays, carbonate, and gypsum at Bakio Beach, thought to be part of the Bakio diapir. D) Composite halokinetic sequence associated with the western flank of the Bakio diapir; HS, halokinetic sequence. E) Pinch-out and onlap of lowermost Black Flysch Group thin-bedded turbidites onto a Gaztelugatxe Limestone clast on the eastern flank of the diapir. F) High-density turbidite abruptly terminating against a block of Gaztelugatxe Limestone in HS3 (BW3).

### Debrites

MTDs and debrites (Table 3.1; Figures 3.6K and 3.8D) observed throughout the succession indicate seafloor, shelf or diapir roof instability. Such sequences are observed in halokinetically-influenced settings globally, where diapir rise rate is high (Giles and Lawton 2002; Giles and Rowan 2012; Doughty-Jones et al. 2019; Wu et al. 2020). Heterogeneities in subsurface fluid flow characteristics can be caused by the presence of reworked thin-beds within debrites (Figure 3.14) which could act as barriers or thief sands, allowing reservoir fluids to migrate further up dip closer to the salt structure (Moscardelli and Wood 2006). Therefore, understanding debrite sourcing can help de-risk seal and trap uncertainty (McKie 2015). Debrites appear chaotic in subsurface data due to



their internal disorder (Soutter et al. 2018; Doughty-Jones et al. 2019) and are therefore difficult to decipher from salt structures (Jones and Davison 2014) which can lead to the overestimation of salt structure width (Charles and Rhyzhikov 2015).

**Description:** Debrites, slumps, and slides (the vast majority being debrites) account for 23% of stratigraphy across all measured sections, with an average thickness of 111 cm. Assuming that all the debrites (Table 3.1; Figures 3.6K and 3.8D) are derived from diapir slopes and all turbidites are derived from far field, a 1:4 ratio of halokinetically to axially derived deposition exists. While this is clearly an oversimplification, and we provide evidence for local, diapirically-derived debrites and regional, slope-derived debrites, it does suggest that locally, extra stratigraphy may be present in salt-confined basins compared to unconfined settings. Therefore, interpreting stacking patterns and correlating between basins may be challenging.

Debrites on the flank of the Jata basin have an average thickness of 140 cm, compared to 119 cm and 73 cm in the axis and flank of the Sollube basin, respectively. 31% of measured stratigraphy on the flank of the Jata basin comprises debrites, compared to 22% and 18% in the flank and axis of the Sollube basin, respectively. Debrite composition shows siliciclastic dominance in the axis of the Sollube basin; debrites with carbonate clasts or matrix become more common on the flank of the Sollube basin and are dominant on the flank of the Jata basin (Figures 3.9, 3.10 and 3.11), in agreement with models of halokinetic sequences (Giles and Rowan 2012). Limestone clasts of similar composition in debrites on both the Jata and Sollube flanks support the presence of a carbonate platform growing on top of the Bakio diapir (García-Mondéjar and Robador 1987; Poprawski et al. 2014; 2016), indicating that these debrites are related to local diapir failures. The proportion of carbonate clasts decreases from the Sollube basin flank to axis (39% in Figure 3.9 and 1% in Figure 3.11) due to distance from the carbonate platform growing on top of the Bakio diapir.

To better understand debrite source areas, debrites were subdivided by type into poorly-sorted mudstones, poorly-sorted muddy sandstone and chaotic clast-rich matrix supported deposit (as per Table 3.2). Clast rich deposits were the most common across all stratigraphy. The axis of the Sollube basin has the highest proportion of clast rich deposits across the measured sections, and the Jata basin flank is the section with the most variable debrite types. Sollube axis and flank contain broadly similar proportions of each type of debrite (Figures 3.9, 3.10 and 3.11). The average thickness of siliciclastic debrite is 145 cm, 63 cm and 137 cm in the Sollube axis, flank and Jata flank settings respectively. Carbonate debrite thickness is highest on the Jata flank (142 cm), 114 cm on the Sollube flank and 74 cm in the Sollube basin axis, based on one observation. Chaotic clast rich deposits are thickest (202 cm) in the Sollube basin axis, compared to the flank (113 cm) and the flank of the Jata basin (101 cm). Poorly-sorted mudstones (27 cm in the axis and 26 cm in the flank) and poorly-sorted muddy sandstones (35 cm in the axis and 37 cm at the flank) of the Sollube basin, are much smaller than the poorly-sorted mudstones (96.5 cm) and muddy sandstones (137 cm) of the Jata basin.

Isolated limestone megaclasts (Figure 3.10 F, 3.12 E and 3.12 F) derived from the Gaztelugatxe Limestone could be out-runner blocks (e.g., De Blasio et al. 2006; Soutter et al. 2018) or fractured blocks of platform limestone that have toppled off during diapiric growth (e.g., Alves et al. 2002; 2003; Martín-Martín et al. 2016). Younger deposits progressively onlap these limestone clasts (Figures 3.12E and 3.12F), showing that subsequent turbidity currents later interacted with this additional seafloor topography (e.g., Kilhams et al. 2012; 2015; Olafiranye et al. 2013).

**Interpretation:** Debrites can be sourced from either collapse on top of the diapir or its flanks, or from failures of the shelf-edge and/or slope (Doughty-Jones et al. 2019; Wu et al. 2020; Rodriguez

et al. 2020). However, the source is difficult to decipher without a dataset covering the coeval shelf and slope succession. The presence of more debrites in the basal active part of the Sollube basin fill (Figures 3.9, 3.10, 3.11 and 3.14) compared to the upper passive part of the basin fill (Figure 3.11) suggests that mass failures are more common during initial development of salt-confined depocenters (Wu et al. 2020). The Sollube basin is more confined than the Jata basin, as it is confined by both the Bakio and Guernica salt structures, and therefore can be expected to receive a larger proportion of material derived from diapir growth. In fact, the Jata basin received more and thicker debrites. This could suggest asymmetric growth of the Bakio diapir, or the carbonate platform above it, creating a steeper slope on the boundary of the Jata basin. However, the apparent difference in the number and thickness of debrites could also be due to limitations of the outcrop, in that the Sollube basin flank location (Gatzelugatxe Island) is more axial than the Jata basin flank outcrop (Figure 3.3). The absence of carbonate clasts in the axis of the Sollube basin, compared to the Sollube and Jata basin flanks, could suggest that diapirically derived mass failures did not extend into the axis of the basin. Subsurface studies show that diapirically-derived debrites may only extend 100s-1000s metres away from the source, which may indicate the axis of the Sollube depocenter is outside the area influenced by halokinetic debrites (Rowan et al. 2012; Giles and Rowan, 2012; Jones et al. 2012; Hearon et al. 2015; Rodriguez et al. 2018; Doughty-Jones et al. 2019; Wu et al. 2020). However, the exposed minibasin stratigraphy is younger than the flanking stratigraphy, and therefore carbonate clasts are expected to be rarer due to a decrease in exposure and availability to be remobilised through time.

Examining the predominant clast type alone, it could be suggested that carbonate-rich debrites decrease away from the diapir and therefore halokinetically-influenced debrites are carbonate rich and shelf-derived debrites are siliciclastic rich. However, passive diapir growth continued during the deposition of the Black Flysch Group (Agirrezabala and García-Mondéjar 1989; Poprawski et al. 2014; 2016; Agirrezabala and López-Horgue 2017; Zamora et al. 2017) and therefore remobilisation of thinly-bedded sandstones deposited on top of diapiric topography probably occurred across the study area, as is evidenced by both siliciclastic and carbonate clast rich debrites at Gatzelugatxe Island (Figure 3.9), and is common during periods of high structural growth (Doughty-Jones et al. 2019).

The average thickness of chaotic clast-rich deposits increases from flank to basin axis in the Sollube basin, this could suggest only the largest diapirically-derived mass failures make it into the basin, and become detached from their up-dip equivalent, with the time-equivalent debrite on the flank being absent due to flow bypass (Moscardelli and Wood 2008). Flow bypass could be driven by steep slopes, and localised fractures associated with the Bakio diapir. Smaller, attached, chaotic-clast rich deposits that thin towards the basin axis may account for the 101-113 m average thickness debrites observed on either flank of the Bakio diapir. The presence of reworked thin-bedded sandstones and rafts of thick-bedded sandstone within chaotic-clast rich debrites suggests they were remobilised from thin-thick bedded sandstones, deposited across the study area, due to diapiric movements. Similar raft blocks, remobilised from diapiric highs have been interpreted in the subsurface (Gee and Gawthorpe 2006; 2007; Oluboyo et al. 2014; Soutter et al. 2018; Doughty-Jones et al. 2019; Rodriguez et al. 2020). Presence of shelly material within these debrites also indicates a local source from the platform atop of the Bakio diapir.

Alternatively, the presence of thicker chaotic clast-rich debrites in the Sollube basin axis could be interpreted as alloeyclic deposition, controlled by up-dip shelf failures. The thickest deposits are interpreted to have exploited lows between diapir-influenced conduits, as is observed in the subsurface (Doughty-Jones et al. 2019; Wu et al. 2020) and apparent thinning towards the Sollube margin and on the Jata margin could be interpreted as debris flows running up topography, and

their deposits thinning, analogous to observations in turbidites (Figure 3.8C). Seismic facies analysis of 'regional' debrites offshore Angola reveals they are mostly composed of chaotic material, and appear to thin towards topographic highs, in agreement with our field-based facies analysis (Doughty-Jones et al. 2019). The Jata basin is only partially confined, therefore the presence of a larger proportion of non-chaotic clast-rich deposits could indicate flows became more dilute due to lack of confinement and transformed into muddier or sandier equivalents.

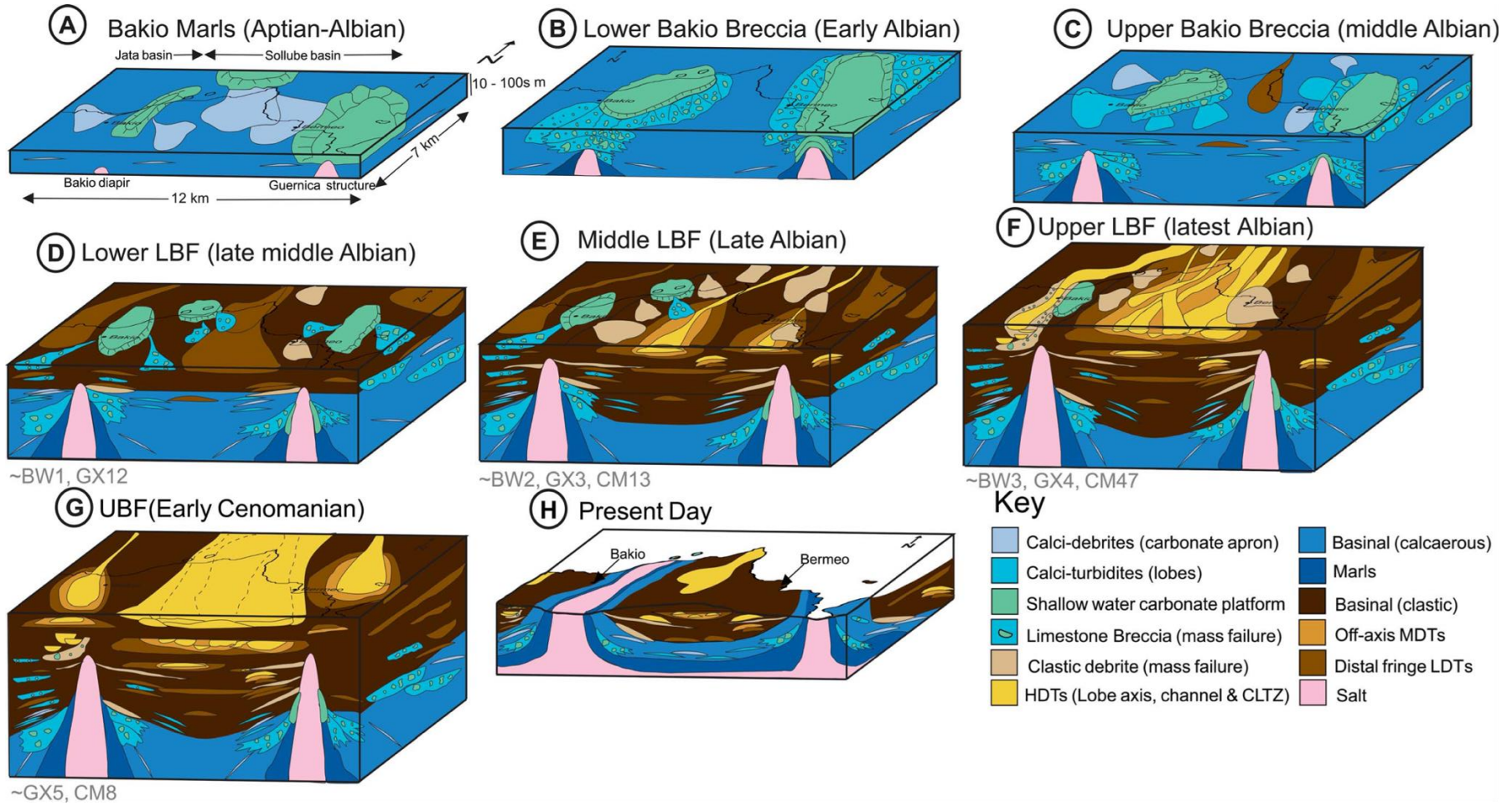
The uplifting Landes massif was located <20 km away from the study area during Black Flysch deposition (Agirrezabala 1996; García-Mondéjar et al. 1996); increased sedimentation due to the uplifting plateau could have caused shelf and/or slope failure resulting in mass flows that made it into the Jata and Sollube basins, as is observed in the subsurface (Wu et al. 2020; Rodriguez et al. 2020). The Landes massif is interpreted as a granitic province and clasts of granite are observed within channel-lobe transition zone deposits to the north of Cabo Matxixako, however clasts of granite are not observed within the debrites which could indicate they are not sourced from the uplifting plateau. The composition of clasts within debrites at Bakio West Bay (Figure 3.10) is different to that observed within the Sollube basin. This could indicate mixing or reworking of halokinetic and shelf-derived debrites or that the Jata basin was tapping into a different, or modulated, source area as it was more open to external forcing than the dual-laterally confined Sollube basin. As the salt beneath the Sollube basin was withdrawn and started to weld, variations in top salt geometry could have caused localised weaknesses within the Sollube basin, promoting development of failures which may be another origin of chaotic clast-rich debrites (Figure 3.14).

Poorly-sorted mudstone and muddy sandstones are comparable in average bed thickness and proportions at the axis and flank of the Sollube basin. This suggests location and thus proximity to the diapir was not a control on these deposits and the flows forming these deposits may have been sourced from the shelf. Average thicknesses and proportions of poorly-sorted mudstones and muddy sandstones are greatest close to the Bakio diapir (at Bakio West Bay), indicating a diapiric source and greatest thickness within the halokinetic sequence, similar to observations adjacent to North Sea diapirs (Davison et al. 2000; Carruthers et al. 2013). If this were the case a similar thickness and proportion would be expected on the opposite side of the Bakio diapir (Gaztelugatxe Island). This difference could further support diapir asymmetry during growth, whereby larger failures were more common on the western flank. It could also indicate that Gaztelugatxe Island is not as marginal as Bakio West Bay, and therefore the Bakio diapir may not exist as far offshore as interpreted (Ferrer et al. 2014; Poprawski et al. 2016) or the Sollube basin may have been steep-sided such that Gaztelugatxe and Cabo Matxixako represent basin off-axis and axis respectively and are outside the direct zone of diapir influence. Due to lack of accessible exposure at Bakio West Bay, and mass flow size being controlled by a number of factors it may not be possible to quantify stratigraphic trends using average debrite thickness and therefore comparison of the Jata and Sollube basins remains tentative.

Regardless of emplacement mechanism, debrites formed additional rugose seafloor topography in both depocenters, confining subsequent gravity flows and further localising deposition (Cronin et al. 1998; Armitage et al. 2009; Madof et al. 2009; Kneller et al. 2016). Halokinetically-derived debrites are likely to increase the area deformed by topography surrounding the salt structures and therefore subsequent flows would be expected to be deposited further from the diapir, in response to topographic influence (Doughty-Jones et al. 2019).

In summary, the presence of complicated variations in thickness, clast type, and debrite style across the study area suggests that mass flows are likely to be both locally derived (from the salt structures) and regionally derived (from the shelf), and therefore debrites were likely both allogenic and halokinetic in origin (Moscardelli and Wood 2008; Doughty-Jones et al. 2019; Wu et al. 2020). The

proximity to salt structures, reduction in mass-failure deposits away from salt structures, and the remobilised intrabasinal clasts within them suggests that the majority of debrites in the study area are locally derived from the Bakio diapir. The wide variety of clasts types in Jata basin debrites (Table 3.3: Figure 3.10) and the association of these deposits with channelised turbidites above could suggest that some of the Jata basin debrites were regionally derived, and deposited as part of channel-axis depositional elements. The absence of these possible regionally derived debrites in the Sollube basin could be due to confinement by the offshore part of the Bakio diapir, or different up-dip sediment routing. The difference in thicknesses and numbers of debrites between the Jata and Sollube basins suggests that they developed, at least partially, as separate depocenters influenced by different controls (Figures 3.9, 3.10 and 3.11).



**Figure 3.13:** Schematic depositional models showing the geological evolution of the system through time, specifically detailing deep-water sub-environments and their interactions with salt-induced topography. Black lines on top of each model outline the present-day coastline. Bakio and Guernica structures are indicated. Geometry of the Guernica salt body is hypothetical. Extrapolations between localities are based on topography, outcrop pattern, and UAV imagery. Parts A–C are after Poprawski et al. 2014, Parts D–G are based on this study. Locations of stratigraphic units discussed in the text (e.g., GX1, CM1) are shown. A–G) Schematic with dimensions indicated in Part A. H) Present day and to scale based on Figures 3.3 and 3.4, with two times vertical exaggeration, representing post-Cretaceous inversion, uplift and erosion. LDT, low-density turbidite; MDT, medium-density turbidite; HDT, high-density turbidite; CLTZ, Channel lobe transition zone.

### 3.9 Discussion

The discussion initially focuses on the Sollube basin, then compares the Sollube and Jata basins, before comparing our observations to similar depocenters developed in other salt-influenced basins.

#### ***Architecture of the Sollube Basin***

The Sollube basin is of a similar size and geometry to previously reported subsurface minibasins (Figure 3.14; e.g., Pratson and Ryan 1994; Booth et al. 2003; Madof et al. 2009; Doughty-Jones et al. 2017). Therefore, this rare, exhumed example of a halokinetically-influenced deep-water succession provides an excellent exposure of small-scale minibasin depositional architecture, providing an analogue for subsurface minibasins.

**Distribution of Facies and Architecture:** The Sollube basin is 8 km wide and confined to the east and west by the Guernica and Bakio structures, respectively (Figure 3.4; Robles et al. 1998; Poprawski and Basile 2018). Repeated stratigraphy and facies distribution on either side of Cabo Matxitxako, the change in bedding angle between the Lower Black Flysch and Upper Black Flysch groups, and sedimentological evidence for syn-depositional topography support the presence of a broadly symmetrical basin confined by the Bakio and Guernica structures.

Early stratigraphy (the Lower Black Flysch Group) in the siliciclastic fill of the Sollube basin is dominated by thin-bedded sandstones, with localised debrites on the flanks (Figures 3.9, 3.11 and 3.14). As the basin developed, thicker-bedded sandstones representing channel fills and lobes were deposited in topographic lows (basin axis), consistent with subsurface analogues (e.g., Booth et al. 2003; Madof et al. 2009; Mayall et al. 2010; Doughty-Jones et al. 2017) and numerical models (e.g., Sylvester et al. 2015; Wang et al. 2017). Towards the flanks, the lower-density parts of the flows responsible for the thick-bedded sandstones may run up topography, depositing thin-bedded sandstones. Therefore, allocyclically-controlled, often thick stratigraphy is observed in the axis of the minibasin. Halokinetically controlled (e.g., debrites) or -influenced (e.g., thickness variations) stratigraphy occurs towards the basin margins. These interpretations are consistent with subsurface studies (e.g., Doughty-Jones et al. 2017; Wu et al. 2020; Rodriguez et al. 2020).

Oluboyo et al. (2014) suggest that a fundamental control on the type of confinement developed is the incidence angle between the strike of the salt structure and the paleoflow direction. “Fill-and-spill” architecture is observed in deep-water environments where topographic highs strike perpendicular to the gravity-flow direction (i.e., at a high incidence angle) (e.g., Piper and Normark 1983; Hay 2012; Prather et al. 2012; Soutter et al. 2019). This study documents a rare example of an exhumed halokinetically influenced deep-water succession where paleoflow is at a low incidence angle to structural strike (i.e., oblique-parallel). In such scenarios, spill between basins is rare, and sedimentary systems are deflected to run broadly parallel to salt walls in minibasins for several kilometres (Figures 3.14, 3.15 and 3.16; e.g., Oluboyo et al. 2014). The four-fold model of the fill of a confined basin (Sinclair and Tomasso 2002) is not appropriate where paleoflow is oblique or parallel to salt structures, and there is a down-dip exit (i.e., not confined in all directions). Our study indicates that the dominant style of interaction between gravity flows and topography is

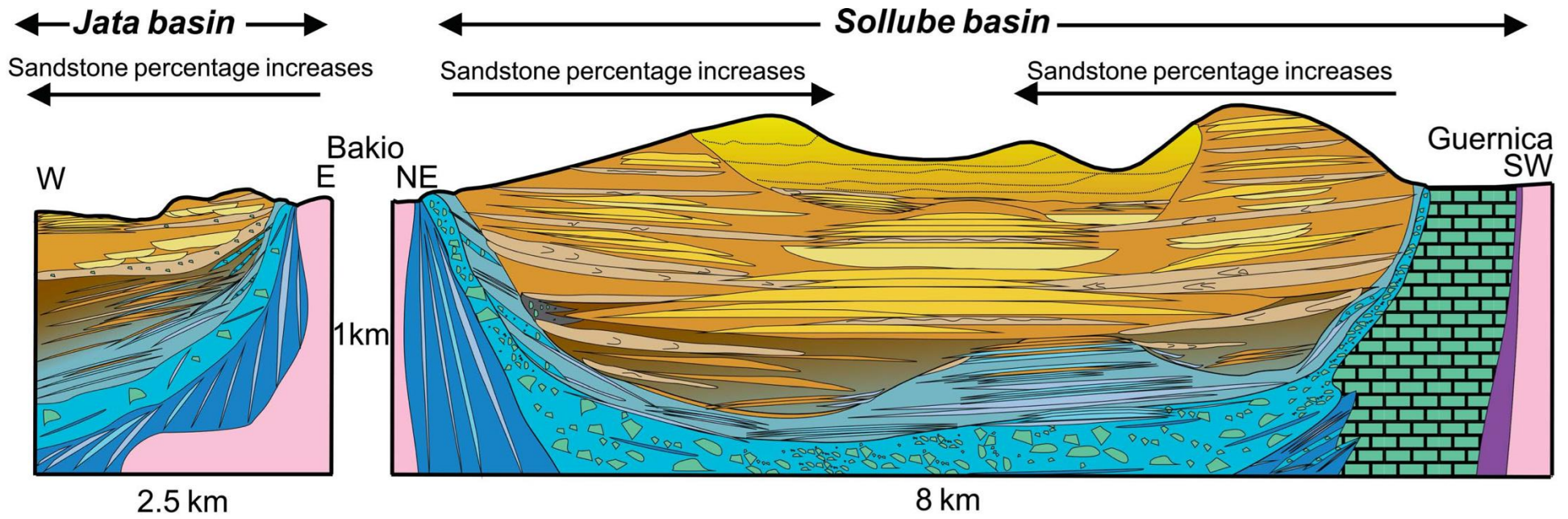
lateral confinement, with channels and lobes in the Sollube basin being thickest in the axis and elongated parallel to the margins of the salt-controlled basin. The presence of MTDs is somewhat overlooked in both the confinement model proposed by Oluboyo et al. (2014), and the earlier “fill-and-spill” model (Winker 1996; Prather et al. 1998; Sinclair and Tomasso 2002). MTDs sourced from either up-dip (i.e., extrabasinal; detached) or from local mass failures (i.e., intrabasinal; attached) related to growing salt structures, can generate additional syn-depositional relief and flow confinement (Figure 3.15; Moscardelli and Wood 2008; Rodriguez et al. 2020).

The hierarchical scheme for classifying deep-water systems developed in the Karoo basin (Prélat et al. 2009) is widely accepted, but must be used with caution, or be adapted for confined systems (Prélat et al. 2010; Etienne et al. 2012; Marini et al. 2015). Prélat et al. (2010) recognised that width-to-thickness ratios and areal extent-to-thickness ratios are different for confined and unconfined systems, with width-to-thickness ratios of 100:1 measured in selected subsurface confined settings, compared to 1000:1 in unconfined settings, and areal extent-to-maximum-thickness ratios 30 times greater in unconfined systems compared to confined systems (Prélat et al. 2010). All examples used in Prélat et al. (2010) are from settings where paleoflow is perpendicular (high angle) to slope.

In terms of areal extent, stratigraphy in the Sollube basin (c. 8 km wide) would be best classified as a lobe element (c. 5 km wide) using the Prélat et al. (2009) framework. However, in terms of thickness each lithostratigraphic unit observed at Cabo Matxitxako (18–124 m thick, Figure 3.11) would be classified as a lobe complex (c. 50 m thick). The width-to-thickness ratio of lobes in the Sollube basin is c. 160:1 (taking a midpoint thickness of 53 m), in agreement with confined examples reported by Prélat et al. (2010). This suggests similar basic geometries for confined lobes regardless of incidence angle between paleoflow and topographic strike. The dimensions observed in the salt-influenced minibasins in the study area are comparable to those of intraslope lobe complexes documented in the Karoo (6–10 km wide, 10–15 m thick; Sychala et al. 2015), which are an order of magnitude smaller than their basin-floor counterparts (Prélat et al. 2009).

Confined-lobe complexes are predicted to have smaller areal extents because radial spreading is minimal due to topographic confinement (e.g., Marini et al. 2015; Soutter et al. 2019). The ratio of axis to fringe deposition is likely to be increased in confined settings where flows stay turbulent for longer, flow deceleration is limited, and development of a wide fringe is hindered due to presence of topography (Etienne et al. 2012; Soutter et al. 2019). The presence of thicker axial deposits due to confinement by topography, and less space for lateral lobe switching to occur, may make axis identification easier in a confined setting; however, this may change through time if topography is healed and depositional systems become less confined (Marini et al. 2015).

This study supports recent work (Oluboyo et al. 2014; Rodriguez et al. 2020) which suggests that elongate systems are common adjacent to topography, on all scales. This is in contrast with the roughly equant geometries predicted in unconfined systems (Prélat et al. 2009). Multi-scale analysis suggests that all confined hierarchical elements would have greater lengths than widths, lesser areal extents, and greater thicknesses (lower aspect ratios) than unconfined settings when deposited adjacent to topography that is oblique-parallel to flow (Booth et al. 2003; Oluboyo et al. 2014; Rodriguez et al. 2020).



- |                   |   |                              |   |                                      |
|-------------------|---|------------------------------|---|--------------------------------------|
| ■ Salt            | ■ Limestone Breccias (megabed) [mass failure] | ■ Calci-turbidites [lobes]   | ■ Aptian-Albian platform carbonates             | ■ Jurassic-Barremian deposits        |
| ■ Marls [basinal] | ■ Calci-debrites and slumps [distal apron]    | ■ Limestone talus [tectonic] | ■ Mudstones and siltstones [basin (calcareous)] | ■ Debrites and slumps [mass failure] |
| ■ HDTs [CLTZ]     | ■ LDTs and mudstone [basin (siliciclastic)]   | ■ MDT-HDT [lobe axis]        | ■ HDTs [submarine channels]                     | ■ LDT-HTD [lobe fringe- off-axis]    |

**Figure 3.14:** Schematic deep-water facies and architectural elements observed on both flanks of the Bakio diapir showing the sub-seismic-scale heterogeneity that can be associated with these systems and diapir flank plays. Section is two times vertically exaggerated. Sollube and Jata Basins are indicated. Note change in orientation at the Bakio diapir.



**Development of Axial Systems:** The overall upward thickening of beds and coarsening of grain size from south to north at Cabo Matxitxako is associated with a transition in depositional environment from lobe distal fringe to channel-lobe transition zone (Figures 3.11 and 3.13). Coarsening and thickening upwards elsewhere is widely interpreted to represent progradation (e.g., Mutti 1974; Macdonald et al. 2011; Kane and Pontén 2012); however, this could also represent (a component of) lateral compensational stacking of lobes (e.g., Prélat and Hodgson 2013).

Throughout the Pyrenean, the Black Flysch Group is interpreted to have been controlled by allocyclic progradation (Robles et al. 1988; Agirrezabala and Bodego 2005), driven by increases in sediment supply following the uplift of the Landes Massif (García-Mondéjar et al. 1996; Martín-Chivelet et al. 2002; Puellas et al. 2014) and/or increased flow efficiency from confinement (Hodgson et al. 2016). This regional progradation, along with our field observations, provides compelling evidence that, on a lobe to lobe-complex scale, the stratigraphic architecture of the study area is controlled primarily by system progradation. Lateral switching may be reduced due to confining topography decreasing the amount of space available for switching to take place (e.g., Mayall et al. 2010; Oluboyo et al. 2014).

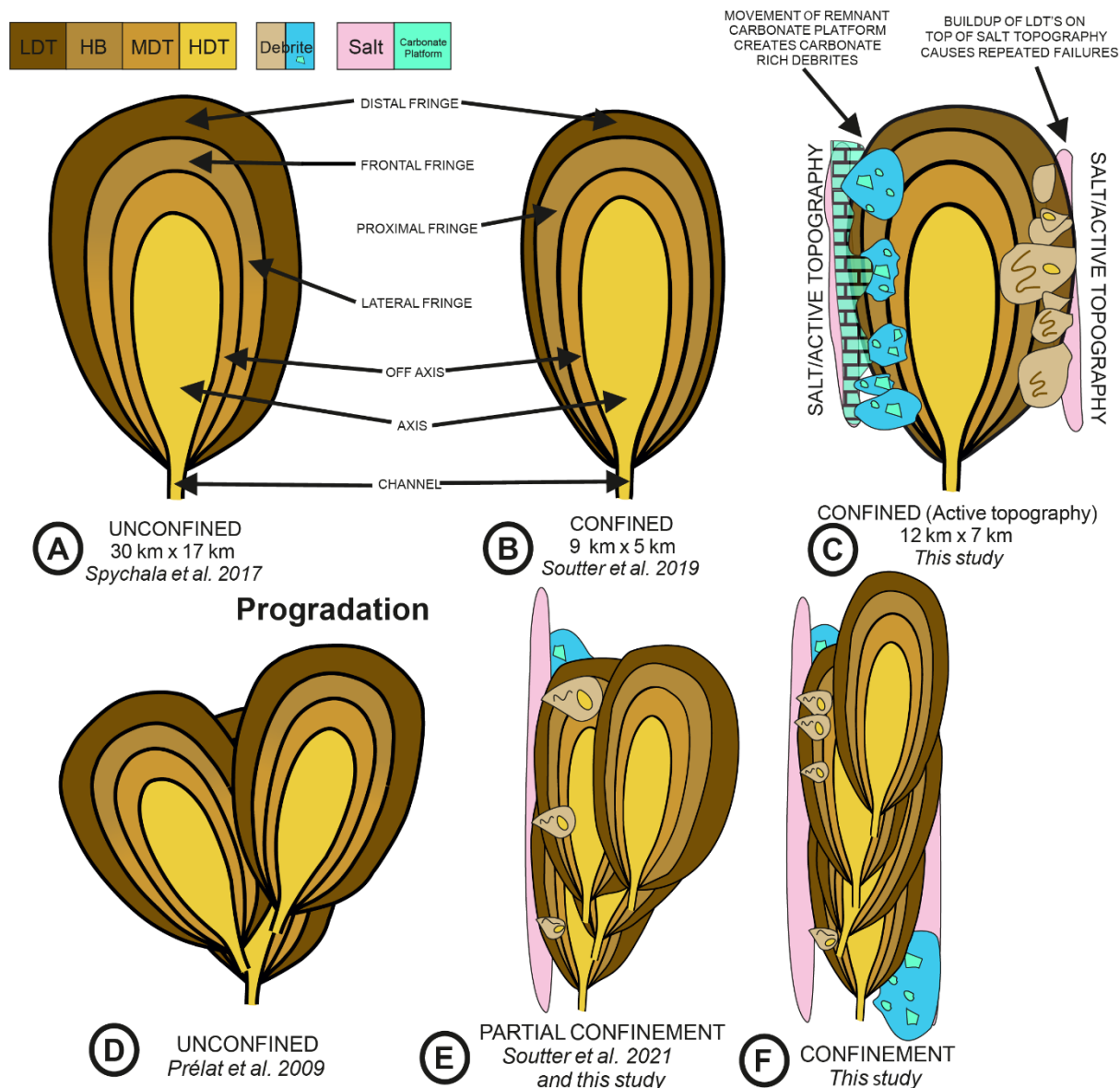
By definition, only two lobe elements would be able to fit laterally within the Sollube basin during Lower Black Flysch deposition (Prélat et al. 2009), suggesting that lateral stacking due to confinement in our study area is feasible only at the bed scale (Marini et al. 2015). The apparent retrogradation observed between CM5–7 could be a result of bed to lobe-scale lateral shifting and compensational stacking modulating an otherwise progradational lobe complex (e.g., Gervais et al. 2006; Pickering and Bayliss 2009; Etienne et al. 2012; Morris et al. 2014).

The lack of lateral stacking suggests that lateral topography maintains flow velocity in the absence of overspill and deceleration, and therefore the system remains turbulent for longer. This causes a basinward shift in deposition effectively acting to magnify the effects of progradation (e.g., Kneller and McCaffrey 1999; Talling et al. 2012; Patacci et al. 2014). This concept accounts for numerous, thick, high-density turbidites (UBF) along the axis of the Sollube basin formed by gravity flows that were guided between the two structures (Figures 3.14, 3.15C, 3.15F and 3.16; e.g., Scott et al. 2010; Oluboyo et al. 2014; Counts and Amos 2016; Howlett et al. 2021).

Using observations from Bakio, a range of stacking patterns may result from progradation of a deep-water system in an unconfined, partially confined, and dual-confined setting (Figure 3.16). Unconfined fans have a higher aspect ratio, surface area, and avulsion angle than confined systems as the ability of the flows to spread radially was not restricted by topography (Prélat et al. 2009; Sychala et al. 2017). Where only one lateral confinement is present, deposits may be asymmetrical, as flows are confined by diapir topography in one direction but are able to spread radially away from it, as is seen in the deposits of the Jata basin (Figure 3.10; Soutter et al. 2021). In settings with lateral confinement, deep-water systems are elongated axially, subparallel with bounding relief (Figures 3.14; 3.15 and 3.16; Oluboyo et al. 2014; Soutter et al. 2021). Funnelling of axial gravity flows, and therefore bed amalgamation, is interpreted to be enhanced where two salt structures are present, resulting in thicker deposits but areally smaller depositional architectures than unconfined settings (Kneller and McCaffrey 1999; Patacci et al. 2014; Soutter et al. 2021).

Diapir growth is not continuous through time, and phases of rapid growth (e.g., Figure 3.16, t2–t3, t5–t6) and quiescence (e.g., Figure 3.16, t1, t4) cause destabilisation and remobilisation of the diapir roof, overburden or flank deposits (Figures 3.9, 3.10 and 3.11). This can drive rerouting of subsequent systems to avoid failure topography, potentially resulting in lateral or compensational stacking (Figures 3.10, 3.13F, 3.15E and 3.16; Kane et al. 2012; Doughty-Jones et al. 2017; 2019; Rodriguez et al. 2018, 2020). In fully confined settings, there is no space for rerouting and lateral

MTDs could be amalgamated with, or eroded away by, flows depositing axial turbidites (Figures 3.8C, 3.11, 3.13, 3.14, 3.15 and 3.16).



**Figure 3.15:** Simplified comparison between lobes in unconfined and A–C) confined settings and D–F) progradation style in these settings. Parts A and B compare the nomenclature of sub-environments of Spychala et al. (2017) and Soutter et al. (2019) from the Karoo and Annot basins, respectively. Confined systems are smaller and more elongate and have more frequent hybrid beds. Part C shows how active topography would modify the model proposed by Soutter et al. (2019). One salt body has a carbonate roof and one a siliciclastic roof purely for completeness. Part D shows compensational stacking occurring during system progradation in an unconfined setting. Part E shows that downstream distance prograded per lobe is increased due to parallel topography, based on flume tank experiments that show a 20% increase in velocity adjacent to topography by Soutter et al. (2021; Appendix D) and Bakio West Bay. Part F shows how the downstream distance prograded per lobe is further increased as gravity-flow deposits are funnelled through dual-confinement. Both siliciclastic and carbonate failures are shown in parts E and F to indicate that the depositional system avoids the debris topography away from the salt structure, thereby illustrating the diapiric influence on axial deposition. LDT, low-density turbidite; HB, hybrid bed; MDT, medium-density turbidite; HDT, high-density turbidite.

**Active or Passive Topography:** The geometry and number of the debris, and thin-bedded sandstones that pinch-out, is controlled by the presence of actively growing topography during LBF deposition. The absence of debris in the UBF suggest that diapir growth ceased following uplift of the Landes Massif (Garc a-Mond jar et al. 1996; Puelles et al. 2014).

We infer that, following the cessation of diapir growth, an underfilled synclinal basin remained due to remnant topography of the buried Bakio and Guernica structures, which appears to have constrained UBF deposition until it was filled (Figures 3.3, 3.13G and 3.14). The LBF represents early-stage “active” deposition, perhaps comparable to syn-kinematic megasequences observed in the subsurface. The UBF represents late-stage “passive” deposition, infilling antecedent topography, comparable to post-kinematic megasequences observed in the subsurface (e.g., Pratson and Ryan 1994; Warren 1999; 2006; Jackson and Hudec 2017). UBF deposits are less confined due to the lesser influence of salt-influenced topography during deposition, and therefore through time may evolve to represent semi-confined or unconfined deep-water systems, more capable of lateral stacking (Marini et al. 2015).

### ***Comparison of Sollube and Jata Basins***

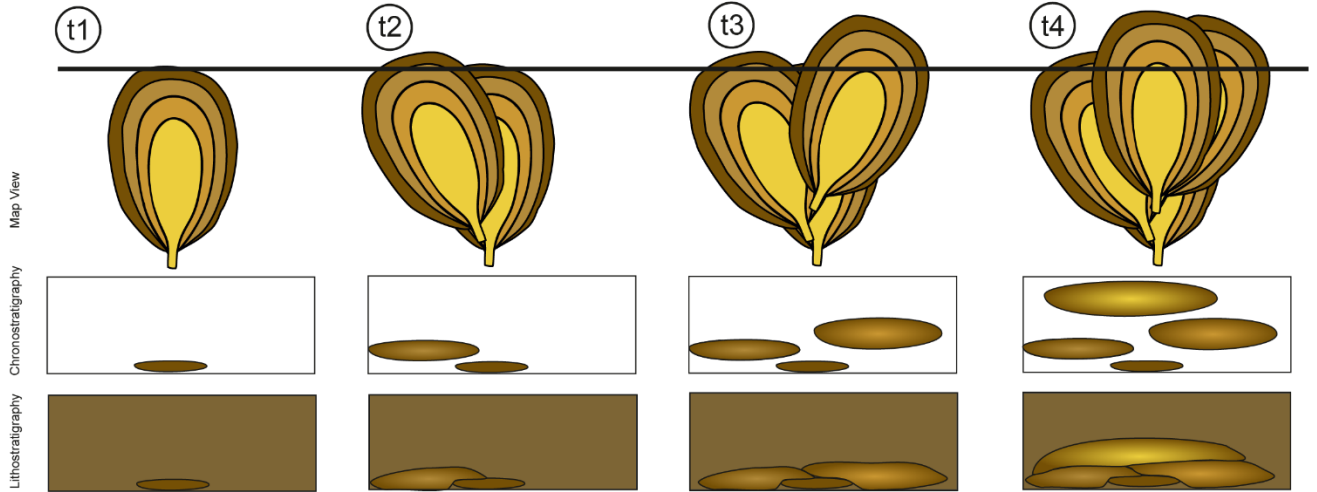
Facies distributions on either side of the Bakio diapir varied during BFG times according to the degree of confinement and distance from diapir crest (Figures 3.13 and 3.14). In the BBF, clast- and matrix-supported breccias are common in the Sollube and Jata basins, respectively (Poprawski et al. 2016), suggesting that minibasin individualisation is long-lived. The lack of confining topography to the west of the Jata basin may have caused flows to dilute, resulting in muddier, more-matrix-rich breccias (e.g., Hampton 1972; Sohn et al. 2002; Baas et al. 2009).

LBF stratigraphy in the Jata basin thins towards the Bakio diapir (Figure 3.12D), showing more evidence for topography than comparable strata in the Sollube basin, supporting the idea that halokinetic deformation is greatest closest to salt structures (Giles and Lawton 2002; Giles and Rowan 2012). Richness in limestone clasts in LBF MTDs in the Jata basin (Figure 3.10C; Table 3.3) could indicate asymmetric build-up and failure of the carbonate platform above the Bakio diapir, preferentially filling the Jata basin (Rosales and Pérez-García 2010; Li et al. 2016). Asymmetric growth and failure of either the carbonate platform or the diapir itself is further supported by thicker, more prevalent debrites observed in the Jata basin compared to the Sollube basin (discussed above: Figures 3.9, 3.10 and 3.11). The diverse range of clast types in the Jata basin (Table 3.3; Figure 3.10) could suggest different depositional routing relative to the Sollube basin, possibly due to the presence of salt topography causing different source areas to be tapped (e.g., Mayall et al. 2010; Oluboyo et al. 2014).

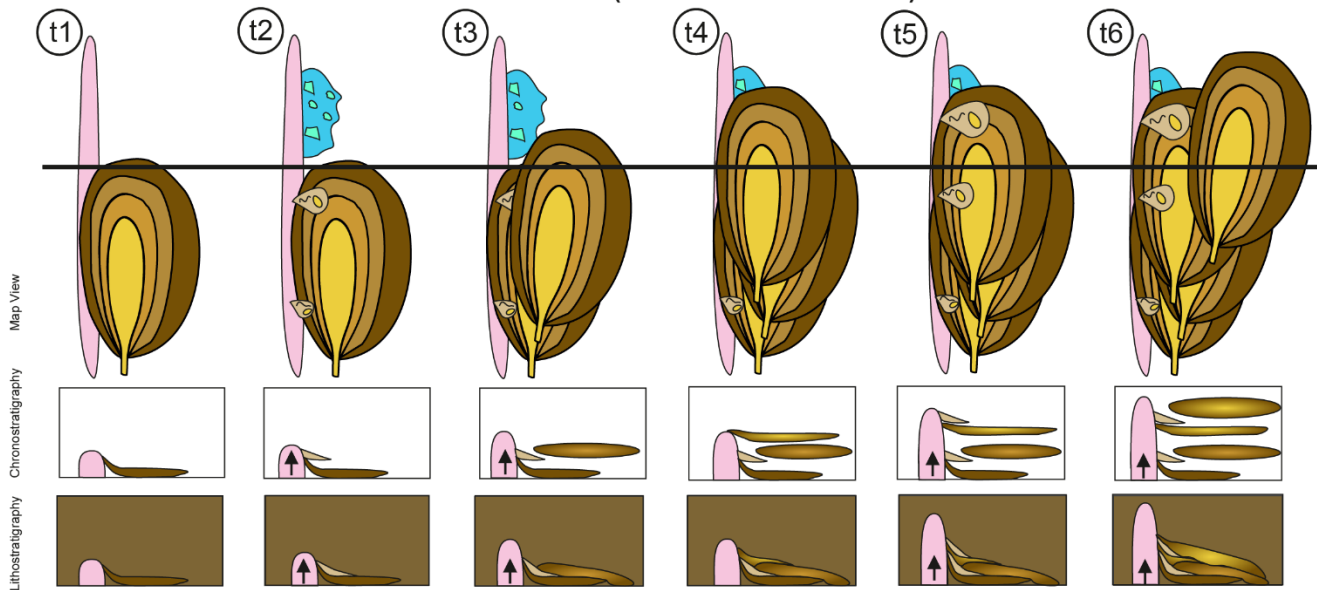
Another key difference is the architecture of thick-bedded sandstones. In the Jata basin, individual depositional elements are often erosionally based, concave-upwards, and thinner, and show more tractional structures (e.g., ripple lamination and planar lamination) than those in the Sollube basin. Where lateral confinement occurs along one margin, sandstones could represent sinuous low-relief channel fills that ran subparallel to topography (e.g., Mayall et al. 2010; Oluboyo et al. 2014). These channels were able to migrate because they were only partially confined (e.g., Mayall et al. 2010; Oluboyo et al. 2014). Such systems are less modulated by halokinetic controls than those that develop under dual-lateral confinement (e.g., Oluboyo et al. 2014; Rodriguez et al. 2020). Subsurface observations indicate that channels migrate away from growing structures (Mayall et al. 2010; Kane et al. 2012); however, those at Bakio West Bay appear to step towards the diapir in 2D (Figures 3.7F and 3.8B). This could suggest a temporary reduction in diapir growth, due to the episodic nature of halokinesis (Kane et al. 2012), which may be unresolvable in subsurface data. Alternatively, the debrites underlying the thick-bedded sandstones could form pathways that controlled sandstone deposition, and therefore the apparent movement towards the diapir was in fact controlled by the deep-water systems infilling debrite-related palaeotopography (Armitage et al. 2009). However, deciphering detailed interpretations of 3D sinuous channels from 2D exposure remains challenging (Li et al. 2016).

The Jata and Sollube basins had unique tectonostratigraphic histories throughout the deposition of the BBF and LBF due to the interplay of halokinetic, allocyclic, and autocyclic controls. Inaccessible UBF stratigraphy to the west of Bakio (Figure 3.12D) appears, from UAV photographs, to exhibit facies and geometries similar to UBF stratigraphy at northern Cabo Matxitxako (Figure 3.11; Vincente Bravo and Robles 1991a; 1991b; 1995) suggesting that influence of halokinesis decreased through time. This supports the idea that sediment accumulation rate ultimately outpaced diapir growth rate, possibly due to the increase in sediment supply associated with the uplift and erosion of the Landes Massif (Martín-Chivelet et al. 2002; Puelles et al. 2014). Partial or complete welding of salt bodies could also be, at least partially, responsible for the reduction of influence of halokinesis through time (Jackson and Hudec 2017).

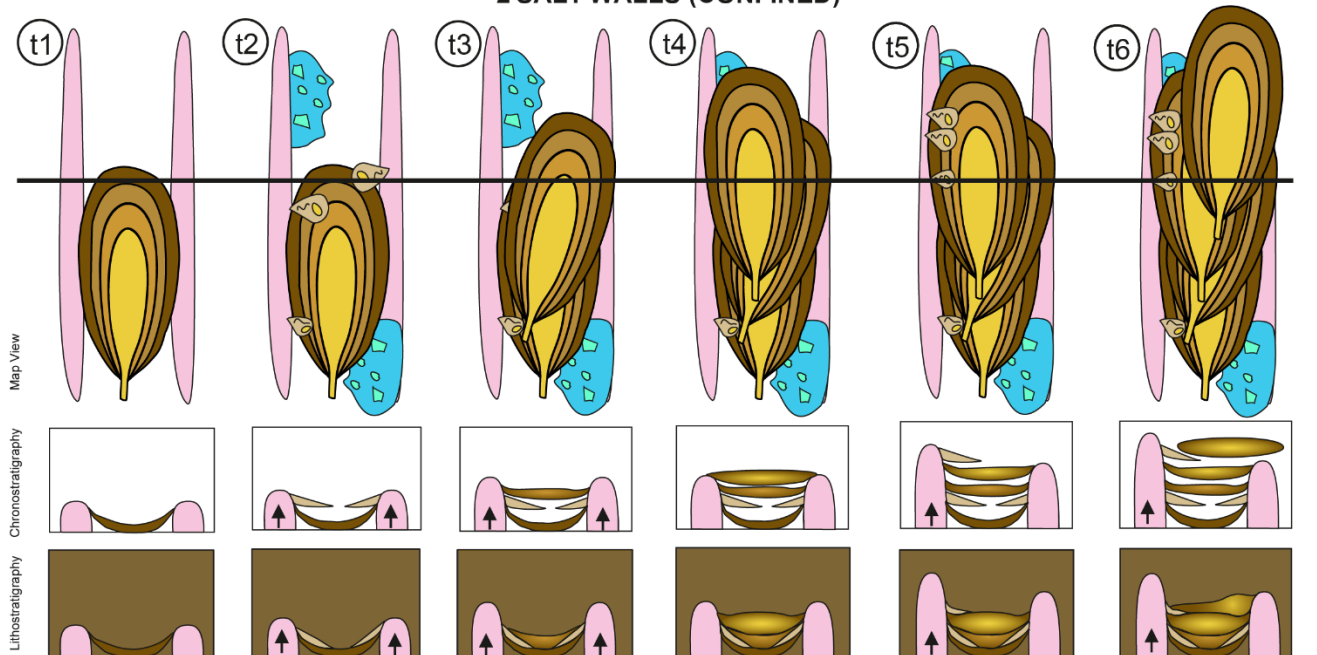
UNCONFINED



1 SALT WALL (PARTIALLY CONFINED)



2 SALT WALLS (CONFINED)



**Figure 3.16:** Thought experiment comparing the effects of variable topography in the evolution of deep-water systems. Unconfined settings are based on Prélat et al. (2009) and Spychala et al. (2017). One salt wall (partially confined) is based on the Jata basin and flume-tank experiments (Soutter et al. 2021). Two salt walls (confined) are based on Sollube basin. Black line shows line of section shown in chronostratigraphy and lithostratigraphy, and represents a fixed point for comparing extent of progradation across the models. The thought experiment highlights how compensational stacking is restricted when topography is present, particularly when two topographic barriers are present, and how topography acts to ‘funnel’ deep-water deposits, appearing to enhance the effects of progradation compared to their unconfined counterparts. Key is the same as Figure 3.15. Arrows on salt structures indicate periods of salt rise; lack of arrows suggests relative quiescence. No scale is implied.

### **Comparison to Other Depositional Settings**

Here, for ease of comparison with subsurface examples, we use mass transport deposit (MTD), instead of debrite, to describe deposits from varied subaqueous mass flows, including a mixture of slides, slumps, and debris flows in agreement with previous subsurface studies (e.g., Nardin et al. 1979; Posamentier and Kola 2003; Pickering and Hiscott 2015; Doughty-Jones et al. 2019; Wu et al. 2020).

**Recognition of Halokinetically Influenced Stratigraphy in the Field:** Before this study, most understanding of halokinetically-influenced deep-water systems came from subsurface datasets (e.g., Booth et al. 2003; Madof et al. 2009; Carruthers et al. 2013; Doughty-Jones et al. 2017; 2019). Features that are common across several depositional settings where halokinetic movements are observed include multi-scalar thinning and onlap, growth faulting, pebble conglomerates, mixed siliciclastic–carbonate lithologies, MTDs, variable paleocurrents, angular unconformities, and abrupt facies variability (Dalgarno and Johnson 1968; Dyson 1999; Kernen et al. 2012, 2018; Carruthers et al. 2013; Counts and Amos 2016; Counts et al. 2019).

Deposition of thick-bedded sandstones along the axis of the Sollube basin, and thinner beds and mudstones on the flanks of the Sollube and Jata basins, is comparable to fluvial facies distribution (Banham and Mountney 2013a; 2013b; 2014; Ribes et al. 2015) where channel-fill sandstones dominate axial settings and floodplain mudstones are observed closer to the diapir.

Individual beds in the BBF are comparable in size (tens- to hundreds-of- metres packages) and composition to stacked MTDs reported overlying bounding unconformities in halokinetic sequences in the La Popa Basin (10–120 m in thickness) associated with remobilisation of diapir roof or cap rock (Giles and Lawton 2002; Poprawski et al. 2014; 2016). Smaller carbonate breccias with wedge-shaped geometries (metre-scale packages; Figure 3.8E) are similar in geometry and composition to “lentils” (1 metre to 100s of metre thick) described by McBride et al. (1974), but differ in thickness and areal extent. Lentils, MTDs, and breccias represent talus-like failure from diapir roof stratigraphy (Giles and Lawton 2002; Poprawski et al. 2014, 2016).

Presence of evaporite clasts in fluvial successions (Banham and Mountney 2013b; Ribes et al. 2015), suggest that the nearby diapir was exposed during deposition. Such clasts are not observed in our study area, suggesting that the Bakio and Guernica structures may have only episodically been exposed at the seabed, if at all. This fits the interpretation of carbonate-platform growth above the structures, preventing salt exposure (García-Mondéjar 1990; Rosales and Pérez-García 2010; Poprawski et al. 2014; 2016). The consistency of our observations and previously described halokinetically influenced settings suggests that the criteria for recognising halokinetically influenced systems is similar regardless of depositional environment, suggesting that halokinetic controls are dominant over allocyclic ones. Multiple directions of ripple lamination, presence of hybrid beds, range of MTD types, and abrupt juxtaposition of deep-water depositional facies can be used to identify halokinetically influenced deep- water systems in core and outcrop.

**Comparison between Quickly and Slowly Deforming Basins:** The gravity flows responsible for the Eocene to Oligocene Annot Sandstone, SE France, were confined during deposition by Alpine fold-and-thrust belt topography (Apps 1987; Sinclair 1994). When compared with the rate of topographic deformation associated with diapir growth, the rate of orogenic deformation is minor.

Like the BFG, the stratigraphy of the Grès d'Annot is broadly progradational, and rapid facies changes occur over tens of metres towards pinch-outs (Soutter et al. 2019). Unlike Bakio, where paleoflow was consistently subparallel to structural trend, sub-basins in the Annot area were eventually filled and bypassed sediment into down-dip basins (Sinclair and Tomasso 2002; Salles et al. 2014), indicating that paleoflow was perpendicular to at least one of the complex structural trends (Oluboyo et al. 2014).

Debrites in the Grès d'Annot were slope-derived and infrequent compared with our study area, which were sourced laterally from failures of stratigraphy above salt structures that are intercalated with axially derived deep-water deposits (Figures 3.13, 3.14, 3.15 and 3.16). This is a reflection of a more active slope in diapiric settings.

The stratigraphy in this study is characterised by an axial deep-water depositional system and a series of lateral systems dominated by debrites fed from the growing salt structures. This interplay of two distinct depositional systems is common in deep-water environments influenced by active rift topography, such as the Gulf of Corinth, Greece (Leeder and Gawthorpe 1987; Pechlivanidou et al. 2018; Cullen et al. 2019) and the Gulf of Suez, Egypt (Sharp et al. 2002; Jackson et al. 2002, 2005; Leppard and Gawthorpe 2006). Here the continually evolving footwall scarps feed lateral MTD-rich systems coevally with axial, allocyclically controlled depositional systems. Deposits in syn-rift settings are often narrow and elongated parallel to the strike of normal-fault segments (Carr et al. 2003; Jackson et al. 2005; Cullen et al. 2019), indicating the control on stratigraphic architecture by footwall physiography. Analogous variability of depositional facies occurs due to salt-structure evolution in halokinetically influenced settings.

### **3.10 Conclusions**

This study documents deep-water facies distributions, with variable amounts of topographic confinement, adjacent to growing salt structures from a rare exposed example. We compare observations from two minibasins, one confined (Sollube) and one partially confined (Jata), which are comparable in size and facies heterogeneity to subsurface minibasins in salt provinces globally. Stratigraphic variability and juxtaposition of architectural elements in the Jata and Sollube basins is high and controlled by the interplay of halokinetic, autocyclic, and allocyclic processes. The low angle between the paleoflow and the strike direction of salt structures results in the depositional system being focused between two salt structures in the Sollube basin, and against one salt structure in the Jata basin, but with no evidence of downdip flow confinement. Confinement against topography increases the effects of allocyclic progradation. Failure of carbonate platforms developed above the crests of the active Bakio diapir and Guernica structure created lateral debrites in the flanking basins, and generated local topography to further constrain axial depositional systems. Debrites can also be sourced axially from up-dip failures on the shelf, and the compositional differences of debrites suggests that the Jata and Sollube basins were subject to different influences.

Indicators of active topography include hybrid beds, remobilised strata, lateral thickness changes over short distances, reversal in ripple cross-lamination in beds, and intercalation of debrites throughout the stratigraphy. These indicators individually are not diagnostic of salt-influenced topography, but collectively they provide a set of features that support interpretation of halokinetic modulation of a deep-water setting. Following the cessation of diapir growth, topography does

not heal instantly, and the “passive” palaeotopography continues to confine subsequent depositional systems despite diapir inactivity.

Closely related depositional systems can be highly variable depending on their complete or partial confinement. Stacked, amalgamated sandstones are observed between the confining barriers in the Sollube basin, whereas more variable architectures are observed in the Jata basin, where only partial confinement is present. These architectures are due to the modulation of a broadly progradational system by halokinetically-influenced lateral barriers and the coeval development of axial allocyclic and lateral debrite-rich depositional systems.

Using outcrop analogues combined with a good regional understanding of source area and salt movement and extracting insights from multi-scalar depositional analogues are advised when exploring in the salt–sediment interface for carbon storage or geothermal or hydrocarbon reservoir targets.



## Chapter 4: External signal preservation in halokinetic stratigraphy: A discrete element modelling approach

Zoë A. Cumberpatch<sup>1</sup>, Emma Finch<sup>1</sup>, Ian A. Kane<sup>1</sup>, Leonardo M. Pichel<sup>2</sup>, Christopher A-L. Jackson<sup>1</sup>, Ben A. Kilbams<sup>3</sup>, David M. Hodgson<sup>4</sup> and Mads Huuse<sup>1</sup>.

<sup>1</sup>Department of Earth and Environmental Sciences, University of Manchester, Oxford Road, Manchester M13 9PL, U.K.

<sup>2</sup>Department of Earth Science, Bergen University, Bergen, Norway

<sup>3</sup>Shell Upstream International, York Road, London SE1 7LZ, U.K.

<sup>4</sup>The Stratigraphy Group, School of Earth and Environment, University of Leeds, Leeds LS2 9JT, U.K.

**Status:** Part published in *Geology*, part accepted in *Basin Research*

Cumberpatch, Z.A., Finch, E., and Kane, I. A., 2021, *External signal preservation in halokinetic stratigraphy: A discrete element modelling approach: Geology*, v. 49 (6), p. 687-692. (Appendix A)

Cumberpatch, Z.A., Finch, E., Kane, I.A., Pichel, L.M., Jackson, C.A-L., Kilbams, B.A., Hodgson, D.M., and Huuse, M., 2021, *Halokinetic modulation of sedimentary thickness and architecture: a numerical modelling approach: Basin Research*, accepted, available online. (Appendix B)

### 4.1 Abstract

Subsurface salt movement in the absence of external tectonic forces can affect contemporaneous sediment deposition, mask allocyclic signals, and deform older strata. Studying salt-sediment interactions is challenging in the subsurface due to poor imaging adjacent to salt, and in the field due to the dissolution of halite. Discrete Element Modelling provides an efficient and inexpensive tool to model stratigraphy and deformation around salt structures, which is advantageous over other modelling techniques as it realistically recreates brittle processes such as faulting. We used a discrete element model (DEM) to better understand salt-related modification of sedimentary sequences, this permitted quantification of thinning rates and analysis of the lateral extent of syn-kinematic layers. Six 2D experiments were run representing 4.6 Myr (46,000 timesteps) to determine the effect of salt growth on syn-kinematic stratigraphy. Halokinetic deformation of stratigraphic architecture was assessed by varying sediment input rates (slow, intermediate, and fast), and increasing and decreasing sediment input through time. Results show the realistic formation and evolution of salt-related faults which define a zone of halokinetic influence that is ~3 times the width of the initial diapir. Outside of this, early diapiric and syn-kinematic stratigraphy are undeformed. Within this zone, syn-kinematic strata are initially isolated into primary salt withdrawal basins, onlapping and thinning towards the salt-cored high. In most models, syn-kinematic strata eventually thin across and cover the diapir roof. Thinning rates are up to six times greater within 350 metres of the diapir, compared to further afield, and typically decrease upwards (with time) and laterally (with distance) from the diapir. Outputs are compared to a subsurface example from the Pierce field, UK North Sea, which highlights the importance of considering local fluctuations in diapir rise rate. These can create stratigraphic architectures that may erroneously be interpreted to represent ‘apparent’ increases/decreases in sedimentation rate, rather than local changes in salt tectonics. Exposed examples, such as the Bakio diapir, northern Spain, are used to make inferences of the expected depositional facies, below model resolution. Our models aid prediction of sedimentary unit thickness and thinning rates, and can be used to test interpretations arising from incomplete or low-resolution subsurface and outcrop data when building geological models for subsurface energy.

### 4.2 Introduction

Deformation by salt-tectonics influences over 120 sedimentary basins globally (e.g., Hudec and Jackson 2007). These basins include some of the world’s largest subsurface energy-producing

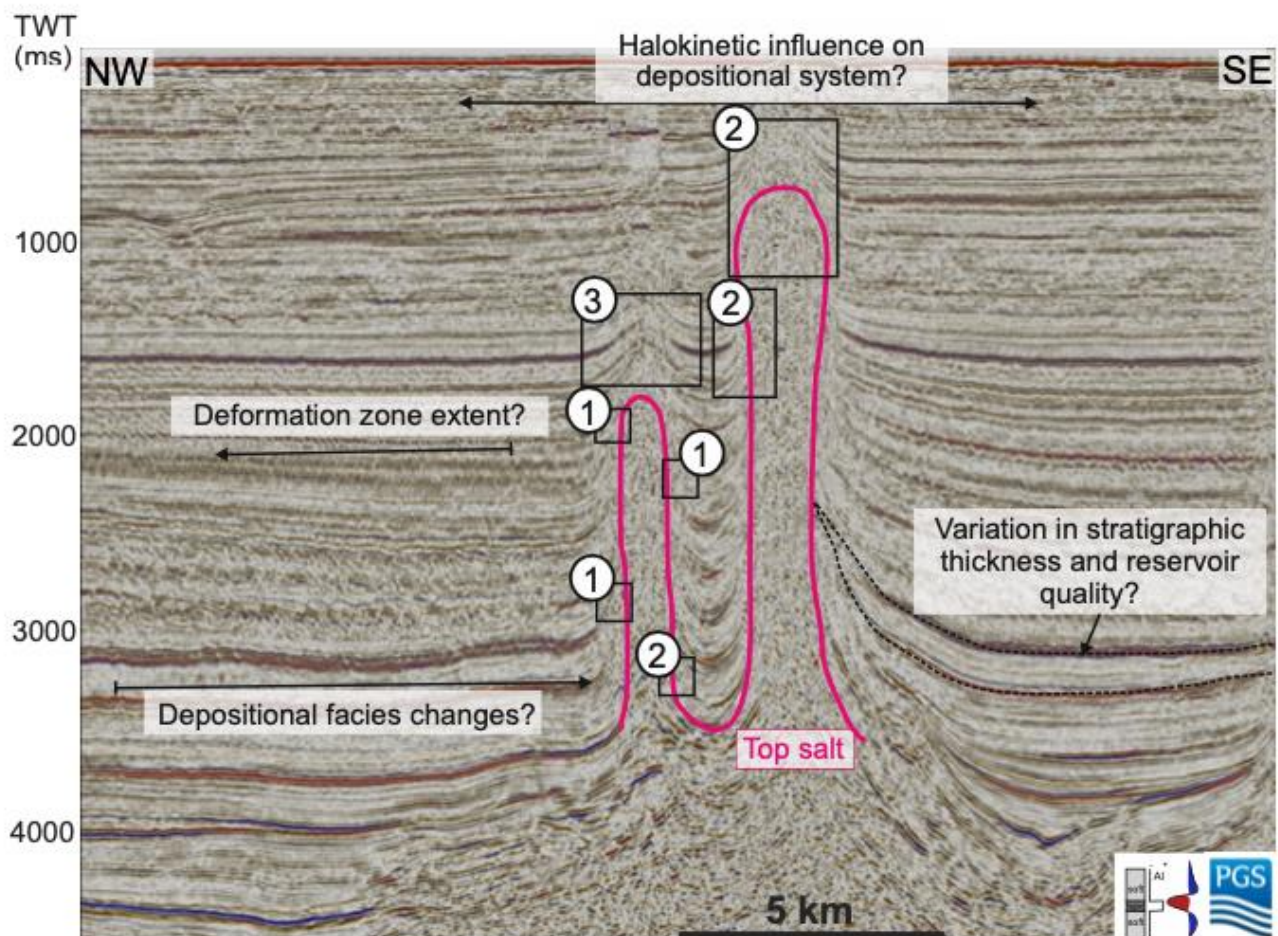
provinces, such as the Gulf of Mexico (e.g. Booth et al. 2003; Hudec et al. 2013), the North Sea (e.g., Mannie et al. 2014; 2016; Charles and Ryzhikov 2015; Stricker et al. 2018; Figure 4.1), offshore Angola (e.g. Oluboyo et al. 2014; Doughty-Jones et al. 2017; Howlett et al. 2020), offshore Brazil (e.g. Rodriguez et al. 2018; 2020; Pichel et al. 2019), and the Precaspian Basin (e.g. Duffy et al. 2017; Pichel and Jackson 2020). There is therefore a need to understand the interactions of sedimentary processes with topographic relief associated with salt tectonics to provide insight into the routing of sedimentary systems and their resultant stratigraphic architecture (e.g., Ribes et al. 2015; Cumberpatch et al. 2021b; Giles and Lawton 2002; Rowan et al. 2003; Pichel and Jackson, 2020). This can improve predictions of reservoir distribution and trap geometry and style for carbon storage (e.g., Maia da Costa et al. 2018; Roelofse et al. 2019; Lloyd et al. 2021), geothermal energy (e.g., Harms 2015; Daniilidis and Herber 2017; Andrews et al. 2020), and hydrocarbons (Figure 4.1; e.g., Hodgson et al. 1992; Jackson and Hudec 2017; Pichel and Jackson 2020).

Thickness variations and stratigraphic pinch-outs adjacent to salt are observed in the subsurface (e.g., Trusheim 1960), at outcrop (e.g., Giles and Rowan, 2012), and with physical models (e.g., Dooley et al. 2007). Salt movement is often proposed to cause stratigraphic modification of allocyclic signatures (Mayall et al., 2010; Giles and Rowan, 2012). However, because natural analogues represent a “snapshot” in time of a complicated evolution controlled by the dynamic interplay of parameters (sedimentation rate, salt supply, etc.), it is often impossible to discern exact controls and therefore constraining the dynamic evolution of the sediment-salt interface through time and space remains challenging. Despite advances in the quantity and quality of 3D seismic reflection data, the salt-sediment interface remains difficult to image due to poor velocity control, steep to overturned bedding and near-diapir deformation (Figure 4.1; Jones and Davison 2014). Resolution issues caused by variable lithological distributions, both within the salt and its overburden, further complicate seismic reflection-based, subsurface analysis (Davison et al. 2000; Jones and Davison 2014). This leads to uncertainty in prediction of facies and thicknesses via seismic methods (Figure 4.1; e.g., Berton and Vesely 2016; Hossain 2019).

Therefore, detailed depositional facies models of halokinetically-influenced depositional systems (or portions of such systems) benefit from calibration with outcrop analogues (e.g., Lerche and Petersen 1995; Madof et al. 2009; Banham and Mountney 2013a; b; 2014; Jackson and Hudec 2017; Rodriguez et al. 2020; Cumberpatch et al. 2021b) to provide a useful framework that can be applied to salt-influenced basins globally. Outcrop examples, however, possess their own set of uncertainties; exposed examples are often limited in the rock record, largely due to dissolution of halite forming the core of the salt bodies (Jackson and Hudec 2017). Rare exposures provide sub-seismic scale facies information for shallow- (e.g., Giles and Lawton, 2002; Giles and Rowan 2012), deep- (e.g., Poprawski et al. 2014; 2016; Cumberpatch et al. 2021a) and non-marine stratigraphy (e.g., Banham and Mountney 2013a; b; 2014; Ribes et al. 2015; 2017). Many field examples are small in size compared to subsurface basins and therefore provide only small-scale details of, for example, sedimentary structures and stratal stacking patterns, rather than the larger, basin-scale tectonostratigraphic context of salt-sediment interactions provided by integrated subsurface datasets. While useful, each subsurface or field example represents a unique record of the ratio of relative salt rise and sedimentation rate. Also, subsurface and field examples provide only a snapshot in time (Figure 4.1). Physical models have an advantage in recreating the evolution of specific subsurface analogues (Dooley et al. 2013; 2015; 2020; Dooley and Hudec, 2017; Ferrer et al. 2017; Roma et al. 2018) and studying sediment gravity flow distribution and evolution adjacent to salt topography (Gauillier and Vendeville, 2005; Sellier and Vendeville, 2010; Soutter et al. 2021).

A number of remaining questions can be addressed by taking a numerical modelling approach that allows modification and isolation of the key controls on salt-sediment interactions. These include: 1) How does salt topography influence depositional systems, and thus depositional facies, and how

does this vary laterally and temporally? 2) How do unconformities, onlap contacts, and faults and fractures vary in salt-influenced settings? 3) How does sedimentation rate influence the width of the roof and basin salt-related deformation zones? and 4) How do stratigraphic thinning rates associated with salt growth vary with sedimentation rate and distance from the salt structure?



**Figure 4.1:** Seismic reflection cross-section from the Pierce diapirs, Eastern Central Graben, UK North Sea (located in Figure 4.12) highlighting some of the key questions and uncertainties of subsurface interpretation in salt-influenced basins. Mapping top salt, visualizing pinch-outs and onlap geometries in areas of lower-quality data adjacent to the salt (1), confidently mapping top salt (2) and studying the lateral and vertical extent of syn-kinematic deformation and sedimentation (3), are challenging. Seismic data courtesy of PGS (MegaSurvey Plus 3D seismic data).

### 4.3 Numerical modelling of salt tectonics

Numerical models have been used in various forms to study different aspects of geologic systems. Large-strain numerical models have long been used to understand the mechanics associated with the evolution of regional and crustal systems (Willett et al. 1993; Johnson et al. 2013). The significant contribution of numerical methods to salt tectonics is the ability to use representative material constitutive laws to accurately simulate the behaviour of both salt and wall rocks. In addition, scaling of numerical models to natural analogues is relatively straightforward compared to physical experiments. Numerical methods also offer the flexibility to examine the role of a variety of geological parameters, including depositional history, tectonic loading, and initial basin geometry (Nikolinakou et al. 2019). There are two main types of numerical modelling applied to salt tectonics, namely Discrete Element Modelling (DEM) and Finite Element Modelling (FEM). They each have different benefits and limitations when used to study salt tectonics. Put most simply DEM deal with discontinuous problems and FEM deals with continuum problems (Zhu et al. 2008; Ucgul et al. 2018).

### ***Recent advances in modelling salt tectonics***

Most recent advances in modelling salt tectonics have used Finite Element Modelling (FEM; Figure 4.2). Such studies have focused on the physical conditions required for the initiation and development of diapirism (Figure 4.2; Poliakov et al. 1993; Gemmer et al. 2004; 2005; Chemia et al. 2008; Fuchs et al. 2011; Fernandez and Kaus 2015; Nikolinakou et al. 2017; Hamilton-Wright et al. 2019; Peel et al. 2020), the stratigraphic architecture of subsiding minibasins (Sylvester et al. 2015; Wang et al. 2017; Fernandez et al. 2020), reconstructing evolutionary history of salt-affected stratigraphy (Ismail-Zadeh et al. 2001; 2004; Pichel et al. 2017; 2019), and salt-related stress (and strain) analysis (Figure 4.2; Luo et al. 2012; 2017; Nikolinakou et al. 2012; 2014a; b; 2018; Heidari et al. 2017).

### ***Finite Element Modelling***

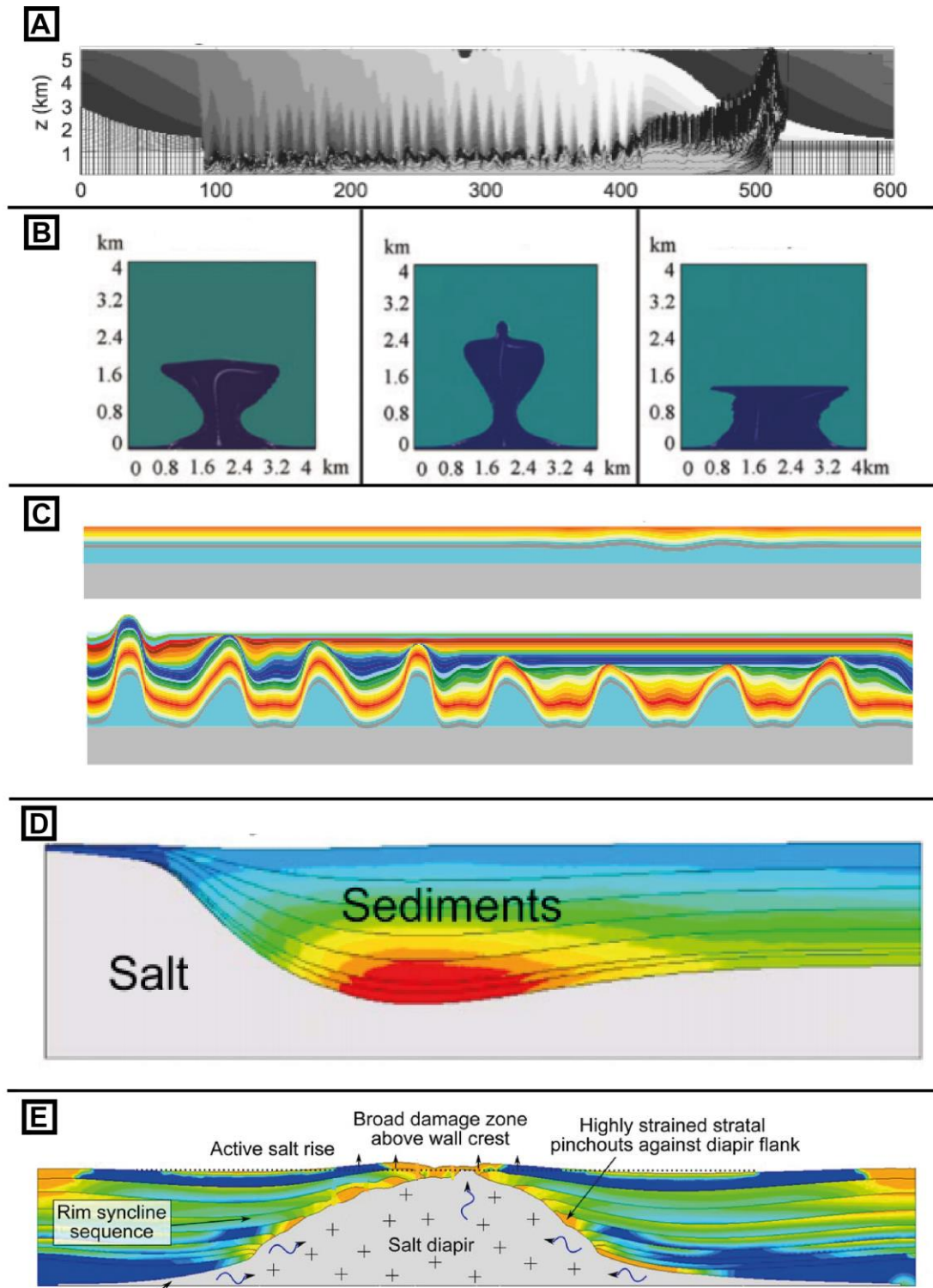
In its most basic form, FEM is an approximation method that subdivides a complex problem space, or domain, into numerous small, simpler pieces (the finite elements) whose behaviour can be described with comparatively simple equations (Figure 4.2). FEM was originally developed in engineering to model and analyse complex systems in mechanical, civil, and aeronautical engineering (Baguley and Hose 1994; 1997). It has, as its foundation, the basic concepts of mechanics, such as Newton's laws of motion, conservation of mass and energy, equilibrium, and the laws of thermodynamics (Baguley and Hose 1994; 1997; Bathe 2006). FEM can be used, for example, to determine the structural mechanics of parts of a bridge under different loading conditions, the heat flow through an engine, or the distribution of electromagnetic radiation from an antenna (Zhu et al. 2008). An important aspect of FEM is how the domain is subdivided. Computer-aided design (CAD) software is useful in this regard, because it defines the three-dimensional shape of an object and can easily subdivide the object into appropriately sized elements according to the desired mesh, or three-dimensional grid that defines the elements (Bathe 2006; Zhu et al. 2008). Depending on the problem to be solved, the mesh can define elements of uniform size and shape (such as cubes or pyramids), or have elements of different shapes and sizes in different parts of the domain (Bathe 2006). The strength of FEM lies in its ability to deal with partial differential equations (Bathe 2006; Zhu et al. 2008).

### ***Finite Element Modelling of Salt Tectonics***

Different authors use different FEM approaches in salt tectonics. Lagrangian approaches deal with individual particles and calculate the trajectory of each particle separately, whereas the Eulerian approach deals with concentration of particles and calculates the overall diffusion and convection of a number of cells (Saidi et al. 2014). Gemmer et al. (2004) uses the plane-strain viscous-plastic finite element model (Lagrangian-Eulerian formulation; Fullsack 1995; Willet 1999) to study salt tectonics driven by differential sediment loading. The model solves the equilibrium force balance equations for incompressible flows in two-dimensions and is velocity-based, designed for large deformation fluid Stokes, or creeping, flows (Figure 4.2). Fuchs et al. (2011) use the Eulerian 2D Finite Difference code (FDCON) to study diapir formation by down-building and examine the role of sedimentation rate, viscosity contrast, initial amplitude and wavelength (Figure 4.2). This is based on stream function formulations, and is used in combination with a marker approach based on a predictor-corrector Runge-Kutta fourth order scheme (Weinberg and Schmeling 1992). Recent geomechanical modelling of salt systems (Nikolinakou et al. 2012; 2014a; b; 2018; Heidari et al. 2017) have used a transient evolutionary model (ELFEN), which depends on a finite-strain quasistatic, finite-element formulation, and complemented by automated adaptive-remeshing techniques (Peric and Crook 2004). This model uses both Lagrangian and Eulerian reference frames, for the mechanical and fluid phases respectively. Fernandez et al. 2019 use a 2D finite element code (MVEP) to study the kinematic interactions between minibasins during density-driven sub-

sidence (Thielmann and Kaus 2012; Johnson et al. 2013). MVEP2 solves the equations of conservation of mass and momentum for incompressible materials with visco-elasto-plastic rheologies. The code uses a Lagrangian approach, where material properties are tracked by randomly distributed markers that are advected according to the velocity field that is calculated in a deformable numerical grid (Kaus 2010). Remeshing of the grid is performed every time step (Kaus 2010). For preliminary studies authors often use more simplified models and simulation techniques. For example, Peel (2014) used a simple Microsoft Excel based arithmetic simulation to investigate the initiation and growth of salt withdrawal minibasins and the effect of changing initial conditions and Peel et al. (2020) used a simple, fast, analytical model to study salt diapir down building (Figure 4.2).

FEM often treats the overburden as a continuous frictional-plastic or viscous-plastic material, which prevents the development of realistic brittle deformation (e.g., fracturing and faulting) in overburden stratigraphy (Figure 4.1). Most FEM packages currently have limited capacity to generate faults during simulations, and therefore either have no faults or faults that are pre-defined at the start of the model simulation (e.g., Heirdari et al. 2016; Nikolinakou et al. 2014; 2018). FEM is advantageous for studying ductile deformation and salt flow dynamics (Albertz and Ings 2012).



**Figure 4.2:** Recent examples of Finite Element Model (FEM) used in salt tectonics. Progradational system deposited over salt layer after 25 Myr. Salt is grey and sedimentary overburden is light grey (Gemmer et al. 2004). B) Three end member diapir 'down-building' models, from left to right 'normal', 'higher' and 'lower' salt viscosity. Blue is salt and turquoise is sediment. Sedimentation rate is 0.25 mm/year throughout all experiments (Fuchs et al. 2011). C) DRAWL numerical model of the formation of salt withdrawal minibasins. Top image shows the initial conditions, completely flat stratigraphy apart from an initial seed point. Bottom image shows the generation of six daughter minibasins, due to a cascading of the seed point (Peel 2014). D) Overpressure development in sediments over time during sedimentation and rise of the salt wall in transient analysis after 7 Myr (Luo et al. 2017). E) Model developed from an initial long-wavelength salt pillow, after 8 Myr. Fracture development is suggested above the crest of the salt wall, and within strained stratal tips above the diapir flanks (Hamilton-Wright et al. 2019).

### ***Discrete Element Modelling***

Discrete Element Modelling (DEM) is a first principal physics method that treats each particle of a granular bed individually. Each particle is represented through a representative shape and size that interacts with other particles. These interactions are at the heart of the DEM implementation, and they are captured through different user-specified material properties (shape and size distribution, density, Young's Modulus, Poisson's ratio, adhesion, thermal conductivity, specific energy for breakage, etc.). DEM is a particle-scale numerical method for modelling the bulk behaviour of granular materials and many geomaterials such as coal, ores, soil, rocks, aggregates, pellets, tablets and powders. This method has been applied to simulate and analyse flow behaviour in a wide range of disciplines including pharmaceutical and process engineering, mechanical engineering, materials science, agricultural engineering and geoscience (Cundall and Strack 1979; Donzé et al. 1994; Finch 1998; Finch et al. 2003; 2004; Imber et al. 2004; Hardy and Finch 2005; 2006; Zhu et al. 2008).

### ***Suitability of DEM to Salt Tectonics***

The DEM applied here is a discontinuous numerical method, which derives from the Particle Dynamics Method and Lattice Solid Model (Mora and Place 1993; 1994). DEMs have been successfully used in physics and chemistry to study liquid and gas behaviours (Allen and Tildesley 1987; Hardy and Finch 2006). In geoscience, DEMs have been applied in two- and three-dimensions (Longshaw et al. 2009; Finch and Gawthorpe 2017; Deng et al. 2018) to forecast geological hazards, often associated with mining (Cil and Alshibli, 2012; Thoeni et al. 2014; Lu et al. 2014; Zhao et al. 2016; Benseghier et al. 2020), to investigate deformation caused by faulting and folding (Donzé et al. 1994; Finch 1998; Finch et al. 2003; 2004; Imber et al. 2004; Hardy and Finch 2005; 2006; Schöpfer et al. 2006; Bellheine et al. 2009; Longshaw et al. 2012; Abe and Urai 2012; Katz et al. 2014), and to study regional-scale salt tectonics (Pichel et al. 2017; 2019).

DEMs offer advantages over FEM in that scale is not a restriction, complex re-meshing is not required, and results are easily reproducible. DEMs are fundamentally discontinuous, and therefore each element simulates the specific physical properties of a given rock. These conditions make it a fit-for-purpose method to quantitatively study syn-kinematic deformation.

The contact between each element is treated as a slip surface in DEM and therefore DEM are able to replicate spontaneous, realistic, localised fault nucleation and growth (Pichel et al. 2017; 2019; Cumberpatch et al. 2021c;d) and are therefore appropriate for studying the interactions between salt-related topography, sedimentation, and stratigraphic evolution. DEMs do have limitations, including the need for careful calibration of element parameters (Abe et al. 2011; Botter et al. 2014), and the limited number of elements and the duration of simulations (Zhu et al. 2008). Despite this, DEM provides a quick, efficient and inexpensive method to investigate system evolution through time (Allen and Tildesley 1987; Donzé et al. 1994; Finch et al. 2003; 2004). It is therefore possible to test a number of scenarios and collect structural growth and syn-kinematic sediment thinning rate data during deformation. This helps to improve recognition of the processes involved with salt-sediment interactions. DEM studies have recently been adapted to salt tectonics so that elements representing salt behave as viscous-plastic materials (Pichel et al. 2017; 2019; Cumberpatch et al. 2021c;d). This has allowed for studying regional-scale compressional salt tectonics (Pichel et al. 2017), the effect of base salt relief on salt flow and overburden deformation styles (Pichel et al. 2019) and the evolution of stratigraphy adjacent to salt structures (Cumberpatch et al. 2021c;d).

### ***Aims of this DEM study***

Here, we use, for the first time, a DEM approach to isolate sedimentation rate from salt rise rate in order to understand how sedimentation rate effects stratal geometries in salt basins experiencing diapirism (Figure 4.1). Our ultimate intention was to test the hypothesis that halokinesis can modulate stratigraphy and mask allocyclic signals. First, we generate a baseline model with no sediment fill, to determine the effect of salt growth on the early diapiric ‘overburden’ sequence. In line with recent work (Cumberpatch et al. 2021c), we define ‘early diapiric sequence’ as layers deposited prior to our simulation, they are discordant to the diapir and thus represent the early diapiric syn-kinematic strata related to the phase of diapirism that is assumed to have emplaced the diapir into our model (Jackson and Hudec 2017). We then vary sedimentation rate and patterns to study how these control the stratigraphic record of halokinesis. The aims of this study are to: 1) investigate variable syn-kinematic sedimentation rates adjacent to a dynamic salt diapir using a DEM; 2) quantify near-diapir thinning rates and how this is controlled by varying sedimentation rates and patterns; 3) analyse lateral and temporal variation in stratigraphic architecture and 4) compare the results to subsurface and field analogues to test the validity of our approach and our model predictions.

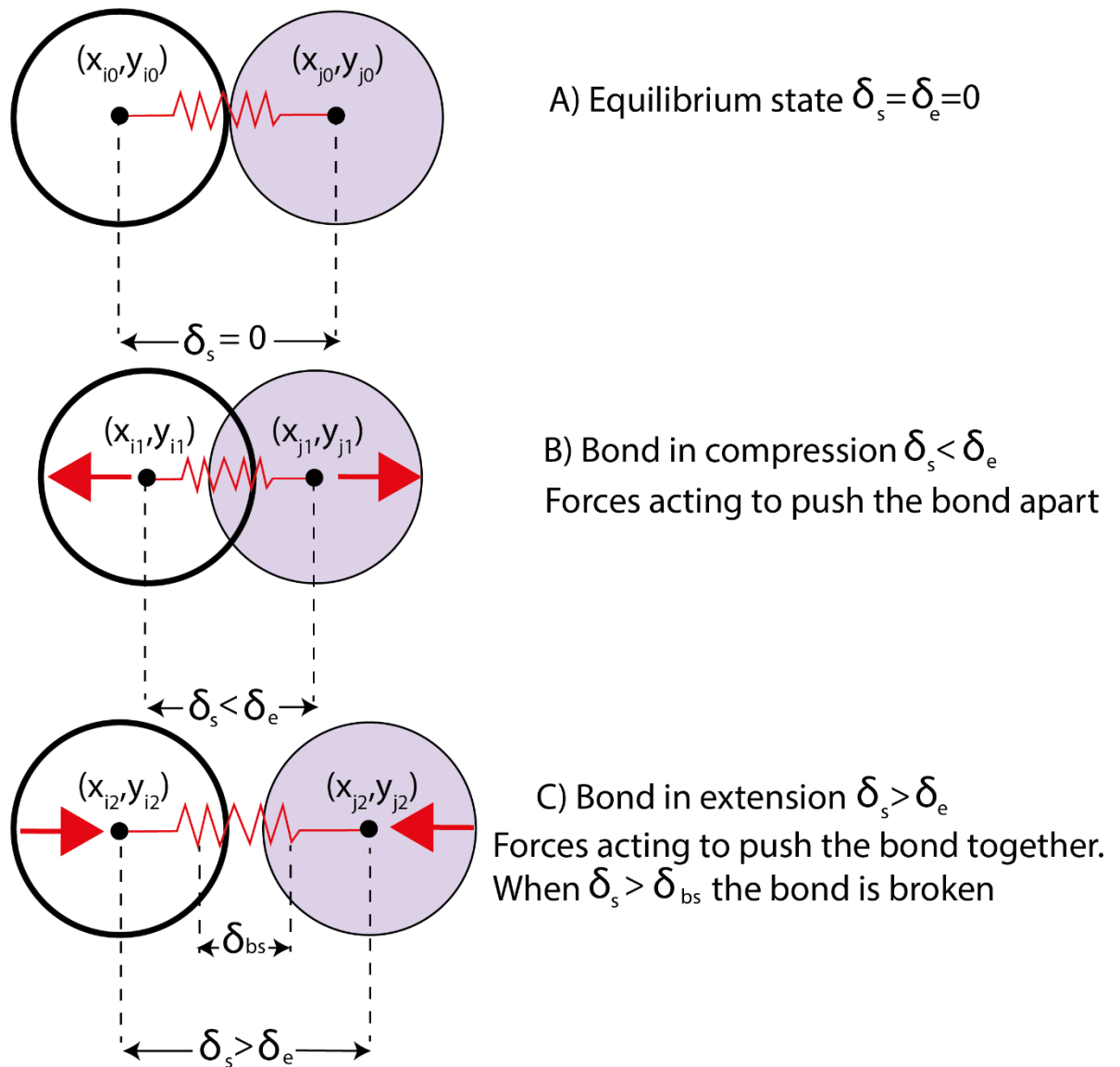
### **4.4 Data and Methods**

DEM treats objects as assemblages of circular elements, connected by breakable elastic bonds through a ‘repulsive-attractive’ force. Elements remain bonded until their breaking separation (defined as the relative strength of the assemblage) is exceeded (Figure 4.3; Donzé et al. 1994; Finch et al. 2004). Once these bonds break, previously connected elements experience no further ‘attractive’ force, if these elements return to contact with each other a ‘repulsive’ force acts between them, preventing the healing of bonds (Figure 4.3; Finch et al. 2003; 2004; Hardy and Finch 2006). Motion of elements is frictionless and cohesionless with elasto-plastic behaviour (Finch et al. 2003; Hardy and Finch 2007). Forces are resolved in the x and y directions and elements are subject to gravity ( $F_g$ ) (Finch et al. 2003). The equations that define the inter-relationship of all forces acting on the DEM are:

$$F_x = F_{i,n} - V\dot{X}$$
$$F_y = F_{i,n} - V\dot{Y} + F_g$$

Where  $F_{i,n}$  corresponds to the total elastic force acting on an element,  $V$  represents the viscosity and  $\dot{X}$  and  $\dot{Y}$  correspond to the velocity of the element in the x- and y- directions. A viscous term is added to counteract the elastic behaviour within a closed system, making it ideal for studying quasi-steady state tectonic processes (Finch et al. 2004; Pichel et al. 2017; 2019). For a comprehensive description of the equations governing DEM, see Mora and Place (1994), Finch et al. (2003; 2004), and Hardy and Finch (2005, 2006).





$\delta_{bs}$  Bond breaking separation  $\delta_e$  Equilibrium separation  $\delta_s$  Current element pair separation

**Figure 4.3:** Example of the relationships that can exist between a particle  $i$  (white) and a neighbouring particle  $j$  (purple).  $x$  and  $y$  are the midpoints of the respective particles. The particles are connected through their midpoints by breakable elastic springs at a separation ( $\delta_s$ ) determined by their relative positions. Red arrows denote the direction of the force exerted on the bond connecting the particle pair. After Mora and Place (1994) and Finch (1998).

Pichel et al. (2017; 2019) recently used a DEM to examine salt-tectonics for the first time, studying regional-scale compressional salt tectonics (Pichel et al. 2017), and the effect of base salt relief on salt flow and overburden deformation styles (Pichel et al. 2019). Cumberpatch et al. (2021c;d) adapted these models to focus on the modulation of stratigraphy by salt diapir growth. Here, the elements representing salt were adjusted so they behaved as a viscous-plastic material in order to represent rock-salt (Pichel et al. 2017; 2019). This requires inter-element interactions to be adjusted so they behave macroscopically as viscous-plastic materials and deform microscopically by dislocation creep, which is expected for dry rock salt (Spiers et al. 1990; Pichel et al. 2017; 2019). This does not completely naturally scale to reproduce salt, which typically deforms on a spectrum of mechanisms including diffusion and dislocation creep (Spiers et al. 1990; Jackson and Hudec 2017; Pichel et al. 2017), and usually contains traces of brines (Warren 1999; 2006), but is considered a satisfactory assumption for studying salt tectonics (following the methodology of Pichel et al.

2017). Pichel et al. (2017) tested breaking separations using biaxial compression tests. Values representing tenths of a model unit (e.g., 0.05) develop defined fault segments, and produced responses typical of brittle materials; these values are therefore used to represent overburden sediment in this study. Values representing hundredths of a unit (e.g. 0.001), however, show a minor elastic component (e.g.  $F_{i,\alpha} \approx 0$ ), representing ductile viscous-plastic materials that accumulate strain without significant stress variations. Consequently, a breaking separation of 0.001 for salt elements is used in this study (see also Pichel et al., 2017), and other physical (Spiers et al. 1990) and numerical (Li and Urai 2016) experiments of salt deformation. By using this value, we ensure salt element motion is entirely controlled by the viscosity and gravity of the system (viscous-plastic behaviour). The scaled viscosity of the salt is  $1.1 \times 10^9$  Pa s, which is lower than its real-world counterpart ( $10^{17}$ - $10^{18}$  Pa s; Hudec and Jackson 2007; Jackson and Hudec 2017), but works as a reasonable approximation when compared with physical models (e.g., Vendeville et al. 1995; Dooley et al. 2009; 2012).

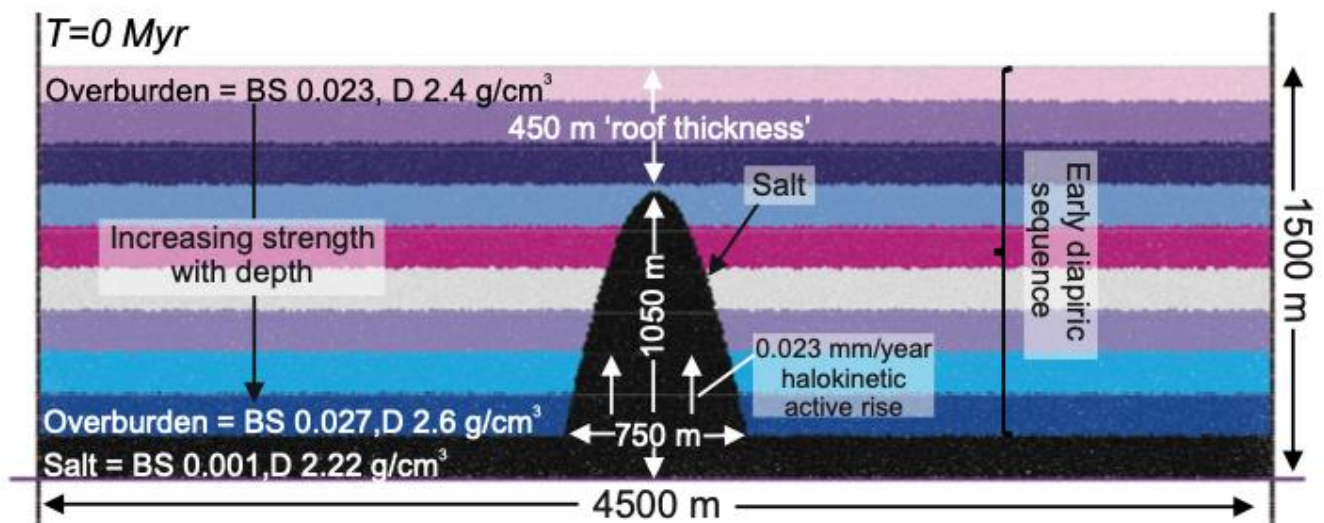
The modelled media in this study consists of a simulated 4.5 km by 1.5 km box, to ensure that the outer boundaries do not influence the structural evolution of the model centre. The media consist of an undeformable base and  $\sim 44,500$  elements with varying radii (0.175-0.35 units, representing 5.25-9.75 metres); these are randomly distributed to reduce failure in preferential orientations within the matrix. A 150 m-thick salt layer is overlain by nine coloured 150 m thick early diapiric overburden layers. A salt density of  $2.2 \text{ g cm}^{-3}$  is used, to mimic a slightly impure halite composition, comparable to many global salt basins (e.g., Warren 1996; 2006; Hudec and Jackson 2007; Jackson and Hudec 2017; Grant et al. 2019) and previous models (Pichel et al. 2017; 2019; Cumberpatch et al. 2021c).

We do not investigate the initial stages of diapir evolution, which have been well-studied elsewhere (Trusheim 1960; Vendeville and Jackson 1992; Costa and Vendeville 2002; Hudec and Jackson 2007), and instead focus on late stage diapir growth. Therefore, we simplify a complicated three-dimensional process into a two-dimensional model, where we assume a linear salt wall or radially symmetric diapir was emplaced by an earlier phase of diapirism; such as assumptions used in other numerical (Pichel et al. 2017; 2019) and physical models (Davison et al. 1993; Dooley et al. 2009; 2012). This allows us to focus on the coupled deformation-sedimentation characterising the late stage of diapir growth, when a tall pre-existing diapir may be rejuvenated by compression (not modelled here) or rise due to buoyancy (active diapirism). During the experiment the diapir is assumed to grow by passive diapirism (initially by halokinetic active rise; Rowan and Giles 2021), driven by the pressure of the overburden on the salt source layer and to a lesser extent by the density difference between the salt and the overlying stratigraphy (Jackson and Hudec 2017). Such growth can happen in the absence of regional tectonics, although mild far-field compression or extension, which can enhance deformation rates, are likely in most natural settings (Jackson and Hudec 2017). Active rise is retarded by roof thickness and strength, and salt viscosity. Therefore, diapir height must be  $>66$ - $75\%$  of the surrounding overburden thickness for substantial halokinesis to occur and the roof thickness must be  $<750$  m (Schultz-Ela et al. 1993). In adhering to this rule, we invoke an individual sinusoid, 750 m (base width) wide, 1050 m (70% of the 1500 m overburden) tall diapir and thus a 450 m roof (Figure 4.4; Supplementary Figure 1, Appendix A). The diapir geometries used in our models are comparable to those observed in natural examples (Davison et al. 2000; Jackson and Hudec 2017). Overburden breaking separation (relative strength) increases with depth linearly from 0.023 – 0.027, in agreement with increasing rock strength with depth. An overburden density of  $2.4$ - $2.6 \text{ g cm}^{-3}$  is used in agreement with natural and modelled examples, and increases with depth in accordance with nature (e.g., Dooley et al. 2009; 2012; Fuchs et al. 2011).

In nature, diapir growth periods are hugely variable in duration, ranging from 100,000s of years to 100s of millions of years (Jackson and Hudec, 2017). Our focus on late-stage of diapir growth and using seismic stratigraphic observations from natural examples (Oluboyo et al. 2014; Grimstad 2016), and run times of previous numerical models (Pichel et al. 2017; 2019), supports our experimental run times of 46,000 timesteps with a timestep equivalent to 100 years (4.6 Myr in total). We impose an upwards motion of 0.023 mm/year, based on North Sea diapirs (Davison et al. 2000) to all elements representative of salt to mimic diapir growth rate (Figure 4.4); this replicates the volumetric salt supply rate (Q) described by Peel et al. (2020). The diapir grows for 2.2 Myr (22,000 timesteps) to allow it to equilibrate creating seabed or surface topography, prior to the addition of sediment (Figure 4.5).

Sediment is added from 2.2 Myr with a constant density of  $2.3 \text{ g cm}^{-3}$ , in agreement with natural examples of near seabed sediment (Tenzer and Gladkikh 2014; Rider and Kennedy 2018) and a breaking separation of 0.023. Sediment is added in three 0.8 Myr (8,000 time steps) stages (S1-S3, Table 4.1). Sedimentation rates in nature are extremely variable (Sadler 1981). Here, the sedimentation rate was varied between 0.15-0.45 mm/year to match Cenozoic rates measured in the North Sea (de Haas et al. 1996) and the North Atlantic (Whitman and Davies 1979).

We present results from six experiments: a baseline zero sedimentation model, and five models with variable sedimentation rates and patterns (slow, intermediate and fast constant sedimentation, increasing and decreasing). Increasing and decreasing sedimentation rates are used to replicate the local advance and retreat of depositional sedimentary systems (progradation and retrogradation). Model set-up and parameters have been rigorously tested (Finch et al. 2003; 2004; Pichel et al. 2017; 2019) and are summarised in Supplementary Table 1 (Appendices A and B).



**Figure 4.4:** Initial set up of the DEM ( $T=0$ ) and key parameters. Initial geometry and rise rates taken from North Pierce diapir (Davison et al. 2000). See text for discussion and Table 4.1 and Supplementary Table 1 (Appendices A and B) for further details. BS; Breaking separation (relative strength).

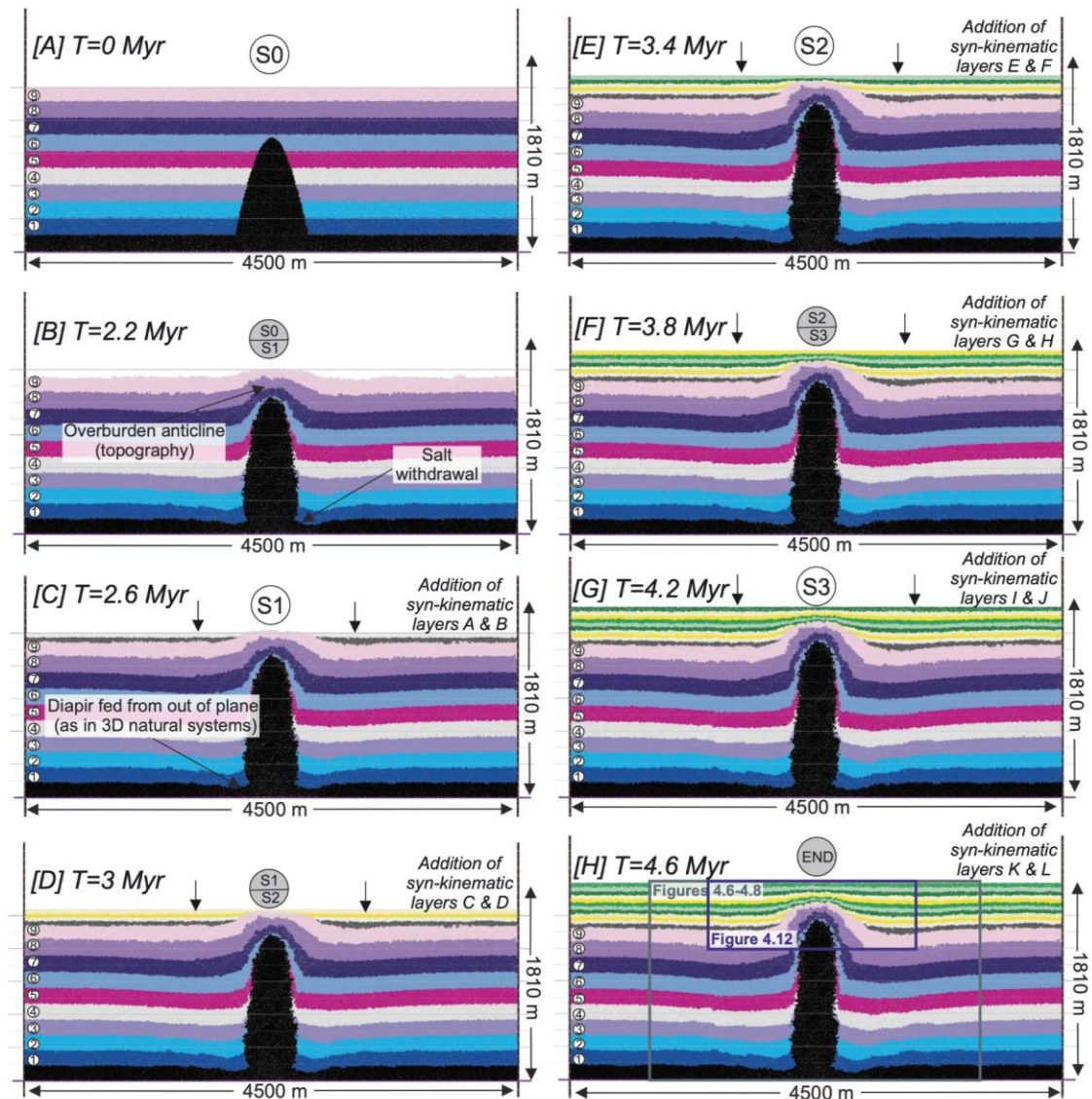
**Table 4.1:** Details of the different sedimentation patterns and rates used in the six experiments. S1-3 refer to sedimentation intervals.

Model	Sedimentation Type	Sedimentation Interval		
		S1 (2.2-3.0 Myr) [22000 – 30000 time steps]	S2 (3.0-3.8 Myr) [30000 – 38000 time steps]	S3 (3.8-4.6 Myr) [3800 – 46000 time steps]
<b>Sedimentation Rate (mm/year)</b>				

<b>M1</b>	None	0.0	0.0	0.0
<b>M2</b>	Slow consistent sedimentation (Aggradation)	0.15	0.15	0.15
<b>M3</b>	Intermediate consistent sedimentation (Aggradation)	0.30	0.30	0.30
<b>M4</b>	Fast consistent sedimentation (Aggradation)	0.45	0.45	0.45
<b>M5</b>	Increasing sedimentation (Progradational)	0.15	0.30	0.45
<b>M6</b>	Decreasing sedimentation (Retrogradational)	0.45	0.30	0.15

### ***Model limitations***

In addition to considering how modelled rock properties (density, viscosity, breaking separation; Supplementary Table 1, Appendices A and B) scale to nature it is important to note that these values are often an oversimplification as they assume homogeneity in a given rock property for an entire layer (e.g., 4500 m laterally or the entire 1050 m tall diapir). The natural heterogeneity within stratigraphy, driven by depositional facies variability, differential diagenetic processes and products, and proximal to distal trends, are not incorporated in our models, which are employed to replicate non-unique stratigraphic variations rather than specific, subtle, unique changes in depositional character. The complex three-dimensional processes occurring in salt basins are simplified into a two-dimensional model for this study. Therefore, we assume our models represent a cross-section through a three-dimensional linear salt wall or radially symmetric diapir (e.g., Pichel et al. 2017; 2019; Cumberpatch et al. 2021c); this is likely to be an oversimplification based on the complex, often asymmetric, geometries of salt structures (Hudec and Jackson 2007), but allows for the assumption that salt is continuously flowing in two-dimensions, essentially being fed from out of the two-dimensional plane (Vendeville et al. 1995; Tvedt et al. 2013; 2016). Modelling in two-dimensions also assumes that all processes (such as salt withdrawal and stratigraphic bed rotation) are equal in all directions, which is an obvious reduction in complexity (e.g., Ismail-Zadeh et al. 2004; Dutta et al. 2016; Jackson and Hudec 2017; Mattson et al. 2020; Pichel and Jackson 2020). This is a suitable assumption in simple models that focus primarily on the role of sedimentation rate variability on the halokinetic depositional record. In order to prevent circular reasoning, our model inputs do not attempt to recreate a specific real world diapir, but rather a simplified universally-applicable structure. The absence of more complicated salt geometries (e.g., salt overhangs or welds) prevent direct comparison of the models to specific settings with complicated three-dimensional salt structures (e.g., the Gulf of Mexico). This approach allows the generation of universal, possibly portable, insights that are applicable to global salt basins. Finally, sedimentation rates are extremely variable and non-linear (Sadler 1981); thus, when comparing to certain analogues, ‘slow’ and ‘fast’ sedimentation (stated in Table 4.1) should be taken as relative rates rather than absolute values. Sediments can be deposited above the diapir relief suggesting they are applicable to subaqueous settings, and are assumed to aggrade evenly, preventing direct comparison to deltaic systems (clinoforms).



**Figure 4.5:** Model 3, the intermediate aggradation experiment with a sedimentation rate of  $0.3\text{mm/year}$ . Diapir growth rate is continuous and constant throughout ( $0.023\text{mm/year}$ ). Outputs begin at the start of the experiment during a stage of no sedimentation ( $T=0\text{ Myr}$ , circle S0 (sedimentation stage 0)). At  $T=2.2\text{ Myr}$  (B) the diapir has generated surface topography and sedimentation begins to be added (S0/S1). Subsequent outputs are generated at  $0.4\text{ Myr}$  intervals across the three equal stages of sedimentation (open circles S1-S3) from 2.2 to 4.6 Myr. Active sediment input is constant in stages 1-3 and the boundaries are highlighted by the grey circle (e.g.,  $T=3\text{ Myr}$  represents the end of sedimentation 1 and the beginning of sedimentation event 2). The final output is at  $4.6\text{ Myr}$  (H), following the final sedimentation from S3. Due to minimal deformation in the outer section of all models, for clarity, subsequent figures will focus on only the central  $3000\text{ m}$  around the diapir (shown by the grey outline,  $T=4.6\text{ Myr}$ ). Subsequent figures are shown at  $T=4.6$  (H).

## 4.5 Results

The model with intermediate sedimentation rate (M3) is first presented (Figure 4.5) to examine the relationship between the rates of salt diapir rise and sedimentation. Subsequent sections describe and compare diapir growth, deformation and stratigraphic architectures across all models (Figure 4.6-4.8; Tables 4.2, 4.3).

### **Summary of temporal relationship between halokinesis and sedimentation**

The initially horizontal basal salt layer thins adjacent to the diapir, and the diapir geometry changes from initially triangular/sinusoidal to vertically elongated during evolution (Compare H with A in

Figure 4.5); this is consistent across all 6 models (Figure 4.5-4.6). Up to 45% thinning of the salt layer, ~450 m either side of the diapir base, occurs in all final model outputs (Figure 4.5H), and is accommodated by thinning in the first 2.2 Myr of evolution, as the initial model calibrates for diapir growth. This thinning appears not to continue throughout the model as the diapir is assumed to be fed by salt flow from out of plane (in three-dimensions), allowing diapir rise to be maintained, and preventing welding. The growth of the diapir is accompanied by withdrawal effects in the adjacent stratigraphy, which is indicated by thinning of the source layer and faulting in the basal layers (layers 1-3, Figure 4.5; M3 on Figure 4.7B). Salt withdrawal and evidence for upwards salt growth are shown by the basal part of the diapir narrowing slightly between  $T=0$  and  $T=2.2$  Myr (0 to 22,000 time steps; A-B on Figure 4.5). Sediment is first introduced to all models after 2.2 Myr (22,000 timesteps; Figure 4.5B). Up to this time, the diapir has risen such that 'early diapiric' layers 4 and 5 are folded during its rise and thin dramatically towards the salt due to structural attenuation, assumed to be accommodated by layer-parallel slip. The early diapiric sequence, originally overlying the diapir (layers 6-9, Figure 4.5), are passively folded as the diapir rises. This results in 'post-depositional' layer thickening on the flanks and thinning over the crest (Figure 4.5B). Above the diapir, a topographic high is generated with associated faulting in layers 6-9 observed in  $T=2.2$  Myr (Figure 4.5B). The topographic high influences subsequent sedimentation (layers A-L) and is the focus of our study of stratigraphic modulation (Figure 4.5C-H).

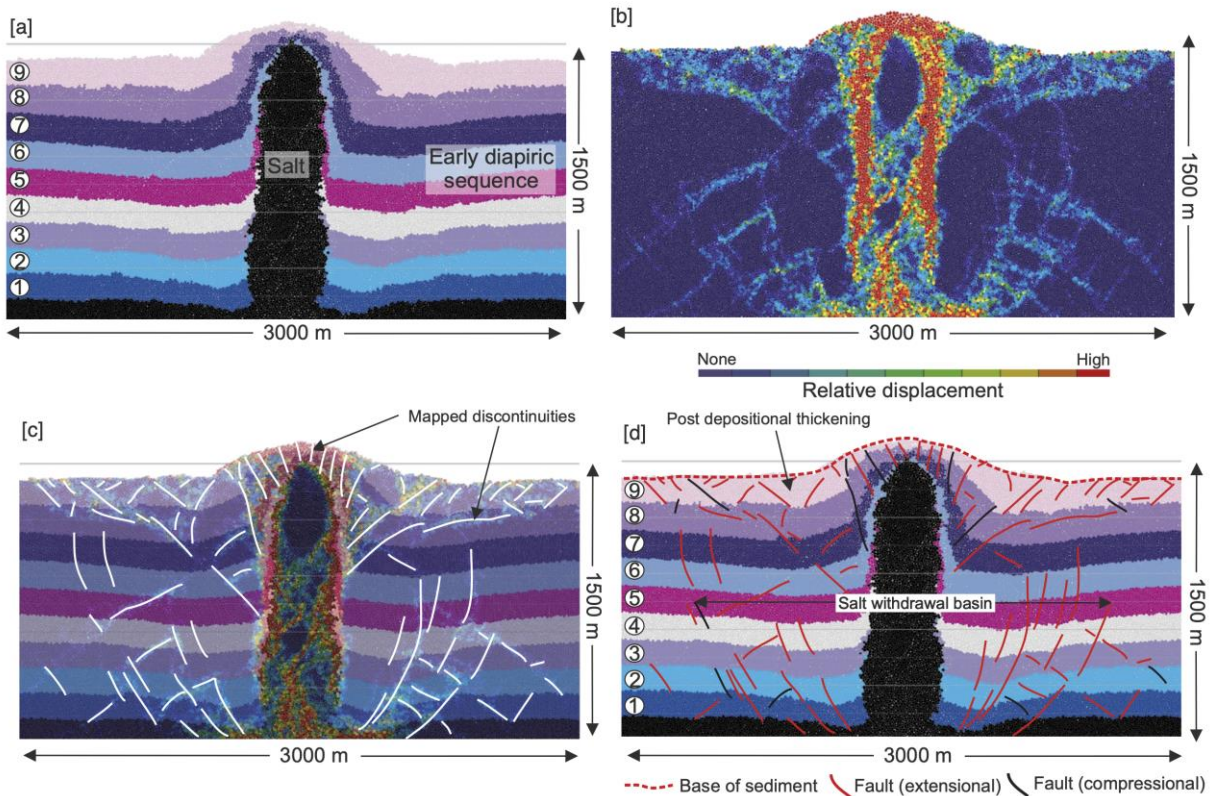
Sediment is added in Stage 1 (S1,  $T= 2.2$  Myr, 22,000 time steps; Figure 4.5C), filling two salt withdrawal basins either side of the diapir. For simplicity, following the methodology of Pichel et al. (2017), the first syn-kinematic layer, Layer A, fills to a flat, standardised base level in all models, to allow consistent comparison across them and subsequent layers are input by assigned sedimentation rate (in the case of M3, 0.3mm/yr). Later in S1 ( $T= 3$  Myr, 30,000 time steps, Figure 4.5), the rate of deposition outpaces diapir rise. Layers extend across the salt rather than onlapping it (Figure 4.5C, D). Throughout diapir rise, the early diapiric sequence is rotated away from the diapir crest, thickening in the adjacent depocentres, again assumed to be due to structural layer-parallel slip. The diapir stem narrows throughout evolution (compare H and A, Figure 4.5). The thinning of early diapiric layers above the rising diapir continues into S2, where early diapiric Layer 5 approaches vertical at the salt-sediment interface (Figure 4.5E, F). Upward movement of the diapir is associated with, and driven by, salt withdrawal underneath the basins, and increased displacement of faults at the base of the model (layers 1-4; Figure 4.5; M3 in Figure 4.7B).

In the final stage (S3), the early diapiric and syn-kinematic stratigraphy thin above the diapir crest, and are further rotated and thicken into the salt withdrawal basins (Figure 4.5G, H). Faulting is present above the diapir tip propagating through the early diapiric sequence and into the syn-kinematic sediment (M3 in Figure 4.7B). Throughout diapir evolution, the dip of the early diapiric layers increases towards the structure, and thus the overburden anticline steepens and narrows as sedimentation progresses (compare H with B in Figure 4.5). The deformation in the early diapiric overburden sequence, described here, is similar across all models (M1-6).

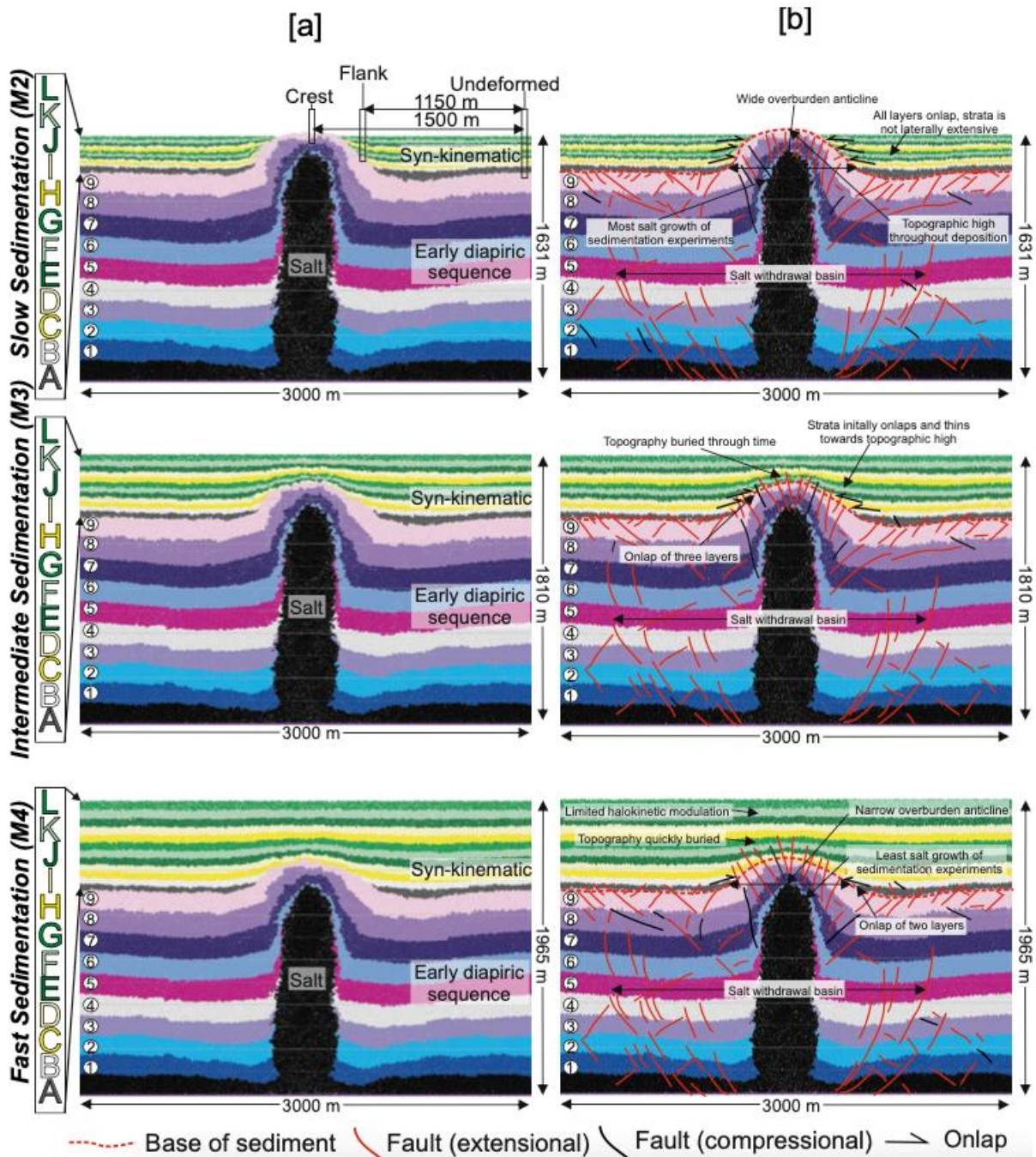
The fault furthest from the diapir is taken as the edge of the halokinetically-influenced part of the succession, which is ~1150 m wide on either flank (from diapir centre to fault edge), resulting in a ~2300 m zone of diapiric influence, in all scenarios. Outside this zone, early diapiric and syn-kinematic strata appear undeformed. Salt mobility has a limited influence on sediments at the extremities of M3, which is consistent across all simulations, so in subsequent figures only the central 3000 m is shown (grey box,  $T = 4.6$  Myr, Figure 4.5).

To permit comparison of stratigraphic variability across all models, subsequent figures (Figures 4.6-4.8) present the result of the models (M1-M6) at the end of the experiment ( $T=4.6$  Myr). In the following section, we describe and compare diapir growth and roof folding, and stratigraphic

architecture (Supplementary Figure 1, Appendix B). In each case, we first present and discuss M1, the case where there is no sediment input for comparison with models in which sedimentation rate is constant (M2-M4), increasing (M5) and decreasing (M6).

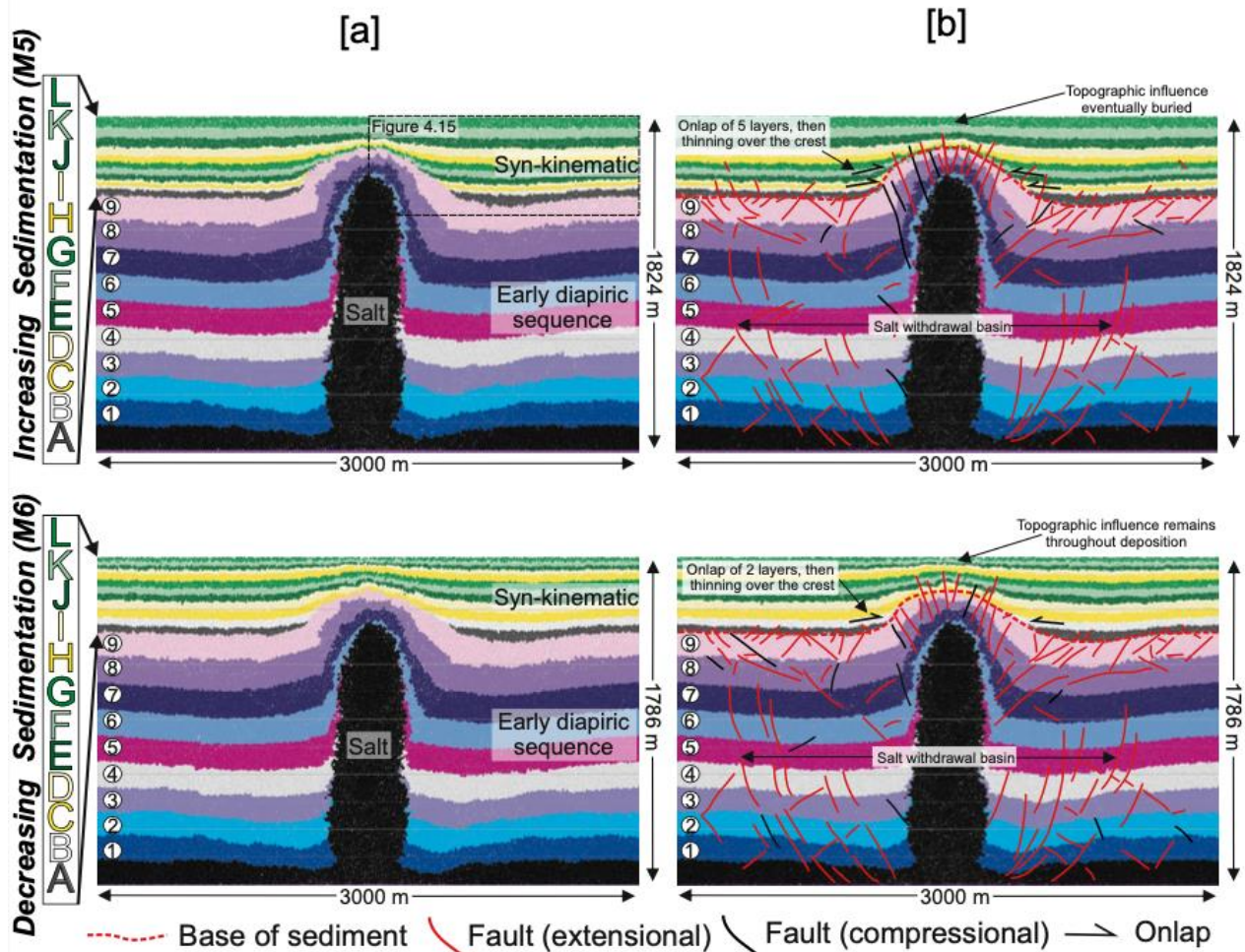


**Figure 4.6:** M1, the model with no sedimentary fill, after 4.6 Myr. Displayed outputs represent the central 3000 m of the original output model (located in Figure 4.5). A) Model output, uninterpreted, early diapiric layers are numbered for clarity, and ease of subsequent discussion. B) Static image of element displacement relative to initial neighbours for M1 after 4.6 Myr (provided for M1-M6 in Supplementary Figure 2, Appendix B). Cold colours represent elements that are in contact with their original neighbour and hot colours indicate high displacement. This is used to show discontinuities and is a proxy for fault location. C) (A) overlain with (B), interpreted with locations of discontinuities, highlighting the methodology used to interpret structures for all models. Note how the majority of the internal salt has remained in connection with its original neighbouring element and the radial faults are associated with salt withdrawal. The maximum displacement shows the relative movement of the salt, the neighbouring overburden, and the high mobility of layers in close proximity to the diapir. Note the lack of deformation outside of the salt withdrawal basin. D) Interpreted static DEM for 4.6 Myr, faults are taken from discontinuities in (C), and overlain onto (A).



**Figure 4.7:** Uninterpreted and interpreted static images of the DEM for M2-M4 (constant sedimentation rate models) after 4.6 Myr. A) Uninterpreted models, sedimentary layers are coloured and assigned letters for easier discussion. Crest, flank and undeformed labels for M2 reflect the locations of thickness measurements taken to calculate thinning rates, this location is consistent across all models (M2-M6), B) Interpreted versions of each model. Fault interpretations use displacement from initial neighbour methodology (see Figure 4.6, Supplementary Figure 2, Appendix B). Interpretations highlight the width of salt withdrawal basins (deformed zones), height of diapirs, fault and fracture distributions, stratigraphic thickness variation and variable halokinetic influence vertically and laterally, discussed in text.





**Figure 4.8:** Uninterpreted and interpreted static image of the DEM with variable sedimentation (M5 and M6) after 4.6 Myr. Displayed output represent the central 3000 m of the original output model (located in Figure 4.5). A) Uninterpreted models, sedimentary layers are coloured and assigned letters for easier discussion. Crest, flank and undeformed zones mentioned in text reflect those shown in M2 (Figure 4.7). B) Interpreted versions of each model. Fault interpretations use displacement from initial neighbour methodology (see Figure 4.6, Supplementary Figure 2, Appendix B). Interpretations highlight the width of salt withdrawal basins (deformed zones), height of diapirs, fault and fracture distributions, stratigraphic thickness variation and variable halokinetic influence vertically and laterally discussed in text.

### Diapir growth and roof folding

**Diapir Rise with No Sedimentation (M1):** In M1, the diapir crest rises a total of 425 m, and the final width of the early diapiric folded roof, taken from the greatest change in dip in Layer 9, is 961 m (Figure 4.6; Supplementary Figure 1, Appendix B). These values represent the base-case to compare the effect of different sedimentation rates on the final geometry of the salt structure and the early diapiric and syn-kinematic stratigraphic architectures (Table 4.2, 4.3; Figure 4.7, 4.6).

**Constant sedimentation rates (M2-M4):** Under slow (M2), intermediate (M3) and fast (M4) constant sedimentation rates the diapir rises by 393 m, 363 m and 297 m, respectively (Figure 4.7). Diapir growth compared to M1 is reduced by 8%, 15% and 30% for the different aggradation cases, respectively (Table 4.2). The width of the early diapiric folded roof decreases from 961 m in M1 to 770 m (M2), 760 m (M3) and 734 m (M4), which accounts for 20-24% reduction relative to M1. Where syn-kinematic stratigraphy is present across the model (i.e., not in M2), the syn-kinematic folded roof is measured from the point within Layer F where there is the greatest change in dip (Supplementary Figure 1, Appendix B). Layer F is chosen as it is the first layer that is laterally

extensive across all models (M3-6). The syn-kinematic folded roof is 839 m and 890 m wide in M3 and M4, respectively. The syn-kinematic roofs are therefore 110% and 120% greater than the width of the early diapiric folded roof in the same models (Supplementary Figure 1, Appendix B).

**Variable Sedimentation Rates:** In M5, under increasing sedimentation rate, the diapir rises by 368 m, a decrease of 14% compared to M1. Under decreasing sedimentation rate conditions (M6) the diapir rises by 346 m, a 19% reduction when compared to the base case M1 (Table 4.2; Figures 4.8 and 4.10). The early diapiric folded roof width is reduced to ~750 m in both models, a decrease of 22% compared to M1 (Table 4.2; Figure 4.10). The syn-kinematic folded roof is 723 m and 872 m in M5 and M6, respectively, representing a 4% reduction and 16% increase compared to the early diapiric folded roof in the same model.

**Table 4.2:** Comparison of diapir growth and overburden anticline width across all six experiments at T=4.6 Myr. Measurements are taken from model simulations (Figures 4.4, 4.5 and 4.6). Initial diapir height (1050 m at T=0 Myr) is subtracted from final diapir height to give diapir growth. M2-6 are compared to M1 to show the percentage reduction that occurs when different amounts of sediment are added. Early diapiric anticline measurements are taken from the stratal termination of Layer A, in M1 they are taken from the top of the overburden at the location of the greatest change in dip. For M2-M6 the width of the overburden is compared to M1 to show the percentage reduction in overburden anticline width that occurs when different amounts of sediment are added. Syn-kinematic folded roof measurements are taken from location of greatest dip change in Layer F (Supplementary Figure 1, Appendix B). Value only calculated where layers extend across the entire structure (M3-M6). Ratio of syn-kinematic to early diapiric folded roof thickness is calculated.

Model	Diapir growth (upward movement) (m)	Percentage reduction compared to base case (M1)	Early diapiric folded roof width (m)	Percentage reduction compared to base case (M1)	Syn-kinematic folded roof width (m)	Ratio of syn-kinematic: early diapiric folded roof (m)
M1, No sedimentation	425	n/a	961	n/a	n/a	n/a
M2, Slow sedimentation rate	393	8	770	20	n/a	n/a
M3, Intermediate sedimentation rate	363	15	760	21	839	1.1
M4, Fast sedimentation rate	297	30	734	24	890	1.21
M5, Increasing sedimentation rate	368	14	750	22	723	0.96
M6, Decreasing sedimentation rate	346	19	753	22	872	1.16

### **Effect of sedimentation rate on stratigraphic architecture**

Here, we discuss the lateral extent, thinning rates, and termination styles of stratigraphy onto the topographic high for M2-6. In all models, Layer A fills to a fixed base level, and therefore does not represent the sedimentation rate of S1, so the first layer described is Layer B. Across all models, Layer A heals the topography. This step reduces inconsistencies with the upper surface of Layer 9 that might influence syn-kinematic sedimentation. This partial healing of topography, which is comparable to hemipelagic deposition prior to the onset of the active depositional system, allows for direct comparison across all models (Pichel et al. 2017; 2019; Cumberpatch et al. 2021c) alt-

hough reduces the effect of thinning and folding of subsequent layers (B-L). Stratigraphic architecture and thinning rates (Table 4.3) are discussed with reference to three points that remain fixed throughout all models: the crest, flank and undeformed zone (see uninterpreted M2 in Figure 4.7).

**Constant sedimentation rates (M2-M4):** Syn-kinematic layers (B-L) are not laterally extensive in M2; this model is defined by slow sedimentation rates. In this case, deposition is restricted to primary salt withdrawal basins, with no sedimentation occurring over the crest of the early diapiric anticline. All layers terminate adjacent to the diapir, with the uppermost layers (I –L) onlapping the remnant topography created by the layers below (Figure 4.7). The entire stratigraphic package thins by 34%, at a rate of 0.029%/m from the undeformed zone to salt flank, before pinching-out towards the crest.

In M3, the model defined by intermediate sedimentation rates, the earliest syn-kinematic strata (Layers B and C) are preserved only in the salt withdrawal basin, offset some distance from the diapir (Table 4.3). However, in contrast to M2, layers D-L are laterally extensive across the model, extending across the diapir crest (Table 4.3). The overall stratigraphic thinning for intermediate aggradation is 55% from undeformed zone to crest, at a rate of 0.037%/m, with over one-third of this occurring between the undeformed zone and flank, accounting for 19% thinning at a rate of 0.017%/m. Thinning rates of 0.1%/m, totalling 35% stratigraphic thinning (almost two-thirds of the overall thinning observed across M3) are observed from flank to crest. The thinning rate between the salt flank and the crest is 6.1 times greater than that between the undeformed section and the flank (Table 4.3).

In the fast sedimentation model, M4, all layers are extensive across the model except for Layer B (Figure 4.7; Table 4.3). The overall stratigraphic thinning for fast aggradation is 33% from the undeformed section to the crest at a rate of 0.022%/m. Over one-third of this total thinning is between the undeformed section and the salt flank, accounting for 12% stratigraphic thinning at a rate of 0.01%/m, and the other almost two-thirds occurs between the salt flank and the crest with a thinning rate of 0.06% accounting for 21% stratigraphic thinning. The thinning rate between the salt flank and the crest is 5.9 times greater than that between the undeformed section and the flank (Table 4.3).

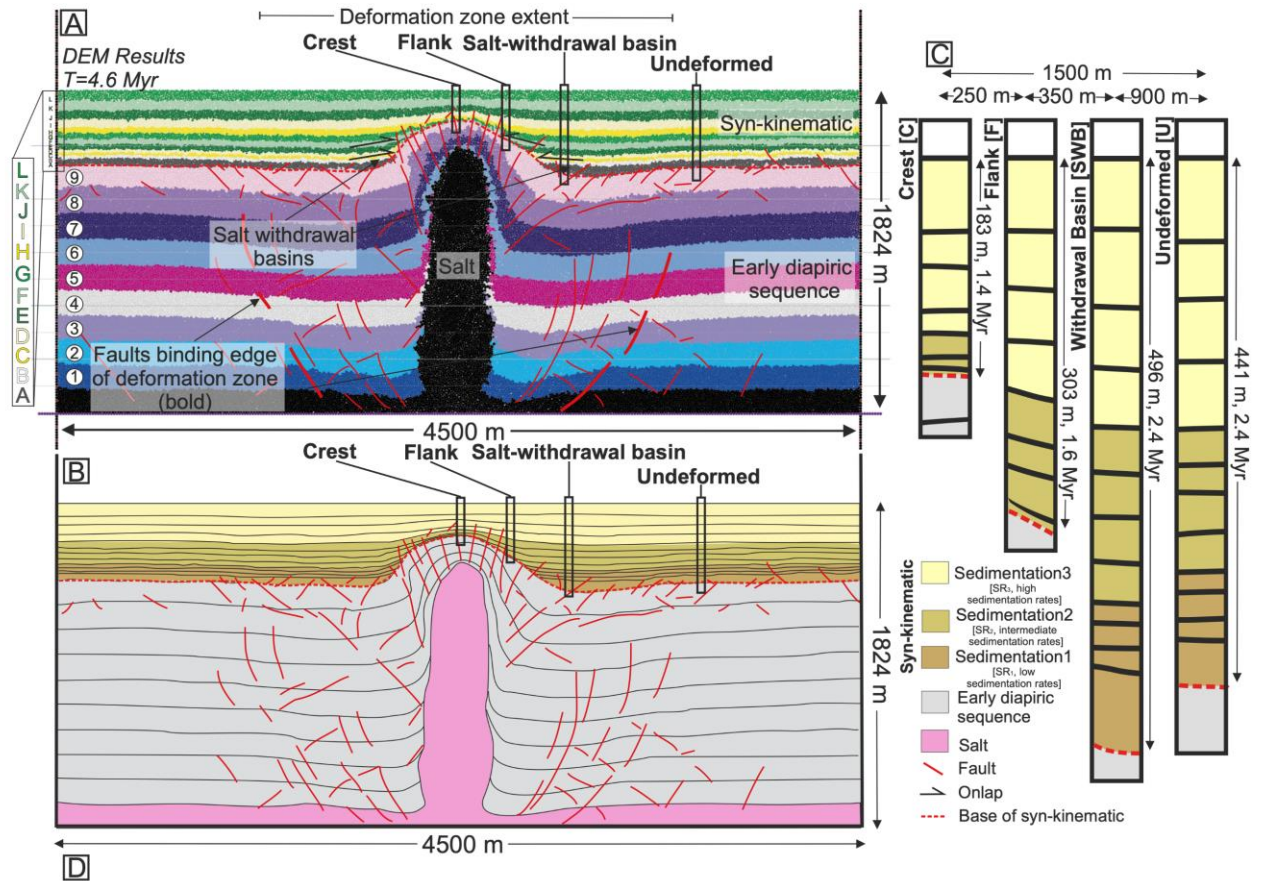
**Increasing (M5) and Decreasing (M6) sedimentation rates:** In M5 (increasing sedimentation rate), layers B-D represent slow sedimentation and thicken into the salt withdrawal basin by 3.5% (over 900 m from the undeformed zone; Figure 4.9) at 0.004%/m, before pinching-out toward the diapir. Layers E-H were deposited under intermediate sedimentation rates. Layer E does not extend across the model and thins towards the flank (across 1250 m) by 0.053%/m, before pinching-out towards the crest (Figure 4.9). Layers F–H extend across the model but thin at 0.045%/m over 1500 m, from the undeformed zone to the crest (Figure 4.9). Layers I-L were deposited under the fast sedimentation rate, and are laterally extensive across the entire model (Figures 4.8 and 4.9; Table 4.3). Thinning rates halve, from 0.032%/m in I to 0.015%/m in L, showing a rapid decrease in salt influence with time. This reduced modulation of the late syn-kinematic sedimentary sequence is a product of increased sedimentation rate (Cumberpatch et al. 2021c). Overall, thinning in the increasing sedimentation model accounts for 58% total stratigraphic thinning at an average rate of 0.039%/m; two-thirds of this thinning takes place between the salt flank and the crest, accounting for 39% stratigraphic thinning at a rate of 0.11 %/m. The remaining third of the thinning occurs between the undeformed section and the salt flank, at a rate of 0.017%/m accounting for 19% stratigraphic thinning. Thickening of 12% (over 900 m) at 0.014%/m is observed between the undeformed zone and the withdrawal basin (Figure 4.9). The thinning rate between the salt flank and the crest is 6.6 times greater than that between the undeformed section and the salt flank (Table 4.3).

In M6 (decreasing sedimentation rate), layers B-D represent fast sedimentation. Layer B is isolated to either side of the diapir and thins between the undeformed section and the flank before terminating towards the diapir (Table 4.3). Layers C and D are laterally extensive. Layers E-H represent intermediate sedimentation, and are deposited across the entire model. Layers I-L are deposited under slow sedimentation and are extensive across the whole model, but thin markedly over the crest (Figure 4.8; Table 4.3). The overall stratigraphic thinning for the decreasing sedimentation rate model is 52% at a rate of 0.035%/m. Just over one-third of this thinning takes place between the undeformed section and the diapir flank, accounting for 19% stratigraphic thinning at a rate of 0.016%/m, and the remaining two-thirds thinning occurs between the flank and crest, at a rate of 0.097%/m, accounting for 34% stratigraphic thinning. The thinning rate between the salt flank and the crest is 5.9 times greater than that between the undeformed section and the salt flank (Table 4.3).

**Table 4.3:** Comparison of stratigraphic thinning across M2-M6. Bold headings indicate each model and show the total thinning for all stratigraphy, beneath each heading this is divided by sedimentary package. Layer A is excluded as it fills to base level in all models. Layers are subdivided based on observational differences (e.g., lateral extent across the model) and are broadly grouped into their sedimentation stage (S1, S2, S3). Percentage thinning and normalised thinning rates (%/m) are shown for U-C (Undeformed to Crest, i.e., the total model), U-F (Undeformed to Salt Flank) and F-C (Salt Flank to Crest). In layers which do not extend across the entire model no results exist for U-C and F-C. The final column displays the ratio of the normalised thinning rate between the Undeformed to Salt Flank and the Salt Flank to Crest sections, to show how much more thinning is observed adjacent to the diapir. Locations of undeformed, flank and crest measurements are shown on Figure 4.7, and are the same for all models to ensure direct comparison.

Model	U-C (%)	U-C (%/m)	U-F (%)	U-F (%/m)	F-C (%)	F-C (%/m)	U-F:F-C
<b>Slow (M2)</b>	-	-	34.4	0.029	-	-	-
<b>Intermediate (M3)</b>	54.5	0.037	19.2	0.017	35.3	0.1	1:6.1
Layers B & C [~S1]	-	-	26.4	0.023	-	-	-
Layers D-H [~S2]	60.1	0.040	14.5	0.011	45.6	0.13	1:10.3
Layers I-L [S3]	23.2	0.015	6.3	0.005	16.9	0.048	1:8.8
<b>Fast (M4)</b>	32.5	0.022	11.6	0.010	20.9	0.060	1:5.9
Layer B [Early S1]	-	-	47.0	0.041	-	-	-
Layers C & D [Late S1]	38.4	0.026	12.9	0.011	25.5	0.073	1:6.5
Layers E-H [S2]	29.7	0.019	8.6	0.007	21.1	0.06	1:8
Layers I-L [S3]	2.35	0.0016	1.04	0.0009	1.3	0.037	1:4.1
<b>Increasing (M5)</b>	58.3	0.039	19.3	0.017	38.9	0.11	1:6.6
Layers B-D [S1]	-	-	61.1	0.053	-	-	-
Layer E [Early S2]	-	-	24.8	0.0022	-	-	-
Layers F-H [Late S2]	60.6	0.040	15.9	0.014	44.8	0.128	1:9.2
Layers I-L [S3]	21.5	0.014	6.7	0.006	14.7	0.042	1:7.2

<b>Decreasing (M6)</b>	52.4	0.035	18.6	0.016	33.9	0.097	1:5.9
Layer B [Early S1]	-	-	37.4	0.017	-	-	-
Layers C&D [Late S1]	39.6	0.026	10.3	0.009	29.3	0.084	1:9.3
Layers E-H [S2]	42.3	0.028	11.4	0.009	30.8	0.088	1:8.8
Layers I-L [S3]	43.9	0.029	19.5	0.017	24.5	0.069	1:4.1



Layer	U-C (%)	U-C (%/m)	U-SWB (%)	U-SWB (%/m)	SWB-F (%)	SWB-F (%/m)	F-C (%)	F-C (%/m)	U-SWB:SWB-F:F-C
<b>Entire Model</b>	58.5	0.039	-12.5	-0.014	38.9	0.111	39.6	0.158	-1:3.12:3.18
Layers B-D [SR <sub>1</sub> ]	/	/	-3.5	-0.004	/	/	/	/	/
Layer E [Early SR <sub>2</sub> ]	/	/	-13.6	-0.015	70.7	0.202	/	/	/
Layers F-H [SR <sub>2</sub> ]	68.1	0.045	-16.5	-0.018	32.9	0.094	59.1	0.236	-1:2:3.59
Layers I-L [SR <sub>3</sub> ]	32.5	0.022	-1.6	-0.002	9.9	0.029	26.3	0.105	-1:6.07:15.98

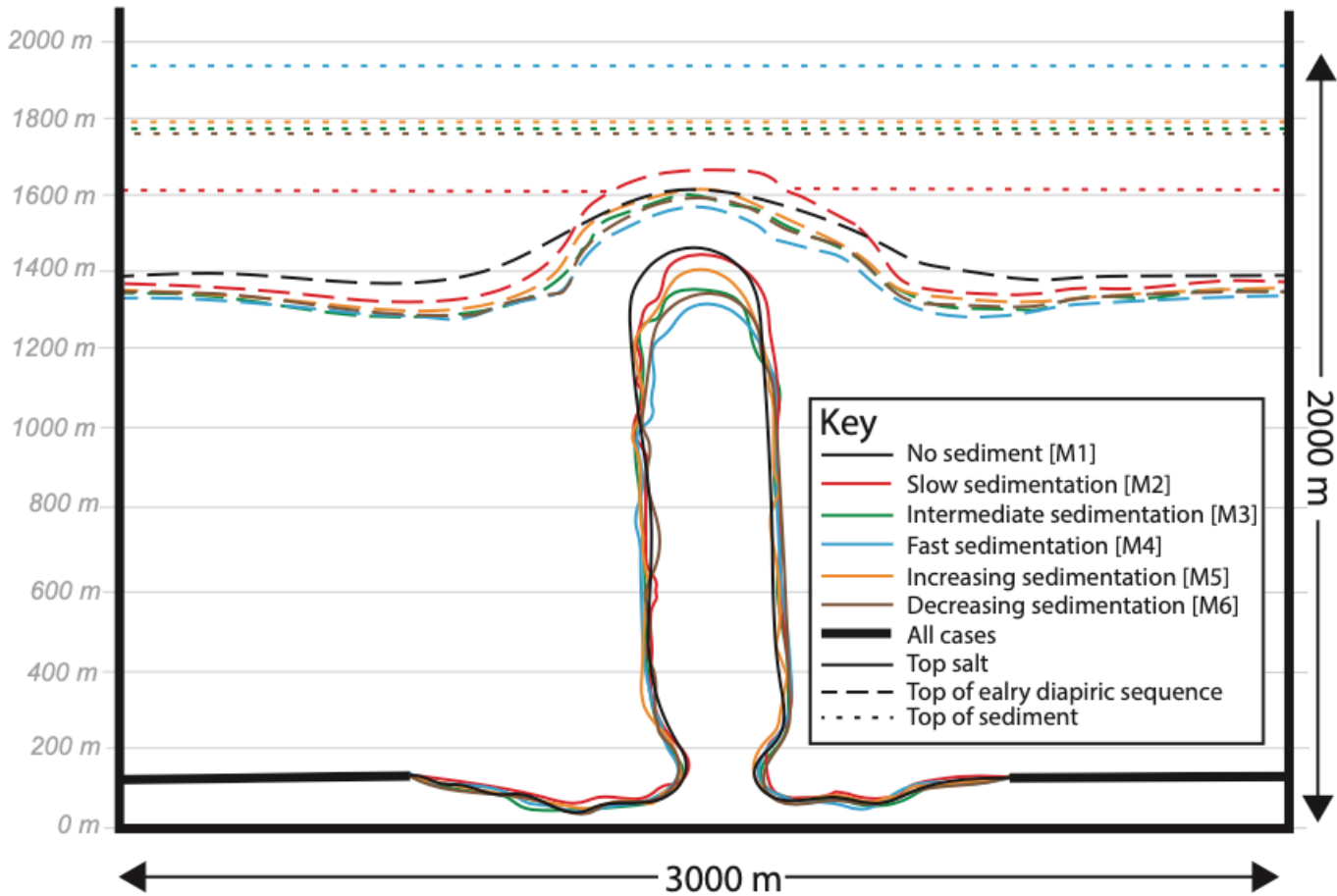
**Figure 4.9:** (A) Interpretation of M5 based on Figure 4.7. (B) Salt-related stratigraphic deformation, including salt-withdrawal basin: Crest (C), flank (F), salt-withdrawal basin (SWB), and undeformed (U) represent stratigraphic zones. (C) Expanded zones. (D) Thinning rates for U-C, U-SWB, SWB-F, and F-C for stratigraphic packages. Layer A is excluded, as it fills to base level. Negative values indicate stratigraphic thickening.

#### 4.6 Summary of halokinetic influence

##### ***Diapir growth and roof folding***

In our model, we invoke a constant upward movement, or growth, of the salt diapir. Therefore, our models show how different sedimentation rates can dampen the late-stage growth of diapirs. The greatest upward movement of the diapir is observed in the model with no sedimentation (M1) (Table 4.2; Figure 4.10), because in this case there is no roof to resist the upward flux of salt. M1 is taken as the base case. Upward movement (growth) of the diapir is reduced with the addition of sediment (Table 4.2; Figure 4.7, 4.8), which in essence increases the roof thickness towards the limit where diapir growth can occur (i.e., diapir height approaches <66% of overburden: Schultz-Ela et al. 1993). The amount of growth decreases, compared to the base case (M1), with increasing sedimentation rate (being limited to 70% in M4), showing that sedimentation rate is a key control on burial of salt topography. This observation is in agreement with existing models (Giles and Lawton 2002; Hudec and Jackson 2007; Fuchs et al. 2011; Jackson and Hudec 2017; Peel et al. 2020).

We also note that the anticline defining the *early diapiric* folded roof is widest in M1 and decreases with increasing sedimentation rate (Table 4.2; Figure 4.10, 4.10). In models which include sedimentation (M2-M6), the early diapiric roof anticline is 20-24% narrower than in M1 (no sedimentation). The lack of variability in stratigraphic architecture between different sedimentation conditions may imply that sedimentation rate has only a minor control on early diapiric anticline width, with other controls such as salt supply, salt viscosity and regional tectonics (not modelled) being more important (Koyi 1998; Fuchs et al. 2011). However, the anticline within the *syn-kinematic* folded roof is widest in M4, appearing to increase with increasing stratigraphic thickness (i.e., sedimentation rate). Syn-kinematic folded roof thicknesses are more variable across the models, because they are controlled by the sedimentation rate. Increasing syn-kinematic folded roof width with sedimentation rate supports fold wavelengths being larger for thicker overburdens (Davison et al. 2000b; Bonini 2003; Hudec and Jackson 2011; Duffy et al. 2018).



**Figure 4.10:** Diagrammatic comparison of static 4.6 Myr DEM across all models. Comparison between top salt (solid line), top of the overburden (dashed line) and top of the sediment (dotted line). The top of sediment is not shown in M1 as none is added. All cases have a similar top salt outside the deformed zone (shown by a bold black line). Diapir growth and width of the early diapiric overburden anticline are reduced in M2-M6 when compared to M1 due to overpressure caused by sedimentation (see Table 4.2). Grey lines indicate 200 metre divisions vertically. Located on Figure 4.5.

### **Fault distribution and deformation zone extent**

Fault distribution and salt withdrawal basin extent are interpreted using a relative displacement algorithm, that calculates the nearest neighbour outputs (Figure 4.6; Supplementary Figure 2, Appendix B). Nearest neighbour outputs highlight the amount of displacement that has occurred during 4.6 Myr, relative to an element's initial neighbours; this is used to highlight discontinuities as a proxy for faults. Fault distributions are broadly similar across all models (Figures 4.6-4.8) and are summarised here. Numerous predominantly extensional faults, with variable dip directions, are identified in the early diapiric sequence in all experiments. These faults have displacements of metres to 100's of metres, with the greatest throws being observed between layers 1-7 (Figures 4.6-4.8). More compressional structures are observed in M4 and M6 compared to the other models. This corresponds with diapirs experiencing the greatest reduction in growth (Figure 4.7, 4.8; Table 4.2), and could suggest that localised compressional stresses increase as the diapir is restrained beneath early thick sedimentation due to overpressure (Jackson and Hudec 2017). However, this could also be an artefact of subtle differences in early diapiric and syn-kinematic anticlines and variations in salt topography. Steep structures appear to develop over the crest of the growing diapir, but are difficult to decipher in terms of slip style (i.e., normal or reverse) due to the relatively small number of displaced neighbouring elements. These crestal structures extend into the syn-kinematic strata (layers A-J) overlying the overburden anticline (M3-M6); these discontinuities are largest and extend furthest into the syn-kinematic overburden under greater sedimentation rates

(compare M4 with M3; Figure 4.7). Away from the crest, in all experiments, layers 8 and 9 are dominated by small-scale faults that are localised to those layers.

The edge of the salt withdrawal basin is taken as the distance of the furthest faults from the diapir. These faults are associated with smaller synthetic and antithetic structures (Figures 4.6-4.8). Outside this zone the strata are undeformed (Figure 4.6-4.8). The salt withdrawal basin, and associated deformation zone, is ~2300 m wide in all models, accounting for three times the initial maximum width of the diapir (Figure 4.6-4.8). The similar extent of the salt withdrawal basin across all experiments suggests that syn-kinematic sedimentation only has a minor control on deformation of early diapiric layers and structural configuration.

### ***Stratigraphic architecture variability with sedimentation rate***

Here, the variability in thinning rate is compared between different models with syn-kinematic sedimentation. Layer A is excluded from descriptions in all models, and thus from our comparisons, as it fills to a linear, instantaneous base level and therefore does not always represent the sedimentation rate of S1. In the absence of Layer A, more layers would onlap and less would be laterally extensive across the models as more bathymetry would need to be healed. However, the inclusion of a consistently thick Layer A across all models enables easier comparison, and could represent a pelagic drape that partially heals topography prior to the incursion of siliciclastic sediment. Therefore 11 layers (B-L) are described and compared in Table 4.3.

Under slow sedimentation rate (M2) all 11 layers onlap topography and are not laterally extensive. Under intermediate sedimentation rate (M3) two layers onlap and nine are laterally extensive. In fast sedimentation (M4) and decreasing sedimentation (M6) this rises to 10 laterally extensive layers and one onlapping layer. Under increasing sedimentation rate (M5), the initial four layers (including three which are deposited under slow sedimentation) onlap topography and the remaining 7 are laterally extensive (Figure 4.7). As expected, layers are more laterally extensive under higher sedimentation suggesting that the effects of halokinetic modulation decrease more rapidly upwards under higher sedimentation rates (Peel et al. 2014; Sylvester et al. 2015; Cumberpatch et al. 2021c). The final stratigraphic thickness is greatest under fast sedimentation rate (M4, 570 m), least under slow sedimentation rate (M2, 228 m), and at a similar intermediate level for intermediate (M3, 401 m), increasing (M5, 441 m) and decreasing (M6, 382 m) sedimentation rates, logically showing that net sediment volume is the most important control on sediment thickness (Figures 4.8-4.10). Overall stratigraphic thinning, from the undeformed zone to the flank, is greatest under slow sedimentation rate (M2, 34% thinning) and least under fast sedimentation rate (M4, 12% thinning) (Table 4.3). This shows that stratigraphic thinning rates decrease with increasing sedimentation, suggesting that diapir modulation (thickness and dip variability) decreases quicker under higher sedimentation rate (Pratson and Ryan 1994; Koyi 1998; Fuchs et al. 2011).

In almost all of the models, the thinning rate is between 5.9 and 6.1 times greater between the salt flank and the crest than it is between the undeformed section and the salt flank (Table 4.3; Figure 4.12). This rate is higher (6.6 times) under increasing sedimentation (M5), which suggests that salt structures have greater influence on stratal architecture and thinning rates in models where sedimentation rate is initially slow (e.g., S1 in M5; Giles and Lawton 2002; Fuchs et al. 2011; Giles and Rowan 2012; Jackson and Hudec 2017).

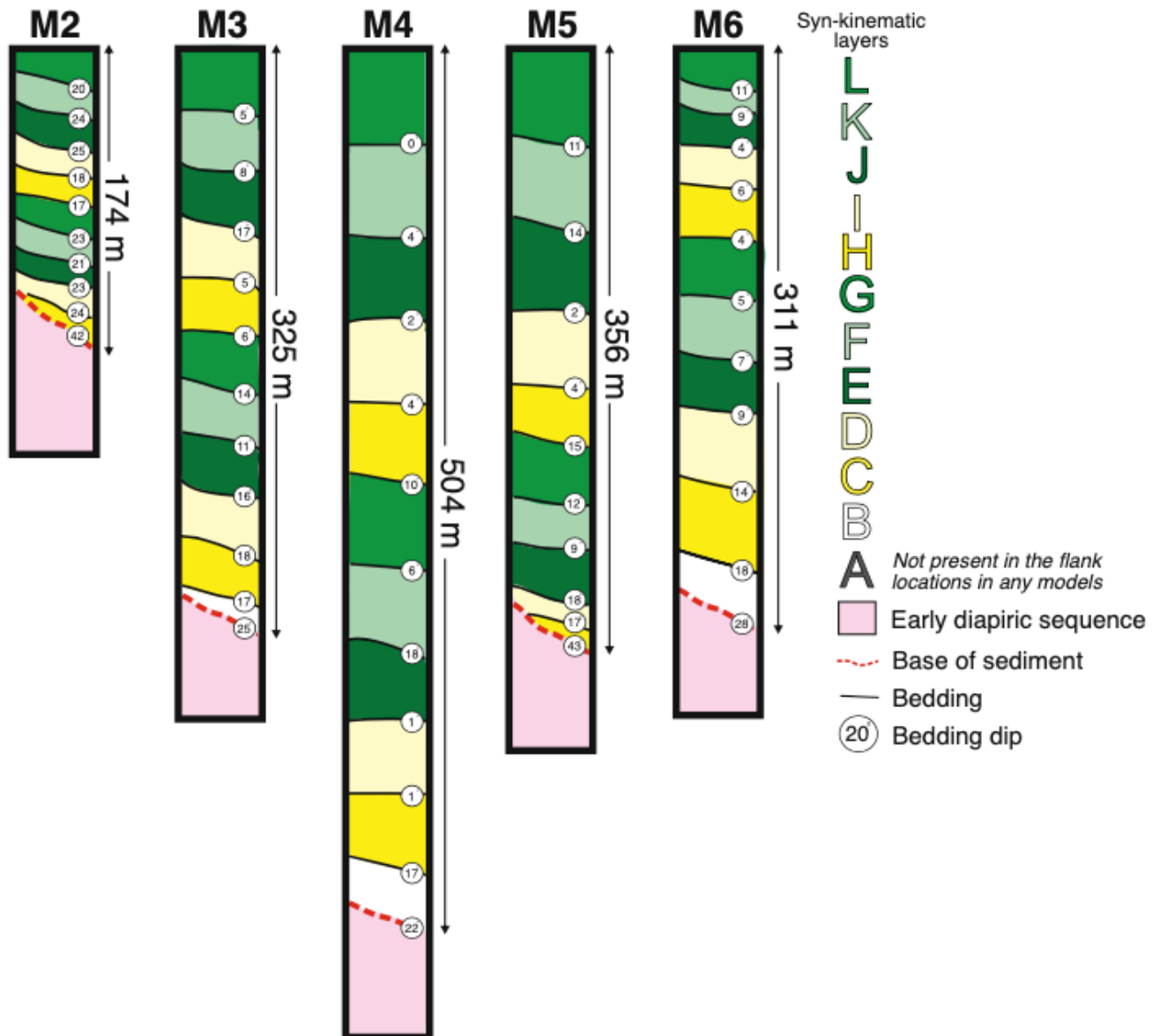
Whilst the primary mechanism modulating the stratigraphic architecture is stratigraphic thinning, stratigraphic thickening into basins driven by salt withdrawal at depth must not be disregarded. Localised thickening into salt withdrawal basins is observed in all models. Such thickening is observed in all models, accounting for 13% of the stratigraphic thickening in M5 (Cumberpatch et al. 2021c). This highlights how the presence of a growing diapir can be associated with localised



additional accommodation (as well as a reduction of accommodation) due to the at-depth evacuation of salt from the source layer to feed the growing diapir, as is evidenced by subtle thickening into the basin (Figures 4.7 and 4.8). Accommodation reduction over the crest of the diapir is driven by diapir growth, which is recorded by stratigraphic thinning. Accommodation increases in salt withdrawal basins are accounted for by stratigraphic thickening and salt migration at depth.

Through time, thickening and thinning are eventually reduced as the halokinetic modulation on stratigraphy is minimised with the burial of the salt-cored topographic high and its flanking depocentres. In all experiments with layers that extend across the entire model, the thinning rate and bedding orientation change up-section (Table 4.3, Figure 4.11). In M2-M5, a decrease in thinning rate up-section is observed. Bedding orientations are variable but generally decrease (flatten) upwards in M2-5. However, under decreasing sedimentation (M6) an overall increase in thinning rate up-section is observed (Figure 4.8; Table 4.3), in addition to a slight increase in bedding dip between layers J, K and L. This suggests that initially thicker layers are less deformed, but that as diapir growth continues and sedimentation decreases, thin layers are still deformed by topography associated with rising salt (Giles and Lawton 2002; Hudec and Jackson 2007; Giles and Rowan 2012; Sylvester et al. 2015; Soutter et al. 2019). Overall, halokinetic modification reduces with increasing sedimentation rate as halokinetic bathymetry is buried. Typically, such alteration decreases up stratigraphy, and laterally outwards from the diapir in agreement with outcrop and subsurface analogues globally (Figures 4.12, 4.14 and 4.15; e.g., Pratson and Ryan 1994; Giles and Lawton 2002; Mayall et al. 2010; Giles and Rowan 2012; Kernen et al. 2012; 2018; Banham and Mountney 2013a; 2013b; 2014; Oluboyo et al. 2014; Poprawski et al. 2014; 2016; Ribes et al. 2015; Doughty-Jones et al. 2017; Wu et al. 2020; Rodriguez et al. 2020; Cumberpatch et al. 2021b).

## Flank stratigraphy comparison



**Figure 4.11:** Comparison of the flank section stratigraphy across all models with sediment (M2-M6). See Figure 4.7 for location of flank profile, which is the same across all models. Thicknesses and bedding orientation highlighted. The flank location shows the most deformation in all models, greatest modulation is observed in M2, and least modulation is observed in M4, generally modulation decreases upwards, however in M6 bed dip increases in layers K and L. Models give an indication of the sedimentary thickness and bed rotation expected adjacent to salt diapirs under different sedimentation rates, aiding prediction of sediment thickness and bed rotation in the subsurface salt sediment interface.

### 4.7 Discussion

#### **Salt Models**

DEM is not intended as a substitute for FEM, but to complement these approaches in salt tectonics. DEM can replicate localised fault growth, evolution, and propagation (Figures 4.5-4.9, 4.10) making it appropriate for studying the interactions of halokinesis, stratigraphy, and tectonics (Pichel et al. 2017, 2019). FEM packages have limited capacity to generate faults during simulations, unless they are predefined (e.g., Heidari et al. 2016; Nikolinakou et al. 2018). DEM treats the contacts between elements as potential displacement surfaces; this is realistic when studying areas with multi-scalar salt-related faulting. As well as seismically resolvable faults, outcrop and borehole data indicate brittle deformation is significant in salt basins (e.g., Koestler and Ehrmann

1991; Giles and Lawton 2002; Giles and Rowan 2012; Poprawski et al. 2014; 2016; Cumberpatch et al. 2021b). Our DEM replicates this brittle deformation (Figures 4.5-4.9); as in nature, extreme thinning and termination of layers are in part accommodated by small-scale displacements. Understanding sub-seismic-scale fault distribution is important for predicting reservoir compartmentalisation and seal integrity in the subsurface. DEM is therefore advantageous due to its replication of diapir-related brittle deformation, while FEM is useful for modelling salt flow (e.g., Albertz and Ings 2012).

### ***Halokinetic Modulation of Stratigraphy***

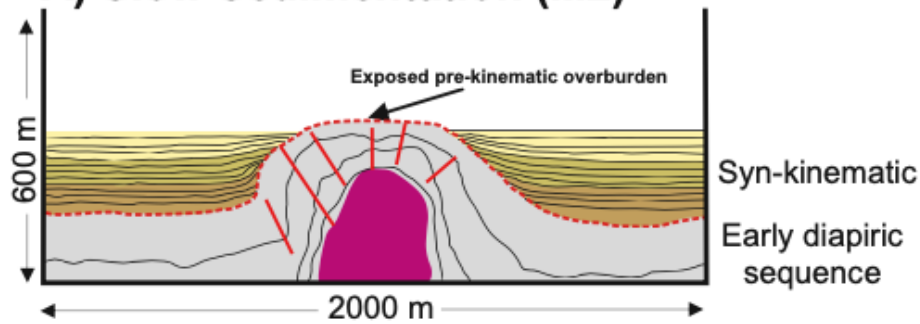
In the absence of salt tectonics, loading and compaction are considered to be the drivers for subsidence, and structures are controlled by regional tectonics. Here, we use M5, the increasing sedimentation model, as an example to test the hypothesis that salt tectonics modulates stratigraphy (Figure 4.9). The undeformed zone shows syn-kinematic strata thicken upwards during an allocyclic increase of sedimentation rate (Figure 4.9). Here, salt topography results in stratigraphic onlap and thickness variations, which are absent in models, or zones, without salt influence (Figures 4.5-4.9), confirming assumptions from subsurface and outcrop examples (e.g., Davison et al., 2000; Giles and Rowan, 2012). Lateral variations in syn-kinematic geometry are significant, defining the relationship between early diapiric and syn-kinematic strata. Syn-kinematic strata (441 m, 2.4 m.y.) conformably overlie early diapiric strata in the undeformed zone (Figure 4.9C) with no evidence of salt influence. Sub-parallel strata (496 m, 2.4 m.y.) thicken into the salt-withdrawal basin to form a subtle, low-angle unconformity over the early diapiric sequence (Figure 4.9C). Syn-kinematic strata (303 m, 1.6 m.y.) dip at a shallower angle than early diapiric strata, creating an angular unconformity at the flank, which is difficult to differentiate from a regional unconformity (Trudgill 2011). Parallel deposition (183 m, 1.4 m.y.) is observed over the crest. Here, the early diapiric to syn-kinematic contact is conformable, but condensed (Jackson and Hudec 2017).

When viewed in isolation (Figures 4.9 and 4.11), the stratigraphic profile across the crestal suggests that the increasing sedimentation trend occurs later and over a shorter time period than the rest of the model (i.e. the basal section is missing and the stratigraphic profile is reduced), indicating that salt growth can modify and mask allocyclic signatures. However, from the undeformed zone to the crestal regions (lateral distance of  $\sim 1500$  m), 258 m of strata representing 1.0 m.y. are missing, as sediment was either not deposited, or it was removed by erosion or failure during growth. This missing stratigraphy clearly demonstrates the effect of halokinesis on allocyclic signal preservation. Growing salt is associated with additional accommodation, as evidenced by thickening into salt-withdrawal basins (Figure 4.9B). Up the stratigraphic section, late syn-kinematic thickness variability is reduced as halokinetic modulation is also reduced by the increased sedimentation rate, healing topography (Figures 4.8 and 4.9). Such relationships are assumed in data where strata cannot be discerned close to the diapir (Pratson and Ryan 1994; Giles and Lawton 2002; Mayall et al. 2010; Giles and Rowan 2012; Kernén et al. 2012; 2018; Banham and Mountney 2013a; 2013b; 2014; Oluboyo et al. 2014; Poprawski et al. 2014; 2016; Ribes et al. 2015; Doughty-Jones et al. 2017; Wu et al. 2020; Rodriguez et al. 2020; Cumberpatch et al. 2021b). Our model confirms this and predicts lateral and temporal thinning rate evolution and stratigraphic geometries in the presence of growing salt. This is vital when exploring and developing subsurface energy resources in crest and flank regions where imaging of overlying and onlapping syn-kinematic strata is difficult (e.g., Jones and Davison 2014; Charles and Ryzhikov 2015).

### ***Comparison to natural examples***

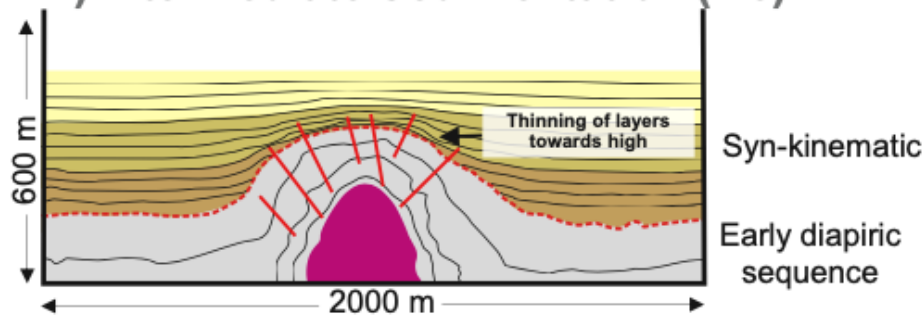
A key challenge for numerical models is ground-truthing against natural prototypes (Oreskes et al. 1994; Burgess 2012). Here, the key findings and predictions from the DEM (Figure 4.12) are compared to published subsurface (Figures 4.13 and 4.14) and field analogues (Figure 4.15) to understand their applicability and limitations.

### A) Slow Sedimentation (M2)



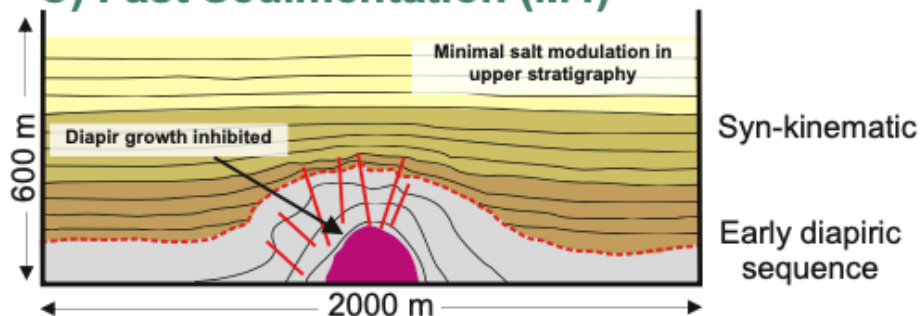
- Non-extensive layers
- Diapir forms topographic high
- Thinning towards the diapir
- Onlap onto the overburden
- Wide overburden anticline
- Long-lived salt influence

### B) Intermediate Sedimentation (M3)



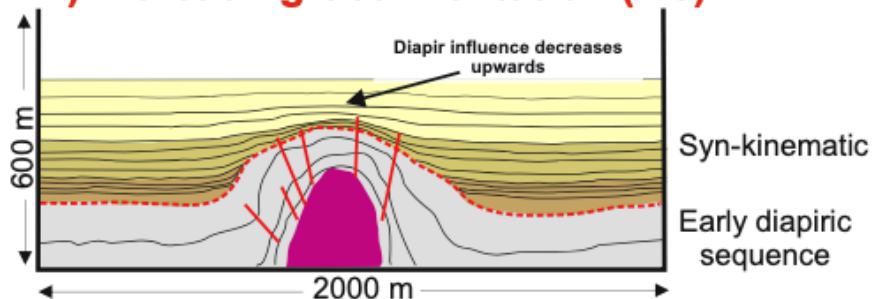
- Initially non-extensive layers
- Early overburden onlap
- Layers thin towards diapir
- Percentage thinning decreases upwards
- Halokinetic influence decreases upwards

### C) Fast Sedimentation (M4)



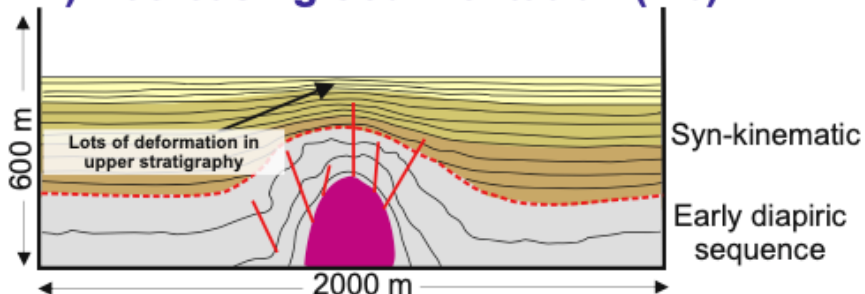
- Laterally extensive layers
- Diapir quickly buried
- Initial onlap, then thinning
- Halokinetic influence decreases upwards
- Narrow overburden anticline
- Reduced salt growth

### D) Increasing Sedimentation (M5)

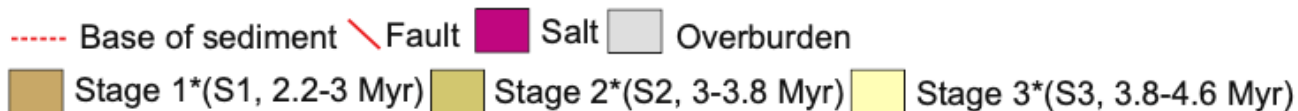


- Sedimentation rate rises to simulate progradation
- Initially non-extensive onlapping layers
- Then thinning of layers
- Halokinetic influence decreases upwards
- Top layer not deformed

### E) Decreasing Sedimentation (M6)



- Sedimentation rate decreases to simulate retrogradation
- First layer non-extensive
- Thinning rate increases upwards
- Halokinetic influence increases upwards
- Top layers thin rapidly towards high



**Figure 4.12:** Schematic interpretations of M2-M6, focussed on the central 2000 m of the syn-kinematic stratigraphy, located in Figure 4.5. Bullet points highlight the key observations specific to each modelled scenario. Crestal faults are simplified from Figures 4-6 to better visualise syn-kinematic stratigraphy.

**Comparison to subsurface: stratigraphy around the Pierce diapirs, Eastern Central Graben, UK North Sea:** Jurassic-Pleistocene syn-kinematic stratigraphy around the north and south Pierce diapirs, Eastern Central Graben, UK North Sea (Figure 4.13) shows evidence for halokinetically-driven changes in bed thickness and dip (Figure 4.14C, 12E; Birch and Haynes 2003). Pierces' tectonostratigraphic history spans ~200 Myr and is summarised as Jurassic reactive-active diapirism, followed by Cretaceous-Cenozoic passive diapirism, and contraction-driven active diapirism during Alpine compression (Scott et al. 2010). Despite a longer-lived and more complex evolution, the Pierce diapirs show geometrical similarities with several of our DEM results (Figures 4.12 and 4.14). In the Pierce example, stratigraphy is near horizontal ~2 km away from both diapirs, but is upturned adjacent to them, comparable with all model results (Figures 4.7, 4.8, 4.10, 4.12). An average seismic velocity of 2000 m/s was used for approximate depth conversion of the time-migrated seismic data to calculate thinning rate for stratigraphy adjacent to the Pierce field. This is an over simplification of seismic velocity, which varies with depth and lithology. However, it is suitable to give a broad comparison to our modelled values (Supplementary Table 2, Appendix B). The generation of brittle deformation throughout the Cenozoic stratigraphy over the crest of both north and south Pierce (Figure 4.14; Carruthers et al. 2013) corresponds to high zones of relative displacement across the crest of the diapir, in M3-M6, which extend into the syn-kinematic stratigraphy (Figures 4.7 and 4.8; Supplementary Figure 1, Appendix B). Similar crestal deformation has been demonstrated in physical models (e.g., Davison et al. 1993). Different model outputs may be applicable to different parts of stratigraphy due to the changing ratio of diapir rise rate and sedimentation rate. For example, stratigraphic architectures comparable to M2, M3 and M5 are observed in different stratigraphic packages around the Pierce diapirs (Figure 4.14).

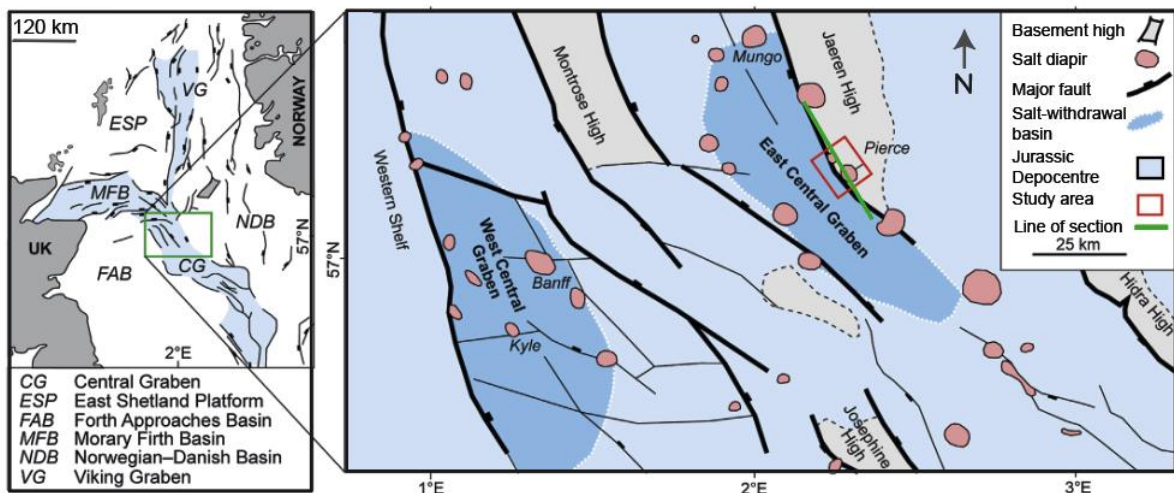
The unique observation from M2 (slow sedimentation) is non-extensive layers that thin towards and eventually onlap and pinch out against the long-lived, salt-related topographic high (Figure 4.12A). M2 results are analogous to the Top Cretaceous (lime green) to Mid Eocene (red) stratigraphy around the Pierce diapirs (Figure 4.14C), which is not laterally extensive across the diapirs (Davison et al. 2000a; Birch and Haynes 2003; Scott et al. 2010; Carruthers et al. 2013). The Top Cretaceous – Mid Eocene package, equivalent to S1-S3 in the models, thins significantly towards both diapirs, before onlapping the flanks (Figures 4.12A; 4.13A and 4.13C). The amount and rate of thinning reduce through time, from 51% at 0.044%/m in the Paleocene (Top Cretaceous – Top Lista interpretations) to 21.3% at 0.019%/m between in the Eocene (Tay and Eocene interpretations (Supplementary Table 2, Appendix B) in agreement with model observations showing thinning rates reducing upwards. These values are similar to the overall thinning of the slow sedimentation model (34%, at 0.029%/m; Table 4.3). Despite this apparent correspondance in thinning rate values, regional sediment volumes are high throughout the Palaeocene (10,000 km<sup>3</sup>/my; Lui and Galloway 1997). Specific lithostratigraphic units such as the Forties Sandstone are associated with ~200 m of sandstone deposited in c. 1 million years (Kilhams et al. 2014; Eldrett et al. 2015). Sedimentation rates for the UK Palaeocene stratigraphy are uncertain, and spatially and temporarily variable around the Pierce diapirs, with rates ranging from 0.085 - 0.4 mm/yr (Liu and Galloway 1997; Kilhams et al. 2014; Eldrett et al. 2015). The lower values are in broad agreement with our slow sedimentation input values. The upper end, however, indicates intermediate – fast sedimentation rates in our models, which have probably been coeval with very high diapir rise rates to form an overall geometry typical of slow sedimentation rates (Carruthers et al. 2013). This is further evidenced by the steep upturning of stratigraphy adjacent to the diapirs (Figure 4.14C; Giles and Lawton 2002; Hudec and Jackson 2007). In our model, we isolate and vary sedimentation rate, whilst in reality the dynamic ratio of sedimentation rate and diapir rise rate control stratigraphic architecture. It is suggested that during the Paleocene – Eocene sedimentation rates were high, but diapir rise rates were higher, likely driven by sediment loading (Carruthers et al. 2013) creating a relative effect of a 'low sedimentation rate' akin to our M2.

In M3 (intermediate sedimentation rates), layers are initially non-extensive (S1), displaying early onlap and thinning (26.4% at 0.023 %/m; Table 4.3; Figure 9B; 10B) similar to Eocene (orange) to Oligocene (peach) stratigraphy adjacent to the north Pierce diapir (Figure 4.14), which thin by 16% at 0.014 %/m. Subsequent modelled layers (S2) are extensive but thin towards the diapir high (60% at 0.04 %/m; Table 4.3), analogous to the Oligocene (peach) to Mid-Miocene (light peach) across north Pierce (65% at 0.044 %/m; Supplementary Table 2, Appendix B; Figure 11C; Carruthers et al. 2013). In our model simulations, 65% of the total thinning occurs between the flank and crestal locations, similar to subsurface observations of 85% of the total thinning around north Pierce occurring between the flank and the crest. After this initial modulation (S1, S2), subsequent M3 stratigraphy (S3) records a reduction in thinning rates and halokinetic influence on stratigraphy upwards (reduction from 60% to 23% total thinning; Table 4.3; Figure 4.12B; 4.12B). This is also observed, albeit at a less extreme rate, between the Middle Miocene and Pliocene interval around the Pierce diapirs (reduction from 65% to 49% total thinning; Supplementary Table 2, Appendix B; Figure 4.14). Much of the excess thinning in the Pierce example, compared to the model, occurs between the undeformed and flank position (28% of thinning, compared to 6% in M3; Table 4.3). This is likely due to Cenozoic compressional forces driving diapir growth and upturn of stratigraphy (Birch and Haynes 2003; Scott et al. 2010; Carruthers et al. 2013), resulting in a less gradual reduction in halokinetic alteration upwards with respect to M3. Based on this comparison of the lateral extent of layers, it is possible to infer that these examples represent intermediate sedimentation rates, relative to diapir rise rate. Sedimentation volumes for the Eocene to Oligocene are  $\sim 4000 \text{ km}^3/\text{Myr}$ , lower than for the Top Cretaceous-Eocene. This suggests that overall diapir rise rate had been slower during the Eocene to Oligocene, with respect to the Top Cretaceous-Eocene time, giving a stratigraphic architecture typical of lower diapir rise rates relative to sedimentation rates (Carruthers et al. 2013).

In M5 (increasing sedimentation rate), S1 and early S2 are initially isolated either side of the diapir in salt-withdrawal basins and onlap salt-cored topography (Table 4.3). Late S2 stratigraphy is extensive across the model, thinning towards the topographic high, with modulation decreasing up-stratigraphy (S3, Figure 4.12D). When combining the Cretaceous to Eocene (M2 analogue, Figure 4.14) and Eocene to Mid-Miocene (M3 analogue) stratigraphy adjacent to the Pierce diapirs, we observe an increasing-upwards sedimentation trend overall, relative to diapir rise rate (Den Hartog Jager et al. 1993; Jennette et al. 2000; Birch and Haynes 2003; Kilhams et al. 2014). The Cretaceous to Eocene was deposited when sedimentation rate < diapir rise rate, leading to isolation of salt withdrawal basins, and stratigraphic thinning and upward rotation of onlap towards the diapir flanks (S1, M5, Figure 4.14D; Carruthers et al. 2013). Rapid thickness changes and pinchouts suggest diapir growth was fastest during the Paleocene–Eocene (Carruthers et al. 2013). The Eocene – Mid Miocene (S2 equivalents) were likely deposited when sedimentation rates were higher relative to diapir rise rates, or when salt supply was equal to sedimentation rate (S2, M5, Figure 4.14D; Carruthers et al. 2013). Subsequent layers (Mid-Miocene – Pleistocene) are broadly extensive across the diapirs, similar to S3 in M5. The sedimentation volume for this interval is fairly low ( $\sim 2000 \text{ km}^3/\text{Myr}$ ; Liu and Galloway 1997), so this observed reduction in halokinetic influence upwards is likely driven by a slowing or cessation of diapir growth rather than being driven purely by high sedimentation rates (Carruthers et al. 2013). Pliocene to Pleistocene stratigraphy is extensive across north Pierce (S2 and S3, M5), but only the Pleistocene is present extensively across south Pierce, due to differential diapir growth histories and cessations (Scott et al. 2010; Carruthers et al. 2013). The upwards reduction in sedimentary thinning observed in the increasing sedimentation model (61% in S2 to 22% in S3) is similar to that observed between the Eocene to Mid-Miocene (88%) and the Mid-Miocene to Pleistocene (18%) in the subsurface example, highlighting the potential applicability of the results from our models. While these subsurface thinning rates are similar to our models, it is important to note that our models do not take into account erosion, or periods of non-deposition once sedimentation begins at 2.2 Myr. Therefore, in nature ‘apparent

thinning rates' could actually be derived from periods of erosion, removing stratigraphy and generating halokinetic unconformities. This is particularly noticeable at the Mid-Miocene unconformity where 'thinning' is at least partly accommodated by Cenozoic compression rejuvenating diapir growth and increasing diapir rise rate, causing erosion of the diapirs overburden, without variation in sedimentation rate (Carruthers et al. 2013). Our models generate realistic halokinetic unconformities, with variable bedding orientations between the early diapiric sequence and the syn-kinematic sequence due to a period of uplift and non-deposition prior to the commencement of sedimentation (Figure 4.11).

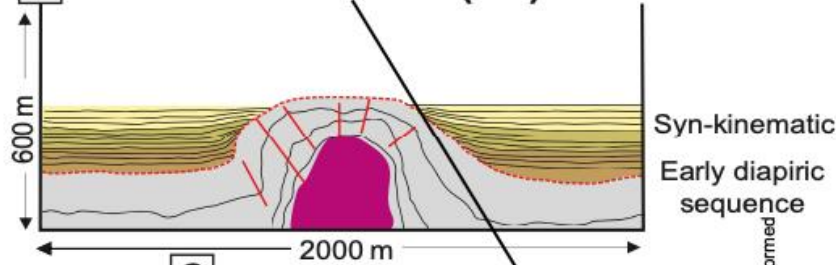
In nature, halokinetic sequence architecture is controlled by the dynamic ratio between sedimentation rate and diapir rise rate (e.g., Giles and Rowan 2012; Pichel and Jackson 2020), such that an 'apparent' increase in sedimentation (reducing halokinetic influence upwards) could represent a slowing of diapir growth due to regional tectonic quiescence or depletion of the salt source layer. Our observations and comparison to DEMs with variable sedimentation rates, are consistent with diapir rise to sedimentation rate ratios derived from halokinetic sequence studies (Carruthers et al. 2013). The role halokinesis plays in shaping the stratigraphic architecture of the north and south Pierce diapirs is reduced from the Oligocene and Pliocene respectively, due to source layer depletion, resulting in halokinetic bathymetry being gradually buried (Figure 4.14; Birch and Haynes 2003). Integration of, and comparison between DEM and subsurface data, demonstrates the importance of understanding local (salt layer variations) and regional (tectonic and sedimentation rate) controls when disentangling salt basin evolution.



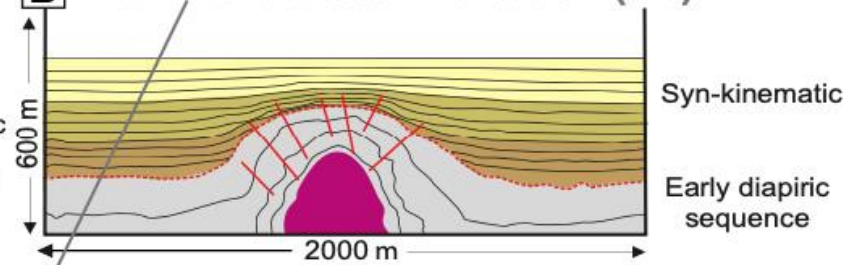
**Figure 4.13:** Tectonic framework of the North Sea rift system, and structural map of the Central Graben showing the location of salt diapirs related to major basin faults and Jurassic salt withdrawal basins (Carruthers et al. 2013). Red box locates subsurface analogue used for comparison to models and green line locates Figure 4.14.



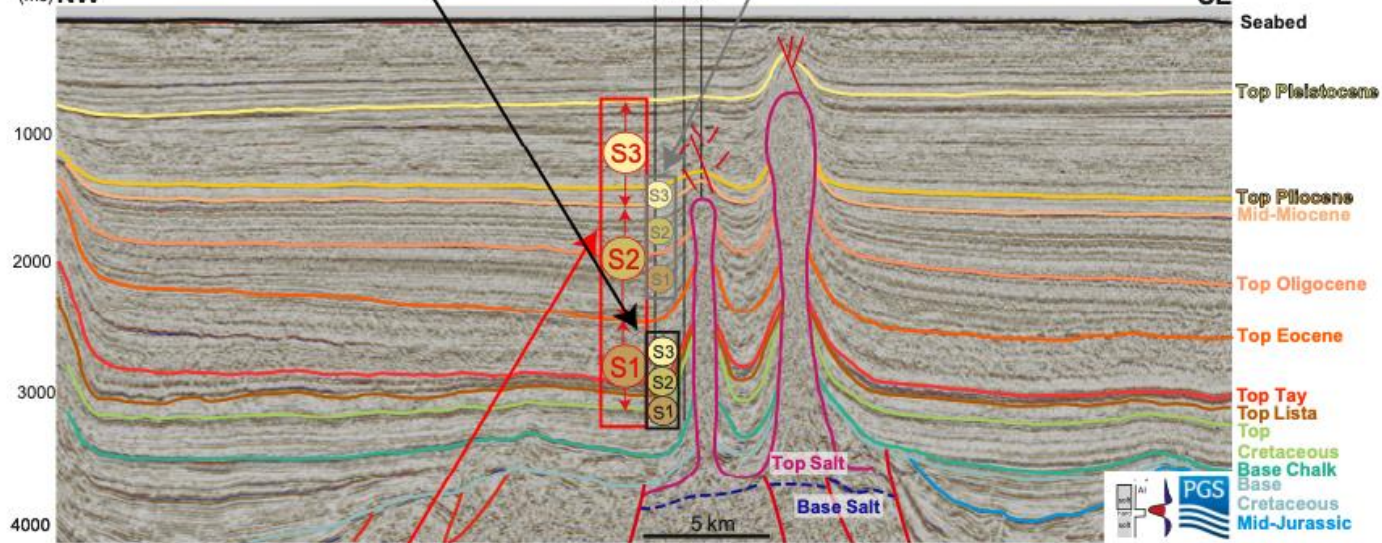
**A Slow Sedimentation (M2)**



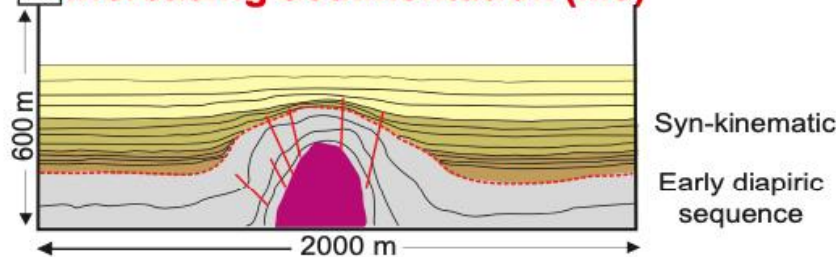
**B Intermediate Sedimentation (M3)**



**C**  
TWT (ms)  
NW



**D Increasing Sedimentation (M5)**



**Key for all models**

- Base of sediment
  - Fault
  - Salt
  - Overburden
  - Stage 1\*(S1, 2.2-3 Myr)
  - Stage 2\*(S2, 3-3.8 Myr)
  - Stage 3\*(S3, 3.8-4.6 Myr)
- \*Text and outline coloured by model*

**Figure 4.14:** *Subsurface example of model application comparing some of the modelled results to stratigraphy from the Pierce Field, Eastern Central Graben, UK North Sea. A, B and D) Models 2, 3 and 5 which are analogous to different parts of the stratigraphy around the Pierce diapirs. C) Interpreted time-migrated seismic profile across the Pierce diapirs. S1, S2, S3 highlight the likely sequences for comparison to models. The colour of the text represents which model those packages could represent (e.g., red represents M5). The location of the undeformed, flank and crest stratigraphic locations used for thinning rate calculations are shown for north Pierce, and are the same spacing as those used for model calculations (Figure 4.7; Table 4.3). Thinning values are calculated in Supplementary Table 2 (Appendix B). Seismic data courtesy of PGS (MegaSurvey Plus 3D seismic data) from Cumberpatch et al. (2021c).*

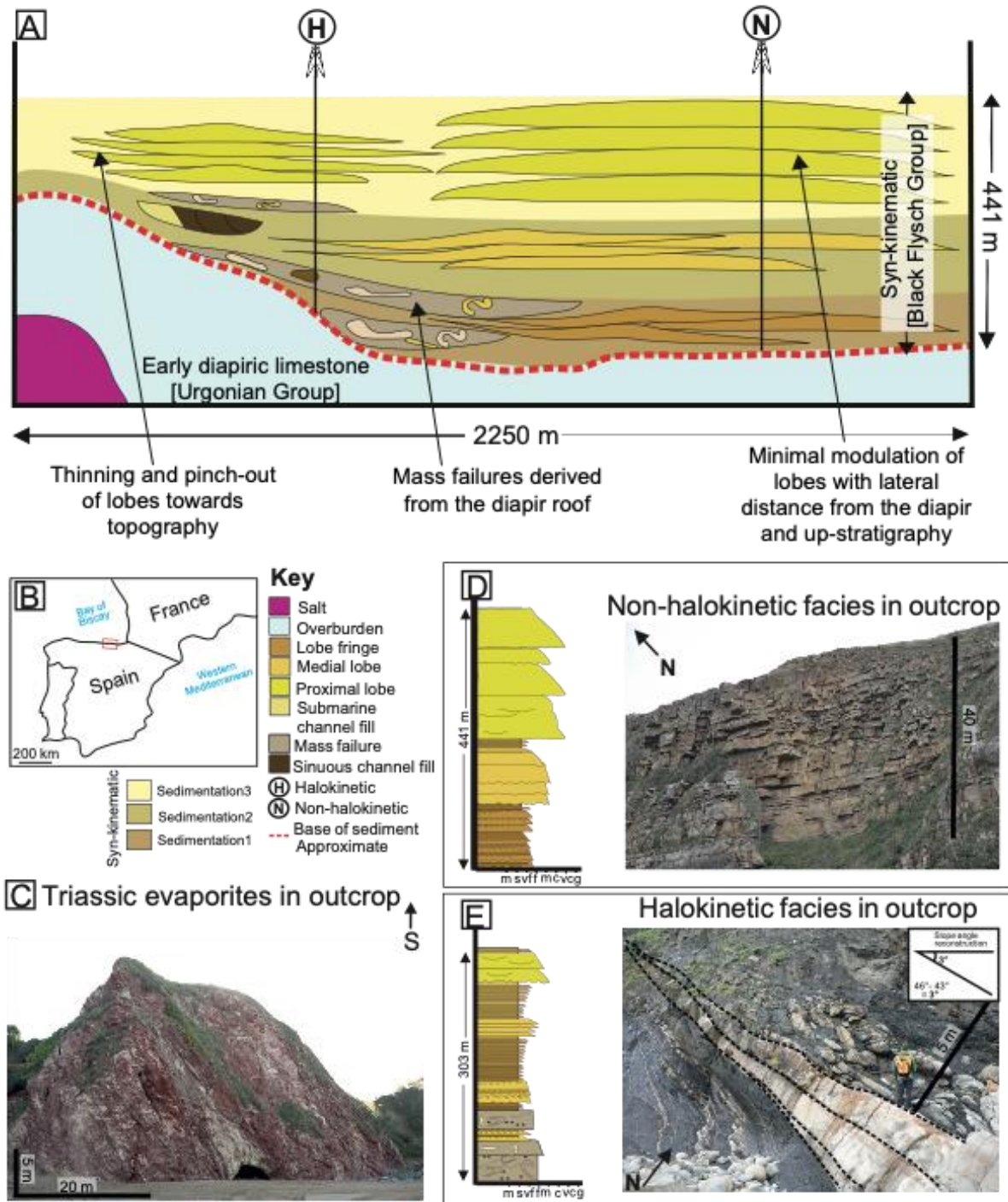
**Comparison to outcrop: stratigraphy around the Bakio diapir, northern Spain:** The model simulations presented here document stratigraphic architectures and structural deformation, but do not invoke a specific sedimentary environment. Different compositions (e.g., carbonate or siliciclastic) and sedimentary environments (e.g., fluvial or deep-water) will respond differently to salt influence (Adams and Kenter 2012). In our models, slow sedimentation (M2) leads to the natural exposure of the early-diapiric sequence above the diapir in the absence of a syn-kinematic cover or roof (Figure 4.7). This is likely to be common in marginal marine or terrestrial environments where the crest is often documented to be exposed, eroded and reworked into the syn-kinematic succession (Giles and Rowan 2012; Banham and Mountney 2013 a; b; 2014; Ribes et al. 2015; 2017; Counts and Amos 2016; Counts et al. 2019). As long as accommodation is available (i.e., below sea level) in deep-water environments there will almost always be a pelagic drape across the crest of the diapir, while sandstones remain limited to the flanks (Rowan et al. 2003; Giles and Rowan 2012; Poprawski et al. 2014; 2016; Cumberpatch et al. 2021b). Our models are applicable to all depositional environments, but fundamental controls on depositional architecture (accommodation, sedimentary processes) must not be overlooked. Below, we compare the observations of M5 (increasing sedimentation) to a well-exposed halokinetically-influenced deep-water succession, and describe how integrating DEM results with outcropping examples can help reduce uncertainty in subsurface energy reservoir prediction.

Exposed Aptian-Cenomanian strata adjacent to the Bakio Diapir, northern Spain document an increase in sedimentation rate associated with an increase in erosion of the hinterland (Figure 4.15; García-Mondéjar 1996; Martín-Chivelet et al. 2002; Puelles et al. 2014), similar to M5 increasing from ‘slow’ to ‘fast’ relative sedimentation (Figures 4.8 and 4.12D). The resulting progradational pattern manifests in the deep-water succession as an upward change from thin-bedded low-density turbidites, deposited in the lobe fringe, (equivalent to S1) to thick-bedded high-density turbidites deposited in a lobe axis (equivalent to S3) (Cumberpatch et al. 2021b). Early diapiric (the Urgonian Group: Figure 4.15) and syn-kinematic (the Black Flysch Group) depositional elements are deformed closest to the diapir, and deformation intensity decreases away from the diapir, being minimal outside the halokinetically-influenced sequence (~700 m wide either side at Bakio); this observation is consistent with the predictions of our model (Figures 4.8 and 4.15). Outside the zone of halokinetic deformation, strata look similar to those deposited in an unconfined, salt-free setting, in terms of their architecture and facies distributions (e.g., Prélat et al. 2009: Figure 4.15D).

The Aptian-Albian is initially isolated either side of the diapir, representing relatively slow sedimentation rates with respect to diapir growth. Individual thin beds representing distal deposition are observed to thin (by up to 1%/m; Figure 4.15E) and pinch out towards the salt-cored topographic high, in accordance with layers A-D in the increasing sedimentation model (S1, Figure 4.15) or the entirety of the slow sedimentation model (M2) (Cumberpatch et al. 2021b;c). At Bakio, different sediment routing systems develop when stratigraphy is restricted to either side of the diapir due to varying controls on deposition (Cumberpatch et al. 2021b). Under increasing sedimentation rates, the Albian-Cenomanian (Black Flysch Group: Figure 4.15) stratigraphy is laterally extensive, representing ‘intermediate’ sedimentation conditions in our model (S2 in M5 and the entirety of M3), but in nature both representing an increased sediment supply from the Landes

Massif (García-Mondéjar 1996; Martín-Chivelet et al. 2002; Puelles et al. 2014) and a reduction in salt rise rate (Poprawski et al. 2014; 2016; Roca et al. 2021). In the field, this stratigraphy shows a reduction in the numbers of mass transport deposits (MTD) upwards, which cannot be resolved in the models, but can be compared to the decrease in stratigraphic dip upwards (from 12° to 2° between layer E and I, Figure 4.11), reducing instability. The lower Black Flysch stratigraphy show a reduction in halokinetic deformation and thinning rate upwards (S2) that is comparable to modelled results, where thinning rates decrease from 0.053 – 0.006%/m through time. Eventual deposition of the upper Black Flysch Group, across the diapir, akin to relatively ‘fast sedimentation’ in our model (S3 in M5 or the entirety of M4) heals the remnant diapiric topography, and shows almost no halokinetic influence (in similarity to layers I-L in the increasing sedimentation model), except for its depositional location within remnant diapiric topography (Cumberpatch et al. 2021c). The relative increase in sedimentation rate at Bakio is driven primarily by an increase in sedimentation supply due to the uplifting source area, which is comparable to M5. However, a coeval reduction of salt supply due to welding between the Bakio and Guernica diapirs cannot be ruled out (Poprawski et al. 2014; 2016; Cumberpatch et al. 2021b; Roca et al. 2021).

In the syn-kinematic stratigraphy, particularly those equivalent to S2 in M5, thick-bedded sandstones deposited in channels and lobes dominate topographic lows, where sedimentary flows were focussed around salt-cored topographic relief (Figure 4.15D; Mayall et al. 2010; Sylvester et al. 2012; Doughty-Jones et al. 2017; 2019; Rodriguez et al. 2020). Towards the highs, the lower-density part of the flows may run-up topography depositing thinly-bedded muddier sandstones towards the pinch out (Figure 4.15E; Kneller and McCaffrey 1999; Soutter et al. 2019). At Bakio, crestal deposition is assumed to be limited to a thin pelagic drape during S1 and much of S2 due to elevation, which is comparable to M5, often leading to remobilisation and the formation of MTDs. MTDs are not explicitly modelled in the models, showing the importance of combining facies information from field observations with stratigraphic architecture and thinning rates from models. During S3 halokinetic bathymetry is healed, and crestal deposition is extensive, with minimal modulation (the upper Black Flysch Group).



**Figure 4.15:** Conceptual facies diagram for a deep-water succession based on integration of field-based facies analysis around the Bakio diapir, Basque Cantabrian Basin Northern Spain (see *Cumberpatch et al. 2021b* for summary), overlain onto the result of M5. A) Interpretation for deep-water facies (based on field facies analysis) overlain on the upper part of the increasing sedimentation model (located on Figure 4.8). Syn-kinematic layers from the model are grouped (S1-S3) and coloured and depositional elements derived from field studies are overlain to show facies variability. H and N are theoretical stratigraphic profiles in the halokinetically-influenced and non-halokinetically-influenced zones respectively. B) Location map of the field analogue, for a full geological discussion see *Cumberpatch et al. in 2021b* (Chapter 3). C) Outcropping Triassic evaporites on Bakio Beach, believed to be part of the Bakio Diapir. D) Non-halokinetic succession showing a classic progradational deep-water system (controlled by allogenic and autogenic processes), accompanied by an example of non-halokinetically influenced strata from the field. E) Halokinetic stratigraphic profile showing a thinner, modulated succession which is rich in MTDs, accompanied by a field analogue of an outcrop-scale bed pinch-out and an overlying MTD.

### ***Implications for subsurface energy***

Despite advances in extent and resolution of 3D seismic reflection imaging, the salt-sediment interface remains difficult to image, yet determining its position and precise geometry is crucial in helping to appraise stratigraphic-structural traps for hydrocarbon, carbon storage, and geothermal prospects globally (Jones and Davison 2014; Warren 2016). Utilising outcrop analogues (Figure 4.15) can help provide sub-seismic scale depositional facies information, helping reduce uncertainty in reservoir quality and distribution. Numerical modelling results do not represent specific analogue conditions nor a ‘snapshot’ in time, and they can therefore help to quickly identify generic depositional architectures, deformation patterns and sediment thickness relationships as a function of several forcing parameters, such as variations in sedimentation rates.

Using stratigraphic architectures from our DEM and sedimentological data from field examples, we can improve predictions of the likely architecture of syn-kinematic stratigraphy and sedimentology around salt structures, which are poorly-imaged in seismic reflection data. Understanding this requires a multi-scalar and multi-technique approach. For example, models provide details about gross thickness changes and geometry, whereas field analogues enable inferences about reservoir quality and net-to-gross.

**Depositional reservoir quality:** Regardless of the amount of sedimentation, our models show that stratigraphy thins as it approaches the diapir, suggesting a reduction in the amount of net reservoir close to the structure (Figure 4.11; Jackson and Hudec 2017). Siliciclastic depositional environments show a thinning of sandstone towards the topographic high and an overall concentration of units with high porosity and permeability at the base of topography (Figures 4.15A and 4.15D), such that a salt-related combined structural-stratigraphic trapping mechanism becomes unlikely (Figure 4.16; Kane et al. 2012; Stricker et al. 2018). Muddier (lower reservoir quality) and thinner (lower net-to-gross) units are expected closer to the diapir (Figures 4.11 and 4.14-4.16); Banham and Mountney 2013; Cumberpatch et al. 2021b). These units are more likely to be over-pressured due to upward rotation, creating a large pressure head, with the topseal rocks unable to hold back a significant hydrocarbon column (Figure 4.15; Nikolinakou et al. 2014a; b; 2018; Heidari et al. 2017; 2019). In carbonate environments, shallow platform or reef facies which may have excellent reservoir potential are often present over salt highs (e.g., Riding 2002; Burgess et al. 2013; Teixell et al. 2017). As salt growth continues, fractures are generated in the overburden, which could form significant secondary porosity within the carbonate reservoirs, increasing quality and producibility (He et al. 2014; Howarth and Alves 2016; Saura et al. 2016).

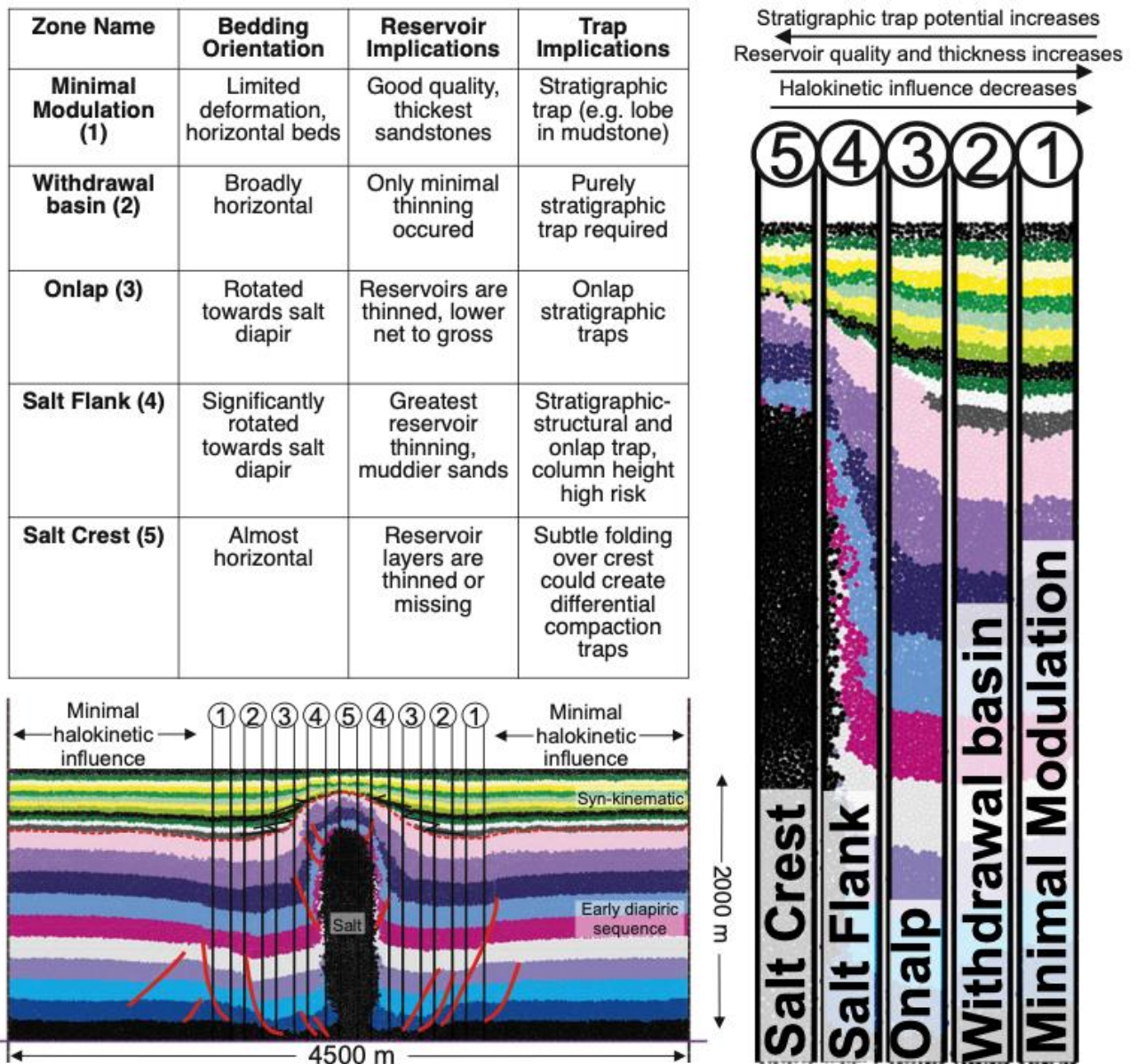
Supplementing subsurface data with modelled stratal architectures and depositional facies observations from exhumed halokinetically influenced settings globally (e.g., Banham and Mountney 2013a; 2013b; 2014; Poprawski et al. 2014; 2016; Counts and Amos 2016; Ribes et al. 2015; 2017; Counts et al. 2019; Cumberpatch et al. 2021b) is recommended as a useful workflow for building reservoir models for salt basins with limited data. Observations from multiple scales and types of models can be combined to further reduce the uncertainty associated with reservoir quality prediction, for example recent finite element modelling (FEM) has shown porosity is lower than expected near the vertical parts of salt structures and higher than expected at the base of diapirs, due to mean principal stress variations (Nikolinakou et al. 2014).

**Halokinetic zonation:** Model results show that a deformation zone exists either side of the diapir in all experiments (Figure 4.6-8). Outside of this zone, the syn-kinematic and early diapiric stratigraphy are undeformed (Figure 4.16). The extent of this salt withdrawal basin is 1150 m on either side of the diapir (2300 m in total). Therefore, the total zone of halokinetic influence in all models is approximately three times the original diapirs’ maximum width (750 m), with a deformed zone of 1.5 diapir widths either side of the structure. The width of the deformation zone is comparable

across all models (Figure 4.10), and therefore it is shown that sedimentation rate is unlikely to have a significant control on the width of the zone of halokinetic influence (Giles and Rowan 2012; Hearon et al. 2014). Other factors such as salt supply, salt viscosity, and style and magnitude of regional tectonics (which are not modelled) will in nature, influence the width of the halokinetically deformed zone (Koyi 1998; Fuchs et al. 2011). The model can be further divided into zones based on onlap geometry and thinning rates, which highlight the ‘trade off’ between reservoir thickness and stratigraphic trap potential in subsurface plays (Figure 4.16). In flank locations, bedding dips and thinning rates are shown to be greater under slower sedimentation rates compared to higher ones (Figure 4.11; Table 4.3), which is important when predicting hydrocarbon column height. Significant overpressures on reservoirs below can be created by fast sedimentation rates (Figure 4.16; Peeters et al. 2018).

**Fault distribution:** Radial faults associated with salt diapirs are shown to cause compartmentalisation of reservoirs (Birch and Haynes 2003; Scott et al. 2010; Charles and Ryzhikov 2015; Peeters et al. 2018; Coleman et al. 2018). Our DEM replicates localised fault growth, evolution and propagation because the contacts between elements are treated as potential displacement surfaces. Our models all document a similar fault pattern, suggesting that faulting, and therefore fault compartmentalisation is not heavily influenced by sedimentation rate. However, sediment composition (e.g., sandstone versus mudstone, not modelled here) will influence structural compartmentalisation (Coleman et al. 2018). As well as seismically resolvable faults, outcrop and borehole data indicate brittle deformation is significant in salt basins (e.g., Koestler and Ehrmann 1991; Cumberpatch et al. 2021b). Our DEM replicates this brittle deformation (Figures 4.6-4.8); as in nature, extreme thinning, and termination of layers is in part accommodated by small-scale displacements. Understanding sub-seismic scale fault distribution is important for predicting reservoir compartmentalisation and seal integrity in the subsurface. Faults, when sealing, could act as lateral permeability barriers, especially if the faults and surrounding reservoir rocks become cemented with salt and salt-related breccia (Van Bergen and de Leeuw 2001; Li et al. 2017). DEM is therefore advantageous in predicting potential traps, conduits and baffles, due to its replication of diapir-related brittle deformation.

### Example of Halokinetic Zonation (M3)



**Figure 4.16:** Halokinetic zonation scheme shown for M3. The model is divided into 5 zones, 4 of which experience some form of halokinetic influence. Minimal deformation zones 1 and all stratigraphy outside of it show virtually no modulation by salt diapirism. Halokinetic influence increases towards the diapir-cored high, and changes from minor thickness changes in the 'withdrawal basin' zone to onlap and abrupt pinch out in the 'onlap' and 'salt flank' zones. Thinned and reduced stratigraphy are observed over the diapirs crest. The table highlights that while stratigraphic trap quality may be greater closer to the diapir, reservoir thickness and quality are likely higher further from the diapir, showing a 'trade-off' exists for subsurface energy exploration and production. Similar zonation is possible for all models.

#### 4.8 Future work

The DEM presented here is useful for predicting local trends around diapirs and studying generic interactions of salt structures and stratigraphy, but further work is required to recreate specific complicated salt geometries. Other suggestions for further development of this model are to incorporate reactivation and cessation of halokinesis, studying the impact on stratigraphic architectures and the development of halokinetic unconformities, due to periods of diapiric rejuvenation, uplift, erosion and non-deposition. Incorporating erosion and remobilisation into the model would also more realistically represent natural settings where entrainment and failure influences thickness patterns, stratigraphic architectures and can remove the diapiric roof. Another line of enquiry

would be to study salt geometry evolution under different salt thicknesses. In nature, salt diapirs are rarely isolated structures, and therefore subsequent studies will focus on the interaction of multiple salt structures, with numerous growth histories on varied sedimentary successions. Many of the limitations of the model, are due to its two-dimensional nature. The ultimate aim of future work is developing a three-dimensional DEM to better understand the four-dimensional variability in halokinetically-influenced stratigraphy and associated subsurface energy reservoirs.

#### **4.9 Conclusions**

Discrete element modelling (DEM) can form an integral part of the workflow when studying salt-sediment interactions. Here, a DEM is used to study the variability in stratigraphic architecture and deformation patterns around a growing salt structure under different sedimentation rates. This work has shown that:

- 1) A DEM approach can be employed to test different scenarios for the development of halokinetic stratigraphy and fault patterns.
- 2) The models generate realistic salt-related faults. In all models, structural deformation and extent of halokinetic influence are similar, and syn-kinematic strata, at least initially, are isolated to either side of the diapir, thinning and onlapping towards the high. Laterally, we observe a zone of 1150 m to either side of the diapir that is influenced by halokinesis, and beyond this zone, strata are undeformed.
- 3) Under slow sedimentation rate (M2) deposition is restricted to salt withdrawal basins either side of the diapir throughout evolution, while in M3-M6 sedimentation eventually occurs over the diapir crest, often associated with significant lateral thickness variability. Diapir growth is most inhibited under fast aggradation (M4) and the halokinetic influence on stratigraphy reduces quickly with time.
- 4) Thinning of syn-kinematic stratigraphy from the undeformed section to the diapir flanks, is greatest under slow aggradation (M2, 34%), and least under fast aggradation (M4, 12%). In all models, thinning is about six times greater between the salt flank and crest, compared to the undeformed section and the salt flank, indicating more intense deformation close to the diapir.
- 5) Thinning rate decreases through time (up stratigraphy), showing a reduction of halokinetic modulation with increased sediment thickness, as halokinetic bathymetry is 'healed'. This is true for all models except for decreasing sedimentation (M6), which experiences a slight increase up stratigraphy.
- 6) Our simplified two-dimensional models provide useful analogues for salt-influenced basins with complicated four-dimensional evolutions. Natural examples record the interplay between sedimentation rate and diapir rise rate, whilst models isolate and vary sedimentation rate. Comparison to the Pierce field diapirs, North Sea, shows how different models can be applicable to distinct parts of stratigraphy and suggest how interpreters could infer likely sedimentation rates and conditions from subsurface stratigraphic geometries.
- 7) Facies, and thus reservoir distribution, around salt diapirs will vary from unconfined settings due to halokinetic modulation, both vertically and laterally. A deep-water analogue from stratigraphy adjacent to the Bakio diapir, shows that halokinetically influenced facies (e.g., the salt flank) contain thin beds, sandstone pinch-outs and increased mass transport deposits in comparison with the allogenic deposits (e.g., the undeformed zone), which are difficult to decipher from deep-water strata in non-salt influenced settings.
- 8) Integrating DEM with subsurface and outcrop data helps to reduce reservoir and trap uncertainty in subsurface energy exploration and development.



## Chapter 5: How confined is confined? An investigation into the effect of diapir-induced topographic spacing on deep-water sediment dispersal in the Paleocene Eastern Central Graben (ECG), UK

Zoë A. Cumberpatch<sup>1</sup>, Ben A. Kilhams<sup>2</sup>, Ian A. Kane<sup>1</sup>, Emma Finch<sup>1</sup>, Christopher A-L. Jackson<sup>1</sup>, David M. Hogdson<sup>3</sup>, Mads Huuse<sup>1</sup> and Ross J. Grant<sup>4</sup>

<sup>1</sup>*Department of Earth and Environmental Sciences, University of Manchester, Oxford Road, Manchester M13 9PL*

<sup>2</sup>*Shell Upstream International, York Road, London, UK*

<sup>3</sup>*The Stratigraphy Group, School of Earth and Environment, University of Leeds, Leeds, LS2 9JT*

<sup>4</sup>*Equinor ASA, Margrethe Jørgensens vei 4, 9406 Harstad, Norway*

**Status:** In preparation for submission to *Petroleum Geoscience*

### 5.1 Abstract

The influence of salt tectonics on deep-water depositional systems remains challenging to study. We use data from the Eastern Central Graben, UK, and numerical modelling, to study stratigraphic modulation by variably-spaced salt diapirs. Depositional facies are controlled by the amount, type and spacing of diapiric, and overarching graben topography. We use 11 natural (1000-15000 m) and six modelled (1500-9000 m) variably spaced diapirs to show that stratigraphy associated with closely-spaced diapirs (<3000 m) is deformed between them. In widely-spaced diapirs (>3000 m), a flat, plateau-like zone is developed between the deformation zones, where halokinetic-modulation is reduced. Modelled stratigraphy experiencing no deformation is a simplification of natural examples which are likely to be influenced by subtle topography (e.g., non-piercing diapirs). Salt-influence on stratigraphy typically decreases temporally following active growth, and spatially away from the diapirs towards a zone of ‘minimal deformation’, unless the diapirs are closely-spaced where there is no minimal deformation zone. Here, the zone between is subject to deformation. Diapir spacing controls the presence, extent and width of the minimal modulation zone between the salt diapirs, suggesting that for subsurface energy prospects between closely-spaced diapirs, combined stratigraphic-structural trap potential is probable, but reservoirs may be laterally-confined, whilst between widely-spaced diapirs, reservoirs may be extensive, but trapping mechanisms may be limited. Prospects may be influenced by subtle salt-related topography 10s of kilometres away from diapirs.

### 5.2 Introduction

Many of the world’s largest petroleum producing provinces are located within basins whose fills are deformed by salt-tectonics (e.g., Ziegler 1992; Coward and Stewart 1995; Davison et al. 2000; Booth et al. 2003; Oluboyo et al. 2014; Charles and Ryzhikov 2015; Stewart 2017; Rodriguez et al. 2018, 2020; Grant et al. 2019a, 2019b, 2020; Pichel et al. 2020). Recently salt basins have become attractive prospects for carbon and hydrogen storage (e.g., Maia de Costa et al. 2018; Roelofse et al. 2019; Lloyd et al. 2021) and geothermal energy (e.g., Harms 2015; Daniilidis and Herber 2017; Andrews et al. 2020).

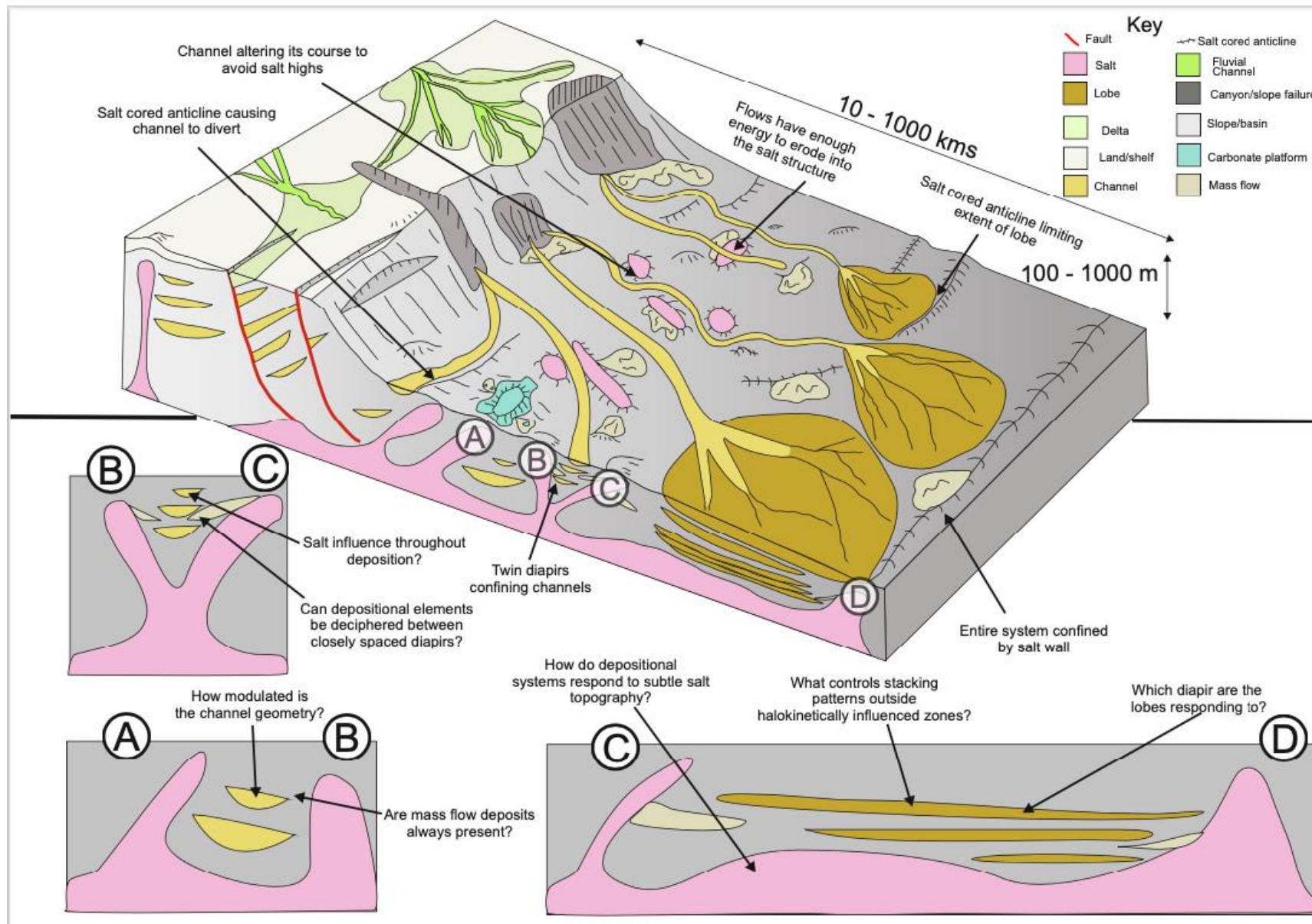
Subsurface studies have shown that salt structures that deform the seafloor can exert substantial control on the location, pathway, and architecture of deep-water depositional elements including: lobe, channel-fill, levee, and mass-transport deposits (Figure 5.1: e.g., Mayall et al. 2006, 2010; Jones et al. 2012; Doughty-Jones et al. 2017;2019; Wu et al. 2020; Howlett et al. 2020). Sediment gravity flow deposits ponded, diverted, deflected, and confined by salt structures (Figure 5.1) are well documented in the eastern Mediterranean (e.g. Clark and Cartwright 2009; 2011), offshore Angola (e.g. Gee and Gawthorpe 2006; 2007; Howlett et al. 2020), the Gulf of Mexico (e.g. Booth

et al. 2003), offshore Brazil (e.g. Rodriguez et al. 2018, 2020), the North Sea (e.g. Davison et al. 2000; Kilhams et al. 2012; 2014; 2015; Mannie et al. 2014) and the Precaspian Basin (e.g. Pichel and Jackson 2020).

Salt-influenced successions are often poorly-imaged in seismic reflection data due to ray path distortion at the salt-sediment interface, steep stratigraphic dips, and deformation associated with salt rise (Davison et al. 2000; Jones and Davison 2014). These complications mean that subsurface salt-influenced systems benefit from calibration to outcrop analogues (Lerche and Petersen 1995; Kernén et al. 2012; 2018; Poprawski et al. 2014; 2016; Counts et al. 2019; Cumberpatch et al. 2021b), numerical models (e.g., Fuchs et al. 2011; Weijermars et al. 2015; Pichel et al. 2017; 2019; Fernandez et al. 2020; Cumberpatch et al. 2021c; 2021d) and physical models (Dooley et al. 2005; 2007; Ferrer et al. 2012; 2017; Soutter et al. 2021). Unfortunately, outcrops are often incomplete and models simplified. Therefore, deciphering the controls on sediment distribution (e.g., halokinetic versus allocyclic) remains challenging without good control on the regional tectono-stratigraphic evolution (Doughty-Jones et al. 2019).

The lateral influence of salt diapirism on deep water sedimentation is poorly understood. Sedimentation immediately adjacent to salt topography (within 1500 m), has been shown to respond to salt movement (Giles and Rowan 2012; Banham and Mountney 2013a; b; 2014; Ribes et al. 2015; Cumberpatch et al. 2021b). Between closely-spaced (~1000 m apart) rising diapirs, such as the Pierce Diapirs in the UK North Sea, stratigraphy is clearly deformed (Birch and Haynes 2003; Scott et al. 2010; Hale et al. 2020). Between two wider-spaced diapirs, a central zone where depositional systems experience lower halokinetic influence has been observed (Mayall et al. 2010; Oluboyo et al. 2014; Doughty-Jones et al. 2017). When diapirs are ~10000 m apart, the stratigraphy between is more strongly influenced by other factors (faulting, original salt geometry etc.) rather than diapir growth, shown in the southwestern Lower Congo Basin, offshore Angola (Oluboyo et al. 2014). Questions remain about how diapir spacing and morphology influences the geometry of depositional systems and how depositional systems respond to subtle topography between salt structures (Figure 5.1). In the Central North Sea, and other salt basins globally, improved understanding of the lateral spacing of diapirs relative to depositional systems is essential for reservoir prediction and production, for example, in order to efficiently sweep hydrocarbon fields (Charles and Ryzhikov 2015) or to understand capacity and containment for carbon sequestration.

This study uses a wealth of subsurface data from the well-studied salt-influenced Paleocene basin floor system in the Eastern Central Graben (ECG) of the UK North Sea, to study deep-water facies and architecture distribution around diapirs, and the effects of lateral spacing of salt diapirs on halokinetic modulation of stratigraphy. The aim of this study is to aid prediction of reservoir architecture in subsurface energy production and carbon sequestration. As such, the objectives of this study are to: 1) analyse salt-influenced deep-water facies and characterise their distribution in terms of halokinetic or allocyclic influences; 2) compare stratigraphic architectures between variably-spaced salt structures; 3) describe the extent of halokinetically-modified stratigraphy between different distances of confinement. To achieve these objectives, we firstly use an integrated multi-scalar dataset to study the distribution and controls on the distribution of facies and architectures around salt diapirs. Secondly, we compare the modification of deep-water stratigraphy between variably spaced diapirs in the subsurface to the results of a simple two-dimensional discrete element model (DEM).



**Figure 5.1:** Sketch summarising the structural controls, with respect to gravity-driven processes, on depositional systems from the shelf to the basins floor (modified from Mayall et al. 2010; redrawn from Cumberpatch et al. 2021 b). A, B, C and D are salt structures, which are spaced at different distances from each other, creating variable geometrical configurations and basin fill. Sketches highlight some of the key uncertainties related to topographic confinement of depositional systems, many of these are discussed within.

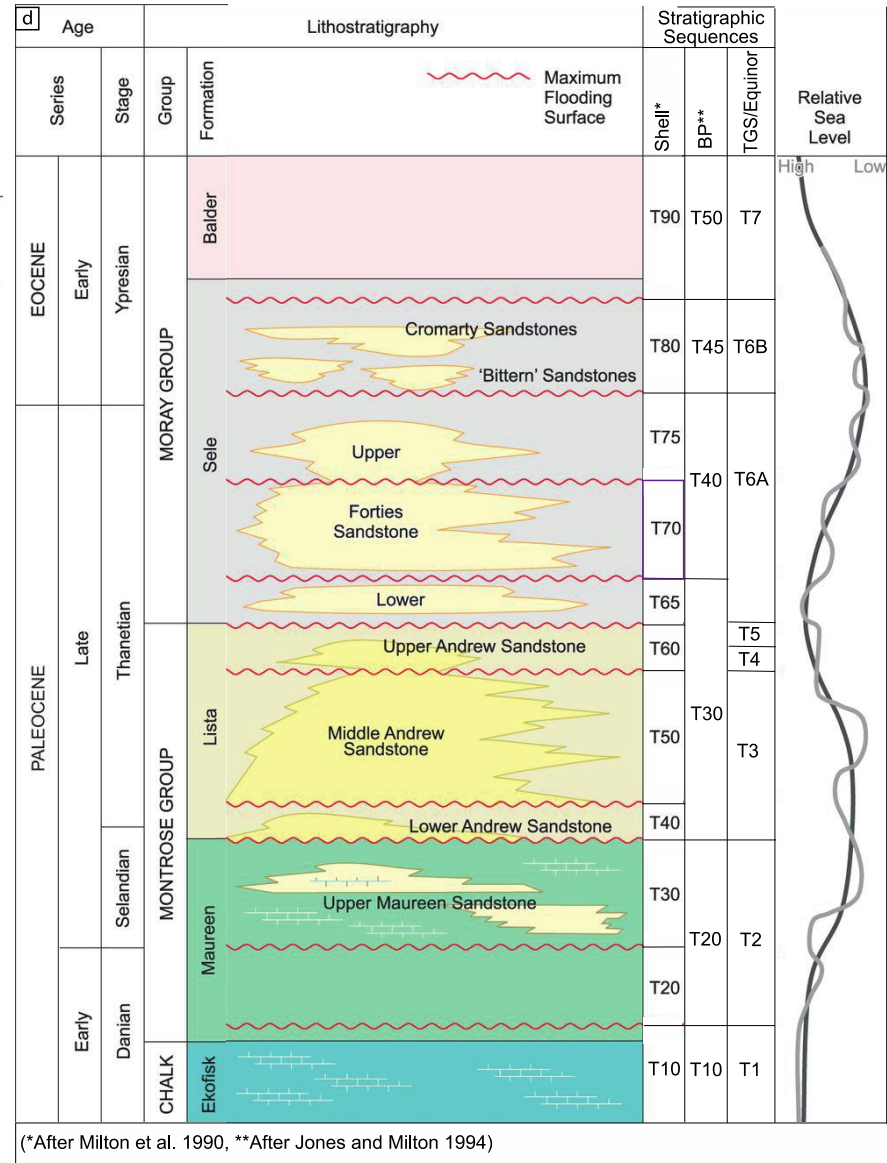
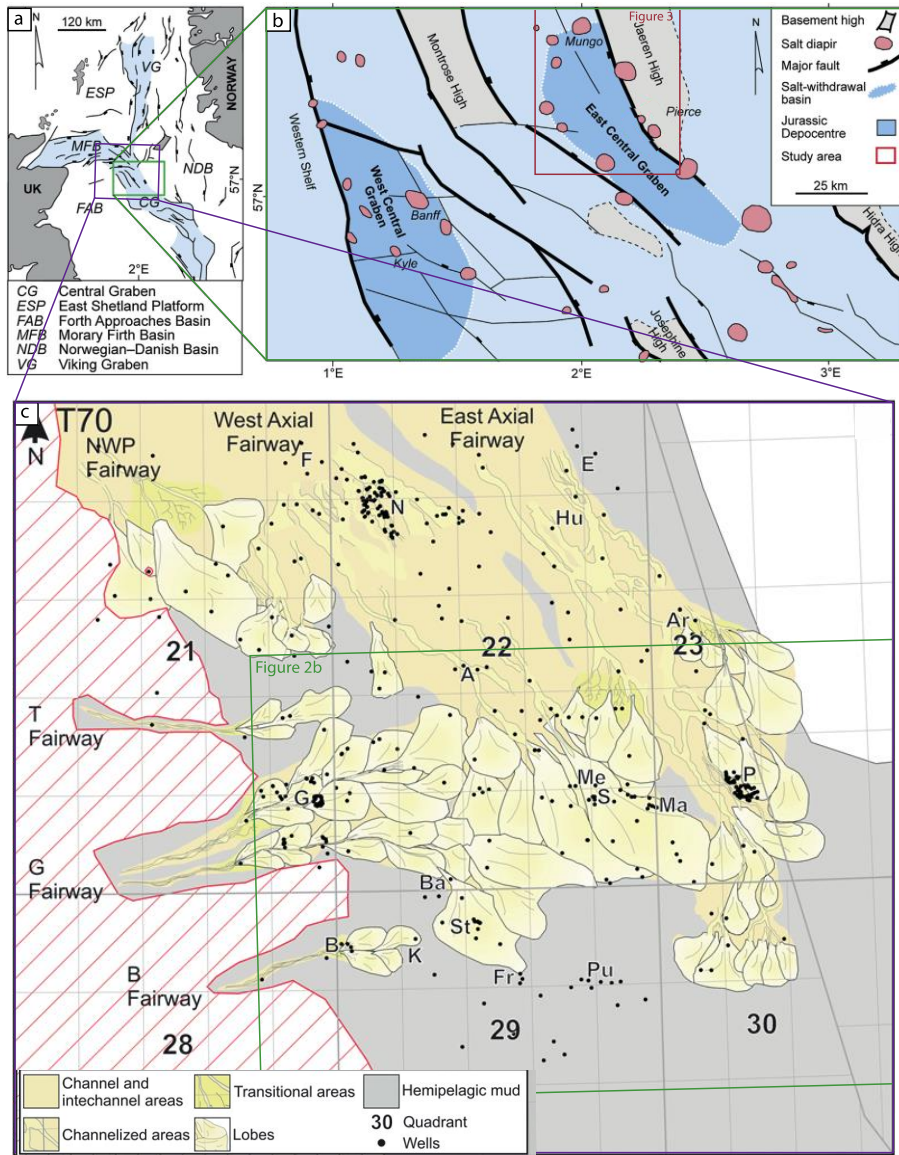
### 5.3 Geological Setting

#### ***Regional Geological Setting***

The case study area is located above the southern branch of the tri-partite North Sea rift system (Figure 5.2A; Glennie 1995), covers UK hydrocarbon quadrants 22 and 23, and includes the North Pierce, South Pierce, Mungo, Monan, Mirren, Machar, Merganser and Scoter salt structures. It is located in the Eastern Central Graben (ECG), and bound by the NNW-SSE trending boundary faults of the Jæren High to the East and the Forties Montrose High to the West (Figure 5.2; Birch and Haynes 2003; Scott et al. 2010; Hale et al. 2020).

The structure and evolution of the ECG is well documented (Hodgson et al. 1992; Erratt et al. 1999; Davison et al. 2000; Charles and Ryzhikov 2015). Halokinesis, in response to polyphase (Triassic-Jurassic) rifting and Cretaceous-Paleocene sediment loading, has been a key control on the grabens' development since the Middle Triassic (Davison et al. 2000; Charles and Ryzhikov 2015). During the Late Permian, 2000-3000 m of Zechstein salt accumulated in the basin depocentre (Davison et al. 2000). Gravitational loading from Late Permian – Early Triassic siliciclastic sedimentation, combined with regional extension, triggered movement of the Zechstein salt and formation of salt walls, and many other salt structures, within the ECG (Hodgson et al. 1992; Carruthers et al. 2013; Charles and Ryzhikov 2015). These salt structures ultimately became hydrocarbon traps for the fields used in this study. An Upper Jurassic period of major extension re-initiated halokinesis and salt ridge growth along the faults bounding Jurassic basins, strongly influencing syn-rift Mesozoic sedimentation (Erratt 1993; Hoiland et al. 1993; Rattey and Hayward 1993; Grant et al. 2019a; 2019b; 2020).

Thermal subsidence during the Late Jurassic-Cretaceous, along with sediment loading led to the formation of km-scale circular diapirs running parallel to basinal faults (including the Pierce diapirs on the Jaeren High and the Machar, Scoter, Merganser and Mirren diapirs on the Erskine Ridge, south of the Forties Montrose High; Figure 5.2B). During the Cretaceous and into the Cenozoic, diapirs that remained connected to the main salt reservoirs continued to grow passively, driven by further sediment loading. A buoyancy equilibrium formed until the mid-Miocene when Alpine-related inversion and compression led to late active growth in many of the Central Graben diapirs (Oakman and Partington 1984; Evans et al. 1993; Davison et al. 2000; Charles and Ryzhikov 2015). Most salt diapirs stopped growing, and became welded, in the late Miocene following a reduction in salt supply (Davison et al. 2000; Carruthers et al. 2013).



**Figure 5.2:** A) Tectonic framework of the North Sea rift system, B) Structural map of the Central Graben showing distribution of salt diapirs related to major basin faults and Jurassic salt-withdrawal basins (Carruthers et al. 2013), red box highlights location of Figure 5.3, most northern part of Figure 5.3 not shown. C) Summary map of the gross depositional setting showing the distribution of the Sele T70 fan systems within the UK sector of the North Sea from Eldrett et al. (2015). The extent of Figure 5.2b is highlighted. NWP, Northwest Platform; N, Nelson Field; F, Forties Field; E, Everest Field; A, Arbroath Field; Me, Merganser Field; Ma, Machar Field S, Scooter Field; St, Starling Field; G, Gannet Field; B, Bittern Field; Pu, Puffin Field; P, Pierce Field; K, Kyle Field; Fr, Fram Field; Hu, Huntington Field; Ar, Arran Field. D) Generalised stratigraphic framework for the Paleocene of the East Central Graben (Charles and Ryzhikov 2015). The lithostratigraphic nomenclature is consistent with that in Knox et al. (1981) and Mudge and Copestake (1992). The relative sea-level cycles highlight the lowstand submarine fan deposits and are modified after Den Hartog Jager et al. (1993) and Jennette et al. (2000). Stratigraphic 'T' surface frameworks of Shell (Milton et al. (1990)), BP (Jones and Milton 1994) and TGS/Equinor are compared. Purple box indicated the stratigraphic interval represented in C.

### **Palaeocene Stratigraphy**

The stratigraphy and sedimentology of the Central North Sea Paleocene basin floor fan systems have been described extensively (e.g., Den Hartog Jager et al. 1993; Jennette et al. 2000; Hempton et al. 2005; Kilhams et al. 2012; 2014; 2015; Eldrett et al. 2015). Siliciclastic sedimentation commenced in the study area during the Danian, which curtailed deposition of the Ekofisk chalk (Figure 5.2D). Paleocene-Eocene phases of uplift associated with the North Atlantic Igneous province shed siliciclastic sediments into the Central Graben during multiple lowstand systems tracts (Den Hartog Jager et al. 1993; Evans et al. 2003; Carruthers et al. 2013). These lowstands lasted ~1-2 Ma in duration and are represented by turbidite fan complexes overlain by highstand hemipelagic shale units (Figure 5.2D; Den Hartog Jager et al. 1993; Kilhams et al. 2012; 2014; 2015; Charles and Ryzhikov 2015).

The Palaeocene-Eocene succession contains several cycles of deep-water sedimentation, restricted laterally by the graben (Eldrett et al. 2015). These cycles have traditionally been lithostratigraphically divided into the Maureen, Lista and Sele Formations, and sequence stratigraphically into 'T-sequences' (Figure 5.2D; Milton et al. 1990; Mudge and Copestake 1992; Jones and Milton 1994; Den Hartog Jager et al. 1993; Jennette et al. 2000). The lowermost Maureen Formation makes up the lower Montrose Group, and lies stratigraphically above the Cretaceous-Danian (Ekofisk) Chalk (Figure 5.2D). The Maureen Formation is overlain by the Lista Formation and associated Mey (informally 'Andrew') Sandstone Member (56.8-59.8 Ma), also of the upper Montrose Group (Figure 5.2D; Den Hartog Jager et al. 1993; Jennette et al. 2000; Kilhams et al. 2015). The main reservoir interval across the Central Graben is the Upper Paleocene to Lower Eocene (56.8-45 Ma) Sele Formation, of the lower Moray Group, which includes the Forties Sandstone Member (Kilhams et al. 2014). The Sele Formation is overlain by the Balder Formation, which comprises thin successions of clays and volcanic tuffs (Figure 5.2D; Hempton et al. 2005).

The Sele Formation is dominated by a submarine fan system (the Forties Sandstone Member). The 'Forties fan' is a large-scale NW-SE trending fairway, characterised by anastomosing complexes of submarine channels and lobes that cover much of the Central Graben (Wills and Peattie 1990; Whyatt et al. 1991; Ahmadi et al. 2003; Hempton et al. 2005; Eldrett et al. 2015). Sandstone distribution patterns throughout the Palaeocene are complicated by the interaction of the axial 'side fans' sourced from the west (Hempton et al. 2005; Kilhams et al. 2014; Eldrett et al. 2015), which could extend as far east as Merganser and Scoter (Figure 5.2C; Charles and Ryzhikov 2015).

Reservoir thickness and net to gross are highly variable throughout the Paleocene, and across the Central Graben, although there is a clear proximal-to-distal trend in reservoir quality (Hempton et al. 2005; Kilhams et al. 2012; 2014; 2015). Core data reveal a comparable reduction in porosity and permeability from proximal to distal locations, which is attributed to the gradual reduction in grain size and increasing detrital clay content in more distal locations (Hempton et al. 2005; Kilhams et

al. 2012; 2014; 2015; Charles and Ryzhikov 2015). The Pierce diapirs (North and South Pierce) form the primary study area for facies analysis, and neighbouring diapirs (Mungo, Monan, Mirren, Merganser, Scoter and Machar) are used to study the effect of diapir spacing on depositional systems (Figure 5.3). All of these diapirs form salt-related traps for hydrocarbon accumulations with a primary reservoir in the Paleocene (Sayer et al. 2020; Freeman et al. 2020; Hale et al. 2020; Baniak et al. 2020). Charles and Ryzhikov (2015) demonstrated that detailed understanding of halokinetically-influenced reservoirs is important to efficiently sweep these fields. Below, we investigate how the presence of two salt structures, at variable distances, can further complicate reservoir distribution and architectures, and thus hydrocarbon recovery factors.

### ***Summary of hydrocarbon fields in the study area***

**The Pierce Field:** The stratigraphy and structural evolution of the Pierce Field (Figures 5.2 and 5.3), operated by Shell, has been studied by Birch and Haynes (2002), and more recently Scott et al. (2010), Carruthers et al. (2013) and Hale et al. (2020). The Pierce Field trap is formed by two salt diapirs, North and South Pierce. The field contains an estimated P50 of 472 million barrels of oil in place (Hale et al. 2020) stored within the Paleocene deep marine Forties Sandstone that is believed to abut against the diapir walls (Hale et al. 2020). Smaller volumes exist in the Ekofisk Formation. The Paleocene units are composed of a 300 m thick sequence of mounded, sand-rich, gravity-flow deposits of the Maureen and Lista Formations (Eldrett et al., 2015; Birch and Haynes 2003; Hempton et al., 2005; Davis et al., 2009) and turbidite deposits of the Forties Formation (Davis et al. 2009; Scott et al. 2010) (Figure 5.2), reflecting the distal location of Pierce along the depositional fairway (Figure 5.2C). Paleocene deposition in thin channel fairways around the eastern and western flanks of the Pierce Field, progressive onlap and thinning up-dip towards the diapir crests indicates that topographic relief of the diapirs had the ultimate control on sediment distribution (Birch and Haynes 2003).

**The Merganser and Scoter fields:** Merganser and Scoter (Figure 5.3) are both operated by Shell, as part of the Shearwater Field development (Freeman et al. 2020). The Merganser field consists of a normally-pressured proven gas-condensate column of 500 m, trapped in a structural attic on the flanks of a fully penetrating salt diapir. Gas and condensate are produced from a composite reservoir in deep marine sandstones of the Maureen, Lista and Sele formations (Charles and Ryzhikov 2015). The depositional provenance is from the NW, and facies analysis indicates proximal channels to distal lobe environments (Kilhams et al. 2012; Eldrett et al. 2015). A large salt overhang obscures the field and structural definition is challenging owing to poor seismic imaging. Poor imaging resulted in an underestimation of volumes, pre drill (Charles and Ryzhikov 2015). Field development plans estimated recovery of 100 billion cubic feet (bcf) gas (Charles and Ryzhikov 2015); to date 185 bcf have been produced (Freeman et al. (2020)).

The Scoter gas field is located nearby Merganser and as such has recently been reviewed by Freeman et al. (2020). Scoter was discovered in 1989, and comprises a 360 m thick Forties Sandstone reservoir, trapped in an anticline above the Scoter salt diapir. To date 280 bcf of gas has been recovered (Freeman et al. 2020).

**Machar, Mungo, Mirren and Monan fields:** Machar, Mungo, Monan and Mirren (Figures 5.2 and 5.3) are part of the Eastern Trough Area Project, an integrated development of nine different fields, also including Marnock, Madoes, Heron, Egret and Skua (Sayer et al. 2020; Baniak et al. 2020). All of the 'M' fields are operated by BP. These fields were not commercially viable for standalone developments due to their small scale, but their combined recoverable reserves (550 million barrels of oil equivalent to date) make production viable (Sayer et al. 2020).

The Machar field (Figure 5.3) was discovered in 1976, with a STOIIP of 500 million barrels (Sayer et al. 2020). The field comprises of a 1300 m light-oil column contained in steeply-dipping Cretaceous Chalk and Paleocene sandstones in the Maureen, Lista and Sele formations, trapped by a four-way dip-closing dome developed over a high-relief Zechstein salt diapir (Sayer et al. 2020). There is connection between the two reservoirs (Paleocene and Cretaceous) via faults and the field is managed as a single reservoir unit (Sayer et al. 2020). To date 120 million barrels of oil and 65 bcf of gas have been produced (Sayer et al. 2020).

Mungo (Figures 5.2 and 5.3) was discovered in 1989 and is a pierced, four-way dip closure against a salt diapir (Baniak et al. 2020) which reservoirs in Late Paleocene sandstones (Maureen, Lista and Sele formations) and early Cretaceous – Late Paleocene Chalk. The sandstones contain a 965 m light oil column, and overlying gas cap (Baniak et al. 2020). Mungo has an estimated 440 million barrels oil and 585 bcf gas in place, having produced 176 million barrels oil and 163 bcf gas to date (Baniak et al. 2020).

Eastern Trough Area Project fields are sourced by Jurassic source rocks, principally the Kimmeridge clay (Baird 1986). Monan is a small oil and gas field which reservoirs in Paleocene turbidites associated with a salt diapir, and was first discovered in 1990 (Goffey et al. 2020). Mirren is a small field with oil reserves of 13 million barrels and 57 bcf gas, which reservoirs in Paleocene sandstone (Goffey et al. 2020).

#### **5.4 Methods and data**

##### ***Subsurface***

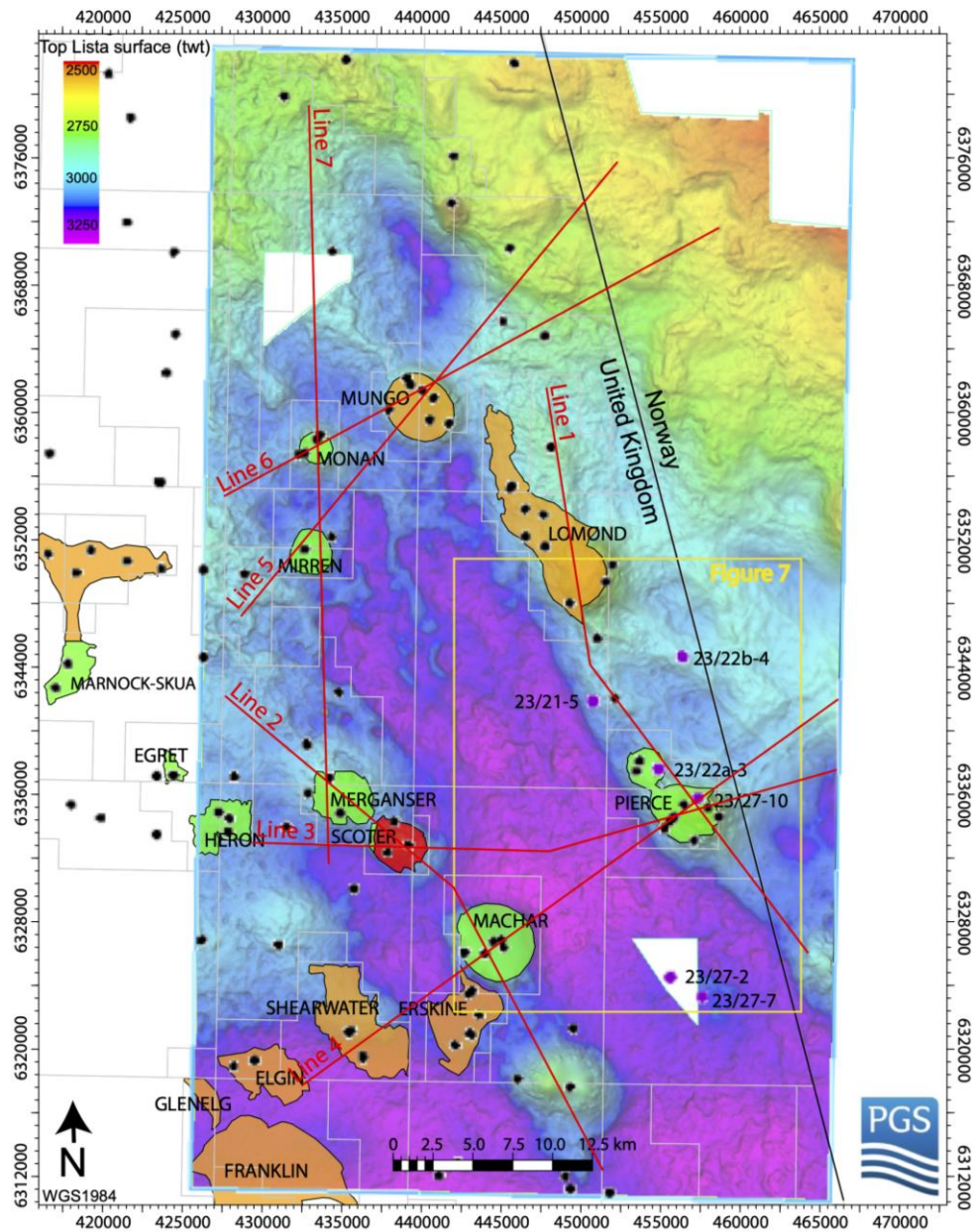
A 2890 km<sup>2</sup> subset of the multiclient PGS CNS MegaSurvey Plus full-offset pre-stack Kirchhoff time-migrated (KPSTM) 3-D seismic dataset formed the primary database for this study (Figure 5.3). Inline and crossline spacing is 12.5 x 12.5 m, sample rate is 4 ms and the data has been processed to zero-phase. The seismic is Society of Exploration Geophysicists (SEG) reverse (European) polarity and a downward increase in acoustic impedance (trough) is displayed with a red loop. Vertical resolution within the Paleocene interval of interest is 25-33 m (based on an interval velocity of 3-4 km s<sup>-1</sup> and a dominant frequency of ~30 Hz). The study area is focussed around eight salt diapirs and is calibrated by over 60 wells.

Synthetic seismograms were created for wells 23/27-7, 23/22b-4 and 23/22a-3, which had continuous log coverage and good borehole integrity (consistent calliper readings). These were used to generate seismic-to-well ties. Eight seismic horizons (base salt, top salt, base Cretaceous, top Cretaceous, top Paleocene, Top Eocene, Top Miocene and seabed) were interpreted between well tops and correlated to standard stratigraphic markers known throughout the region (e.g., Kilhams et al. 2012, 2015; Carruthers et al. 2013). These interpretations allowed for analysis of thickness and orientation variability between differently spaced diapirs. Interpretations were extrapolated with increasing uncertainty to the limits of the seismic image at the salt-sediment interface. Time structure maps along with spectral frequency decomposition maps were used for analysis of the Paleocene. Core observations were used to ground-truth seismic observations of facies distributions (Kilhams 2011). Five cored wells with a good coverage in the Paleocene Forties Sandstone were selected to study facies variability adjacent to, and at distance from, diapirs (Table 5.1, Supplementary Figure 1, Appendix B). The purpose of the wells (for hydrocarbon exploration) has meant core data have a significant sampling bias towards potential reservoir intervals (e.g., high-density turbidites).

Subsurface data (seismic and core) are first used to assess facies distribution around diapirs in order to better understand the controls on sediment distribution (objective 1), and then seismic data are



used alongside DEM results to compare stratigraphic architectures between variably spaced salt structures and describe the extent of halokinetically modified stratigraphy (objectives 2 and 3).



**Figure 5.3:** Subsurface dataset map, overlain onto the Top Lista formation time-surface, showing the location of the diapirs used in this study (North and South Pierce, Merganser, Machar, Scoter, Mirren, Monan and Mungo). Outline of part of the map is shown in Figure 5.2. The data used is a 2890 km<sup>2</sup> subset of the PGS CNS MegaSurvey 3D (outlined by the blue box). Blank areas within the data polygon indicate areas of missing data. Black dots indicate wells within the study area, and purple dots, labelled with well number, indicate wells used for this study (either for core analysis or creating synthetic well ties). Known hydrocarbon fields are shown and labelled (green: oil, orange: condensate, red: gas). Yellow box highlights the location of the spectral (frequency) decomposition map shown in Figure 5.7 and red numbered lines represent seismic cross-sections in Figure 5.8. UTM Zone 31N coordinates annotated in metres.

**Table 5.1:** Core data used for facies analysis across the study area. Selected wells had core through the Paleocene interval and were located at different distances from diapirs to study changes in facies on and off the diapirs flanks. Core data is publically available from the British Geological Survey (BGS). T6A is located and correlated to other ‘T-sequence’ nomenclature on Figure 5.2D.

Well	Location	Cored Palaeocene interval	Studied core interval (m MD)
23/21-5	Between Lomond and North Pierce	T6A, Forties Sandstone Member, Sele Formation	3088-3100
23/22a-3	South flank of North Pierce	T6A, Forties Sandstone Member, Sele Formation	2713-2768
23/27-2	Between Machar and South Pierce	T6A, Forties Sandstone Member, Sele Formation	3116-3156
23/27-7	Between Machar and South Pierce	T6A, Forties Sandstone Member, Sele Formation	3103-3187
23/27-10	South flank of North Pierce	T6A, Forties Sandstone Member, Sele Formation	2657-2732

### **Discrete Element Model (DEM)**

A Discrete Element Model (DEM) based on the methodology of Cumberpatch et al. (2021c; d; Chapter 4) is used here to complement subsurface observations and study the effect that variably-spaced diapirs have on stratigraphic architecture. DEM is a discontinuous numerical method that treats objects as assemblages of circular elements, connected by breakable elastic bonds (Finch et al. 2004). Forces are resolved in the  $x$  and  $y$  directions, and elements are subject to gravity (Finch et al. 2003). The equations that define all forces acting on the DEM are:

$$F_x = F_{i,n} - V\dot{X}. \quad (1)$$

$$F_y = F_{i,n} - V\dot{Y} + F_g. \quad (2)$$

where  $F_{i,n}$  is the elastic force acting on a particle,  $V$  is viscosity, and  $\dot{X}$  and  $\dot{Y}$  are particle velocity. DEM has been used to study deformation processes (Hardy and Finch 2006), and salt tectonics (Pichel et al. 2017, 2019; Cumberpatch et al. 2021c;d). For a discussion of the equations governing DEM, and DEM limitations, see Finch et al. (2003, 2004) and Botter et al. (2014). Further details of the models applicability to salt tectonics are covered in recent work (Pichel et al. 2017; 2019; Cumberpatch et al. 2021c;d, Chapter 4). Our modelled parameters build on previous work and have been rigorously tested (summarised in Supplementary Table 1, Appendix B; Finch et al. 2003, 2004; Pichel et al. 2017, 2019; Cumberpatch et al. 2021c;d). The model in this study comprised a 13500 m-wide by 1500 m-deep cross-section with a rigid base containing ~150,000 elements of varying radii (representing 6-15 m), which are randomly distributed, to reduce failure in preferred orientations. A 150 m thick salt layer is overlain by nine 150 m thick overburden layers (Figure 5.4).

This work is not intended to investigate initial diapir evolution (e.g., Vendeville and Jackson 1992), but rather the interaction between diapir spacing and evolving halokinesis. As such, to simplify a complex three-dimensional process into a two-dimensional model, we assume two linear salt walls or radially symmetric diapirs, emplaced by an earlier phase of diapirism (Pichel et al. 2017; 2019; Cumberpatch et al. in 2021c;d). During the experiment, these diapirs are assumed to actively rise, driven by overburden loading of the salt layer and a salt-overburden density contrast, without invoking regional tectonics (Jackson and Hudec 2017). Active rise is restricted by roof thickness; diapir height must be greater than 66-75% of the surrounding overburden for substantial halokinesis to occur (Schultz-Ela et al. 1993). We model two sinusoidal 750 m wide (maximum width), 1050 m high (70% of the overburden) diapirs, and vary the spacing between them. The geometries used in our models are based on North Pierce diapir, and are therefore comparable to those observed in natural examples in the ECG (Davison et al. 2000; Jackson and Hudec 2017). We impose an upwards motion of 0.028 mm/year (based on the 0.02 – 0.04 mm/year growth of Kyle, Monan,

North and South Peirce diapirs, documented by Davison et al. 2000), to all elements representative of salt, to simulate a diapir growth rate which is modulated by syn-kinematic stratigraphy (Figure 5.4). This replicates the volumetric salt supply rate (Q) described by Peel et al. (2020). We model the late-stage of diapir growth, to enable closer comparison to seismic stratigraphic observations from natural examples (Oluboyo et al. 2014; Grimstad 2016), and employ run times of previous numerical models (Pichel et al. 2017; 2019; Cumberpatch et al. 2021c;d). Our experiments were run for 46,000 timesteps with a timestep equivalent to 100 years (4.6 Myr in total). The diapirs grow for 2.2 Myr (22,000 timesteps) to allow the model to equilibrate creating seabed or surface topography, prior to the addition of sediment. Before the addition of sediment, the diapir growth deforms the ‘early diapiric’ sequence. We define the ‘early diapiric sequence’ as layers deposited prior to the simulation; they are discordant to the diapir and thus represent the early diapiric syn-kinematic strata related to the phase of diapirism that is assumed to have emplaced the diapir into our model (Jackson and Hudec 2017).

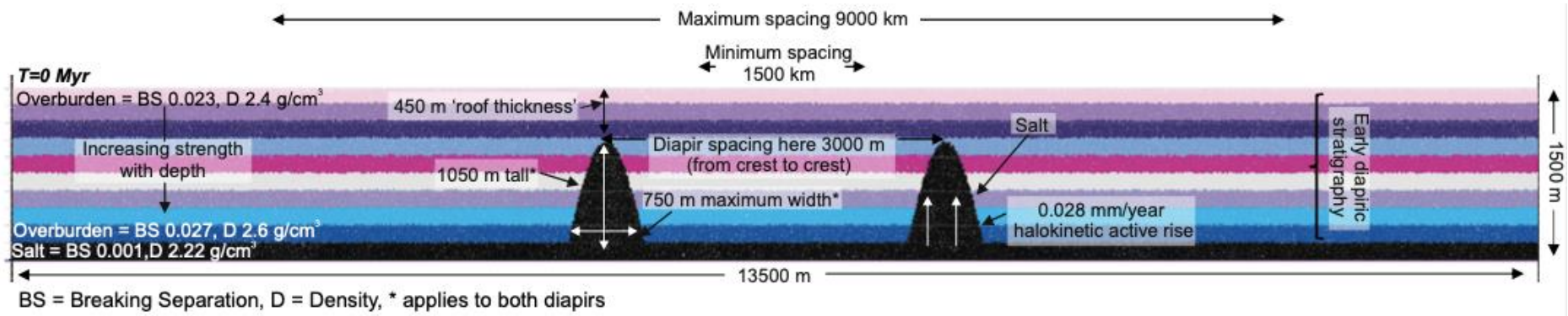
Sediment is added in three 0.8 Myr (8,000 timesteps) stages (S1-S3). Following addition of sediment, diapir rise is passive and is modulated by syn-kinematic sedimentation (Rowan and Giles 2021). Sedimentation rates adjacent to the Pierce diapirs range from 0.085 - 0.4 mm/yr (Liu and Galloway 1997; Kilhams et al. 2014; Eldrett et al. 2015). Here, we use an increasing sedimentation rate, consistent with Cumberpatch et al. (2021c,d), whereby sedimentation rate increases from 0.15 mm/year (2.2-3 Myr), to 0.3 mm/year (3-3.8 Myr), to 0.45 mm/year (3.8-4.6 Myr). This ‘increasing sedimentation rate’ could reflect absolute increases (in the model) or relative increases with respect to salt rise (North Sea analogue).

The relative strength of each model layer is defined by its breaking separation; particles are bonded until this is exceeded (Donzé et al. 1994). Particle motion is frictionless and cohesionless (Finch et al. 2003). Overburden breaking separation (strength) and density increase linearly with depth from 0.023 to 0.027 and 2.4 g cm<sup>-3</sup> to 2.6 g cm<sup>-3</sup> to simulate increasing compaction with depth. Salt and sediment are assigned densities of 2.2 g cm<sup>-3</sup> and 2.3 g cm<sup>-3</sup> respectively, in agreement with measurements from comparable natural systems (Jackson and Hudec 2017) and as used in previous modelling experiments (Pichel et al. 2017; 2019; Cumberpatch et al. 2021c;d; Supplementary Table 1, Appendix B). A viscosity of 1.1 x 10<sup>9</sup> Pa-s is used to represent ductile rock-salt and viscous-plastic behaviour is mimicked by weakening the breaking separation by an order of magnitude (0.001 for salt compared to 0.023 in syn-kinematic strata; Pichel et al. 2017).

We ran multiple experiments with two diapirs with varying horizontal separation to investigate the effects of diapir spacing on stratigraphic architecture. Diapir spacing is measured from the crest of each diapir, here we present six models, with variable diapir spacing (Table 5.2; Figure 5.4).

**Table 5.2:** Details of the different spacing distances between diapirs (measured from crest to crest) used in each model

Model	Spacing of diapirs (model units)	Spacing of diapirs (metres)
M1	50	1500 m
M2	100	3000 m
M3	150	4500 m
M4	200	6000 m
M5	250	7500 m
M6	300	9000 m



**Figure 5.4:** Initial set up of DEM ( $T=0$ ) with two diapirs, showing key parameters. Diapir spacing was the only variable changed throughout the experiments. See text for discussion and Table 5.2 and Supplementary Table 1 (Appendix B) for further details.

## 5.5 Results: Paleocene Facies Distribution

### *Lithofacies and facies associations*

Lithofacies presented in Table 5.3 and Figure 5.5 represent ‘event beds’ and are classified based on core observations. Facies associations are interpreted based on an integration of dominant cored lithofacies (Figure 5.5), gamma ray (GR) profile, seismic and spectral frequency decomposition observations (Table 5.4). Five facies associations [A-E] are interpreted (Figure 5.6). In agreement with recent work, we describe Mass Transport Deposit (MTD) as deposits from varied subaqueous mass flows including slides, slumps and debris-flows (e.g., Nardin et al. 1979; Posamentier and Kolla 2003; Doughty-Jones et al. 2019; Wu et al. 2020; Nwoko et al. 2020). The following section addresses the distribution of these facies associations throughout the study area, with specific focus on proximity to diapirs.

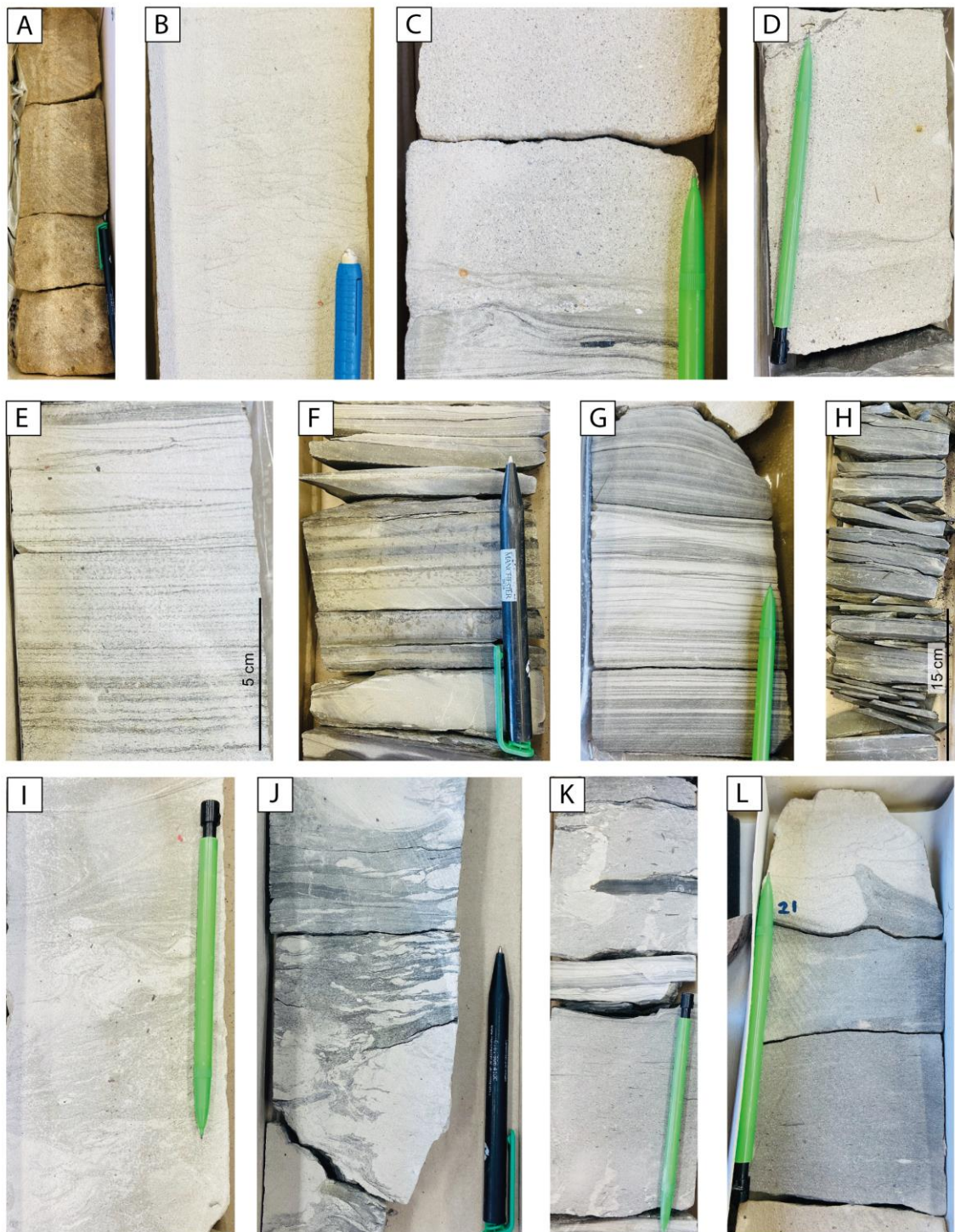
*Table 5.3: Siliciclastic facies table based on core observations from the studied cores in Tabel 5.1. Five lithofacies were identified that comprise the Forties Sandstone Member of the Sele Formation (T6A).*

Facies	Description	Interpretation
<b>Thick-bedded sandstones [A]</b>	<ul style="list-style-type: none"> <li>• 0.5 m to 1+ m thick brown-orange or pale cream-beige fine-coarse grained, moderately- to well-sorted sandstones (Figure 5.5A).</li> <li>• Can be extensive across numerous core sticks and may be amalgamated.</li> <li>• Normally-graded or non-graded typically lacking in any primary depositional structures.</li> <li>• Erosive, flat and loaded bases are observed.</li> <li>• Occasionally beds have cm-thick granular lags at their bases (Figure 5.5B), or contain sporadic limestone granules throughout.</li> <li>• Mud-clasts can be observed throughout.</li> <li>• Dewatering structures such as dish and pillars (Figure 5.5C), syn-sedimentary faulting and injectites are observed, along with evidence for remobilisation of original bedding.</li> <li>• Occasionally, mud content increases upwards and this facies grades into [C] or [D].</li> <li>• Often hydrocarbon stained (Figure 5.5A).</li> </ul>	<p><b>High density turbidites:</b>  The general massive nature, coarse grain size and amalgamation of these deposits suggests that they represent rapid aggradation beneath a highly-concentrated but dominantly turbulent flow, and are thus interpreted as high-density turbidites (Lowe 1982; Mutti 1992; Kneller and Branney 1995). The presence of coarse granular fragments at the base of some beds could indicate the transition from highly-concentrated debris flows into highly-concentrated turbulent flows (Mulder and Alexander 2001; Sohn et al. 2002), due to the deposition of the coarsest grain size fraction and the entrainment of ambient water (Postma et al. 1988). The presence of dewatering structures suggests overpressured fluids within high porosity layers which could indicate slope instability (Cheel and Rust 1986; Yamamoto 2014). Mud content increasing upwards and the grading into [D] could indicate flow transformation due to deceleration or increased concentration of fines (Barker et al. 2008; Kane et al. 2017). Hydrocarbon staining suggests moderate-good reservoir porosity and permeability (Scott et al. 2010).</p>
<b>Medium-bedded sandstones [B]</b>	<ul style="list-style-type: none"> <li>• As [A], but with bed thicknesses of 0.1 to 0.5 m, and occasional mud draped laminations present (Figure 5.5D).</li> </ul>	<p><b>Medium-density turbidites:</b>  Based on their similarity to thick-bedded sandstones these deposits are suggested to also represent rapid aggradation beneath a turbulent flow and are thus interpreted as turbidites (Lowe 1982). Their thinner bed thickness suggests they are medium-density turbidites (Soutter et al. 2019; Cumberpatch et al. 2021a).</p>
<b>Thin-bedded sandstones and silstones [C]</b>	<ul style="list-style-type: none"> <li>• 0.1 to 1+ m packages comprising of 0.001 to 0.1 m thick interbeds which consist of cream-beige very</li> </ul>	<p><b>Low-density turbidites:</b>  Thin-bedded, normally-graded, traction structure-rich sandstones are interpreted to be deposited from</p>

	<p>fine-sandstone and siltstone and grey muddy siltstone (Figure 5.5E-G).</p> <ul style="list-style-type: none"> <li>• Often normally-graded or non-graded.</li> <li>• Tractional structures (cross, ripple, planar, unilobe and wispy laminations) observed (Figures 5.5E and 5.5F).</li> <li>• Flat or loaded bases.</li> <li>• Core is often broken up along bedding planes.</li> <li>• Ripples with opposing palaeoflow directions and bed-thickness variations, across the width of the core, are observed (Figure 5.5G).</li> <li>• Cm-scale muddy fine-sandstones with starry night texture, sporadic granules and mud-clasts are observed within the packages.</li> </ul>	<p>low- concentration turbidity currents (Mutti 1992; Jobe et al. 2012; Talling et al. 2012) and are therefore interpreted as low-density turbidites. Common banding and presence of muddy-sandstones may reflect some periodic suppression of turbulence associated with flow deceleration or increased concentration (Lowe and Guy 2000; Barker et al. 2008). Ripples indicating opposing palaeoflow suggests topographic interference (e.g., Kneller et al. 1991).</p>
<p><b>Deformed mudstones and sandstones [D]</b></p>	<ul style="list-style-type: none"> <li>• 0.01 to 1+ m moderately - poorly-sorted, deformed, matrix-supported deposits.</li> <li>• Matrix ranges from claystone to fine-grained sandstone.</li> <li>• Heterogeneous facies, with lots of variability. Individual deposits contain a lot of lateral variability at core scale (Figures 5I-L).</li> <li>• Undulose, flat, gradational and stepped tops and bases observed.</li> <li>• Remobilised, non-continuous bedding with evidence for soft sediment deformation is common (Figure 5.5I).</li> <li>• Sandstone deformation and cm-scale injectites within a muddy-sandstone matrix frequently observed (Figures 5J &amp; 5K).</li> <li>• Mud-clasts and sporadic granules common throughout (Figure 5.5K).</li> <li>• Mud-rich sandstones with starry night texture observed throughout (Figure 5.5L).</li> </ul>	<p><b>Mass failure deposits:</b></p> <p>The poorly-sorted matrix, deposit heterogeneity and clast-rich nature are suggestive of ‘flow freezing’ (Inverson et al. 2010) indicating ‘en masse’ deposition from a cohesive debris flow (Nardin et al. 1979; Inverson 1997; Sohn 2000).</p> <p>Folded, remobilised, thinly-bedded sandstones [C] and intra-basinal clasts indicate localised mass failure and reworking (Cumberpatch et al. 2021a). Small scale injectites indicate fluid overpressure (Cobain et al. 2016).</p> <p>Grading into [A] and [E] suggests some turbulence was influencing the flow and therefore periodic deposition from a transitional flow regime is interpreted (Baas et al. 2009; 2013; Sumner et al. 2013). The mass failure deposits described here refer to sedimentary bodies that are translated downslope as a result of gravity-induced mass failure and encompasses a vari-</p>

	<ul style="list-style-type: none"> <li>• This facies is observed to grade into [A] and [E].</li> </ul>	<p>ety of processes including slumping, sliding and laminar flow transport (Moscardelli and Wood 2008; Nwoko et al. 2020)</p>
<b>Mudstone [E]</b>	<ul style="list-style-type: none"> <li>• 0.1 to 1+ m packages comprising of dark homogenous siltstones and claystones.</li> <li>• Planar laminations, and colour variations sometimes visible due to alternations between silt and clay grain sizes.</li> <li>• Friable packages often not in tact in core, broken along lamination planes (Figure 5.5H).</li> <li>• Can be heavily bioturbated.</li> <li>• Occasional laterally non-extensive silstone- fine-grained sandstone.</li> <li>• This facies often grades into [C].</li> </ul>	<p><b>Background/low-density turbidites:</b>  Fine grain-size indicates low-energy conditions, representative of background sedimentation via suspension fallout. Discontinuous siltstones and grading into thin-bedded sandstones [C] suggest laminations may be present below the scale visible in core, representing deposition from a dilute turbidity current (Boulesteix et al. 2019; 2020). These mudstones could also represent contourites deposited by density driven bottom currents (Talling et al. 2012; Kane et al. 2020; Furhmann et al. 2020).</p>





**Figure 5.5:** Photographs of type examples of facies from core, see Table 5.3 for description and interpretation. All core photographs are from T6A, from the wells in Table 5.1. All photographs are taken younging upwards. Pen, pencil and eraser are all 16 cm. A-C) Thick-bedded sandstones. D) Medium-bedded sandstones. E-G) Thin-bedded sandstones. H) Mudstone. I-L) Alternating, deformed, and chaotic sandstones and mudstones.

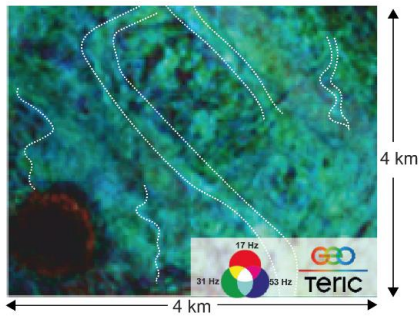
**Table 5.4:** Summary of characteristics of subsurface facies observed in the Paleocene across a number of different data types and scales of data, shown on Figure 5.6. ‘Complex’ and ‘element’ scales refer to scales describe by Pr elat et al. 2009. Interpretations are consistent with other deep-water halokinetically-influenced systems elsewhere (e.g., Oluboyo et al. 2014; Eldrett et al. 2015; Doughty-Jones et al. 2017; Rodr iguez et al. 2020). *ms* = millisecond two way travel time.

Facies Association	Observations			Interpretation	
	Spectral Frequency decomposition	Seismic (Complex scale)	Gamma Ray (GR)	Core (Element scale)	
<b>Channel</b> (Figure 5.6A)	Km long, 100’s m wide, sinuous to straight moderate-high frequency bodies (e.g. Kilhams 2011; Eldrett et al. 2015; Hale et al. 2020)	100’s m wide, 10’s ms thick discontinuous, concave up, upwards-widening geobodies with moderate amplitude. Commonly stacked vertically and laterally (e.g. Scott et al. 2010; Eldrett et al. 2015; Charles and Ryzhikov 2015; Hale et al. 2020).	Low GR values at base (20-80 API) increasing upwards over 10’s m to higher values of 80-150 API (e.g. 3138 – 3154 m in well 23-27-2 (T6A)).	Stacked metre-scale packages of lithofacies A and B. A are often erosively based, normally-graded and transition upwards into C or E (e.g. 3125 – 3130 m in well 23-37-2).	Sinuous to straight submarine channel complexes composed of individual channel elements, with predominantly sand-rich fill (Eldrett et al. 2015; Charles and Ryzhikov 2015; Hale et al. 2020).
<b>Proximal Lobe</b> (Figure 5.6C)	10’s km long, kms wide, lobate geobodies. Speckled facies throughout. Brighter in proximal areas and dimmer and darker at the distal equivalents (e.g. Kilhams 2011;	Km wide, 10’s ms thick sub-parallel, semi-continuous, high amplitude reflections. Tabular to mounded morphology with bidirectional downlap. Stacked vertically, commonly with dimmer reflectors described below (e.g. Scott et al. 2010 Kilhams et al. 2012; 2014; Eldrett et al. 2015; Charles and Ryzhikov 2015).	Clean, low API (10-50), 10’s m scale packages of blocky GR signature, divided by subsidiary <m scale higher values, between 50-80 (e.g. 2635-2735 m in well 23/27-10 (T6A))	Stacked metre-scale packages of lithofacies A and B. Sandstones are sharp-based, and often amalgamated. Dewatering structures are common. Generally massive or normally-graded into C (e.g. 2690 – 2705 m in well 23/27-10).	Submarine lobe complexes comprised of individual lobes and lobe elements. Bright amplitudes, low GR and sandstone-rich lithofacies are suggestive of a lobe axis sub-environment (e.g. Pr�elat et al. 2009; Kilhams et al. 2012; 2014; Eldrett et al. 2015).
<b>Distal Lobe</b> (Figure 5.6C)	Kilhams et al. 2014; 2015; Hale et al. 2020).	The moderate- low amplitude edges, and dimmer km wide, 10 ms thick reflections between, the geobodies described	‘Ratty’, irregular and jagged GR profile reflecting variable lithological	Stacked metre-scale packages of lithofacies C. Cm scale interbeds of variable lithologies. Tractional structures within	Submarine lobe complexes comprised of individual lobes and lobe elements. Dimmer amplitudes, high GR and mixed lithology lithofacies suggest a

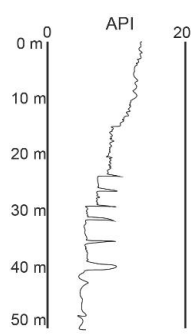
		above (Scott et al. 2010; Kilhams et al. 2015; Eldrett et al. 2015).	composition. Values between 50 and 120 API (e.g. 2700 – 2750 m in well 23/22a-3(T6A)).	sandstones. Can transition into E (e.g. 2648 -2668 m in well 23/22a-3).	lobe fringe sub-environment (e.g., Prélat et al. 2009; Scott et al. 2010; Kilhams et al. 2015).
<b>Mass Transport Deposit (MTD)</b> (Figure 5.6B)	Kms long, 100's m- km wide, undulose geobodies often associated with salt structures. Speckled low-moderate frequency character (e.g. Kilhams 2011; Kilhams et al. 2015; Eldrett et al. 2015; Soutter et al. 2018; Hale et al. 2020).	Km wide, 40+ ms thick, disorganised, low-moderate amplitude, discontinuous, semi-transparent reflectors. Irregular upper and lower surfaces. Internal 100's m wide clasts. Discontinuous reflectors are laterally offset (e.g. Scott et al. 2010; Eldrett et al. 2015; Charles and Ryzhikov 2015; Soutter et al. 2018).	Variable dependent on composition of MTD. Often 'ratty' and irregular GR signature reflecting internal deposit heterogeneity. Values between 80 and 150 API (e.g. 3135-3150 m in well 23/27-7 (T6A)).	Stacked, metre-scale packages of lithofacies D. Variable lithology, often mixed, commonly containing chalk (Kilhams et al. 2015). Common soft sediment deformation, fluidisation and isolated clasts and mud-clats. Poorly-sorted deposits with irregular bases and tops (e.g. 3137 -3146 m in well 23/27-7).	Products of gravity driven mass failure processes (including slides, slumps and debris flows), collectively termed mass transport deposits (MTDs). Often diapiroically derived (e.g., Giles and Rowan 2012; Kilhams et al. 2015; Soutter et al. 2018; Doughty-Jones et al. 2019; Wu et al. 2020).
<b>Background deposition</b> (Figure 5.6D)	Kms long, kms wide extensive areas of high frequency, dark, speckled character, with no resolveable features (e.g. Kilhams 2011; Soutter et al. 2018; Hale et al. 2020).	Km wide, 100s ms thick packages of parallel, low-moderate amplitude, continuous reflections (e.g. Kilhams et al. 2012; 2014; 2015; Eldrett et al. 2015).	Homogeneously high GR signature values over 100 API (e.g. 3190-3240 m in well 23/21-5 (T6A)).	Stacked, metre-scale packages of lithofacies E. Often transitions upwards into C. Commonly broken during coring process (e.g. 3103 - 3108 m in well 23/27-7).	Representing deposition either by background hemipelagic suspension fall out or mud-rich dilute distal submarine fans (e.g. Kilhams 2011; Eldrett et al. 2015; Boulesteix et al. 2019; 2020).

**[A] - Submarine Channel**

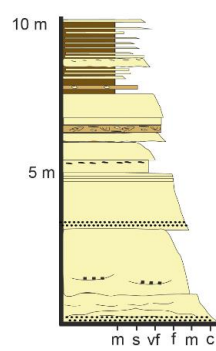
Spectral Decomposition



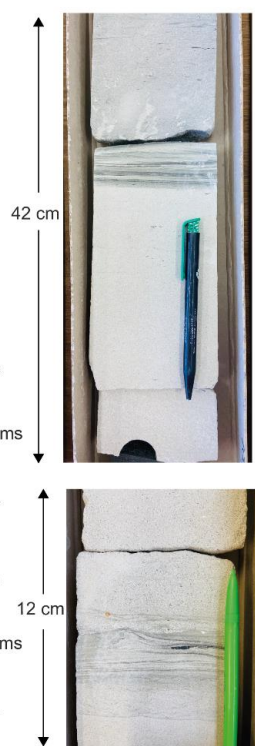
Gamma Ray Profile



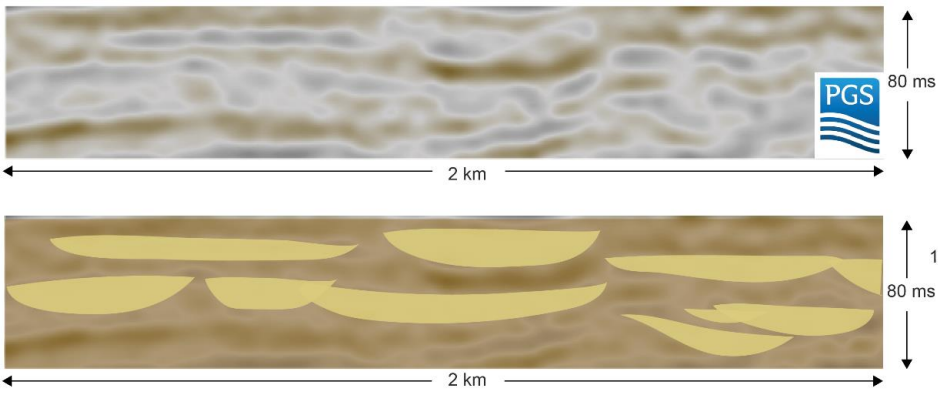
Sedimentary Log



Core Photograph

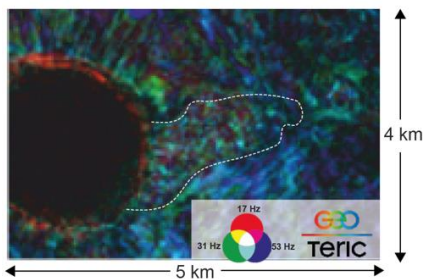


Seismic Section

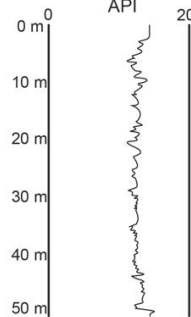


**[B] - Mass Transport Deposit (MTD)**

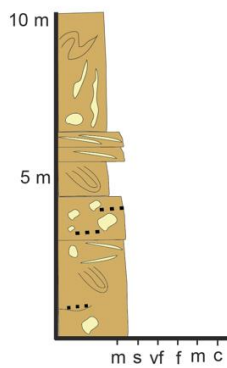
Spectral Decomposition



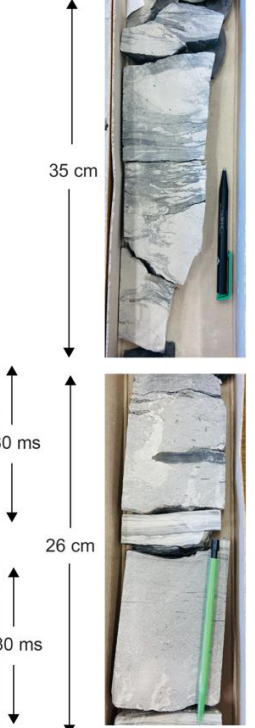
Gamma Ray Profile



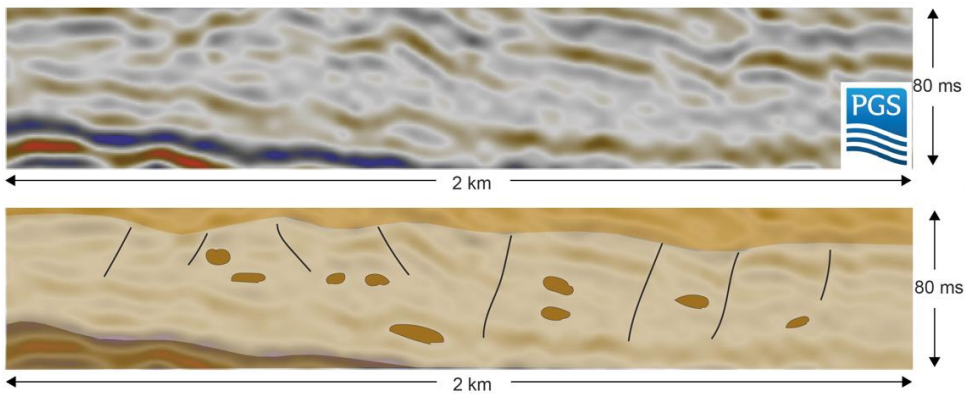
Sedimentary Log



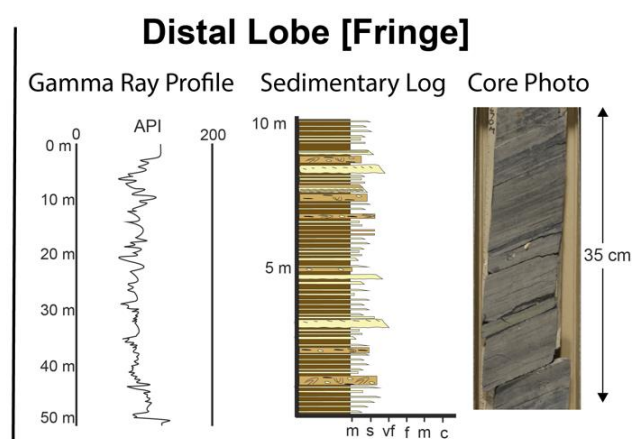
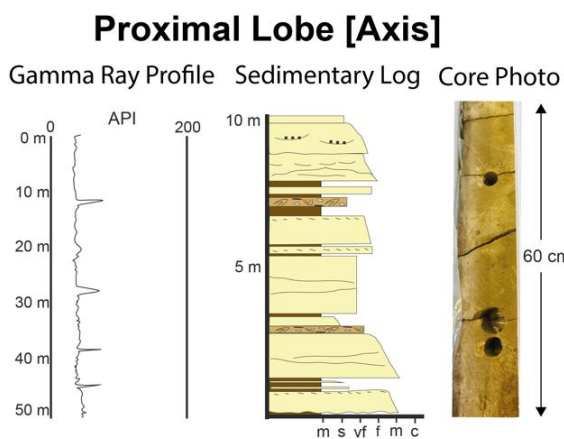
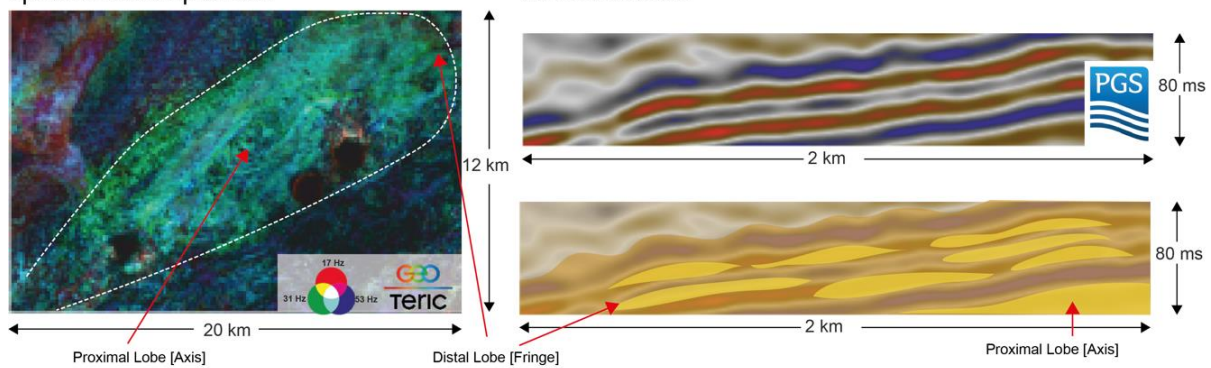
Core Photograph



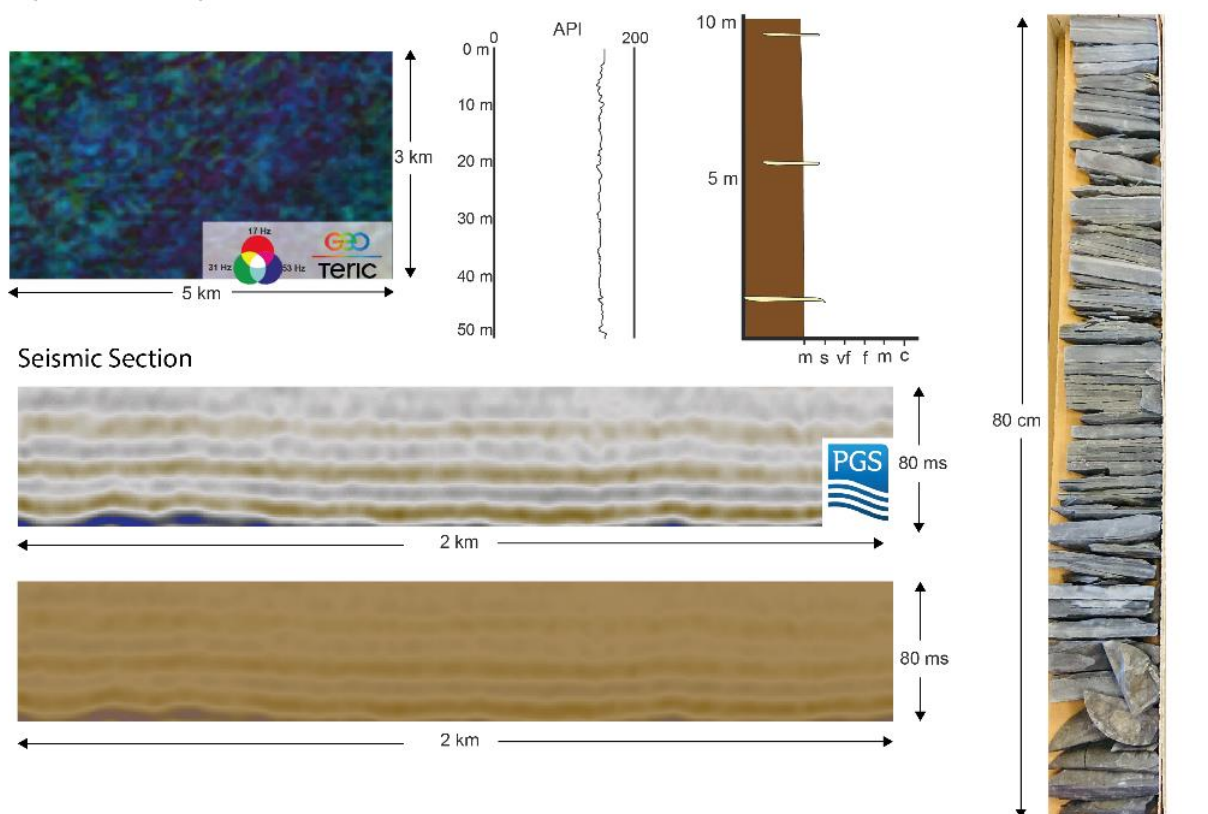
Seismic Section



**[C] - Submarine Lobe**  
Spectral Decomposition



**[D] - Background Deposit**  
Spectral Decomposition



*Figure 5.6: Summary figure showing the anticipated observations across different types of data and scales in different depositional environments within the study area. All data is from the study area and provides a visual representation of the descriptions and*

examples from Table 5.4 A) Submarine Channel. B) Mass Transport Deposit. C) Submarine Lobe. D) Background Deposit. All frequency decompositions are taken from the Top Lista Formation time slice shown in Figure 5.7, seismic reflection data represents Paleocene stratigraphy and core data are from the Forties formation (3<sup>rd</sup> order sea level cycle TA6).

### ***Facies Distributions***

Here we use the integrated subsurface facies associations to analyse salt-influenced deep-water facies and characterise their distribution in terms of halokinetic or allocyclic controls (objective 1).

**Observations:** The depositional system is revealed by spectral frequency decomposition across a window 20 milliseconds either side of the Top Lista Formation interpretation. To the east of the Pierce diapirs, the system forms an elongate bright NW-SE trending bulb-like geometry with thin sinuous features (Figure 5.7A). This system is cross-cut by a red-purple diverging bulb-shaped geometry trending to the north east of the Lomond Diapir (Lo). Well 23/21-5 is located in the centre a cross-cutting bulb-like geometry, which widens to the SW (Figure 5.7A). Depositional systems with speckled, undulose morphologies can also be observed on the eastern side of Machar and the south-eastern side of South Pierce diapirs. Outside of these more defined depositional elements, dark, high frequency, mounded and speckled deposits can be seen. In addition, a number of dark radiating linear features are present around the diapirs.

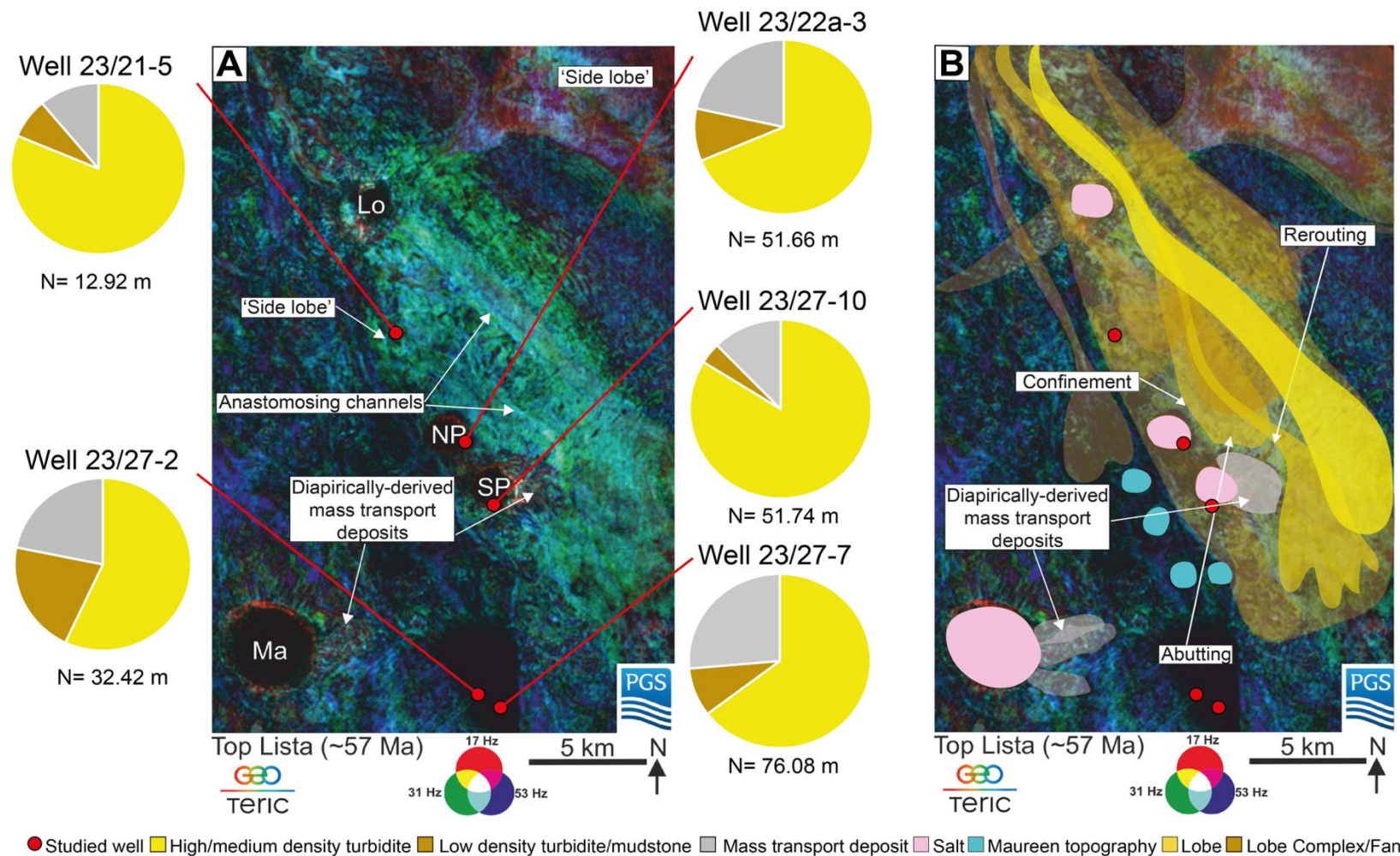
In the T6A sequence, high- to medium- density turbidites are the most common facies throughout the depositional system, accounting for 84% and 81% of cored facies in 23/27-10 and 23/21-5 respectively. Well 23/27-2 has the lowest percentage of high- to medium- density turbidites (57%) (Figure 5.7A). Overall, the percentage of high- to medium- density turbidites decreases southward in the study area. MTDs are common south of South Pierce (23/27-7 (26%) and 23/27-2 (22%)) and on the southern flank of North Pierce (23/22a-3; 21%). Wells 23/21-5 and 23/27-10 have 11% and 12% MTDs respectively. Low-density turbidites and mudstones account for 21% of 23/27-2, between 8 and 10% in wells 23/21-5, 23/22a-3 and 23/27-7, and only 4% of 23/27-10 (Figure 5.7A).

**Interpretations:** The spatial distribution of depositional facies is a complicated three-dimensional problem that cannot be completely understood using a small subsample of cored data. However, our observations support the NW-SE trending channelised submarine lobe complex interpretation of previous workers (Figure 5.7B; Den Hartog Jager et al. 1993; Jennette et al. 2000; Kilhams et al. 2012; 2014; 2015; Eldrett et al. 2015). Cross-cutting bulb-like geometries and their locations are consistent with the proposed transverse ‘side lobes’ of Hempton et al. (2005) and Eldrett et al. (2015) (Figure 5.7A). Speckled, undulose geometries adjacent to Machar and South Pierce are interpreted as diapir-derived MTDs based on their chaotic appearance, and apparent attachment to diapirs (Figure 5.7B). This is similar to ‘locally’-derived MTDs reported elsewhere (e.g., Moscardelli and Wood 2008; Doughty-Jones et al. 2019; Wu et al. 2020). The radiating linear structures around diapirs are similar to radial faults reported elsewhere (Coleman et al. 2018).

The high proportions of high- to medium-density turbidites in the T6A sequence, and an overall decrease in percentage of this facies to the south is consistent with the proximal to distal trend of the eastern fairway of the ‘Forties fan’ (Figure 5.2C). This is supported by an increasing percentage of thin-bedded turbidites and mudstones in the distal part of the depositional system, to the South of South Pierce (Figure 5.7A). Particularly high percentages of high- to medium-density turbidites around South Pierce could reflect a preferential flow pathway. Well 23/27-10 is slightly off flank in location and thus could penetrate part of the salt withdrawal basin. Visually 23/27-10 also appears to be outside of the easterly-trending MTD derived from South Pierce, indicating why it has one of the highest proportions of high- to medium-density turbidites. The high proportion of

high- to medium-density turbidites in well 23/21-5 is potentially due to the well's off-axis position in the side lobe (Figure 5.7B) as well as its overall proximal location.

The high proportion of MTDs in wells 23/27-2 and 23/27-7 could represent failures from the Machar diapir, or previous failures (for example within the Maureen or Lista formations) that were remobilised by subsequent gravity flows (Kilhams et al. 2012; 2014). The location of these wells, over 5000 m from diapirs, could suggest the MTD facies were allocyclically-influenced and related to regional failures of the coeval shelf and slope rather than derived from individual diapirs (Johnson 1987; Moscardelli and Wood 2008; Soutter et al. 2018; Doughty-Jones et al. 2019). Well 23/27-10 could represent a 'failure shadow' where certain flanks of the diapir were more stable and therefore less prone to failure. The MTDs adjacent to Machar and the Pierce diapirs are likely to be halokinetically-derived rather than allocyclic due to their attachment and proximity (Moscardelli and Wood 2008; Doughty-Jones et al. 2019).



**Figure 5.7:** A) Spectral Frequency Decomposition map for the Top Lista Formation. Black areas indicate salt diapirs piercing the Top Lista surface: Ma; Machar, Lo; Lomond, NP; North Pierce, SP; South Pierce. Pie charts for five wells with core in the Paleocene Forties formation (3<sup>rd</sup> order sea level cycle TA6) are shown and located on the map. N refers to the thickness in metres of the cored stratigraphy. The Top Lista Formation is equivalent to the base of TA6. Core was simplified into three facies classifications (high- to medium-density turbidite, low-density turbidites and mudstones, and mass failure deposits: Table 5.3; Figure 5.5). Black polygon around Well 23/27-2 and 23.27-7 is a data gap. MegaSurvey Plus 3D seismic data courtesy of PGS. B) Interpretation of depositional elements and salt structures.



## 5.6 Results: Effects of lateral spacing in subsurface and models

Analysing the effects of variable diapir spacing (Table 5.5; Figures 5.3 and 5.8) provides insights into how the presence of multiple diapirs influence stratigraphy, and how changes in the lateral and temporal extent of a diapir is recorded. Observations from seismic (Figure 5.8) and the variably-spaced diapirs in the DEM (Figure 5.9) are used to interpret and investigate halokinetic modulation. Here, we address objectives 2 and 3 by comparing stratigraphic architectures between variably spaced salt structures and describing the extent of halokinetically-modified stratigraphy between different distances of confinement.

**Table 5.5:** Variably spaced diapirs used in this study, shown on Figure 5.8. Discussed in text.

Diapirs	Spacing	Line Number (Figure 5.3 and 5.8)
North Pierce – South Pierce	1000 m	1
Merganser - Scoter	1000 m	2
Monan - Mungo	4000 m	6
Mirren - Monan	4200 m	7
Scoter - Machar	4440 m	2
Machar – Southerly diapir	5200 m	2
Mirren - Mungo	8300 m	5
Machar – South Pierce	10000 m	4
Merganser - Mirren	12900 m	7
Lomond – North Pierce	13200 m	1
Scoter – South Pierce	15000 m	3

### **Subsurface Observations**

Thickness variations are common regardless of diapir spacing (Figure 5.8) and are greatest in salt withdrawal basins above areas of thinned salt, either between or adjacent to diapirs (e.g., between Merganser and Scoter, and Scoter and Machar, Line 2, and between Monan and Mungo, Line 6, Figure 5.8). Thickening is most prominent in the Triassic-Jurassic section, and is also seen within the Cretaceous and Paleocene units. Both symmetrical (synclinal) (e.g., between Merganser and Scoter, Line 2, and to the southeast of South Pierce, Line 1, Figure 5.8) and asymmetrical mini-basins (e.g., between Monan and Mungo, Line 6, and Mirren and Mungo, Line 5, Figure 5.8) are observed.

Thinning is commonly observed adjacent to the diapirs, and is most extreme in the Paleocene stratigraphy around South Pierce (Line 1, 3 and 4, Figure 5.8). Here, the overall package almost pinches out towards the diapir over ~2000 m, and individual reflectors can be seen to onlap. Elsewhere thinning is subtle and constrained to within 500–1000 m of the diapir (e.g., Line 2-3, 5-7, Figure 5.8). Within ~500 m of diapirs there is typically a change from clear, resolvable seismic facies with continuous reflections, to a dimmer, chaotic facies (e.g., Line 3 and 4, Figure 5.8).

### **Model Observations**

Across all models the thickest part of the syn-kinematic stratigraphy is located where the salt is thinnest and has the least elevation. This usually coincides with the base of the salt structure (Figure 5.9). Where diapir spacing is large (<4500 m, models M3-M6) two salt withdrawal basins, represented by depositional maxima, form either side of the diapirs. A slight thinning to background conditions occurs away from the salt withdrawal basins. With narrow spacing (1500 m, model M1) the thickest strata is concentrated within the centre of basin between the two diapirs. Where diapir

spacing is slightly greater (e.g., 3000 m, model M2, Figure 5.9), there is a consistently thick succession that extends between the two diapirs. Thickening away from the diapirs is also observed in the early-diapiric stratigraphy.

Thinning of all syn-kinematic layers towards both diapirs is observed in all models and is most apparent between the salt flank and crest. All models also show the upper five layers thinning across the crest of the diapirs (Figure 5.9). Early diapiric layers thin towards the diapir, and in places are absent from the diapir crest where the salt has pierced through. Thinning rates are greatest in model M1 (0.043%/m), where the diapirs are closely spaced. For both the early diapiric and syn-kinematic sections thinning is most apparent in the deformation zone associated with each diapir, defined as the distance between the two furthest faults related to salt withdrawal. Outside this zone, stratigraphic modulation by salt growth is minimal, comparable to stratigraphy >5000 m away from salt structures in the seismic examples (Figure 5.8).

### ***Interpretations***

**Stratigraphic thickness variability:** Thickening of stratigraphy adjacent to salt structures is consistent with salt withdrawal basin formation (Hudec et al. 2009; Peel et al. 2014; Jackson et al. 2020; Rodriguez et al. 2020; Howlett et al. 2020). M1 and M2 show that the thickest part of the syn-kinematic stratigraphy is in the axis of the depocenter between them, in agreement with observations of closely spaced subsurface diapirs (e.g., Scoter and Merganser, Scoter and Machar, Line 2, North and South Pierce, Line 1, Figure 5.8). Abrupt stratigraphic thickness changes are likely due to the high degree of confinement. In models where the diapirs are more widely spaced (>3000 m) or in subsurface examples that do not have other laterally confining diapirs (e.g., NE of Mungo in Line 5 and 6, Figure 5.8), the thickest part of the stratigraphy is adjacent to the diapir and is influenced by salt withdrawal. The thickening at the base of the diapir slope observed from the seismic in the study area and the models is consistent with field observations of thick sandstones at the base of topography, typically the result of rapid flow deceleration (Kneller and McCaffrey 1999; Reilly and Lang 2003; Aschoff and Giles 2005; Soutter et al. 2019; 2021). Asymmetrical thickening packages may reflect a shift in minibasin axis through time (Mayall et al. 2006; 2010; Jones et al. 2012; Wang et al. 2017; Ge et al. 2020) likely related to differential growth of the diapirs confining the stratigraphy (Warsitzka et al. 2013; Harding and Huuse 2015; Jackson and Hudec 2017).

Thinning in close proximity to the diapirs suggests that these packages represent halokinetic sequences (<1000 m wide) related to individual diapirs (Giles and Lawton 2002; Rowan and Giles 2021), rather than broader-scale minibasin syn-kinematic sequences. This is in agreement with previous work around the Pierce diapirs (Carruthers et al. 2013). In the models, thinning rates appear to be more exaggerated when stratigraphy is confined between closely-spaced diapirs (e.g., in M1 stratigraphic thinning is 0.043%/m). In contrast, in seismic observations the amount of thinning is more subtly influenced by diapir spacing (e.g., 0.0126%/m thinning between North and South Pierce (1000 m) and 0.006%/m between Machar and the Southerly diapir (5200 m)). In some cases, closely-spaced diapirs (North and South Pierce in Line 1, Figure 5.8) show the thickest part of stratigraphy to be in the axis between the diapirs, and thinning occurring towards either diapir (at a rate of 0.0126%/m). In other cases, in the absence of dual confinement, more dramatic thinning (0.058%/m in the Paleocene SE of South Pierce, Line 1, Figure 5.8) is observed showing that thinning rates are influenced by a number of variables, including diapir rise rate (Vendeville and Jackson 1992; Rowan et al. 2003; Giles and Rowan 2012; Rowan and Giles 2021; Cumberpatch et al. 2021c;d). Our models replicate the thinning over diapiric crests observed in subsurface data (e.g., the Cretaceous – Eocene thinning over the Scoter diapir in Line 3; Figure 5.8). Thinning over

the diapir crest suggests that the topography from the diapirs continue to have influence on deposition even when they are not penetrative or present at the surface (Pratson and Ryan 1994; Oluboyo et al. 2014; Saura et al. 2016; Doughty-Jones et al. 2017; Cumberpatch et al. 2021 b;c;d).

The apparent dimming of seismic facies towards diapirs could represent a change in depositional character when systems approach the salt structures. This could be reflective of an increase in mud proportion, as well as a thinning, of units towards the diapir as the higher density part of the flow is unable to run up topography (Kneller and McCaffrey 1999; Birch and Haynes 2003; Counts et al. 2019; Soutter et al. 2019; 2021; Cumberpatch et al. 2021 b;c). Alternatively, this change in seismic facies could reflect an upwards rotation in stratigraphy causing seismic imaging problems, and/or tuning effects due to thinly bedded units, potentially masking lithological variations (Jones and Davison 2014).

**Lateral and temporal evolution of stratigraphic modulation:** Stratigraphic thickness variations and rotation of bedding decreases laterally away from individual diapirs (Figure 5.8) in agreement with current understanding (Alsop et al. 1995; 2000; Giles and Rowan 2012; Doughty-Jones et al. 2017; Rowan and Giles 2021). Between closely spaced diapirs (e.g., North and South Pierce Line 1, Figure 5.8) the halokinetic influence of one diapir is laterally connected to the halokinetic influence of the diapir, such that the zone between diapirs is influenced by both. When diapirs are >5000 m apart, there is often a zone of consistent stratigraphic thickness and stratal dip between them where minimal modulation occurs (e.g., Scoter to South Pierce, Line 3 and Merganser to Mirren, Line 7, Figure 5.8). Between these wider spaced diapirs, stratigraphy does not respond to diapir separation. This stratigraphic sequence may be difficult to decipher from strata outside salt provinces, although the bedding may still be influenced by long wavelength deformation. Subtle topography associated with irregularities in the autochthonous salt, smaller diapirs and earlier (Triassic) rifting can influence subsequent stratigraphy without the need for a long-lived salt diapir (e.g., southeast of South Pierce in Line 1, northeast of Mungo in Line 6, Figure 5.8).

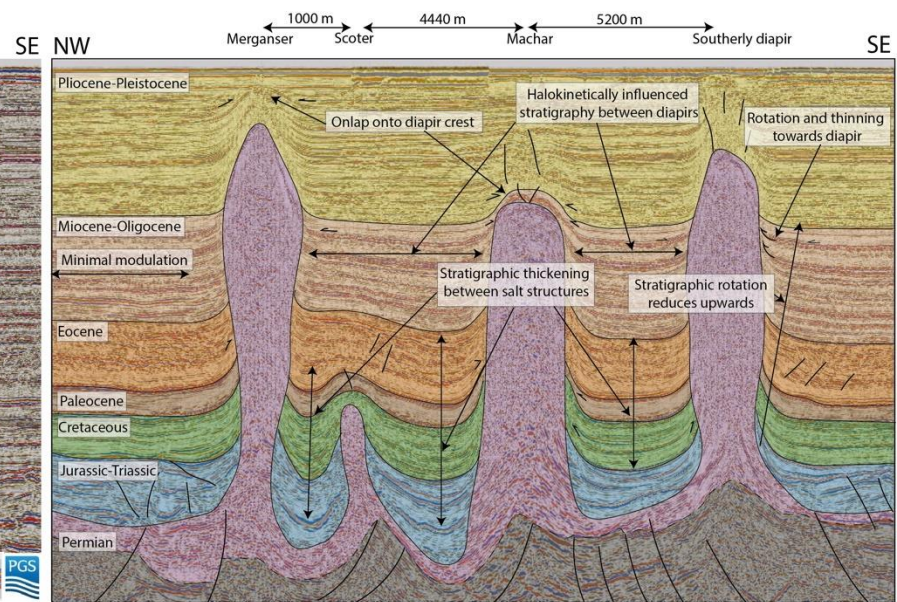
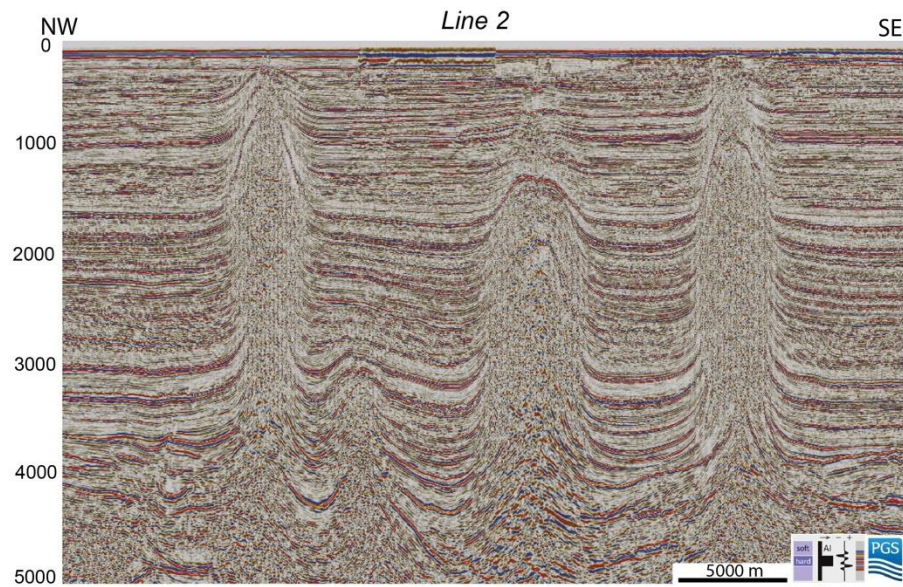
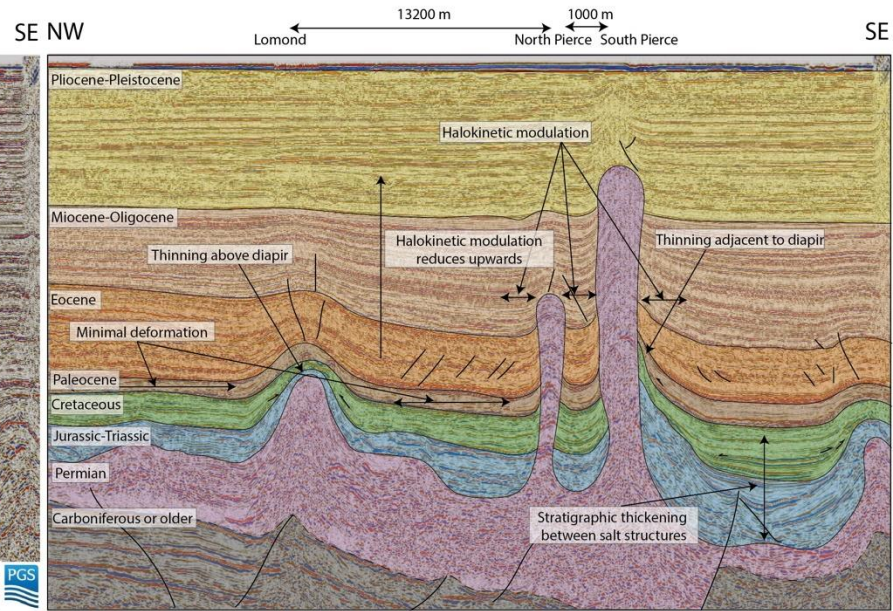
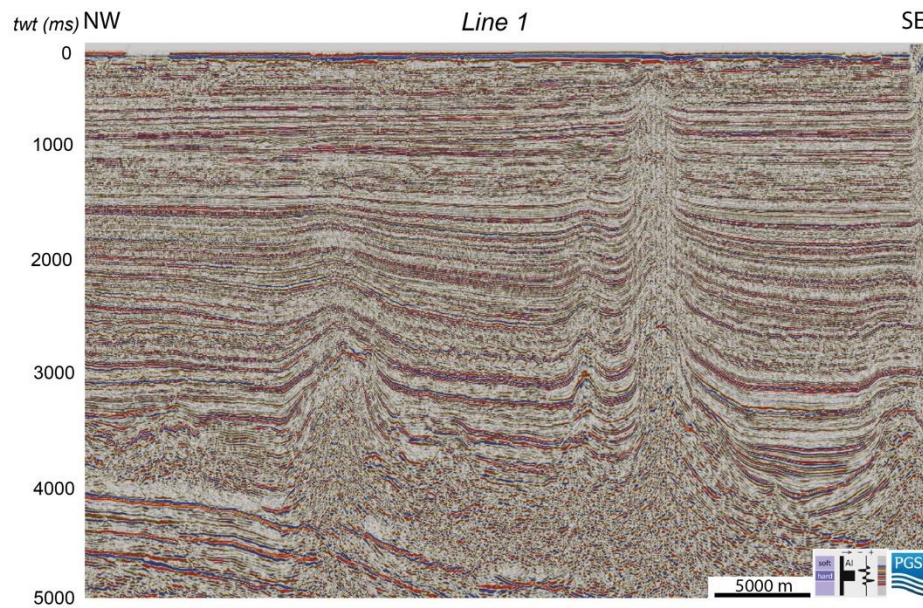
The halokinetic influence on stratigraphy reduces upwards, reflected by less thickness variability, fewer pinch outs and less rotation of beds in younger stratigraphy (Figure 5.8). Several diapirs have long-lived influences on stratigraphy, causing thickness variations and termination of stratigraphy often until the Pliocene-Pleistocene, resulting in topography only being healed at the seabed (e.g., Merganser, Line 2, Figure 5.8). The Scoter diapir has an influence on stratigraphy until the end of the Eocene, after which its remnant topography appears healed (Line 2 and 3, Figure 5.8). In the models, halokinetic modulation reduces away from diapirs in both directions to the minimal deformation zone (undeformed zone). Stratigraphic modulation also reduces with time (upwards) (Figure 5.9). Through time, the amount of stratigraphic upturn shallows out, with the syn-kinematic strata being upturned less than the early diapiric sequence. Even the uppermost syn-kinematic layer is influenced by diapiric topography and exhibits minor thinning, however subsequent deposition would probably heal the diapir topography. This reduction in halokinetic influence upwards reflects the increasing sedimentation input within the model, and does not appear to be influenced by diapir spacing.

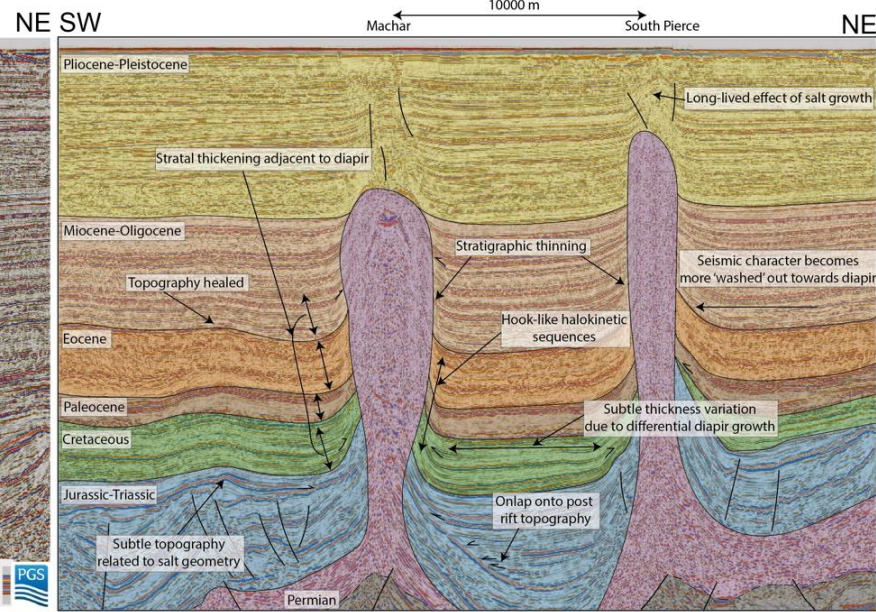
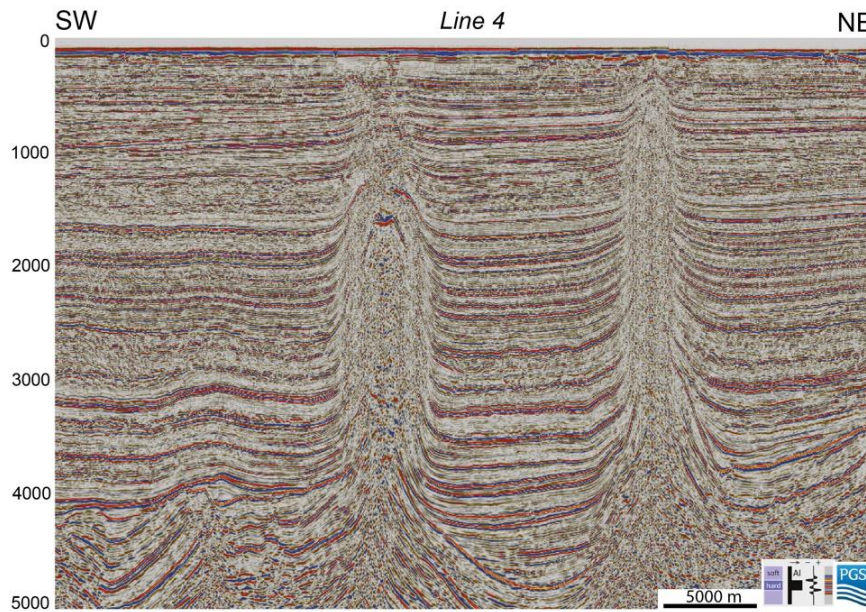
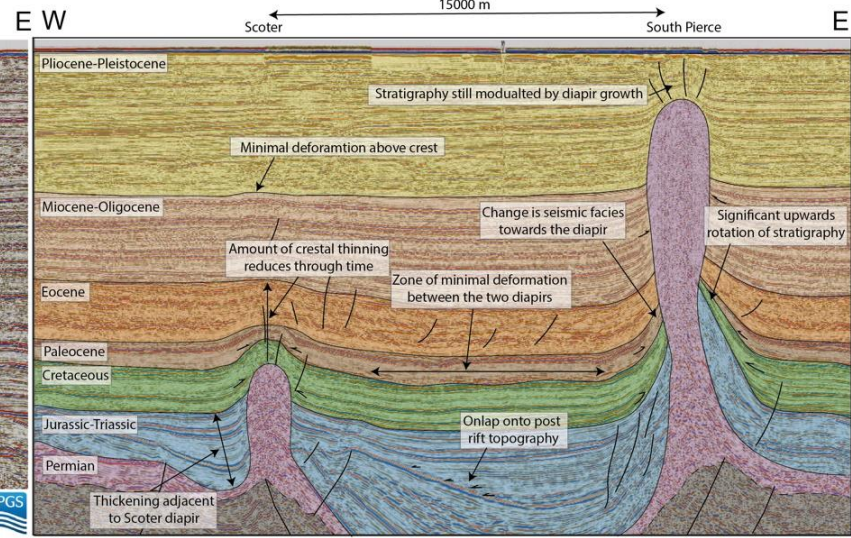
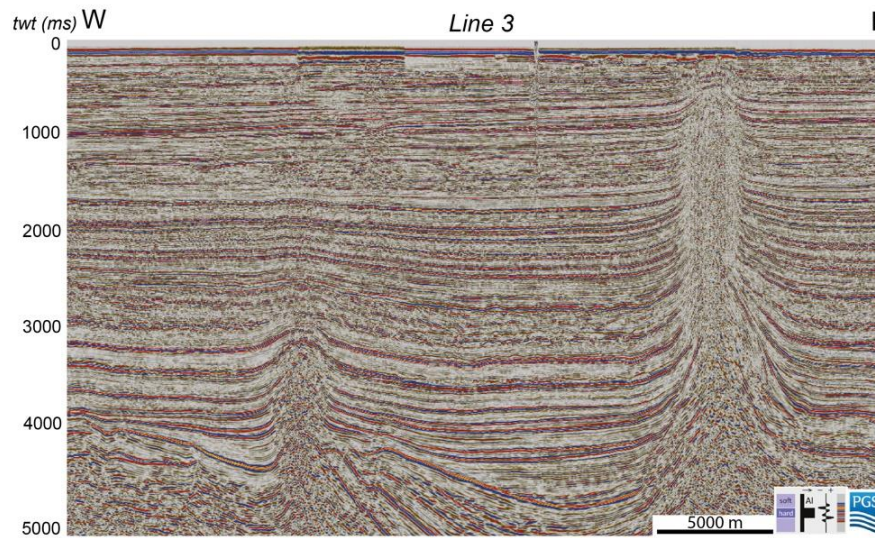
Modelled results indicate that stratigraphic modulation is more intense where diapirs are closer together. This could be due to overlapping deformation zones between diapirs (Booth et al. 2003; Fernandez et al. 2020). Previous work (Cumberpatch et al. 2021c;d) has shown that a deformation zone of 1150 m either side of a 750-metre wide diapir is expected. Therefore, in M1 the deformation zones of each individual diapir overlap, increasing the intensity of deformation. Thus, while it is poorly imaged, it is likely that the 1000 m between North and South Pierce, and Merganser and Scoter (Figure 5.8), do not have an undeformed section at the centre. Our model results show that once diapirs are spaced more widely than 3000 m, an area of non-deformation between them

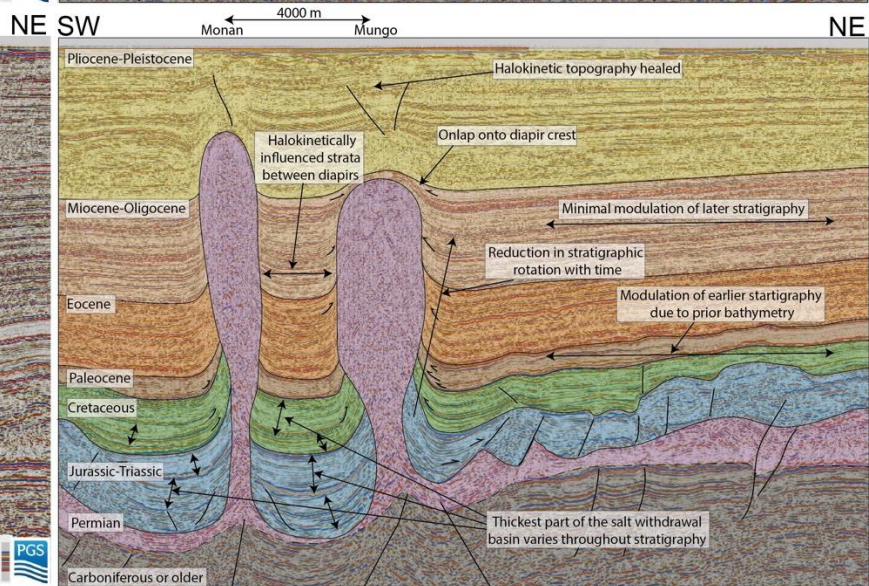
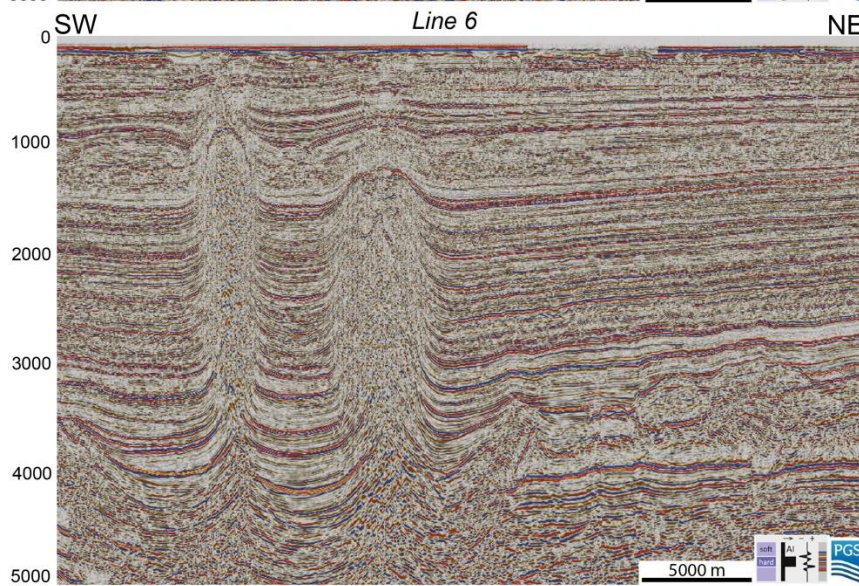
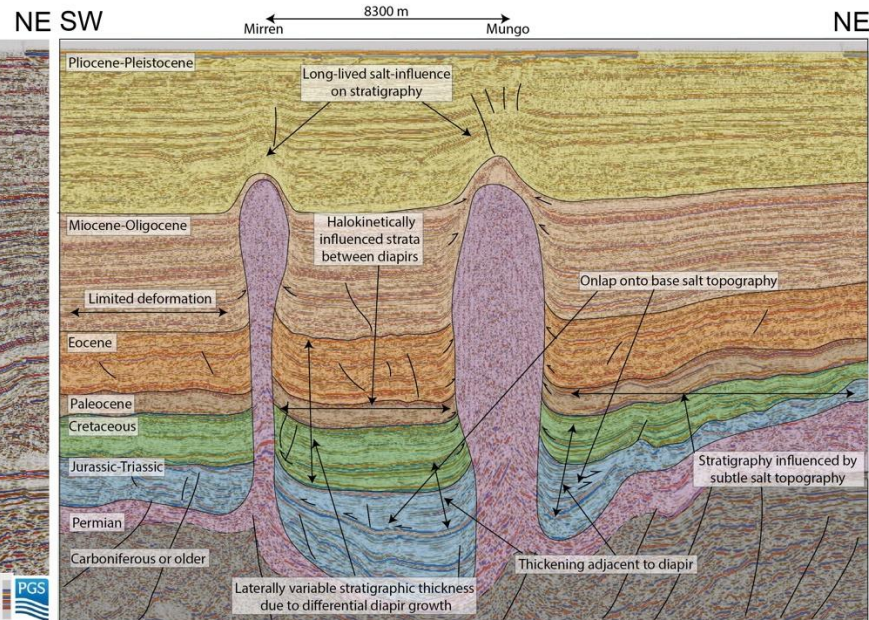
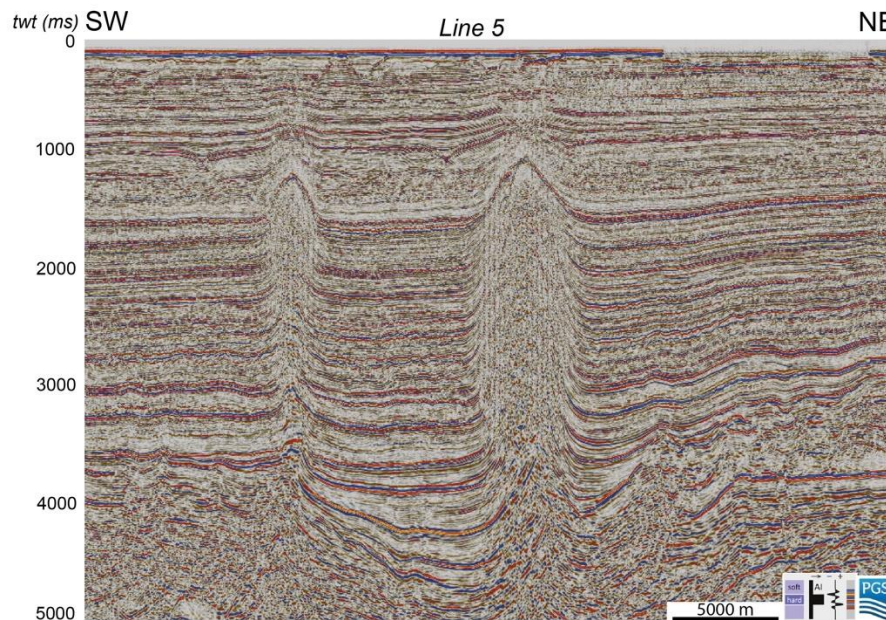
akin to the ‘undeformed zones’ described in Cumberpatch et al. (2021c;d) develops. Subsurface diapirs that are spaced at ~4000-5000 m (e.g., Monan and Mungo, Scoter and Machar, Figure 5.8), have <1000 m of the ‘minimally deformed’ zone between them. Examples of diapirs that are further away from each other (>5000 m), show a central section which appears undeformed or experiences minimal deformation, owing to the distance from the salt structures (Alsop et al. 2000; Oluboyo et al. 2014; Doughty-Jones et al. 2017).

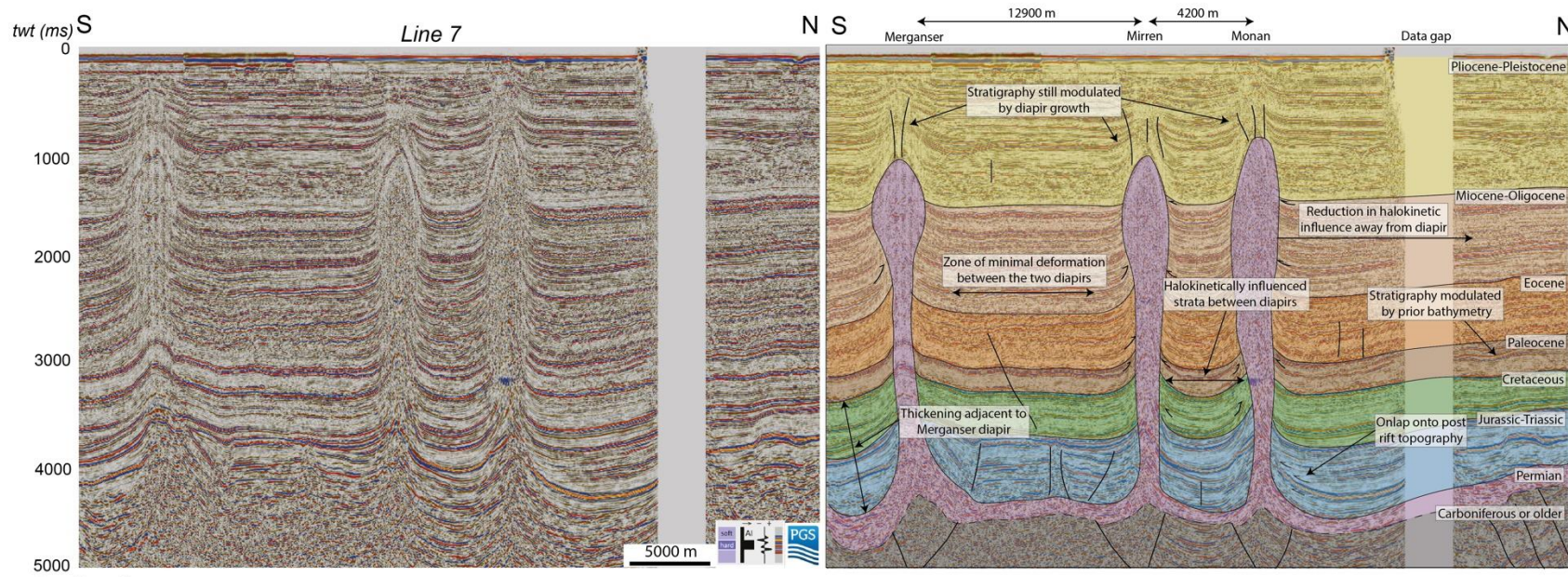
For simplicity, our models do not include an irregular top salt geometry or any early diapiric rift topography. Therefore, the subtle amounts of deformation seen between diapirs in the subsurface examples (e.g., Triassic to Eocene stratigraphy being modulated by a subtle top salt irregularity NE of Mungo in Line 5, and over Lomond in Line 1, Figure 5.8) are not replicated. In the modelled ‘undeformed zones’ between diapirs it is likely that antecedent topography and deformation would cause subtle ‘minimal’ halokinetic modulation in nature, despite the distance from penetrative diapirs as is observed in the North Sea, Offshore Angola and Bolivia (Hodgson et al. 1992; Poliakov and Podladchikov 1992; Penge et al. 1993; Erratt et al. 1999; Birch and Haynes 2003; Borsa et al. 2008; Oluboyo et al. 2014; Charles and Ryzhikov 2015; Howlett et al. 2020). This suggests that while modulation of stratigraphy by a specific diapir is improbable several kilometres away, salt-influenced basins are unlikely to contain purely ‘undeformed’ stratigraphy.

The overall reduction in salt influence through time is consistent across models and subsurface observations (Figures 5.8 and 5.9). Prior to that, subsurface observations show that regardless of whether the diapir was growing or static, there would still have been topography influencing depositional systems and thus stratigraphic architectures (Pratson and Ryan 1994; Prather et al. 1998; 2012; Cumberpatch et al. 2021b). Once topography is buried, the subsequent depositional system and stratigraphic architecture will be ‘undeformed’, unless the salt structure is reactivated by subsequent movements (Harding and Huuse 2015; Wu et al. 2016; Dooley and Hudec 2020).







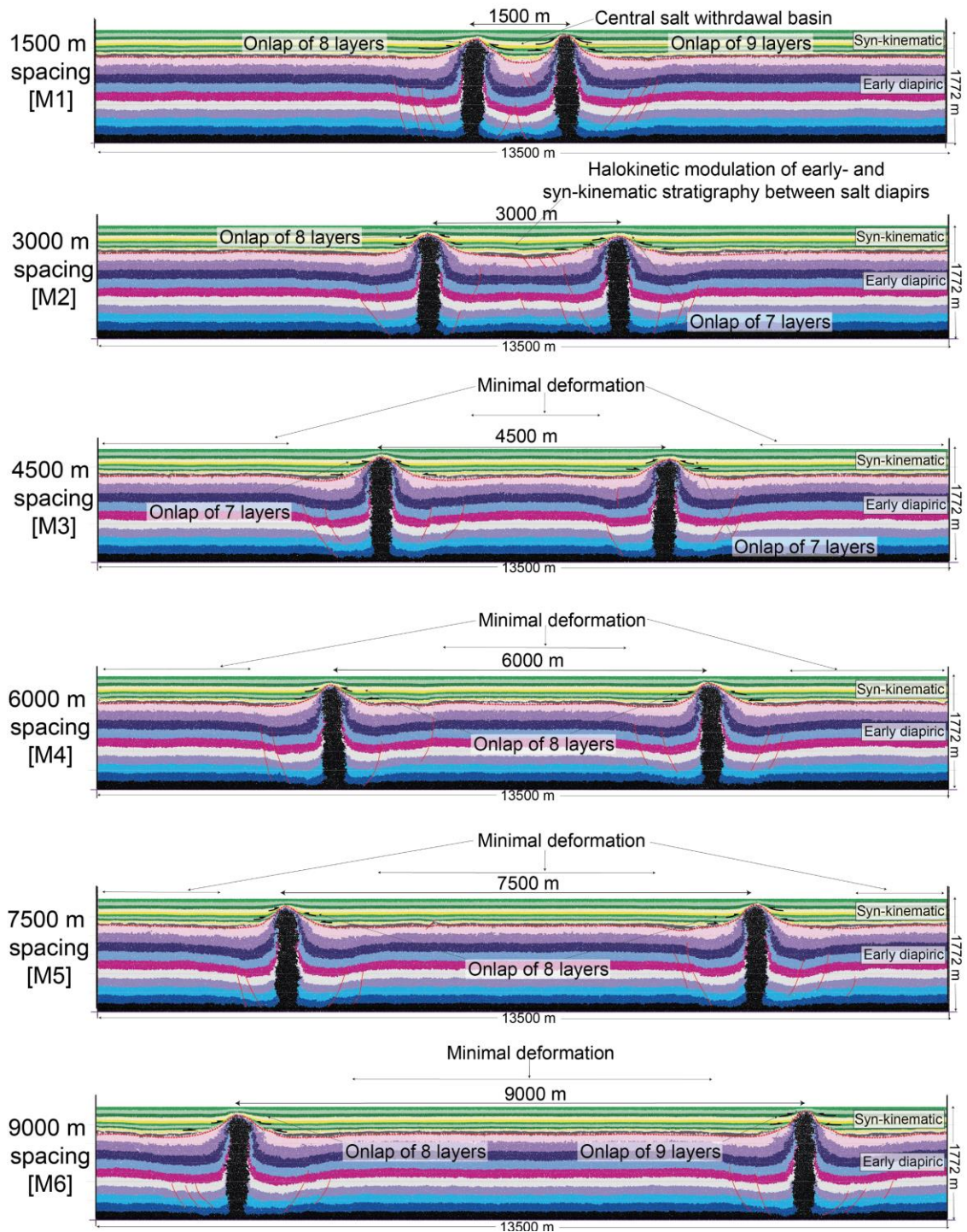


Key for all seismic interpretations

- Carboniferous or older
- Permian
- Triassic-Jurassic
- Cretaceous
- Paleocene
- Eocene
- Miocene-Oligocene
- Pliocene-Pleistocene
- Fault
- ← Onlap
- - - Uncertain base salt

**Figure 5.8:** Uninterpreted and interpreted two-way travel-time seismic reflection cross-sections across the Eastern Central Graben, showing the modulation of stratigraphy between diapirs of different spacing. Location of seismic lines is shown in Figure 5.3. MegaSurvey Plus 3D seismic data courtesy of PGS. Faults, onlap, stratigraphic thickness variations and extent of modulation highlighted. All sections are shown at 6 times vertical exaggeration.





**Figure 5.9:** Interpreted static images of the DEM for M1-M6 after 4.6 Myr. Early diapiric and syn-kinematic sedimentary layers are coloured and assigned numbers and letters respectively for easier discussion. Fault interpretations use displacement from initial neighbour methodology (see Cumberpatch et al. 2021d). Interpretations highlight the width of deformation zones associated with salt structures, major faults, stratal termination and architecture, and variable halokinetic influence vertically and laterally, discussed in text.

## 5.7 Discussion

### *Controls on Paleocene facies distribution*

Facies distribution is controlled on a number of scales across the Eastern Central Graben (ECG) (Den Hartog Jager et al. 1993; Jennette et al. 2000; Hempton et al. 2005; Eldrett et al. 2015), which correspond to 2<sup>nd</sup> -5<sup>th</sup> order topography (Kane et al. in prep). One of the most fundamental controls on facies distribution is the basin-bounding horst and grabens, which controls the distribution of depositional sinks (2<sup>nd</sup> order topography; Penge et al. 1993; Erratt et al. 1999; Bouroulllec et al. 2018; Phillips et al. 2019; Tilhams et al. 2021). Basin-floor fans were supplied along the graben axis, either directly from these fluvial-dominated shorelines or from shelf collapse and bypass, by a combination of turbidity currents and mass flow processes (Jennette et al. 2000).

Salt structures, such as diapirs, are thought to influence depositional processes and subsequent deposits at a smaller scale due to flow re-routing and the formation of depositional shadows (3<sup>rd</sup>-4<sup>th</sup> order topography; Figures 5.1 and 5.7; Mayall et al. 2010; Rodriguez et al. 2020). Diapiric influence on depositional systems is typically radial around a diapir on a kilometre scale (Giles and Lawton 2002; Giles and Rowan 2012). Diapirs in the ECG act to re-route, confine and cause termination of localised parts of depositional systems (Figure 5.7; Hempton et al. 2005; Eldrett et al. 2015; Charles and Ryzhikov 2015). On a local scale, (specifically within 3 kilometres radially), the diapirs act to influence depositional sedimentary processes, stratigraphic thickness, architecture, facies variability, distribution and transitions, diagenesis and subsequent fluid flow and migration (Davison et al. 2000; Hempton et al. 2005; Eldrett et al. 2015; Kilhams et al. 2015). On the scale of the entire graben, however, the diapirs have only a subtle influence on the overall depositional system (i.e., the 3<sup>rd</sup> – 4<sup>th</sup> order topography in superimposed on the 2<sup>nd</sup> order topography).

Other structures observed in our subsurface data include saddle zones between diapirs, an irregular base and top salt surface, and smaller diapirs where growth has ceased (3<sup>rd</sup>-4<sup>th</sup> order topography; Figure 5.8; Hodgson et al. 1992; Poliakov and Podladchikov 1992; Penge et al. 1993; Erratt et al. 1999; Borsa et al. 2008; Oluboyo et al. 2014; Charles and Ryzhikov 2015; Hale et al. 2020; Howlett et al. 2020). These topographic features, like the diapirs, have a localised control on depositional facies and stratigraphic architecture, but their effects are unlikely to be felt a few kilometres away (Giles and Rowan 2012; Rowan and Giles 2020; Cumberpatch et al. 2021a). Additionally, local topography that can cause re-routing of sedimentary facies throughout the Paleocene stratigraphy are associated with diapirically-derived mass transport deposits (Figures 5.6B and 5.7; Scott et al. 2010; Carruthers et al. 2013), and the palaeotopography of earlier depositional systems (3<sup>rd</sup>-5<sup>th</sup> order topography; Eldrett et al. 2015).

The distribution of depositional facies around diapirs (Figure 5.7), whilst controlled by the type, amount and spacing of confining topography, is perhaps more influenced by the allogenic and autogenic controls related to the depositional system itself (e.g., Ferguson et al. 2020). The extent and facies of the axial Paleocene deep-water systems (i.e., the Forties Fan) is ultimately controlled by sediment supply and accommodation availability (Den Hartog Jager et al. 1993; Evans et al. 2003). Source area geomorphology, predominantly controlled by steep basin margins, combined with high sedimentation rates, ultimately influence the size, geometry and distribution of deep marine systems in the study area (Den Hartog Jager et al. 1993; Charles and Ryzhikov 2015). The overall axial system is modulated by interspersed deposition of lateral ‘side lobes’ (Figure 5.7; Eldrett et al. 2015; Kilhams et al. 2015).

MTDs in the study area are reported to be either regionally-derived from up-dip slope failures (Kilhams et al. 2015; Soutter et al. 2018; Cox et al. 2020) or locally-derived from diapir crests (Davison et al. 2000; Back et al. 2011; Kilhams et al. 2015; Arfai et al. 2016; Grimstad 2016). Our

sampling of wells in close proximity to diapirs could be biased towards locally-derived MTDs. In our spectral frequency decomposition data, MTDs derived locally from diapirs are observed (Figures 5.6 and 5.7), typically displaying undulating geometries and chaotic facies. Their apparent attachment to, radial nature around, and thinning away from salt diapirs suggest that these are diapir-sourced and likely to consist of translated material that has moved no more than a few kilometres down the flanks of an individual salt structure (Doughty-Jones et al. 2019). This is further supported by remobilised clasts and thin beds evident in cored wells on diapir flanks (Figures 5.5I-L and 5.6B; Kilhams et al. 2015; Doughty-Jones 2019; Cumberpatch et al. 2021b). Our observations of local, diapirically-derived failures within ~2000 m of diapirs is consistent with global observations of structural deformation (Alsop et al. 1995; 2000), halokinetic sequences (Giles and Rowan 2012) and sedimentary facies (Doughty-Jones et al. 2019; Rodriguez et al. 2020; Wu et al. 2020; Poprawski et al. 2021). MTDs that contain seismically-resolvable clasts, are not connected or derived from diapirs, do not show significant lateral thickness variation (Figure 5.6B) and are more likely to be regionally-derived (Soutter et al. 2018; Doughty-Jones et al. 2019; Cox et al. 2020).

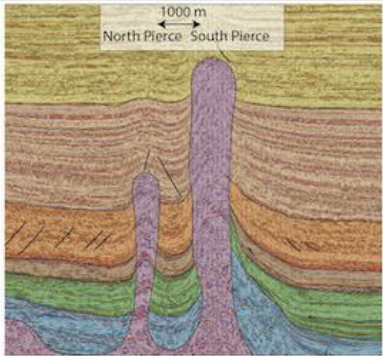
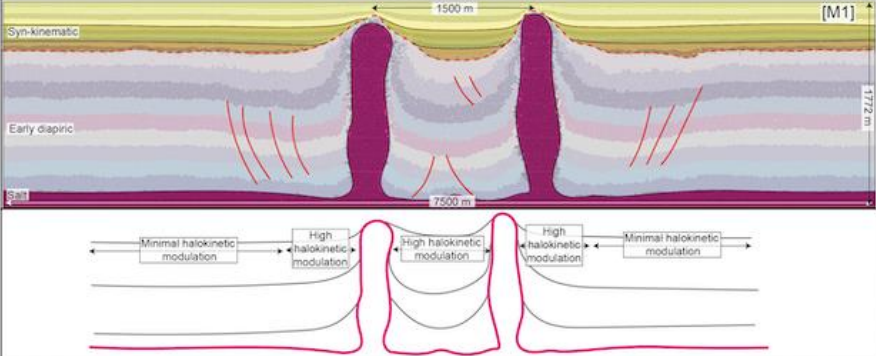
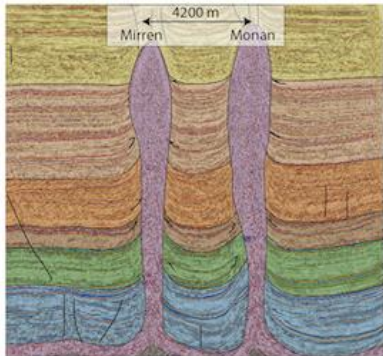
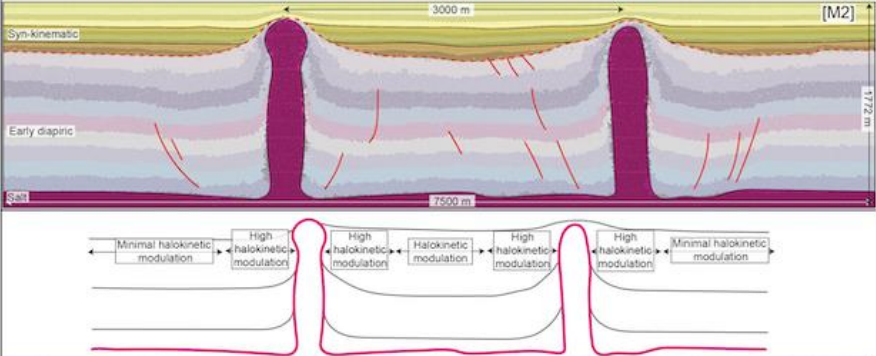
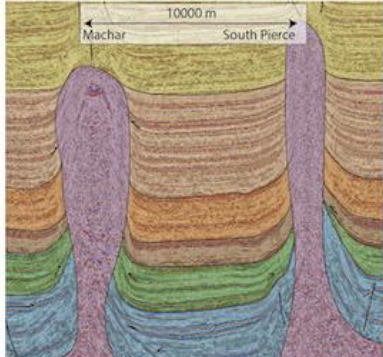
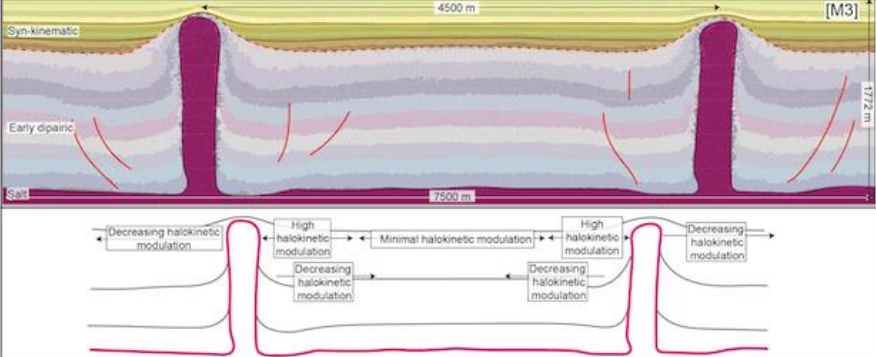
### ***How confined is confined?***

In this study, we show that the modulation of stratigraphy by confinement is influenced by diapir spacing (Figures 5.8-5.10). Where diapirs are very close together we observe intensely modified zones between them, with the highest amount of bed rotation, stratal terminations and thickness variability (e.g., thinning rates of 0.0126%/m between North and South Pierce Line 1, Figure 5.8 and 0.043%/m in M1, Figures 5.9 and 5.10). In natural systems (Figure 5.8), closely spaced (<3000 m) diapirs may have different growth histories and the internal stratigraphic architectures may be asymmetric reflecting the shift in minibasin axis through time due to differential growth of the diapirs and palaeotopography of previous deposits (Mayall et al. 2006; 2010; Jones et al. 2012; Wang et al. 2017; Doughty-Jones et al. 2017; Ge et al. 2020). When diapirs are more widely-spaced (>3000 m), a zone of minimal or 'non' deformation appears to develop between the two structures, which occupies more than half of the lateral distance between the diapirs, where both early diapiric and syn-kinematic stratigraphy experience minimal deformation related to salt diapirs, and the stratigraphic thickness and bedding orientation remain constant, in agreement with natural global analogues (Booth et al. 2003; Oluboyo et al. 2014; Sylvester et al. 2015; Rodriguez et al. 2020). It is, however, unlikely that these areas will be completely free from deformation due to the nature and complexity of salt basins. Minor modulation of stratigraphy is likely to exist across salt-influenced basins regardless of the distance from active, penetrative salt structures due to the presence of subtle structurally- and stratigraphically-controlled topography described above (Penge et al. 1993; Erratt et al. 1999; Birch and Haynes 2003; Borsa et al. 2008; Charles and Ryzhikov 2015; Hale et al. 2020; Howlett et al. 2020).

Fundamentally our study shows that, where zones of halokinetically-influenced stratigraphy associated with two closely spaced (<1500 m) diapirs interact, a zone of intense modulation with highly deformed strata, and thinning rates in the order of 0.0126-0.058%/m, is created (Figure 5.10). By comparison, when diapirs are widely-spaced (>4500 m) a central broad plateau, which occupies more than half of the lateral distance between the diapirs, appears to develop in models, which experiences very limited deformation (Figure 5.10). The same zone is represented by extensive, flat depositional lows between diapirs in subsurface examples (Figure 5.8, Harding and Huuse 2015; Jackson and Hudec 2017; Pichel et al. 2017; 2019; Grant et al. 2019). In diapirs that are intermediately spaced (1500 – 4500 m) a central modulation zone between the two diapirs is predicted, but deformation appears to decrease from the diapirs towards the centre of the modulation zone, suggesting there may be a small zone of 'non-deformation' which is difficult to decipher (Figure 5.10). This is in agreement with observations of polygonal faulting variation and intensity around and between salt diapirs (Stewart 2006).

This manuscript has focussed on the confinement of stratigraphic packages by salt structures, specifically focussing on diapirs. As previously discussed, there are other types of confining features present in the ECG and other salt-influenced basins including topography created by: broad-scale rifting (Davison et al. 2000; Borsa et al. 2008; Jackson et al. 2017; Bouroullec et al. 2018; Tilhams et al. 2021), previous mass transport deposits (Armitage et al. 2009; Ortiz-Karpf et al. 2015; 2016; Soutter et al. 2018; Doughty-Jones et al. 2019; Wu et al. 2020; Cumberpatch et al. 2021a) and previous lobes (Jennette et al. 2000; Hempton et al. 2005; Prélat et al. 2009; Kilhams 2012; 2014; 2015; Eldrett et al. 2015; Doughty-Jones et al. 2017; Bell et al. 2018; Hansen et al. 2019). Therefore, it is most useful to have an integrated understanding of all scales and types of topography operating in salt basins, regionally and locally (Clark and Cartwright 2009), in order to be in the best place to predict how sediment routing may occur, rather than treating individual topography styles as isolated.

So far, we have focussed on how spacing of diapirs controls the amount of modulation experienced by early diapiric and syn-kinematic stratigraphy, and have discussed the influence of different types of topography. However, the amount of modulation is influenced by a number of other factors, which we consider here. Put simply, it is likely that the higher the number of diapirs or salt structures in a basin, the more complicated the confining topography is, and therefore the more complicated the sediment routing pathways are. Diapirs, somewhat randomly distributed across a basin, are more likely to cause a complicated, variable sediment routing pathway and therefore facies distribution compared to linear salt walls (Oluboyo et al. 2014). The geometry of the salt will also have a control on the amount of stratigraphic modulation experienced. An overhanging complex geometry, for example in the Gulf of Mexico (Murray 1966; Ratcliff et al. 1991; Talbot 1993; Jackson and Hudec 2017), will have a more complicated influence on stratigraphy than a radial diapir or salt wall. Overhanging allochthonous salt may reduce the imaging quality of sub-salt topography, such as variations in salt geometry and sub-salt faulting, preventing a detailed analysis of different scales of topography and their influence on stratigraphy (Ratcliff et al. 1991; Jones and Davison 2014, Chen et al. 2018). Salt walls are likely to exhibit a more regionally extensive impact on stratigraphic architecture and facies distribution compared to salt diapirs, because confinement is more extensive laterally (for 10s to 100s of kms), rather than only being influential for a few kilometres around the diapirs (Oluboyo et al. 2014; Doughty-Jones et al. 2017; Rodriguez et al. 2020). Diapir size, specifically width, can also exhibit a significant control on the extent of deformation zones formed by salt diapirs (Cumberpatch et al. 2021b,d), with wide, tall diapirs having the most laterally and temporarily extensive effects on stratigraphy (Giles and Rowan 2012; Jackson and Hudec 2017). Salt layer initial thickness has been shown to control diapir spacing and thus the amount of stratigraphic modulation, at a ratio of 1:12 to 1:20 (Hernandez et al. 2018). Another control on stratigraphic modulation between diapirs is the relative ratio between salt rise and sedimentation rate. If sedimentation rate is higher than diapir rise rate the topography will become subdued, and thus the sedimentary architecture unconfined. In this case the stratigraphic character will exhibit an upwards reduction in confinement over relatively short time intervals, on the order of millions of years (Booth et al. 2003; Sylvester et al. 2015; Wang et al. 2017; Ge et al. 2020; Cumberpatch et al. 2021b).

	Subsurface Example	Modelled Example Schematic	Key Observations
<b>Narrow diapir spacing</b> ( $<1500$ m between)			<ul style="list-style-type: none"> <li>• Central high modulation zone formed between diapirs, in early and syn-kinematic</li> <li>• Difficult to image in subsurface data</li> <li>• Thickest stratigraphy between diapirs, thins towards diapirs</li> <li>• Halokinetic influence decreases upwards and away from diapir, in absence of confinement</li> </ul>
<b>Intermediate diapir spacing</b> ( $1500$ - $4500$ m between)			<ul style="list-style-type: none"> <li>• Central modulation zone formed between diapirs, in early and syn-kinematic</li> <li>• Highest modulation adjacent to diapirs, and decreases away from them, and upwards</li> <li>• Thickest stratigraphy in salt withdrawal basins</li> <li>• Thickness variability can be resolved in subsurface data</li> </ul>
<b>Wide diapir spacing</b> ( $>4500$ m between)			<ul style="list-style-type: none"> <li>• Central plateau between diapirs which experiences minimal to no diapiric modulation</li> <li>• Highest modulation adjacent to diapirs, and decreases away from them, and upwards</li> <li>• In the subsurface, subtle topography between diapirs (rifts, buried diapirs) influences deposition so this zone is not entirely 'undeformed'</li> </ul>

**Figure 5.10:** Comparative diagram showing examples of different spaced diapirs in subsurface and model datasets used in this study, and the key observations associated with those different amounts of diapir spacing. Seismic data is from Figure 5.8, models are from Figure 5.9 (numbered), and represent the central 7500 m of the 13500 m model. Models overlain with a stratigraphic interpretation, the different shades of brown-yellow represent different stages of sedimentation (2.2-3 Myr, 3-3.8 Myr, 3.8-4.6 Myr). Schematics show the key modulation zones and trends.

### **Implications for reservoir quality and stratigraphic traps**

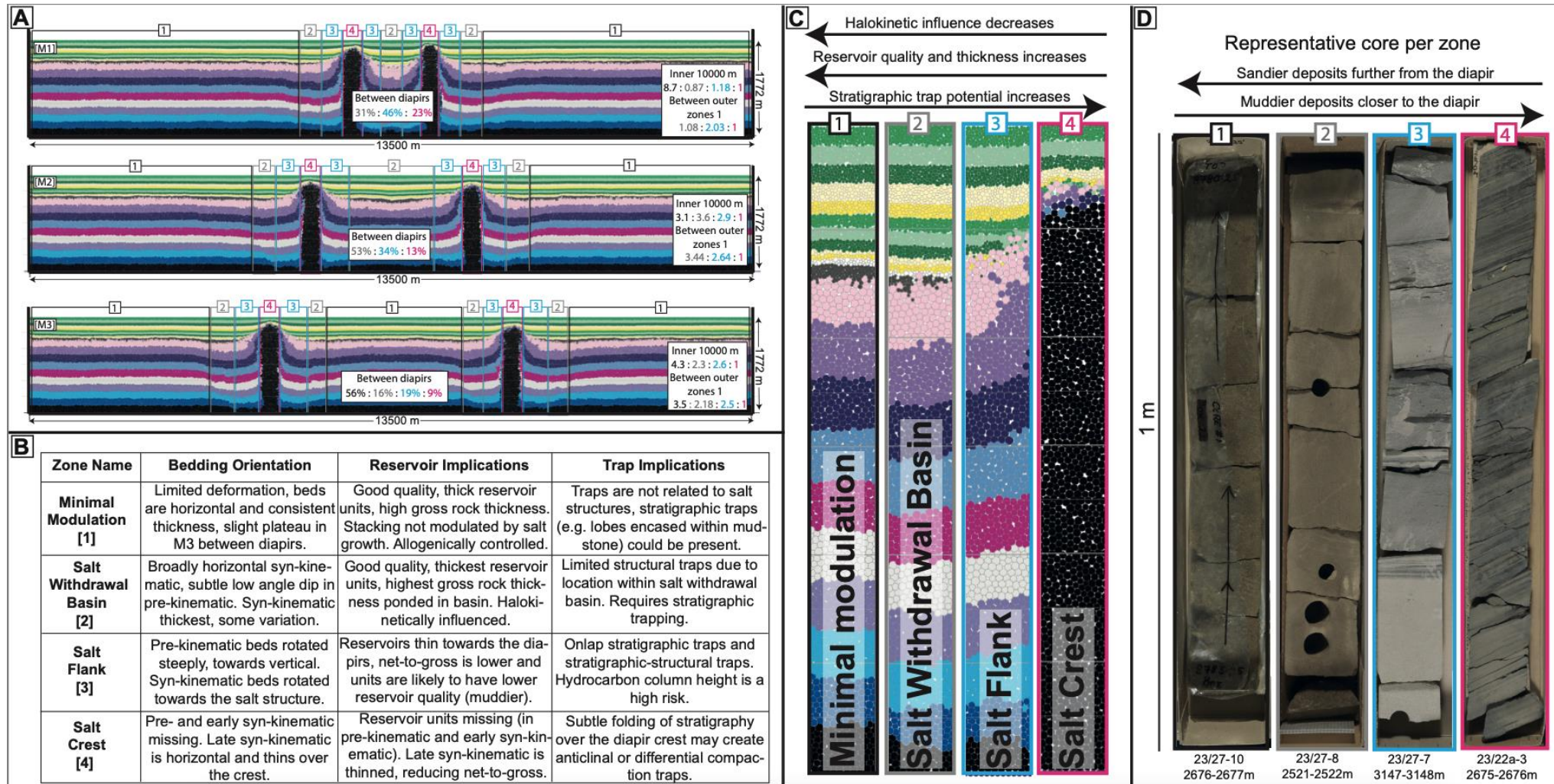
Despite advances in extent and resolution of 3D seismic reflection imaging, the salt-sediment interface remains difficult to image, yet determining its position and precise geometry is crucial in helping to appraise stratigraphic-structural traps for hydrocarbon, carbon storage, and geothermal prospects globally (Jones and Davison 2014; Warren 2016).

This work has enabled the subdivision of the region between two diapirs in salt-influenced settings into four zones; minimal modulation, salt withdrawal basin, salt flank and salt crest (Figure 5.11A, B). Overall, the halokinetic influence decreases away from the diapirs, from the salt crest to the undeformed zones, and thus reservoir quality and thickness increases away from diapirs, whilst the stratigraphic trap potential increases towards them (Figure 5.11C). Diapir spacing controls the presence, extent and width, of the minimal modulation zone between the salt withdrawal zone between diapirs (Figure 5.11). Between narrowly spaced diapirs (M1), each individual zone is small, with a strip of salt withdrawal basin between them (that accounts for 31% of the distance between the diapirs). In this zone, good, thick, amalgamated reservoirs are likely to develop, but structural traps are limited (Figure 5.11D). In intermediate spaced diapir scenarios (M2), the salt withdrawal basin between the diapirs is larger than in the narrow spaced diapirs (accounting for 53% of the distance between the diapirs), but the other halokinetic zones have similar lateral extents. Deformation decreases towards the centre of the salt withdrawal basin, but there appears to remain some subtle modulation of stratigraphy at the centre, suggesting that reservoir units will not be completely undeformed, and still experience some deformation due to halokinetic-influence however this is difficult to decipher from the ‘minimal modulation’ (Figure 5.11D). Where diapirs are widely spaced (>3000m, M3-6) giving a zone of ‘minimal modulation’ (responsible for over 56% of the distance between the diapirs in M3) good quality reservoir properties may be expected (Figure 5.11D). With increasing diapir spacing, the zone of ‘minimal modulation’ lengthens, and therefore thick reservoir units could be laterally extensive (Figure 5.11 A, D). However, this zone may be influenced by other types of topography described above. Regardless of diapir spacing, the salt crest and flank zones are generally the same size, with a ratio of ~1:2-2.6 between the outer ‘minimal deformation zones’ in all models. Reservoir thickness and quality decreases in these locations as the high-density part of flows, responsible for thickest sandstones are unable to run up topography (Figure 5.11D; Kneller and McCaffrey 1999; Soutter et al. 2019).

There is a trade-off in terms of play suitability due to lack of trapping mechanism (Figure 5.11B). Combined structural-stratigraphic traps are more likely to develop where diapirs are closely spaced (Figure 5.11), but any resources will be laterally confined and limited in size (at least in two-dimensions). Furthermore, steep dips will result in large column heights such that higher sealing capacity will be needed to form a working trap. Nonetheless, due to the topography of the top and base salt, non-piercing diapirs and salt related faults at depth, there may also be structural closures further away from salt diapirs, reaffirming knowledge that subsurface energy plays in salt basins do not always require penetrative diapirs (Jackson and Hudec 2017). Deep-water fans with limited petroleum trapping potential may still be useable for carbon dioxide storage as long as they do not lead to leakage points at diapir flanks or areas where the aquifer is less than 800 metres below sea level where the CO<sub>2</sub> would enter its gaseous phase (Lloyd et al. 2021).

Whilst this study has focussed on a specific basin, its combination of numerical modelling and a wealth of data from the North Sea make it useful globally for gaining a better understanding of

the effects of diapir spacing on stratigraphic architectures. Whilst our simulations are an oversimplification, with stratigraphic and structural evolutions well known and controlled, they are useful for providing generic end member scenarios, which can be populated with basin specific data and understanding. The overall aim of this work is to improve understanding to help better predict halokinetic modulation in salt basins. Due to a number of limitations arising from using a two-dimensional model to simulate such complicated three-dimensional systems further work is intended using three-dimensional models.



**Figure 5.11:** A) Halokinetic zonation scheme shown for M1, M2 and M3. The models are divided into 4 zones, 3 of which experience some form of halokinetic-influence. Minimal deformation zones [1] show virtually no modulation by salt diapirism. Halokinetic influence increases towards the diapir-cored high, and changes from thickening in the 'salt withdrawal basin' zone to onlap and thinning in the 'salt flank' zones. Thinned and reduced stratigraphy are observed over the diapir crest. Ratios of the different zones across each model are shown between diapires, within the inner 10 km of the models and between the outer limits of zone 1, B) Table highlighting reservoir and trap implications of each zone, note that while stratigraphic trap quality may be greater closer to the diapir, reservoir thickness and



quality are likely higher further from the diapir, showing a 'trade-off' exists for subsurface energy exploration and production. Central zone between the two diapirs in M3 represents a zone of stratigraphy with minimal deformation, this zone is more extensive in M4-M6. Net-to-gross (NTG) and porosity values taken from Everest and Arran fields of the Eastern Central Graben (Nagatomo and Archer 2015), C) Zoom ins of representative model observations for each zone. D) Equivalent metre sections of core from each zone taken from the Eastern Central Graben (ECG) study area, core viewings available at the British Geological Survey.

## 5.8 Conclusions

We integrate results from subsurface data and a discrete element model (DEM) to better understand the halokinetic modulation of stratigraphic architectures by variably-spaced salt diapirs, in order to reduce reservoir and trap uncertainty in subsurface energy exploration and development. We have demonstrated that:

- 1) In the Paleocene of the Eastern Central Graben, channels and lobes are influenced (re-routed and confined) by salt growth on a range of scales (from centimetre-scale sedimentological character in core, to kilometre-scale geomorphological attributes in seismic). Mass transport deposits are present and appear to be diapir-derived. The distribution of depositional facies around diapirs is influenced by the type, amount and spacing of confining diapir topography.
- 2) Comparison between models and subsurface data have shown that diapir spacing strongly influences stratigraphic thicknesses, minibasin geometries and extent of the halokinetically influenced zone, such that when the spacing between diapirs is:
  - a) **Close (<3000 m e.g., M1 and North to South Pierce diapirs):**
    - (i) The thickest part of the stratigraphy is within the axis of the salt withdrawal basin.
    - (ii) A synclinal-shaped minibasin with steeply rotated flanks develops between diapirs recording their growth.
    - (iii) The zone of halokinetic influence of one diapir is laterally connected to the other, such that the zone between them is influenced by both structures (46% of the space between the diapirs is salt flank zone, compared to 19% in wider spaced models). This creates a region of intense constructive interference (modulation) and topographic perturbation where stratigraphy is highly deformed.
  - b) **Intermediate (3000-4500 m e.g., M3 and Mirren to Monan diapirs):**
    - (i) Thinning directly adjacent to diapirs is common, and thickest stratigraphy is in salt withdrawal basins.
    - (ii) Halokinetic influence is highest adjacent to salt structures and decreases away from them.
    - (iii) A central minimal modulation zone is present between the two diapirs in early diapiric and syn-kinematic stratigraphy, this occupies 53%-72% of the distance between the diapirs and comprises of a transition between the salt withdrawal basin and minimal modulation zones which is often hard to decipher.
  - c) **Wide (>4500 e.g., M5 and Machar to South Pierce diapirs):**
    - (i) The thickest stratigraphic succession is directly adjacent to the diapir.
    - (ii) Between diapirs there is a zone where stratigraphy is relatively flat, forming a plateau.
    - (iii) There is an extensive zone of minimal deformation that develops between the diapirs, this occupies more than 65% of the distance between the diapirs.
- 3) Due to the complexity of salt basins, and therefore the presence and variability in the early diapiric stratigraphy and salt-related faults, even these 'minimal modulation' zones are likely to contain gently modulated stratigraphy. Subsurface energy prospects are likely to be influenced by subtle salt-related topography even 10s of kilometres away from diapirs.

## Chapter 6: Synthesis

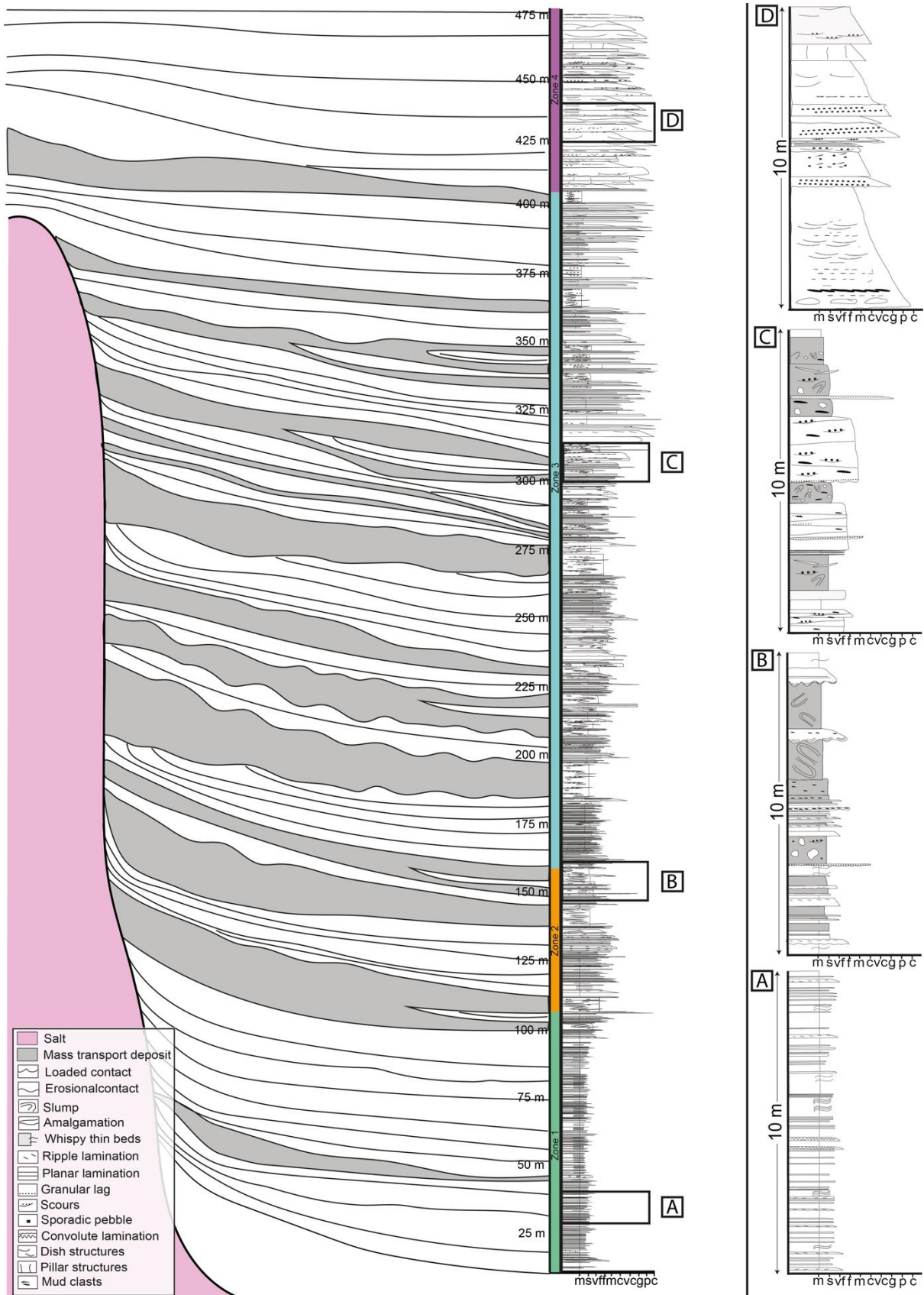
This chapter intends to provide a synthesis of the results, discussions, conclusions and applications of the previous chapters, within the context of the three broad research aims set out in Chapter 1. It also aims to evaluate the importance of using multiple different data sets and methodologies to further our multi-scalar understanding of the salt sediment interface, with focus on the implications for subsurface energy exploration and production. Future research questions and directions generated by this study are also proposed.

### 6.1 How do deep-water facies and architecture vary around salt structures?

#### *Summary*

Stratigraphic packages that thin and rotate towards salt structures (halokinetic sequences) are responsible for progressive facies changes adjacent to diapirs (Giles and Rowan 2012). These sequences are bound by progressive unconformities, and steepen towards the diapir (Giles and Lawton 2002). These steep sections are subject to intense brittle and plastic deformation. Brittle deformation is characterised by fault and fracture density, which decrease away from diapirs (Alsop et al. 2000). Plastic deformation is characterised by soft sediment deformation, driven by movement of the mobile substrate, and is common outside (and stratigraphically above) the brittle deformation zone (Birch and Haynes 2003). Common features in salt basins include: hybrid beds, injectites, soft sediment deformation, ripple reflections and amalgamated sandstones (Booth et al. 2003). Mass transport deposits (MTDs) are often intercalated with these sequences, and could be regionally- or locally- derived (Hunnicuttt 1998; Giles and Rowan 2012; Doughty-Jones et al. 2019; Wu et al. 2020; Poprawski et al. 2021). While none of these features alone is diagnostic of the presence of evolving seafloor topography, the combination and repetitive patterns described can give some indication.

A typical stratigraphic profile (Figure 6.1) is characterised by an upwards thickening and coarsening associated with the progradation of the sedimentary system, intercalated with MTDs. This often represents a transition from initial poorly developed or distal channel and/or lobe sub-environments (thin-bedded sandstones interbedded with mudstones) to more developed, longer lasting or more proximal channels and lobes (medium to thick-bedded, often amalgamated sandstones) upwards (Figure 6.1; Booth et al. 2003; Mayall et al. 2010; Oluboyo et al. 2014; Doughty-Jones et al. 2017; Jackson and Hudec 2017). This shallowing-upwards trend reflects an increase in sedimentation rate relative to diapir rise rate (Giles and Rowan 2012). Vertical trends adjacent to diapirs typically represent a loss of confinement (Sylvester et al. 2015) and are associated with a reduction in the number of MTDs up-section (Figure 6.1; Booth et al. 2003; Doughty-Jones et al. 2019; Wu et al. 2020).



**Figure 6.1:** Stratigraphic architectural panel through the Black Flysch Group at Cabo Matxixako, Bakió, Spain (Cumberpatch et al. 2021b), thought to be representative of halokinetically-influenced deep-water settings. Stratigraphy is divided into 4 zones (coloured on the log) based on stratigraphic observations. A detailed 10 metre section, representative of each zone is shown on the right. Grey indicates mass failure deposits.

Outcrop observations around the Bakio diapir, Northern Spain (Chapter 3) provide bed to lobe scale observations of facies and architectures variability. These observations confirm the typical stratigraphic profile, often recognised in seismic data sets, whereby relative deformation rate decreases through time, relative sedimentation rate increases through time, and as such confinement decreases temporally (Figure 3.11; Booth et al. 2003; Doughty-Jones et al. 2019; Wu et al. 2020).

The lowermost siliciclastic fill (Black Flysch Group) of the Sollube basin is dominated by thin-bedded sandstones, with localised debrites on the flanks (Figures 3.9, 3.11 and 3.14). As the basin developed, thicker-bedded sandstones representing channel fills and lobes were deposited in topographic lows (basin axis), consistent with subsurface analogues (e.g., Booth et al. 2003; Madof et al. 2009; Mayall et al. 2010; Doughty-Jones et al. 2017) and numerical models (e.g., Sylvester et al. 2015; Wang et al. 2017). Towards the flanks, the lower-density parts of the flows responsible for the thick-bedded sandstones may run up topography, depositing thin-bedded sandstones (Kneller et al. 1991; McCaffrey and Kneller 2001; Barr et al. 2004). Therefore, allocyclically-controlled, axially-derived, and often the thickest stratigraphy is observed in the axis of the minibasin. Halokinetically-controlled (e.g., debrites) or -influenced (e.g., thickness variations) stratigraphy occurs towards the basin margins. These interpretations are consistent with those from other subsurface studies (e.g., Doughty-Jones et al. 2017; Wu et al. 2020; Rodriguez et al. 2020), which suggest that stratigraphy closer to the diapir experience more deformation, showing higher proportions of MTDs. Whilst in the axis of the minibasin, further from the diapir, sandstone deposition with minor modulation may be observed as gravity flows respond to the remnant topography of the diapir (Figure 3.14).

Model observations show that stratigraphic architectures, thinning rates and modulation on a stratigraphic to mega-sequence scale are heavily influenced by relative sedimentation rates (Chapter 4). Thinning rates are shown to be up to six times greater in the 350 m immediately adjacent to the diapir compared to 1500 m away, therefore allocyclically controlled stratigraphic architectures, and associated facies (not modelled) are confirmed to be modulated by halokinesis. Relative sedimentation rate controls the amount of stratigraphic architecture variability, with deposition under slow sedimentation rates being restricted to salt withdrawal basins either side of the diapir throughout evolution, while other sedimentation rates and styles (intermediate, fast, increasing and decreasing) eventually occurs over the diapir crest, often associated with significant lateral thickness variability (Figures 4.5 and 4.6).

Core observations at bed scale, reveal very similar facies in the Eastern Central Graben (ECG) to those identified in outcrop and previous subsurface studies (Figure 5.5; Birch and Haynes 2003; Scott et al. 2010; Eldrett et al. 2015; Doughty-Jones et al. 2019). Facies analysis of the Paleocene stratigraphy in the ECG study area (Chapter 5) reveals that channels and lobes are influenced (re-routed and confined) by salt growth on a number of different scales, from centimetre-scale sedimentological character in core, to kilometre-scale geomorphological attributes in seismic datasets. Overall, there is a proximal to distal decrease in thick-bedded high density turbidites, and increase in lower density turbidites, consistent with reported reductions in reservoir quality distally (Hemp-ton et al. 2005; Kilhams et al. 2012; 2014; 2015; Charles and Ryzhikov 2015). These predominantly allocyclic depositional systems are influenced by mass transport deposits, which appear to be diapirically-derived. The distribution of Paleocene facies radially around diapirs in the ECG is influenced by the type, amount and spacing of confining diapir topography. Facies distributions are not symmetrical around the diapirs due to a complex interaction of these controlling parameters and different scales and types of topography.

### ***Development of a coeval deep-water axial and debrite rich lateral depositional system***

Both the outcrop (Chapter 3; Cumberpatch et al. 2021b) and subsurface (Chapter 5) analogues record coeval development of axial deep-water depositional systems and transverse debrite rich depositional systems (Figure 6.2). Field observations from Bakio, provide compelling evidence that, on a lobe to lobe-complex scale, the stratigraphic architecture is controlled primarily by system progradation. This is likely driven by the increase in sediment supply from the Landes Massif (García-Mondéjar et al. 1996; Martín-Chivelet et al. 2002; Puelles et al. 2014), and/or increased flow efficiency from confinement (Hodgson et al. 2016). Lateral switching of lobes, which is expected in unconfined settings, appears to be limited in confined settings due to a reduction in the amount of space available for switching to take place due to the confining topography (e.g., Mayall et al. 2010; Oluboyo et al. 2014).

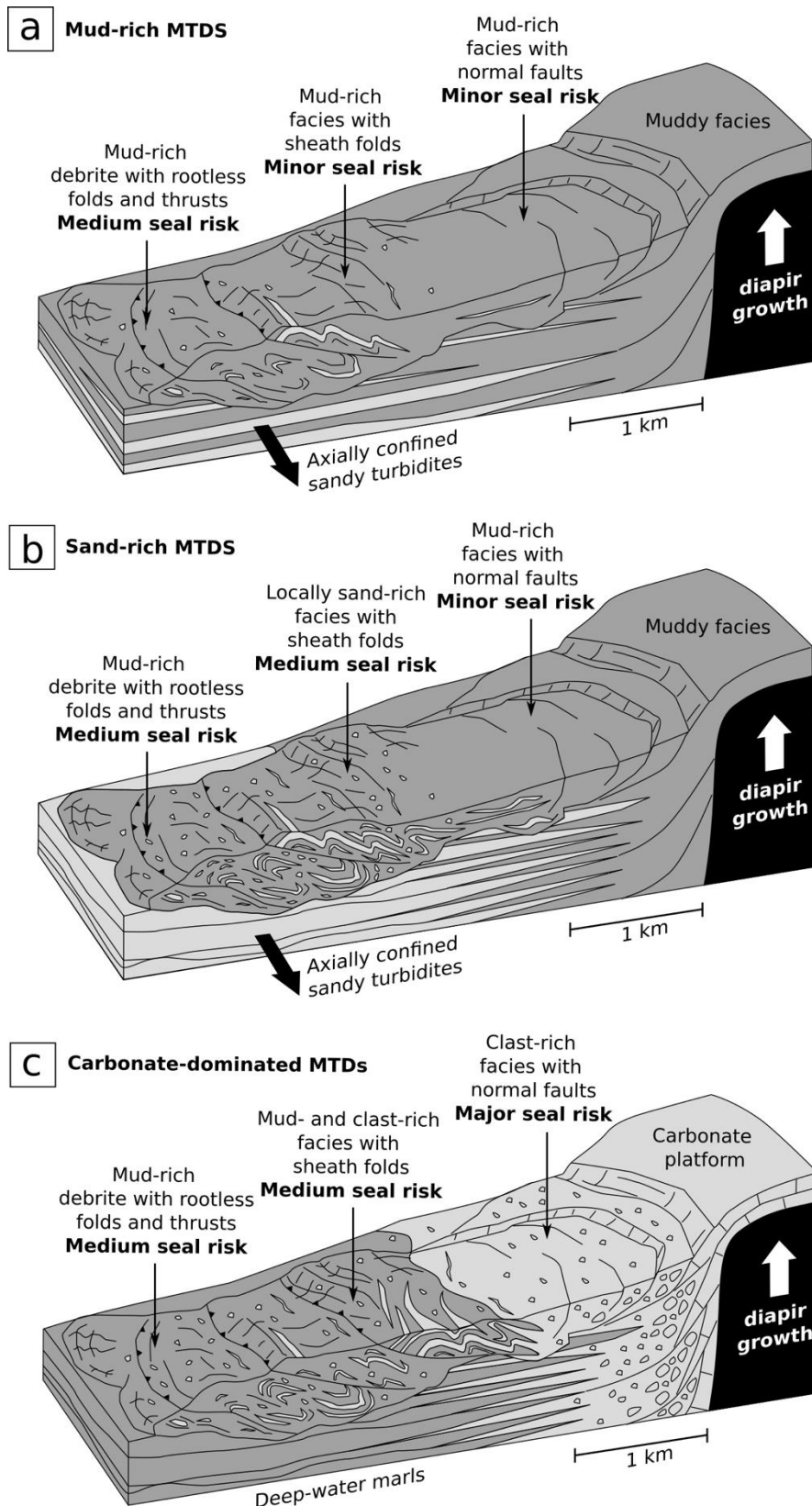
The field work study indicates that the dominant style of interaction between gravity flows and topography is lateral confinement, with channels and lobes in the Sollube (dual confinement) basin being thickest in the axis and elongated parallel to the margins of the salt-controlled basin. This ‘funneling’ arises because lateral topography reduces flow loss to overspill and causes flow deceleration resulting in the system remaining turbulent for longer. Ultimately this manifests as a basinward shift in deposition, magnifying the effects of progradation (Figures 3.14, 3.15C, 3.15F and 3.16; Kneller and McCaffrey 1999; Machado et al. 2004; Scott et al. 2010; Talling et al. 2012; Patacci et al. 2014; Oluboyo et al. 2016; Howlett et al. 2020). Funneling of axial gravity flows, and therefore bed amalgamation, is interpreted to be more enhanced where two salt structures are present, resulting in thicker, but areally smaller, depositional architectures compared to unconfined settings (Figure 3.16; Kneller and McCaffrey 1999; Patacci et al. 2014; Soutter et al. 2021). This observation substantiates the dominant stacking pattern being compensational stacking in unconfined settings and progradational or aggradational stacking in confined settings (Straub et al. 2009; Prélat et al. 2009; 2010; Prélat and Hodgson 2013; Sztanó et al. 2013; Grandvåg et al. 2014; Sahoo et al. 2020; Liu et al. 2020).

The presence of MTDs is somewhat overlooked in both the confinement model proposed by Oluboyo et al. (2014), and the earlier “fill-and-spill” model (Winker 1996; Prather et al. 1998; Sinclair and Tomasso 2002). MTDs sourced from either up-dip (i.e., extrabasinal; detached) or from local mass failures (i.e., intrabasinal; attached) related to growing salt structures, can generate additional syn-depositional relief and flow confinement (Figure 3.15; Moscardelli and Wood 2008; Nascimento et al. 2020; Rodriguez et al. 2020). Regionally-derived MTDs in salt-controlled basins commonly consist of debrites associated with rafted blocks and are usually associated with long run-out distances (Gamboa et al. 2011; Jackson 2012; Omosanya and Alves 2013; Ward et al. 2018; Soutter et al. 2018; Doughty-Jones et al. 2019). Locally-derived MTDs have better preserved internal architectures, including slide deposits, folded strata, normal faults in their headwall and imbricate thrusts in their toe (Madof et al. 2009; Gamboa and Alves 2016; Doughty-Jones et al. 2019), consistent with their run out distances (Poprawski et al. 2021).

The presence of complicated variations in thickness, clast type, and debrite style across the study area suggests that mass flows are likely to be both locally-derived (from the salt structures) and regionally-derived (from the shelf), and therefore debrites were likely both allogenic and halokinetic in origin (Moscardelli and Wood 2008; Doughty-Jones et al. 2019; Wu et al. 2020). The proximity to salt structures, and the reduction in mass-failure deposits away from salt structures, combined with the nature of remobilised intrabasinal clasts within them suggests that the majority of debrites in the study area are locally derived from the Bakio diapir (Figure 6.2). Based on measurements of slump fold axes, run out distance (100 to 2000m), proximity to structures, along with facies analysis, preservation of strata, and studying reworked facies, Poprawski et al. (2021) suggests that majority of MTDs in the Bakio study area are locally-sourced from the Bakio salt wall,

or the footwalls of the nearby Armintza and Bermeo sub-salt extensional faults. Only MTD 5 (BWB in Chapter 3) from their study, is interpreted to have a regional signature because of the wider variety of clast compositions and debritic character observed, consistent with the regional source from the Landes Massif (Figure 3.10; Chapter 3; Figure 6.2).

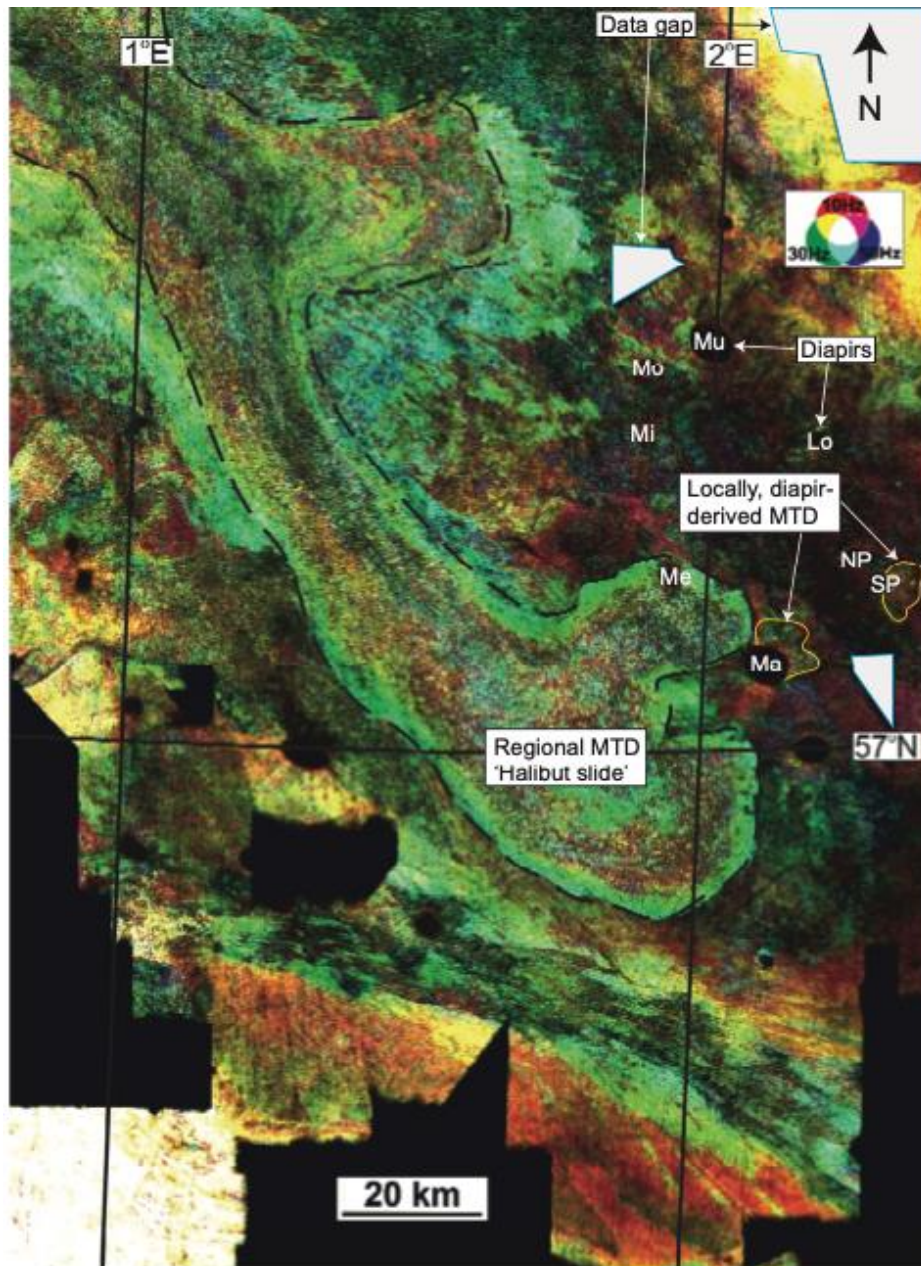
Regardless of emplacement mechanism, debrites formed additional rugose seafloor topography in the field study area, confining subsequent gravity flows and further localising deposition (Cronin et al. 1998; Armitage et al. 2009; Madof et al. 2009; Kneller et al. 2016; Cumberpatch et al. 2021a). Halokinetically-derived debrites are likely to increase the area deformed by topography surrounding salt structures and therefore subsequent flows would be expected to be deposited further from the diapir, in response to topographic influence (Doughty-Jones et al. 2019; Figure 6.2).



**Figure 6.2:** Conceptual model for locally-derived MTDs in salt-controlled basin (Poprawski et al. 2021). A) Locally-derived siliciclastic MTD in a deep-water environment with limited interaction with coarse-grained facies (mud-rich MTDs; lower Black Flysch Group). B) Locally-derived siliciclastic MTD in deep-water environment with coeval interaction of coarse-grained facies (sand-rich MTDs; upper Black Flysch Group). C) Locally-derived carbonate-dominated MTD linked with syn-kinematic carbonate platform growth in the photic zone at the apex of diapirs (carbonate-dominated MTDs; Urgonian Group). Implications for subsurface energy seal risks are highlighted and vary laterally.



Subsurface observations from the ECG study area confirm the presence of the NW-SE trending channelised submarine lobe complex, recognised by previous workers (Figure 5.7; Den Hartog Jager et al. 1993; Jennette et al. 2000; Kilhams et al. 2012; 2014; 2015; Eldrett et al. 2015). This axial deep-water system, regionally known as the ‘Forties fan’, is coeval with cross-cutting, transverse ‘side lobes’ and diapirically-derived, attached (local) MTDs (Figure 5.7B; Hempton et al. 2005; Moscardelli and Wood 2008; Eldrett et al. 2015; Doughty-Jones et al. 2019; Wu et al. 2020). The areal extent of the subsurface study area is substantial enough to observe an along-axis decrease in high-density and medium-density turbidites, and an increase in low-density turbidites distally, providing greater resolution of the source to sink coverage than is possible in the outcropping analogue. Due to the regionally extensive data set and understanding, it is possible to get better control on the local-versus regional nature of MTDs, compared to the field example. Similar to the stratigraphy around Bakio, there is evidence for both regionally- and locally-sourced MTDs (Figure 6.3). In the subsurface study area, the MTDs adjacent to Machar and Pierce diapirs are likely to be halokinetically-derived rather than regionally-derived due to their attachment, radial nature, thinning away from, and proximity to salt diapirs (Moscardelli and Wood 2008; Doughty-Jones et al. 2019). This ‘local’ origin of the MTDs is supported by remobilised clasts and thin beds observed in cored wells on diapir flanks (Kilhams et al. 2015; Doughty-Jones et al. 2019; Cumberpatch et al. 2021c). These observations of local, diapirically-derived failures within ~2 km of diapirs is consistent with global observations of structural deformation (Alsopp et al. 1995; 2000), halokinetic sequences (Giles and Rowan 2012) and sedimentary facies (Doughty-Jones et al. 2019; Rodriguez et al. 2020; Wu et al. 2020; Poprawski et al. 2021). Where MTDs are located over 5 km from diapirs, they do not appear to show attachment to the diapirs, contain seismically-resolvable clasts, and do not vary significantly in thickness laterally and can often be linked to regional up-dip shelf failures (Figure 6.3; Johnson 1987; Moscardelli and Wood 2008; Soutter et al. 2018; Doughty-Jones et al. 2019; Cox et al. 2020).



**Figure 6.3:** Spectral decomposition of a horizon slice within the Halibut Slide (Maureen Formation, Paleocene, UK North Sea) showing speckled internal seismic facies. The Halibut slide is a 290 km long MTD formed by plume-related instability on the up-dip Cretaceous chalk slopes (Soutter et al. 2018). Diapirically-derived local MTDs are present around diapirs (yellow) showing different characteristics and length scales to the regional MTD. Diapirs are labelled in white: Mu; Mungo, Mo; Monan, Mi; Mirren, Me; Merganser, Lo; Lomond, Ma; Machar, NP; North Pierce, SP; South Pierce.

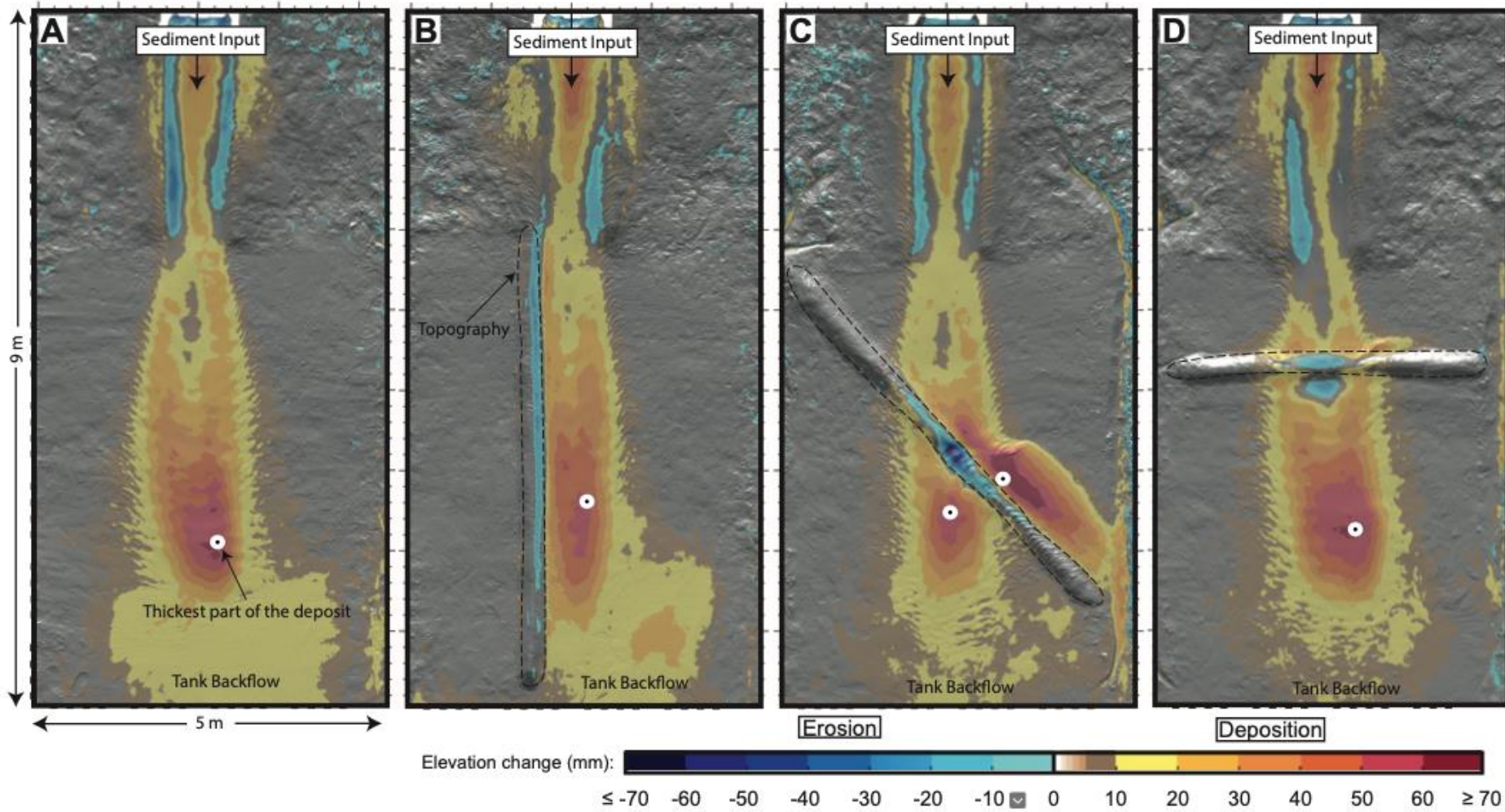
### ***Facies and architecture variability under different amounts and types of confinement***

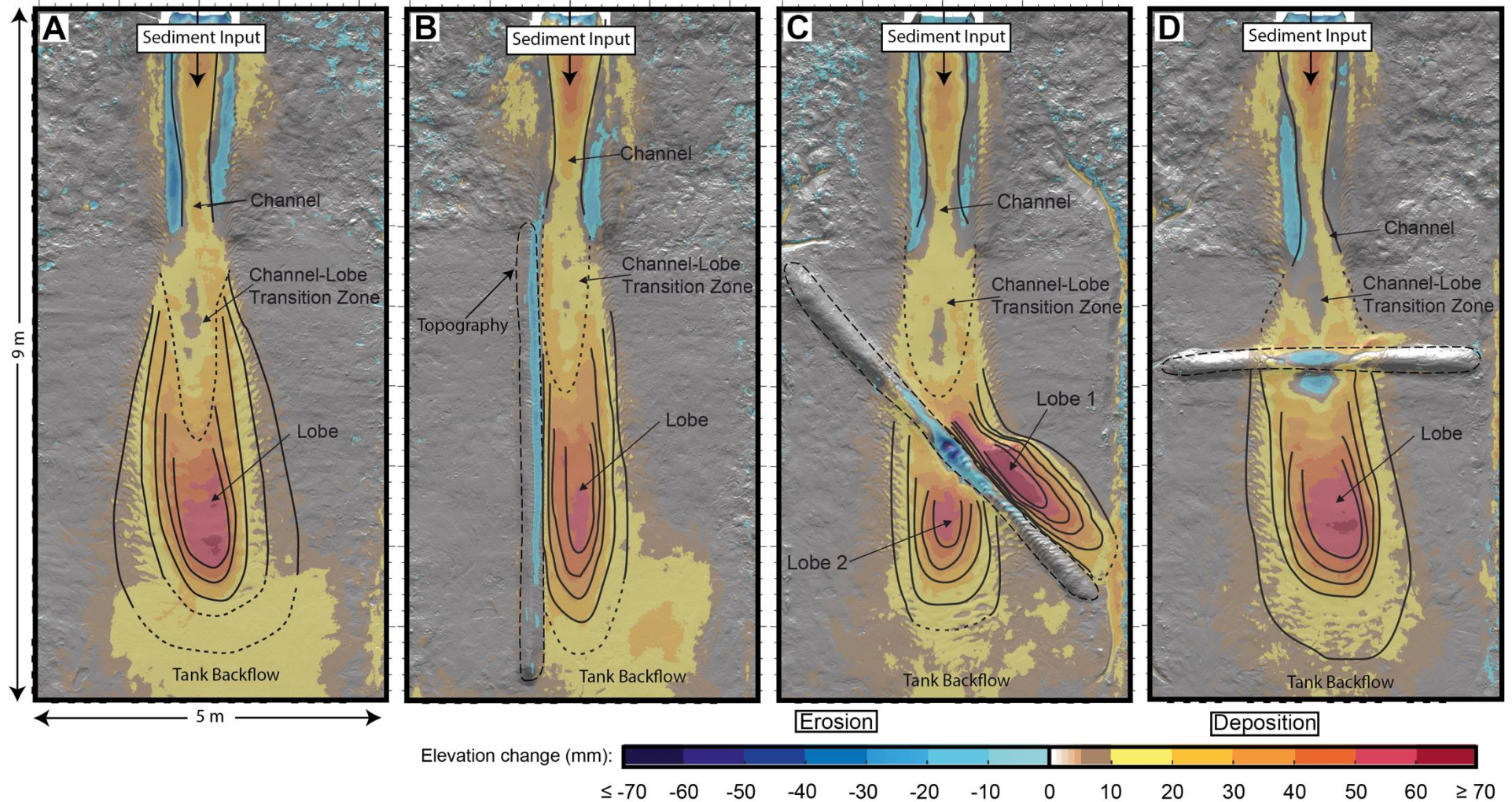
Field (Chapter 3), subsurface and numerical modelling (Chapter 5), and physical modelling (Appendix D; Soutter et al. 2021) results provide insight into how facies and architectures vary around different amounts and types of salt confinement, from bed-scale to mega-sequence scale.

Facies distributions on either side of the Bakio diapir varied during Black Flysch Group times according to the degree of confinement and distance from the diapirs crest (Figures 3.13 and 3.14). In the Bakio Breccia Formation, clast- and matrix-supported breccias are common in the Sollube and Jata basins, respectively (Poprawski et al. 2016), suggesting long-lived minibasin individualisation. The lack of confining topography to the west of the Jata basin may have caused flows to dilute, resulting in muddier, more-matrix-rich breccias (e.g., Hampton 1972; Sohn et al. 2002; Baas et al. 2009).

Another key difference is the architecture and facies of thick-bedded sandstones. In the Jata basin (one lateral confining topography) individual depositional elements are often erosionally based, concave-upwards, and thinner, and show more tractional structures (e.g., ripple lamination and planar lamination) than those in the Sollube (dual lateral confinement) basin. Where lateral confinement occurs along one margin, sandstones could represent sinuous low-relief channel fills that ran subparallel to topography (e.g., Mayall et al. 2010; Oluboyo et al. 2014). These channels were able to spread laterally and migrate because they were only partially confined (e.g., Mayall et al. 2010; Oluboyo et al. 2014). Such systems are less modulated by halokinetic controls than those that develop under dual-lateral confinement (e.g., Oluboyo et al. 2014; Rodriguez et al. 2020). Between the two diapirs deposits are amalgamated and stacked, perhaps more analogous to fluvial braided systems (Figure 3.13F; Nascimento et al. 2020).

Field results allow the comparison of individual and dual lateral confinement, but represent a specific angle of sediment input to structural strike, and therefore prevent discussion of how type, or orientation, of topography influences deep-water depositional systems. Results of physical modelling of turbidity currents interacting with topographic barriers at incidence angles of 0, 45, and 90° were created in a study supplemental to this work (Soutter et al. 2021; Appendix D). These physical experiments aimed to study the effect topographic orientation has on natural turbidity currents and their deposits (Figure 6.4). The results of these experiments were used to better understand how topography influenced depositional systems at the scale of an individual sediment gravity flow. These models show how bed-scale depositional architecture varies with orientation and type of confinement (Figure 6.4). Unconfined turbidity currents are able to spread radially over the basin-floor, forming a lobate deposit that thickens, then thins distally. Laterally confined turbidity currents are prevented from spreading on one side, forming an asymmetric deposit. Down-dip thinning rates are also reduced in a laterally confined setting, allowing flows to deposit farther into the basin. These flows are associated with a 20% increase in velocity adjacent to topography compared to unconfined equivalents. Oblique confinement resulted in an upstream deflected deposit and a downstream deposit, which has implications for deposit correlation in deep-water outcrop and subsurface datasets. Frontal confinement caused lateral spreading, with inferred trapping of coarse grains higher on the slope, compared to unconfined deposits (Soutter et al. 2021). Flow stratification is also shown to be important for confinement, with the higher-concentration base of turbulent flows more affected by the topography than the lower-concentration upper parts of flows, resulting in both highly confined and weakly confined deposits being produced by one individual flow (Figure 6.11).





**Figure 6.4:** Two-dimensional difference maps for the flume tank experiments discussed in Soutter et al. 2021 (Appendix D). The maps are made by subtracting the laser scan derived elevation of the pre-experiment tank surface from the post-experiment tank surface. Above – uninterpreted difference maps, white circle indicates the thickest part of the deposit. Sediment input point, topography and tank backflow (reflection off the back of the tank) highlighted. Below – maps interpreted with deep-water depositional elements and overarching fan geometries, highlighting asymmetry. A) Unconfined; B) laterally confined; C) obliquely confined, and D) frontally confined. Erosion is shown in blue and deposition in orange-red.

Oluboyo et al. (2014) suggest that a fundamental halokinetic control on the type of confinement developed is the incidence angle between the strike of the salt structure and the palaeoflow direction. “Fill-and-spill” stratigraphic evolution is observed in deep-water environments where topographic highs strike perpendicular to the gravity-flow direction (i.e., at a high incidence angle; e.g., Piper and Normark 1983; Hay 2012; Prather et al. 2012; Soutter et al. 2019). Bakio (Chapter 3) documents a rare example of an exhumed halokinetically-influenced deep-water succession where palaeoflow is at a low incidence angle to structural strike (i.e., oblique-parallel). In such scenarios, spill between basins is rare, and sedimentary systems are deflected to run broadly parallel to salt walls in minibasins for several kilometres (Figures 3.14, 3.15 and 3.16; e.g., Oluboyo et al. 2014).

A simple thought experiment, based on field observations and flume tank experiments (Chapter 3, Appendix D) showed the range of possible stacking patterns which may form during progradation of a deep-water system in an unconfined, partially confined and dual-confined setting (Figure 3.16). Unconfined fans have a higher aspect ratio, surface area, and avulsion angle than confined systems as the ability of the flows to spread radially was not restricted by topography (Prélat et al. 2009; Spychala et al. 2017). Where only one lateral confinement is present, deposits may be asymmetrical, as flows are confined by diapir topography in one direction but are able to spread radially away from it, as is seen in the deposits of the Jata basin, and the laterally confined flume tank experiment (Figures 3.10 and 6.4; Soutter et al. 2021). In settings with lateral confinement, deep-water systems are elongated axially, subparallel with bounding relief (Figures 3.14; 3.15, 3.16, and 6.4; Oluboyo et al. 2014; Soutter et al. 2021), with flows being suggested to be fed between two salt structures resulting in areally smaller depositional architectures, but thicker deposits, than unconfined settings (Soutter et al. 2021).

Analysis of the subsurface combined with numerical modelling (Chapter 5) shows that stratigraphic architecture is influenced by the spacing of confining topography (i.e., diapir spacing; Figures 5.8, 5.9, 5.10). The study demonstrates that where the zones of halokinetically-influenced stratigraphy are associated with two closely spaced (<1500 m) diapirs interact and a zone of intense modulation with highly-deformed strata is created (Figure 5.10). In this zone the highest amount of bed rotation, stratal terminations and thickness variability are seen. By comparison when diapirs are widely-spaced (>4500 m) a central broad plateau appears to develop between the diapirs in models which experience very limited deformation (Figure 5.10). This ‘minimal’ or ‘non’ deformation zone is represented by extensive, flat depositional lows (with consistent thicknesses and bedding orientations) between diapirs in subsurface examples (Figure 5.8; Harding and Huuse 2015; Jackson and Hudec 2017; Pichel et al. 2017; 2019; Grant et al. 2019 a;b; 2020). In diapirs which are intermediately spaced (1500 – 4500 m) a central modulation zone between the two diapirs is predicted, but deformation appears to decrease from the diapirs towards the centre of the modulation zone, suggesting there may be a small zone of ‘non-deformation’ which is difficult to decipher (Figure 5.10). In similarity to subsurface and model observations, fieldwork observations show that the ~8000 m zone between the Bakio and Guernica diapirs (widely spaced diapirs) shows minimal modulation in the central zone between the diapirs (at Cabo Matxitaxako). In the field example the deformation is condensed to ~1000 m zones flanking either salt structure, in similarity to halokinetic sequence models (Giles and Rowan 2012).

Ultimately, it is unlikely that stratigraphy in these ‘non-deformation’ zones will be completely free from any deformation due to the nature and complexity of salt basins. Minor modulation of stratigraphy is likely to exist across salt-influenced basins regardless of the distance from active, penetrative salt structures due to the presence of subtle structurally- and stratigraphically-controlled confining topography (Penge et al. 1993; Erratt et al. 1999; Birch and Haynes 2003; Borsa et al. 2008; Charles and Ryzhikov 2015; Hale et al. 2020; Howlett et al. 2020).

### ***Characterising controls on distributions of facies and architectures***

Regional subsurface analysis (Chapter 5) explores controls on facies and architectures. The most fundamental control on facies distribution in the ECG is the horst and graben morphology which controls the distributions of depositional sinks (2<sup>nd</sup> order static topography; Penge et al. 1993; Erratt et al. 1999; Bouroullec et al. 2018; Phillips et al. 2019; Tilhams et al. 2021). On the scale of the entire graben the diapirs have only a subtle influence on the overall depositional system. Nevertheless, on a local scale, within 3 kilometres radially of the diapirs, the effects of the diapirs (3<sup>rd</sup> order active topography) are substantial, acting to influence depositional processes, stratigraphic thickness, architecture, facies variability, distribution and transitions, diagenesis and subsequent fluid flow and migration (Davison et al. 2000; Hempton et al. 2005; Eldrett et al. 2015; Kilhams et al. 2015). Other subsurface features, such as saddle zones between diapirs, irregular base and top salt, and smaller diapirs where growth has ceased (3<sup>rd</sup>-4<sup>th</sup> order static or active topography; Figure 5.8; Hodgson et al. 1992; Poliakov and Podladchikov 1992; Penge et al. 1993; Erratt et al. 1999; Borsa et al. 2008; Oluboyo et al. 2014; Charles and Ryzhikov 2015; Hale et al. 2020; Howlett et al. 2020) act as additional topographic features, having localised control on depositional facies and architecture, but their effects are unlikely to be felt a few kilometres away (e.g. halokinetic rather than allocyclic). While halokinetic controls act to modify stratigraphy local to diapirs, overall deposition might also be influenced by the allogenic and autogenic controls related to depositional systems themselves (Ferguson et al. 2020). The extent and facies deposited within the axial Paleocene deep-water systems (i.e., the Forties Fan) is controlled by sediment supply and accommodation availability (Den Hartog Jager et al. 1993; Evans et al. 2003). Source area geomorphology, controlled by steep basin margins, combined with high sedimentation rates, ultimately influence the size, geometry and distribution of deep marine systems in the study area (Den Hartog Jager et al. 1993; Charles and Ryzhikov 2015).

The multi-disciplinary study has shown the importance of understanding the interplay between halokinetic (salt layer variations, diapir rise rate, salt withdrawal, salt related faulting, MTD distribution) controls that typically influence depositional systems and stratigraphy within >5 km of the salt, and allocyclic (tectonics, sedimentation rate, hinterland dynamics) controls, which are further extensive regionally, when disentangling salt basin evolution controls. Fundamentally halokinetic sequence architecture is controlled by the dynamic ratio between sedimentation rate and diapir rise rate (e.g., Giles and Rowan 2012; Pichel and Jackson 2020), such that an apparent increase in sedimentation (reducing halokinetic influence upwards) could represent a slowing of diapir growth due to regional tectonic quiescence or depletion of the salt source layer.

## **6.2 How does this modulation of stratigraphic architectures vary laterally and temporally?**

### ***Summary***

The different techniques used in this study all show that halokinetic modulation (the alteration of stratigraphy by salt growth) reduces stratigraphically and laterally away from the salt structure, in agreement with outcrop and subsurface analogues globally (Pratson and Ryan 1994; Giles and Lawton 2002; Mayall et al. 2010; Giles and Rowan 2012; Kernen et al. 2012; 2018; Banham and Mountney 2013a; 2013b; 2014; Oluboyo et al. 2014; Poprawski et al. 2014; 2016; Ribes et al. 2015; Doughty-Jones et al. 2017; Wu et al. 2020; Rodriguez et al. 2020). A summary of the findings from the studies presented in this thesis are given below.

In numerical models (Chapter 4), thinning rates decrease through time (up stratigraphy), and reflects a reduction of halokinetic modulation with increased sediment thickness as halokinetic bathymetry is 'healed'. This is true for all models except for the decreasing sedimentation rate (M6) model, which demonstrates a slight increase up stratigraphy. Thinning rates, and deformation increase towards the diapir (laterally) in all models. Bedding orientations are variable around the

diapir, but decrease (flatten) upwards in models. Thinning rates are shown to be up to six times greater in the 350 m immediately adjacent to the diapir compared to 1500 m away, and thus deformation style is highly variable. Stratigraphy is undeformed outside of the zone of halokinetic influence (~1150 m either side of the diapir), in all models, suggesting that the extent of the halokinetic zone of influence is not controlled by sedimentation rate.

In the subsurface study (Chapter 5) stratigraphic thickness variations and rotation of beds decrease laterally away from individual diapirs (Figure 5.8) in agreement numerical models (Chapter 4; Cumberpatch et al. 2021c;d) and with current understanding (Alsop et al. 1995; 2000; Giles and Rowan 2012; Doughty-Jones et al. 2017; Rowan and Giles 2021). Between closely spaced diapirs (<1.5 km) the halokinetic influence of one diapir is laterally connected to the halokinetic influence of the other diapir, such that the zone between the diapirs is influenced by both diapirs. When diapirs are >5 km apart, there is often a zone of consistent stratigraphic thickness and orientation between the diapirs where minimal modulation occurs (Figure 5.8). Between these wider spaced diapirs stratigraphy does not respond to the effects of the diapirs due to distance and this stratigraphy may be difficult to decipher from stratigraphy outside salt provinces. Modelled results indicate that modulation is more intense where diapirs are closer together (<1.5km), and suggest that once diapirs are spaced more widely than 3000 m away from each other an area of non-deformation between them is predicted. Subsurface diapirs which are spaced at ~4-5 km have <1 km of this 'minimally deformed' zone between them. Examples of diapirs that are further away from each other (>5 km) show a broad, central zone which appears to be undeformed, or experiences minimal deformation, between the diapirs, owing to the larger distance from the salt structures (Alsop et al. 2000; Oluboyo et al. 2014; Doughty-Jones et al. 2017).

The halokinetic influence on stratigraphy reduces upwards in combined DEM-subsurface observations, reflected by less thickness variability, fewer pinch outs and less rotation of beds in younger compared to older stratigraphy (Figures 5.8 and 5.9). Several diapirs have long-lived influences on stratigraphy, causing thickness variations and termination of the youngest stratigraphy, resulting in topography only being healed at the seabed (Pratson and Ryan 1994; Prather et al. 1998; 2012).

In the Basque-Cantabrian Basin (Chapter 3), deformation and bedding orientation decrease laterally away from the Bakio diapir on the western flank, in agreement with halokinetic sequence models of deformation (Giles and Lawton 2002; Rowan et al. 2003; Giles and Rowan 2012). Between the Bakio and Guernica diapirs, deformation decreases towards the axis of the Sollube basin (i.e., reduction of MTDs, reduction in bed thinning). The axis of the Sollube basin is comparable on scale and sediment routing capabilities to the 'minimal deformation' zones described in Chapter 5. Halokinetic modulation is shown to reduce stratigraphically upwards; with the lower Black Flysch Group containing a much higher number of debrites controlled by actively growing topography, than the latter upper Black Flysch Group. It can be inferred that following the cessation of diapir growth, an underfilled synclinal basin remained due to remnant topography of the buried Bakio and Guernica structures, which appears to have constrained upper Black Flysch Group deposition until it was filled (Figures 3.3, 3.13G and 3.14). The lower Black Flysch Group represents early-stage "active" deposition, perhaps comparable to syn-kinematic megasequences observed in the subsurface, whereas the upper Black Flysch Group represents late-stage "passive" deposition, infilling antecedent topography, comparable to post-kinematic megasequences observed in the subsurface (e.g., Pratson and Ryan 1994; Warren 1999; 2006; Jackson and Hudec 2017) and models (Chapter 4; Cumberpatch et al. 2021c;d). This reduction in halokinetic influence upwards results in the minibasin becoming less confined upwards, due to healing of the salt topography (Marini et al. 2015). This reduction of halokinetic influence through time (transition from "active" to "passive" deposition) supports the idea that sediment accumulation rate outpaced diapir growth rate, due to a combination of increased sediment supply associated with the uplift and erosion of the



Landes Massif (Martín-Chivelet et al. 2002; Puelles et al. 2014) and partial or complete welding of salt bodies (Jackson and Hudec 2017).

### ***Sedimentation rate versus diapir rise rate through time***

In all data sets used in this study, an upwards increase in relative sedimentation rate associated with a decrease in halokinetic influence is observed (Figure 6.5). For ease of comparison, each example is divided into 3 phases in Figure 6.5. In the field (Chapter 3), the Aptian-Albian is initially isolated, representing slow sedimentation rates relative to diapir growth (grey on Figure 6.5). Observations are similar to the slow sedimentation model (Chapter 4), where sediment is isolated to individual depocentres due to relatively rapid diapir growth (blue on Figure 6.5). In the subsurface example (Chapter 5) stratigraphy within phase 1 are not laterally extensive and reflect relative sedimentation rates lower than diapir rise rates (green on Figure 6.5). This is supported by steeply upturned Paleocene stratigraphy adjacent to diapirs reflecting rapid diapir rise rates.

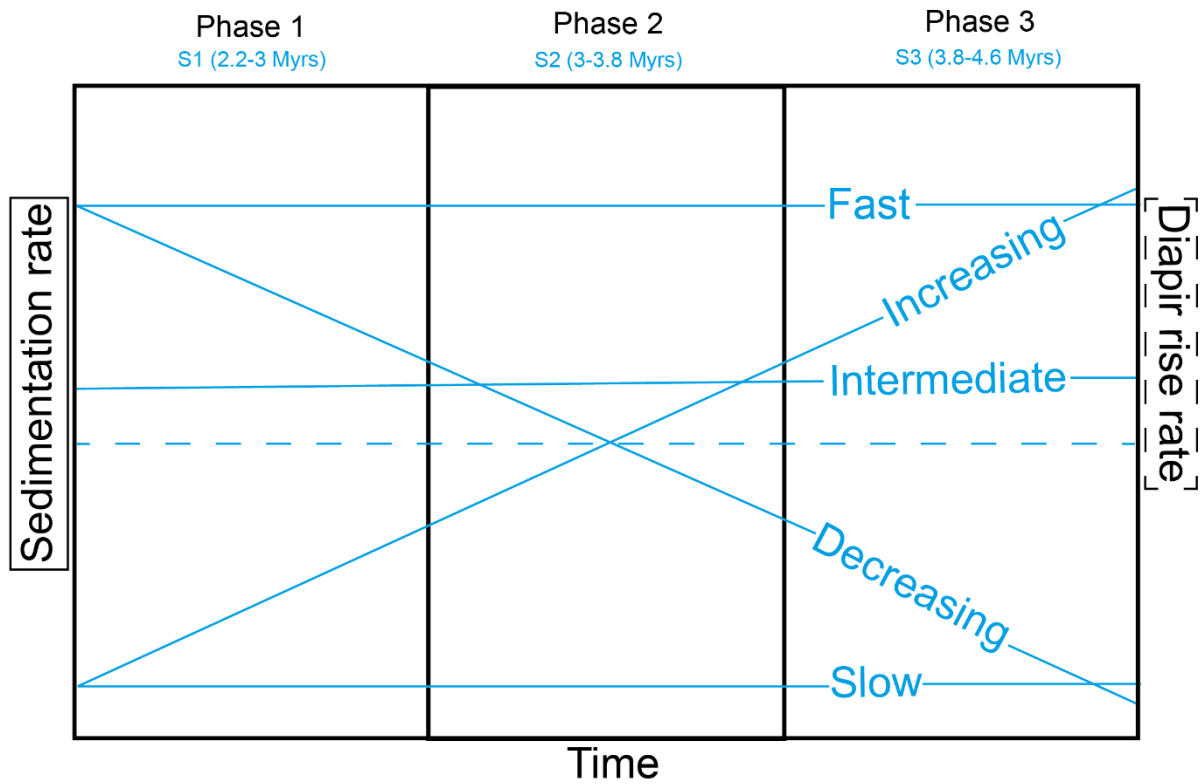
Under relative increasing sedimentation rates the Albian-Cenomanian (phase 2) is laterally extensive across both sides of the diapir, at Bakio, reflecting the intermediate sedimentation model. At Bakio, the increase in sedimentation is driven by a regional progradation related to the uplift, and erosion of a northerly source area (Martín-Chivelet et al. 2002; Puelles et al. 2014), coupled with a reduction in salt rise rate (Poprawski et al. 2014; 2016; Roca et al. 2021). Facies analysis reveals a reduction of MTDs upwards, associated with a reduction of halokinetic influence. MTDs cannot be resolved in numerical models, however, a reduction in stratigraphic dip upwards is observed in all models (Figure 6.5) providing evidence for decreasing instability and salt influence waning. In the subsurface example thinning rates decrease upwards (phase 2) and diapir rise rate slows in phase 3 due to regional tectonic quiescence or depletion of the salt source layer. This causes a reduction of halokinetic modulation on the latest stratigraphy as the halokinetic bathymetry is gradually buried. In the ECG, during the Eocene, sediment supply rates and diapir rise rates were equally paced (Figure 6.5; Carruthers et al. 2013), reflecting an increase in diapir rise rate, which is attributed to Cenozoic compressional forces driving diapir growth (Figure 6.5; Birch and Haynes 2003; Scott et al. 2010; Carruthers et al. 2013).

Deposition of the upper Black Flysch Group (phase 3) across the diapir under relatively high sedimentation conditions is consistent with ‘fast sedimentation’ in models. The upper Black Flysch group heals remnant topography and shows almost no halokinetic influence, except for its depositional location within remnant diapiric topography. The relative increase in sedimentation rate at Bakio is driven primarily by an increase in sediment supply due to the uplifting source area, however, a coeval reduction of salt supply due to welding between the Bakio and Guernica diapirs cannot be ruled out (Poprawski et al. 2014; 2016; Cumberpatch et al. 2021b; Roca et al. 2021).

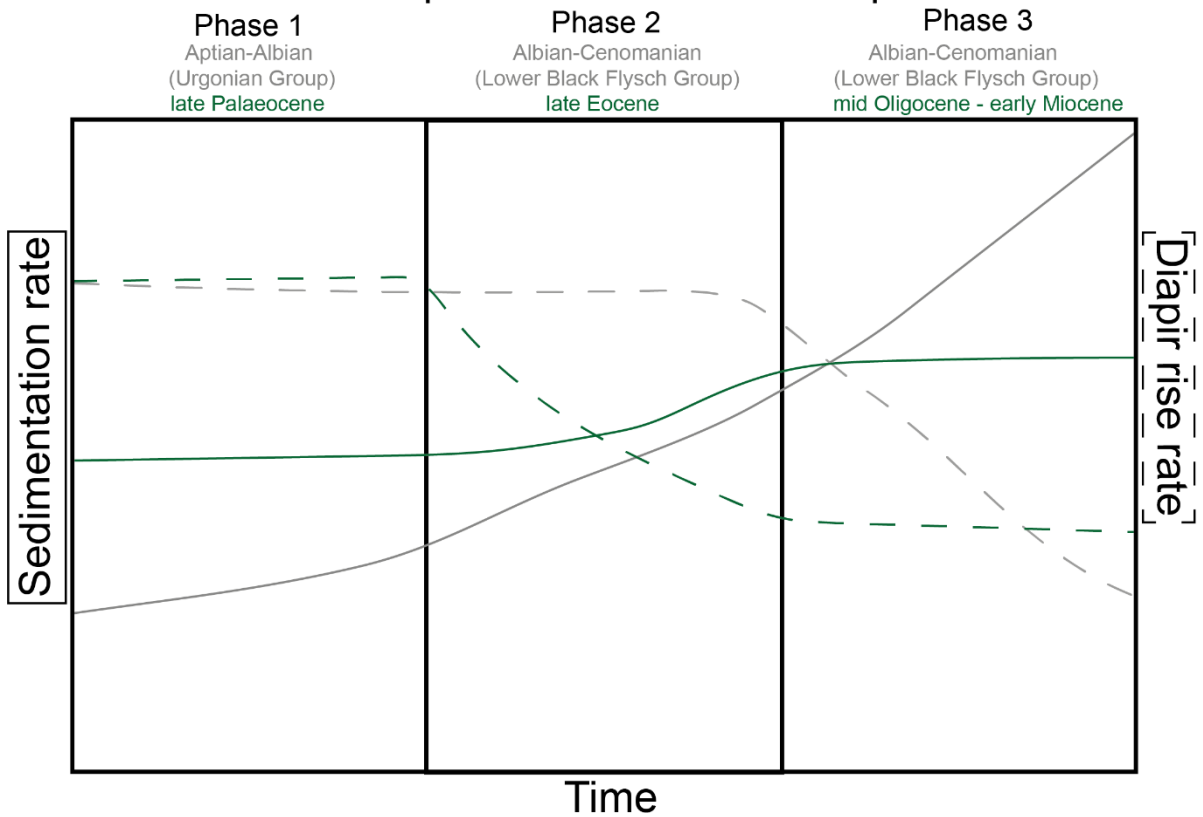
The ‘slow’, ‘intermediate’ and ‘fast’ numerical models (Chapter 4) are absolute sedimentation rates, as the diapir rise rate remains fixed (Figure 6.5). The patterns and geometries of these models therefore represent one part of system evolution, which is by nature dynamic and changing. Increasing and decreasing sedimentation rate models are more likely to reflect changing relative sedimentation rates in nature, because in natural examples, diapir rise rate also varies through time. A relative decrease in sedimentation rate (upwards), could be caused by subsequent phases of tectonism reactivating diapir growth, as is observed in the Cenozoic in the ECG (Birch and Haynes 2003; Scott et al. 2010; Carruthers et al. 2013). The increasing sedimentation model is consistent across the entirety of the field and subsurface examples, representing a relative increase in sedimentation rate temporarily (upwards), usually linked to a reduction in salt supply due to welding or an increase in absolute sedimentation rate, in agreement with global observations (Pratson and Ryan 1994; Giles and Lawton 2002; Mayall et al. 2010; Giles and Rowan 2012; Kernen et al. 2012;

2018; Banham and Mountney 2013a; 2013b; 2014; Oluboyo et al. 2014; Poprawski et al. 2014; 2016; Ribes et al. 2015; Doughty-Jones et al. 2017; Wu et al. 2020; Rodriguez et al. 2020).

## Modelled examples



## Outcrop and subsurface examples



— Field example: Bakio (Chapter 3) — DEM examples (Chapter 4) — Subsurface example: Pierce field (Chapter 5)

**Figure 6.5:** Schematic charts plotting sedimentation rate and diapir rise rate evolution through time, across the different methods used in our study (above: models and below: field and subsurface examples). Time is split into 3 phases, which are of different lengths

for each method, and are indicated in different colours (see key). Sedimentation rate is solid line and diapir rise rate is dashed. For models, diapir rise rate is consistent throughout, and sedimentation rates are shown and labelled.

### **6.3 Criteria for the recognition of halokinetically-influenced deep-water systems**

#### ***Summary***

Chapters 3-5 have provided criteria for recognition of halokinetically-influenced stratigraphy in outcrop (Chapter 3), DEM (Chapter 4) and subsurface data (Chapter 5), respectively. On a bed scale, similar sedimentary structures and stacking patterns are observed in field data (Chapter 3), core data (Chapter 5) and flume tank experiments (Appendix D). On a larger architectural scale, similar thinning rates, geometries and deformation zone extents are observed in numerical models (Chapter 4) and subsurface data (Chapter 5).

Before this study, most understandings of halokinetically-influenced deep-water systems came from subsurface datasets (e.g., Booth et al. 2003; Madof et al. 2009; Carruthers et al. 2013; Doughty-Jones et al. 2017; 2019). Features that are common across several depositional settings where halokinetic movements are observed include multi-scalar thinning and onlap, growth faulting, pebble conglomerates, mixed siliciclastic–carbonate lithologies, MTDs, variable paleocurrents, angular unconformities, and abrupt facies variability (Dalgarno and Johnson 1968; Dyson 1999; Kernen et al. 2012, 2020; Carruthers et al. 2013; Counts and Amos 2016; Counts et al. 2019).

Criteria for recognition of halokinetically-influenced deep-water systems across multiple scales and data types include short length scale architectures with high variability (e.g., lobate geometries that pinch out, stratigraphy that thins towards a diapir). For this reason, it can be difficult to trace individual depositional elements for several kilometres, and difficult to correlate them across diapirs due to the individualisation of sediment routing. Rapid pinch out and rotation of beds is observed in proximity to diapirs in outcrop, models and subsurface data (Chapters 3-5), showing substantial halokinetic modulation relative to nearby undeformed zones. Mass failure deposits that are sourced from, and thus radiate around and thin away from diapirs, are observed in outcrop and subsurface data sets, providing evidence for an unstable seabed during diapir growth. Therefore, stratigraphic profiles where the overall depositional (allocyclic) stacking is interspersed with MTDs (especially those that contain remobilised thin beds) are strongly indicative of a salt influence. Failures in the early diapiric sequence in models could also represent similar MTDs. The presence of a preserved salt structure (in subsurface data and models) is obviously a strong indicator of a halokinetically-influenced environment, but where this is missing or partially missing due to dissolution or welding, it may still be possible to infer its existence based on geomorphological lows, (e.g., the Guernica salt structure, Chapter 3), or stratigraphic architecture analysis. Typically, allocyclicity (external controls such as sea level and sediment supply) has a strong control on the depositional system, and therefore lobes and channels are likely to be recognised via pre-existing methodologies (e.g., Prélat et al. 2009; Sychala et al. 2017; Ferguson et al. 2020). Halokinesis acts to modify these depositional elements, and is the primary control over diapirically-derived mass failure deposits (e.g., Doughty-Jones et al. 2019; Wu et al. 2020), which may be subsequently re-worked, or cause the re-routing of future depositional systems.

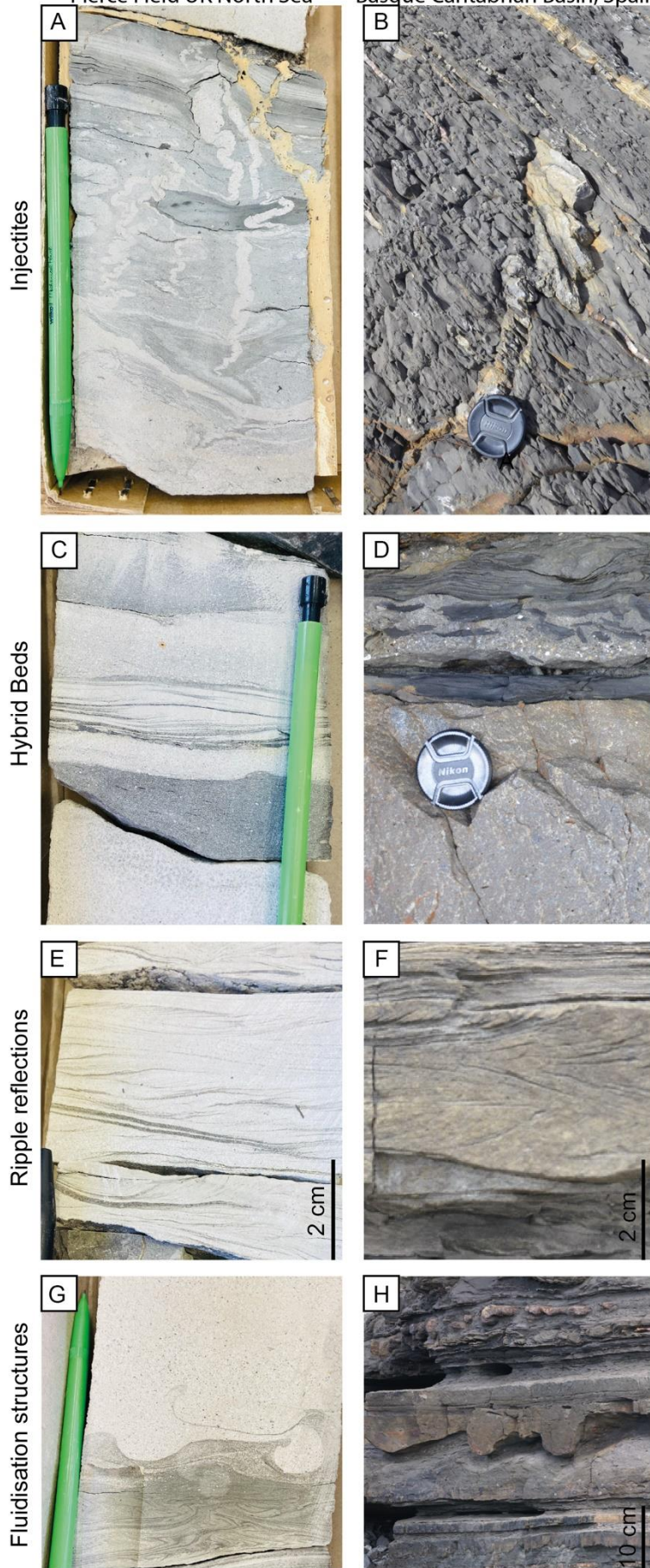
#### ***Identification criteria for salt-influenced stratigraphy in one dimensional data***

Multiple directions of ripple lamination, injectites, fluidisation structures, presence of hybrid beds (Figures 6.1 and 6.6), range of MTD types, and abrupt juxtaposition of deep-water depositional facies and MTDs can be used to identify halokinetically-influenced deep-water systems in core and outcrop. These sedimentary structures and bed types give indications of the presence of topography, in agreement with field observations from salt-influenced stratigraphy in outcrop (Ribes et al. 2015; Counts et al. 2019; Cumberpatch et al. 2021b). Injectites (Figure 6.6 A,B) have been recognised in halokinetically-influenced deep-water provinces globally due to over-pressured sandstones

(Svendsen et al. 2010; Monnier et al. 2014; Cobain et al. 2017). Hybrid beds seen throughout the distal parts of a depositional fan (Figure 6.6 C,D) indicate that topography influenced the transformation from turbulent to laminar flow (Barker et al. 2008; Spsychala et al. 2017b; Soutter et al. 2019). Ripple laminations in opposing directions are common in confined settings (Figure 6.6 E,F) and have been attributed to flow reflection or deflection from seafloor topography (e.g., Kneller et al. 1991; McCaffrey and Kneller 2001; Barr et al. 2004; Hodgson and Haughton 2004). Soft sediment deformation structures (Figure 6.6 G,H) provide evidence for a fluidised, mobile, substrate during deposition possibly due to growing topography (Aschoff and Giles 2005; Fossen 2010; Shanmugam 2017). Individually these criteria are not diagnostic of salt-influenced environments, however, when combined with seismic observations of salt structures and bedding orientation and dip variability, along with regional understanding, they can be used to confirm the presence of local topography, and the influence it has on depositional facies (Pratson and Ryan 1994; Mayall et al. 2010; Oluboyo et al. 2014; Doughty-Jones et al. 2017; Wu et al. 2020; Rodriguez et al. 2020; Cumberpatch et al. 2021b). Physical models (flume tank experiments) show ripples with opposing palaeocurrent directions around topography and the vertical juxtaposition of lower density flow deposits above those of higher density flows adjacent to topography, suggesting velocity segregation and flow transformation due to topography (Soutter et al. 2021; Appendix D). These observations show, that even on the scale of an individual bed, topography can have a significant influence on deposition, in agreement with observations from multiple stacked beds (e.g., in core and outcrop).

Core Photo  
Pierce Field UK North Sea

Outcrop Photo  
Basque Cantabrian Basin, Spain



**Figure 6.6:** Sedimentological evidence for topography during deposition of deep-water successions. Core photos from T6A of the Palaeocene Forties Member, Sele Formation, from wells in the study area (Table 5.1). Outcropping equivalents are from the Albian-Cenomanian Black Flysch Group around the Bakio Diapir, northern Spain (Chapter 3). Lens cap is 52 mm and pencil is 16 cm.

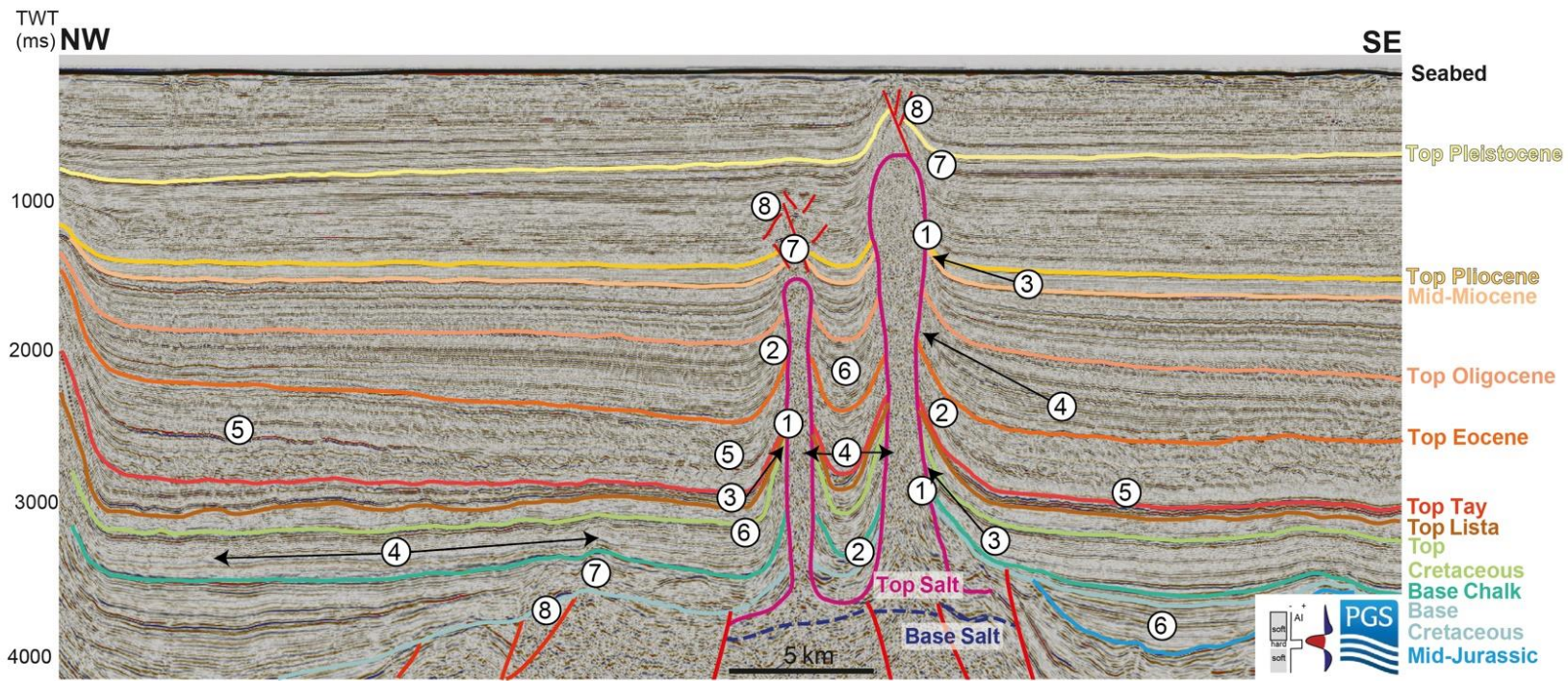
### **Identification criteria for salt-influenced stratigraphy in two-dimensional data**

In two-dimensional data (e.g., cross-sections from seismic data and numerical models, and extensive outcrops) lateral variability (e.g., thinning, thickening and upturn) within stratigraphy forms a key part of the recognition criteria (Figure 6.7). Stratigraphy which thin towards, and in some cases eventually pinch out or abut against salt topography, suggest the presence of a mobile topographic high during deposition (Giles and Lawton 2002; Rowan et al. 2003; Giles and Rowan 2012; Rowan and Giles 2021). This thinning and eventual termination is often consistent with depositional flows losing energy (reduction in velocity) as they run up topography, resulting in a thicker deposit at the base of the salt, compared to the flank or crest (Kneller et al. 1991; McCaffrey and Kneller 2001; Barr et al. 2004). Numerical modelling has shown that thinning rates can be up to 0.13%/m between the salt flank and the salt crest (Table 4.2), and that these thinning rates are commonly six times more extreme when compared to thinning rates from the undeformed section to the salt flank. Therefore, lateral variability in thinning rates, and drastic thinning to termination (pinch out) across two-dimensional data sets can be diagnostic of the presence of salt (Figure 6.7). Pinch outs can be difficult to image in seismic data due to resolution and velocity issues, and difficulty resolving salt versus stratigraphy at the salt-sediment interface (Jones and Davison 2014). Stratigraphy can also be seen to thicken into, and sometimes be confined to, deposition lows created by salt withdrawal, which are common at the base of salt topography (Figure 6.7). In numerical models, stratigraphy thickens into salt withdrawal basins adjacent to salt structures by a maximum of 13% (Figure 4.9). Observations of thick isolated sandstones in depositional lows adjacent to topography are consistent across outcrop studies (Figure 3.8), numerical models (Figures 4.5, 4.6, 4.7, 5.9, 5.10, and 5.11), subsurface data (Figures 5.8 and 5.10) and physical models (Figure 6.11), as well as in previous work (Figure 6.7; Pratson and Ryan 1994; Mayall et al. 2010; Oluboyo et al. 2014; Doughty-Jones et al. 2017; Wu et al. 2020; Rodriguez et al. 2020).

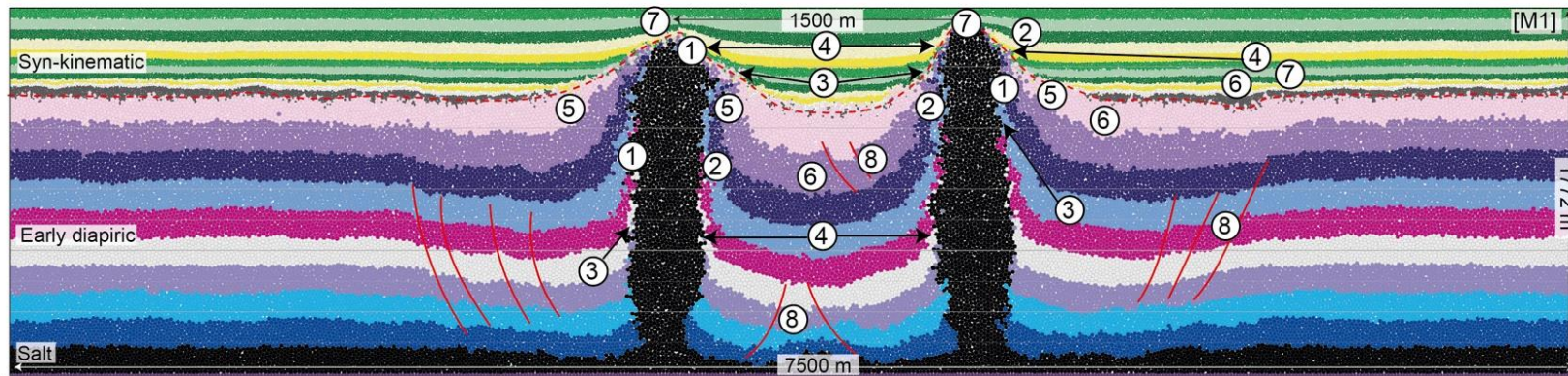
Aside from thickness variations, other characteristics that can identify salt-influenced stratigraphy include rotated, and often overturned, strata (Figure 6.7). Stratigraphy that abruptly steepen towards salt structures (often rotating by 40-90° across ~1-2 km) are observed in outcrop (Figure 3.12), numerical models (Figures 4.5, 4.6, 4.7, 4.9 and 5.9) and subsurface data (Figures 5.8 and 5.10) and are consistent with near diapir deformation reported elsewhere (Alsopp et al. 2000; Giles and Lawton 2002; Rowan et al. 2003; Giles and Rowan 2012; Jackson and Hudec 2017; Rowan and Giles 2021). Another characteristic that can be recognised in seismic data, but is more difficult to resolve in models are MTDs (Doughty-Jones et al. 2019; Wu et al. 2020), which typically appear on seismic data to have a chaotic internal character. The presence of active salt influenced seafloor topography can trigger MTDs due to the oversteepening and failure of salt-influenced seafloor topography, and as such deposits often thin to a pinch out away from such areas (Figures 3.6, 3.8 and 6.7). In outcrop, MTDs have a variety of compositions (muddy debrites, limestone breccias, slumps, slides etc.), which leads to their chaotic seismic character. Supra-salt faults and anticlinal structures formed stratigraphically above salt structures provide further evidence of salt topography (Figure 6.7). Therefore, the variability in stratigraphic thickness, bedding orientation, faulting and MTD character is itself a key identification criterion for halokinetically-influenced deep-water systems. Compared to depositional environments that are not influenced by topography, stratigraphy is highly modulated and deformed and facies are heterogeneous and spatially variable, in salt-influenced settings (e.g., Banham and Mountney 2013a; b; 2014; Poprawski et al. 2014; 2016; 2021; Ribes et al. 2015; 2017; Counts and Amos 2016; Doughty-Jones et al. 2017; Counts et al. 2019; Wu et al. 2020).

Diapir growth is often not continuous through time, and phases of rapid growth and quiescence cause destabilisation and remobilisation of the diapir roof, overburden and flank deposits (Figures 3.9, 3.10, 3.11 and 3.16). These salt-triggered, remobilised deposits (MTDs), that radiate outwards from the underlying salt structure, can drive re-routing of subsequent systems to avoid the newly created failure topography (Kane et al. 2012; Doughty-Jones et al. 2017; 2019; Figure 5.7; Chapter 5). At Bakio, stratigraphy commonly shows variable bedding orientations that radiate around salt structures (Figure 3.12). Facies and thinning rates are often highly variable in three-dimensional data and asymmetry cannot be assumed due to the high proportion of controls on depositional sequences (Mayall et al. 2010; Oluboyo et al. 2014; Ribes et al. 2015; 2017).





1; Pinch out of Beds, 2; Rotation of Stratigraphy, 3; Stratigraphic Thinning, 4; Lateral Variability, 5; Mass Transport Deposit, 6; Stratigraphic Thickening, 7; Long-lived influence on Stratigraphy, 8; Salt-related Faulting



**Figure 6.7:** Some of the criteria used to identify halokinetically-influenced stratigraphy in two dimensions, in this case in a time-migrated seismic cross-section from the Pierce field (Figure 4.14) and a cross-section through DEM (M1, Figure 5.9). Examples of key features are highlighted by numbers 1-8, see figure for definition and text for description. Locations of transport deposits in DEM are hypothetical.

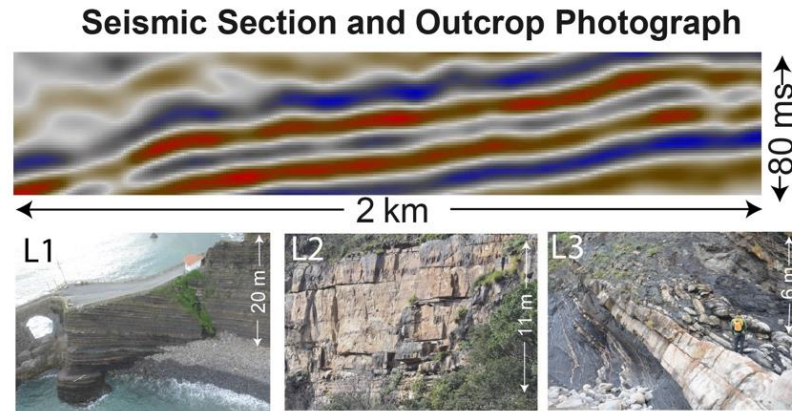
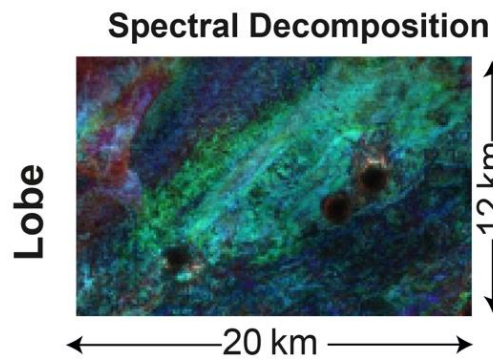
### ***Multi-scalar architectural analysis: the importance of field analogues***

Depositional architectures can be recognised in different data types and at different scales (Figure 6.8). In seismic reflection data it is often possible to resolve channels, lobes and mass transport deposits at complex scale (*sensu* Prélat et al. 2009). Core and well data can be helpful in providing fine resolution details (e.g., bed to element scale), but only represent a one-dimensional profile. Due to the inherent lateral variability in salt-influenced settings, outlined above, outcrop analogues are often utilised when creating subsurface energy reservoir models. Properties which are below the scale of seismic, but can be resolved in outcrop data (such as individual bed thinning rates, lateral facies variability, extent of potential 'thief' sandstones and MTDs, and diagnostic sedimentary structures) can enhance understanding of the processes, stratigraphy and uncertainties associated with deep-water halokinetically-influenced settings.

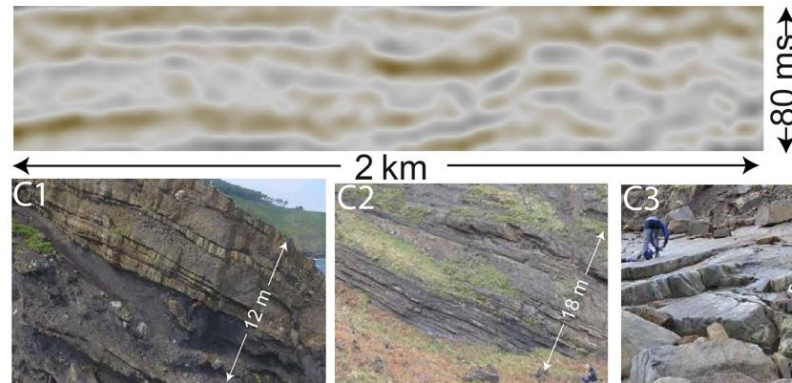
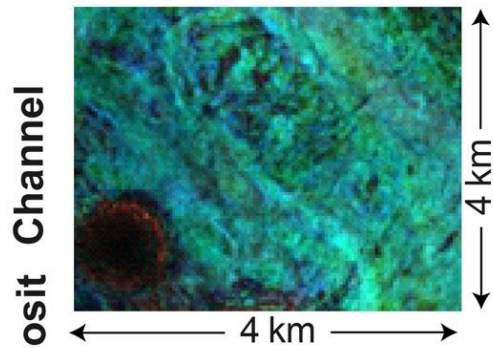
Due to interbedding of deep-water 'axial' stratigraphy with lateral MTDs, the overall depositional signal can be altered on a bed to lobe scale (e.g., the progradational trend in the Black Flysch Group (Chapter 3) is interspersed with mass failure deposits). This small-scale interbedding often gets 'upscaled out' in seismic and well data, where an 'average' of the rock properties is displayed. For example of 100 metre section of metre thick sandstones stacked with metre thick MTDs may instead be resolved as a 100 metre section of muddy-sandstones, which has huge implications for subsurface energy reservoir estimates. Identifying the bed-scale interactions, juxtaposition of facies and possible end- members observed in outcrop data (e.g., mud-rich distal lobes and sand-rich proximal lobes) can help to provide a better understanding of the depositional system when interpreting subsurface data. While field analogues are unique, and not direct replications of any specific subsurface setting, it is helpful to have a wide range of possible models (Figure 6.8). Depositional elements are shown to be unique, and get increasingly complicated the more 'zoomed in' observations are (e.g., from megasequence scale thickness variability down to variable clay coating in grains).

The facies variations visible in outcrop emphasise that depositional elements are unlikely to be thick, extensive 'tanks' of sandstone, and rather much more heterogeneous (Figure 6.8). An appreciation of the variability observed in outcrop helps to understand, and guide rock physics interpretations. Likewise, having an appreciation for the rock complexities (e.g., beds are very steeply dipping, lots of breccia, lithological variations, salt overhangs) can help to understand the imaging issues around salt diapirs, allowing some comprehension of what the salt-sediment interface may look like, rather than simply concluding the data is poor quality.

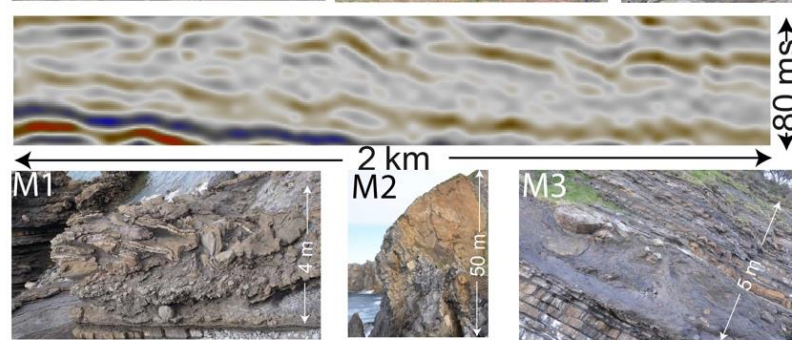
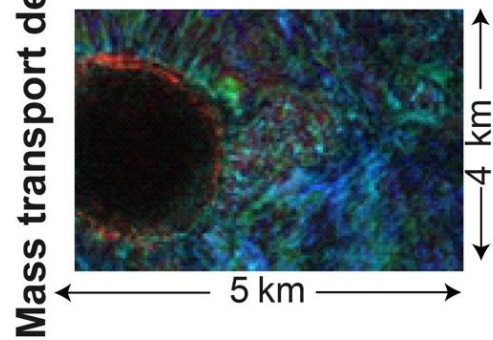
The multi-dimensional, multi-technique approach used in this thesis shows that similar processes are in operation at multiple scales. For example, one individual mass transport event may re-route to avoid the previous one (5<sup>th</sup> order topography, compensational stacking). A subsequent lobe may then migrate to avoid the resulting MTD topography (4<sup>th</sup> order topography). Ultimately these processes occur within a depositional complex that is being deflected, and re-routed to avoid a salt-cored high (3<sup>rd</sup> order topography). The observations of re-routing to avoid topography and pinch out (Figure 6.11) means that we can often apply small scale learning to large scale problems, and vice versa.



- Lobe**
- Elongated adjacent to topography
  - Mounded geometry
  - Thin and pinch out towards topography (L3)
  - Thickest sandstone in topographic lows at the base of salt (L3)
  - Transition laterally from sandstone rich (axial; L2) to mudstone rich (distal; L1)
  - Interspersed with MTDs



- Channel**
- Deflect and re-route around salt topography and diapirically-derived MTDs
  - Concave upwards geometries
  - Thickest sandstones in the channel axis (C1,C3), mudstone percentage increases towards margin (C2)
  - Often interspersed with, and ponded into MTDs



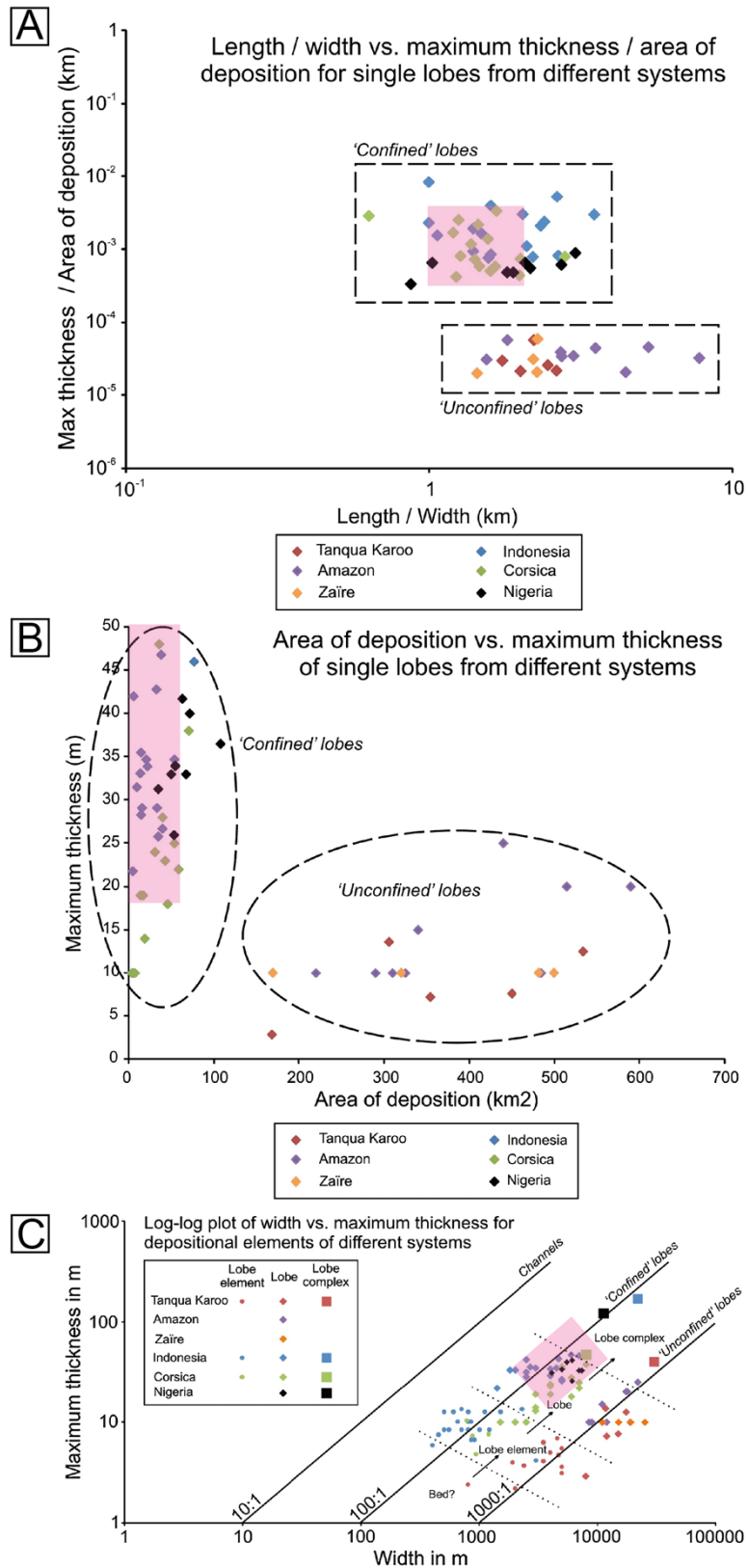
- MTD**
- Derive from diapirs, radiate around, and thin away from, them
  - Speckled or chaotic seismic signature
  - Undulose base and top surface
  - Contains remobilised beds and clasts (M1, M2, M3)
  - Variable composition and character (M1, M2, M3)

**Figure 6.8:** *Analysis of halokinetically-influenced deep-water depositional elements across different data sets. The key diagnostic characteristics of lobes, channels and mass transport deposits in spectral decomposition, seismic and outcrop data from this study is displayed. A variety of different outcrop photographs are shown to display the variability of each architectural element. Key observations across multiple scales and data types are highlighted.*

### **Recognition of confined depositional hierarchies in the field**

The widely accepted hierarchical scheme for classifying deep-water systems that was developed from the analysis of Permian outcrops of the Karoo Basin, South Africa (Prélat et al. 2009) must be used with caution, or be adapted for confined systems (Prélat et al. 2010; Etienne et al. 2012; Marini et al. 2015). Prélat et al. (2010) recognised that width-to-thickness ratios and areal extent-to-thickness ratios are different for confined and unconfined systems, with width-to-thickness ratios of 100:1 measured in selected subsurface confined settings, compared to 1000:1 in unconfined settings, and areal extent-to-maximum-thickness ratios 30 times greater in unconfined systems compared to confined systems (Figure 6.9; Prélat et al. 2010). The width-to-thickness ratio of lobes in the confined Sollube basin is c. 160:1 (taking a midpoint thickness of 53 m; Figure 6.9), in agreement with confined examples reported by Prélat et al. (2010), from subsurface observations. Lobe data collected in the field at Bakio plot in the confined lobes portion of all classification charts used by Prélat et al. (2010) demonstrating the scalability of lobe geometries between the typical scales of outcrop and subsurface observations. The dimensions observed in the salt-influenced minibasins in the outcropping study area are comparable to those of intraslope lobes complexes documented in the Karoo Basin (6–10 km wide, 10–15 m thick; Spychala et al. 2015), which are an order of magnitude smaller than their basin-floor counterparts (Prélat et al. 2009).

This multi-scalar study suggests that confined setting hierarchical elements have greater lengths than widths (Figure 6.9A) and smaller areal extents compared with the roughly equant geometries predicted in unconfined systems (Prélat et al. 2009), because radial spreading is limited due to topographic confinement (e.g., Marini et al. 2015; Soutter et al. 2019; 2021; Figure 6.9B). Confined deposits often have greater thicknesses due to axial routing of gravity flow deposits creating stacked, amalgamated sandstones (Kneller and McCaffrey 1999; Scott et al. 2010; Talling et al. 2012; Patacci et al. 2014; Oluboyo et al. 2016; Howlett et al. 2020), and result in lobes with lower width-to-thickness ratios than unconfined lobes (Figure 6.9C). These findings support recent work (Oluboyo et al. 2014; Soutter et al. 2019; Rodriguez et al. 2020; Howlett et al. 2020) suggesting that elongate systems are common adjacent to topography, on all scales. The difference between stratal geometries in confined and unconfined lobes highlights the importance of adapting methodologies and models developed for unconfined deep-water systems to be fit for purpose for deep-water topographically confined settings (Prélat et al. 2009; 2010; Patacci et al. 2014; Oluboyo et al. 2014; Spychala et al. 2015; 2017; Soutter et al. 2019).



Extent of observations in the Black Flysch Group, Bakio (Chapter 3)

**Figure 6.9:** Characteristic stratigraphic geometry plots for confined and unconfined lobes from Prélat et al. (2010), overlain with data from a confined field example (the Black Flysch Group adjacent to the Bakio diapir, Chapter 3). Previous 'confined lobes' observations are from subsurface datasets. A) Log-log plot of the length-to-width vs. maximum thickness-to-area of deposition. B) Graph of the area of deposition vs. maximum thickness. C) Log-log plot of width vs. maximum thickness for different depositional elements of the lobe hierarchy of Prélat et al. (2009). Adapted from Prélat et al. (2010). Measurements of individual lobes are not

*certain in the field area, due to lack of outcrop extent and therefore the data on the charts for the Black Flysch Group represents end member thicknesses, areas and lengths based on the extent of the Sollube basin, assuming lobes would fill it completely.*

## **6.4 The importance of integrated workflows**

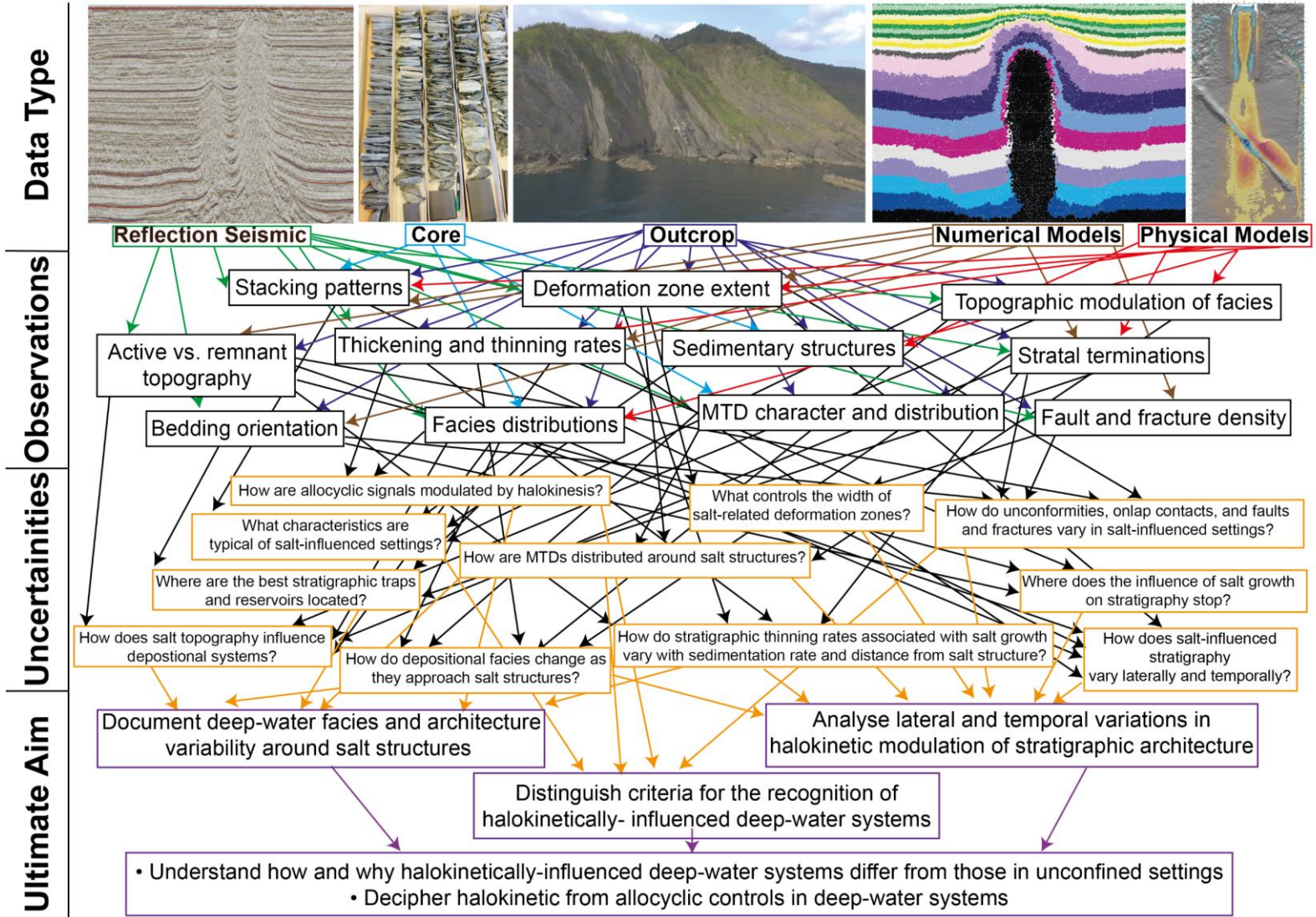
### ***Summary***

Integrating a variety of datasets can help to improve understanding of complex multi-scalar, or scale independent processes (Figures 6.10 and 6.11). The increasing availability of high-quality 3D seismic data has formed the foundation for a large part of recent work on halokinetically-influenced deep water systems (Mayall et al. 2006; 2010; Jones et al. 2012; Carruthers et al. 2013; Olu-boyo et al. 2014; Charles and Ryzhikov 2015; Doughty-Jones et al. 2017; 2019; Coleman et al. 2018; Rodriguez et al. 2020; Howlett et al. 2020). Such seismic-based studies are helpful for determining bedding orientations, stacking patterns, deformation zone extents, stratal terminations, thickening and thinning rates, and fault and fracture density, but are limited in terms of the small-scale (sub-seismic) observations of depositional facies, topographic modulation of facies, mass transport deposit character and sedimentary structures (Figure 6.10). Well data, in particular core, provide the only true calibration points in the subsurface and can often be underutilised or overlooked. Core provides important sedimentological data, such as information on lithology, sedimentary structures, stacking patterns, MTD character etc., that ground-truth interpretations away from the well using the variety of subsurface imaging techniques available. Core is, however, one-dimensional, so does not allow for two-dimensional calculations such as thinning rates which are important in understanding halokinetically influenced systems (Figure 6.10). Numerical models provide observations on a similar scale to seismic reflection data, and as such are useful for studying fault and fracture distribution, stratal terminations, deformation zone extent, bedding orientations and thickness changes (Figure 6.10). These models still leave gaps in knowledge with respect to depositional facies and MTD distribution and character, which are beyond the scope of the ‘mega-sequence’ scale models (Figure 6.10). DEMs are highly advantageous as a variety of different parameters can be altered such that observations (stacking patterns, bedding orientation etc.) can be made across a variety of different end members in a short amount of time (without requiring numerous different, inherently more complex subsurface or outcrop analogues). In this study numerical models were used to provide quantitative data (thinning rates etc.) that is difficult to extract from incomplete, or complicated outcrop or subsurface data sets. Physical models provide information of small scale (bed-scale) sedimentary and stratigraphic processes, allowing for the calculation of thinning rates (Figure 6.10). Whilst, these flume tank experiments do not provide any larger scale observations such as fault and fracture density or active vs. remnant topography, they do allow for variables to be altered and different end members to be generated (in the case of Soutter et al. 2021; Appendix D, the orientation of topography relative to sediment input). Outcrop data provides the broadest amount of information across a variety of scales (from sedimentary structures to deformation zone extent; Figure 6.10), but these are often limited to a few data points, with high uncertainties on exact sedimentation rates, diapir rise rates, source areas and three-dimensional stratigraphic geometries.

The combined observations from multiple data sources such as the ones used in this study can help to address some of the questions remaining about the nature of the salt-sediment interface. For example, understanding MTD character, bedding orientations, facies distributions and thickening and thinning rates can help to understand the longevity of halokinetic-influence on stratigraphy (Figure 6.10). Meanwhile, understanding facies distributions, fault and fracture density, deformation zone extent, stratal terminations and stacking patterns (which requires a multi-scalar, multi-discipline approach) can aid prediction of the highest quality reservoir sandstones and stratigraphic-structural traps (Figure 6.10).

The integrated workflow used within this study has helped to increase understanding of how halokinetically-influenced deep-water systems differ from their unconfined counterparts, and what

controls these differences. Figure 6.10 highlights the importance of a multi-scalar approach to supplement knowledge gaps that exist when using only one data type or scale. Utilising all available data and employing multi-scalar workflows are always recommended when working in salt basins.

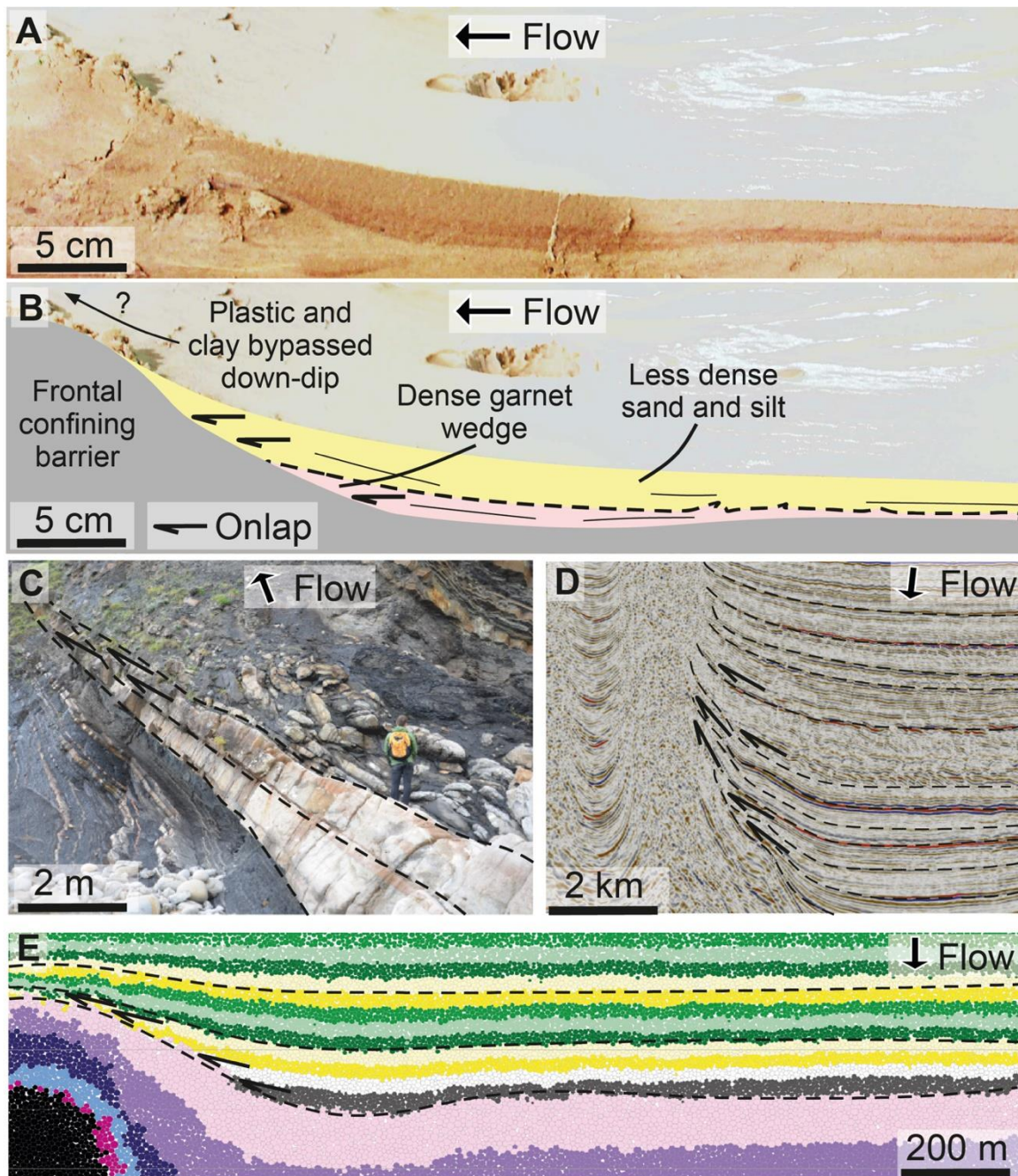




**Figure 6.10:** Workflow diagram showing the different types of data in this study (coloured boxes) and how they can be used to generate different observations (black boxes), which aim to address some of the key uncertainties (orange boxes) present in halokinetically-influenced deep-water environments. Addressing these uncertainties ultimately leads to a better understanding of deep-water sediment routing around salt topography (purple boxes). The list of observations and uncertainties is non-exhaustive, but highlights the importance of using a multi-scalar approach to supplement knowledge gaps that exist when using only one data type.

### **Scale independent observations**

Some observations are specific to a certain data type or scale, for example sedimentary structures are often bed scale, while deformation zone extent is often ‘mega sequence’ scale. Other identifying characteristics in deep-water halokinetically-influenced systems are scale independent, such as thinning, and eventual termination of beds towards topography (Figure 6.11). At individual flow (bed) scale, the high-density part of the flow is confined at the base of the topography, demonstrated in the flume tank experiments by the concentration of higher-density garnet at the base of the flow. The less-dense sand and silt parts of the flow run further up slope and onlap topography, and the lowest-density plastic and clay grains bypass the topographic barrier and flow down-dip (Figure 6.11A, B). Similar observations were made in the Black Flysch Group where, at a lobe element scale, high-density flow deposits were confined at the base of the topography, comprising thick, stacked sandstones, while lower-density flow deposits ran up topography, comprising increasingly muddier, thinner sandstones which onlap the slope due to a reduction in flow velocity (Figure 6.11C). At the lobe complex to mega sequence scale, seismic packages of Jurassic – Miocene stratigraphy in the ECG, show upwards rotation, thinning and termination against the Pierce salt structures (Figure 6.11D). The apparent termination of these stratigraphic reflectors helps to illuminate the top salt. The upwards rotation of beds is a product of rapid diapir rise rate (Giles and Rowan 2012). On a similar scale to seismic datasets, DEM observations, show thinning towards the topographic high of all layers, and eventual pinch out and onlap of the basal layers (grey-yellow layers, Figure 6.11E). Thinning, pinch out and onlap towards depositional slope occurs across multiple scales because low-density flows require less energy to overcome the increased gravitational potential when being transported up topography, and topographic barriers can exist from bed to megasequence scale (e.g., Ericson et al. 1952; Gorsline and Emery 1959; Al-Ja’aidi 2000; Bakke et al. 2013). Thus, it’s clear that some halokinetically-influenced processes are scale independent and also scalable. For example, one seismic reflector pinch out represents a series of bed pinch outs which are difficult to resolve at the resolution of seismic data. Therefore, observations of large-scale pinch-outs (e.g. in seismic data) represent many smaller scale (bed – lobe scale) pinch outs. This shows that the primary observation of a large-scale pinch out represents numerous internally complex smaller scale pinch outs. The observations of small-scale pinch-outs or core-scale bed thinning for example, are likely to upscale, representing a larger more prominent stratigraphic pinch out. Bed-scale data can provide details of grain size and type segregation across a pinch out, whilst larger scale data (seismic data) can show length scale variabilities in rock and fluid properties approaching a pinch out, often in three- or four- dimensions. Understanding of these characteristics as multi-scalar is helpful in extracting learnings and knowledge from different scales of data and applying a ‘zoom in zoom out’ approach to subsurface energy exploration and production.



**Figure 6.11:** Observations of onlap and pinch out across multiple scales and datasets, predominant direction of sediment flow is highlighted. Arrows indicate onlap and dashed lines highlight specific bedding surfaces to trace thickness variations. A) Uninterpreted and B) interpreted cross-section photographs from the frontally-confined flume tank experiment (Soutter et al. 2021; Appendix D). This section is taken ~20 cm off-axis. The image shows onlap of a red garnet-rich layer (higher density part of the deposit), and later onlap of a more sand-silt rich dominated layer (lower density part of the deposit). C) Onlap and thinning to pinch out of sandstone in the Black Flysch Group at Cabo Matxixako; higher density sandstones are confined to the base of slope while muddier and thinner bedded units (lower density) run further up topography. D) Halokinetic sequences adjacent to the South Pierce diapir, showing steep onlap geometries approaching the diapir (specifically in the basal (Jurassic-Palaeocene) stratigraphy). E) Extract from the upper part (syn-kinematic stratigraphy) of the intermediate sedimentation model (M3) showing onlap getting progressively closer to the crest of the diapiric overburden. Subsequent layers thin over the crest but do not pinch out or terminate.

### **Integration of numerical modelling data**

Numerical modelling data is extremely beneficial at complementing existing datasets by providing the ability to vary lots of parameters and therefore allow for testing of a variety of scenarios. For example, thinning rates, deformation rates and fault density under different simulated conditions.

DEM is not intended to substitute Finite Element Models, physical models or standard subsurface workflows, but rather to complement these approaches in salt tectonics.

A key challenge for numerical models is ground-truthing against natural prototypes (Oreskes et al. 1994; Burgess 2012). The integrated nature of this study has compared findings and predictions from the DEM to outcropping and subsurface analogues to assess their applicability and limitations (Chapter 4 and 5). Comparison of variable sedimentation models to Pierce Field diapirs in the UK North Sea (Chapter 4) shows how different models can be applicable to different parts of stratigraphy, a benefit of the ability to run multiple scenarios to best simulate natural complexity. Model-derived thinning rates, onlap geometries and deformation zone extents, under different sedimentation conditions, could be used to guide interpreters of likely sedimentation rates and conditions present in subsurface examples from analysis of broad scale stratigraphic geometries. Natural examples record the interplay between diapir rise rate and sedimentation rate, however, the models used here are a simplification and only sedimentation rate was varied. Therefore, if using numerical models to predict subsurface conditions, it is important to remember that natural stratigraphic architectures represent relative, and not absolute, sedimentation rates.

Variably spaced diapirs imaged in the subsurface and modelled data (Chapter 5) are in agreement about the extent of halokinetically-influenced zones between diapirs at different spacing (e.g., intense modulation between closely-spaced diapirs, and a zone of non-deformation between more widely-spaced diapirs). The ease of generating multiple models quickly enables comparison to a wide variety of subsurface analogues, and allow the evaluation of governing processes. Models, do however, simplify the subsurface expression of top salt topography, subsalt faulting, and other salt related topography (i.e., short-lived salt diapirs). This shows, again, that ‘real examples’ are more complicated than modelled results, but that models can provide useful and quick broad insight, as well as confirming and supplementing subsurface observations.

Models are of similar resolution (e.g., depositional element complex – mega-sequence scale) to seismic observations, so it is encouraging that similarities in thinning rates, diapir spacing, deformation zone extents and stratigraphic geometries are consistent. Observations that are often sub-seismic resolution, such as facies and MTD distribution, and lateral and temporal variability of these properties, are therefore not possible to resolve in DEM. Integrating facies information from outcrop analogues (Chapter 4) with geometries from DEM, can allow the prediction of sandstone and MTD distribution and likely lateral variability. While such integrations are simplistic, they may quickly highlight the likely presence or absence of key components of subsurface energy play concepts.

Fundamentally, the similarity of observations across multiple data types provides increasing confidence in validity of interpretations. Integrating DEM with subsurface and outcrop data helps to reduce uncertainty in halokinetically-influenced deep-water systems, by allowing the quick and efficient ability to vary and isolate key parameters.

## **6.5 Comparison to other depositional settings**

### ***Subsurface halokinetically-influenced deep-water settings***

Mayall et al. (2010) show that at a seismic-scale salt topography can confine, re-route or cause the abutting of gravity flow deposits. Observations of sediment routing around the Bakio diapir have established that at an outcrop scale these alterations to sediment pathways also exist, suggesting they are scale-independent processes. Field observations of kilometre to tens of kilometre wide salt-influenced basins, are consistent with minibasins of 10 – 100s kilometre, and diapir spacing as narrow as 2 kilometres, observed in the subsurface (Mayall et al. 2006, 2010; Scott et al. 2010; Carruthers et al. 2013; Oluboyo et al. 2014; Doughty-Jones et al. 2017; 2019; Howlett et al. 2020;

Nascimento et al. 2020). Classic deep-water systems are predicted to become less confined down dip (i.e., from channel confined to unconfined lobes; Pr elat et al. 2009; Talling et al. 2009; Spychala et al. 2017a). Nascimento et al. (2020) show that with increased salt topography down dip, deep-water systems can actually, counter-intuitively become more confined down dip, for example where channels and lobes are confined between salt walls.

Progressive onlap and thinning up-dip of the Paleocene Forties Sandstone member, towards the crest of many ECG diapirs (Chapter 5) is similar to that observed in the Black Flysch Group stratigraphy around Bakio (Chapter 3). This onlap pattern indicates that the topographic relief of the diapirs had a significant control on sediment distribution across much of the ECG, UK North Sea (e.g., Jennette et al. 2000; Kilhams et al. 2012; 2014; 2015; Hale et al. 2020). Anastomosing channels are common between diapirs in the ECG showing that ‘funneling’ of these systems, predicted to be responsible for stacked thick sandstone deposits in the Sollube basin is possible (Figure 5.7). MTDs, derived from diapirs are seen to further confine and influence subsequent gravity flow deposits, across the ECG (Jenette et al. 2000; Birch and Haynes 2003; Scott et al. 2010; Kilhams et al. 2012; 2014; 2015; Hale et al. 2020), in agreement with observations of outrunner blocks derived from the diapir high influencing subsequent deposition in the Black Flysch Group at Bakio (De Blasio et al. 2006; Soutter et al. 2018).

Deep-water unconformities in seismic data from the Gulf of Mexico (e.g., Rowan et al. 2003) and the North Sea (e.g., Carruthers et al. 2013) are associated with bright continuous pairs of amplitudes (Giles and Rowan 2012). In the Gulf of Mexico these reflectors represent condensed hemipelagic mud deposited between third-order lowstand systems tracts (Prather et al. 1998; Weimer and Link 1991; Weimer 1994). Field observations from Bakio suggest that deposition is most extensive during lowstand (Haq et al. 1987; Haq 2014) and therefore unconformities associated with halokinetic sequence boundaries could be formed during highstand. A late Albian highstand (Haq et al. 1987; Haq 2014), associated with increased mudstone deposition, could be responsible for the unconformable contact separating halokinetic sequences 3 and 4 on the western flank of the Bakio Diapir (Figures 3.10 and 3.12D; Roca et al. 2021).

Oluboyo et al (2014) recognise salt minibasins between 5 – 20 km wide in the Miocene of the Lower Congo Basin, Angola, which are comparable in geometry and stratigraphic fill to the Bakio-Gaztelugatxe salt-influenced basins. Across the Lower Congo Basin, elongated lobes are confined by binding salt walls, and there is evidence for enhanced progradation between two salt walls Oluboyo et al. 2014). These observations appear consistent across outcropping examples (the Sollube basin) and physical models (Soutter et al. 2021; Appendix D), and are representative of depositional systems where flow is at a low angle to structural strike (Oluboyo et al. 2014; Jackson and Hudec 2017). In the Kwanza Basin, offshore Angola, Howlett et al. (2020) recognised a three-part evolution (initiation, maturation and decay) of contractional salt structures that influence sediment gravity flows, and their deposits. During the decay stage, remnant structures still exert a subtle, but key, control on the development and position of deep-water sedimentary systems (Howlett et al. 2020). This is in similarity to the residual topography of the Bakio and Guernica diapirs, which influences the geometry of the Sollube basin into the Cenomanian, following the cessation of diapir growth, and thus controls the position and architecture of the Upper Black Flysch Group, despite the fact the topography was static during deposition. Recognition of similar observations at different scales reiterates the importance of a fully integrated, multi-scalar understanding of depositional systems (Figure 6.10). The outcrops around the Bakio diapir are of seismic-scale, and therefore it is unsurprising that they show similarities to the subsurface variability in halokinetically-influenced deep-water environments.

### ***Deep-water systems developed under variable amounts and types of topography***

Much of our understanding of deep-water settings in general is derived from outcrop observations from the Tanqua-Karoo Basin of South Africa, the southern Pyrenees, Spain, the Clare Basin, Ireland and the Annot Basin, France (e.g., Apps 1987; Mutti et al. 1987; Martinsen et al. 2000; Elliott 2000; Apps et al. 2004; Kane and Hodgson 2011; Patacci et al. 2014; Hansen et al. 2019; Soutter et al. 2019). This section describes and compares the Bakio study area to other deep-water depositional settings confined by non-halokinetically influenced topography, specifically focussing on examples from the Eastern Greater Caucasus, Azerbaijan (Cumberpatch et al. 2021a; Appendix C) and the subbasins of the Annot Area, SE France (Soutter et al. 2019).

**Orientation of topography:** ‘Fill and spill’ is commonly observed in deep water slope settings where topography is perpendicular to flow direction (Figure 6.15; e.g., Prather et al. 2012; Oluboyo et al. 2014; Soutter et al. 2019; 2021). In these settings, the thick high density turbidites tend to remain ponded in up-dip basins while the more dilute low-density turbidites can ‘spill’ into the down-dip basin (Normark et al. 1983; Normark and Piper 1991; Sinclair and Tomasso 2002). Oluboyo et al. (2014) showed that where regional flow direction was at a high angle to structural strike (i.e., oblique to perpendicular) transport pathways passed progressively through multiple intra-slope basins in a fill and spill manner. By comparison, when regional flow direction was at a low angle to structural strike, sediment transport pathways ran parallel to structure and were confined into individual intra-slope basins for many tens of kilometres. In the latter, often poorly-studied or documented, configuration spill between adjacent intra slope basins is rare (Prather et al. 2012; Oluboyo et al. 2014). A similar phenomenon has been documented in outcropping halokinetically-influenced fluvial successions where channels develop parallel to salt-walls (Banham and Mountney 2013a; b; 2014).

The Bakio study area provides the only known exposed example of a deep-water salt influenced basin where flow direction is at a low angle to structural strike. A broadly progradational sequence, which thickens and coarsens upwards, and runs parallel-oblique to the confining salt walls on a similar scale and distance to the configurations in the Lower Congo Basin (Oluboyo et al. 2014), is observed in the field area (Cumberpatch et al. 2021b; Chapter 3). A ‘secondary’ westerly palaeoflow orientation is indicated by Vicente Bravo and Robles (1988), and supported by palaeocurrent data collected as part of this study (Figure 3.12A) to represent fill and spill over (Prather et al. 2012) the Guernica diapir into the Sollube basin (Roca et al. 2021). This suggests that in settings with dynamic topography, neighbouring basins can behave independently.

In confined settings, such as the Annot Basin (slowly deforming) and the Basque-Cantabrian Basin (quickly deforming), similar broad, fan-shaped geometries and facies are observed to unconfined settings such as Tanqua-Karoo (Bouma and Wickens 1994; Sinclair 1994; Robles et al. 1998; 1999; Sinclair and Tomasso 2002; Apps et al. 2004; Hodgson et al. 2006; Prélat et al. 2009; Flint et al. 2011; Salles et al. 2014; Patacci et al. 2014; Spychala et al. 2015; 2017; Soutter et al. 2019), however systems are smaller and more elongate (Figures 3.15 and 6.16 Soutter et al. 2019; 2021). Flume tank observations (Soutter et al. 2021; Appendix D; Figure 6.4) highlight that on the scale of an individual event, beds that eventually stack to form lobes are of similar broad geometry, but exhibit vital differences dependent on the presence or absence of topography during their deposition. Broadly lobate symmetrical deposits form under the ‘unconfined’ experiment. Similar geometries form under frontal confinement but with some confinement and lateral dispersal up dip of the topographic barrier (compare Figure 6.4A and D). When lateral topography is present, flow velocities are 20% higher adjacent to the topographic barrier, and thus the deposit reaches further into the basin, suggesting the flow velocity was enhanced due to the presence of topography. The resultant deposit is also asymmetric with a smaller areal extent (Figure 6.4B). In experiments with oblique confinement, two lobate deposits form (down dip and laterally re-routed up-dip of the

topographic barrier), here the deposit geometry is highly modulated compared to that deposited with no topography (Figure 6.4). Differences exist, not only in terms of depositional system geometry, but also in terms of how facies are distributed across these settings. A difference in facies distribution between unconfined and confined deep-water fans is that flow transformation is influenced by topography and therefore hybrid beds are common throughout the proximal fringe (i.e., frontal and lateral) in tectonically active confined settings, while in unconfined systems they are restricted to the frontal fringe (Barker et al. 2008; Sychala et al. 2017; Soutter et al. 2019; Barker et al. 2008).

**Mass transport deposits as indicators of topography:** A common facies association in deep-water topographically influenced settings is the interbedding of MTDs and turbidites, giving evidence for coeval seabed instability with deposition. Between the proto-Boltaña and Mediano anticlines, in the Tremp-Pamplona Basin, Pyrenees, slide and debris flow deposits are interbedded with coarse-grained sand-rich channel and scour-fill deposits throughout the Eocene stratigraphy, on a similar scale and facies distribution to those in the Black Flysch Group at Cabo Matxixako (Clark 1995; Pickering and Corregidor 2000; Schwab et al. 2007). Interbedding of slumps and turbidites in the Carboniferous Ross Formation of Western Ireland is attributed to lateral mass failure from the basin margin interacting with axial turbidity currents (e.g., Gill 1979; Gill and Kuenen 1958; Elliot 2000), in resemblance to the coeval axial (allocyclic) and lateral (halokinetic) systems operating during the Albian in the Bakio study area. At Tremp, these deposits have been attributed to mass-wastage from the upper and mid-slope, which were likely triggered by growth of the proto-Boltaña and Mediano anticlines (e.g., Gupta and Pickering 2008; Dakin et al. 2013). The evolution of the Ross Formation is influenced by mud diapirism such that channels are often bound by such structures. Put simply, mud diapirism is a similar process to salt diapirism, and therefore the topographic barriers cause similar instabilities and therefore similar depositional facies (e.g., Fusi and Kenyon 1996; Hanafy et al. 2017). At Bakio, remobilised carbonates (from the Aptian platform growing on top of the diapir), and low-density turbidites (deposited on the crest or flanks of the topographic high during the Albian-Cenomanian) are frequently reworked as mass transport deposits, and thus interact with the deep-water axial system, and in some cases these mass failures act to further control and confine subsequent axial flows and lateral failures (Figures 3.15 and 3.16).

Mass transport deposits (MTDs) are well known to influence and promote ponding and partial confinement of the overriding sediment gravity flows (Figure 6.15; e.g., Kneller et al. 2016). They can also produce gentle seabed relief, with gradients as low as  $0.05^{\circ}$ - $1.4^{\circ}$  (Bugge et al. 1988; Gee et al. 1999; Haflidason et al. 2004; Frey-Martinez et al. 2006; Ortiz-Karpf et al. 2015; 2016; Cumberpatch et al. 2021a; Appendix C) and impact the overlying strata, as is evidenced by halokintically-derived MTDs influencing subsequent deep-water sedimentary systems (Chapters 3 and 5). Van der Merwe et al. (2009) documented on a bed scale, sandstones that underwent foundering into an underlying debrite, driven by instability due to the density contrast of sand deposited above the liquefied debrite (density loading) and lateral changes in sediment load (uneven loading) (Owen 2007). A similar phenomenon is described by Martinez-Doñate et al. (in prep), in the Jurassic Los Molles formation, Neuquén basin, Argentina, where disconnected sand bodies between 0.5-3 metre thickness and 5-25 metre width overlie a mud-rich debrites, similar to disconnected channel or scour fill sandstones assumed to be deposited in depositional lows on MTD topography at Bakio Bay West (Chapter 3; Cumberpatch et al. 2021b). These sandstones are present in the topographic lows of the upper surface of the debrite, where the debrite is thinnest (Figure 6.15; Martinez-Doñate et al. in prep) and are characterised by onlap and thinning towards the edges of depressions within the upper surface of the MTD. The accumulation of thick-bedded sandstones is the product of the dynamic nature of the upper surface of the MTD rather than a pronounced depositional

topography (Martinez-Doñate et al. in prep), similar to how thick-bedded sandstones are preferentially deposited in areas of reduced salt thickness (Cumberpatch et al. 2021 b;c;d).

Together, Bakio and the Annot and Eastern Greater Caucasus examples, discussed below, offer excellent outcropping analogues for confined deep-water successions, providing end members for type of topography, angle of topography, and orientation of topography to depositional flow (Figure 6.15).

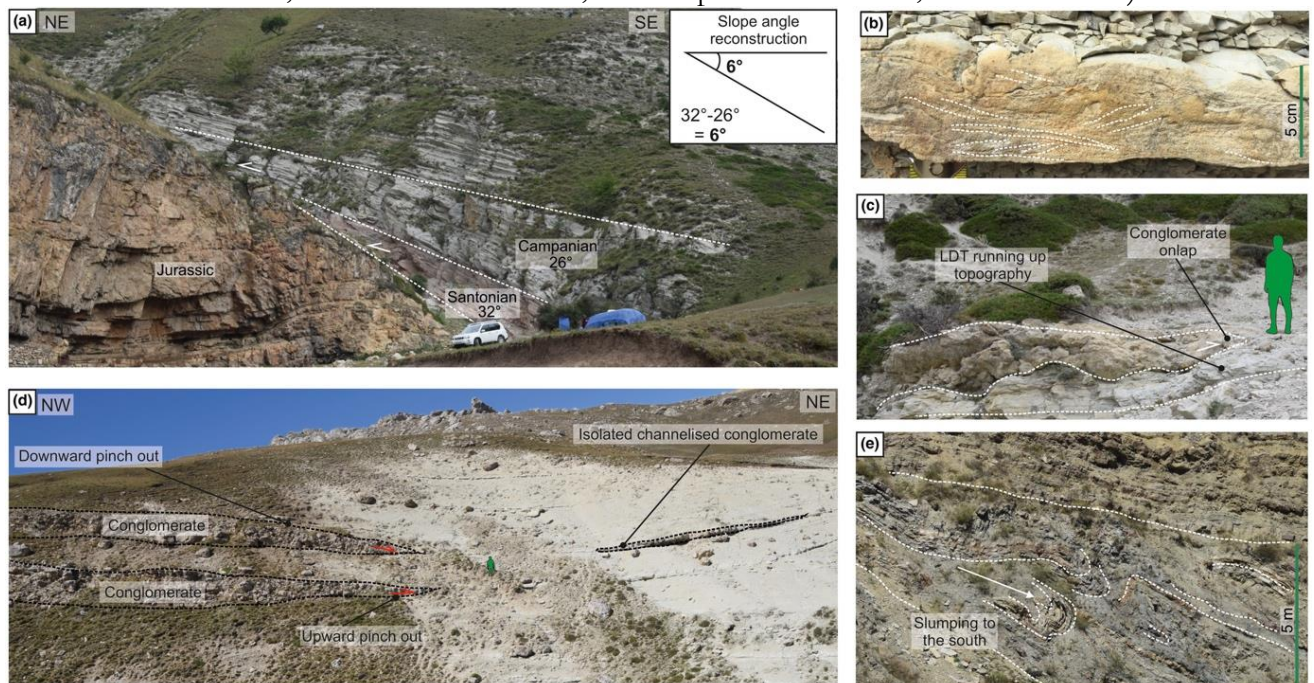
**Eastern Greater Caucasus, Azerbaijan:** The well-exposed Late Cretaceous mixed systems on the northern side of the Eastern Greater Caucasus, Azerbaijan, shows an evolutionary history influenced by early Cretaceous topography formed by a mass transport deposit (Cumberpatch et al. 2021a; Appendix C). Evidence for irregular bathymetry is recorded by opposing palaeoflow indicators and frequent MTDs throughout the Late Cretaceous stratigraphy (Figure 6.12), such observations are consistent with observations around the Bakio diapir (Chapter 3). Facies analysis reveals a Cenomanian–early Turonian siliciclastic submarine channel complex that abruptly transitions into a Mid Turonian–Maastrichtian mixed lobe-dominated succession. The channels are entrenched in lows on the palaeoseafloor but are absent 10 km towards the west where an Early Cretaceous submarine landslide complex acted as a topographic barrier to deposition (Figure 6.13). By the Campanian, this topography was largely healed allowing extensive deposition of the mixed lobe-dominated succession, acting to ‘bury’ previous topography (Figure 6.14), as is observed in salt-influenced deep-water environments globally (Mayall et al. 2006, 2010; Scott et al. 2010; Caruthers et al. 2013; Oluboyo et al. 2014; Doughty-Jones et al. 2017; 2019; Howlett et al. 2020; Nascimento et al. 2020).

The MTD in Azerbaijan influences subsequent depositional systems, which re-route around it, and are in some places absent adjacent to it (Figures 6.15 and 6.16). The overall stratigraphic architecture shows evidence for the infilling of ‘residual topography’, thinning towards the margins, similar to the Upper Black Flysch Group at Cabo Matxixako, but perhaps not as highly modulated as depositional systems deposited on the actively deforming seabed (e.g., salt-influenced). The presence of decametre-scale allochthonous blocks and submarine landslide deposits throughout the Cretaceous stratigraphy indicates a highly unstable margin (Figure 6.13).

In the western part of the Azerbaijan study area, Late Cretaceous deep-marine sandstones are observed to thin towards, and onlap, Late Jurassic platform limestones (Figures 6.13 – 6.15). Stratigraphy is observed to thin from metres to centimetres across the scale of the outcrop (10's–100's metres) towards Late Jurassic limestones around Cek (Figure 6.12). Late Jurassic limestones must, therefore, have formed 100s of metres of relief on the Cretaceous seafloor. The most likely mechanism for the generation of seafloor topography is through allochthonous block emplacement. These blocks, or “megaclasts” (e.g., Blair and McPherson 1999), were likely derived from Late Jurassic carbonate platform limestones (Figure 6.13), similarly to the megaclasts in the Black Flysch Group at Bakio being derived from the Aptian limestones above the diapiric highs (Figure 6.15). Interpretations of basin-scale submarine landslide deposits, which partially form the Qizilqaya and Shahdag mountains (Figure 6.13), further validates this interpretation of an unstable Jurassic margin forming highly rugose seabed bathymetry which influenced deep water depositional systems throughout the Cretaceous (Bochud 2011; Gavrillov 2018). The megaclasts in the west of the study area possibly formed part of this much larger deposit (Figures 6.13-6.15). This MTD is most likely to represent a regional MTD, related to margin-scale collapse, and thus is extensive for 10s' – 100s' of kilometres, rather than the locally (e.g., diapirically)-derived MTDs observed in the Black Flysch Group (Figure 6.15; Doughty-Jones et al. 2019; Wu et al. 2020). However, similarities exist, in that these MTDs have a substantial influence on the basal part of the stratigraphic architecture. Similar relationships to those formed as the Cretaceous stratigraphy infilled the irregular surface created

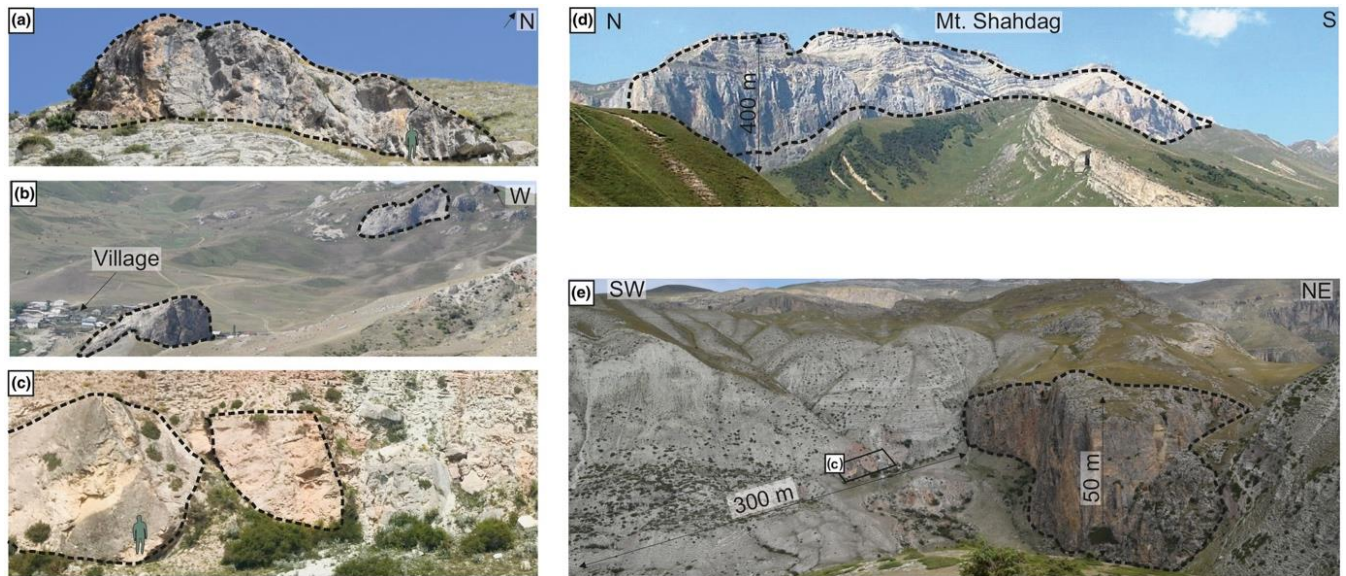
by earlier submarine landslide deposits, have been observed elsewhere at outcrop (e.g., Burbank et al. 1992; Armitage et al. 2009; Kneller et al. 2020) and in the subsurface (e.g., Soutter et al. 2018; Casson et al. 2020). The Late Jurassic blocks (Figure 6.13) within the Cretaceous stratigraphy can be interpreted as either: (a) Late Cretaceous failures from an exposed Jurassic shelf; (b) out-running blocks from Early Cretaceous failures (e.g., De Blasio et al. 2006) that were subsequently onlapped during the Late Cretaceous, or; (c) blocks that were periodically remobilised throughout the Late Cretaceous from high-relief Early Cretaceous slope submarine landslides identified in the west (Figure 6.14).

Differential compaction around these rigid blocks will have resulted in the steepening of strata adjacent to the block, which may contribute to the gradual rotation and steepening of stratigraphy identified (Figure 6.12). This compaction has been reported elsewhere around allochthonous blocks (e.g., Burbank et al. 1992). Rotation and steepening of stratigraphy due to differential compaction has a similar signature to rotation and steepening of stratigraphy experienced in halokinetic sequences adjacent to growing salt diapirs (Figure 6.15; Giles and Lawton 2002; Rowan et al. 2003; Giles and Rowan 2012; Rowan and Giles 2021; Cumberpatch et al. 2021b; Roca et al. 2021).

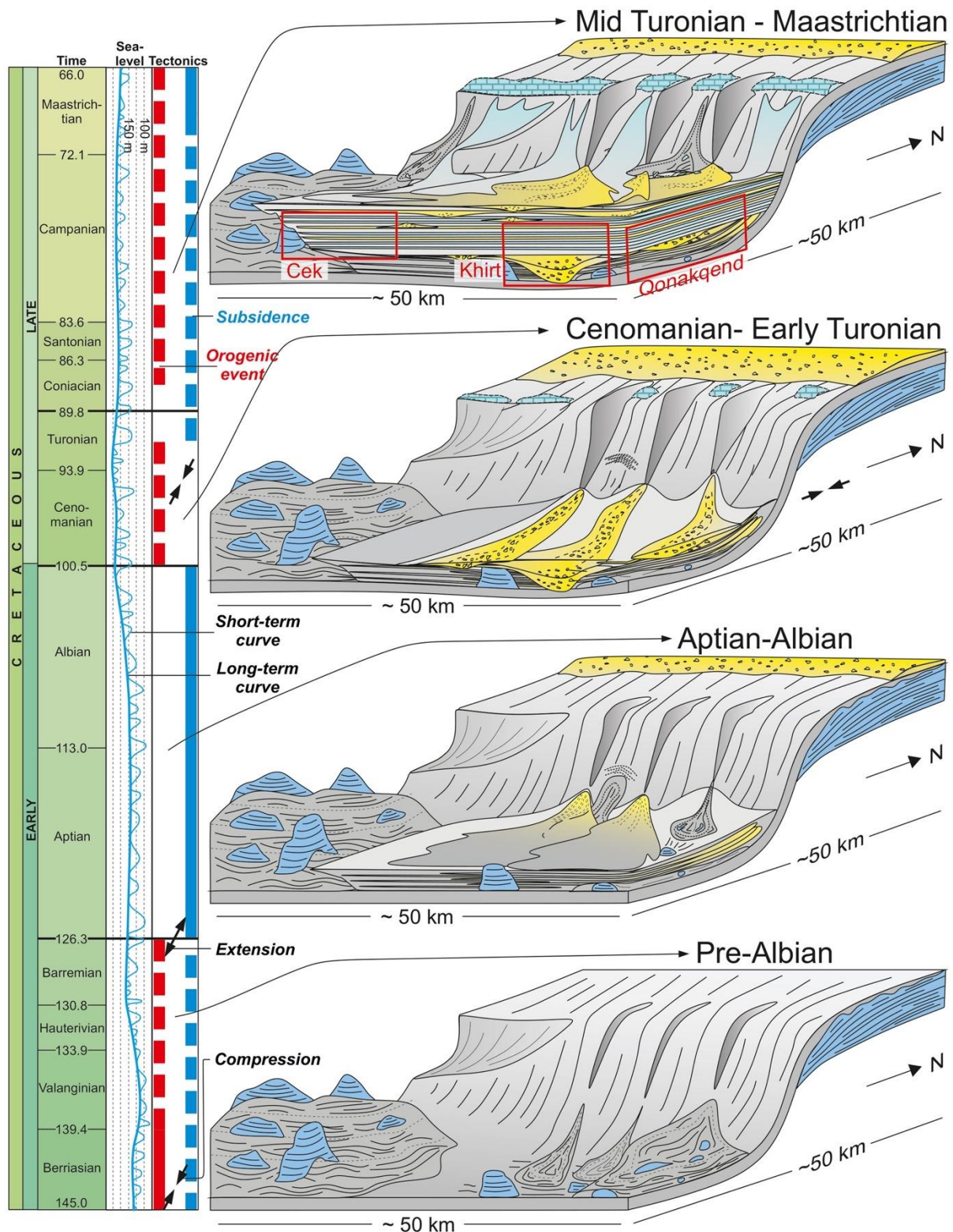


**Figure 6.12:** Evidence for palaeotopography in the Eastern Greater Caucasus. Scale is either person (1.74 m), car (1.9 m) or indicated. A) Cretaceous stratigraphy thinning and onlapping Jurassic limestone, slope angle reconstructed. B) Evidence for opposing ripple directions suggesting flow deflection. C) Thickness and pinch-out variability of different deposits on a metre-scale laterally. D) Cliff section containing three conglomerate bodies that vary in architecture and termination style as indicated. E) Submarine landslide deposit showing evidence for slumping towards the south.





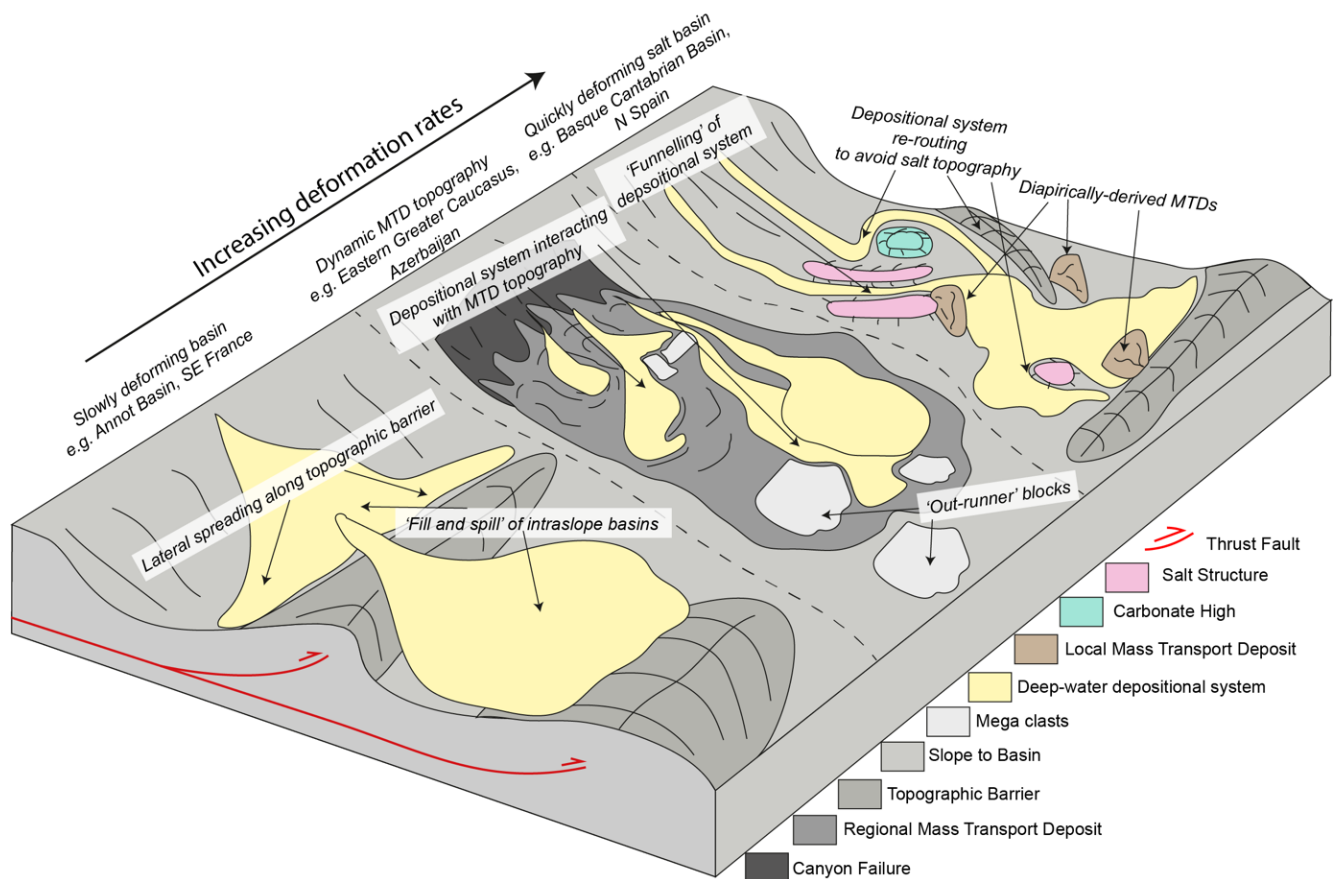
**Figure 6.13:** Evidence for allochthonous block model as the most likely for the generation of Cretaceous topography in the Eastern Greater Caucasus of Azerbaijan. Scale is either person (1.74 m) or indicated. Blocks are drawn around with black dashed line. A–C are examples of metre-decametre scale clasts around Cek. D) Shahdag Mountain, is interpreted as a kilometre-scale olistostrome (Bochud 2011), which moved up to 20 km without significantly affecting the internal stratigraphy (Garrilov 2018). E) Block with both margins exposed and overlapped by mixed stratigraphy, black box locates C.



**Figure 6.14:** Evolutionary model for the Cretaceous of the Eastern Greater Caucasus of Azerbaijan. Studied stratigraphic sections highlighted. Topography, thought to be formed by a mega-clast, is present throughout the Cretaceous and influences deposition, discussed in detail in *Cumberpatch et al. 2021a (Appendix C)*. Extract from the geological time scale, sea-level fluctuations (Haq 2014) and local tectonic events highlighted on the left. Tectonic events are compiled by *Bochud 2011, after Zonenshain and Le Pichon (1986), Philip et al. (1989), Brunet et al. (2003), Saintot et al. (2006) and Barrier et al. (2008)*. The Pre-Albian was dominated by limestone blocks on a muddy slope. Thin-bedded siliciclastic turbidites of a distal lobe were deposited during the Aptian-Albian. Siliciclastic channels are prominent throughout the Cenomanian-early Turonian. In the mid Turonian-Maastrichtian mixed calcareous and siliciclastic lobes, of different sub-environments interact, and are likely sourced from the same northern margin, discussed in text. Locations in red boxes are stratigraphically, and not spatially, representative.

**Grès d'Annot, France:** The gravity flows responsible for the Eocene to Oligocene Annot Sandstone, SE France, were confined during deposition by Alpine fold-and-thrust belt topography (Figure 6.15; Apps 1987; Sinclair 1994; Apps et al. 2014; Salles et al. 2014; Soutter et al. 2019). When compared with the rate of topographic deformation associated with diapir growth, the rate of orogenic deformation is more minor. The stratigraphic evolution of the Grès d'Annot is very similar to that of the Black Flysch Group; broadly progradational, initially with thin-bedded low-density turbidites of a distal fringe environment, which drape basinal topography. These beds are overlain by hybrid beds representing proximal lobe fringe deposition (Soutter et al. 2019), with continued progradation resulting in sandstones deposited in the lobe off-axis and eventually, lobe axis. Low sinuosity systems, similar to those observed between the diapiric walls of Bakio and Guernica are reported in the axis of basins in Annot area (Clark et al. 2008).

Rapid facies changes over 10s metres towards pinch outs are observed in the Annot basin (Apps 1987; Soutter et al. 2019), while halokinetic facies variation is seen over 100's metres at Bakio and in the ECG. Unlike Bakio, where palaeoflow was consistently at a low angle to structural trend, sub-basins in the Annot region were eventually filled and bypassed sediment into down-dip basins (Figure 6.15; Sinclair and Tomasso 2002; Prather et al. 2012; Salles et al. 2014; Soutter et al. 2019), indicating that paleoflow was perpendicular to at least one of the complex structural trends (Oluboyo et al. 2014). The slope angle is a scale of magnitude greater at Annot than Bakio ( $11^\circ$  at Col de Fa compared with  $3^\circ$  at Cabo Matxitaxako; Figure 3.8C). The correlation of steeper slope angle with shorter length scale changes in facies towards pinch outs suggests that slope angle controls facies distribution and variability adjacent to slopes (Soutter et al. 2019). Despite the steeper slopes, debrites in the Grès d'Annot are infrequent compared to those in the Black Flysch Group, and are slope derived (regionally), instead of deriving from diapiric highs (Figures 3.13, 3.14, 3.15, 3.16 and 6.15). This is a reflection of a more active, quickly-deforming basin floor in diapiric settings. Notwithstanding the difference in slope angle and the configuration of flow direction to structural strike, the stratigraphic evolution of Bakio and Annot remains broadly similar, suggesting that confined deep-water successions are broadly predictable (Kane et al. in prep).



**Figure 6.15:** Comparison of different types of topography that influence deep-water depositional systems, under increasing deformation rates (After Martínez-Doñate et al. (in prep); Kane et al. (in prep)). Slowly deforming example is based on field observations from the Annot Basin, SE France (Soutter et al. 2019) and flume tank experiments of frontal topography (Soutter et al. 2021; Appendix D). The example of the topography formed by a mass transport deposit is based on field observations in the Eastern Greater Caucasus of Azerbaijan (Cumberpatch et al. 2021a; Appendix C) and in the Nequén Basin, Argentina (Martínez-Doñate et al. (in prep)). Quickly deforming salt basin schematic is based on field observations from the Bakio diapir (Cumberpatch et al. 2021b; Chapter 3) and subsurface observations from the ECG, UK North Sea (Chapter 5).

**Axial and lateral system interplay:** The interplay of two distinct depositional systems (axial and lateral) is common in deep-water environments influenced by active rift topography, such as the Gulf of Corinth, Greece (Leeder and Gawthorpe 1987; Pechlivanidou et al. 2018; Cullen et al. 2019) and the Gulf of Suez, Egypt (Sharp et al. 2002; Jackson et al. 2002, 2005; Leppard and Gawthorpe 2006). In rift settings, the continually evolving footwall scarps feed lateral MTD-rich systems coevally with axial, allocyclicly-controlled depositional systems. Deposits in syn-rift settings are often narrow and elongated parallel to the strike of normal-fault segments (Carr et al. 2003; Jackson et al. 2005; Cullen et al. 2019; Tilhams et al. 2021), indicating the control on stratigraphic architecture by footwall physiography, analogous to salt wall controls on stratigraphic architecture. Some syn-rift tectono-sedimentary models propose that sediment supply to deep-water sinks is predominantly locally-derived from uplifted intra-basin footwall topography, either from the steep footwall scarp or down the gentler hanging wall dip-slope (e.g., Gawthorpe and Leeder 2000). Recent work by Tilhams et al. (2021), emphasises the importance of hinterland drainage sourcing major syn-rift gravity flow depositional systems (Scholz et al. 1990; Pivnik et al. 2003; Zhang et al. 2014; Zhang and Scholz 2015; Ford et al. 2017; Gawthorpe et al. 2018; Cullen et al. 2019). This supports the importance of a hinterland/regional depositional system, in addition to local diapirically-derived sediment source areas, in deep-water halokinetically-influenced environments (Mayall et al. 2006; 2010; Jones et al. 2012; Oluboyo et al. 2014; Doughty-Jones et al. 2017; 2019; Howlett et al. 2020).

### ***Recognition of halokinetically-influenced settings, across all depositional environments***

Sedimentological and stratigraphic features that are common across several depositional settings where halokinetic movements are observed include: multi-scalar thinning and onlap, growth faulting, pebble conglomerates, mixed siliciclastic–carbonate lithologies, MTDs, variable paleocurrents, angular unconformities, and abrupt facies variability (Figure 6.16; Dalgarno and Johnson 1968; Dyson 1999; Kernén et al. 2012, 2020; Carruthers et al. 2013; Counts and Amos 2016; Counts et al. 2019).

Deposition of thick-bedded sandstones along the axis of the Sollube basin, and thinner beds and mudstones on the flanks of the Sollube and Jata basins, is comparable to fluvial facies distribution (Figure 6.16; Banham and Mountney 2013a; 2013b; 2014; Ribes et al. 2015) where channel-fill sandstones dominate axial settings and floodplain mudstones are observed closer to the diapir. In subsurface examples from shallow marine stratigraphy in the Jurassic of the Norwegian North Sea, Mannie et al. (2014; 2016) observe thinning of 65% from axis of minibasin to diapir flank. Depositional thinning is also observed in marine-non-marine stratigraphy at El Papalote, La Popa (Giles and Lawton, 2002; Giles and Rowan 2012) and in the mixed stratigraphy in the Adelaide Rift Complex (Counts et al. 2019).

Individual beds in the Bakio Breccia formation are comparable in size (tens- to hundreds-of-metres packages) and composition to stacked MTDs reported overlying bounding unconformities in halokinetic sequences in the La Popa Basin (10–120 m in thickness) associated with remobilisation of diapir roof or cap rock (Figure 6.16; Giles and Lawton 2002; Poprawski et al. 2014; 2016). Smaller carbonate breccias with wedge-shaped geometries (metre-scale packages; Figure 3.8E) are similar in geometry and composition to “lentils” (1 metre to 100s of metre thick) described by McBride et al. (1974), but differ in thickness and areal extent. Lentils, MTDs, and breccias represent talus-like failure from diapir roof stratigraphy (Giles and Lawton 2002; Poprawski et al. 2014, 2016). Remobilised and reworked thin-bedded sandstones adjacent to diapirs often reflect remobilisation due to diapir growth, of stratigraphy that was deposited on top of the diapirs (Figure 6.16; e.g., Kilhams et al. 2012; 2014; 2015; Poprawski et al. 2014; 2016; Doughty-Jones et al. 2019; Howlett et al. 2020). The absence of these facies in fluvial settings probably reflects the fact that diapirs maintained surface topography during deposition, and therefore stratigraphy was not deposited above them (Banham and Mountney 2013 a;b; 2014; Ribes et al. 2015; 2017). Convolute laminated slump deposits in salt-withdrawal basins close to diapirs are reported in the Adelaide Rift Complex showing similar geometries to the reworked thin-beds observed in siliciclastic MTDs in this study (Counts and Amos 2016), suggesting these deposits are common in sub-aerial settings when accommodation exists above diapiric highs.

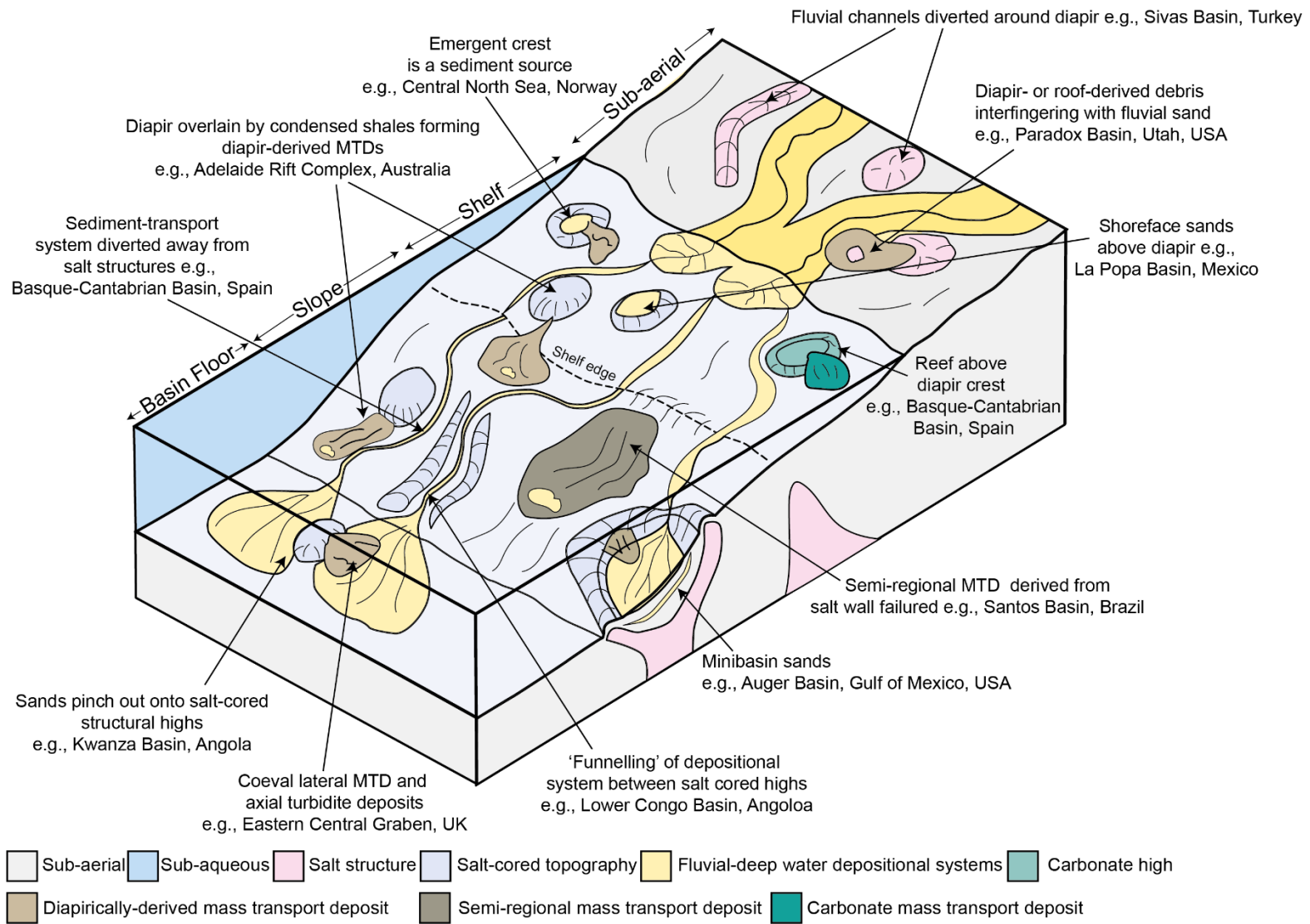
Evaporite clasts and beds can be observed in halokinetic stratigraphy if a nearby diapir was exposed during deposition. Interbedding of anhydrite and gypsum beds and clasts occurs within the fluvial succession in the Sivas Basin (Ribes et al. 2015) and the Paradox Basin (Figure 6.16; Banham and Mountney 2013b). No such salt layers or clasts are preserved in the Bakio study area suggesting the salt structures of Bakio and Guernica were only episodically exposed at the seabed, if at all. This fits the interpretation of carbonate-platform growth above the structures, preventing salt exposure (García-Mondéjar 1990; Rosales and Pérez-García 2010; Poprawski et al. 2014; 2016).

Extra formational clasts within syn-kinematic stratigraphy surrounding the Mount Frome diapir, Adelaide Rift Complex (Counts and Amos 2016; Counts et al. 2019) are thought to represent isolated exotic clasts brought to the surface from deep within the basin by the salt diapirs and redeposited into the younger basin fill. This process could explain the presence of metre-scale mafic breccias within the Triassic succession at Bakio (Poprawski et al. 2016; Roca et al. 2021). Active diapirs in present-day basins (e.g., The Persian Gulf (Edgell 1996; Talbot and Pohjola 2009)), which contain abundant, variable, brecciated clasts from deeper in the basin, are deposited

onto a subaerial or subaqueous surface, providing a modern analogue for such extra formation clasts, observed in ancient halokinetically-influenced stratigraphy (Bruthans et al. 2009).

Giles and Lawton (2002) report abrupt lateral facies changes within 1 km of the syn-depositionally active El Papalote diapir, in the La Popa Basin, Mexico. In the salt-influenced Sivas Basin, Turkey, fluvial facies distributions are mostly controlled by halokinesis; minibasin axis are dominated by channelised sandstone bodies and floodplain mudstones are observed closer to the diapir (Ribes et al. 2015; 2017). Counts et al. (2019) describe a mudstone condensed section closest to the diapir again suggesting finer grained deposition closer to diapirs (Figure 6.16). The Bakio study area also highlights sandstone deposited in the basin axis while thin-beds, MTDs and mudstones occupy the flanks, suggesting that sandstones are preferentially confined in the centre of the basin (Figure 6.16). The high amount of deformation and facies variability observed in halokinetically-influenced deep-water stratigraphy is in agreement with other halokinetically-influenced settings globally (e.g., Dalgarno and Johnson 1968; Dyson 1999; Kernen et al. 2012; 2020; Banham and Mountney 2013 a;b; 2014; Poprawski et al. 2014; 2016; Counts and Amos 2016; Ribes et al. 2015; 2017; Counts et al. 2019; Davison and Barreto 2021). This study supports recent work of Counts et al. (2019), who suggest that unevenly distributed and highly variable facies are distinguishing of halokinetic influence, and are common in areas where depositional thinning, onlap and growth strata are present.

The consistency of field observations collected in a deep-water halokinetically-influenced setting and previously described halokinetically-influenced settings suggests that the criteria for recognising halokinetically-influenced systems (e.g., pinch out, onlap, stratigraphic thickness variations, variations in facies and facies distributions and unconformities) is similar regardless of depositional environment, suggesting that halokinetic controls are central to stratigraphic architecture and evolution modulation. Multiple directions of ripple lamination, presence of hybrid beds, range of MTD types (particularly slumps containing remobilised thin-bedded sandstones), and abrupt juxtaposition of deep-water depositional facies can be used to specifically identify deep-water stratigraphy influenced by salt tectonics in core and outcrop.



**Figure 6.16:** Summary diagram showing how diapir topography can influence facies distribution throughout all depositional environments (after Hudec and Jackson 2017). Salt topography acts to confine, re-route and modulate sedimentary systems in similar ways regardless of depositional environment (e.g., failures, pinch out, over-steepened stratigraphy, multiple paleocurrent directions). Sub-aerial environments are based on outcropping observations from Permian-Triassic stratigraphy in the Paradox Basin, Utah (Banham and Mountney 2013a; b; 2014) and the Miocene strata of the Sivas Basin, Turkey (Ribes et al. 2015; 2017). Shallow marine observations are based on outcrop observations from the Cretaceous of the La Popa Basin, Mexico (Giles and Rowan 2002; Rowan et al. 2003; Giles and Rowan 2012), the Cretaceous stratigraphy around the Bakio diapir, Spain (Poprawski et al. 2014; 2016), and Precambrian stratigraphy in the Adelaide Rift Complex, Australia (Counts and Amos 2016; Counts et al. 2019), and subsurface observation from the Jurassic of the Central Norwegian Sea (Mannie et al. 2014; 2016). Deep-water observations are based on the Cretaceous Black Flysch Group around the Bakio diapir, Spain (Cumberpatch et al. 2021b; Chapter 3), subsurface observations from the Paleocene of the ECG, UK North Sea (Kilbams et al. 2012; 2014; 2015; Chapter 5) and supplementary literature (Booth et al. 2003; Mayall et al. 2006; 2010; Oluboyo et al. 2014; Doughty-Jones et al. 2017; 2017; Rodríguez et al. 2018; 2020).

## 6.6 Reducing facies uncertainty in the subsurface

Utilising outcrop analogues (Figure 4.15) can help provide sub-seismic scale depositional facies information, helping reduce uncertainty in reservoir quality and distribution. Numerical modelling results do not represent specific analogue conditions nor a ‘snapshot’ in time. They can therefore help to quickly identify generic depositional architectures, deformation patterns and sediment thickness relationships as a function of several parameters, such as variations in sedimentation rates. Using stratigraphic architectures from our DEM and sedimentological data from field examples, we can improve predictions of the likely architecture of syn-kinematic stratigraphy and sedimentology around salt structures, which are poorly-imaged in seismic reflection data. For example, models provide details about gross thickness changes and geometry, whereas field analogues enable inferences about reservoir quality and net-to-gross.

The DEM models presented in Chapter 4 document changes in stratigraphic architectures (thickening and thinning of layers) and deformation. For simplicity and applicability to all depositional settings the models do not assume a specific sedimentary process, and therefore no depositional setting is implied. Composition (e.g., carbonate or siliciclastic) controls the overarching processes experienced in a depositional setting, and therefore the likelihood of halokinetic modulation (Adams and Kenter 2012). Type of depositional setting (e.g., fluvial or deep-water) is associated with different depositional processes (e.g., suspension fall out, laminar flow, turbulent flow) and therefore all sedimentary environments will respond differently to salt influence, and their depositional facies will be differently distributed (Figure 6.17; Davison and Barreto 2021). Due to the natural variability (internal and external controls) operating across all depositional environments there are already a number of sub-facies present which would control reservoir distribution in a basin absent of salt (e.g., Ferguson et al. 2020). Salt tectonics further complicates the facies heterogeneities (Figure 6.17), making visualising sub-seismic scale variability extremely difficult, requiring an integrated multi-discipline, multi-scalar approach to understanding.

The schematic conceptual models presented in Figure 6.17 are created using the stratigraphic architecture of the intermediate aggradational model (M3, Chapter 4) and overlaying depositional facies observations from published halokinetically-influenced settings globally (Banham and Mountney 2013 a; b; 2014; Poprawski et al. 2014; 2016; Ribes et al. 2015; 2017; Counts et al. 2019; Cumberpatch et al. in 2021b; Chapter 3). Outcropping halokinetically-influenced successions are rare (Jackson and Hudec 2017) and therefore Figure 6.17 does not provide an exhaustive list of all possible depositional environments. Each reported field example is unique in terms of stratigraphic age, global location and proximity to salt structure, but the population of models with depositional facies from different environments gives some insight into the expected variability in the subsurface.



### ***Deep-Water Environments***

Field-based observations from the Albian-Cenomanian Black Flysch Group adjacent to the Bakio diapir, are used to populate the model for the deep-water depositional environment. A broadly thickening-upwards stratigraphic trend can be seen with a transition from thinly-bedded, finer-grained sandstones to thicker-bedded coarser-grained sandstones with intercalated MTDs (Cumberpatch et al. 2021b). Early diapiric overburden and syn-kinematic depositional elements are deformed closest to the diapir with deformation rate decreasing away from the diapir, and being minimal outside of the halokinetic sequence (Figure 6.17). The tapered composite halokinetic sequence at Bakio is ~700 m wide, with stratigraphic packages, and individual beds, shown to pinch towards the diapir (Chapter 3). The width of the halokinetic sequence is akin to the width of the zone of halokinetic influence in the DEM. Thicker bedded sandstones representing channels and lobes are deposited in topographic lows (in minibasins adjacent to the salt structures) while towards the flanks, the lower density part of the flows responsible for the thick-bedded sandstones may run-up topography depositing thinly-bedded muddier sandstones towards the pinch-out (Kneller and McCaffrey 1999). Field evidence and subsurface examples (Mayall et al. 2010; Sylvester et al. 2012; Doughty-Jones et al. 2017; Rodriguez et al. 2020) show that submarine channels often re-route to a path of least resistance (commonly a depositional low) and increase sinuosity, depositing lateral accretion packages, to avoid salt-cored topography.

Crestal and flank deposition is limited due to elevation, with suspension fall-out and low-density turbidity currents depositing mudstones and thinly-bedded sandstones respectively. This sediment is often re-worked into MTDs which thin away from the diapir. Similar observations are seen in subsurface examples of salt-influenced systems (Oluboyo et al. 2014; Doughty-Jones et al. 2017; Rodriguez et al. 2020) and in outcropping examples of deep-water sedimentation during rift propagation (Cullen et al. 2019). The number of MTDs decreases upwards in the Black Flysch Group which, as shown by the DEM, reflects reduction in halokinetic influence upwards and thus less topography generation to promote failures (Figure 6.17). Not all MTDs in deep-water halokinetically-influenced environments derive from diapirs; outside the zone of halokinetic influence any MTDs observed are likely to be sourced from failures of the shelf up dip (Soutter et al. 2018; Poprawski et al. 2021).

Stratigraphy, both vertically and laterally, outside the zone of halokinetic deformation would be difficult to decipher using facies analysis, without looking more regionally, if you were in a deep-water salt influenced basin, or a unconfined salt free-setting (e.g., Prélat et al. 2009). Directly above the diapirs crest, even in the third phase of sedimentation in the DEM, lobe geometries appear to thin slightly towards remnant topographic highs and be confined by the palaeotopography (Figure 6.17). This is ground-truthed by observations that suggest Upper Black Flysch deposition was partially confined and controlled by remnant topography despite diapir growth and MTD generation ceasing. Overall, the depositional environment shows a deep-water axial system which is modulated by and intercalated with, transverse MTDs (Figure 6.17).

### ***Fluvial Environments***

Findings from examples of dryland fluvial stratigraphy in the Triassic Moenkopi Formation in the Salt Anticline region of SE Utah, USA (Banham et al. 2013a; b; 2014) are combined with outcropping observations from fluvio-lacustrine facies distribution in the Oligocene Sivas minibasins, Turkey (Ribes et al. 2015; 2017) to conceptualise the fluvial halokinetically-influenced depositional environment model (Figure 6.17). Early diapiric stratigraphy is rotated upwards towards the salt structures (Ribes et al. 2017). Gypsum clasts and debris remobilised from salt glaciers are observed in the Sewemup member of the Moenkopi formation, representing periods of salt diapir exposure, and remobilisation at the surface (6.17; Banham and Mountney 2013b). MTDs are rarely reported in the Sivas minibasins (Ribes et al. 2015; 2017). Isolated shallow evaporitic lakes are found in

depositional lows adjacent to topographic highs in the Tenderfoot Member of the Moenkopi formation, signifying localised sediment starvation, in agreement with subsurface observations from the Pre-Caspian Basin of Kazakhstan (Barde et al. 2002). Isolated lacustrine facies exploit topographic lows in fluvial-lacustrine settings, such as the lower member of the Karayün formation (Ribes et al. 2017), in agreement with sedimentation phase 1 in the DEM.

Outside the lateral zone of halokinetic-influence aeolian dunes experience minimal topographic modulation (Jordan and Mountney 2012). Further up stratigraphy (sedimentation phase 2) both outcropping examples show fluvial channels are absent from topographic highs. Channel deposition in the Ali Baba and Parriott members is confined to the minibasins between the diapirs whilst overbank and floodplain facies are present over diapir highs (Banham and Mountney 2013b). Multi-lateral, multi-stacked braided channel belts in the Moenkopi Formation are confined between two salt structures (Banham and Mountney 2013), perhaps with amalgamation of thicker sandstones units increased due to confinement (Cumberpatch et al. 2021b). Channel elements within the lower and upper member of the Karayün formation are also confined to minibasins (Ribes et al. 2017). Reduction of halokinetic modulation up-stratigraphy (sedimentation phase 3) results in further braided fluvial environments with reduced diapir influence (Banham and Mountney 2013; Ribes et al. 2017), or deltaic build out (Barde et al. 2002; Ribes et al. 2015). These depositional systems remain isolated by diapir topography and are not extensive over the palaeohigh showing that remnant topography controls deposition (Figure 6.17). Ribes et al. (2015; 2017) highlights how minibasins can be highly individualised, with higher variability in depositional sub-environments due to halokinetic, autocyclic and allocyclic controls making halokinetically-influenced fluvial systems less predictable than their non-halokinetically influenced counterparts (e.g., Priddy and Clarke 2020).

### ***Mixed Siliciclastic-Carbonate Environments***

Mixed siliciclastic-carbonate environments are relatively common and found in a variety of depositional settings, including: lagoonal (Mitchell et al. 2001), shoreface (Zonneveld et al. 1997) and deep marine (Bell et al. 2018a; Cumberpatch et al. 2021a). Often these environments are misinterpreted as 'transition zones' rather than distinct settings (Chiarella et al. 2017; Moscardelli et al. 2019; Casson et al. 2020; Cumberpatch et al. 2021a). The Ediacaran-Cambrian of the Adelaide Rift Complex, South Australia, documents stratigraphic-scale mixing (*sensu* Chiarella et al. 2017) of a halokinetically-influenced mixed succession (Counts and Amos 2016; Counts et al. 2019). The early kinematic modelled layer, which represents the Wonoka Formation is interpreted as a marginally modulated storm-dominated carbonate shallow shelf (Counts et al. 2019). Infrequent, isolated debris-rich conglomeratic channels originating from the salt-cored high are observed outside of the zone of halokinetic influence (Figure 6.17) suggesting that MTD deposits may have been re-distributed by small-scale channels (Counts et al. 2019). MTDs are also observed close to the topographic highs due to slumping during passive folding over the diapir topography. This agrees with alluvial fan deposits which are continuous for tens of metres on the flanks of the diapir in the upper Wonoka Formation (Counts et al. 2019).

The Bonney Sandstone, equivalent to sedimentation phase 1 in the DEM, is interpreted as a broadly subsiding siliciclastic floodplain with infrequent small channels. This is a result of salt withdrawal beneath the minibasin (Von der Borch et al. 1982; Counts and Amos 2016; Counts et al. 2019). Channel stacking is rare, and isolated to topographic lows (directly adjacent to the diapir) where there is reduced space, so stacking occurs. During late Bonney Sandstone times the central topographic high was failing and shedding conglomerates from the ridge, in agreement with modelled observations of a thin and partially re-mobilised roof (Figure 6.17).

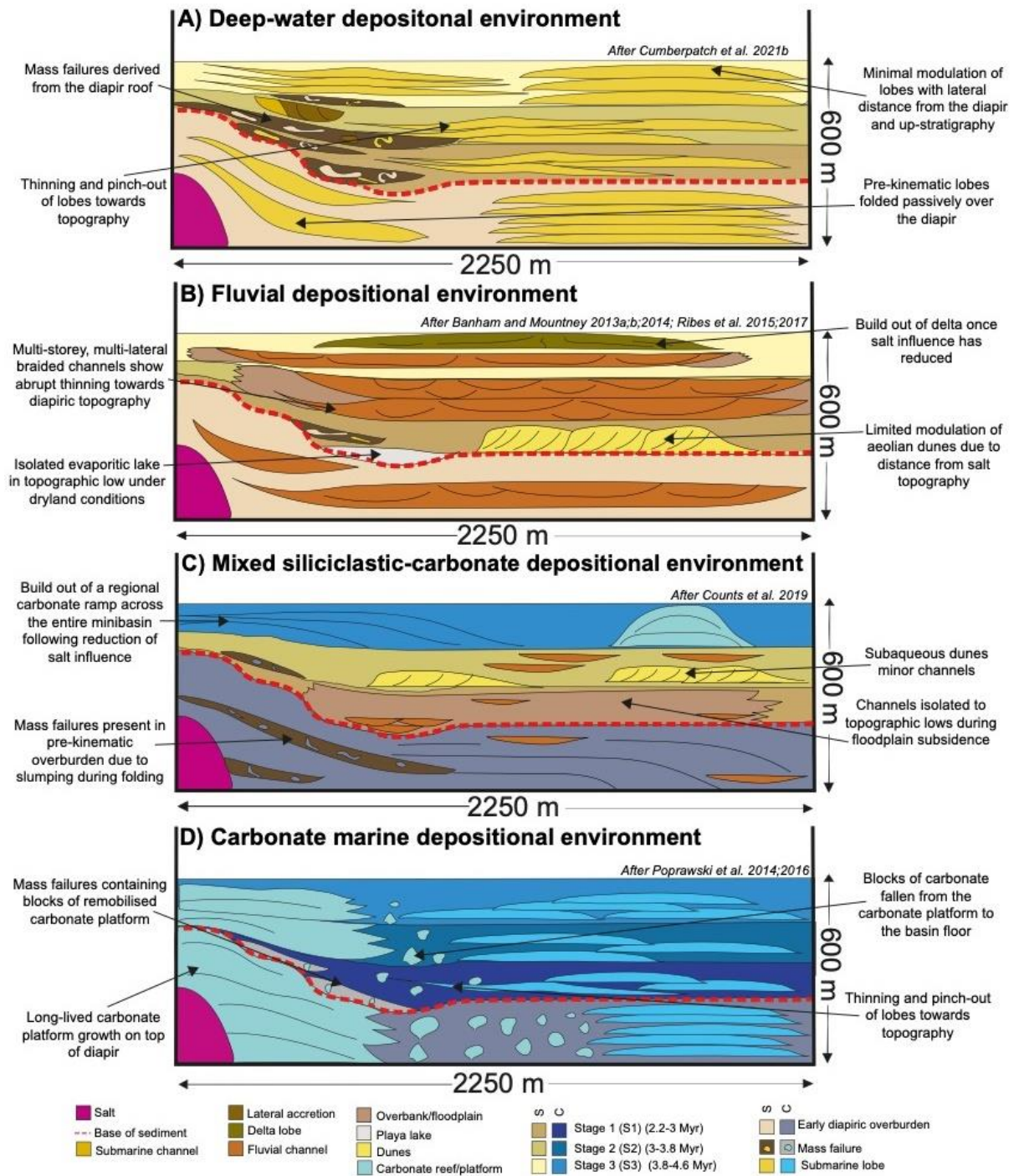
The Rawnsley Quartzite, which is equivalent to sedimentation phase 2 in the model, represents the deposition of subaqueous dunes and minor channels, which dominate outside of the halokinetically-influenced zone. The dunes themselves do not appear to pinch out towards the topographic high, but the entire stratigraphic formation does, in agreement with the DEM and halokinetic sequence models (Giles and Rowan 2012). Dunes experience minor modulation, but are notably absent within proximity to the diapiric high, probably because the topography promoted sub-aerial conditions (Counts et al. 2019). The reduction in halokinetic influence upwards and burial of salt topography observed in models agrees with the deposition of the carbonate Wilkawillina Formation extensively across the top of the diapir (Figure 6.16). A regional carbonate ramp builds out across the entire minibasin following the reduction of salt influence (Counts et al. 2019); the palaeohigh above the diapir acts as a nucleation point for ramp progradation (Figure 6.17; Giles 2014). Mixed systems are often inherently more complicated than their siliciclastic- or carbonate-only counterparts, and in salt-influenced settings record the interplay of not only siliclastic and carbonate systems, but also halokinesis, creating a complex array of depositional facies. Therefore, halokinetically-influenced mixed systems are unlikely to follow a predictable trend and ought to be treated on a case-by-case basis.

### ***Carbonate Environments***

Field observations from the Barremian-Albian Urgonian Group adjacent to the Bakio diapir were used to create a conceptual model for deposition in a carbonate-dominated marine environment (Poprawski et al. 2014; 2016). The Urgonian limestone is known regionally to form isolated shallow marine carbonate platforms on top of topographic highs such as footwalls and diapirs (Rosales and Pérez-García 2010). The locally known Gaztelugatxe limestone is interpreted to represent a long-lived carbonate platform developed on top of the Bakio diapir during growth (Figure 6.17). Distal equivalents to the Gaztelugatxe Limestone, the Bakio Marls, are interpreted to represent downdip deposition in a deep-water environment dominated by calcareous turbidity and debris flows. Adjacent to the diapir at Bakio these deposits are steeply-rotated into a composite halokinetic sequence (Giles and Rowan 2012; Poprawski et al. 2014; 2016).

Throughout the stratigraphic evolution of the carbonate marine system at Bakio, a platform continues to build up on top of the diapir, with a regional sequence boundary suggesting a period of uplift and karstification (Agirrezabala and López-Horgue 2017). MTDs that appear to be sourced directly from the carbonate platform above the diapir are visible at Gaztelugatxe Island and pinch-out away from the diapir (Figure 6.17), in agreement with halokinetically-influenced lentil geometries observed elsewhere (McBride et al. 1974; Hunnicut 1998; Giles and Lawton 2002; Cumberpatch et al. 2021b). Remobilised limestone clasts make up the majority of the Bakio Breccia Formation, deriving from platform failures during diapir growth. Blocks of Gaztelugatxe limestone are found outside of MTDs (Figures 6.16 and 6.18) and form subtle basin floor topography for subsequent siliclastic deposits (Cumberpatch et al. 2021b), possibly having slid from the platform or been carried as out-runner blocks ahead of MTDs (e.g., Soutter et al. 2018).

Poprawski et al. (2016) interpret a laterally-equivalent, calcareous deep-water depositional system downdip of the carbonate platform which is evidenced by calcareous thin-bedded debrites and turbidites overlying the Bakio Breccia formation in certain outcrops. Outside of the zone of halokinetic influence the stratigraphy is assumed to be horizontal, with calcareous lobes showing negligible salt influence, however, outcrop is limited. An overall broadly predictable facies distribution for marine carbonate environments, consisting of carbonate platforms on the diapir high (crest), diapirically-derived MTDs and carbonate blocks on the salt flank and deeper water distal facies in the undeformed section is apparent from the conceptual facies model (Figure 6.17) in agreement with subsurface examples (Bosence 2005; Lukasik and Simo 2008; Warren 2016; Jackson and Hudec 2017).



**Figure 6.17:** Schematic conceptual models for facies distribution in different halokinetically-influenced depositional settings. Published observations from outcrop analysis are overlain over the stratigraphic geometries observed in half of the intermediate aggradation model (M3, Chapter 4). Deep-water halokinetically-influenced model is created using outcrop data from the Aptian-Cenomanian Black Flysch Group adjacent to the Bakio diapir, northern Spain (see Cumberpatch et al. 2021b; Chapter 3 for comprehensive discussion). Fluvial halokinetically influenced model is created using outcrop data from the Triassic Moenkopi Formation of SE Utah, USA (see Banham and Mountney 2013a,b;2014 for comprehensive discussion) and the Oligocene-Miocene of the Sivas Basin, Turkey (see Ribes et al. 2015; 2017 for a comprehensive discussion). Mixed siliciclastic-carbonate halokinetically-influenced model is created using outcrop data from the Ediacaran-Cambrian of the Mt. Frome minibasin, South Australia (see Counts et al. 2019 for a comprehensive discussion). Carbonate marine halokinetically-influenced model is created using outcrop data from the Barremian-Albian Urganian Group adjacent to the Bakio diapir, northern Spain (see Poprawski et al. 2014; 2016 for comprehensive discussion). See labels and text for description of various key points.

## 6.7 Subsurface energy implications

### ***Summary***

Deep-water gravity flow deposits provide excellent hydrocarbon reservoirs, carbon storage sites and geothermal aquifers. Salt is a near-perfect seal (Warren 2016) and can provide a high-quality sealing unit or combination trap for these deposits. The dimensions, facies, and lateral and vertical distributions of sand bodies from seismic scale outcrop analogues (Chapter 3) are often used as inputs into reservoir models for salt influenced basins. It is vital in reducing uncertainty to use outcropping examples which are comparable to subsurface examples (Abegg 2004). Facies distributions and other learnings from fieldwork around the Bakio diapir are fit-for-purpose in reservoir models of salt-controlled minibasins globally and locally.

The Gaviota storage facility, 8 km offshore from Cabo Matxixako (Bakio coastline), which provides 1/6<sup>th</sup> of Spain's annual gas requirement, demonstrates the suitability of deep-water salt-influenced settings as reservoirs for gas storage, or the trapping of hydrocarbons. Gaviota was previously a hydrocarbon field. Gas is stored within stratigraphy of similar age and facies to that outcropping onshore (e.g., the siliciclastic Albian-Cenomanian Black Flysch Group), and is trapped by a complex positive flower structure cored by Triassic salt (Cámara and Gentou 1990; Nieto et al. 2003; Varela et al. 2003; Shesa 2018). The halokinetically-influenced exposures in the Basque Cantabrian basin were used as direct analogues for both the original hydrocarbon discovery and the present-day gas storage site, highlighting the importance and relevance of outcropping analogues in subsurface energy exploration, production and storage (Cámara and Gentou 1990; Cámara 2017). The capability of Gaviota to store gas without leaking, suggests that similar reservoir-trap pairs globally may also be suitable for long term storage, such as the storage of carbon dioxide or hydrogen.

### ***Reservoir quality predictability***

In the subsurface, salt appears chaotic due to poor velocity controls (Jones and Davison 2014). MTDs also appear chaotic due to their internal disorder and therefore it can be difficult to decipher them from salt structures in subsurface seismic data, often leading to the overestimation of salt thickness due to difficulty identifying the top of the salt, which can underestimate reservoir thickness (i.e., some of the reservoir is characterised as salt; Charles and Rhyzhikov 2015). Where seismic resolution and quality allows, halokinetically-influenced facies may be decipherable from allocyclically-controlled facies. Chaotic units which originate at salt structures and thin away from salt are likely to represent mass transport complexes, typically representing poorer-quality reservoirs, which are difficult to produce from. More ordered units which thin towards salt structures and may show lobate or channelised geometries are likely to represent lobe or channel complexes, typically represent good quality, producible reservoirs. Core through one of these halokinetically-influenced successions would show a wide range of facies which are difficult to correlate in two-dimensions, demonstrating the need to integrate outcrop analogues to better understand multi-dimensional reservoir facies distributions. The presence of ripples reflections, frequent hybrid beds and common mass transport deposits in core can be indicative of halokinetically-influenced deep-water successions in subsurface datasets (Figure 6.6).

The distribution of sandstones in halokinetically-influenced deep-water successions is controlled by location relative to the salt structure. Sandstones between two diapirs, deposited in a syncline where gravity flow deposits have been deposited between two structures are likely to be well stacked and amalgamated and therefore provide an extensive, connected reservoir, with a greater capacity for hydrocarbon or carbon storage than a non-stacked reservoir sandstone. In these configurations the reservoir sandstones are further away from the stratigraphic-structural trap and therefore trapping uncertainty is increased (Figure 4.16). Sandstones deposited on one flank of the diapir, which are not influenced by another nearby diapir are less likely to be well stacked, because

they are less confined, and distributed, isolated reservoirs are more likely. These sandstones tend to occur closer to the stratigraphic-structural trap than those in minibasins and therefore trap risk is reduced, however, these sandstones will not necessarily be connected and hence reservoir thickness and connectivity remains uncertain (Figure 4.16). Overall, net-to-gross is shown to increase away from salt diapirs in field observations (Chapter 3), with zones closest to the diapir being occupied by the most chaotic and 'gross' facies and those further away from the diapir being associated with thicker, better connected 'net' sandstones suitable as aquifers or hydrocarbon reservoirs.

Similar observations are seen in our numerical models, where, regardless of depositional system or amount of sedimentation, stratigraphy appears to thin as it approaches the diapir suggesting a reduction in the amount of 'net reservoir' close to the salt structure (Figures 4.9 and 6.17; Jackson and Hudec 2017). Siliciclastic depositional environments (deep-water and fluvial) show a thinning of sandstone lobes and channels towards the topographic high and an overall concentration of high-quality reservoir sandstones at the base of topography (Figures 4.13 and 6.17). These sandstones are most likely to be of highest reservoir quality and producibility, but are often deposited far from the diapir such that trapping mechanism becomes an uncertainty (Kane et al. 2012; Stricker et al. 2018).

In the siliciclastic depositional models muddier, thinner and lower reservoir quality units are expected closer to the diapir, for example distal fringes of lobes in deep-water successions and overbank and flood plain deposits in fluvial settings (Figure 6.17; Banham and Mountney 2013 a; b; 2014; Ribes et al. 2015; 2017; Cumberpatch et al. in 2021b). This causes typically lower quality reservoirs, which are more likely to be over-pressured due to upward rotation of stratigraphy and therefore less likely to hold a significant hydrocarbon column, despite being close to a potentially high quality structural-stratigraphic trap (Figures 4.13 and 4.14; Nikolinakou et al. 2014; 2018; Heidari et al. 2017; 2019).

In carbonate-dominated depositional environments salt highs may promote a topographic high in otherwise relatively deep-water conditions which may allow for the build-up of isolated carbonate platforms or reefs which may have excellent reservoir potential (Figure 6.17; Riding 2002; Burgess et al. 2013; Teixell et al. 2017). Potential carbonate reservoirs are likely to experience a subsequent changes in reservoir quality, as the continued growth of the salt diapir generates fractures in the overburden which could form significant secondary porosity (He et al. 2014; Howarth and Alves 2016; Saura et al. 2016), increasing reservoir quality and producibility. Subsequent diagenesis can also occur, which can cause the reduction of reservoir quality, for example due to dolomitization. In mixed systems where carbonate and siliciclastic systems are intercalated, siliciclastic mudstones deposited on top of diapirs may act as a significant seal to carbonate platform or reef reservoirs below (Figure 6.17; Moscardelli et al. 2019; Casson et al. 2020; Cumberpatch et al. 2021a; Appendix C).

### ***Mass Transport Deposits***

MTDs contribute to uncertainty in hydrocarbon production and carbon storage (Figure 6.2). MTDs can act as reservoirs, where there is enough reworked amalgamated sandstone to allow fluid flow (e.g., the Frigg Formation of the North Sea (Jenette et al. 2000)). They are more often associated with barriers and partial seals (Figure 6.2; Moscardelli et al. 2006; Poprawski et al. 2021). Heterogeneities in flow characteristics caused by the presence of reworked thin-beds within MTD deposits could act as thief sands, allowing reservoir fluids to migrate further up dip closer to the salt structure and be lost from the overall accumulation, reducing the hydrocarbon volume associated in petroleum exploration and causing leakage risks in carbon storage (Tyagi et al. 2008; Souche et al. 2015; McKie et al. 2015), creating seal and trap uncertainty.

Locally-derived MTDs are often assumed to be mud-rich (Madof et al. 2009) related to remobilisation of mud which drapes the diapirs roof. Davison et al. (2000) reported locally-derived Palaeocene MTDs including clasts of Cretaceous chalk mixed inside a muddy-matrix, derived from adjacent diapirs. Similar highly variable MTD facies have been documented throughout the Palaeocene formations in the Central Graben (Kilhams et al. 2012; 2014; 2015). In addition, Wu et al. (2020), described locally-derived MTDs containing from 40 – 60% sandstones, showing the wide variety of locally-derived MTDs within salt-controlled basins (Cumberpatch et al. 2021b).

When the apex of the diapir remains in deep-water environments, they are assumed to experience mudstone and fine-grained turbidite deposition (Mayall et al. 2010; Poprawski et al. 2021) and consequently, slope failure creating MTDs is assumed to occur by the diapir flank steepening (Figure 6.2). During their downslope trajectory, MTDs may interact with other allocyclically-derived facies deposited on the sea floor (e.g., turbidites). If MTDs are transported above a muddy substrate, they will remain relatively muddy (Figure 3.6) and thus have relatively good sealing properties in a subsurface energy system, both near and at distance from the diapirs (Figure 6.2; Madof et al. 2009; Poprawski et al. 2021). Such MTDs are identified in the Jata Basin (Figure 3.10; Chapter 3; Poprawski et al. 2021).

If the trajectory of a locally-derived muddy MTD passes over coarser grained facies (e.g., turbidites), these may become incorporated into the MTD (Figure 3.6; e.g., Ogata et al. 2014; Sobiesiak et al. 2016; 2018; Cardona et al. 2020), and therefore the percentage of sandstone clasts or reworked thin-bedded sandstones may increase over a short length scale away from the diapir (Figure 6.2). An increase in the number of porous clasts may decrease the sealing properties of these MTDs away from the diapirs, and even enhance reservoir, or thief sandstone, potential (Figure 6.2; Poprawski et al. 2021). Such MTDs are identified in the Sollube Basin at Bakio (Figure 3.11; Chapter 3; Poprawski et al. 2021).

The Bakio field analogue shows that shallow-water carbonate clasts can be transported to deep-water environments, where the facies developed above diapiric highs (carbonate platforms growing in the photic zone) strongly differ from the facies in adjacent minibasins (deep-water facies; Poprawski et al. 2016). The MTDs in the Bakio Breccia Formation (Figure 3.5) are results of failures of the over-steepened carbonate highs into deep-water basins (Figure 6.2; Giles and Rowan 2012; Poprawski et al. 2014; 2016; 2021). The percentage of limestone clasts within this type of MTD is shown to decrease away from the diapirs, and consequently such MTDs may have increased reservoir potential close to the diapir, whilst their distal toe may be muddier with higher sealing potential (Figure 6.2).

Characterising the nature of the diapir roof and the surrounding seafloor can aid in prediction of the reservoir and sealing properties of locally-derived MTDs (Figure 6.2; Poprawski et al. 2021). For siliciclastic-dominated MTDs, the seal risk may be reduced by drilling near the diapir, as postulated by Madof et al., (2009), since porous, high density turbidites facies are often restricted to the axial part of the salt withdrawal basins. By contrast, the seal risk increases near the diapir for carbonate-dominated MTDs, since redeposited carbonates with increased porosity relative to the muddy matrix are deposited near the diapir. Irrespective of MTD composition, the geometries of the internal structures (e.g., soft sediment deformation) must be studied as these may form paths for fluids (e.g., Wu et al. 2020; Cardona et al. 2020).

### ***Halokinetic zonation of salt-influenced stratigraphy using DEM results***

The model results show that a deformation zone exists either side of the diapir in all experiments (Figures 4.4-4.6). Outside of this zone the early diapiric and syn-kinematic stratigraphy are undeformed. The extent of this salt withdrawal basin is 1150 m on either side of the diapir (2300 m in total). Therefore, the total zone of halokinetic influence in all models is approximately 3 times the original diapirs maximum width (750 m), with a deformed zone of 1.5 diapir widths either side of the structure (Figure 4.16). The width of the deformation zones is comparable across all models (Figure 4.10) and therefore it is shown that sedimentation rate is unlikely to have a significant control on the width of the zone of halokinetic influence (Giles and Rowan 2012; Hearon et al. 2014). The models suggest the width of the halokinetically-influenced zone is proportional to the width of the salt diapir, which may prove helpful for well planning, pressure analysis and reservoir quality prediction in subsurface energy exploration and development (Cedeño et al. 2019). Other factors such as salt supply, salt viscosity, and style and magnitude of regional tectonics (which are not modelled) will, in nature, influence the width of the halokinetically-deformed zone (Koyi 1998; Fuchs et al. 2011).

The models can be further divided into zones (1-5) based on onlap geometry and thinning rates, which highlight the 'trade off' between reservoir thickness and stratigraphic trap potential in subsurface plays (Figure 4.16). In the flank locations, bedding dips and thinning rates are shown to be greater under slower sedimentation rates compared to higher sedimentation rates (Figure 4.11; Table 4.3), which is important when predicting hydrocarbon column height. Significant overpressures on reservoirs below can be created by fast sedimentation rates (Figure 4.16; Peeters et al. 2018).

Zone 1 is outside the zone of halokinetic influence, and as such only experiences negligible deformation. Stratigraphy is deposited horizontally throughout evolution in these zones and therefore stratigraphic pinch-out trap potential is likely to be low. Due to minimal modulation, reservoir sandstones may be of the best quality and thickest in this location. Halokinetic-influence increases towards the diapir, and in general, reservoir quality and thickness decrease while stratigraphic trap potential increases (Figure 4.16; Wilkinson et al. 2013; Ward et al. 2016; Jackson and Hudec 2017). Reservoir units will be thicker and less modulated up-stratigraphy once they have passed the vertical/temporal halokinetic influence of the diapir (Blanchard et al. 2018). At this point reservoir units could be more laterally extensive with better quality and thicknesses than those isolated either side of the diapir (compare layers B and L; Figure 4.16). With vertical distance from the diapir, however, structural-stratigraphic combination traps become unlikely, and stratigraphic trapping styles observed in unconfined basins (e.g., lobes enclosed within mudstone; Cobain et al. 2017; Sattar et al. 2017; Hansen et al. 2019) will become increasingly important.

In the withdrawal basin zone (Zone 2) only minimal thinning is observed (Table 4.3) and beds remain broadly horizontal. Structural-stratigraphic trapping potential is still low, and reservoir quality is still high although minor reservoir thinning may have occurred (e.g., 0.04 %/m; Table 4.3; Figure 4.16). In the onlap zone (Zone 3) more obvious thinning of potential reservoir units are observed, suggesting a reduction in reservoir thickness, but still a potentially economic net-to-gross. In Figure 4.16 (Zone 3) Layer A (grey) is shown to abruptly terminate on the overburden high, while layer B (white) pinches out towards an onlap, providing good quality stratigraphic trapping mechanisms for subsurface energy resources. Layers in the later stratigraphy thin in the onlap zone, however, the effect of the halokinetic modulation decreases upwards.

At the salt flanks (Zone 4) the highest thinning rates are observed (Table 4.3) for all layers, across all models, showing that this zone has the strongest influence on reservoir presence, potential and producibility. Facies analysis (Kane et al. 2012; Souche et al. 2015; Soutter et al. 2019; Cumberpatch



et al. 2021b) shows that thinner, finer-grained, muddier beds intercalated with MTDs are more common in this zone. The steepest onlap and pinch-out configurations are observed in the salt flank which could provide excellent stratigraphic-structural trapping mechanisms (Gardiner 2006; Stanbrook et al. 2008). The steep upwards rotation of the strata in these locations may pose drilling hazards due to over-pressured reservoirs, and inability to hold a significantly economic column could be encountered (Nikolinakou et al. 2014; 2018; Heidari et al. 2017; 2019). Syn-kinematic strata over the salt apex (Zone 5) are almost horizontal and show minimal folding over the crest which could act as subtle stratigraphic traps caused by differential compaction over the topographic high (Dietrich 1993; Jackson and Hudec 2017; Ward et al. 2018; Cedeño et al. 2019). Layers are thinner than in the undeformed stratigraphy, and some are completely absent, for example if Layer C was the reservoir unit it would not be present above the diapiric high (Figure 4.16).

Where multiple diapirs are present (Chapter 5) diapir spacing controls the presence, extent and width, of the minimal modulation zone between the salt withdrawal zone in the middle of diapirs (Figures 5.10 and 5.11). The best reservoirs are likely located in the minimal modulation zone, and therefore diapir spacing controls reservoir distribution, and producibility. Between narrowly-spaced diapirs ( $M1 < 3000$  m), each halokinetic zone is small, with a thin strip of salt withdrawal basin between the diapirs. In this zone, good, thick, amalgamated reservoirs are likely to develop, but structural traps are limited (Figures 5.10 and 5.11). Between intermediately-spaced (3000-4500m) diapirs the salt withdrawal basin between the diapirs is larger than in narrowly spaced diapirs, but the other halokinetic zones are similar widths. Deformation decreases towards the centre of the salt withdrawal basin, but there appears to remain some subtle modulation of stratigraphy at the centre, suggesting that reservoir units will not be completely undeformed, and will still experience some deformation due to halokinetic-influence. Therefore, these reservoir units may have higher reservoir complexity and lower reservoir quality than is expected for an 'undeformed', non-halokinetically influenced reservoir (Figures 5.10 and 5.11). Where diapirs are widely spaced ( $>4500$ m) giving a zone of 'minimal modulation' between them, good quality reservoir properties may be expected (Figures 5.10 and 5.11), exemplified by the thick, sandstones stacked between the Bakio and Guernica salt structures (Cumberpatch et al. 2021b). With increasing diapir spacing the zone of reduced halokinetic influence is extensive, and therefore thick reservoir units would be laterally extensive (Figure 5.11), potentially analogous to the sandstones at Cabo Matxixako between the Bakio and Guernica diapirs. Nonetheless, due to the topography of the top and base salt, non-piercing diapirs and salt related faults at depth, there may also be structural closures further away from salt diapirs, reaffirming knowledge that subsurface energy plays in salt basins do not always rely on penetrative diapirs (Jackson and Hudec 2017).

In areas of poor data coverage adjacent to salt structures this scheme, derived from numerical modelling, can be used as a predictive tool for what types of deformation and stratigraphic geometry to expect in the subsurface. The model highlights the trade-off between reservoir thickness and quality and stratigraphic trap potential, and the onlap zone is suggested as the optimum location for both suitable net-to-gross and stratigraphic trap potential. The combination of numerical modelling and the wealth of data from the North Sea used in Chapter 5, make the halokinetic zonation scheme useful globally, for gaining a better understanding of the effects of diapir spacing on stratigraphic architectures. Whilst our models are an oversimplification, with stratigraphic and structural evolutions well known, and controlled, they are useful for providing generic end members, which can be populated with basin specific data and understanding.

### ***Fault distribution***

DEM is advantageous in predicting potential traps, conduits and baffles, due to its replication of diapir-related brittle deformation. The DEM presented in Chapter 4 replicates localised fault growth, evolution and propagation because the contacts between elements are treated as potential

displacement surfaces. Subsurface examples of faults associated with salt diapirs are shown to cause compartmentalisation of reservoirs (Birch and Haynes 2003; Scott et al. 2010; Charles and Ryzhikov 2015; Peeters et al. 2018; Coleman et al. 2018). As well as these significant, seismically-resolvable faults, outcrop and borehole data indicate brittle deformation is significant across multiple-scales in salt basins (e.g., Koestler and Ehrmann 1991; Cumberpatch et al. 2021b), influencing fluid flow pathways and reservoir and stratigraphic trap complexities. Understanding sub-seismic scale fault distribution is therefore important for predicting reservoir compartmentalisation and seal integrity in the subsurface. Faults, when sealing, could act as lateral permeability barriers, especially if the faults and surrounding reservoir rocks become cemented with salt and salt-related breccia (Van Bergen and de Leeuw 2001; Li et al. 2017).

### ***Towards an integrated workflow***

Supplementing subsurface data with modelled stratal architectures and depositional facies observations from exhumed halokinetically-influenced settings globally (e.g., Banham and Mountney 2013a;b; 2014; Poprawski et al. 2014;2016; Counts and Amos 2016; Ribes et al. 2015; 2017; Counts et al. 2019; Cumberpatch et al. 2021b) is recommended as a useful workflow for building subsurface energy reservoir models for salt basins with limited data (Figure 6.10). Integrated, cross-discipline working and thinking has helped to increase understanding of how halokinetically-influenced deep-water systems differ from their unconfined counterparts, and what controls these differences. Observations from multiple scales and types of data help to supplement knowledge gaps that exist when using only one data type or scale (Figure 6.10). Utilising all available data, and employing multi-scalar workflows is recommended when working in salt basins.

## **6.8 Future research directions**

### ***Outcrop studies***

Future directions for outcrop studies at Bakio should focus on widening the scales of observations (i.e., grain-scale) and improving the understanding of data that can be input into subsurface reservoir models of salt influenced deep-water basins. Such studies could: 1) assess the applicability of the conceptual models generated as part of this study to other diapirs across the Basque-Cantabrian Basin, 2) perform grain-scale petrographic analysis on different facies within the Black Flysch Group, to understand small-scale heterogeneities and the associated effects on reservoir deterioration in salt-influenced deep-water settings, 3) reappraise the structural configuration of Gaztelugatxe Island in order to better understand along strike variability in halokinetic sequences, and 4) extract architectural data, bedding orientations and net-to-gross estimations from virtual outcrop models of the study area to provide quantification on lateral and temporal variability.

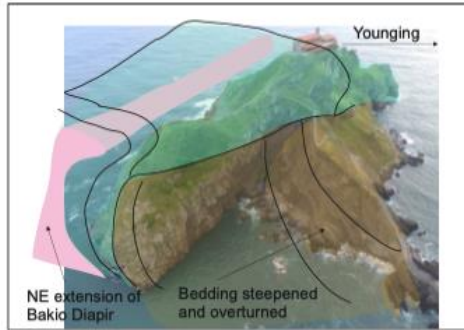
Comparing the Sollube and Jata basin architectures to basins surrounding other Basque-Cantabrian diapirs (e.g., the Murguia, Orduña and Vilassana de Mena diapirs which outcrop south of Bakio and are assumed to be coeval within Aptian-Albian limestone deposition (Cámara 2017)) would help to validate models generated in our study area, and further analyse different controls effecting stratigraphic architecture and facies (e.g., diapir spacing, regional source areas etc.). These conceptual models could also be tested in deep-water halokinetically-influenced basins globally (in the subsurface, outcrop and modern day).

Grain-scale petrographical analysis of different facies in the Black Flysch Group, would allow for analysis of how they vary across different deep-water sub-environments in salt-influenced settings, and consequently give insights into flow processes. Such a study could also help to decipher local versus regional MTDs by studying petrographical indicators of MTD evolution, such as provenance, source area and run out distance.

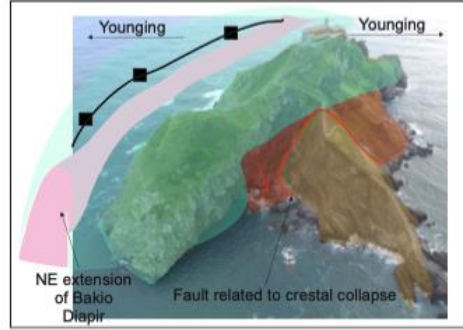
The structure of Gaztelugatxe Island has been debated (Poprawski et al. 2014; 2016; Roca et al. 2021) and is problematic to conclusively appraise, due to difficulties separating bedding planes from fracture surfaces, and due to accessibility issues on the most northerly part of the island. Virtual outcrop models help to provide an insight into bedding orientations and structuration on the inaccessible part of this island, and preliminary analysis suggests four possible models; a meg-aflap, a salt cored anticline, a fault and a tertiary weld (Figure 6.18). Detailed structural mapping would be required to resolve the most likely explanation for the complex structuration. Disentangling this problem would confirm the extent of the offshore Bakio diapir, and provide insight into 'sub-seismic' along-strike diapir variability. This has industrial implications for prediction of structural traps, de-risking seal integrity and estimating migration pathways.

Extracting quantitative data from virtual outcrop models, created as part of this study, would aid comparison to unconfined, and differently confined deep-water systems globally, and provide direct inputs into subsurface reservoir models. Such data could also allow for synthetic seismic models (e.g., Bakke et al. 2013) to be created, and tested across different resolutions, to see what resolutions are required to identify deep-water sub-environments transitions and bed pinch out geometries in salt-confined basins in the subsurface.

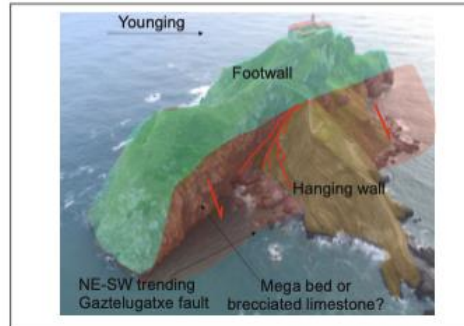
The Azerbaijan field example presented in Appendix C (Cumberpatch et al. 2021a) studied only one structural zone of the Greater Caucasus. There remain extensive outcrops of Cretaceous-aged sediments in other structural zones within the Greater Caucasus. Future research should focus on extending the sedimentological and stratigraphic findings of Cumberpatch et al. (2021a) across the entire Cretaceous post-rift basin. These findings could increase understanding of both the palaeogeographic evolution of the basin, such as sediment input points and lateral-distal facies variations. As well as the response of the basin to the external controls outlined in Cumberpatch et al. (2021; Appendix C), for example whether tectonic activity was a greater influence on the stratigraphic record of the basin closer to the locus of activity in the Black Sea toward the west. Analysis of different structural zones would provide further insight into the mixed carbonate-siliciclastic system evolution across a larger scale, particularly if extent of carbonate platforms and siliciclastic sediment input systems can be discerned. Regional analysis could allow the tracing of the Shahdag mountain MTD across multiple structural zones, which would provide further opportunity to study the evolution of deep-water systems adjacent to mass transport topography (Figure 6.14).



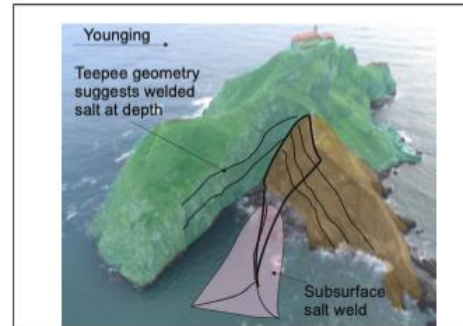
**Salt flap** causing steepening and local overturning of stratigraphy. Bakio Diapir extension present seaward of island.



**Salt cored anticline** trending NE-SW is an extension of Bakio Diapir. Gaztelugatxe fault is related to crestal collapse.

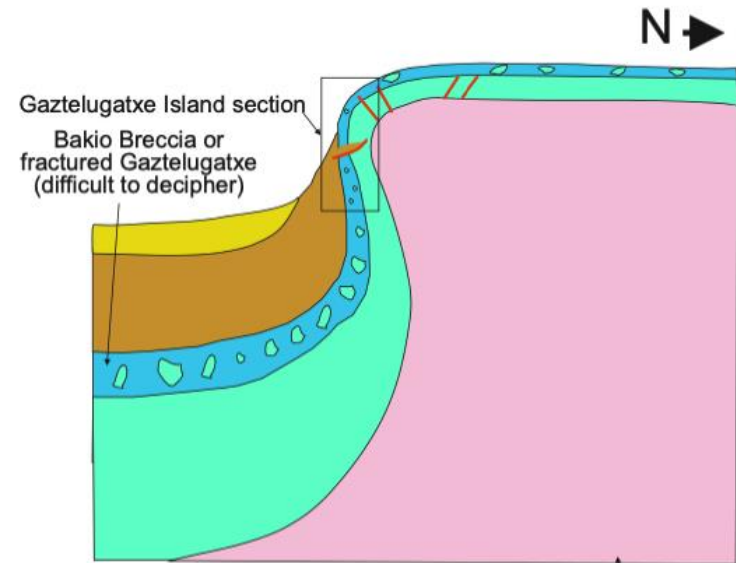
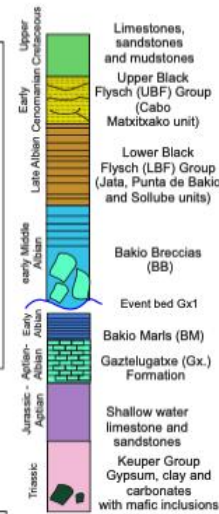


**Gaztelugatxe Fault** is a regional fault zone responsible for the reactive growth of the Bakio Diapir. Reactivated in Pyrenean.



The Bakio Diapir is expressed as a **tertiary weld** in the subsurface creating the teepee geometry and steep stem.

### Stratigraphy



Bakio Diapir 'mega flap' located offshore (north of Gaztelugatxe Island).

**Figure 6.17:** Four of the potential models proposed for the structural configuration of Gaztelugatxe Island. The salt flap hypothesis suggests that the Bakio Diapir extends offshore to the NE to Gaztelugatxe Island and is present offshore to the north of the island. The diapiric structure here is somewhat overturned, due to Pyrenean compression, and this causes the complete overturning of the limestone and over-steepening of the Lower Black Flysch Group. In the salt-cored anticline hypothesis the Bakio Diapir is also still present to the north of Gaztelugatxe Island. The Gaztelugatxe Limestone is folded over the salt which results in a heavily fractured limestone unit. The Lower Black Flysch is interpreted to have been deposited above the Gaztelugatxe Limestone and subsequent flank collapse resulted in the juxtaposition observed today. Similar salt cored, extensionally-forced folds have been recently documented in the Burgalesa Platform (western Basque Cantabrian Basin) (Tavani and Granado 2015; Bodego et al. 2018). In the fault model the Bakio Diapir does not extend to Gaztelugatxe Island. The north of the island therefore represents a footwall high, where carbonate build up was common and the south of the island represents the downthrown side. Fault activity may have occurred during deposition of the Lower Black Flysch Group, supporting the steepening of the beds towards the fault. Poprawski et al. (2014; 2016) suggests this fault, the Gaztelugatxe Fault, is the reactive fault responsible for the initial growth of the Bakio Diapir during its reactive phase in the Albian. Subsequent movement in the Pyrenean has created the complex geometry observed today. The weld model suggests that the Bakio Diapir extends through the middle of Gaztelugatxe Island, but has changed in structural configuration along strike to become a tertiary weld at depth beneath the island. This suggests that the Bakio Diapir once extended to the island but subsequent withdrawal and compression formed a tertiary weld resulting in the teepee geometry observed in the bedding at the island.

### **Numerical modelling studies**

The two-dimensional DEM presented in Chapter 4 and 5 (Cumberpatch et al. 2021c;d) is useful for predicting regional trends and studying generic interactions of salt structures and stratigraphy, however there are many limitations due to its' two-dimensional nature, for example diapir growth, sedimentation and salt withdrawal are assumed to be radially symmetrical. Further work is required using three-dimensional models to better simulate the complicated three-dimensional systems that are observed in nature. The overall aim of this work would be to improve predictions of halokinetic alteration in salt basins.

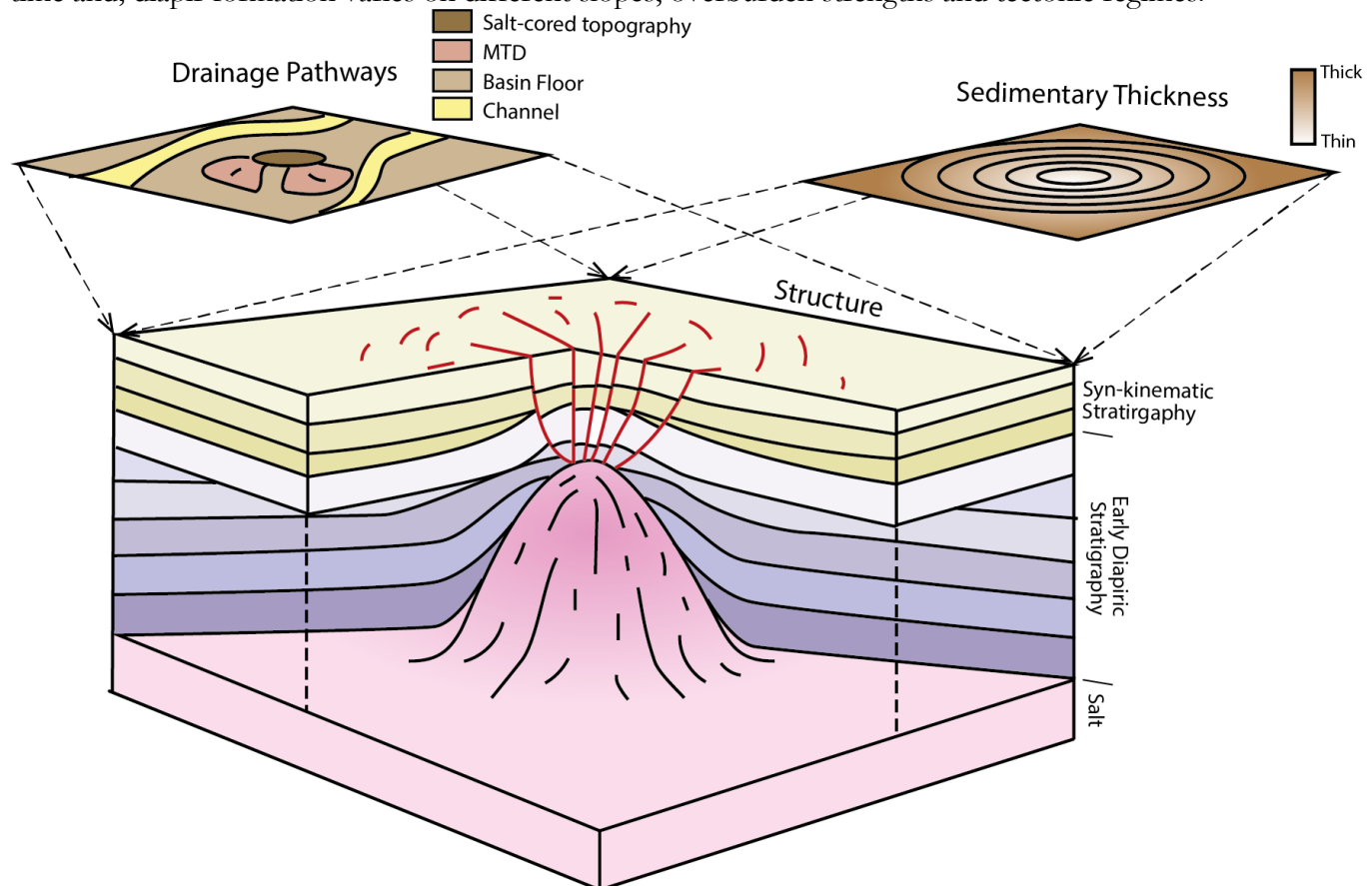
3D simulations could provide insight into the four-dimensional evolution of stratigraphy adjacent to salt diapirs, salt-related faulting, the processes controlling expulsion and withdrawal of source layer salt into diapirs and variability in stratigraphic architecture and stacking, all of which would supplement subsurface models (Figure 6.19; e.g., Pichel and Jackson 2020). Coupling a 3D DEM with a landscape evolution model could enable realistic representation of drainage pathways, depositional fairways and preferential failure directions (Figure 6.19) helping to supplement depositional models of halokinetically-influenced environments based on specific analogues, and provide non-specific end members which may be more broadly applicable in exploring and producing energy resources in global salt basins.

It is suggested that further 2D and 3D DEM work should focus on: 1) attempting to replicate specific complicated salt geometries such as those present in the subsurface Gulf of Mexico, 2) incorporating erosion, remobilisation, reactivation and cessation of halokinesis into the simulations to better comprehend the controls on halokinetic unconformity generation and, 3) varying different parameters (salt thickness, viscosity, rise rate, width etc.) to validate numerous hypothesis in salt tectonics (Jackson and Hudec 2017).

The nature of this modelling technique, means the models are highly adaptable and a number of parameters can be quickly varied to address multiple uncertainties in salt basins. Re-creating complex overhanging geometries, such as those in the Gulf of Mexico would improve understanding of the tectonic evolutions that lead to their development. Modelling these geometries would provide insights into sub-salt stratigraphic relationships that are often difficult to decipher beneath overhangs (Jones and Davison 2014) alleviating some uncertainty in subsurface exploration and production.

Incorporating erosion, remobilisation and rejuvenation into the model would also more realistically represent natural settings where entrainment and failure influences thickness patterns, stratigraphic architectures and can remove the diapiric roof. If failures could be better simulated, models could provide insights into the coeval deposition of axial and lateral systems.

When modelling there is the potential to change many variables and not really appreciate the implications of such changes. In these cases results could become geologically unrealistic. Therefore, future simulations should attempt to address and supplement current salt tectonic research, such as how: original salt layer thickness effects diapir evolution; initial diapir geometry evolves through time and; diapir formation varies on different slopes, overburden strengths and tectonic regimes.



**Figure 6.18:** Expected result of a three-dimensional DEM based on the two-dimensional models used within this study. The three-dimensional study would allow the original geometry to be varied and made asymmetric, in order to better replicate reality. The three-dimensional nature of the model would allow cross-sections to be extracted from different orientations which would enable the studying of diapiric spacing and the effects on stratigraphic geometries for easier comparison to natural examples. Time slices of various attributes (relative displacement/structure, sedimentary thickness, landscape evolution and drainage) could be exported, in a similar way to attribute maps created in subsurface software. Such three-dimensional models would allow the salt-sediment interface to be studied in four-dimension (i.e., throughout evolution in three-dimensions) helping to supplement existing depositional and structural models created from subsurface and outcropping data sets. As with the two-dimensional models, the three-dimensional model would be heavily adaptable to different salt geometries, overburden properties, tectonic settings, slope conditions etc.

### **Subsurface studies**

Future subsurface studies could focus on the testing of locally-derived models on global data sets and expanding the current study and understanding in terms of detail (comprehensive mapping of individual geobodies), extent (additional core data) and data types (petrophysical data). Work could involve: 1) mapping individual geobody evolution around salt structures, to understand the interplay between salt growth and channel/lobe migration, 2) analysing more core data to provide a more detailed regional understanding of reservoir quality and facies associations in different spatial

settings, 3) testing the applicability of models generated in the North Sea in other subsurface examples (e.g., Gulf of Mexico and Offshore Brazil), to see how universal relationships between diapir spacing and stratigraphic architecture are, and 4) integrating petrophysical well data, pressure data, and drilling data to provide quantitative estimations of reservoir producibility and variability, and likely over-pressured units.

Mapping geobody evolution would improve the understanding of depositional element stacking during active and quiet periods of diapir growth, and help to delineate interplay between axial and lateral deposition. A higher resolution seismic dataset would be required, so studies would currently be limited to around hydrocarbon fields where dedicated, more permanent seismic acquisition techniques are involved (e.g., ocean bottom cable) that provide improved resolution. Access to such data may be difficult if the surveys are proprietary.

Only five wells were analysed in the subsurface study presented here to gain a representative understanding of spatial variability, of course such relationships are complicated and many local controls can influence depositional system evolution. Collecting more core data and quantitatively evaluating this data (using similar bed statistics methods used in the Azerbaijan study (Appendix C)), may reveal trends in axial versus lateral depositional systems and locally- versus regionally-derived MTDs.

Whilst the North Sea data set is not as high resolution as Angolan data used recently to postulate the different types of MTDs in salt basins (Doughty-Jones et al. 2019), it does provide a unique opportunity to integrate well and core data into the current characterisation scheme. Understanding how the applicability of confinement models produced in this study hold up globally, will help to decipher what additional complexities need to be considered when comprehending the relationship between diapir spacing and stratigraphic geometries.

Additional data sets (petrophysical, drilling, pressure etc.) would broaden the number of techniques used in the study, providing validity and acting to fill the gap in scale between seismic and core data. Applicability of this study to subsurface energy resource exploration and production would be improved by providing porosity and permeability estimates from petrophysical data. This could quantifiably demonstrate how reservoir quality varies and potentially deteriorates towards diapirs, in order to reduce uncertainty when producing from deep-water halokinetically-influenced reservoirs.

### ***Physical modelling studies***

Scaled physical models (Appendix D; Soutter et al. 2021) could be used to: 1) investigate the effect of including erodible topographic barriers with different geometries, such as salt-diapir-analogous mounds, 2) perform experiments with multiple confining topographic barriers on one slope, such as two laterally confining barriers, 3) release sequential flows into the basin to assess the stacking pattern predictions made in this study, and 4) using barriers composed of a different sand colour to the ‘turbidity current’ to evaluate the interplay of lateral and axial deposition. These additional experiments may help further validate many hypotheses proposed for deposition in salt-diapir influenced deep-water basins, and support observations in subsurface and outcrop.

Performing experiments with different topographic geometries would be useful for quantifying flow velocity around different types of structures, assessing depositional flow routing over complex seafloor bathymetry and evaluating the control of topographic geometry, as well as orientation on subsequent deposit geometry. Using two topographic barriers would allow for the hypothesis that deep-water gravity flows are ‘funnelled’ between topographic barriers, to be tested. These

topographic barriers could be spaced at different distances to analyse how diapir spacing influences deposition at a bed/flow scale. Using a tracer/dye in the sand that created the topography, would allow observations of ‘mass failures’ interaction with axial deposition (from the input pipe). This would be advantageous in predicting MTD distribution around different types of topography and analysing potential bedforms, facies and bed types (e.g., hybrid beds) that form on a flow scale due to the interaction of two coeval systems.

### ***Integrated studies***

This study has benefited from its integrated approach, enabling multi-scalar observations to be made across multiple different data types (Figure 6.10). Further attempts to integrate more data sets to better understand the salt-sediment interface should focus on: 1) grain-scale observations of facies, cement and reservoir quality across outcrop and cored subsurface examples to improve quantification of reservoir quality trends, 2) utilising a quantitative approach in facies analysis (e.g., grain size versus bed thickness) of field and core data to create predictive stacking pattern relationships, 3) combining offshore and outcrop data to understand how salt structures vary along strike (Figure 6.20), and 4) testing field, subsurface and modelling findings developed in this study on different data sets to comprehend their global applicability.

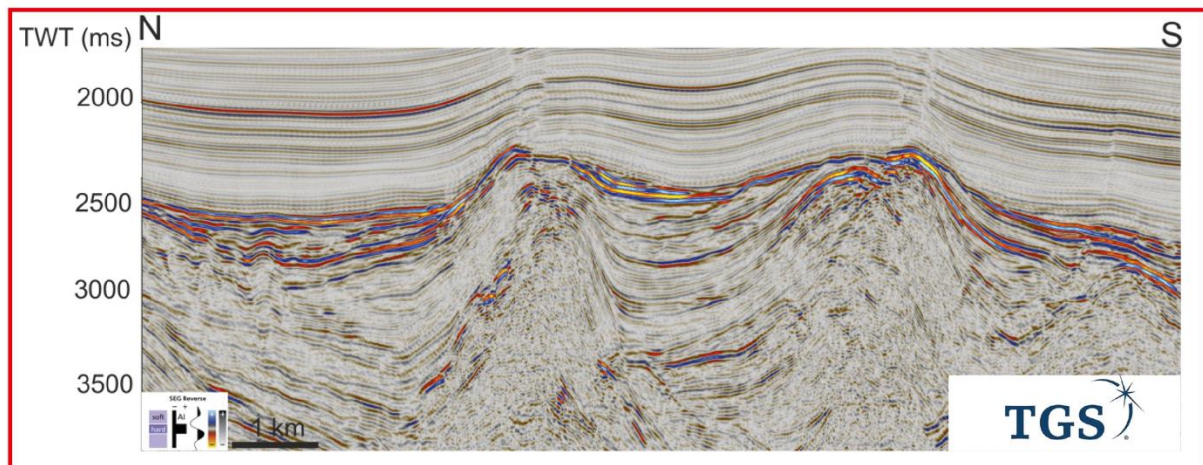
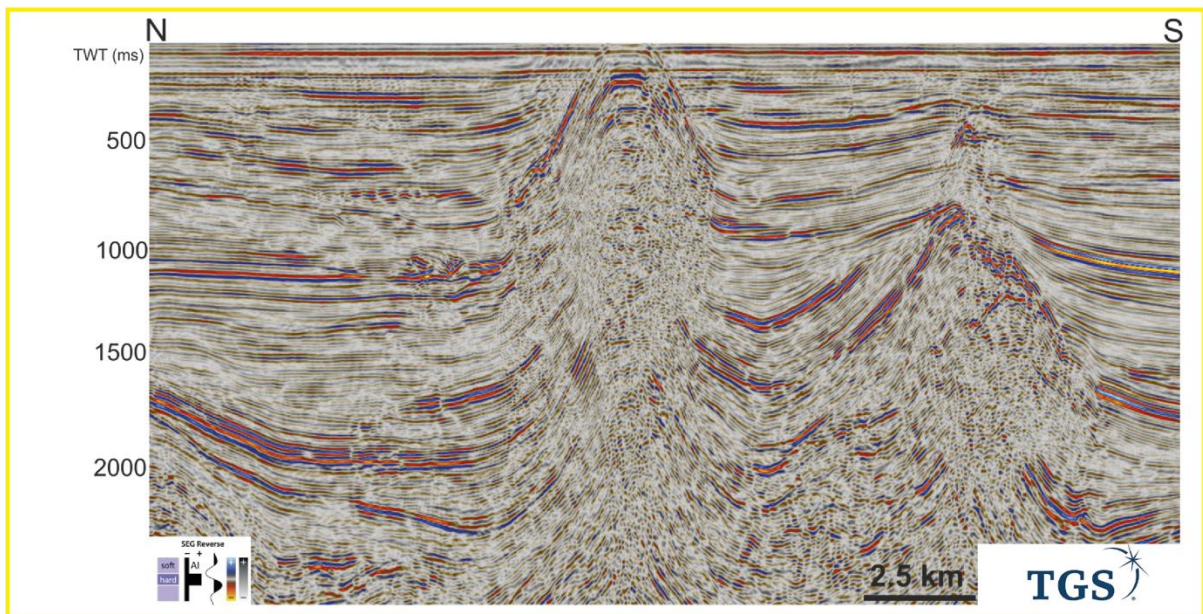
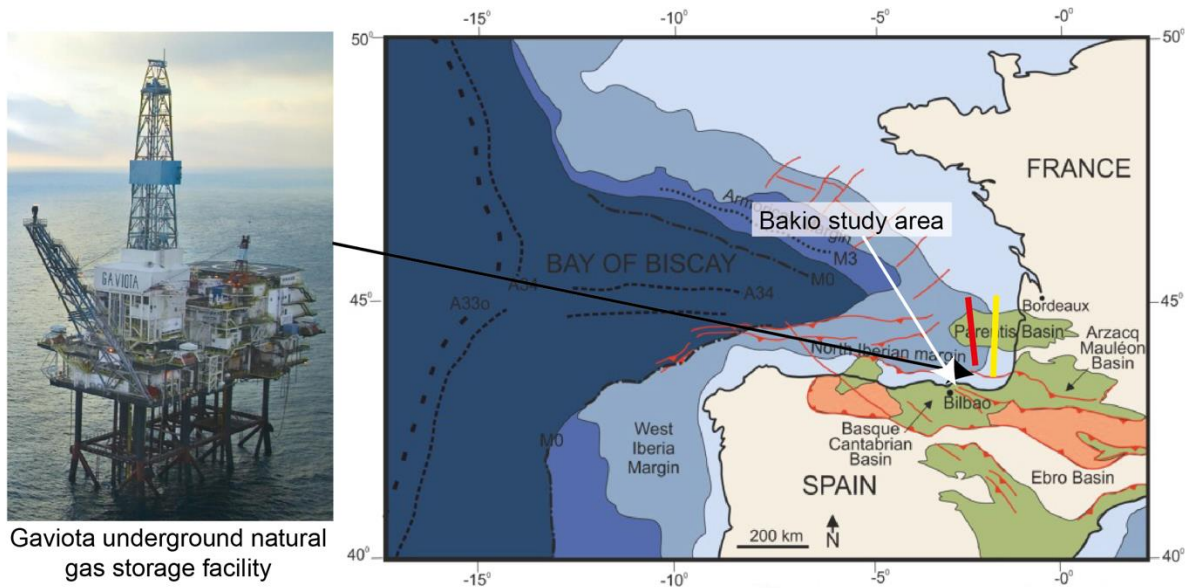
These approaches would add increased detail (grain/pore scale) to the study and increase its reliability for use globally. Petrographic analysis of samples from the Basque-Cantabrian basin and ECG would provide quantitative grain-scale reservoir quality information, that could be compared between the two examples for similarities (that may be consistent across multiple deep-water halokinetically-influenced basins), and local differences, enabling further understanding of halokinetic versus allocyclic controls.

Undertaking quantitative facies analysis of these data sets (similar to the approaches used in Appendix C) would enable evaluative comparison of the data sets in terms of stacking patterns, evolutionary trends and halokinetic versus allocyclic controls. Such statistics would also be useful when comparing to different types of confined basin, or different halokinetically-influenced depositional environments.

Combining subsurface data from the Bay of Biscay (Figure 6.20; offshore Bakio), and field data from the Bakio area could provide a unique opportunity to sufficiently improve the understanding of sub-surface along strike variability in salt structure, and thus along strike variability in halokinetic sequences and stratigraphic architectures. Unfortunately, because the Gaviota platform remains in commercial use as a gas storage site (Figure 6.20) key parts of this potential data set (e.g., well data, core data, and field scale seismic data) remain unattainable for research purposes.

Finding natural examples of the oblique physical experiment in the subsurface or field, would enable comparison of bed scale observations and stratigraphic architecture scale (which is possible in the Annot region for the frontal topography experiment and the Bakio region for the lateral topography experiment). Ultimately, the only way to substantiate the conceptual and numerical models and concepts derived from this integrated study is to test them against different data sets (e.g., different orientations of topography, different amounts of sedimentation, different geological evolutions, different shapes of topography, different water depths etc.).





**Figure 6.19:** Examples of seismic data from in the Bay of Biscay which is suggested to be used alongside outcrop observations to better understand along strike variability for salt structures and halokinetic sequences. Location map from Jammes et al. (2009). Red and yellow line locate the seismic sections shown in red and yellow boxes which are representative of the data quality and salt structures in the two-dimensional Bay of Biscay survey. Some of this two-dimensional data set has previously been analysed by Ferrer

*et al. (2008). The commercial interest of the Gaviota gas storage site (pictured) prevents access to a more subsurface data. Seismic data courtesy of TGS (Bay of Biscay Scanning 2013 seismic data).*

## Chapter 7: Conclusions

This thesis has presented an integrated analysis of deep-water sediment gravity flow interaction with active salt topography, and how this is expressed on the seafloor, in the rock record and in numerical simulations. Field, subsurface, numerical modelling and physical experiments were used to improve understanding of deep-water facies and architecture variability around salt structures, plus halokinetic modulation of allocyclic architectures. These integrated methods were also used to distinguish a multi-scalar recognition criterion for halokinetically-influenced deep-water systems globally, across different data sets. Three key approaches were presented to address the broad aims set out in Chapter 1, in the context of the current understanding highlighted in Chapter 2: 1) An outcrop-based study of a deep-water depositional environment which was deposited coevally with halokinesis (Chapter 3); 2) Two-dimensional discrete element modelling of stratigraphic architecture modulation by salt growth (Chapter 4); 3) a subsurface study from a well-documented deep-water fan which was influenced by multiple, variably-spaced salt structures (Chapter 5); the findings of these three approaches were integrated to understand how and why halokinetically-influenced deep-water systems differ from those in unconfined settings (Chapter 6). This has contributed to our understanding of how: sediment gravity flows and their subsequent deposits are distributed around active topography; halokinesis can modulate stratigraphy and mask allocyclic signals; facies and stratigraphic architectures vary spatially and temporally in salt basins; and how sedimentation rates and variable confinement impact halokinetic modulation.

### 7.1 Interactions between deep-water gravity flows and active salt tectonics: an exposed example from the Bakio Diapir, Basque-Cantabrian Basin, Northern Spain

Chapter 3 (Cumberpatch et al. 2021b) introduced a rare exposed example of halokinetically-influenced deep-water stratigraphy in order to: 1) document lateral and vertical changes in deep-water facies and architecture with variable amounts of salt-induced confinement; 2) document the evolution of coeval deep-water axial and debrite-rich lateral depositional systems; and 3) distinguish criteria for the recognition of halokinetically-influenced deep-water systems. Facies analysis of the Aptian-Cenomanian stratigraphy around the Bakio diapir shows that stratigraphic variability and juxtaposition of architectural elements in the studied basins is high and controlled by the interplay of halokinetic, autocyclic, and allocyclic processes. Confining topography (such as the Bakio and Guernica diapirs) is demonstrated to increase the effects of allocyclic progradation. Different types of topography (e.g., complete or partial confinement) are demonstrated to strongly influence depositional systems, even those in close proximity. Stacked, amalgamated sandstones are observed between two confining barriers, whereas more variable architectures are observed where only partial confinement is present. This variability is due to the modulation of a broadly progradational system by halokinetically-influenced lateral barriers and the coeval development of axial allocyclic and lateral debrite-rich depositional systems. Temporally, following the cessation of diapir growth, topography does not heal instantly, and the “passive” paleotopography continues to confine subsequent depositional systems despite diapir inactivity. Throughout the Black Flysch Group there are a number of indicators for active topography including: hybrid beds; remobilised strata; lateral thickness changes over short distances; reversal in ripple cross-lamination in beds; and intercalation of debrites throughout the stratigraphy. These indicators individually are not diagnostic of salt-influenced topography, but collectively they provide a set of features that support interpretation of halokinetic modulation of a deep-water setting. Furthermore, this work has provided an exposed example of a halokinetically-influenced deep-water system to complement the global atlases of other halokinetically-influenced environments, and deep-water settings influenced by static, relatively static or absent in, topography. This study provides a useful outcropping analogue for subsurface energy exploration and production in salt basins globally.

## **7.2 External signal preservation in halokinetic stratigraphy: A discrete element modelling approach**

In Chapter 4 (Cumberpatch et al. 2021c;d) a Discrete Element Model (DEM) was developed to understand how sedimentation rate effects stratal geometries in salt basins experiencing diapirism, and to test the hypothesis that halokinesis can modulate stratigraphy and mask allocyclic signals. The chapter aimed to: 1) identify and quantify thickness variations and pinch-out geometries in a salt-influenced depositional system; 2) investigate how halokinetic modulation of stratigraphic architecture changes with variable syn-kinematic sedimentation rates adjacent to a dynamic salt diapir; and 3) compare the results to subsurface and field analogues to test the validity of our model predictions. Six two-dimensional numerical models were ran with different sedimentation rates (no sediment, constant (slow, medium and fast), increasing and decreasing sedimentation rates) and the same salt rise rate, to analyse how allocyclic signature is altered by halokinesis. In all models, laterally, a zone of ~1150 m either side of the diapir that is influenced by halokinesis is observed, and beyond this zone, strata are undeformed. Unlike Finite Element Models, the DEM used in this study are able to generate realistic salt-related faults, which account for near-diapir deformation and act as ‘edges’ to the halokinetically-influenced zone. In all models, structural deformation and the extent of halokinetic influence are similar, and syn-kinematic strata, at least initially, are isolated to either side of the diapir, thinning and onlapping towards the high. Across all simulations, thinning is ~six times greater between the salt flank and crest, compared to the undeformed section and the salt flank, indicating more intense deformation close to the diapir. This modulation decreases with distance from the diapir. Thinning rate and amount of onlap decrease through time (up stratigraphy), showing a reduction of halokinetic modulation with increased sediment thickness, as halokinetic bathymetry is ‘healed’. While the overall modulation style close to the diapir is stratigraphic thinning, stratigraphic thickening is also observed in the salt-withdrawal basins. This study highlights that DEM can form an integral part of the workflow when studying salt-sediment interactions, and integrating DEM with subsurface and outcrop data can help to reduce reservoir and trap uncertainty in subsurface energy exploration and development. This technique can be used to test different scenarios for the development of halokinetically-influenced stratigraphy.

## **7.3 How confined is confined? An investigation into the effect of diapir-induced topographic spacing on deep-water sediment dispersal in the Eastern Central Graben, UK**

Chapter 5 uses a wealth of subsurface data and understanding from the well-studied salt-influenced Paleocene basin floor system in the Eastern Central Graben of the UK North Sea, to study deep-water facies and architecture distribution around diapirs, and the effects of lateral spacing of salt diapirs on halokinetic modulation. This study compared modification of deep-water stratigraphy between differently-spaced diapirs in the subsurface, to results of a simple two-dimensional DEM with variably spaced diapirs, and aimed to: 1) Analyse salt-influenced deep-water facies and characterise their distribution in terms of halokinetically versus allocyclically controlled; 2) compare stratigraphic architectures between variably spaced salt structures; and 3) describe the extent of halokinetically-modified stratigraphy between different distances of confinement. Facies analysis in the Paleocene of the Eastern Central Graben, UK North Sea, reveals that channels and lobes are influenced (re-routed and confined) by salt growth on a number of different scales, from centimetre-scale sedimentological character in core, to kilometre-scale geomorphological attributes in seismic. Stratigraphic thickness variations are common regardless of diapir spacing. Thickening is observed in the salt withdrawal basin in subsurface and models, as is most common above areas of autochthonous thinned salt. In closely spaced diapirs (<3km) a synclinal shaped minibasin develops with steeply rotated flanks, reflecting diapir growth. In more widely spaced diapirs (>4km) there is a zone between the diapirs where stratigraphy is relatively flat, forming a broad plateau.

Between closely spaced diapirs (<3 km) the zone of halokinetic influence of one diapir is laterally connected to the halokinetic influence of another diapir, such that the zone between the diapirs is influenced by both structures. When diapirs are more than 4 km apart a zone of minimal deformation develops. However, due to the complexity of salt basins, and therefore the presence and variability in the early kinematic stratigraphy and salt-related faults, even these ‘minimal modulation’ zones are unlikely to contain stratigraphy which is completely undeformed. Therefore, subsurface energy prospects are likely to be influenced by subtle salt-related topography even far away from diapirs. This study highlights the importance of integrating subsurface data with DEM to gain a better multi-scalar understanding of the effects of diapir spacing on stratigraphic architecture. This combined approach is advantageous in predicting stratigraphic geometries and halokinetic-influence on stratigraphy, in order to reduce reservoir and trap uncertainty in subsurface energy exploration and development.

Overall, the novel application of the diverse dataset used in this work serves to advance understanding of halokinetically-influenced deep-water systems.

#### **7.4 Controls on halokinetically-influenced deep-water successions**

Mass transport deposits (MTDs) are commonly recognised in salt-influenced systems across field and core data, and shown in spectral decomposition data to be diapirically-derived. This often results in ‘allocyclic’ stratigraphy being intercalated with these laterally-derived debrites. The presence of MTDs is somewhat overlooked in previous models of confined deep-water settings, however regardless of their emplacement mechanism such debrites form additional rugose seafloor topography, confining subsequent gravity flows. Deep-water sedimentary system development is shown to be controlled by orientation, number and proximity of topographic barriers; in flume tank experiments with flow-lateral topography deposits being elongated and asymmetric, appearing to have experienced some degree of ‘funneling’ in agreement with observations of thick, amalgamated sandstones between diapirs in the subsurface and outcrops. Where two topographic barriers are present, in the field, depositional flows were not able to radially spread and therefore thick sandstones are deposited between diapirs, by ‘braided’ channels. With only one topographic barrier, flows were able to dilute and re-route around the topography, in similarity to sinuous channels. With flow-frontal topography deposits exhibit a more classic ‘fill and spill’ morphology, and flow-oblique topography causes deep-water fan deposits to diverge. Combined subsurface and model learnings show that where diapirs are closely spaced (<1500 m) a zone of highly deformed strata is present. By comparison, when diapirs are widely spaced (>4500 m) a central broad plateau appears to develop between the diapirs. In intermediately spaced diapirs (1500-4500 m) a central modulation zone between the diapirs is predicted. In these zones of ‘non-modulation’, other subsurface features, such as saddle zones between diapirs, irregular base and top salt, and smaller diapirs where growth has ceased (3<sup>rd</sup>-4<sup>th</sup> order static or active topography) may act as additional topographic features, having a localised control on depositional facies and architecture, however their effects are unlikely to be felt several kilometres away. Outside the zone of halokinetic influence stratigraphy appear to be undeformed, and challenging to recognise from non-deformed stratigraphy, and facies are difficult to decipher from unconfined deep-water systems. External to the halokinetic controls outlined above, a number of other controls are influential on the development of deep-water systems, including: larger scale (i.e., 2<sup>nd</sup> order) topography (basin bounding faults), allocyclic controls on the deposition of the deep-water system itself (sediment supply, accommodation availability, source area geometry, potential ‘side fans’ etc.), tectonics and hinterland dynamics. This multi-disciplinary study has shown the importance of understanding halokinetic (salt layer variations, diapir rise rate, salt withdrawal, salt related faulting, MTD distribution) controls, which typically influence depositional systems and stratigraphy within >5 km of the salt and allocyclic (tectonics, sedimentation rate, hinterland dynamics) controls, which are extensive more regionally, when disentangling salt basin evolution.

## **7.5 Lateral and temporal variations in halokinetic modulation of stratigraphic architectures**

Across all the different techniques used in this study halokinetic modulation (the alteration of stratigraphy by salt growth) is shown to reduce stratigraphically (with time) and laterally (with distance) from the salt structure, in agreement with outcrop and subsurface analogues globally. Halokinetic bathymetry is shown to have a 'passive' influence on subsequent depositional systems (influencing sediment routing, but not forming diapirically-derived MTDs) until it is eventually 'healed'. In all data sets used in this study an upwards increase in relative sedimentation rate is associated with a decrease in halokinetic influence, and thus a 'healing' of diapiric topography. This relative increase in sedimentation rate could be due to an absolute increase in sedimentation rate (in the numerical simulations) or, in the case of many natural examples a combination of a reduction in salt supply due to welding (causing diapir rise rate to reduce relative to sedimentation rate) and an increase in absolute sedimentation rate.

## **7.6 Criterion for the recognition of halokinetically-influenced deep-water systems**

Recognition criterion for deep-water halokinetically-influenced settings includes: multiple directions of ripple lamination, injectites, fluidisation structures, presence of hybrid beds, range of MTD types, and abrupt juxtaposition of deep-water depositional facies and MTDs. Stratigraphy which thin towards and in some cases eventually pinch out or abut against salt topography suggest the presence of a mobile topographic high during deposition. Lateral variability in thinning rates, and drastic thinning to termination (pinch out) across two-dimensional data sets can be diagnostic of the presence of salt. Stratigraphy can also be seen to thicken into, and sometimes be confined to, deposition lows created by salt withdrawal, which are common at the base of salt topography. Aside from thickness variations, other characteristics that can identify salt-influenced stratigraphy include rotated, and often overturned, strata. Compared to similar depositional environments that are not influenced by topography, stratigraphy is highly modulated and deformed, mass transport deposits are commonly derived from diapirs, and facies are heterogeneous and spatially variable in deep-water salt-influenced settings. Therefore, hierarchical schemes, fan geometries, sub-environment distribution, and facies models developed in unconfined deep-water systems, must be used with caution, or adapted for use in halokinetically-influenced settings.

## **7.7 Comparison to other salt, or topographically influenced basins**

Halokinetically-influenced deep-water systems are fundamentally similar to the other topographically-influenced (e.g., rift, fold and thrust belt or mass transport deposit) deep-water systems in that MTDs, onlap, facies changes and stratigraphic thickness variations are common. The interplay of two distinct depositional systems (axial and lateral) is also common in deep-water environments influenced by different types of topography. The distinguishing feature of salt-topography in deep-water environments, as opposed to other types of topography, are debrites-derived from the salt structure, the presence of halokinetic sequences, radial bedding orientations and dramatic increases in bedding dip and thinning rates laterally towards the topography. The consistency of observations in a deep-water halokinetically-influenced setting and previously described halokinetically-influenced settings suggests that the criteria for recognising halokinetically-influenced systems (e.g., pinch out, onlap, stratigraphic thickness variations, variations in facies and facies distributions, and unconformities) is similar regardless of depositional environment, suggesting that halokinetic controls are central to stratigraphic architecture and evolution modulation. Multiple directions of ripple lamination, presence of hybrid beds, range of MTD types (particularly slumps containing remobilised thin-bedded sandstones), and abrupt juxtaposition of deep-water depositional facies can be used to specifically identify deep-water stratigraphy influenced by salt tectonics. Due to their long-lived sub-aqueous nature, deep-water halokinetically-influenced basins are unlikely to

contain remobilised anhydrite or halite, which are diagnostic of sub-aerial halokinetically-influenced environments.

Overall, integrating modelled stratal architectures and depositional facies observations from exhumed halokinetically-influenced settings globally is recommended as a useful workflow for building the sub-seismic geology into subsurface energy reservoir models for salt basins. This can help to reduce uncertainty of reservoir quality and stratigraphic trap prediction around salt structures. Integrated, cross-discipline working and thinking has helped to increase understanding of how halokinetically-influenced deep-water systems differ from their unconfined counterparts, and what controls these differences. Observations from multiple scales and types of data have been shown to bridge knowledge gaps that exist when using only one data type or scale. Utilising all available data, and employing multi-scalar workflows is recommended when disentangling halokinetic from allocyclic controls salt basins.

## 7.8 Summary

The key take home messages presented in this thesis are:

- The integration of these diverse techniques allows for the spatial and temporal distribution of deep-water facies and architectures in salt-influenced basins to be recognised.
- Deep-water depositional systems are influenced by salt growth across all scales, from centimetre-scale sedimentological characteristics identified in core and outcrop, to kilometre-scale geomorphological attributes visible in seismic data.
- Axially-derived deep-water depositional systems are heavily modified by laterally impinging mass transport deposits formed in response to salt-controlled topographic growth of the sea bed.
- Recognition criteria for deep-water halokinetically-influenced settings include: multiple directions of ripple lamination, a range of MTD types, bedding orientation and thickness variations and abrupt juxtaposition of deep-water depositional facies and MTDs.
- Halokinetically-influenced processes including re-routing and ‘funelling’ of gravity flows and rotation, thinning and termination of stratigraphy are scale independent and scalable.
- Thinning rates are up to six times greater within 350 m of a salt diapir, compared to further afield.
- Stratigraphy between closely (<3 km) spaced diapirs is more highly deformed than stratigraphy between widely (>3km) spaced diapirs.
- In halokineitcally-influenced deep-water successions the dominant controls are often allocyclic (external), but these successions are heavily influenced by halokinesis (salt growth) which drives autocyclic (internal) modulation of the primary depositional signal.

## References

- Ábalos, B., 2016, Geologic map of the Basque-Cantabrian Basin and a new tectonic interpretation of the Basque Arc: *International Journal of Earth Sciences*, v. 105, p. 2327-2354.
- Abe, S., and Urai, J.L., 2012, Discrete element modelling of boudinage: insights on rock rheology, matrix flow, and evolution of geometry: *Journal of Geophysical Research. Solid Earth*, v. 117.
- Abe, S., Van Gent, H., and Urai, J.L., 2011, DEM simulation of normal faults in cohesive materials: *Tectonophysics*, v. 512, p. 12-21.
- Abreu, V., Sullivan, M., Pirmez, C., and Mohrig, D., 2003, Lateral accretion packages (LAPs): An important reservoir element in deep water sinuous channels: *Marine and Petroleum Geology*, v. 20, p. 631–648.
- Adam, J., Z. Ge, and Sanchez, M., 2012, Salt-structural styles and kinematic evolution of the Jequitinhonha deepwater fold belt, central Brazil passive margin: *Marine and Petroleum Geology*, v. 37(1), p. 101-120.
- Adams, E., and Kenter, J., 2012, So Different, Yet So Similar: Comparing and Contrasting Si-iclastic and Carbonate Slopes: AAPG Search and Discovery Article 50683.
- Agirrezabala, L.M., 1996, El Aptiense-Albiense del Anticlinorio Nor-Vizcaino entre Gernika y Azpeitia. PhD Thesis. Euskal Herriko Unibertsitatea, Bilbao, 429 p.
- Agirrezabala, L.M., and Bodego, A., 2005, Interbedded mudstone slope and basin-floor sandy deposits in the Ondarroa turbidite system (Albian, Basque-Cantabrian Basin): *Geogaceta*, v. 38, p. 83-86.
- Agirrezabala, L.M., and Dinarés-Turell, J., 2013, Albian syndepositional block rotation and its geological consequences, Basque–Cantabrian Basin (Western Pyrenees): *Geological Magazine*, v. 150, p. 986–1001.
- Agirrezabala, L.M., and García-Mondéjar, J., 1989, Evolución tectosedimentaria de la plataforma urgoniana entre Cabo Ogoño e Itziar durante el Albiense inferior y medio (Región Vasco-Cantábrica nor-oriental): Del XII Congreso Español de Sedimentología simposio: Leioa, p. 11-20.
- Agirrezabala, L.M., and López-Horgue, M., 2017, Environmental and ammonoid faunal changes related to Albian Bay of Biscay opening: Insights from the northern margin of the Basque-Cantabrian Basin: *Journal of Sea Research*, v. 130, p. 36-48.
- Ahmadi, Z. M., Sawyers, M., Kenyon-Roberts, S., Stanworth, C. W., Kugler, K. A., Kristensen, J. and Fugelli, E. M. G. 2003., Paleocene, in: Evans, D., Graham, C., Armour, A., and Bathurst, P., eds., *The Millennium Atlas: Petroleum Geology of the Central and Northern North Sea*. The Geological Society, London, p. 235–259.
- Ala, M.A., 1974, Salt diapirism in southern Iran: *AAPG Bulletin*, v. 58, p. 1758–1770.



Albertz, M., and Ings, S.J., 2012, Some consequences of mechanical stratification in basin-scale numerical models of passive margin salt tectonics, in: Alsop, G.I., Archer, S.G., Hartley, A.J., Grant, N.T., and Hodgkinson, R., eds., *Salt Tectonics, Sediments and Prospectivity*: Geological Society, London, Special Publications, v. 363, p. 303-330.

Al Ja'Aidi, O.S., 2000, The influence of topography and flow efficiency on the deposition of turbidites. PhD Thesis. University of Leeds, UK, 162 p.

Al Ja'Aidi, O.S., McCaffrey, W.D., and Kneller, B.C., 2004, Factors influencing the deposit geometry of experimental turbidity currents: implications for sand-body architecture in confined basins, in: Lomas, S., and Joseph, P., eds., *Confined Turbidite Basins*: Geological Society of London, Special Publications, v. 222, p. 45–58.

Albertz, M., and Ings, S.J., 2012, Some consequences of mechanical stratification in basin-scale numerical models of passive margin salt tectonics, in: Alsop, G.I., Archer, S.G., Hartley, A.J., Grant, N.T., and Hodgkinson, R., eds., *Salt Tectonics, Sediments and Prospectivity*: Geological Society, London, Special Publications, v. 363, p. 303-330.

Alexander, J., and Morris, S., 1994, Observations on experimental, non-channelized, high-concentration turbidity currents and variations in deposits around obstacles: *Journal of Sedimentary Research*, v. 64, p. 899-909.

Allen, J.R.L., 1985, *Principles of Physical Sedimentology*: London, George Allen and Unwin, 272 p.

Allen, M.P., and Tildesley, D.J., 1987, *Molecular Simulation of Liquids*: Clarendon, Oxford.

Alves, T.M., Gawthorpe, R.L., Hunt, D.H., and Monteiro, J.H., 2002, Jurassic tectono-sedimentary evolution of the northern Lusitanian Basin (offshore Portugal): *Marine Petroleum Geology*, v. 19, p. 727–754.

Alves, T.M., Manuppella, G., Gawthorpe, R.L., Hunt, D.W., and Monterio, J.H., 2003, The depositional evolution of diapir- and fault-bounded rift basins: examples from the Lusitanian Basin of West Iberia: *Sedimentary Geology*, v. 162, p. 273–303.

Alsop, G.I., 1996, Physical modelling of fold and fracture geometries associated with salt diapirism, in: Alsop, G.I., Blundell, D.J., and Davison, I., eds., *Salt Tectonics*: Geological Society London Special Publication, v. 100, p. 227–241.

Alsop, G.I., Jenkins, G., and Davison, I., 1995, A preliminary study of drag zone geometry adjacent to salt diapirs, in: *Salt, sediment and hydrocarbons: Gulf Coast Section, SEPM 16th Annual Research Conference*, p. 1–9.

Alsop, G. I., Brown, J.P., Davison, I., and Gibling, M.R., 2000, The geometry of drag zones adjacent to salt diapirs: *Journal of the Geological Society, London*, v. 157, p. 1019–1029.

Alsop, G. I., Weinberger, R., Levi, T., and Marco, S., 2016, Cycles of passive versus active diapirism recorded along an exposed salt wall: *Journal of Structural Geology*, v. 84, p. 47-67.

Amy, L.A., McCaffrey, W.D., and Kneller, B.C., 2004, The influence of a lateral basin-slope on the depositional patterns of natural and experimental turbidity currents, in: Lomas, S.A., and Joseph, P., eds., *Confined Turbidite Systems: Geological Society of London, Special Publications*, v. 222, p. 311-330.

Amy, L.A., Talling, P.J., Peakall, J., Wynn, R.B. and Thynne, R.A., 2005, Bed geometry used to test recognition criteria of turbidites and (sandy) debrites: *Sedimentary Geology*, v. 179, p. 163-174.

Amy, L.A., Kneller, B.C. and McCaffrey, W.D., 2007, Facies architecture of the Gres de Peira Cava, SE France: landward stacking patterns in ponded turbiditic basins: *Journal of the Geological Society*, v. 164, p. 143-162.

Anderson, A. V., Sickafoose, D. K., Fahrer, T. R., and Gottschalk, R.R., 2012, Interaction of Oligocene–Miocene deep-water depositional systems with actively evolving structures: The Lower Congo Basin, offshore Angola, in D. Gao, ed., *Tectonics and sedimentation: Implications for petroleum systems: AAPG Memoir*, v. 100, p. 291–313.

Anderson, J. E., Cartwright, J., Drysdall, S. J., and Vivian, N., 2000, Controls on turbidite sand deposition during gravity-driven extension of a passive margin: Examples from miocene sediments in block 4, Angola: *Marine and Petroleum Geology*, v. 17, p. 1165–1203.

Anderson, K.S., Graham, S.A. and Hubbard, S.M., 2006, Facies, architecture, and origin of a reservoir-scale sand-rich succession within submarine canyon fill: insights from Wagon Caves Rock (Paleocene), Santa Lucia Range, California, USA: *Journal of Sedimentary Research*, v. 76, p. 819-838.

Andrews, B.J., Cumberpatch, Z.A., Shipton, Z.K., and Lord, R., 2020, Collapse processes in abandoned pillar and stall coal mines: Implications for shallow mine geothermal energy: *Geothermics*, v. 88, 101904.

Apps, G., 1987, Evolution of the Grès d'Annot Basin, SW Alps. PhD. thesis, University of Liverpool, 434 p.

Apps, G., Peel, F., and Elliott, T., 2004, The structural setting and palaeogeographical evolution of the Grès d'Annot basin, in: Lomas, S., and Joseph, P., eds., *Deep-Water Sedimentation in the Alpine Basin of SE France: New Perspectives on the Grès d'Annot and Related Systems: Geological Society of London, Special Publication*, v. 221, p. 65-96.

Arbués, P., Ferrer, O., Roca, E., Giles, K., Rowan, M., De Matteis, M. and Muñoz, J.A., 2012, The Bakio salt wall and its effects on synkinematic deepwater sedimentation (Basque Pyrenees, Northern Spain): *EGU General Assembly Conference Abstracts*, v. 14, p. 9659.

Archer, S.G., G.I. Alsop, A.J. Hartley, N.T. Grant, and R. Hodgkinson, 2012, Salt tectonics, sediments and prospectivity: an introduction: *Geological Society, London, Special Publications*, v. 363(1), p. 1-6.

Arfai, J., Lutz, R., Franke, D., Gaedicke, C., and Kley, J., 2016, Mass-transport deposits and reservoir quality of Upper Cretaceous Chalk within the German Central Graben, North Sea: *International Journal of Earth Sciences*, v. 105, p. 797-818.

Armitage, D.A., Romans, B.W., Covault, J.A., and Graham, S.A., 2009, The influence of mass-transport-deposit surface topography on the evolution of turbidite architecture: the Sierra Contreras, Tres Pas Formation (Cretaceous), Southern Chile: *Journal of Sedimentary Research*, v. 79, p. 287-301.

Aschoff, J.L., and Giles, K.A., 2005, Salt diapir-influenced, shallow-marine sediment dispersal patterns: insights from outcrop analogs: *AAPG Bulletin*, v. 89, p. 447-469.

Asl, M. E., Faghieh, A., Mukherjee, S., and Soleimany, B., 2019, Style and timing of salt movement in the Persian Gulf basin, offshore Iran: insights from halokinetic sequences adjacent to the Tonb-e-Bozorg diapir: *Journal of Structural Geology*, v. 122, p. 116-132.

Assier-Rzadkieicz, S., Heinrich, P., Sabatier, P.C., Savoye, B. and Bourillet, J.F., 2000, Numerical modelling of a landslide-generated tsunami: the 1979 Nice event: *Pure and Applied Geophysics*, v. 157, p. 1707-1727.

Atwater, G.I., and Forman, M.J., 1959, Nature of growth of southern Louisiana salt domes and its effect on petroleum accumulation: *AAPG Bulletin*, v. 43, p. 2592-2622.

Azpiroz-Zabala, M., Cartigny, M.J.B., Talling, P.J., Parsons, D.R., Sumner, E.J., and Clare, M.A., 2017, Newly recognized turbidity current structure can explain prolonged flushing of submarine canyons: *Science Advances*, v. 3, e1700200.

Baas, J.H. and Best, J.L., 2002, Turbulence Modulation in Clay-Rich Sediment-Laden flows and some implications for sediment deposition: *Journal of Sedimentary Research*, v. 72, p. 336-340.

Baas, J.H., 2004, Conditions for formation of massive turbiditic sandstones by primary depositional processes: *Sedimentary Geology*, v. 166, p. 292-310.

Baas, J.H., McCaffrey, W.D. and Knipe, R.J., 2005, The Deep-Water Architecture Knowledge Base: towards an objective comparison of deep-marine sedimentary systems: *Petroleum Geoscience*, v. 11, p. 309-320.

Baas, J.H., Best, J.L., Peakall, J., and Wang, M., 2009, A phase diagram for turbulent, transitional, and laminar clay suspension flows: *Journal of Sedimentary Research*, v. 79, p. 162-183.

Baas, J.H. Best, J.L., and Peakall, J., 2011, Depositional processes, bedform development and hybrid bed formation in rapidly decelerated cohesive (mud-sand) sediment flows: *Sedimentology*, v. 58, p. 1953-1987.

Baas, J.H., Davies, A.G., and Malarkey, J., 2013, Bedform development in mixed sand-mud: The contrasting role of cohesive forces in flow and bed: *Geomorphology*, v. 182, p. 19-32.

Babel, M. and B.C. Schreiber, 2014, Geochemistry of evaporites and evolution of seawater: *Treatise on geochemistry*, p. 483-560.

Back, S., Van Gent, H., Reuning, L., Grötsch, J., Niederau, J., and Kukla, P., 2011, 3D seismic geomorphology and sedimentology of the Chalk Group, southern Danish North Sea: *Journal of the Geological Society*, v. 168, p. 393-406.

Baguley, D., and Hose, D. R., 1994, *Why Do Finite Element Analysis*, Hamilton, NAFEMS.

- Baguley, D., and Hose, D. R., 1997, *How to Plan a Finite Element Analysis*, Hamilton, NAFEMS.
- Baird, R.A., 1986, Maturation and source rock-evaluation of Kimmeridge Clay, Norwegian North Sea: *AAPG Bulletin*, v. 70, p. 1–11.
- Bakke, K., Gjelberg, J., and Agerlin Petersen, S., 2008, Compound seismic modelling of the Ainsa II turbidite system, Spain: Application to deep-water channel systems offshore Angola: *Marine and Petroleum Geology*, v. 25, (10) p. 1058–1073.
- Bakke, K, Kane, I.A., Martinsen, O.J., Petersen, S.A., Johansen, T.A., Hustoft, S., Hadler, J., and Groth, A., 2013, Seismic modelling in the analysis of deep-water sandstone termination styles: *AAPG Bulletin*, v. 97, p. 1395-1419.
- Bally, A. W., 1981, Thoughts on the tectonics of folded belts, in: McClay, K.R., and Price, N.J., eds., *Thrust and nappe tectonics*: London, Geological Society, Special Publication v. 9, p. 13–32.
- Bally, A. W., 1982, Musings over sedimentary basin evolution, in: Kent, P., Bott, M. H. P., McKenzie, D.P., and Williams, C.A., eds., *The evolution of sedimentary basins*: London, Royal Society, p. 325–338.
- Banham, S.G., and Mountney, N.P., 2013a, Evolution of fluvial systems in salt-walled mini-basins: a review and new insights: *Sedimentary Geology*, v. 296, p. 142–166.
- Banham, S.G., and Mountney, N.P., 2013b, Controls on fluvial sedimentary architecture and sediment-fill state in salt-walled mini-basins: Triassic Moenkopi Formation, Salt Anticline Region, SE Utah, USA: *Basin Research*, v. 25, p. 709–737.
- Banham, S.G., and Mountney, N.P., 2014, Climatic versus halokinetic control on sedimentation in a dryland fluvial succession: *Sedimentology*, v. 61, p. 570–608.
- Baniak, G.M., Sayer, Z., Patterson, H., Gooder, R., Laing, N., and Love, A., 2020, The Mungo Field, Blocks 22/20a and 23/16a, UK North Sea, in: Goffey, G., and Gluyas, J.G., eds., *United Kingdom Oil and Gas Fields: 50<sup>th</sup> Anniversary Commemorative Volume*, Geological Society, London, *Memoirs*, v. 52, 537-549.
- Barde, J-P., Chamberlain, P., Galavazi, M., Gralla, P., Harwijanto, J., Marsky, J., and Van Den Belt, F., 2002, Sedimentation during halokinesis: Permo-Triassic reservoirs of the Saigak Field, Precaspian Basin, Kazakhstan: *Petroleum Geoscience*, v. 8, p. 177-187.
- Barker, S.P., Haughton, P.D.W., McCaffrey, W.D., Archer, S.G., and Hakes, B, 2008, Development of rheological heterogeneity in clay-rich high-density turbidity currents: Aptian Britannia Sandstone Member, UK continental shelf: *Journal of Sedimentary Research*, v. 78, p. 45–68.
- Barr, B.C., Slinn, D.N., Pierro, T., and Winters, K.B., 2004, Numerical simulation of turbulent, oscillatory flow over sand ripples: *Journal of Geophysical Research, Oceans* v. 109 (C9).
- Barrier, E., Vrielynck, B., Bergerat, F., Brunet, M.-F., Mosar, J., Poisson, A., and Sosson, M., 2008, Paleotectonic maps of the Middle East : Tectono-sedimentary-palaeogeographic maps from Late Norian to Pliocene. Retrieved from <https://www.worldcat.org/title/palaeotectonic-maps-of->

the-middle-east-tectono-sedimentary-palinspastic-maps-from-late-norian-to-pliocene/oclc/784218423

Barton, D. C., 1933, Mechanics of formation of salt domes with special reference to Gulf Coast salt domes of Texas and Louisiana: AAPG Bulletin, v. 17, p. 1025–1083.

Barton, M., O'Byrne, C., Pirmez, C., Prather, B., Van der Vlugt, F., Alpak, F.O. and Sylvester, Z., 2010, Turbidite channel architecture: Recognizing and quantifying the distribution of channel-base drapes using core and dipmeter data: AAPG Memoir, v. 92, p. 195-210.

Bathe, K.J., 2006, Finite Element Procedures. Cambridge, MA: Klaus-Jürgen Bathe.

Bauer, K., Moeck, I., Norden, B., Schulza, A., Weber, M., and Wirth, H., 2010, Tomographic P wave velocity and vertical velocity gradient structure across the geothermal site Groß Schönebeck (NE German Basin): Relationship to lithology, salt tectonics, and thermal regime: Journal of Geophysical Research: Solid Earth, v. 115 (B8).

Beaubouef, R.T., 2004, Deep-water leveed-channel complexes of the Cerro Toro Formation, Upper Cretaceous, southern Chile: AAPG Bulletin, v. 88, no. 11, p. 1471–1500.

Beaubouef, R.T., and Friedman, S.J., 2000, High Resolution Seismic/Sequence Stratigraphic Framework for the Evolution of Pleistocene Intra Slope Basins, Western Gulf of Mexico: Depositional Models and Reservoir Analogs, in: Weimer, eds., Deep-water reservoirs of the World, v. 20.

Belheine, N., Plassiard, J.P., Donzé, F. V., Darve, F., and Seridi, A., 2009, Numerical simulation of drained triaxial test using 3D discrete element modeling: Computers and Geotechnics, v. 36, p. 320-331.

Bell, D., Stevenson, C.J., Kane, I.A., Hodgson, D.M., and Poyatos-Moré, M., 2018a, Topographic controls on the development of contemporaneous but contrasting basin-floor depositional architectures: Journal of Sedimentary Research, v. 88, p. 1166-1189.

Bell, D., Kane, I.A., Pontén, A.S.M., Flint, S.S., Hodgson, D.M., and Barret, B.J., 2018b, Spatial variability in depositional reservoir quality: Marine and Petroleum Geology, v. 98, p. 97-115.

Benseghier, Z., Cuéllar, P., Luu, L.H., Bonelli, S., and Philippe, P., 2020, A parallel GPU-based computational framework for the micromechanical analysis of geotechnical and erosion problems: Computers and Geotechnics, v. 120, 103404.

Bersezio, R., Felletti, F. and Micucci, L., 2005, Statistical analysis of stratal patterns and facies changes at the terminations of “turbiditic” sandstone bodies: the Oligocene Cengio Unit (Tertiary Piedmont Basin): GeoActa, v. 4, p. 83-104.

Berton, F., and Vesely, F. F., 2016, Seismic expression of depositional elements associated with a strongly progradational shelf margin: northern Santos Basin, southeastern Brazil: Brazilian Journal of Geology, v. 46(4), p. 585-603.

Birch, P., and Haynes, J., 2003, The Pierce Field Blocks 23/22a, 23/27, UK North Sea, in: Gluyas, J.G., and Hichens, H.M., eds., United Kingdom Oil and Gas Fields Commemorative Millennium Volume: Geological Society, London, Memoir 20, p. 618-647.

Bird, D.E., Burke, K., Hall, S.A., and Casey, J.F., 2005, Gulf of Mexico tectonic history: Hotspot tracks, crustal boundaries, and early salt distribution: AAPG bulletin, v. 89(3), pp. 311- 328.

Bjørkum, P.A., Oelkers, E.H., Nadeau, P.H., Walderhaug, O., and Murphy, W.M., 1998, Porosity prediction in quartzose sandstones as a function of time, temperature, depth, stylolites frequency, and hydrocarbon saturation: AAPG Bulletin, v. 82, p. 637– 648.

Blair, T. C., and McPherson, J. G., 1999, Grain-size and textural classification of coarse sedimentary particles: Journal of Sedimentary Research, v. 69(1), p. 6–19.

Blanchard, S., Matheson, E.J., Fielding, C.R., Best, J.L., Bryk, A.B., Howell, K.J., Monson, C.C., Mahoney, G. and Peakall, J., 2018, Early burial mud diapirism and its impact on stratigraphic architecture in the Carboniferous of the Shannon Basin, County Clare, Ireland: Sedimentology, v. 66 (1), p. 329-361.

Blum, M.D. and Hattier-Womack, J., 2009, Climate change, sea-level change, and fluvial sediment supply to deepwater depositional systems, in: Kneller, B., Martinsen, O.J. and McCaffrey, B., eds., External Controls on Deep Water Depositional Systems, SEPM, Special Publication, v. 92, p. 15-39.

Bochud, M., 2011, Tectonics of the Eastern Greater Caucasus in Azerbaijan. PhD Thesis. University of Freiburg, Switzerland, 202 p.

Bodego, A., and Agirrezabala, L.M., 2013, Syn-depositional thin- and thick-skinned extensional tectonics in the mid Cretaceous Lasarte sub-basin, western Pyrenees: Basin Research, v. 25, p. 594-612.

Bodego, A., Iriarte, E., López-Horgue, M.A., and Álvarez, I., 2018, Rift-margin extensional forced folds and salt tectonics in the eastern Basque-Cantabrian rift basin (western Pyrenees): Marine and Petroleum Geology, v.91, p. 667-682.

Bondevik, S., Mangerud, J., Dawson, S., Dawson, A., and Lohne, Ø., 2003, Record- breaking height for 8000-year-old tsunami in the North Atlantic: Eos, Transactions American Geophysical Union, v. 84, no. 31, p. 289.

Bonin B., 2010, The Scientific Basis of Nuclear Waste Management, in: Cacuci D.G. eds., Handbook of Nuclear Engineering. Springer, Boston, MA.

Bonini, M., 2003, Detachment folding, fold amplification, and diapirism in thrust wedge experiments: Tectonics, v. 22 (6), p. 1065.

Booth, J. R., DuVernay, A.E., Pfeiffer, D.S., and Styzen, M.J., 2000, Sequence stratigraphic framework, depositional models, and stacking patterns of ponded and slope fan systems in the Auger basin: Central Gulf of Mexico slope, in: Deep-water reservoirs of the world: Tulsa, OK, Society of Economic Paleontologists and Mineralogists, Gulf Coast Section, 20th annual research conference, p. 82–103.

Booth, J.R., Dean, M.C., Duvernay, A.E., and Styzen, M.J., 2003, Paleo-bathymetric controls on the stratigraphic architecture and reservoir development of confined fans in the Auger Basin: Central Gulf of Mexico slope: Marine and Petroleum Geology, v. 20, p. 563–586.

Bornhauser, M., 1969, Geology of Day dome (Madison County, Texas) A study of salt emplacement: AAPG Bulletin, v. 53, p. 1411–1420.

Borsa, A.A., Fricker, H.A., Bills, B.G., Minster, J-B., Carabajal, C.C. and Quinn, K.J., 2008, Topography of the salar de Uyuni, Bolivia from kinematic GPS: Geophysical Journal International, v. 172 (1), p. 31-40.

Bosence, D., 2005, A genetic classification of carbonate platforms based on their basinal and tectonic settings in the Cenozoic: Sedimentary Geology, v. 175, p. 49-72.

Botter, C., Cardozo, N., Hardy, S., Lecomte, I., and Escalona, A., 2014, From mechanical modeling to seismic imaging of faults: A synthetic workflow to study the impact of faults on seismic: Marine and Petroleum Geology, v. 57, p. 187-200.

Boulesteix, K., Poyatos-More, M., Flint, S.S., Taylor, K., Hodgson, D.M., and Hasiotis, T. M., 2019, Transport and deposition of mud in deep-water environments: processes and stratigraphic implications: Sedimentology, v. 66, p. 2894-2925.

Boulesteix, K., Poyatos-Moré, M., Hodgson, D.M., Flint, S.S., and Taylor, K.G., 2020, Fringe or background: Characterizing deep-water mudstones beyond the basin-floor sandstone pinchout: Journal of Sedimentary Research, v. 90 (12), p. 1678-1705.

Bouma, A.H., 1962, Sedimentology of some Flysch deposits; a graphic approach to facies interpretation. Amsterdam: Elsevier, 168 p.

Bouma, A.H., 2000, Coarse-grained and fine-grained turbidite systems as end member models: applicability and dangers: Marine and Petroleum Geology, v. 17 (2) p. 137–143.

Bouma, A.H., 2001, Fine-grained submarine fans as possible recorders of long- and short- term climatic changes: Global and Planetary Change, v. 28 (1), p. 85–91.

Bouma, A.H., and Wickens, H. de V., 1994, Tanqua Karoo, ancient analog for fine-grained submarine fans, in: Weimer, P., Bouma, A.H., and Perkins, B.F. eds., Submarine Fans and Turbidite Systems—Sequence Stratigraphy, Reservoir Architecture and Production Characteristics Gulf of Mexico and International, Geological Society of America.

Bourget, J., Zaragosi, S., Ellouz-zimmermann, N., Mouchot, N., Garlan, T., Schneider, J.L., Lanfumey, V. and Lallemand, S., 2011, Turbidite system architecture and sedimentary processes along topographically complex slopes: the Makran convergent margin: Sedimentology, v. 58, p. 376-406.

Bouroullec, R., Verreussel, C.H., Geel, C.R., De Bruin, G., Zipp, M.H.A.A., Kőrösi, D., Munsterman, D.K., Janssen, N.M.M., and Kerstholt-Boegehold, S.J., 2018, Tectonostratigraphy of a rift basin affected by salt tectonics: synrift Middle Jurassic-Lower Cretaceous Dutch Central Graben, Tershelling Basin and neighbouring platforms, Dutch offshore, in: Kilhams, B., Kukla, P.A., Mazur, S., McKie, T., Mijnlief, H.F., and van Ojik, K., eds., Mesozoic Resource Potential in the Southern Permian Basin, Geological Society, London, Special Publications, v. 469, 269-303.

Bowie, W., 1927, Isostasy – The science of the equilibrium of the Earth's crust: New York, E. P. Dutton, 275 p.

- Brooks, H.L., Hodgson, D.M., Brunt, R.L., Peakall, J., Hofstra, M. and Flint, S.S., 2018, Deep-water channel-lobe transition zone dynamics: Processes and depositional architecture, an example from the Karoo Basin, South Africa: *GSA Bulletin*, v. 130, p. 1723-1746.
- Brunet, M.-F., Korotaev, M. V., Ershov, A. V., and Nikishin, A. M., 2003, The South Caspian Basin: A review of its evolution from subsidence modelling: *Sedimentary Geology*, v. 156(1-4), p. 119-148.
- Brun, J. P., and Fort, X., 2004, Compressional salt tectonics (Angolan margin): *Tectonophysics*, v. 382, p. 129-150.
- Brun, J. P., and Fort, X., 2011, Salt tectonics at passive margins: Geology versus models: *Marine and Petroleum Geology*, v. 28, p. 1123-1145.
- Brunet, M.F., 1994, Subsidence in the Parentis Basin (Aquitaine, France): implications of the thermal evolution, in: *Hydrocarbon and Petroleum Geology of France*, eds., Mascle, A. European Association of Petroleum Geoscientists, Special Publication 4, p.187-198.
- Bruthans, J., Filippi, M., Asadi, N., Zare, M., Šlechta, S., Churáčková, Z., 2009, Surficial deposits on salt diapirs (Zagros Mountains and Persian Gulf Platform, Iran): Characterization, evolution, erosion and the influence on landscape morphology: *Geomorphology*, v. 107 (3-4), p. 195-209.
- Bryn, P., Berg, K., Forsberg, C.F., Solheim, A. and Kvalstad, T.J., 2005, Explaining the Storegga slide: *Marine and Petroleum Geology*, v. 22, p. 11-19.
- Buckee, C., Kneller, B., and Peakall, J., 2001, Turbulence structure in steady, solute-driven gravity currents, in: McCaffrey, W.D., Kneller, B.C., and Peakall, J., eds., *Particulate Gravity Currents*, IAS Special Publication, p. 173-187.
- Bugge, T., Befring, S., Belderson, R.H., Eidvin, T., Jansen, E., Kenyon, N.K., Holtedahl, H. and Sejrup, H.J., 1987, A giant three-stage submarine slide off Norway: *Geo-Marine Letters*, v. 7, p. 191-198.
- Bull, S., Cartwright, J. and Huuse, M., 2009, A review of kinematic indicators from mass-transport complexes using 3D seismic data: *Marine and Petroleum Geology*, v. 26, p. 1132-1151.
- Burbank, D. W., Vergés, J., Munoz, A., and Bentham, P., 1992, Coeval hindward- and forward-imbricating thrusting in the south-central Pyrenees, Spain: Timing and rates of shortening and deposition: *GSA Bulletin*, v. 104, p. 3-17.
- Burgess, P.M., Winefield, P., Minozoni, M., and Elders, C., 2013, Methods for identification of isolated carbonate buildups from seismic reflection data: *AAPG Bulletin*, v. 97 (7), p. 1071-1098.
- Burgess, P.M., 2012, A brief review of developments in stratigraphic forward modelling, 2000-2009, in: Roberts, D.G., and Bally, A.W., eds., *Regional Geology and Tectonics: Principles of Geologic Analysis*, v. 1A, Elsevier, p. 864.
- Burgreen, B., and Graham, S., 2014, Evolution of a deep-water lobe system in the Neogene trench-slope setting of the East Coast Basin, New Zealand: Lobe stratigraphy and architecture in a weakly confined basin configuration: *Marine and Petroleum Geology*, v. 54, p. 1-22.



Burke, K., 1972, Longshore drift, submarine canyons, and submarine fans in development of Niger Delta: AAPG Bulletin, v. 56 (10) p. 1975–1983.

Callot, J.P., Salel, J-F, Letouzey, J., Daniel, J-M., Ringenbach, J-C., 2016. Three-dimensional evolution of salt-controlled minibasins: Interactions, folding, and megaflap development: AAPG Bulletin, v. 100 (9), p. 1419-1442.

Callot, J.P., Ribes, C., Kergaravat, C., Bonnel, C., Temiz, H., Poisson, A., Vrielynck, B., Salel, J.F., and Ringenbach, J.C., 2014, Salt tectonics in the Sivas basin (Turkey): crossing salt walls and minibasins. Bulletin de la Société Géologique de France, v. 185, p. 33-42.

Calvès, G., Huuse, M., Clift, P.D., and Brusset, S., 2015, Giant fossil mass wasting off the coast of West India: The Nataraja submarine slide: Earth and Planetary Science Letters, v. 432, p. 265–272.

Cámara, P., 2017, Salt and Strike-Slip Tectonics as Main Drivers in the Structural Evolution of the Basque-Cantabrian Basin, Spain, in: Soto, J.I., Flinch, J.F., Tari, G., eds., Permo-Triassic Salt Provinces of Europe, North Africa and the Atlantic Margins: Elsevier, p. 371-393.

Cámara, P., 2020, Inverted turtle salt anticlines in the Eastern Basque-Cantabrian basin, Spain: Marine and Petroleum Geology, v. 117, p. 104-358.

Campion, K.M., Sprague, A.R., Mohrig, D., Lovell, R.W., Drzewiecki, P.A., Sullivan, M.D., Ardill, J.A., Jensen, G.N. and Sickafoose, D.K., 2003, Outcrop expression of confined channel complexes: Bulletin of South Texas Geological Society, v. 44. P. 13-37.

Cardona, S., Wood, L.J., Dugan, B., Jobe, Z., and Strachan, L.J., 2020, Characterization of the Rapanui mass-transport deposit and the basal shear zone: Mount Messenger Formation, Taranki Basin, New Zealand: Sedimentology, v. 67 (4), p. 2111-2148.

Carr, I.D., Gawthorpe, R.L., Jackson, C.A-L., Sharp, I.R., and Sadek, A., 2003, Sedimentology and sequence stratigraphy of early syn-rift tidal sediments: the Nukhul Formation, Suez Rift, Egypt: Journal of Sedimentary Research, v. 73, p. 407–420.

Carruthers, D., Cartwright, J., Jackson, M.P.A., and Schutjens, P., 2013, Origin and timing of layer-bound radial faulting around North Sea salt stocks: new insights into the evolving stress state around rising diapirs: Marine and Petroleum Geology, v. 48, p. 130-148.

Cartwright, J., M. Jackson, T. Dooley, and S. Higgins, 2012, Strain partitioning in gravity- driven shortening of a thick, multilayered evaporite sequence, in: Alsop, G.I., S. G. Archer, S.G., Hartley, A.J., Grant, N.T., and Hodgkinson, R.T., eds., Salt tectonics, sediments and prospectivity: London, Geological Society, Special Publication Geological Society, London, Special Publications, v. 363, pp. 449-470.

Carvajal, C., Paull, C.K., Caress, D.W., Fildani, A., Lundsten, E., Anderson, K., Maier, K.L., McGann, M., Gwiazda, R. and Herguera, J.C., 2017, Unraveling the channel– lobe transition zone with high-resolution AUV bathymetry: Navy Fan, offshore Baja California, Mexico: Journal of Sedimentary Research, v. 87, p. 1049-1059.

Casson, M., Calvès, G., Huuse, M., Sayers, B., and Redfern, J., 2020, Cretaceous continental margin evolution revealed using quantitative seismic geomorphology, offshore northwest Africa. *Basin Research*, v. 33 (1), p. 66-90.

Castañares, L.M. and Robles, S., 2004, El vulcanismo del Albiense-Santonense en la Cuenca Vasco- Cantábrica, in: Vera, J.A. ed., *Geología de España*. Sociedad Geológica de España: Instituto Geológico y Minero de España, Madrid, p. 306–308.

Castañares, L.M., Robles, S., Gimeno, D., and Vicente Bravo, J.C., 2001, The submarine volcanic system of the Errigoiti Formation (Albian–Santonian of the Basque–Cantabrian Basin, northern Spain): stratigraphic framework, facies and sequences: *Journal of Sedimentary Research*, v. 71, p. 318–333.

Cedeño, A., Alberto Rojo, L., Cardozo, N., Centeno, L., and Escalona, A., 2019, The impact of salt tectonics on the thermal evolution and the Petroleum System of confined rift basins: insights from Basin Modeling of the Nordkapp Basin, Norwegian Barents Sea: *Geosciences*, v. 9 (7), p. 316.

Chadwick Jr, W.W., Dziak, R.P., Haxel, J.H., Embley, R.W. and Matsumoto, H., 2012, Submarine landslide triggered by volcanic eruption recorded by in situ hydrophone: *Geology*, v. 40, p. 51-54.

Chapple, W.M. and Spang, J.H., 1974, Significance of layer-parallel slip during folding of layered sedimentary rocks: *GSA Bulletin*, v. 85 (10), p. 1523-1534.

Charles, R., and Ryzhikov, K., 2015, Merganser Field: managing subsurface uncertainty during the development of a salt diapir field in the UK Central North Sea, in: McKie, T., Rose, P.T.S., Hartley, A.J., Jones, D.W., and Armstrong, T.L., eds., *Tertiary Deep-Marine Reservoirs of the North Sea Region*: Geological Society of London, Special Publications 403, p. 261-298.

Cheel, R.J. and Rust, B.R., 1986, A sequence of soft-sediment deformation (dewatering) structures in Late Quaternary subaqueous outwash near Ottawa, Canada: *Sedimentary Geology*, v. 47, p. 77-93.

Chemia, Z., Koyi, H. and Schmeling, H., 2008, Numerical modelling of rise and fall of a dense layer in salt diapirs: *Geophysical Journal International*, v. 172 (2), p. 798–816.

Chen, C., and Hiscott, R.N., 1999, Statistical analysis of facies clustering in submarine-fan turbidite successions: *Journal of Sedimentary Research*, v. 69, p. 505-517.

Chen, J., Sixta, D., Raney, G., Mount, V., Riddle, E., Nicholson, A., Ma, H., Ji, H., and Peng, C., 2018, Improved subsalt imaging from reflection full-waveform inversion-guided salt scenario Interpretation: A case history from deepwater Gulf of Mexico: *SEG Technical Program Expanded Abstracts 2018*.

Chiarella, D., Longhitano, S. G., and Tropeano, M., 2017, Types of mixing and heterogeneities in siliciclastic-carbonate sediments: *Marine and Petroleum Geology*, v. 88, p. 617–627.

Cil, M.B., and Alshibli, K.A., 2012, 3D assessment of fracture of sand particles using discrete element method: *Géotechnique Letters*, v. 2 (3), p. 161-166.

Clare, M.A., Clarke, J.H., Talling, P.J., Cartigny, M.J., and Pratomo, D.G., 2016, Preconditioning and triggering of offshore slope failures and turbidity currents revealed by most detailed monitoring yet at a fjord-head delta: *Earth and Planetary Science Letters*, v. 450, p. 208-220.

Clark, J.D., 1995, Detailed section across the Ainsa II Channel Complex, south central Pyrenees, Spain, in: Pickering, K.T., Hiscott, N., Kenyon, N.H., Ricci Lucchi, F., Smith, R.D.A., eds., *Atlas of Deep-Water Environments - Architectural Style in Turbidite Systems*. Chapman and Hall, London, p. 139-144.

Clark, J.D. and Pickering, K.T., 1996, Architectural elements and growth patterns of submarine channels: application to hydrocarbon exploration: *AAPG Bulletin*, v. 80, p. 194-221.

Clark, J.D., Stanbrook, D., and Gardiner, A., 2008, Architecture and Facies of Confined Deep-water Clastics in the Grand Coyer Remnant, Grès d'Annot, France, in: Nilsen, T., Shew, R.D., Steffens, G., and Studlick, J., eds., *Atlas of Deep-Water Outcrops: AAPG Studies in Geology*.

Clark, I.A., and Cartwright, J.A., 2009, Interactions between submarine channel systems and deformation in deepwater fold belts: examples from the Levant Basin, Eastern Mediterranean Sea: *Marine and Petroleum Geology*, v. 26, p. 1465-1482.

Clark, I.A., and Cartwright, J.A., 2011, Key controls on submarine channel development in structurally active settings: *Marine and Petroleum Geology*, v. 28, p. 1333-1349.

Clarke, F., 1924, The Data of Geochemistry: *US Geological Survey Bull*, v. 770, p. 841.

Cloos, H., 1939, Hebung – Spaltung – Vulkanismus – Elemente einer geometrischen Analyse irdischer Großformen: *Geologische Rundschau*, v. 30, p. 405-527.

Cloos, E., 1955, Experimental analysis of fracture patterns: *GSA Bulletin*, v. 66, p. 241-256.

Cloos, E., 1968, Experimental analysis of Gulf Coast fracture patterns: *AAPG Bulletin*, v. 52, p. 420-444.

Cobain, S.L., Hodgson, D.M., Peakall, J. and Shiers, M.N., 2017, An integrated model of clastic injectites and basin floor lobe complexes: implications for stratigraphic trap plays: *Basin Research*, v. 29 (6), p. 816-835.

Cobbold, P. R., and Szatmari, P., 1991, Radial gravitational gliding on passive margins: *Tectonophysics*, v. 188, p. 249-289.

Coleman, A.J., Jackson, C.A-L., Duffy, O.B., and Nikolinakou, M.A., 2018, How, where, and when do radial faults grow near salt diapirs?: *Geology*, v. 46 (7), p. 655-658.

Collie, A.J., and Giles, K., 2011, Comparison of Lower Cambrian carbonate facies and halokinetic sequences in minibasins developed on opposite sides of the Wirrealpa Diapir, Central Flinders Ranges, South Australia: *AAPG Search and Discovery Article #50442*.

Collins, J., Kenyon-Roberts, S., Cullen, B., White, J., Bordas-Le Floch, N., and Downey, J., 2015, Arran Field: a complex heterolithic reservoir on the margins of the Forties Fan System, in:

McKie, T., Rose, P.T.S., Hartley, A.J., Jones, D.W., and Armstrong, T.L. eds., Tertiary Deep-Marine Reservoirs of the North Sea Reservoirs of the North Sea, The Geological Society of London, v. 403, p. 185-217.

Costa, E., and Vendeville, B.C., 2002, Experimental insights on the Geometry and Kinematics of Fold-and-Thrust Belts Above Weak, Viscous Evaporitic Décollement: *Journal of Structural Geology*, v. 24, p. 1729-1739.

Counts, J.W., and Amos, K.J., 2016, Sedimentology, depositional environments and significance of an Ediacaran salt-withdrawal minibasin, Billy Springs Formation, Flinders Ranges, South Australia: *Sedimentology*, v. 63, p. 1084-1123.

Counts, J.W., Dalgarno, C.R., Amos, K.J., and Hasiotis, S.T., 2019, Lateral facies variability along the margin of an outcropping salt-withdrawal minibasin, South Australia: *Journal of Sedimentary Research*, v. 89, p. 28-45.

Coussot, P., and Meunier, M., 1996, Recognition, classification and mechanical description of debris flows: *Earth Science Reviews*, v. 40, p. 209-227.

Covault, J.A., and Romans, B.W., 2009, Growth patterns of deep-sea fans revisited: Turbidite-system morphology in confined basins, examples from the California Borderland: *Marine Geology*, v. 265, p. 51-66.

Covault, J.A., Fildani, A., Romans, B.W. and McHargue, T., 2011, The natural range of submarine canyon-and-channel longitudinal profiles: *Geosphere*, v. 7(2), p. 313-332.

Covault, J.A., Shelef, E., Traer, M., Hubbard, S.M., Romans, B.W., and Fildani, A., 2012, Deep-water channel run-out length: Insights from seafloor geomorphology: *Journal of Sedimentary Research*, v. 82, p. 21-36.

Covault, J.A., Sylvester, Z., Hubbard, S.M., Jobe, Z.R. and Sech, R.P., 2016, The stratigraphic record of submarine-channel evolution: *The Sedimentary Record*, v. 14, p. 4-11.

Coward, M., and Stewart, S., 1995, Salt-influenced structures in the Mesozoic–Tertiary cover of the southern North Sea, U.K., in: Jackson, M.P.A., Roberts, D.G., Snelson, S., eds., *Salt Tectonics: a Global Perspective*: AAPG Memoir, v. 65, p. 229–250.

Cox, D.R., Huuse, M., Newton, A.M.W., Gannon, P., and Clayburn, J., 2020, Slip sliding away: Enigma of large sandy blocks within a gas-bearing mass transport deposit, offshore northwestern Greenland: *AAPG Bulletin*, v. 104 (5), p. 1011-1043.

Crimes, T.P., 1973, From limestones to distal turbidites: a facies and trace fossil analysis in the Zumaya flysch (Paleocene-Eocene), North Spain: *Sedimentology*, v. 20, p. 105-131.

Cronin, B.T., 1995., Structurally-controlled deep-sea channel courses: examples from the Miocene of south-east Spain and the Alboran Sea, south-west Mediterranean., in: Hartley, A.J., Prosser, D.J., eds., *Characterization of Deep Marine Clastic Systems*. Geological Society of London, Special Publication, v. 94, p. 113-133.

- Cronin, B.T., Owen, D., Hartley, A.J., and Kneller, B., 1998, Slumps, debris flows and sandy deep-water channel systems: implications for the application of sequence stratigraphy to deep-water clastic sediments: *Journal of the Geological Society of London*, v. 155, p. 429–432.
- Cullen, T.M., Collier, R.E.L., Gawthorpe, R.L., Hodgson, D.M., and Barrett, B.J., 2019, Axial and transverse deep-water sediment supply to syn-rift fault terraces: Insights from the West Xylokastro Fault Block, Gulf of Corinth, Greece: *Basin Research*, v. 32 (5), p. 1115-1149.
- Cullis S, Patacci M, Colombera L, Bührig L, and McCaffrey W.D., 2019, A database solution for the quantitative characterisation and comparison of deep-marine siliciclastic depositional systems: *Marine and Petroleum Geology*, v. 102, p. 321-339.
- Cullis S, Colombera L, Patacci M, and McCaffrey W.D., 2019, Hierarchical classifications of the sedimentary architecture of deep-marine depositional systems: *Earth-Science Reviews*, v. 179, p. 38-71.
- Cumberpatch, Z.A., Soutter, E.L., Kane, I.A., Casson, M., and Vincent, S.J., 2021a, Evolution of a mixed siliciclastic-carbonate deep-marine system on an unstable margin: the Cretaceous of the Eastern Greater Caucasus, Azerbaijan. *Basin Research*, v. 33 (1), p. 612-647.
- Cumberpatch, Z.A., Kane, I.A., Soutter, E.L., Hodgson, D.M., Jackson, C. A-L., Kilhams, B.A., and Poprawski, Y., 2021b, Interactions of deep-water gravity flows and active salt tectonics, *Journal of Sedimentary Research*, v. 91, p. 34-65.
- Cumberpatch, Z.A., Finch, E., and Kane, I.A., 2021c, External signal preservation in halokinetic stratigraphy: A Discrete Element Modeling (DEM) approach: *Geology*, v. 49 (6), p.687-692.
- Cumberpatch, Z A., Finch, E., Kane, I.A., Pichel, L.M., Jackson, C.A-L., Kilhams, B.A., Hodgson, D.M., and Huuse, M., 2021d in press. Halokinetic modulation of sedimentary thickness and architecture: a numerical modelling approach: *Basin Research*, 2021d, accepted, in press, available online.
- Cundall, P.A., and Strack, O.D., 1979, A Discrete Element Method for Granular Assemblies: *Geotechnique*, v. 22, p. 47-65.
- Cunha, R.S., Tinterri, R., and Magalhaes, P.M., 2017, Annot Sandstone in the Peira Cava basin: An example of an asymmetric facies distribution in a confined turbidite system (SE France): *Marine and Petroleum Geology*, v. 87, p. 60-79.
- Dakin, N., Pickering, K.T., Mohrig, D., and Bayliss, N.J., 2013, Channel-like features created by erosive submarine debris flows: Field evidence from the Middle Eocene Ainsa Basin, Spanish Pyrenees: *Marine and Petroleum Geology*, v. 41 (1), p. 62-71.
- Dalgarno, C.R., and Johnson, J.E., 1968, Diapiric structures and late Precambrian–early Cambrian sedimentation in Flinders Ranges, South Australia, in: Braunstein, J., and O’Brien, G.D., eds., *Diapirism and Diapirs: AAPG, Memoir v. 8*, p. 301–314.
- Daly, R.A., 1936, Origin of submarine ‘canyons’: *American Journal of Science*, v. 31, p. 402-420.
- Daniilidis, A., and Herber, R., 2017, Salt intrusions providing a new geothermal exploration target for higher energy recovery at shallower depths: *Energy*, v. 118, p. 658-670.

Davis, D.M., and Engelder, T., 1987, Thin-skinned deformation over salt, in: Lerche, I., O'Brien, J.J., eds., *Dynamical Geology of Salt and Related Structures*. Academic Press, Orlando, Florida, p. 301–338.

Davis, C., Haughton, P., McCaffrey, W., Scott, E., Hogg, N. and Kitching, D., 2009, Character and distribution of hybrid sediment gravity flow deposits from the outer Forties Fan, Palaeocene Central North Sea, UKCS: *Marine and Petroleum Geology*, v. 26, p. 1919-1939.

Davison, I., 2007, *Geology and tectonics of the South Atlantic Brazilian salt basins*: Geological Society, London, Special Publications, v. 272, pp. 345-359.

Davison, I., and Barreto, P., 2021, Deformation and sedimentation processes, and hydrocarbon accumulations on upturned salt diapir flanks in the Lusitanian Basin, Portugal: *Petroleum Geoscience*, v. 27, p. 138-144.

Davison, I., Insley, M., Harper, M., Weston, P., Blundell, D., McClay, K., and Quallington, A., 1993, Physical modelling of overburden deformation around salt diapirs: *Tectonophysics*, v. 228, p. 255-274.

Davison, I., Bosence, D., Alsop, G.I. and Al-Aawah, M.H., 1996, Deformation and sedimentation around active Miocene salt diapirs on the Tihama Plain, northwest Yemen. *Geological Society London. Special Publication 100*, p. 23–39.

Davison, I., Alsop, I., Birch, P., Elders, C., Evans, N., Nicholson, H., Rorison, P., Wade, D., Woodward, J., and Young, M., 2000a, Geometry and late-stage structural evolution of Central Graben salt diapirs, North Sea: *Marine and Petroleum Geology*, v. 17, p. 499-522.

Davison, I., Alsop, G.I., Evans, N.G., and Safaricz, M., 2000b, Overburden deformation patterns and mechanisms of salt diapir penetration in the Central Graben, North Sea: *Marine and Petroleum Geology*, v. 17, p. 601–618.

Davison, I., Jones, I.F., and Waltham, D., 2013, *Seismic imaging of Salt Diapirs: Problems and Pitfalls*: 13th International Congress of the Brazilian Geophysical Society & EXPOGEF, Rio de Janeiro, Brazil, 26-29<sup>th</sup> August 2013.

Dean, M. C., J. R. Booth, and B. T. Mitchell, 2002, Multiple fields within the sequence stratigraphic framework of the greater Auger basin, Gulf of Mexico: *Society of Economic Paleontologists and Mineralogists Gulf Coast Section, 22nd annual research conference proceedings*, p. 661–680.

De Blasio, F.V., Engvik, L.E., and Elverhøi, A., 2006, Sliding of outrunner blocks from submarine landslides: *Geophysical Research Letters*, v.30 (6).

DeFelipe, I., Pedreira, D., Pulgar, J.A., Iriarte, E., and Medina, M., 2017, Mantle exhumation and metamorphism in the Basque-Cantabrian Basin (N Spain): Stable and clumped isotope analysis in carbonates and comparison with opicalcites in the North-Pyrenean Zone (Urdach and Lherz): *Geochemistry, Geophysics, Geosystems*, v. 18, p. 631-652.

De Haas, H., Okkels, E. and Van Weering, T.C.E., 1996, Recent sediment accumulation in the Norwegian Channel, North Sea. *Norges Geologiske Undersøkelse Bulletin*, v. 430, p. 57-65.

- Demercian, S., Szatmari, P., and P.R., Cobbold, 1993, Style and pattern of salt diapirs due to thin-skinned gravitational gliding, Campos and Santos basins, offshore Brazil: *Tectonophysics*, v. 228, p. 393-433.
- Den Hartog Jager, D., Giles, M.R., and Griffiths, G.R., 1993, Evolution of Paleogene submarine fans of the North Sea in space and time, in: Parker, J.R., ed., *Petroleum Geology of Northwest Europe: Proceedings of the 4th Conference*, The Geological Society, London, p. 59-71.
- Deng, C., Gawthorpe, R.L., Fossen, H., and Finch, E., 2018, How does the orientation of a preexisting basement weakness influence fault development during renewed rifting? Insights from three-dimensional discrete element modeling: *Tectonics*, v. 37 (7), p. 2221-2242.
- Deptuck, M.E., Sylvester, Z., Pirmez, C. and O'Byrne, C., 2007, Migration-aggradation history and 3-D seismic geomorphology of submarine channels in the Pleistocene Benin-major Canyon, western Niger Delta slope: *Marine and Petroleum Geology*, v. 24, p. 406-433.
- Deptuck, M.E., Piper, D.J.W., Savoye, B. and Gervais, A., 2008, Dimensions and architecture of late Pleistocene submarine lobes off the northern margin of East Corsica: *Sedimentology*, v. 55, p. 869-898.
- Di Celma, C.N., Brunt, R.L., Hodgson, D.M., Flint, S.S. and Kavanagh, J.P., 2011, Spatial and Temporal Evolution of a Permian Submarine Slope Channel-Levee System, Karoo Basin, South Africa: *Journal of Sedimentary Research*, v. 81, p. 579–599.
- Dickinson, W. R., and Lawton, T. F., 2001, Carboniferous to Cretaceous assembly and fragmentation of Mexico: *GSA Bulletin*, v. 113, p. 1142 – 1160.
- Dietrich, H., 1993, Differential Compaction and Structural Genesis: Computerized Basin Analysis, p. 47-57.
- Dodd, T.J.H., McCarthy, D.J. and Richards, P.C., 2019, A depositional model for deep-lacustrine, partially confined, turbidite fans: Early Cretaceous, North Falkland Basin: *Sedimentology*, v. 66, p. 53–80.
- Donzé, F., Mora, P., and Magnier, S-A., 1994, Numerical simulation of faults and shear zones: *Geophysical Journal International*, v. 116, p. 46-52.
- Dooley, T.P., McClay, K.R., Hempton, M. and Smit, D., 2005, Salt tectonics above complex basement extensional fault systems: results from analogue modelling, in: Doré, A.G. and Vining, B.A., eds., *Petroleum Geology: North-West Europe and Global Perspectives – Proceedings of the 6<sup>th</sup> Petroleum Geology Conference* 6, p. 1631-1648.
- Dooley, T.P., and Hudec, M.R., 2017, The effects of base-salt relief on salt flow and suprasalt deformation patterns – Part 2: Application to the eastern Gulf of Mexico: *Interpretation*, v. 5(1) p. 25-38.
- Dooley, T.P., and Hudec, M.R., 2020, Extension and inversion of salt-bearing rift systems: *Solid Earth*, v. 11(4), p. 1187-1204.
- Dooley, T.P., Jackson, M., and Hudec, M.R., 2007, Initiation and growth of salt-based thrust belts on passive margins: Results from physical models: *Basin Research*, v. 19, p. 165–177.

Dooley, T.P., Jackson, M.P., and Hudec, M.R., 2009, Inflation and deflation of deeply buried salt stocks during lateral shortening: *Journal of Structural Geology*, v. 31(6), p. 582-600.

Dooley, T.P., Hudec, M.R., and Jackson, M.P., 2012, The structure and evolution of sutures in allochthonous salt: *AAPG Bulletin*, v. 96(6), p. 1045-1070.

Dooley, T.P., Jackson, M.P.A, and Hudec, M.R., 2013, Coeval extension and shortening above and below salt canopies on an uplifted, continental margin: Application to the northern Gulf of Mexico: *AAPG Bulletin*, v. 97(10), p. 1737-1764.

Dooley, T.P., Jackson, M.P.A., Jackson, C.A-L., Hudec, M.R., and Rodriguez, C.R., 2015, Enigmatic structures within salt walls of the Santos Basin- Part 2: Mechanical explanation from physical modelling: *Journal of Structural Geology*, v. 75, p. 163-187.

Dooley, T.P., Hudec, M.R., Pichel, L.M., and Jackson, M.P.A., 2020, The impact of base-salt relief on salt flow and suprasalt deformation patterns at the autochthonous, paraautochthonous and allochthonous level: insights from physical models: *Journal of the Geological Society, Special Publications*, v. 476 (2), p. 287-315.

Dorrell, R.M., Peakall, J., Sumner, E.J., Parsons, D.R., Darby, S.E., Wynn, R.B., Özsoy, E., and Tezcan, D., 2016, Flow dynamics and mixing processes in hydraulic jump arrays: Implications for channel-lobe transition zones: *Marine Geology*, v. 381, p. 181-193.

Doughty-Jones, G., Mayall, M., and Lonergan, L., 2017, Stratigraphy, facies, and evolution of deep-water lobe complexes within a salt controlled intraslope minibasin: *AAPG Bulletin*, v. 101, p. 1879-1904.

Doughty-Jones, G., Lonergan, L., Mayall, M., and Dee, S.J., 2019, The role of structural growth in controlling the facies and distribution of mass transport deposits in a deep-water salt minibasin: *Marine and Petroleum Geology*, v. 104, p. 106-124.

Druke, D. C. 2005., Sedimentology and stratigraphy of the San Jose Lentil, La Popa Basin, Mexico, and its implications for carbonate development in a tectonically influenced salt basin. MS. Thesis. New Mexico State University.

Druke, J., and Giles, K.A., 2008, Depositional setting and distribution of sands within Type A halokinetic sequences: an example from the Paleocene Upper Mudstone Member, Potrerillos Formation, La Popa Basin, Mexico: *AAPG Annual Convention and Exhibition Abstracts* v. 17, p. 47-48.

Dudley, P. R. C., Rehmer, D. E., and Bouma, A. H., 2000, Reservoir scale characteristics of fine-grained sheet sandstones, Tanqua Karoo Subbasin South Africa, in *Deep-Water Reservoirs of the World: GCSSEPM Foundation 20th Annual Research Conference*, (Houston, TX: GCSSEPM Foundation), p. 318-341.

Duffy, O.B., Fernandez, N., Hudec, M.R., Jackson, M.P.A., Burg, G., Dooley, T.P. and Jackson, C. A-L., 2017, Lateral mobility of minibasins during shortening: Insights from the SE Precaspian Basin, Kazakhstan: *Journal of Structural Geology*, v. 97, p. 257-276.

Duffy, O.B., Dooley, T.P., Hudec, M.R., Jackson, M.P.A., Fernandez, N. Jackson, C, A-L. and Soto, J.I., 2018, Structural evolution of salt-influenced fold-and-thrust belts: A synthesis and new



- insights from basins containing isolated salt diapirs: *Journal of Structural Geology*, v. 114, p. 206-221.
- Dutta, U., Baruah, A., and Mandal, N., 2016, Role of source-layer tilts in the axi-symmetric growth of diapirs triggered by a Rayleigh-Taylor instability: *Geophysical Journal International*, v. 206, p. 1814-1830.
- Duval, B., Cramez, C., and Jackson, M. P. A., 1992, Raft tectonics in the Kwanza Basin, Angola. *Marine and Petroleum Geology*, v. 9, p. 389–404.
- Dyson, I.A., 1996, A new model for diapirism in the Adelaide Geosyncline: *MESA Journal*, v. 3, p. 41–48.
- Dyson, I.A., 1999, The Beltana Diapir – a salt withdrawal minibasin in the northern Flinders Ranges: *MESA Journal*, v. 15, p. 40–46.
- Dyson, I.A., 2001, The diapir-base metal association in the northern Flinders Ranges. *MESA Journal*, v. 22, p. 37–43.
- Dyson, I.A., 2004a, Interpreted shallow and deep water depositional systems of the Beltana minibasin in the northern Flinders Ranges, South Australia, in: Post, P.J., Olson, D.L., Lyons, K.T., Palmes, S.L., Harrison, P.F., and Rosen, N.C., eds., *Salt- Sediment Interactions and Hydrocarbon Prospectivity: Concepts, Applications, and Case Studies for the 21st Century*, p. 997–1030.
- Dyson, I.A., 2004b, Christmas Tree Diapirs and Development of Hydrocarbon Reservoirs: a model from the Adelaide Geosyncline, South Australia, in: Post, P.J., Olson, D.L., Lyons, K.T., Palmes, S.L., Harrison, P.F., and Rosen, N.C., eds., *Salt- Sediment Interactions and Hydrocarbon Prospectivity: Concepts, Applications, and Case Studies for the 21st Century*, p. 133–165.
- Dyson, I.A., 2005, Formation of submarine unconformities in halotectonic mini-basins during passive margin development of the Adelaide Geosyncline, South Australia, in: Post, P.J., Rosen, N.C., Olson, D.L., Palmes, S.L., Lyons, K.T., and Newton, G.B., eds., *Petroleum Systems of Divergent Continental Margin Basins* p. 679–721.
- Dyson, I.A., and Rowan, M.G., 2004, Geology of a Welded Diapir and Flanking Mini-Basins in the Flinders Ranges of South Australia, in: Post, P.J., Olson, D.L., Lyons, K.T., Palmes, S.L., Harrison, P.F., and Rosen, N.C., eds., *Salt-Sediment Interactions and Hydrocarbon Prospectivity: Concepts, Applications, and Case Studies for the 21st Century*, p. 69–89.
- Dyson, I.A., and Marshall, T.R., 2007, Neoproterozoic salt nappe complexes and salt-withdrawal mini-basins in the Amadeus Basin, in: Munson, T.J., and Ambrose, G.J., eds., *Proceedings of the Central Australian Basins Symposium (CABS)*, p. 16–18.
- Dzulynski, S., and Sanders, J.E., 1962, Current marks on firm mud bottoms: *Transactions of the Connecticut Academy of Arts and Sciences*, v. 42, p. 58–96.
- Edgell, H.S., 1996, Salt tectonism in the Persian Gulf Basin, in: Alsop, G.I., Blundell, D.J., and Davison, I., eds., *Salt Tectonics*, Geological Society, London, Special Publications, v. 100, p. 129-151.
- Edwards, D.A., Leeder, M.R., Best, J.L. and Pantin, H.M., 1994, On experimental reflected density currents and the interpretation of certain turbidites: *Sedimentology*, v. 41, p. 437-461.

Eggenhuisen, J.T., Tilston, M.C., de Leeuw, J., Pohl, F. and Cartigny, M.J., 2019, Turbulent diffusion modelling of sediment in turbidity currents: An experimental validation of the Rouse approach: *The Depositional Record*, v. 6 (1), p. 203-216.

Ehrenberg, S.N., 1990, Relationship between diagenesis and reservoir quality in sandstones of the Garn Formation, Haltenbanken, mid-Norwegian continental shelf: *AAPG Bulletin*, v. 74, p. 1538-1558.

Eldrett, J., Tripsanas, E., Davis, C., Mckie, T., Vieira, M., Osterloff, P., and Sandison, T., 2015, Sedimentological evolution of Sele Formation deep-marine depositional systems of the Central North Sea, in: McKie, T., Rose, P.T.S., Hartley, A.J., Jones, D.W., and Armstrong, T.L. eds., *Tertiary Deep-Marine Reservoirs of the North Sea*, The Geological Society of London, v. 403, p. 63-98.

Elliott, T., 2000, Megaflute erosion surfaces and the initiation of turbidite channels: *Geology*, v. 28, p. 119-122.

Ericson, D.B., Ewing, M., and Heezen, B.C., 1952, Turbidity currents and sediments in North Atlantic: *AAPG Bulletin*, v. 36, p. 489-511.

Erratt, D., 1993. Relationships between basement faulting, salt withdrawal and Late Jurassic rifting, UK Central North Sea, in: Parker, J.R., ed., *Petroleum Geology of Northwest Europe: Proceedings of the 4th Conference*, Geological Society, London, pp. 1211-1219.

Erratt D., Thomas G. M., and Wall G. R. T., 1999., The evolution of the Central North Sea Rift, in: Fleet A. J., and Boldy S. A. R., eds, *Petroleum Geology of Northwest Europe: Proceedings of the 5th Conference*. Geological Society, London, p. 63–82.

Espejo, J., 1973, Mapa Geológico de España 1:50.000, Hoja 38 (Bermeo). Segunda Serie (MAGNA), Primera Edición IGME.

Espejo, J., and Pastor, F., 1973, Mapa Geológico de España 1:50.000, Hoja 37 (Algorta). Segunda Serie (MAGNA), Primera Edición IGME.

Escosa, F. O., Rowan, M.G., Giles, K.A., Deatrick, K.T., Mast, A.M., Langford, R.P., Hearon T.E., IV, and Roca, E., 2019, Lateral terminations of salt walls and megaflaps: Gypsum Valley diapir, Paradox Basin, Colorado: *Basin Research*, v. 31, p. 191-212.

Espurt, N., F. Wattellier, J. Philip, J.-C. Hippolyte, O. Bellier, and L. Bestani, 2019, Mesozoic halokinesis and basement inheritance in the eastern Provence fold-thrust belt, SE France: *Tectonophysics*, v. 766, p. 60-80.

Etienne, S., Mulder, T., Bez, M., Desaubliaux, G., Kwasniewski, A., Parize, O., Dujoncquoy, E., and Salles, T., 2012, Multiple scale characterization of sand-rich distal lobe deposit variability: Examples from the Annot Sandstones Formation, Eocene–Oligocene, SE France: *Sedimentary Geology*, v. 273-274, p. 1-18.

Evans, N., MacLeod, J.A., Macmillan, N., Rorison, P., and Salvador, P., 1993. The Banff field, blocks 22/27a, 29/2a, UK North Sea, in: Gluyas, J.G., and Hitchens, H.M., eds., *United Kingdom Oil and Gas Fields, Commemorative Millennium Volume*, Geological Society, London, Memoir 20, p. 497-507.

Evans, D., Graham, C., Armour, and A., Bathurst, P., 2003. *The Millennium Atlas: Petroleum Geology of the Central and Northern North Sea*, Geological Society, London.

Falivene, O., Arbués, P., Howell, J., Muñoz, J.A., Fernández, O., and Marzo, M., 2006, Hierarchical geocellular facies modelling of a turbidite reservoir analogue from the Eocene of the Ainsa basin, NE Spain: *Marine and Petroleum Geology*, v. 23 (6), p. 679–701.

Fallgatter, C., Kneller, B., Paim, P.S. and Milana, J.P., 2017, Transformation, partitioning and flow–deposit interactions during the run-out of megaflores: *Sedimentology*, v. 64, p. 359-387.

Farre, J.A., McGregor, B.A., Ryan, W.B. and Robb, J.M., 1983, Breaching the shelfbreak: passage from youthful to mature phase in submarine canyon evolution: *SEPM Special Publication*, v. 33, p 25 – 39.

Felletti, F., 2002, Complex bedding geometries and facies associations of the turbiditic fill of a confined basin in a transpressive setting (Castagnola Fm., Tertiary Piedmont Basin, NW Italy): *Sedimentology*, v. 49, p. 645-667.

Ferguson, R.A., Kane, I. A., Eggenhuisen, J.T., Pohl, F., Tilston, M., Sychala, Y.T. and Brunt, R.L., 2020, Entangled external and internal controls on submarine fan evolution: an experimental perspective: *The Depositional Record*, v. 6 (3), p. 605-624.

Fernandez, N., and Kaus, B.J.P, 2015, Pattern formation in 3-D numerical models of down-built diapirs initiated by a Rayleigh–Taylor instability: *Geophysical Journal International*, v. 202 (2), p. 1253–1270.

Fernandez, N., Hudec, M.R., Jackson, C, A-L., Dooley, T.P., and Duffy, O.B. 2020, The competition for salt and kinematic interactions between minibasins during density-driven subsidence: observations from numerical models: *Petroleum Geoscience*, v. 26 (1), p. 3-15.

Fernández-Mendiola, P.A., Gómez-Pérez, I., and García-Mondéjar, J., 1993, Aptian-Albian carbonate platforms: central Basque-Cantabrian Basin, northern Spain. In: Toni Simo, J.A., Scott, R.W., and Masse, J.P., eds., *Cretaceous Carbonate Platforms: AAPG Memoir*, v. 56, p. 315-324.

Ferrer, O., Roca, E., Benjumea, B., Muñoz, J., and Ellouz, N., 2008, The deep seismic reflection MARCONI-3 profile: Role of extensional Mesozoic structure during the Pyrenean contractional deformation at the eastern part of the Bay of Biscay: *Marine and Petroleum Geology*, v. 25, p 714-730.

Ferrer, O., Jackson, M.P.A., Roca, E., and Rubinat, M., 2012, Evolution of salt structures during extension and inversion of the Offshore Parentis Basin (Eastern Bay of Biscay), 2012, in: Alsop, G.I., Archer, Hartley, A.J., Grant, N.T., and Hodgkinson, R., eds., *Salt tectonics, sediments and prospectivity*: London, Geological Society, Special Publication v. 363, p. 361-380.

Ferrer, O., Arbues, P., Roca, E., Giles, K., Rowan, M.G., De Matteis, M. and Munoz, J.A., 2014, Effect of Diapir Growth on Synkinematic Deepwater Sedimentation: the Bakio Diapir (Basque-Cantabrian Basin, Northern Spain): *AAPG Search and Discovery Article #90189*.

Ferrer, O., McClay, K., and Sellier, N. C., 2017, Influence of fault geometries and mechanical anisotropies on the growth and inversion of hanging-wall synclinal basins: Insights from sandbox models and natural examples, in: Childs, C., Holdsworth, R.E., Jackson, C.A-L., Manzocchi, T.,

Walsh, J.J., and Yielding, G., eds., *The Geometry and Growth of Normal Faults*, Geological Society, London, Special Publications, v. 439(1), p. 487–509.

Fiduk, J. C., and Rowan, M.G., 2012, Analysis of folding and deformation within layered evaporites in Blocks BM-S-8 & -9, Santos Basin, Brazil, in: Alsop, G.I., Archer, Hartley, A.J., Grant, N.T., and Hodgkinson, R., eds., *Salt tectonics, sediments and prospectivity*: London, Geological Society, Special Publication v. 363p. 471–487,

Figueiredo, J.J., Hodgson, D.M., Flint, S.S. and Kavanagh, J.P., 2013, Architecture of a channel complex formed and filled during long-term degradation and entrenchment on the upper submarine slope, Unit F, Fort Brown Fm., SW Karoo Basin, South Africa: *Marine and Petroleum Geology*, v. 41, p. 104-116.

Fildani, A., Hubbard, S.M., Covault, J.A., Maier, K.L., Romans, B.W., Traer, M. and Rowland, J.C., 2013, Erosion at inception of deep-sea channels: *Marine and Petroleum Geology*, v. 41, p.48-61.

Finch, E., 1998, *A Crustal Lattice Solid Model: The Evolution, Geometry and Scaling of Tectonic Extension*. PhD thesis, School of Environmental Sciences, University of Ulster.

Finch, E., Hardy, S., and Gawthorpe, R., 2003, Discrete element modelling of contractional fault-propagation folding above rigid basement fault blocks: *Journal of Structural Geology*, v. 25(4), p. 515–528.

Finch, E., Hardy, S., and Gawthorpe, R., 2004, Discrete-element modelling of extensional fault-propagation folding above rigid basement fault blocks: *Basin Research*, v. 16(4), p. 467–488.

Finch, E., and Gawthorpe, R., 2017, Growth and interaction of normal faults and fault network evolution in rifts: insights from three-dimensional discrete element modelling, in: Childs, C., Holdsworth, R.E., Jackson, C.A-L., Manzocchi, T., Walsh, J.J., and Yielding, G., eds., *The Geometry and Growth of Normal Faults*, Geological Society, London, Special Publications, v. 439 (1) p. 219-248.

Fine, I.V., Rabinovich, A.B., Bornhold, B.D., Thomson, R.E. and Kulikov, E.A., 2005, The Grand Banks landslide-generated tsunami of November 18, 1929: preliminary analysis and numerical modelling: *Marine Geology*, v. 215, p. 45-57.

Fisher, R.V., 1971, Features of coarse-grained, high concentration fluids and their deposits: *Journal of Sedimentary Petrology*, v. 41, p. 916- 927.

Flint, S.S., and Hodgson, D.M., 2005, *Submarine Slope Systems: Processes and Products*, in: Hodgson, D.M., and Flint, S.S., eds., *Submarine Slope Systems: Processes and Products*, Geological Society of London, Special Publication, v. 244, p. 1-6.

Flint, S.S., Hodgson, D.M., Sprague, a. R., Brunt, R.L., Van der Merwe, W.C., Figueiredo, J., Pr lat, a., Box, D., Di Celma, C., and Kavanagh, J.P., 2011, Depositional architecture and sequence stratigraphy of the Karoo basin floor to shelf edge succession, Laingsburg depocentre, South Africa: *Marine and Petroleum Geology*, v. 28 (3) p. 658–674.

Fonnesu, M., Haughton, P., Felletti, F., and McCaffrey, W., 2015, Short length-scale variability of hybrid event beds and its applied significance: *Marine and Petroleum Geology*, v. 67, p. 583-603.

Fonnesu, M., Felletti, F., Haughton, P.D., Patacci, M., and McCaffrey, W.D., 2018, Hybrid event bed character and distribution linked to turbidite system sub-environments: the North Apennine Gottero Sandstone (north-west Italy): *Sedimentology*, v. 65, p. 151- 190.

Ford, M., Hemelsdaël, R., Mancini, M., and Palyvos, N., 2017, Rift migration and lateral propagation: Evolution of normal faults and sediment- routing systems of the western Corinth rift (Greece), in: Childs, C., Holdsworth, R.E., Jackson, C.A-L., Manzocchi, T., Walsh, J.J., and Yielding, G., eds., *The Geometry and Growth of Normal Faults*, Geological Society, London, Special Publications, v. 439, p. 131-168.

Fort, X., Brun, J-P., and Chauvel, F., 2004, Salt tectonics on the Angolan margin, synsedimentary deformation processes: *AAPG Bulletin*, v. 88, p. 1523-1544.

Fossen, H. 2010. *Structural Geology*. Cambridge University Press, Cambridge, UK, 463 p.

Fossen, H., 2010, Deformation bands formed during soft-sediment deformation: observations from SE Utah: *Marine and Petroleum Geology*, v. 27, p. 215-222.

Freeman, C.J.F., Garrard, R.J., and Farwana, A., 2020, The Starling, Scoter and Merganser fields, Blocks 22/30a and 29/3a, UK North Sea, in: Goffey, G., and Gluyas, J.G., eds., *United Kingdom Oil and Gas Fields: 50<sup>th</sup> Anniversary Commemorative Volume*, Geological Society, London, *Memoirs*, v. 52, 589-605.

Frey-Martínez, J., J. Cartwright, and D. James, 2006, Frontally confined versus frontally emergent submarine landslides: A 3D seismic characterization: *Marine and Petroleum Geology*, v. 23, p. 585–604.

Fuchs, L., Schmeling, H., and Koyi, H., 2011, Numerical models of salt diapir formation by down-building: the role of sedimentation rate, viscosity contrast, initial amplitude and wave length: *Geophysical Journal International*, v. 186, p. 390-400.

Fuhrmann, A., Kane, I.A., Clare, M.A., Ferguson, R.A., Schomacker, E., Bonamini, E., and Contreras, F.A., 2020, Hybrid turbidite-drift channel complexes: An integrated multiscale model: *Geology*, v. 48 (6), p. 562-568.

Fullsack, P., 1995, An arbitrary Lagrangian-Eulerian formulation for creeping flows and its applications in tectonic models: *International Journal of Geophysics*, v. 120, p. 1-23.

Fusi, N., and Kenyon, N.H., 1996, Distribution of mud diapirism and other geological structures from long-range sidescan sonar (GLORIA) data, in the Eastern Mediterranean Sea: *Marine Geology*, v. 132, p. 21–38.

Gamboa, D., Alves, T., and Cartwright, J., 2011, Distribution and characterization of failed (mega)blocks along salt ridges, southeast Brazil: Implications for vertical fluid flow on continental margins: *Journal of Geophysical Research: Solid Earth* v. 116.

Gamboa, D., and Alves, T. M., 2016, Bi-modal deformation styles in confined mass-transport deposits: Examples from a salt minibasin in SE Brazil: *Marine Geology*, v. 379, p. 176 - 193.

Gannaway Dalton, C.E., Giles, K.A., Rowan, M.G., Langford, R.P., Hearon, T.E., and Fiduk, C., 2020, Sedimentological, stratigraphic, and structural evolution of minibasins and a megaflap

formed during passive salt diapirism: The Neoproterozoic Witchelina diapir, Wilouran Ranges, South Australia: *Journal of Sedimentary Research*, v. 90 (2), p. 165-199.

García, M.H., 1994, Depositional turbidity currents laden with poorly sorted sediment: *Journal of Hydraulic Engineering*, v. 120, p. 1240–1263.

García, M., and Parker, G., 1989, Experiments on hydraulic jumps in turbidity currents near a canyon-fan transition: *Science*, v. 245, p. 393–396.

García-Mondéjar, J., 1990, The Aptian-Albian carbonate episode of the Basque-Cantabrian basin (northern Spain) general characteristics controls and evolution, in: Tucker, M.E., Wilson, J.L., Crevello, P.D., Sarg, J.F., and Read, J.F., eds., *Carbonate Platforms – facies, sequences and evolution: International Association of Sedimentologists, Special Publication 9*, p. 257-290.

García-Mondéjar, J., 1996, Plate reconstruction of the Bay of Biscay: *Geology*, v. 24, p. 635-638.

García-Mondéjar, J., and Robador, A., 1987, Sedimentación y paleogeografía de la del Complejo Urgoniano (Aptiense-Albiense) en el área de Bermeo (región Vasco-Cantábrica septentrional): *Acta Geologica Hispanica*, v. 22, p. 411-418.

García-Mondéjar, J., Fernández-Mendiola, P.A., Agirrezabala, L.M., Aranburu, A., López-Horgue, M.A. Iriarte, E., and Martínez de Rituerto, S., 2004, El Aptiense-Albiense de la Cuenca Vasco-Cantábrica: *Geologica de España*, p. 291-296.

Gardiner, A.R., 2006, The variability of turbidite sandbody pinchout and its impact on hydrocarbon recovery in stratigraphically trapped fields, in: Allen, M.R., Goffey, G.P., Morgan, R.K., and Walker, I.M., eds., *The Deliberate Search for the Stratigraphic Trap*, Geological Society of London, Special Publications 254, p. 267-287.

Garrison, J. M., and McMillan, N.J., 1999, Evidence for Jurassic continental rift magmatism in northeast Mexico: allochthonous metaigneous blocks in El Papalote diapir, La Popa Basin, Nuevo León, Mexico, in: Bartolini, C., Wilson, J. L., and Lawton, T. F., eds., *Mesozoic Sedimentary and Tectonic History of North-Central Mexico*. GSA, Boulder, Special Papers, v. 340, p. 319–332.

Garrote-Ruiz, A., García-Potero, J. A., Eguiguren-Altuna, E., and García-Pascual, I., 1991, Mapa de la Hoja nº 38-I (Bermeo) del Mapa Geológico del País Vasco a escala 1:25.000. Ente Vasco de la Energía-EVE, Bilbao.

Garrote-Ruiz, A., García-Potero, J. A., Eguiguren-Altuna, E., and García-Pascual, I., 1992, Mapa de la Hoja nº 38-III (Mungia) del Mapa Geológico del País Vasco a escala 1:25.000. Ente Vasco de la Energía-EVE, Bilbao.

Garrote-Ruiz, A., García-Potero, J. A., Eguiguren-Altuna, E., and García-Pascual, I., 1993a, Mapa de la Hoja nº 37-II (Armintza) del Mapa Geológico del País Vasco a escala 1:25.000. Ente Vasco de la Energía-EVE, Bilbao.

Garrote-Ruiz, A., García-Potero, J.A., Eguiguren-Altuna, E., and García-Pascual, I., 1993b, Mapa de la Hoja nº 37-IV (Getxo) del Mapa Geológico del País Vasco a escala 1:25.000. Ente Vasco de la Energía-EVE, Bilbao.

Gavrilov, Y. O., 2018, Architecture of the Southern Marginal Zone of the Upper Jurassic-Valanginian Carbonate Platform of the Northeastern Caucasus (Dagestan, Shakhdag Massif): Lithology and Mineral Resources, v. 53(6), p. 460–472.

Gaullier, V., and Vendeville, B.C., 2005, Salt tectonics driven by sediment progradation: Part II- Radial spreading of sedimentary lobes prograding above salt: AAPG Bulletin, v. 89 (8), p. 1081-1089.

Gawthorpe, R. L., and Leeder, M. R., 2000, Tectono- sedimentary evolution of active extensional basins: Basin Research, v. 12, p. 195– 218.

Gawthorpe, R. L., Leeder, M. R., Kranis, H., Skourtsos, E., Andrews, J. E., Henstra, G. A., Mack, G. H., Muravchik, M., Turner, J. A., and Stamatakis, M., 2018, Tectono- sedimentary evolution of the Plio- Pleistocene Corinth rift, Greece: Basin Research, v. 30, p. 448– 479.

Ge, Z., Gawthorpe, R.L., Rotevatn, A., Zijerveld, L., Jackson, C, A-L. and Oluboyo, A., 2020, Minibasin depocentre migration during diachronous salt welding, offshore Angola: Basin Research, v. 32, p. 875-893.

Gee, M.J.R., and Gawthorpe, R.L., 2006, Submarine channels controlled by salt tectonics: Examples from 3D seismic data offshore Angola: Marine and Petroleum Geology, v. 23, p. 443-458.

Gee, M.J.R., and Gawthorpe, R.L., 2007, Early evolution of submarine channels offshore Angola revealed by three-dimensional seismic data, in: Davies, R.J., Posamentier, H.W., Wood, L.J., and Cartwright, J.A., eds., Seismic Geomorphology: Applications to Hydrocarbon Exploration and Production, Geological Society, London, Special Publications, v. 277, p. 223–235.

Gee, M. J. R., Masson, D.G., Watts, A.B., and Allen, P.A., 1999, The Saharan debris flow: An insight into the mechanics of long runout submarine debrisflows: Sedimentology, v. 46, p. 317–335.

Geluk, M.C., Paar, W.A., and Fokker, P.A., 2007, Salt, in: Wong, T.E., Batjes, D.A.J. and De Jager, J., eds., Geology of the Netherlands. Royal Netherlands Academy of Arts and Sciences, Amsterdam, p. 283-294.

Gemmer, L., Ings, S.J., Medvedev, S., and Beaumont, C., 2004, Salt tectonics driven by differential sediment loading: stability analysis and finite-element experiments: Basin Research, v. 16, p. 199-218.

Gemmer, L., Beaumont, C., and Ings, S.J., 2005, Dynamic modelling of passive margin salt tectonics: effects of water loading, sediment properties and sedimentation patterns: Basin Research, v. 17, p. 382-402.

Georgiopoulou, A., Masson, D.G., Wynn, R.B. and Krastel, S., 2010, Sahara Slide: Age, initiation, and processes of a giant submarine slide: Geochemistry, Geophysics, Geosystems, v. 11. Q07014.

Gervais, A., Savoye, B., Piper, D.J., Mulder, T., Cremer, M., and Pichevin, L., 2004, Present morphology and depositional architecture of a sandy confined submarine system: the Golo turbidite system (eastern margin of Corsica, in: Lomas, S., and Joseph, P., eds., Confined Turbidite Basins: Geological Society of London, Special Publication, v. 222, p. 59-89.

Gervais, A., Savoye, B., Mulder, T. and Gonthier, E., 2006, Sandy modern turbidite lobes: a new insight from high resolution seismic data: *Marine and Petroleum Geology*, v. 23, p. 485–502.

Giles, K., 2014, Attributes of Carbonate Platforms Associated With Passive Diapirism: *AAPG Search and Discovery Article 41386*.

Giles, K., and Lawton, T., 2002, Halokinetic sequence stratigraphy adjacent to the El Papalote diapir, Northeastern Mexico: *AAPG Bulletin*, v. 86, p. 823-840.

Giles, K., and Rowan, M., 2012, Concepts in halokinetic-sequence deformation and stratigraphy, in: Alsop, G.I., Archer, S.G., Hartley, A.J., Grant, N.T., and Hodgkinson, R., eds., *Salt Tectonics, Sediments and Prospectivity: Geological Society of London, Special Publication 363*, p. 7-31.

Giles, K. A., Lawton, T.F., and Rowan, M.G., 2004, Summary of halokinetic sequence characteristics from outcrop studies of La Popa salt basin, northeastern Mexico, in: *Salt–sediment interactions and hydrocarbon prospectivity: Concepts, applications, and case studies for the 21st century: Society of Economic Paleontologists and Mineralogists Gulf Coast Section, 24th annual research conference*, p. 1045–1062.

Giles, K. A., Druke, D.C., Mercer, D.W., and Hunnicutt-Mack, L., 2008, Controls on upper Cretaceous (Maastrichtian) heterozoan carbonate platforms developed on salt diapirs, La Popa basin, northeast Mexico, in: Lukasik, J., and Simo, J.A., eds., *Controls on carbonate platform development: Tulsa, OK, Society of Economic Paleontologists and Mineralogists, Special Publication 89*, p. 107–124.

Gill, D.W., 1979, Syndepositional sliding and slumping in the West Clare Namurian Basin, Ireland: *Geological Survey of Ireland Special Paper*, v. 4, p. 1-30.

Gill, D.W. and Kuenen, P.H., 1958, Sand volcanoes on slumps in the Carboniferous of County Clare, Ireland: *Quarterly Journal of the Geological Society*, v. 113, p. 441-460.

Glennie, K.W., 1995. Permian and Triassic Rifting in Northwest Europe, in: Boldy, S.A.R., ed., *Permian and Triassic Rifting in Northwest Europe*, Geological Society, London, *Special Publications*, v. 91, p. 1.

Goffey, G., Gluyas, J., and Schofield, N., 2020, UK oil and gas fields: an overview, in: Goffey, G., and Gluyas, J.G., eds., *United Kingdom Oil and Gas Fields: 50<sup>th</sup> Anniversary Commemorative Volume*, Geological Society, London, *Memoirs*, v. 52, p. 3-18.

Gómez, M., Vergés, J., and Riaza, C., 2002, Inversion tectonics of the northern margin of the Basque Cantabrian Basin: *Bulletin de la Société Géologique de France*, v. 173, p. 449-459.

Gómez-Pérez, I., Fernández-Mendiola, P.A., and García-Mondéjar, J., 1999, Depositional architecture of a rimmed carbonate platform (Albian, Gorbea, western Pyrenees): *Sedimentology*, v. 46, p. 337-356.

Gorsline, D.S. and Emery, K.O., 1959, Turbidity-current deposits in San Pedro and Santa Monica basins off southern California: *GSA Bulletin*, v. 70, p. 279-290.

Goteti, R., Ings, S. J., and Beaumont, C., 2012, Development of salt minibasins initiated by sedimentary topographic relief: *Earth and Planetary Science Letters*, v. 339–340, p. 103-116.



- Gradmann, S., and Beaumont, C., 2017, Numerical modelling study of mechanisms of mid-basin salt canopy evolution and their potential applications to the Northwestern Gulf of Mexico: *Basin Research*, v. 29 (4) p. 490-521.
- Gradstein, F. M., Ogg, J. G., and Smith, A. G., 2012., *A Geologic Time Scale 2012*, Cambridge University Press, Cambridge.
- Grant, R.J., Underhill, J.R., Hernández-Casado, J., Barker, S.M., Jamieson, R.J. 2019a. Upper Permian Zechstein Supergroup carbonate-evaporite platform palaeomorphology in the UK Southern North Sea: *Marine and Petroleum Geology*, v. 100, p. 484-518.
- Grant, R.J., Underhill, J.R., Hernández-Casado, J., Jamieson, R.J., Williams. R.M. 2019b. The evolution of the Dowsing Graben System: implications for petroleum prospectivity in the UK Southern North Sea: *Petroleum Geoscience*, v. 27, p. 64-81.
- Grant, R.J., Booth, M.G., Underhill, J.R., and Bell, A., 2020, Structural evolution of the Breagh area: implications for carboniferous prospectivity of the Mid North Sea High, Southern North Sea: *Petroleum Geoscience*, v. 26, p. 174-203.
- Grimstad, S., 2016, Salt tectonics in the central and northeastern Nordkapp Basin, Barents Sea. MS Thesis. University of Oslo, Norway, 127 p.
- Groenenberg, R.M., Hodgson, D.M., Prélat, A., Luthi, S.M., and Flint, S.S., 2010, Flow- deposit interaction in submarine lobes: Insights from outcrop observations and realizations of a process-based numerical model: *Journal of Sedimentary Research*, v. 80, p. 252-267.
- Grundvåg, S.A., Johannessen, E.P., Helland-Hansen, W. and Plink-Björklund, P., 2014, Depositional architecture and evolution of progradationally stacked lobe complexes in the Eocene Central Basin of Spitsbergen: *Sedimentology*, v. 61, p. 535-569.
- Gupta, K.D., and Pickering, K.T., 2008, Petrography and temporal changes in petrofacies of deep-marine Ainsa-Jaca basin sandstone systems, Early and Middle Eocene, Spanish Pyrenees: *Sedimentology*, v. 55, p. 1083-1114.
- Gwiazda, R., Paull, C.K., Ussler, W., and Alexander, C.R., 2015, Evidence of modern fine-grained sediment accumulation in the Monterey Fan from measurements of the pesticide DDT and its metabolites: *Marine Geology*, v. 363, p. 125–133.
- Hadler-Jacobsen, F., Johannessen, E.P., Ashton, N., Henriksen, S., Johnson, S.D., and Kristensen, J.B., 2005, Submarine fan morphology and lithology distribution: a predictable function of sediment delivery, gross shelf-to-basin relief, slope gradient and basin topography: *Geological Society, London Petroleum Geology Conference Series*, v. 6, p. 1121-1145.
- Haflidason, H., Sejrup, H.P., Nygard, A., Mienert, J., Bryn, P., Lien, R., Forsberg, C.F., Berg, K., and Masson, D., 2004, The Storegga Slide: Architecture, geometry and slide development: *Marine Geology*, v. 213, p. 201–234.
- Hale, D.N., Hill, R., and Stefani, J., 1992, Imaging salt with turning seismic waves: *Geophysics*, v.57 (11), p. 1396-1524.

Hale, M., Laird, R., Gavnholt, J. and van Bergen, P.F. 2020, The Pierce Field, Blocks 23/22a and 23/27, UK North Sea, in: Goffey, G., and Gluyas, J.G., eds., United Kingdom Oil and Gas Fields: 50<sup>th</sup> Anniversary Commemorative Volume, Geological Society, London, Memoirs, v. 52, p. 550-559.

Hamilton-Wright, J., Dee, S., Von Nicolai, C., and Johnson, H., 2019, Investigating controls on salt movement in extensional settings using finite-element modelling: *Petroleum Geoscience*, v. 25(3), p. 258-271.

Hampton, M.A., 1972, The Role of Subaqueous Debris Flow in Generating Turbidity Currents: *Journal of Sedimentary Petrology*, v. 42, p. 775-793.

Hampton, M.A., Lee, H.J. and Locat, J., 1996, Submarine landslides: *Reviews of Geophysics*, v. 34, p. 33-59.

Hanafy, S., Nimmagadda, S.L., Mahmoud, S.E., and Mabrouk, W.M., 2017, New insights on structure and stratigraphic interpretation for assessing the hydrocarbon potentiality of the off-shore Nile Delta basin, Egypt: *Journal of Petroleum Exploration and Production Technology*, v. 7, p. 317-339.

Hanna, M. A., 1953, Fracture porosity in Gulf Coast: *American Association of Petroleum Geologists Bulletin*, v. 37, p. 266–281.

Hansen, L.A.S., Callow, R.H.T., Kane, I.A., Gamberi, F., Rovere, M., and Cronin, B.T., 2015, Genesis and character of thin-bedded turbidites associated with submarine channels: *Marine and Petroleum Geology*, v. 67, p. 852–879.

Hansen, L., Callow, R., Kane, I., and Kneller, B., 2017, Differentiating submarine channel-related thin-bedded turbidite facies: Outcrop examples from the Rosario Formation, Mexico: *Sedimentary Geology*, v. 358, p. 19–34.

Hansen, L.A.S., Hodgson, D.M., Pontén, A., Bell, D., and Flint, S., 2019, Quantification of basin-floor fan pinchouts: Examples from the Karoo Basin, South Africa: *Frontiers in Earth Science*, v. 7, p. 12.

Haq, B.U., 2014, Cretaceous eustasy revisited: *Global and Planetary Change*, v. 113, p. 44-58.

Haq, B.U., Hardenbol, J., and Vail, P.R., 1987, Chronology of fluctuating sea levels since the Triassic (250 million years ago to present): *Science*, v. 235, p. 1156- 1167.

Harding, R., and Huuse, M., 2015, Salt on the move: Multi stage evolution of salt diapirs in the Netherlands North Sea: *Marine and Petroleum Geology*, v. 61, p. 39-55.

Hardy, S., and Finch, E., 2005, Discrete-element modelling of detachment folding: *Basin Research*, v. 17(4), p. 507-520.

Hardy, S., and Finch, E., 2006, Discrete element modelling of the influence of cover strength on basement-involved fault-propagation folding: *Tectonophysics*, v. 415, p. 225-238.

Harms, G.L., 2015, Numerical modelling of salt diapirism and the temperature field during thin-skinned extension; in search of geothermal and hydrocarbon energy sources. MS Thesis. Utrecht University, The Netherlands, 32 p.

Harris, G. D., and A. C. Veatch, 1899, A preliminary report on the geology of Louisiana, in Geological Survey of Louisiana report: Baton Rouge: Baton Rouge, LA, Louisiana Geological Survey, Part 5, Geology and Agriculture, p. 9–138.

Harris, P.T., and Whiteway, T., 2011, Global distribution of large submarine canyons: geomorphic differences between active and passive continental margins: *Marine Geology*, v. 285, p. 69–86.

Haughton, P.D.W., 1994, Deposits of deflected and ponded turbidity currents, Sorbas basin, Southeast Spain: *Journal of Sedimentary Petrology*, v. B64, p. 233–246.

Haughton, P.D.W., Barker, S.P., and McCaffrey, W.D., 2003, Linked debrites in sand-rich turbidite systems - origin and significance: *Sedimentology*, v. 50 (3), p. 459–482.

Haughton, P., Davis, C., McCaffrey, W., and Barker, S., 2009, Hybrid sediment gravity flow deposits - Classification, origin and significance: *Marine and Petroleum Geology*, v. 26, p. 1900–1918.

Hay, D.C., and Prather, B.E., 2012, Stratigraphic evolution of a tortuous corridor from the stepped slope of Angola. Application of the principles of seismic geomorphology to continental slope and base-of-slope systems: Case studies from sea floor and near-sea floor analogs: *SEPM Special Publication*, v. 99, p. 163-180.

He, L., Zhao, L., Li, J., Ma, J., Lui, R., Wang, S., and Zhao, W., 2014, Complex relationship between porosity and permeability of carbonate reservoirs and its controlling factors: A case study of platform facies in Pre-Caspian Basin: *Petroleum Exploration and Development*, v. 41 (2), p. 225-234.

Hearon, T.E., Rowan, M.G., Giles, K.A., and Hart, W.H., 2014, Halokinetic deformation adjacent to the deepwater Auger diapir, Garden Banks 470, northern Gulf of Mexico: Testing the applicability of an outcrop-based model using subsurface data: *Interpretation*, v. 2 (4), p. 57-76.

Hearon, T.E., Rowan, M.G., Lawton, T.F., Hannah, P.T., and Giles, K.A., 2015, Geology and tectonics of Neoproterozoic salt diapirs and salt sheets in the eastern Willouran Ranges, South Australia: *Basin Research*, v. 27, p. 183–207.

Heidari, M., Nikolinakou, M.A., Hudec, M.R., and Flemings, P.B., 2016, Geomechanical analysis of a welding salt layer and its effects on adjacent sediments: *Tectonophysics*, v. 683, p. 172-181.

Heidari, M., Nikolinakou, M.A., Flemmings, P.B. and Hudec, M.R., 2017, A simplified stress analysis of rising salt domes: *Basin Research*, v. 29 (3), p. 363-376.

Heidari, M., Nikolinakou, M.A., Hudec, M.R., and Flemmings, P.B., 2019, Influence of a reservoir bed on diapirism and drilling hazards near a salt diapir: a geomechanical approach: *Petroleum Geoscience*, v. 25 (3), p. 282-297.

Heiniö, P., and Davies, R.J., 2007, Knickpoint migration in submarine channels in response to fold growth, western Niger Delta: *Marine and Petroleum Geology*, v. 24 (6-9), p. 434-449.

- Heinrich, P., and Piatanesi, A., 2000, Near-field modeling of the July 17, 1998 tsunami in Papua New Guinea: *Geophysical Research Letters*, v. 27 (19), p. 3037–3040.
- Hempton, M., Marshall, J., Sadler, S., Hogg, N., Charles, R., and Harvey, C., 2005. Turbidite reservoirs of the Sele Formation, Central North Sea: geological challenges for improving production, in: Dore, A.G., and Vining, B.A., eds., *Petroleum Geology: North-west Europe and Global Perspectives*, Proceedings of the 6th Petroleum Geology Conference, p. 449-459.
- Hernandez, K., Mitchell, N.C., and Huuse, M., 2018, Deriving relationships between diapir spacing and salt-layer thickness in the Southern North Sea, in: Kilhams, B., Kukla, P.A., Mazur, S., McKie, T., Mijnlieff, H.F., and van Ojik, K., eds., *Mesozoic Resource Potential in the Southern Permian Basin*, Geological Society, London, Special Publications, v. 469, 119-137.
- Hesse, R., 1964, Herkunft und Transport der Sedimente im bayerischen Flyschtrog: *Zeitschrift der Deutschen Geologischen Gesellschaft*, p. 403–426.
- Hiscott, R.N., 1994, Loss of capacity, not competence, as the fundamental process governing deposition from turbidity currents: *Journal of Sedimentary Research*, v. 64, p. 209–214.
- Hiscott, R.N., and Middleton, G. V., 1980, Fabric of coarse deep-water sandstones Tourelle Formation, Quebec, Canada: *Journal of Sedimentary Research*, v. 50, no. 3.
- Hiscott, R.N., Pickering, K.T. and Beeden, D.R., 1986, Progressive filling of a confined Middle Ordovician foreland basin associated with the Taconic Orogeny, Quebec, Canada: *Foreland Basins*, p. 307-325.
- Hiscott, R.N., Hall, F.R. and Pirmez, C., 1997, Turbidity current overspill from Amazon Channel: texture of silt/sand load, paleoflow from anisotropy of magnetic susceptibility, and implications for flow processes, in: Flood, R.D., Piper, D.J.W., Klaus, A., and Peterson, L.C., eds., *Proceedings of the Ocean Drilling Program*, v. 155, p. 53–78.
- Hodgetts, D., 2013, Laser scanning and digital outcrop geology in the petroleum industry: A review: *Marine and Petroleum Geology*, v. 46, p. 335-354.
- Hodgkins, M., and O'Brien, M.J., 1994, Salt sill deformation and its implications for subsalt exploration: *The Leading Edge*, v. 13 (8), p. 849-851.
- Hodgson, D.M., 2009, Distribution and origin of hybrid beds in sand-rich submarine fans of the Tanqua depocenter, Karoo Basin, South Africa: *Marine and Petroleum Geology*, v. 26, p. 1940-1956.
- Hodgson, D.M., and Haughton, P.D.W., 2004, Impact of syndepositional faulting on gravity current behaviour and deep-water stratigraphy: Tabernas-Sorbas Basin, SE Spain, in: Lomas, S.A., and Joseph, P., eds., *Confined Turbidite Systems: Geological Society of London, Special Publication* v. 222, p. 135-158.
- Hodgson, D.M., Flint, S.S., Hodgetts, D., Drinkwater, N.J., Johannessen, E.P., and Luthi, S.M., 2006, Stratigraphic evolution of fine-grained submarine fan systems, Tanqua Depocenter, Karoo Basin, South Africa: *Journal of Sedimentary Research*, v. 76, p. 20–40.

Hodgson, D.M., Di Clema, C.N., Brunt, R.L., and Flint, S.S., 2011, Submarine slope degradation and aggradation and the stratigraphic evolution of channel-levee systems: *Geological Society of London Journal*, v. 168, p. 625-628.

Hodgson, D.M., Kane, I.A., Flint, S.S., Brunt, R.L., and Ortiz-Karpf, A., 2016, Time-transgressive confinement on the slope and the progradation of basin-floor fans: implications for the sequence stratigraphy of deep-water deposits: *Journal of Sedimentary Research*, v. 86, p. 73-86.

Hodgson, D.M., Brooks, H.L., Ortiz-Karpf, A., Sychala, Y., Lee, D.R., and Jackson, C.L., 2019, Entrainment and abrasion of megaclasts during submarine landsliding and their impact on flow behaviour: *Geological Society, London, Special Publications*, v. 477, p. 223-240.

Hodgson, N.A., Farnsworth, J., and Fraser, A.J., 1992, Salt-related tectonics, sedimentation and hydrocarbon plays in the Central Graben, North Sea, UKCS, in: Hardman, R.F.P., ed., *Exploration Britain: Geological Insights for the Next Decade: Geological Society of London, Special Publications*, v. 67, p. 31-63.

Hofstra, M., Hodgson, D.M., Peakall, J., and Flint, S.S., 2015, Giant scour-fills in ancient channel-lobe transition zones: Formative processes and depositional architecture: *Sedimentary Geology*, v. 329, p. 98-114.

Hofstra, M., Peakall, J., Hodgson, D.M., and Stevenson, C.J., 2018, Architecture and morphodynamics of subcritical sediment waves in an ancient channel-lobe transition zone: *Sedimentology*, v. 65, no. 7, p. 2339-2367.

Hoiland, O., Kristensen, J., Monsen, T., 1993, Mesozoic evolution of the Jaeren high area, Norwegian central North Sea, in: Parker, J.R. (Ed.), *Petroleum Geology of Northwest Europe: Proceedings of the 4th Conference*, Geological Society of London, p. 1189-1195.

Hon, K. D., 2001, Salt-influenced growth-stratal geometries and structure of the Muerto Formation adjacent to an ancient secondary salt weld, La Popa Basin, Nuevo Leon, Mexico. M.S. Thesis. New Mexico State University, USA.

Hossack, J., 1995, Geometric rules of section balancing for salt structures, in: Jackson, M.P.A., Roberts, D.G., and Snelson, S., eds., *Salt tectonics: A global perspective: Tulsa, OK, AAPG Memoir* v. 65, p. 29-40.

Hossain, S., 2019, Application of seismic attribute analysis in fluvial seismic geomorphology; *Journal of Petroleum Exploration and Production Technology*.

Howard, J. A., and Bredeson, D.H., 1971, Structural Development of Some Shallow Domes in Louisiana Miocene Productive Belt: *AAPG Bulletin*, v. 55 (2), p. 204-226.

Howarth, V., and Alves, T.M., 2016, Fluid flow through carbonate platforms as evidence for deep-seated reservoirs in Northwest Australia: *Marine Geology*, v. 380, p. 17-43.

Howell, D.G., and Normark, W.R., 1982, Sedimentology of submarine fans: *American AAPG Memoir*, v. 31, p. 365-404.

- Howlett, D.M., Gawthorpe, R.L., Ge, Z., Rotevatn, A., and Jackson, C, A-L., 2020, Turbidites, topography and tectonics: Evolution of submarine channel-lobe systems in the salt-influenced Kwanza Basin, offshore Angola: *Basin Research*, v. 33 (2), p. 1076-1110.
- Hsü K.J., 1972, Origin of saline giants: a critical review after the discovery of the Mediterranean evaporite: *Earth-Science Reviews*, v. 8(4), p. 371-396.
- Hsu, S-K., Kuo, J., Yeh, Y-C., Tsai, C-H., Doo, W., Ku, C-Y., and Sibuet, J-C., 2008, Turbidity Currents, Submarine Landslides and the 2006 Pingtung Earthquakes off SW Taiwan: *Terrestrial Atmospheric and Oceanic Sciences*, v. 1(6), p. 1229.
- Hubbard, S.M., Romans, B.W., and Graham, S.A., 2008, Deep-water foreland basin deposits of the Cerro Toro Formation, Magallanes basin, Chile: architectural elements of a sinuous basin axial channel belt: *Sedimentology*, v. 55, p. 1333-1359.
- Hubbard, S.M., Covault, J.A., Fildani, A. and Romans, B.W., 2014, Sediment transfer and deposition in slope channels: Deciphering the record of enigmatic deep-sea processes from outcrop: *GSA Bulletin*, v. 126, p. 857-871.
- Hudec, M.R., and Jackson, M.P.A., 2004, Regional restoration across the Kwanza Basin, Angola: salt tectonics triggered by repeated uplift of a metastable passive margin: *AAPG Bulletin* v. 88, p. 971–990.
- Hudec, M.R., Jackson, M.P.A., 2006, Growth of allochthonous salt sheets in passive margins and orogens: *AAPG Bulletin* v. 90, p. 1535–1564.
- Hudec, M., and Jackson, M., 2007, Terra infirma: Understanding salt tectonics: *Earth-Science Reviews*, v. 82, p. 1-28.
- Hudec, M. R., and M. P. A. Jackson, 2011, *The salt mine: a digital atlas of salt tectonics*: Austin, TX, The University of Texas at Austin, Bureau of Economic Geology, Udden Book Series 5; Tulsa, OK, AAPG Memoir 99, 305 p.
- Hudec, M.R., Jackson, M.P.A., and Schultz-Ela, D.D., 2009, The paradox of minibasin subsidence into salt: Clues to the evolution of crustal basins: *GSA Bulletin*, 121 (1-2), 201-221.
- Hudec, M., Norton, I.O., Jackson, M.P.A., and Peel, F.J., 2013, Jurassic evolution of the Gulf of Mexico salt basin: *AAPG Bulletin*, v. 97 (10), p. 1638-1710.
- Hughes Clarke, J.E., 2016, First wide-angle view of channelized turbidity currents links migrating cyclic steps to flow characteristics: *Nature Communications*, v. 7, p. 1-13.
- Hunt, J.E., Talling, P.J., Clare, M.A., Jarvis, I., and Wynn, R.B., 2014, Long-term (17 Ma) turbidite record of the timing and frequency of large flank collapses of the Canary Islands: *Geochemistry, Geophysics, Geosystems*, v. 15 (8), p. 3322–3345.
- Hunnicut, L.A., 1998, Tectonostratigraphic interpretation of Upper Cretaceous to Lower Tertiary limestone lentils within the Potrerillos Formation surrounding El Papalote diapir, La Popa basin, Nuevo Leon, Mexico. MS thesis. New Mexico State University, USA.

Ilstad, T., Marr, J.G., Elverhøi, A., and Harbitz, C.B., 2004, Laboratory studies of subaqueous debris flows by measurements of pore-fluid pressure and total stress: *Marine Geology*, v. 213 (1-4) p. 403–414.

Imber, J., Tuckwell, G.W., Childs, C., Walsh, J.J., Manzocchi, T., Heath, A.E., Bonson, C.G., and Strand, J., 2004, Three-dimensional distinct element modelling of relay growth and breaching along normal faults: *Journal of Structural Geology*, v. 26, p. 1897–1911.

Inverson, R.M., 1997, The physics of debris flows: *Reviews of Geophysics*, v. 35, p. 245- 296.

Inverson, R.M., Logan, M., Lahusen, R.G., and Berti, M., 2010, The perfect debris flow? Aggregated results from 28 largescale experiments: *Journal of Geophysical Research: Earth Surface*, v. 115, p. 1-29.

Ismail-Zadeh, A.T., Talbot, C.J., and Volozh, Y.A., 2001, Dynamic restoration of profiles across diapiric salt structures: numerical approach and its applications: *Tectonophysics*, v. 337, p. 23-38.

Ismail-Zadeh, A.T., Tsepelev, I., Talbot, C., and Korotkii, A., 2004, Three-dimensional forward and backward modelling of diapirism: numerical approach and its applicability to the evolution of salt structures in the Pricaspian basin: *Tectonophysics*, v. 387, p. 81-103.

Jackson, C.A-L, 2011, Three-dimensional seismic analysis of megaclast deformation within a mass transport deposit; implications for debris flow kinematics: *Geology*, v. 39, p. 203-206.

Jackson, C.A.L., 2012, The initiation of submarine slope failure and the emplacement of mass transport complexes in salt-related minibasins: A three-dimensional seismic- reflection case study from the Santos Basin, offshore Brazil: *Geological Society of America Bulletin*, v. 124, p. 746-761.

Jackson, C.A.L., and Johnson, H.D., 2009, Sustained turbidity currents and their interaction with debrite-related topography; Labuan Island: *Sedimentary Geology*, v. 219, p. 77-96.

Jackson, C.A.L., Gawthorpe, R.L., and Sharp, I.R., 2002, Growth and linkage of the East Tanka fault zone, Suez rift: structural style and syn-rift stratigraphic response: *Geological Society of London Journal*, v. 159, p. 175-187.

Jackson, C.A.L., Gawthorpe, R.L., Carr, I.D., and Sharp, I.R., 2005, Normal faulting as a control on the stratigraphic development of shallow marine syn-rift sequences: the Nukhul and Lower Rudeis Formations, Hammam Faraun fault block, Suez Rift, Egypt: *Sedimentology*, v. 52, p. 313-338.

Jackson, C.A.L., Zakaria, A.A., Johnson, H.D., Tongkul, F., and Crevello, P.D., 2009, Sedimentology, stratigraphic occurrence and origin of linked debrites in the West Crocker Formation (Oligo-Miocene), Sabah, NW Borneo: *Marine and Petroleum Geology*, v. 26, p. 1957-1973.

Jackson, C. A.L., Jackson, M.P.A., Hudec, M.R., and Rodriguez, C.R., 2014, Internal structure, kinematics, and growth of a salt wall: Insights from 3-D seismic data: *Geology*, v. 42, pp. 307-310.

- Jackson, C., A-L., Rodriguez, C.R., Rotevatn, A., and Bell, R.E., 2014, Geological and geophysical expression of a primary salt weld: An example from the Santos Basin, Brazil: *Interpretation*, v. 2 (4) p. 77-89.
- Jackson, C.A.L., M.P.A. Jackson, M.R. Hudec, and Rodriguez, C.R., 2015, Enigmatic structures within salt walls of the Santos Basin—Part 1: Geometry and kinematics from 3D seismic reflection and well data: *Journal of Structural Geology*, v. 75, p. 135-162.
- Jackson, C. A-L., and Lewis, M.M., 2016, Structural style and evolution of a salt-influenced rift basin margin; the impact of variations in salt composition and the role of polyphase extension: *Basin Research*, v. 28 (1), p. 81-102.
- Jackson, C.A-L., Zhang, Y., Herron, D.A., and Fitch, P.J.R., 2019, Subsurface expression of a salt weld, Gulf of Mexico: *Petroleum Geoscience*, v. 25 (1), p. 102-111.
- Jackson, C. A-L., Duffy, O.B., Fernandez, N., Dooley, T.P., Hudec, M.R., Jackson, M.P.A. and Burg, G., 2020, The stratigraphic record of minibasin subsidence, Precaspian Basin, Kazakhstan: *Basin Research*, v 32 (4), p. 739-763.
- Jackson, J.A. Ed., 1997, *Glossary of Geology*, Fourth Edition. American Geological Institute, Alexandria, Virginia. 769 p.
- Jackson, M.P.A., 1995, Retrospective salt tectonics, in: Jackson, M.P.A., Roberts, D.G., Snelson, S., eds., *Salt Tectonics: a Global Perspective: AAPG Memoir*, v. 65, p. 1–28.
- Jackson, M.P.A., 1997, *Conceptual Breakthroughs in Salt Tectonics: A Historical Review, 1856–1993. Report of Investigations*, v. 246. The University of Texas at Austin, Bureau of Economic Geology. 51 p.
- Jackson, M.P.A., and Harrison, J.C., 2006, An allochthonous salt canopy on Axel Heiberg Island, Sverdrup Basin, Arctic Canada: *Geology*, v. 34, p. 1045–1048.
- Jackson, M.P.A., and Hudec, M.R., 2017, *Salt Tectonics: Principles and Practise*: Cambridge University Press, p. 515.
- Jackson, M.P.A., and Talbot, C.J., 1986, External shapes, strain rates, and dynamics of salt structures: *GSA Bulletin*, v. 97 (3), p. 305-323.
- Jackson, M. P. A., and Talbot, C.J., 1989a, Anatomy of mushroom- shaped diapirs: *Journal of Structural Geology*, v. 11, p. 211–230.
- Jackson, M. P. A., and Talbot, C.J., 1989b, Salt canopies: Society of Economic Paleontologists and Mineralogists Gulf Coast Section, 10th annual research conference program and extended abstracts, p. 72–78.
- Jackson, M. P. A., and Talbot, C.J., 1991, A glossary of salt tectonics: Austin, TX, The University of Texas at Austin, Bureau of Economic Geology, *Geologic Circular* 91-4, 44 p.
- Jackson, M.P.A., and Vendeville, B.C., 1994, Regional extension as a geologic trigger for diapirism: *GSA Bulletin*, v. 106, p. 57–73.



- Jackson, M. P. A., Talbot, C.J., and Cornelius, R.R., 1988, Centrifuge modeling of the effects of aggradation and progradation on syndepositional salt structures: Austin, TX, The University of Texas at Austin, Bureau of Economic Geology, Report of Investigations 173, 93 p.
- Jackson, M.P.A., Cornelius, R.R., Craig, C.H., Gansser, A., Stöcklin, J., and Talbot, C.J., 1990, Salt diapirs of the Great Kavir, Central Iran: Boulder, CO, Geological Society of America, Memoir 177, 139 p.
- Jackson, M.P.A, Vendeville, B.C., and Schultz-Ela, D.D., 1994, Structural dynamics of salt systems: Annual Review of Earth and Planetary Sciences, v. 22, p. 93–117.
- Jackson, M.P.A., Cramez, C., and Fonck, J.M., 2000, Role of subaerial volcanic rocks and mantle plumes in creation of South Atlantic margins: implications for salt tectonics and source rocks: Marine and Petroleum Geology, v. 17, pp. 477-498.
- Jackson, M. P. A., Hudec, M. R., and Hegarty, K. A., 2005, The great West African Tertiary coastal uplift: Fact or fiction? A perspective from the angolan divergent margin: Tectonics, v 24, p. 1–23.
- Jahani, S., Callot, J.-P., Frizon de Lamotte, D., Letouzey, J., and Leturmy, P., 2007, The salt diapirs of the eastern Fars province (Zagros, Iran): a brief outline of their past and present, in: Lacombe, O., Lavé, J., Roure, F., and Vergés, J., eds., Thrust Belts and Foreland Basins. Springer, Berlin, p. 287–306.
- Jammes, S., Mannatschal, G., Lavier, L., and Masini, E., 2009, Tectonosedimentary evolution related to extreme crustal thinning ahead of a propagating ocean: an example of the western Pyrenees: Tectonophysics, v. 28 (4), p. 1-24.
- Janocko, M., Nemec, W., Henriksen, S. and Warchol, M., 2013, The diversity of deep-water sinuous channel belts and slope valley-fill complexes: Marine and Petroleum Geology, v. 41, p.7-34.
- Jegou, I., Savoye, B., Pirmez, C. and Droz, L., 2008, Channel-mouth lobe complex of the recent Amazon Fan: the missing piece: Marine Geology, v. 252, p. 62-77.
- Jennette, D.C., Garfield, T.R., Mohrig, D.C., and Cayley, G.T., 2000, The interaction of shelf accommodation, sediment supply and sea level in controlling the facies, architecture and sequence stacking patterns of the Tay and Forties/Sele basin- floor fans, Central North Sea, in: Weimer, P., Slatt, R.M., Coleman, J., Rosen, N.C., Nelson, H., Bouma, A.H., Styzen, M.J., Lawrence, D.T., eds., Deep Water Reservoirs of the World. GCSSEPM Foundation 20th Annual Bob F. Perkins Research Conference, pp. 402-421.
- Jervey, M.T., 1988, Quantitative geological modeling of siliciclastic rock sequences and their seismic expression. Sea-Level Changes-An integrated approach. SEPM Special Publication, v.42, p. 47–69.
- Jobe, Z.R., Lowe, D.R., and Morris, W.R., 2012, Climbing-ripple successions in turbidite systems: depositional environments, sedimentation and accumulation times: Sedimentology, v. 59, p. 867-898.
- Jobe, Z.R., Howes, N.C., and Auchter, N.C., 2016, Comparing submarine and fluvial channel kinematics: Implications for stratigraphic architecture: Geology, v. 44, p. 931–934.

Jobe, Z.R., Sylvester, Z., Howes, N., Pirmez, C., Parker, A., Cantelli, A., Smith, R., Wolinsky, M.A., O'Byrne, C., Slowey, N., and Prather, B., 2017a, High-resolution, millennial-scale patterns of bed compensation on a sand-rich intraslope submarine fan, western Niger Delta slope: *Geological Society of America, Bulletin*, v. 129, p. 23-37.

Jobe, Z., Sylvester, Z., Bolla Pittaluga, M., Frascati, A., Pirmez, C., and Minisini, D., 2017b, Facies architecture of submarine channel deposits on the western Niger Delta slope: Implications for grain-size and density stratification in turbidity currents: *Journal of Geophysical Research: Earth Surface*, v. 122, p. 473-491.

Jobe, Z.R., Howes, N., Romans, B.W., and Covault, J.A., 2018, Volume and recurrence of submarine-fan-building turbidity currents: *The Depositional Record*, v. 4, p. 160-176.

Johnson, H., 1987, Seismic expression of major chalk reworking events in the Palaeocene of the central North Sea, in: Brooks J., and Glennie K.W., eds., *Petroleum Geology of North West Europe: Proceedings of the 3rd Conference*. Graham and Trotman, London, 591–598.

Johnson, T., Brown, M., Kaus, B., and VanTongeren, J.A., 2014, Delamination and recycling of Archaean crust caused by gravitational instabilities: *Nature Geoscience*, v. 7, p. 47–52.

Johnson, S.D., Flint, S., Hinds, D. and De Ville Wickens, H., 2001, Anatomy, geometry and sequence stratigraphy of basin floor to slope turbidite systems, Tanqua Karoo, South Africa: *Sedimentology*, v. 48, p. 987-1023.

Jones, G., Mayall, M., and Lonergan, L., 2012, Contrasting depositional styles on a slope system and their control by salt tectonics—Through-going channels, ponded fans and mass transport complexes, in: Rosen, N.C., Weimer, P., Coutes Dos Anjos, S., Henrickson, E., Marques, E., Mayall, M., and Fillon, R., eds., *New understanding of the petroleum systems of continental margins of the world: 32nd Annual Gulf Coast Section SEPM Foundation Bob F. Perkins Research Conference*, Houston, Texas, December, v. 2–5, p. 503–533.

Jones, I.F., and Davison, I., 2014, Seismic imaging in and around salt bodies: *Interpretation*. v. 2, p. 1-20.

Jones, R.W., 1959, Origin of Salt Anticlines of Paradox Basin: *AAPG Bulletin*, v. 43 (8), p. 1869-1895.

Jones, R.W., and Milton, N. J., 1994. Sequence development during uplift: Palaeogene stratigraphy and relative sea level history of the Outer Moray Firth, UK North Sea: *Marine and Petroleum Geology*, v. 11, p. 157 –165.

Jordan, O.D., and Mountney, N.P., 2012, Sequence Stratigraphic Evolution and Cyclicity of An Ancient Coastal Desert System: The Pennsylvanian-Permian Lower Cutler Beds, Paradox Basin, Utah, U.S.A.: *Journal of Sedimentary Research*, v. 82 (10), p. 755-780.

Joseph, P., and Lomas, S.A., 2004, Deep-water sedimentation in the Alpine Foreland Basin of SE France: New perspectives on the Grès d'Annot and related systems—an introduction: *Geological Society, London, Special Publications 221*, p. 1-16.

Kane, I.A., and Clare, M.A., 2019, Dispersion, accumulation, and the ultimate fate of microplastics in deep-marine environments: a review and future directions: *Frontiers in Earth Science*, v. 7, p. 80.

Kane, I.A., and Hodgson, D.M., 2011, Sedimentological criteria to differentiate submarine channel levee subenvironments: Exhumed examples from the Rosario Fm. (Upper Cretaceous) of Baja California, Mexico, and the Fort Brown Fm. (Permian), Karoo Basin, S. Africa: *Marine and Petroleum Geology*, v. 28, p. 807-823.

Kane, I.A. and Pontén, A.S.M., 2012, Submarine transitional flow deposits in the Paleogene Gulf of Mexico: *Geology*, v. 40, p. 1119-1122.

Kane, I.A., Kneller, B.C., Dykstra, M., Kassem, A., and McCaffrey, W.D., 2007, Anatomy of a submarine channel-lee: An example from Upper Cretaceous slope sediments, Rosario Formation, Baja California, Mexico: *Marine and Petroleum Geology*, v. 24, p. 540-563.

Kane, I.A., McCaffrey, W.D., and Peakall, J., 2008, Controls on sinuosity evolution within submarine channels: *Geology*, v. 36, p.287-290.

Kane, I.A., Dykstra, M.L., Kneller, B.C., Tremblay, S., and McCaffrey, W.D., 2009, Architecture of a coarse-grained channel-levée system: The Rosario Formation, Baja California, Mexico: *Sedimentology*, v. 56 (7), p. 2207–2234.

Kane, I.A., McCaffrey, W.D., and Martinsen, O.J., 2009, Allogenic vs. Autogenic Controls on Megaflute Formation: *Journal of Sedimentary Research*, v. 79, p. 643-651.

Kane, I.A., Catterall, V., McCaffrey, W.D. and Martinsen, O.J., 2010, Submarine channel response to intrabasinal tectonics: The influence of lateral tilt: *American Association of Petroleum Geologists, Bulletin*, v. 94, p. 189-219.

Kane, I.A., McGee, D.T., and Jobe, Z.R., 2012, Halokinetic effects on slope equilibrium profiles: submarine channel evolution and implications for facies architecture in Magnolia Field, Gulf of Mexico, in: Alsop, G.I., Hartley, A.J., Grant, N.T., and Hodgkinson, R., eds., *Salt Tectonics, Sediments and Prospectivity*, Geological Society of London, p. 289–302.

Kane, I.A., Pontén, A.S.M., Vangdal, B., Eggenhuisen, J.T., Hodgson, D.M., and Spychala, Y.T., 2017, The stratigraphic record and processes of turbidity current transformation across deep-marine lobes: *Sedimentology*, v. 64, p. 1236–1273.

Kane, I.A., Clare, M.A., Miramontes, E., Wogelius, R., Rothwell, J.J., Garreau, P., and Pohl, F., 2020, Seafloor microplastic hotspot controlled by deep-sea circulation: *Science*, v. 368 (6495), p. 1140-1145.

Kane, I.A., Ayckbourn, A., Bell, D., Cumberpatch, Z.A., Ferguson, R.A., Fuhrmann, A., Martínez-Doñate, A. and Soutter, E.L., in prep, Bed-scale indicators of sediment gravity flow sedimentation against topography: *Frontiers in Geoscience*, in preparation.

Karam, P., and Mitra, S., 2016, Experimental studies of the controls of the geometry and evolution of salt diapirs: *Marine and Petroleum Geology*, v. 77, p. 1309-1322.

- Katz, O., Morgan, J.K., Aharonov, E., and Dugan, B., 2014, Controls on the size and geometry of landslides: Insights from discrete element numerical simulations: *Geomorphology*, v. 220, p. 104-113.
- Kaus, B.J.P., 2010, Factors that control the angle of shear bands in geodynamic numerical models of brittle deformation: *Tectonophysics*, v. 484, p. 36-47.
- Kehle, R. O., 1970, Analysis of gravity sliding and orogenic translation: *GSA Bulletin*, v. 81, p. 1641-1664.
- Kehle, R. O., 1988, The origin of salt structures, in: Schreiber, B.C., ed., *Evaporites and hydrocarbons*: New York, Columbia University Press, p. 345-404.
- Kendrick, J. W., 2000, Turbidite reservoir architecture in the northern Gulf of Mexico deep-water: Insights from the development of Auger, Tahoe, and Ram/Powell fields, in *Deep-water reservoirs of the world: Society of Economic Paleontologists and Mineralogists Gulf Coast Section, 20th annual research conference*, p. 450-468.
- Kenyon, N.H., Millington, J., Droz, L. and Ivanov, M.K., 1995, Scour holes in a channel-lobe transition zone on the Rhône Cone: in *Atlas of Deep Water Environments*, Springer, Dordrech, p. 212 - 215.
- Kernen, R.A., Giles, K.A., Rowan, M.G., Lawton, T.F., and Hearon, T.E., 2012, Depositional and halokinetic-sequence stratigraphy of the Neoproterozoic Wonoka Formation adjacent to Patawarta allochthonous salt sheet, Central Flinders Ranges, South Australia: *Geological Society of London, Special Publication*, v. 363, p. 81-105.
- Kernen, R.A., Giles, K.A., Poe, P.L., Gannaway Dalton, C.E., Rowan, M.G., Fiduk, J.C., and Hearon, T.E., 2020, Origin of the Neoproterozoic rim dolomite as lateral carbonate caprock, Patawarta salt sheet, Flinders Ranges, South Australia: *Australian Journal of Earth Sciences*, v. 6, p. 815-832.
- Kilhams, B., 2011, An integrated characterisation of the Paleocene Submarine Fan Systems (Lista and Maureen Formations) in the central Graben of the North Sea. Ph.D. Thesis. University of Aberdeen, UK.
- Kilhams, B., Godfrey, S., Hartley, A., and Huuse, M., 2011, An integrated 3D seismic, petrophysical and analogue core study of the Mid-Eocene Grid channel complex in the greater Nelson Field area, UK Central North Sea: *Petroleum Geoscience*, v. 17 (2), p. 127-142.
- Kilhams, B., Hartley, A., Huuse, M., and Davis, C., 2012, Characterizing the Paleocene turbidites of the North Sea: the Mey Sandstone Member, Lista Formation, UK Central Graben: *Petroleum Geoscience*, v. 18, p. 337-354.
- Kilhams, B.A., Morton, A., Borella, R., Wilkins, A., and Hurst, A., 2014, Understanding the provenance and reservoir quality of the Sele Formation sandstones of the UK Central Graben utilizing detrital garnet suites, in: Scott, R.A., Smyth, H.R., Morton, A.C., and Richardson, N., eds., *Sediment Provenance Studies in Hydrocarbon Exploration and Production*: Geological Society, London, Special Publications, v. 386, p. 129-142.

Kilhams, B.A., Hartley, A., Huuse, M., and Davis, C., 2015, Characterizing the Paleocene turbidites of the North Sea: Maureen Formation, UK Central Graben, in: McKie, T., Rose, P.T.S., Hartley, A.J., Jones, D.W., and Armstrong, T.L., eds., Tertiary Deep-Marine Reservoirs of the North Sea Region: Geological Society of London, Special Publications 403, p. 43-62.

Kneller, B. C., 1995, Beyond the turbidite paradigm: physical models for deposition of turbidites and their implications for reservoir prediction, in: Hartley, A., and Prosser, D.J., eds., Characterisation of Deep Marine Clastic Systems: Geological Society of London, Special Publications, v. 94, p. 29-46.

Kneller, B., 2003, The influence of flow parameters on turbidite slope channel architecture: Marine and Petroleum Geology, v. 20, p. 901-910.

Kneller, B.C., and Bramney, M.J., 1995, Sustained high-density turbidity currents and the deposition of thick massive sands: Sedimentology, v. 42, p. 607-616.

Kneller, B. and Buckee, C., 2000, The structure and fluid mechanics of turbidity currents: a review of some recent studies and their geological implications: Sedimentology, v. 47 (1), p. 62-94.

Kneller, B.C., and McCaffrey, W.D., 1995, Modelling the effects of salt-induced topography on deposition from turbidity currents: SEPM, Gulf Coast Section, p. 137- 145.

Kneller, B. C., and McCaffrey, W.D., 1999, Depositional effects of flow non-uniformity and stratification within turbidity currents approaching a bounding slope: deflection, reflection and facies variation: Journal of Sedimentary Research, v. 69, p. 980-991.

Kneller, B.C., Edwards, D., McCaffrey, W.D., and Moore, R., 1991, Oblique reflection of turbidity currents: Geology, v. 19, p. 250-252.

Kneller, B., Dykstra, M., Fairweather, L., and Milana, J.P., 2016, Mass-transport and slope accommodation: implications for turbidite sandstone reservoirs: AAPG Bulletin, v. 100, p. 213-235.

Kneller, B., Bozetti, G., Callow, R., Dykstra, M., Hansen, L., Kane, I., Li, P., McArthur, A., Santa Catharina, A., dos Santos, T. and Thompson, P., 2020, Architecture, process and environmental diversity in a Late Cretaceous slope channel system: Journal of Sedimentary Research, v. 90 (1), p. 1-26.

Knox R.W., Morton A.C., and Harland R., 1981, Stratigraphical relationships of Palaeocene Sands in the UK Sector of the Central North Sea, in: Illing L.V., and Hobson G.D., eds., Petroleum Geology of the Continental Shelf of Northwest Europe. Heyden, London, p. 267-281.

Koestler, A.G., and Ehrmann, W.U., 1991, Description of brittle extensional features in chalk on the crest of a salt ridge (NW Germany), in: Roberts, A.M., Yielding, G., and Freeman, B., eds., The Geometry of Normal Faults: Geological Society, London, Special Publications, v. 56, p. 113-123.

Kolla, V., Bourges, P., Urruty, J.-M., and Safa, P., 2001, Evolution of Deep-Water Tertiary Sinuous Channels Offshore Angola (West Africa) and Implications for Reservoir Architecture: AAPG Bulletin, v. 85 (8), p. 1373-1405.

- Koyi, H., 1998, The shaping of salt diapirs: *Journal of Structural Geology*, v. 20, p. 321–338.
- Koyi, H., Burliga, S., and Chemia, Z., 2012, Salt supply to and significance of asymmetric salt diapirs: *EGU General Assembly Conference Abstracts*, v. 14.
- Krastel, S., Schmincke, H.U. and Jacobs, C., 2001, Formation of submarine canyons on the flanks of the Canary Islands: *Geo-Marine Letters*, v. 20, p. 160-167.
- Kuenen, P.H., 1957, Sole markings of graded graywacke beds: *The Journal of Geology*, v. 65, p. 231-258.
- Kuenen, P.H. and Migliorini, C.I., 1950, Turbidity Currents as a Cause of Graded Bedding: *The Journal of Geology*, v. 58, p. 91–127.
- Kullberg, J.C., 2000, *Evolução tectónica mesozóica da Bacia Lusitaniana*. PhD Thesis. Universidade NOVA de Lisboa, Lisbon, Portugal.
- Kullberg, J.C., and Kullberg, M.C., 2017, The tectono-stratigraphic evolution of an Atlantic-type Basin: an example from the Arrabida sector of the Lusitanian Basin. *Ciencias da Terra*, v. 19, p. 53–74.
- Kullberg, J.C., Rocha, R.B., Soares, A.F., Rey, J., Terrinha, P., Callapez, P., and Martins, L., 2006., A Bacia Lusitaniana: Estratigrafia, Paleogeografia e Tectónica. in: Dias, R., Araújo, A., Terrinha, P. and Kullberg, J.C., eds., *Geologia de Portugal no contexto da Ibéria*. University of Évora, Évora, Portugal, p. 317–368.
- Kullberg, J.C., Rocha, R.B. et al. 2013. A Bacia Lusitaniana: Estratigrafia, Paleogeografia e Tectónica, in: Dias, R., Araújo, A., Terrinha, P. and Kullberg, J.C., eds., *Geologia de Portugal no contexto da Ibéria*. Escolar Editora, Lisbon, II, p. 195–350.
- Kuswandar, G.Y., Amir Hassan, M.H., Matenco, L.C., Taib, N.I., and Mustapha, K.A., 2018, Turbidite, debrite, and hybrid event beds in submarine lobe deposits of the Palaeocene to middle Eocene Kapit and Pelagus members, Belaga Formation, Sarawak, Malaysia: *Geological Journal*, v. 54 (6), p. 3421-3437.
- Laudon, R.C., 1975, Stratigraphy and petrology of the Difunta Group, La Popa and eastern Pararas Basins, northeastern Mexico. Ph.D. Thesis. University of Texas, Austin, USA.
- Laudon, R.C., 1984, Evaporite diapirs in the La Popa basin, Nuevo Leon, Mexico: *GSA Bulletin*, v. 95, p. 1219– 1225.
- Lawton, T. F., Vega, F. J., Giles, K. A., and Rosales- Dominguez, C., 2001, Stratigraphy and origin of the La Popa Basin, Nuevo León and Coahuila, Mexico, in: Bartolini, C., Buffler, R. T. and Cantú -Chapa, A., eds., *The Western Gulf of Mexico Basin: Tectonics, Sedimentary Basins, and Petroleum Systems*. AAPG, Tulsa, Memoir, v. 75, p. 219–240.
- Leeder, M.R., and Gawthorpe, R.L., 1987, Sedimentary models for extensional tilt-block/half-graben basins, in *Continental Extensional Tectonics*, eds., Coward, M.P., Dewey, J.F., and Hancock, P.L., Geological Society of London, Special Publications, v. 28, p. 139–152.

- Le Heron, D.P., Busfield, M.E., Prave, A.R., Sciences, E., Andrews, S., and Ky, S.A., 2016, Neoproterozoic ice sheets and olistoliths : multiple glacial cycles in the Kingston Peak Formation, California: *Journal of the Geological Society*, v. 171, p. 525–538.
- Lemon, N.M., 1985, Physical modeling of sedimentation adjacent to diapirs and comparison with late Precambrian Oratunga breccia body in central Flinders Ranges, South Australia: *AAPG Bulletin*, v. 69, p. 1327–1338.
- Lemon, N.M., 2000, A Neoproterozoic fringing stromatolite reef complex, Flinders Ranges, South Australia: *Precambrian Research*, v. 100, p. 109–120.
- Leppard, C.W., and Gawthorpe, R.L., 2006, Sedimentology of rift climax deep water systems: Lower Rudeis Formation, Hammam Faraun Fault Block, Suez Rift, Egypt: *Sedimentary Geology*, v. 191, p. 67–87.
- Lerche, I. and Petersen, K., 1995, *Salt and sediment dynamics*, London, 336 p.
- Lerche, I., 2010, Mud diapirs in the South Caspian Basin: dynamical and thermal effects on hydrocarbon generation and retention: *Energy Exploration and Exploitation*, v. 28 (3), p 131-146.
- Lien, T., Midtbø, R.E., and Martinsen, O.J., 2006, Depositional facies and reservoir quality of deep-marine sandstones in the Norwegian Sea: *Norwegian Journal of Geology*, v. 86 (2), p. 71–92.
- Link, T. A., 1930, Experiments relating to salt-dome structures: *AAPG Bulletin*, v. 14, p. 483–508.
- Li, S.Y., and Urai, J.L., 2016, Rheology of rock salt for salt tectonics modelling: *Petroleum Science*, v. 13, p. 712–724.
- Liu, X., and Galloway, W.E., 1997, Quantitative determination of tertiary sediment supply to the North Sea Basin: *AAPG Bulletin*, v. 81 (9), 1482-1509.
- Liu, Q., Kneller, B., Fallgatter, C., Valdez Buso, V., and Milana, J.P., 2018, Tabularity of individual turbidite beds controlled by flow efficiency and degree of confinement: *Sedimentology*, v. 65, p. 2368 - 2387.
- Liu, J., Xian, B., Ji, Y., Gong, C., Wang, J., Wang, Z., Chen, P., Song, D., Wei, W., Zhang, X., and Dou, L., 2020, Alternating of aggradation and progradation dominated clinothems and its implications for sediment delivery to deep lake: The Eocene Dongying Depression, Bohai Bay Basin, east China: *Marine and Petroleum Geology*, v. 114, p. 104-197.
- Lloyd, C., Huuse, M., Barrett, B.J., Stewart, M.A., and Newton, A.M.W., 2021, A regional CO<sub>2</sub> containment assessment on the northern Utsira Formation seal and overburden, northern North Sea: *Basin Research*, v.33 (3), p. 1985-2017.
- Locat, J. and Lee, H.J., 2002, Submarine landslides: advances and challenges: *Canadian Geotechnical Journal*, v. 39, p. 193-212.

- Lomas, S.A., and Joseph, P., 2004, Confined turbidite systems, in Lomas, S., and Joseph, P., eds., *Confined Turbidite Basins: Geological Society of London, Special Publication 222*, p. 1-7.
- Longshaw, S.M., Turner, M.J., Finch, E., and Gawthorpe, R., 2009, Discrete Element Modelling Using a Parallelised Physics Engine: Theory and Practice of Computer Graphics – Eurographics UK Chapter Proceedings, p. 207-214.
- Longshaw, S.M., Turner, M.J., and Finch, E., 2012, Visualizing a Spherical Geological Discrete Element Model of Fault Evolution: Theory and Practice of Computer Graphics – Eurographics UK Chapter Proceedings, p. 77-84.
- López-Horgue, M.A., Owen, H.G., Aranburu, A., Fernández-Mendiola, P.A. and García-Mondéjar, J., 2009, Early late Albian (Cretaceous) of the central region of the Basque-Cantabrian Basin, northern Spain: biostratigraphy based on ammonites and orbitolinids: *Cretaceous Research*, v. 30, p. 385–400.
- Lotze, F., 1953, Salzdiapirismus im nördlichen Spanien: *Deutschen Geologische Gesellschaft, Zeitschrift*, v. 105, p. 814 – 822.
- Lowe, D.R., 1979, Sediment gravity flows: their classification and some problems of application to natural flows and deposits: *SEPM Special Publication 27*, p. 75-82.
- Lowe, D.R., 1982, Sediment gravity flows: II Depositional models with special reference to the deposits of high-density turbidity currents: *Journal of Sedimentary Petrology*, v. 52, p. 279–297.
- Lowe, D.R., and Guy, M., 2000, Slurry-flow deposits in the Britannia Formation (Lower Cretaceous), North Sea: A new perspective on the turbidity current and debris flow problem: *Sedimentology*, v. 47, p. 31–70.
- Lu, C-Y., Tang, C-L., Chan, Y-C., Hu, J-C., and Chi, C-C., 2014, Forecasting landslide hazard by the 3D discrete element method: A case study of the unstable slope in the Lushan hot spring district, central Taiwan: *Engineering Geology*, v. 183, p. 14-30.
- Lukasik, J., and Simo, J.A., 2008, Controls on Carbonate Platform and Reef Development: *SEPM Special Publication*, v. 89.
- Luo, G., Nikolinakou, M.A., Flemings, P.B. and Hudec, M.R., 2012, Geomechanical modeling of stresses adjacent to salt bodies: Part 1—Uncoupled models: *AAPG Bulletin*, v. 96 (1), p. 43–64.
- Luo, G., Hudec, M.R., Flemmings, P.B. and Nikolinakou, M.A., 2017, Deformation, stress, and pore pressure in an evolving suprasalt basin: *Solid Earth*, v. 122 (7), p. 5663-5690.
- Macauley, R.V. and Hubbard, S.M., 2013, Slope channel sedimentary processes and stratigraphic stacking, Cretaceous Tres Pasos Formation slope system, Chilean Patagonia: *Marine and Petroleum Geology*, v. 41, p.146-162.
- Macdonald, H.A., Peakall, J., Wignall, P.B., and Best, J., 2011, Sedimentation in deep-sea lobe-elements: implications for the origin of thickening-upward sequences: *Journal of the Geological Society*, v. 168 (2) p. 319–332.



Machado, L.C.R., Kowsmann, R.O., Almeida, W., Murakami, C.Y., Schreiner, S., Miller, D.J. and Piauilino, P.O.V., 2004, Geometria da porção proximal do Sistema deposicional turbidítico moderno da Formação Carapebus, Bacia de Campos: modelo para heterogeneidade de reservatórios. *Bol. Geociências Petrobras* v. 12, p. 287-315.

Madof, A.S., Christie-Blick, N., and Anders, M.H., 2009, Stratigraphic controls on a salt-withdrawal intraslope minibasin, north-central Green Canyon, Gulf of Mexico: Implications for misinterpreting sea level change: *AAPG Bulletin*, v. 93, p. 636-561.

Maia da costa, A., V., Udebhulu, O., Cabral Azevedo, R., Ebecken, N., Miranda, A., De, Eston, S., De, Tomi, G., R. Meneghini, J., Nishimoto, K., Ruggiere, F., Malta, E., Élis Rocha Fernandes, M., Brandão, C. and Breda, A., 2019, Potential of storing gas with high CO<sub>2</sub> content in salt caverns built in ultra-deep water in Brazil: *Greenhouse Gas Science and Technology*, v. 9, pp. 79-94.

Maier, K.L., Fildani, A., Paull, C.K., McHargue, T.R., Graham, S.A., and Caress, D.W., 2013, Deep-sea channel evolution and stratigraphic architecture from inception to abandonment from high-resolution autonomous underwater vehicle surveys offshore central California: *Sedimentology*, v. 60(4), p. 935-960.

Maier, K.L., Roland, E.C., Walton, M.A.L., Conrad, J.E., Brothers, D.S., Dartnell, P., and Kluesner, J.W., 2018, The tectonically controlled San Gabriel channel-lobe transition zone, Catalina Basin, Southern California Borderland: *Journal of Sedimentary Research*, v. 88 (8) p. 942–959.

Maier, K.L., Gales, J., Paull, C.K., Rosenberger, K., Talling, P.J., Simmons, S.M., Gwiazda, R.H., McGann, M., Cartigny, M.J., Lundsten, E. and Anderson, K., 2019, Linking direct measurements of turbidity currents to submarine canyon-floor deposits: *Frontiers in Earth Science*, v. 7, p. 144.

Mannie, A.S., Jackson, C. A-L., and Hampson, G.J., 2014, Shallow-marine reservoir development in extensional diapir-collapse minibasins: An integrated subsurface case study from the Upper Jurassic of the Cod terrace, Norwegian North Sea: *AAPG Bulletin*, v. 98, p. 2019-2055.

Mannie, A.S., Jackson, C. A-L., Hampson, G.J., and Fraser, A.J., 2016, Tectonic controls on the spatial distribution and stratigraphic architecture of a net-transgressive shallow-marine synrift succession in a salt-influenced rift basin: Middle to Upper Jurassic, Norwegian Central North Sea: *Journal of the Geological Society*, v. 173, p. 901-915.

Marchand, A.M.E., Apps, G., Li, W., and Rotzien, J.R., 2015, Depositional processes and impact on reservoir quality in deepwater Paleogene reservoirs, US Gulf of Mexico: *AAPG Bulletin*, v. 99 (9) p. 1635–1648.

Marini, M., Milli, S., Ravnås, R., and Moscatelli, M., 2015, A comparative study of confined vs. semi-confined turbidite lobes from the Lower Messinian Laga Basin (Central Apennines, Italy): implications for assessment of reservoir architecture: *Marine and Petroleum Geology*, v. 63, p. 142–165.

Marini, M., Patacci, M., Felletti, F., and McCaffrey, W.D., 2016, Fill to spill stratigraphic evolution of a confined turbidite mini-basin succession, and its likely well bore expression: The Castagnola Fm, NW Italy: *Marine and Petroleum Geology*, v. 69, p. 94-111.

Martín-Chivelet, J., Breastegui, X., Rosales, I., Vera, J.A., Vilas, L., Caus, R., Greafe, K-I., Sergua, M., Puig, C., Mas, R., Robles, S., Floquet, M., Quesada, S., Ruiz-Ortiz, P. A., Fregenal-Martinez,

M.A., Salas, R., Garcia, A., Martin-Algaraara, A., Arias, C., Melendez, N., Chacon, B., Molina, J.M., Sanz, J.L., Castro, J.M., Garcia-Hernandez, M., Carenas, B., Garcia-Hibalgom J., and Ortega, F., 2002, Cretaceous, in: Gibbons, W., and Moreno, T., eds., *The Geology of Spain: Geological Society of London*, 668 p.

Martín-Martín, J. D., Vergés, J., Saura, E., Moragas, M., Messenger, G., Baqués, V., Razin, P., Grélaud, C., Malaval, M., Joussiaume, R., Casciello, E., Cruz-Orosa, I., and Hunt, D.W., 2017, Diapiric growth within an Early Jurassic rift basin: the Tazoult salt wall (central High Atlas, Morocco): *Tectonics*, v. 36 (1), p. 2-32.

Martinez-Doñate, A., Privat, A., Sychala, Y., Hodgson, D.M., Jackson, C. A-L., Kane, I.A., Duller, R.A., Stevenson, C., Schwarz, E., and Flint, S.S., in prep. Impact of flow processes and stratal architecture above a dynamic exhumed submarine landslide: In preparation for submission to *Sedimentology*.

Martinsen, O.J., Lien, T., and Walker, R.G., 2000, Upper Carboniferous Deep Water Sediments, Western Ireland, in: Weimer, P., eds., *Analogues for Passive Margin Turbidite Plays: Deep Water Reservoirs of the World*, v. 20.

Marr, J., Harff, P., Shanmugam, G., and Parker, G., 2001, Experiments on subaqueous sandy gravity flows: The role of clay and water content in flow dynamics and depositional structures: *GSA Bulletin*, v. 113 (11) p. 1377–1386.

Masson, D.G., van Niel, B., and Weaver, P.P.E., 1997, Flow processes and sediment deformation in the Canary Debris Flow on the NW African Continental Rise: *Sedimentary Geology*, v. 110 (3), p. 163–179.

Masson, D.G., Harbitz, C.B., Wynn, R.B., Pederson, G. and Løvholt, F., 2006, Submarine landslides: processes, triggers and hazard prediction: *Philosophical Transactions of the Royal Society* v. 364, p. 2009-2039.

Mathey, B., 1987, *Les Flyschs Crétacé supérieur des Pyrénées Basques: âge, anatomie, origine du matériel, milieu de dépôt et la relation avec l'ouverture du Golfe de Gascogne*. PhD. Thesis. Université de Bourgogne, Dijon, France p. 403.

Matthews, W.J., Hampson, G.J., Trudgill, B.D., and Underhill, J.R., 2007, Controls on fluviolacustrine reservoir distribution and architecture in passive salt- diapir provinces: insights from outcrop analogs. *AAPG Bulletin*, v. 91, p. 1367–1403.

Mattson, A.G., Royhan Gani, M., Roesler, T., Gani, N.D., and Ford, J.T., 2020, 3D mapping of intruding salt bodies in the subsurface of the Gulf of Mexico using 3D seismic data: *Results in Geophysical Sciences*, v. 1-4.

Mayall, M. and Stewart, I., 2000, The Architecture of Turbidite Slope Channels, in: Weimer, P., Slatt, R.M., Coleman, J., Rosen, N.C., Nelson, H., Bouma, A.H., Styzen, M.J. and Lawrence, D.T., eds., *20th Annual GCSSEPM Foundation Bob F. Perkins Research Conference 2000: Deep-Water Reservoirs of the World*, Houston, 3-6 December 2000, p. 578-586.

Mayall, M., Jones, E., and Casey, M., 2006, Turbidite channel reservoirs key elements in facies prediction and effective development: *Marine and Petroleum Geology*, v. 23, p. 821–841.

- Mayall, M., Lonergan, L., Bowman, A., James, S., Milles, K., Primmer, T., Pope, D., Rogers, L., and Skeene, R., 2010, The response of turbidite slope channels to growth-induced seabed topography: *AAPG, Bulletin*, v. 94, p. 1011-1030.
- McArthur, A.D., and McCaffrey, W.D., 2019, Sedimentary architecture of detached deep-marine canyons: Examples from the East Coast Basin of New Zealand: *Sedimentology*, v. 66, p. 1067-1101.
- McArthur, A., Kane, I.A., Bozetti, G., Hansen, L., and Kneller, B.C., 2020, Supercritical flows overflowing from bypass-dominated submarine channels and the development of overbank bedforms: *The Depositional Record*, v. 6 (1), p. 21-40.
- McBride, E.F., Weidie, A.E., Wolleben, J.A., and Laudon, R.C., 1974, Stratigraphy and structure of the Parras and La Popa Basins, Northeastern Mexico: *GSA Bulletin*, v. 85, p. 1603-1622.
- McCaffrey, W.D., and Kneller, B.C., 2001, Process controls on the development of stratigraphic trap potential on the margins of confined turbidite systems and aids to reservoir evaluation: *AAPG, Bulletin*, v. 85, p. 971-988.
- McGuinness, D. B. and Hossack, J.R., 1993, The development of allochthonous salt sheets as controlled by the rates of extension, sedimentation, and salt supply: *Society of Economic Paleontologists and Mineralogists Gulf Coast Section, 14th annual research conference, extended abstracts*, 127–139.
- McHargue, T., Pyrcz, M.J., Sullivan, M.D., Clark, J.D., Fildani, A., Romans, B.W., Covault, J.A., Levy, M., Posamentier, H.W., and Drinkwater, N.J., 2011, Architecture of turbidite channel systems on the continental slope: Patterns and predictions: *Marine and Petroleum Geology*, v. 28 (3) p. 728–743.
- McKie, T., Rose, P.T.S., Hartley, A.J., Jones, D.W., and Armstrong, T.L., 2015, Tertiary deep-marine reservoirs of the North Sea region: an introduction, in: McKie, T., Rose, P.T.S., Hartley, A.J., Jones, D.W., and Armstrong, T.L. eds., *Tertiary Deep-Marine Reservoirs of the North Sea Reservoirs of the North Sea*, The Geological Society of London, p. 403.
- McSaveney, M., Goff, J., Darby, D., Goldsmith, P., Barnett, A., Elliott, S., and Nongkas, M., 2000, The 17th July 1998 Tsunami, Sissano Lagoon, Papua New Guinea-evidence and initial interpretation: *Marine Geology*, v. 170, p. 81–92.
- Menard Jr, H.W., 1955, Deep-sea channels, topography, and sedimentation: *AAPG Bulletin*, v. 39, p. 236-255.
- Mercer, D.A., 2002, Analysis of growth strata of the Upper Cretaceous to Lower Paleogene Potrillo Formation adjacent to El Gordo salt diapir, La Popa basin, Nuevo Leon, Mexico. MS. thesis, New Mexico State University, USA.
- Mianaekere, V., and Adam, J., 2020, 'Halo-kinematic' sequence stratigraphic analysis adjacent to salt diapirs in the deepwater contractional province, Liguro-Provençal Basin, Western Mediterranean Sea: *Marine and Petroleum Geology*, v. 115, .104-125.
- Middleton, G. V., 1967, Experiments on density and turbidity currents: III. Deposition of sediment: *Canadian Journal of Earth Sciences*, v. 4 (3), p. 475–505.

- Middleton, G. V., 1993, Sediment deposition from turbidity currents: Review of Earth and Planetary Sciences, v. 21, p. 89–114.
- Middleton, G. V., and Hampton, M.A., 1973, Part I. Sediment gravity flows: mechanics of flow and deposition: p. 1–38.
- Milliman, J.D. and Syvitski, J.P.M., 1992, Geomorphic/tectonic control of sediment discharge to the ocean: The importance of small mountainous rivers: *The Journal of Geology*, v. 100, p. 525–544.
- Millington, J.J., and Clark, J.D., 1995, The Charo/Arro canyon-mouth sheet system, South-Central Pyrenees, Spain: A structurally influenced zone of sediment dispersal: *Journal of Sedimentary Research*, v. 65 (4) p. 443–454.
- Milton N. J., Bertram G. T., and Vann I. R., 1990, Early Palaeogene tectonics and sedimentation in the Central North Sea, in: Hardman R. F. P., and Brooks J., eds, *Tectonic Events Responsible for Britain's Oil and Gas Reserves*. Geological Society, London, Special Publications, v. 55, p. 339–351.
- Mitchell, S.F., Pickerill, R.K., and Stemman, T.A., 2001, The Port Morant Formation (Upper Pleistocene, Jamaica): High resolution sedimentology and paleoenvironmental analysis of a mixed carbonate clastic lagoonal succession: *Sedimentary Geology*, v. 144 (3-4), p. 291-306.
- Mitchell, W.H., Whittaker, A.C., Mayall, M., Lonergan, L., and Pizzi, M., 2020, Quantifying the relationship between structural deformation and the morphology of submarine channels on the Niger Delta continental slope: *Basin Research*, v. 33 (1), p. 186-209.
- Mitchum, R.M., Vail, P.R., and Sangree, J.B., 1977, Seismic Stratigraph and Global Changes of Sea Level Part 6: Stratigraphic Interpretation of Seismic Reflection Patterns in Depositional Sequences, in: Payton, C.E., eds., *Seismic Stratigraphy – Applications to Hydrocarbon Explorations*: AAPG Memoir 26.
- Moeck, I.S., 2014, Catalog of geothermal play types based on geologic controls: *Renewable and Sustainable Energy Reviews*, v. 37, p. 867-882.
- Mohriak, W., and Szatmari, P., 2008, *Introdução às propriedades químicas e físicas dos evaporitos*. Webster Mohriak, Peter Szatmari and Sylvia Couto Anjos, Sal: *Geologia e Tectônica: Exemplos das Bacias Brasileiras*. Rio de Janeiro: Beca, p. 19.
- Mohriak, W., Szatmari, P., and Anjos, S., 2009, *Sal Geologia e Tectônica*: *Terrae Didactica*, 4, p. 90-91.
- Mohriak, W., Szatmari, P., and Anjos, S., 2012, Salt: geology and tectonics of selected Brazilian basins in their global context, in: Alsop, G. I., Archer, S. G., Hartley, A. J., Grant, N. T., and Hodgkinson, R., eds., *Salt Tectonics, Sediments and Prospectivity*. Geological Society, London, Special Publications, v. 363(1), p. 131-158.
- Mohrig, D., and Buttles, J., 2007, Deep turbidity currents in shallow channels: *Geology*, v. 35, p. 155-158.

- Mora, P., and Place, D., 1993, A lattice solid model for the nonlinear dynamics of earthquakes: *International Journal of Modern Physics*, v. 4, p. 1059-1074.
- Mora, P., and Place, D., 1994, Simulation of the frictional stick-slip instability: *Pure Applied Geophysics*, v. 143, p. 61-87.
- Morley, C.K., and Guerin, G., 1996, Comparison of gravity-driven deformation styles and behaviour associated with mobile shales and salt: *Tectonics*, v. 15 (6), p. 1154-1170.
- Morris, W., Scheihing, M., Wickens, D., and Bouma, A. H., 2000, Reservoir architecture of deep-water sandstones: examples from the skoorsteenbergt formation, Tanqua Karoo Sub-Basin, South Africa: in *Deep-Water Reservoirs of the World: GCSSEPM Foundation 20th Annual Research Conference.*, eds., Weimer, P., and Slatt, M., p. 629–666.
- Morris, E.A., Hodgson, D.M., Brunt, R.L. and Flint, S.S., 2014, Origin, evolution and anatomy of silt-prone submarine external levées: *Sedimentology*, v. 61, p. 1734-1763.
- Morris, E.A., Hodgson, D.M., Flint, S., Brunt, R.L., Luthi, S.M., and Kolenberg, Y., 2016, Integrating outcrop and subsurface data to assess the temporal evolution of a submarine channel-levee system: *AAPG Bulletin*, v. 100 (11), p. 1663–1691.
- Moscardelli, L. and Wood, L., 2008, New classification system for mass transport complexes in offshore Trinidad: *Basin Research*, v. 20, p. 73-98.
- Moscardelli, L., and Wood, L., 2015, Morphometry of mass-transport deposits as a predictive tool: *Geological Society of America Bulletin*, v. 128 (1-2), p. 47-80.
- Moscardelli, L., Wood, L. and Mann, P., 2006, Mass-transport complexes and associated processes in the offshore area of Trinidad and Venezuela: *AAPG bulletin*, v. 90, p. 1059-1088.
- Moscardelli, L., Ochoa, J., Lunt, I., and Zahm, L., 2019, Mixed siliciclastic-carbonate systems and their impact for the development of deep-marine turbidites in continental margins: A case study from the Late Jurassic to Early Cretaceous Shelburne subbasin in offshore Nova Scotia: *AAPG Bulletin*, v. 103 (10), p. 2487-2520.
- Mrazec, L., 1907, Despre cute cu sîmbure de străpungere [On folds with piercing core]. *Buletinul Societății de Științe*, v. 16, p. 6-8.
- Mrazec, L., 1910, Über die Bildung der rumänischen Petroleumlagerstätten [On the formation of the Romanian petroleum deposits]: *Congrès International du Pétrole, Troisième Session, Comte Rendu*, v. 2, p. 80-134, Bucharest.
- Muck, M.T., and Underwood, M.B., 1990, Upslope flow of turbidity currents: a comparison among field observations, theory, and laboratory models: *Geology*, v. 18, p. 54-57.
- Mudge, D.C., and Copestake, P., 1992, Revised Lower Palaeogene lithostratigraphy for the Outer Moray Firth, North Sea: *Marine and Petroleum Geology*, v. 9 (1), p. 53-69.
- Mudge D. C., and Jones S. M, 2004, Palaeocene uplift and subsidence events in the Scotland–Shetland and North Sea region and their relationship to the Iceland plume: *Journal of the Geological Society*, London, 161, p. 381–386

- Mueller, P., Patacci, M., and Di Giulio, A., 2017, Hybrid event beds in the proximal to distal extensive lobe domain of the coarse-grained and sand-rich Bordighera turbidite system (NW Italy): *Marine and Petroleum Geology*, v. 86, p. 908-931.
- Mulder, T., and Alexander, J., 2001, Abrupt change in slope causes variation in the deposit thickness of concentrated particle-driven density currents: *Marine Geology*, v. 175, p. 221-235.
- Mulder, T., Savoyet, B., and Syvitski, J.P.M., 1997, Numerical modelling of a mid-sized gravity flow: the 1979 Nice turbidity current (dynamics, processes, sediment budget and seafloor impact): *Sedimentology*, v. 44 (2) p. 305–326.
- Muravchik, M., Henstra, G.A., Eliassen, G.T., Gawthorpe, R.L., Leeder, M., Haralambos, K., Skourtos, E., and Andrews, J., Deep-water sediment transport patterns and basin floor topography in early rift basins: Plio-Pleistocene syn-rift of the Corinth Rift, Greece: *Basin Research*, v. 32 (5), p. 1184-1212.
- Murray, G.E., 1966, Salt Structures of Gulf of Mexico Basin – A review: *AAPG Bulletin*, v. 50 (3), p. 439-478.
- Mutti, E., and Ricci-Lucchi, F., 1972, Le torbiditi dell'Appennino settentrionale: introduzioni all'analisi di facies: *Memoir Society Geologica Italalia*, v. 11/2, p. 161–199.
- Mutti, E., 1974, Examples of ancient deep-sea fan deposits from circum Mediterranean geosynclines in modern and ancient geosynclinal sedimentation, in: Dott, R.H., Jr., and Shaver, R.H., eds., *Modern and Ancient Geosynclinal Sedimentation: Society of Economic Paleontologists and Mineralogists, Special Publication 19*, p. 92–105.
- Mutti, E., 1977, Distinctive thin-bedded turbidite facies and related depositional environments in the Eocene Hecho Group (South-central Pyrenees, Spain): *Sedimentology*, v. 24, p. 107–131.
- Mutti, E., 1992, *Turbidite sandstones: AGIP- Istituto di Geologia, Università di Parma*, p. 275.
- Mutti, E., and Normark, W.R., 1987, Comparing Examples of Modern and Ancient Turbidite Systems: Problems and Concepts, in: Leggett, J.K. and Zuffa, G.G., eds., *Marine clastic sedimentology*, Springer Netherlands, Dordrecht, p. 1–38.
- Muzzi Magalhaes, P., and Tinterri, R., 2010, Stratigraphy and depositional setting of slurry and contained (reflected) beds in the Marnoso-arenacea Formation (Langhian- Serravallian) Northern Apennines, Italy: *Sedimentology*, v. 57 (7), p. 1685–1720.
- Nagatomo, A., and Archer, S., 2015, Termination geometries and reservoir properties of the Forties Sandstone pinch-out, East Central Graben, UK North Sea, in: McKie, T., Rose, P.T.S., Harley, A.J., Jones, D.W., and Armstrong, T.L., eds., *Tertiary Deep-Marine Reservoirs of the North Sea Region: The Geological Society of London, Special Publications*, v. 403, no. 1, p. 133–155.
- Nardin, T.R., Hein, F.J., Gorsline, D.S., and Edwards, B., 1979, A Review of mass movement processes, sediment and acoustic characteristics, and contrasts in slope and base-of-slope systems versus canyon-fan-basin floor systems: *SEPM Special Publications*, v. 27, p. 61–73.

- Nascimento, I., Picanço de Figueiredo, J., Azambuja Filho, N.C.d., Oliveria, J.P., Araújo, A.C., Ferro, R., and Borghi, L., 2020, High resolution stratigraphy of channelized deposits on a continental slope setting with sea-floor topography controlled by halokinetics, uppermost cretaceous, Espírito Santo offshore basin, Brazil: *Journal of South American Earth Sciences*, v. 103, p. 102721.
- Nelson, T. H., 1989, Style of salt diapirs as a function of the stage of evolution and the nature of the encasing sediments, in: *Gulf of Mexico Salt Tectonics, Associated Processes and Exploration Potential*: Austin, TX, Gulf Coast Section SEPM Foundation, Tenth Annual Research Conference Program and Abstracts, p. 109-110.
- Nelson, T.H., 1991, Salt tectonics and listric normal faulting, in: Salvador, A., ed., *The Gulf of Mexico Basin*: Boulder, CO, Geological Society of America, p. 73-89.
- Nettleton, L.L., 1934, Fluid mechanics of salt domes: *AAPG Bulletin* v. 18, p. 1175–1204.
- Newell, A.J., Benton, M.J., Kearsy, T., Taylor, G., Twitchett, R.J. and Tverdokhlebov, V.P., 2012, Calcretes, fluviolacustrine sediments and subsidence patterns in Permo-Triassic salt-walled minibasins of the south Urals, Russia: *Sedimentology*, v. 59, p. 1659–1676.
- Nikolinakou, M.A., Luo, G., Hudec, M.R., and Flemings, P.B., 2012, Geomechanical modeling of stresses adjacent to salt bodies: Part 2—Poroelastoplasticity and coupled overpressures: *AAPG Bulletin*, v. 96 (1), p. 65–85.
- Nikolinakou, M.A., Flemmings, P.B., and Hudec, M.R., 2014a, Modelling stress evolution around a rising diapir: *Marine and Petroleum Geology*, v. 51, p. 230-238.
- Nikolinakou, M.A., Flemmings, P.B., and Hudec, M.R., 2014b, Comparison of evolutionary and static modelling of stresses around a salt diapir: *Marine and Petroleum Geology*, v. 57, p. 537-545.
- Nikolinakou, M.A., Heidari, M., Hudec, M.R., and Flemings, P.B., 2017, Initiation and growth of salt diapirs in tectonically stable settings: Upbuilding and megaflaps: *AAPG Bulletin*, v. 101 (6), p. 887–905.
- Nikolinakou, M.A., Heidari, M., Flemmings, P.B. and Hudec, M.R., 2018, Geomechanical modelling of pore pressure in evolving salt systems: *Marine and Petroleum Geology*, v. 93, p. 272-286.
- Nikolinakou, M.A., Goteti, R., and Heidari, M., 2019, Mechanics of salt systems: state of the field in numerical methods: *Petroleum Geoscience*, v. 25, p. 249-250.
- Nilsen, K.T., Vendeville, B.C., and Johansen, J.T., 1995, Influence of regional tectonics on halokinesis in the Nordkapp Basin, Barents Sea, in: Jackson, M.P.A., Roberts, D.G., Snelson, S., eds., *Salt Tectonics: A Global Perspective*: AAPG Memoir, v. 65, p. 413–436.
- Norden, B., and Förster, A., 2006, Thermal conductivity and radiogenic heat production of sedimentary and magmatic rocks in the Northeast German Basin: *AAPG Bulletin*, v. 90 (6), p. 939-962.
- Normark, W.R., 1970, Growth patterns of deep-sea fans: *AAPG Bulletin*, v. 54, p. 2170-2195.

Normark, W.R., 1978, Fan valleys, channels, and depositional lobes on modern submarine Fans: characters for recognition of sandy turbidite environments: AAPG Bulletin, v. 62 (6) p. 912–931.

Normark, W.R., and Piper, D.J.W., 1991., Initiation Processes and Flow Evolution of Turbidity Currents: Implications for the Depositional Record, in: Osborne, R.H., ed., From Shoreline to Abyss Contributions in Marine Geology in Honor of Francis Parker Shepard, Tulsa, SEPM Special Publication, v. 46, p. 207–230.

Normark, W.R., Piper, D.J.W. and Hess, G.R., 1979, Distributary channels, sand lobes, and mesotopography of Navy submarine fan, California Borderland, with applications to ancient fan sediments: Sedimentology, v. 26, p. 749-774.

Normark, W.R., Piper, D.J.W., and Stow, D.A.V., 1983, Quaternary Development of channels, levees, and lobes on middle Laurentian Fan: AAPG Bulletin, v. 67, p. 1400-1409.

Nwoko, J., Kane, I., Huuse, M., 2020a, Megaclasts within mass-transport deposits: their origin, characteristics and effect on substrates and succeeding flows, in: Georgiopoulou, A., Amy, L.A., Benetti, S., Chaytor, J.D., Clare, M.A., Gamboa, D., Haughton, P.D.W., Moernaut, J. and Mountjoy, J.J., eds., Subaqueous Mass Movements and their Consequences: Advances in Process Understanding, Monitoring and Hazard Assessments, Geological Society of London Special Publications 500 (1), p. 515-530.

Nwoko, J., Kane, I., Huuse, M., 2020b, Mass transport deposit (MTD) relief as a control on post-MTD sedimentation: Insights from the Taranaki Basin, offshore New Zealand: Marine and Petroleum Geology, v. 120, p. 104-148.

Oakman, C.D., Partington, M.A., 1984, Cretaceous, in: Glennie, K.W., ed., Introduction to the Petroleum Geology of the North Sea, fourth ed. Blackwell Science Limited, pp. 294-350.

Ogata, K., Pogačnik, Ž., Pini, G., Tunis, G., Festa, A., Camerlenghi, A. and Rebesco, M., 2014, The carbonate mass transport deposits of the Paleogene Friuli Basin (Italy/Slovenia): Internal anatomy and inferred genetic processes: Marine Geology, v. 356, p. 88-110.

Olafiranye, K., Jackson, C.A-L., and Hodgson, D.M., 2013, The role of tectonics and mass-transport complex emplacement on upper slope stratigraphic evolution: A 3D seismic case study from offshore Angola: Marine and Petroleum Geology, v. 44, p. 196-216.

Oluboyo, A.P., Gawthorpe, R.L., Bakke, K., and Hadler-Jacobsen, F., 2014, Salt tectonic controls on deep-water turbidite depositional systems: Miocene, southwestern Lower Congo Basin, offshore Angola: Basin Research, v. 26, p. 597-620.

Omosanya, K.O., and Alves, T.M., 2013, Ramps and flats of mass-transport deposits (MTDs) as markers of seafloor strain on the flanks of rising diapirs (Espírito Santo Basin, SE Brazil): Marine Geology, v. 340, p. 82-97.

Oreskes, N., Shrader-Frechette, K., and Beltix, K., 1994, Verification, Validation, and Confirmation of Numerical Models in the Earth Sciences: Science, v. 263, p. 641-646.



- Ortiz-Karpf, A., Hodgson, D.M., and McCaffrey, W.D., 2015, The role of mass-transport complexes in controlling channel avulsion and the subsequent sediment dispersal patterns on an active margin: the Magdalena Fan, offshore Colombia: *Marine and Petroleum Geology*, v. 64, p. 58-75.
- Ortiz-Karpf, A., Hodgson, D.M., Jackson, C.A-L., and McCaffrey, W.D., 2016, Mass-Transport Complexes as Markers of Deep-Water Fold-and-Thrust Belt Evolution: Insights from the Southern Magdalena Fan, Offshore Colombia: *Basin Research*, v. 30, p. 65-88.
- Owen, M., Day, S., and Maslin, M., 2007, Late Pleistocene submarine mass movements: Occurrence and causes: *Quaternary Science Reviews*, v. 26, p. 958–978.
- Palanques, A., Kenyon, N.H., Alonso, B., and Limonov, A., 1995, Erosional and depositional patterns in the Valencia Channel mouth: An example of a modern channel-lobe transition zone: *Marine Geophysical Researches*, v. 17 (6) p. 503– 517.
- Pantin, H.M. and Leeder, M.R., 1987, Reverse flow in turbidity currents: the role of internal solitons: *Sedimentology*, v. 34, p. 1143-1155.
- Parker, T. J., and McDowell, A.N., 1951, Scale models as guide to interpretation of salt-dome faulting: *AAPG Bulletin*, v. 35, p. 2076–2086.
- Parker, T. J., and McDowell, A.N., 1955, Model studies of salt-dome tectonics: *AAPG Bulletin*, v. 39, p. 2384–2470.
- Patacci, M., Haughton, P.D., and McCaffrey, W.D., 2014, Rheological complexity in sediment gravity flows forced to decelerate against a confining slope, Braux, SE France: *Journal of Sedimentary Research*, v. 84, p. 270-277.
- Paull, C.K., Talling, P.J., Maier, K.L., Parsons, D., Xu, J., Caress, D.W., Gwiazda, R., Lundsten, E.M., Anderson, K., Barry, J.P., Chaffey, M., O'Reilly, T., Rosenberger, K.J., and Gales, J.A., 2018, Powerful turbidity currents driven by dense basal layers: *Nature Communications*, v. 9 (1) p. 4114.
- Peakall, J., and Sumner, E.J., 2015, Submarine channel flow processes and deposits: A process-product perspective: *Geomorphology*, v. 244, p. 95–120.
- Peakall, J., McCaffrey, B., and Kneller, B., 2000, A process model for the evolution, morphology, and architecture of sinuous submarine channels: *Journal of Sedimentary Research*, v. 70, p. 434-448.
- Peakall, J., Amos, K.J., Keevil, G.M., Bradbury, P.W., and Gupta, S., 2007, Flow processes and sedimentation in submarine channel bends: *Marine and Petroleum Geology*, v. 24, p. 470-486.
- Pechlivanidou, S., Cowie, P.A., Hannisdal, B., Whittaker, A.C., Gawthorpe, R.L., Pennos, C., and Rüser, O.S., 2018, Source-to-sink analysis in an active extensional setting: Holocene erosion and deposition in the Sperchios rift, central Greece: *Basin Research*, v. 30, p. 522-543.
- Peel, F.J., 2014, How do salt withdrawal minibasins form? Insights from forward modelling, and implications for hydrocarbon migration: *Tectonophysics*, v. 630, p. 222-235.

- Peel, F.J., Travis, C.J., and Hossack, J.R., 1995, Genetic structural provinces and salt tectonics of the Cenozoic offshore U.S. Gulf of Mexico: a preliminary analysis, in: Jackson, M.P.A., Roberts, D.G., Snelson, S., eds., *Salt Tectonics: a Global Perspective: AAPG Memoir*, v. 65, p. 153–175.
- Peel, F.J., Hudec, M.R., and Weijermars, R., 2020, Salt diapir downbuilding: Fast analytical models based on rates of salt supply and sedimentation: *Journal of Structural Geology*, v. 141, p. 104–202.
- Peeters, S. Asschert, A., and Werweij, H., 2018, Towards a better understanding of the highly overpressured Lower Triassic Bunter reservoir rocks in the Terschelling Basin, in: Kilhams, B., Kulka, P.A., Mazur, S., McKie, T., Mijnlief, H.F. and van Ojik, K., eds., *Mesozoic Resource Potential in the Southern Permian Basin: Geological Society, London, Special Publications*, v. 469, p. 223–236.
- Pemberton, E.A., Hubbard, S.M., Fildani, A., Romans, B. and Stright, L., 2016, The stratigraphic expression of decreasing confinement along a deep-water sediment routing system: Outcrop example from southern Chile: *Geosphere*, v. 12(1), p. 114–134.
- Pena dos Reis, R., Pimentel, N., Fainstein, R., Reis, M., and Rasmussen, B., 2017, Influence of salt diapirism on the basin architecture and hydrocarbon prospects of the Western Iberian Margin. In: Soto, J.I., Flinch, J.F. and Tari, G., eds., *Permo Triassic Salt Provinces of Europe, North Africa and the Atlantic Margins*. Elsevier, Amsterdam, p. 313–327.
- Penge, J., Taylor, B., Huckerby, J.A., and Munns, J.W., 1993, Extension and salt tectonics in the East Central Graben: *Petroleum Geology Conference Series*, Geological Society, London, v. 4, p. 1197–1209.
- Peric, D, and Crook, A.J.L., 2004, Computational strategies for predictive geology with reference to salt tectonics: *Computer Methods in Applied Mechanisms and Engineering*, v. 193, p. 48–51.
- Pettingill, H.S., 1998, Turbidite plays' immaturity means big potential remains: *Oil and Gas Journal*, v. 96, no. 40, p. 106–111.
- Philip, H., Cisternas, A., Gvishiani, A., and Gorshkov, A., 1989, The Caucasus: An actual example of the initial stages of continental collision: *Tectonophysics*, v. 161, p. 1–21.
- Phillips, T.B., Fazlikhani, H., Gawthorpe, R.L., Fossen, H., Jackson, C.A-L., Bell, R.E., Faleide, J.I., and Rotevatn, A., 2019, The Influence of Structural Inheritance and Multiphase Extension on Rift Development, the Northern North Sea: *Tectonics*, v. 38 (12), p. 4099–4126.
- Pichel, L.M., and Jackson, C.A-L., 2020, Four-dimensional variability of Composite Halokinetic Sequences: *Basin Research*, v. 32 (6), p. 1277–1299.
- Pichel, L. M., Finch, E., Huuse, M., and Redfern, J., 2017, The influence of shortening and sedimentation on rejuvenation of salt diapirs: A new discrete-element modelling approach: *Journal of Structural Geology*, v. 104, p. 61–79.
- Pichel, L.M., Peel, F., Jackson, C. A-L., and Huuse, M., 2018, Geometry and kinematics of salt-detached ramp syncline basins: *Journal of Structural Geology*, v. 115, p. 208–230.
- Pichel, L. M., Finch, E., and Gawthorpe, R.L., 2019, The Impact of Pre-Salt Rift Topography on Salt Tectonics: A Discrete-Element Modeling Approach: *Tectonics*, v. 38, p. 1466–1488.

- Pichel, L.M., Jackson, C.A-L., Peel, F., and Dooley, T.P., 2020, Base-salt relief controls salt-tectonic structural style, São Paulo Plateau, Santos Basin, Brazil: *Basin Research*, v. 32 (3), p. 453-484.
- Pickering, K.T., and Bayliss, N.J., 2009, Deconvolving tectono-climatic signals in deep-marine siliciclastics, Eocene Ainsa basin, Spanish Pyrenees: Seesaw tectonics versus eustacy: *Geology*, v. 37, p. 203-206.
- Pickering, K.T., and Corregidor, J., 2000, 3D reservoir scale study of Eocene confined submarine fans, south central Spanish Pyrenees, in *Deep Water Reservoirs of the World: SEPM, Gulf Coast Section, 20th Annual Bob F. Perkins Research Conference*, SEPM, p. 776–781.
- Pickering, K.T. and Corregidor, J., 2005, Mass-transport complexes (MTCs) and tectonic control on basin-floor submarine fans, middle Eocene, south Spanish Pyrenees: *Journal of Sedimentary Research*, v. 75, p. 761-783.
- Pickering, K.T., and Hiscott, R.N., 1985, Contained (reflected) turbidity currents from the Middle Ordovician Cloridorme Formation, Quebec, Canada: an alternative to the antidune hypothesis: *Sedimentology*, v. 32, p. 373-394.
- Picot, M., Droz, L., Marsset, T., Dennielou, B., and Bez, M., 2016, Controls on turbidite sedimentation: Insights from a quantitative approach of submarine channel and lobe architecture (Late Quaternary Congo Fan): *Marine and Petroleum Geology*, v. 72, p. 423–446.
- Pimentel, N., and Pena dos Reis, R., 2016, Petroleum systems of the Western Iberian margin: a review of the Lusitanian Basin and the deep offshore Peniche Basin: *Journal of Petroleum Geology*, v. 39, p. 305–326.
- Pinto, V., Casas, A., Rivero, L. and Torné, M., 2005, 3D gravity modeling of the Triassic salt diapirs of the Cubeta Alavesa (northern Spain): *Tectonophysics* v. 405, p. 65–75.
- Pinter, P.R., Butler, R.W., Hartley, A.J., Maniscalco, R., Baldassini, N., and Di Stefano, A., 2017, Tracking sand-fairways through a deformed turbidite system: the Numidian (Miocene) of Central Sicily, Italy: *Basin Research*, v. 30, p. 480-501.
- Piper, D.J.W., and Aksu, A.E., 1987, The source and origin of the 1929 Grand Banks turbidity current inferred from sediment budgets: *Geo-Marine Letters*, v. 7 (4), p. 177–182.
- Piper, D., Cochonat, P., and Morrison, M.L., 1999, The sequence of events around the epicentre of the 1929 Grand Banks earthquake: Initiation of debris flows and turbidity current inferred from sidescan sonar: *Sedimentology*, v. 46, p. 79–97.
- Pirmez, C., and Dixon, B.T., 2005, Integrated slope channel depositional models: the key to successful prediction of reservoir presence and quality in offshore West Africa: CIPM, cuarto Eexitep 2005, Veracruz, Mexico, p. 1–13.
- Pirmez, C., Beaubouef, R.T., Friedmann, S.J., and Mohrig, D.C., 2000, Equilibrium Profile and Baselevel in Submarine Channels: Examples from Late Pleistocene Systems and Implications for the Architecture of Deepwater Reservoirs, in: Weimer, P., eds., *Deep-Water Reservoirs of the World*, v. 20.

Pivnik, D. A., Ramzy, M., Steer, B. L., Thorseth, J., El Sisi, Z., Gaafar, I., Garing, J. D., and Tucker, R. S., 2003, Episodic growth of normal faults as recorded by syntectonic sediments, July oil field, Suez rift, Egypt: AAPG Bulletin, v. 87, p. 1015– 1030.

Pohl, F., Eggenhuisen, J.T., Tilston, M. and Cartigny, M.J.B., 2019, New flow relaxation mechanism explains scour fields at the end of submarine channels: Nature Communications, v. 10, p. 1-8.

Pohl, F., Eggenhuisen, J., Cartigny, M., Tilston, M., de Leeuw, J., and Hermidas, N., 2020, The influence of a slope break on turbidite deposits: an experimental investigation: Marine Geology, v. 424, p.106-160.

Poliakov, A., and Podladchikov, Y., 1992, Diapirism and topography: Geophysical Journal International, v. 109 (3), p. 553-564.

Poliakov, A.N.B., Van Belan, R., Podladchikov, Y., Daudre, B., Cloetingh, S. and Talbot, C., 1993, Numerical analysis of how sedimentation and redistribution of surficial sediments affects salt diapirism: Tectonophysics, v. 226, p. 199-216.

Poprawski, Y., and Basile, C., 2018, Long-lasting diapir growth history in the Basque-Cantabrian Basin (northern Spain): a review, Penrose conference presentation.

Poprawski, Y., Basile, C., Aguirrezabala, L.M., Jaillard, E., Gaudin, M., and Jacquin, T., 2014, Sedimentary and structural record of the Albian growth of the Bakio salt diapir (the Basque Country, northern Spain): Basin Research, v. 26, p. 746-766.

Poprawski, Y., Basile, C., Jaillard, E., Gaudin, M., and Lopez, M., 2016, Halokinetic sequences in carbonate systems: An example from the Middle Albian Bakio Breccias Formation (Basque Country, Spain): Sedimentary Geology, v. 334, p. 34-52.

Poprawski, Y., Basile, C., Cumberpatch, Z., and Eude, A., 2021, Mass transport deposits in deep-water minibasins: outcropping examples from the minibasins adjacent to the Bakio salt wall (Basque Country, Northern Spain: Marine and Petroleum Geology, accepted, available online.

Popescu, I., Lericolais, G., Panin, N., Normand, A., Dinu, C. and Le Drezen, E., 2004. The Danube submarine canyon (Black Sea): morphology and sedimentary processes: Marine Geology, v. 206, p. 249-265.

Porten, K.W., Kane, I.A., Warchol, M.J. and Southern, S.J., 2016, A sedimentological process-based approach to depositional reservoir quality of deep-marine sand-stones: an example from the Springar Formation, north- western Vøring Basin, Norwegian Sea: Journal of Sedimentary Research, v. 86 (11), p. 1269–1286.

Posamentier, H.W., 2003, Depositional elements associated with a basin floor channel- levee system: Case study from the Gulf of Mexico: Marine and Petroleum Geology, v. 20, (6-8), p. 677– 690.

Posamentier, H.W., and Kolla, V., 2003, Seismic geomorphology and stratigraphy of depositional elements in deep-water settings: Journal of Sedimentary Research, v. 73, p. 367-388.

- Posamentier, H.W., Erskine, R.D. and Mitchum, R.M., 1991, Models for submarine fan deposition within a sequence stratigraphic framework, in: Weimer, P. and Link, M.H., eds., *Seismic Facies and Sedimentary Processes of Submarine Fans and Turbidite Systems*, Berlin, Springer-Verlag, p. 127–136.
- Postma, G., 1986, Classification of sediment gravity-flow deposits based on flow conditions during sedimentation: *Geology*, v. 14, p. 291–294.
- Postma, G., Nemeč, W., and Kleinspehn, K., 1988, Large floating clasts in turbidites: a mechanism for their emplacement: *Sedimentary Geology*, v. 58 (1), p. 47-61.
- Postma, G., Hilgen, F.J., and Zachariasse, W.J., 1993, Precession-punctuated growth of a late Miocene submarine-fan lobe on Gavdos (Greece): *Terra nova*, v. 5, p. 438-444.
- Postma, G., Hoyal, D.C., Abreu, V., Cartigny, M.J.B., Demko, T., Fedele, J.J., Kleverlaan, K., and Pederson, K.H., 2016, Morphodynamics of supercritical turbidity currents in the channel-lobe transition zone, in: Lamarche, G., Mountjoy, J., Bull, S., Hubble, T., Krastel, S., Lane, E., Miccallef, A., Moscardelli, L., Mueller, C., Pecher, I., and Woelz, S., eds., *Submarine Mass Movements and their Consequences: 7th International Symposium*, Springer International Publishing, Cham, p. 469–478.
- Prather, B.E., 2000, Calibration and visualization of depositional process models for above-grade slopes: a case study from the Gulf of Mexico: *Marine and Petroleum Geology*, v. 17, p. 619-638.
- Prather, B.E., 2003, Controls on reservoir distribution, architecture and stratigraphic trapping in slope settings: *Marine and Petroleum Geology*, v. 20, p. 529–545.
- Prather, B. E., Booth, J.R., Steffens, G.S., and Craig, P.A., 1998, Classification, lithologic calibration, and stratigraphic succession of seismic facies of intraslope basins, deep-water Gulf of Mexico: *AAPG Bulletin*, v. 82, p. 701-728.
- Prather, B.E., Pirmez, C., and Winker, C.D., 2012, Stratigraphy of linked intraslope basins: Brazos-Trinity system western Gulf of Mexico, in Prather B.E., eds., *Application of the Principles of Seismic Geomorphology to Continental-Slope and Base-of-Slope Systems: Case Studies from Seafloor and Near-Seafloor Analogues: SEPM, Special Publication*, v. 99, p. 83-109.
- Pratson, L.F. and Coakley, B.J., 1996, A model for the headward erosion of submarine canyons induced by downslope-eroding sediment flows: *GSA Bulletin*, v. 108, p. 225-234.
- Pratson, L.F., and Ryan, W.B.F., 1994, Pliocene to recent infilling and subsidence of intraslope basins offshore Louisiana: *AAPG Bulletin*, v. 78, p. 1483–1506.
- Prélat, A., and Hodgson, D., 2013, The full range of turbidite bed thickness patterns in Submarine lobes: Controls and implications: *Journal of the Geological Society*, v. 170, p. 209-214.
- Prélat, A., Hodgson, D.M., and Flint, S.S., 2009, Evolution, architecture and hierarchy of distributary deep-water deposits: a high-resolution outcrop investigation from the Permian Karoo Basin, South Africa: *Sedimentology*, v. 56, p. 2132-2154.

Prélat, A., Covault, J.A., Hodgson, D.M., Fildani, A., and Flint, S.S., 2010, Intrinsic controls on the range of volumes, morphologies, and dimensions of submarine lobes: *Sedimentary Geology*, v. 232 (1), p. 66–76.

Price, N. J., and J. W. Cosgrove, 1990, *Analysis of geological structures*: Cambridge, Cambridge University Press, 502 p.

Priddy, C.L., and Clarke, S.M., 2020, The sedimentology of an ephemeral fluvial-aeolian succession: *Sedimentology*, v. 67 (5), p. 2392-2425.

Pringle, J.K., Brunt, R.L., Hodgson, D.M., and Flint, S.S., 2010, Capturing stratigraphic and sedimentological complexity from submarine channel complex outcrops to digital 3D models, Karoo Basin, South Africa: *Petroleum Geoscience*, v. 16, p. 307-330.

Prior, D.B., and Coleman, J.M., 1982, Active slides and flows in underconsolidated marine sediments on the slopes of the Mississippi Delta, in: Saxov, S. and Nieuwenhuis J.K., eds., *Marine slides and other mass movements*, NATO Conference Series, Springer, Boston, v. 6, p. 21-49.

Prior, D.B., Bornhold, B.D., and Johns, M.W., 1984, Depositional characteristics of a submarine debris flow: *The Journal of Geology*, v. 92, p. 707-727.

Prior, D. B., Bornhold, B. D., Wiseman, W. J. Jr., and Lowe, D. R., 1987, Turbidity current activity in a British Columbia fjord: *Science*, v. 237, p. 1330–1333.

Privat, A.M-L.J, Hodgson, D.M., Jackson, C.A-L., Schwarz, E., and Peakall, J., Evolution from syn-rift carbonates to early post-rift deep-marine intraslope lobes: The role of rift basin physiography on sedimentation patterns: *Sedimentology*, online early.

Puelles, P., Ábalos, B., García De Madinabeitia, S., Sanches-Lorda, M.E., Fernández-Armas, S., and Gil Ibarguchi, J.I., 2014, Provenance of quartz-rich metamorphic tectonite pebbles from the 'Black Flysch' (W Pyrenees, N Spain): An EBSD and detrital zircon LA-ICP-MS study: *Tectonophysics*, v. 632, p. 123-137.

Puigdefàbregas, C., Gjelberg, J.M., and Vaksdal, M., 2004, The Grès d'Annot in the Annot syncline: outer basin-margin onlap and associated soft-sediment deformation, in: Lomas, S., and Joseph, P., eds., *Deep-Water Sedimentation in the Alpine Basin of SE France: New Perspectives on the Grès d'Annot and Related Systems*: Geological Society of London, Special Publication, v. 221, p. 367-388.

Pujalte, V., Baceta, J.I., Payros, A., Orue-Etxebarria, X., and Serra-Kiel, J., 1994, Late Cretaceous- Middle Eocene Sequence Stratigraphy and Biostratigraphy of the SW and W Pyrenees (Pamplona and Basque Basins): a Field Seminar of the Groupe de Etude du Paleogene. IGCP Project 286, Universidad del País Vasco/Euskal Herriko Unibertsitatea, 118p.

Pujalte, V., Baceta, J.I., Orue-Etxebarria, X., and Payros, A., 1998, Paleocene strata of the Basque Country, W Pyrenees, N Spain: facies and sequence development in a deep-water, starved basin, in: De Graciansky, P.C., Hardenbol, J., Jacquin, T., and Vail, P.R., eds., *Mesozoic and Cenozoic Sequence Stratigraphy of European basins*: SEPM Special Publication, v. 60, p. 311-325.

- Pyles, D.R. and Jennette, D.C., 2009, Geometry and architectural associations of co-genetic debrite–turbidite beds in basin-margin strata, Carboniferous Ross Sandstone (Ireland): Applications to reservoirs located on the margins of structurally confined submarine fans: *Marine and Petroleum Geology*, v. 26, p. 1974-1996.
- Pyles, D.R., Nilsen, T.H., Shew, R.D., Steffens, G.S. and Studlick, J.R.J., 2007, Architectural elements in a ponded submarine fan, Carboniferous Ross Sandstone, western Ireland: Atlas of deep-water outcrops: *AAPG Studies in Geology*, v. 56, p. 206-209.
- Rabouille, C., Dennielou, B., Baudin, F., Raimonet, M., Droz, L., Khripounoff, A., Martinez, P., Mejanelle, L., Michalopoulos, P., Pastor, L. and Pruski, A., 2019, Carbon and silica megasink in deep-sea sediments of the Congo terminal lobes: *Quaternary Science Reviews*, v. 222, p. 105-185.
- Ramm, M., 2000, Reservoir quality and its relationship to facies and provenance in Middle to Upper Jurassic sequences, northeastern North Sea: *Clay Minerals*, v. 35, p. 77-94.
- Rat, P., 1988, The Basque-Cantabrian Basin between the Iberian and the European Plates. Some facts but still many problems: *Sociedad de Geológica de España Revista*, v.1, p. 3-4.
- Ratcliff, D.W., Gray, S.H., Whitmore, N.D., 1991, Seismic Imaging of Salt Structures in the Gulf of Mexico: SEG Annual Meeting, Houston, Texas, November 1991.
- Ratcliff, D.W., and Weber, D.J., 1997, Geophysical imaging of subsalt geology: *The Leading Edge*, v. 16 (2) p. 115- 119.
- Rattee, R.P., and Hayward, A.B., 1993, Sequence stratigraphy of a failed rift system: the Middle Jurassic to Early Cretaceous basin evolution of the Central and Northern North Sea, in: Parker, J.R., ed., *Petroleum Geology of Northwest Europe: Proceedings of the 4th Conference*, Petroleum Geology, Geological Society of London, p. 215-249.
- Reading, H.G., 1991, The classification of deep-sea depositional systems by sediment calibre and feeder system: *Journal of the Geological Society, London*, v. 148, p. 427–430.
- Reading, H.G., and Richards, M., 1994, Turbidite systems in deep-water basin margins classified by grain size and feeder system: *AAPG Bulletin*, v. 78 (5) p. 792–822.
- Reilly, M., 2001, Deepwater Reservoir Analogue – Bunkers Sandstone, Donkey Bore Syncline, Flinders Ranges Australia. Honours Thesis. University of Adelaide, Adelaide, Australia.
- Reilly, M.R.W., and Lang, S.C., 2003, A ponded basin floor fan outcrop analogue: Bunkers sandstone, Northern Flinders Ranges, Australia: *The Australian Petroleum Production and Exploration Association Journal*, v. 43(1), p. 537-553.
- Remacha, E., Fernández, L.P., and Maestro, E., 2005, The Transition between sheet-like lobe and basin-plain turbidites in the Hecho Basin (South-Central Pyrenees, Spain): *Journal of Sedimentary Research*, v. 75 (5) p. 798–819.
- Rommelts, G., 1995, Fault-related salt tectonics in the southern North Sea, the Netherlands, in: Jackson, M.P.A., Roberts, D.G., and Snelson, S., eds., *Salt tectonics: a global perspective: AAPG Memoir*, v. 65, p. 261-272.

- Remmelts, G., 1996, Salt tectonics in the southern North Sea, the Netherlands, in: Rondeel, H.E., Batjes, D.A.J., and Nieuwenhuijs, W.H., eds., *Geology of Gas and Oil under the Netherlands*. Springer Netherlands, p. 143-158.
- Ribes, C., Kergaravat, C., Bonnel, C., Crumeyrolle, P., Callot, J-P., Poisson, A., Temiz, H., and Ringenbach, J-C., 2015, Fluvial sedimentation in a salt-controlled mini-basin: Stratal patterns and facies assemblages, Sivas Basin, Turkey: *Sedimentology*, v. 62, p. 1513-1545.
- Ribes, C., Kergaravat, C., Crumeyrolle, P., Lopez, M., Bonnel, C., Poisson, A., Kavak, K, S., Callot, J-C., and Ringenbach, J-C., 2017, Factors controlling stratal pattern and facies distribution of fluvio-lacustrine sedimentation in the Sivas mini-basins, Oligocene (Turkey): *Basin Research*, v. 29 (S1), p. 596-621.
- Ricci-Lucchi, F., 1967, Recherches stratonomiques et sedimentologiques sur le flysch Miocene de la Romagna: *Giornal Geologica*, v. 35, p. 163-192.
- Ricci-Lucchi, F., 1975, Depositional cycles in two turbidite formations of northern Apennines: *Journal of Sedimentary Research*, v. 45 (1), p. 3-43.
- Ricci-Lucchi, F., and Valmori, E., 1980, Basin-wide turbidites in a Miocene, oversupplied deep-sea plain: a geometrical analysis: *Sedimentology*, v. 27/3 (3), p. 241-270.
- Richter-Bernburg, G., 1973, Paleogeographical Pre-conditions for the Genesis of Evaporites: *Congresso Brasileiro de Geologia*, v. 27, p. 163-169.
- Rider, M., and Kennedy, M., 2018, *The Geological Interpretation of Well logs*: Glasgow, Bell and Ball, 432 p.
- Riding, R., 2002, Structure and composition of organic reefs and carbonate mud mounds: concepts and categories: *Earth Science Reviews*, v. 58, p. 163-231.
- Ringenbach, J.C., Salel, J.F., Kergaravat, C., Ribes, C., Bonnel, C., and Callot, J.P., 2013, Salt tectonics in the Sivas Basin, Turkey: outstanding seismic analogues from outcrops: *First Break*, v. 31, p. 93-101.
- Robles, S., Pujalte, V., and García-Mondéjar, J., 1988, Evolución de los sistemas sedimentarios del margen continental cantábrico durante el Albiense y Cenomaniense, en la transversal del litoral Vizcaino: *Sociedad de Geológica de España Revista*, v. 1 (3-4), p. 410-441.
- Robles, S., Garrote, A., and García-Mondéjar, J., 1989, XII Congreso Español de Sedimentología: Simposios y conferencias. Universidad del País Vasco, Departamento de Estratigrafía, Geodinámica y Paleontología, Bilbao.
- Roca, E., Ferrer, O., Rowan, M.G., Muñoz, J.A., Butillé, M., Giles, K.A., Arbués, P., and de Matties, M., 2021, Salt tectonics and controls on halokinetic-sequence development of an exposed deepwater diapir: The Bakio Diapir, Basque-Cantabrian Basin, Pyrenees: *Marine and Petroleum Geology*, v. 123. Available online early.
- Rodriguez, C.R., Jackson, C.A-L., Rotevatn, A., Bell, R.E., and Francis, M., 2018, Dual tectonic-climatic controls on salt giant deposition in the Santos Basin, offshore Brazil: *Geosphere*, v. 14, p. 215-242.



- Rodriguez, C.R., Jackson, C.A-L., Bell, R.E., Rotevatn, A., and Francis, M., 2020, Deep-water reservoir distribution on a salt-influenced slope, Santos Basin, offshore Brazil: AAPG Bulletin, in press.
- Roelofse, C., Alves, T.M., Gafeira, J., and Omosanya, K.O., 2019, An integrated geological and GIS-based method to assess caprock risk in mature basins proposed for carbon capture and storage: International Journal of Greenhouse Gas Control, v. 80, p. 103-122.
- Rojo, L. A., and Escalona, A., 2018, Controls on minibasin infill in the Nordkapp Basin: evidence of complex Triassic synsedimentary deposition influenced by salt tectonics: AAPG Bulletin, v. 102, p. 1239-1272.
- Roma, M., Ferrer, O., Roca, E., Pla, O., Escosa, F.O., and Butillé, M., 2018, Formation and inversion of salt-detached ramp-syncline basins. Results from analog modeling and application to the Columbrets Basin (Western Mediterranean): Tectonophysics, v. 745, p. 214-228.
- Romans, B.W., Fildani, A., Hubbard, S.M., Covault, J.A., Fosdick, J.C., and Graham, S.A., 2011, Evolution of deep-water stratigraphic architecture, Magallanes Basin, Chile: Marine and Petroleum Geology, v. 28 (3), p. 612-628.
- Romans, B., Hubbard, S., Stright, L., and Autcher, N., 2013, Variability in Slope Sandstone Bodies: Linkage to Slope Morphology and Evolution: AAPG Search and Discovery Article #50865.
- Rosales, I., 1999, Controls on carbonate platform evolution on active fault blocks: the Lower Cretaceous Castro Urdiales platform (Aptian – Albian, northern Spain): Journal of Sedimentary Research, v. 69, p. 447–465.
- Rosales, I., and Pérez-García, A., 2010, Porosity development, diagenesis and basin modelling of a Lower Cretaceous (Albian) carbonate platform from northern Spain, in: van Buchem, F.S.P., Gerdes, K.D., and Esteban, M., eds., Mesozoic and Cenozoic Carbonate System of the Mediterranean and the Middle East: Stratigraphic and Diagenetic Reference Models: Geological Society of London, Special Publication 329, p. 317-342.
- Rossi, V., Amorosi, A., Sarti, G., and Mariotti, S., 2017, Late Quarternary multiple incised-valley systems: An unusually well-preserved stratigraphic record of two interglacial valley-fill successions from the Arno plain (northern Tuscany, Italy): Sedimentology, v. 64, p. 1901-1928.
- Rotzien, J.R., and Lowe, D.R., 2014, Processes of sedimentation and stratigraphic architecture of deep-water braided lobe complexes: The Pliocene Repetto and Pico Formations, Ventura Basin, U.S.A.: Journal of Sedimentary Research, v. 84, p. 910– 934.
- Rowan, M.G., 2014, Passive-margin salt basins: Hyperextension, evaporite deposition, and salt tectonics: Basin Research, v. 26 (1), p. 154-182.
- Rowan, M. G., 2017, An overview of allochthonous salt tectonics, in: Soto, J.I., Flinch, J.F., and Tari, G., eds., Permo-Triassic Salt Provinces of Europe, North Africa and the Atlantic Margins: Tectonics and Hydrocarbon Potential: Elsevier, Amsterdam, p. 97-114.
- Rowan, M.G., 2020, The South Atlantic and Gulf of Mexico salt basins: crustal thinning, subsidence and accommodation for salt and presalt strata: Geological Society of London, Special Publication 476 (1), p. 333-363.

- Rowan, M.G., 2020, Chapter 11- Salt and shale detached gravity-driven failure of continental margins: *Regional Geology and Tectonics*, v. 2, p. 205-234.
- Rowan, M.G., and Giles, K.A., 2021, Passive versus active salt diapirism: *American Association of Petroleum Geologists*, v. 105 (1), p. 53-63.
- Rowan, M. G., and Weimer, P., 1998, Salt-sediment interaction, northern Green Canyon and Ewing Bank (offshore Louisiana), northern Gulf of Mexico: *AAPG Bulletin*, v. 82, p. 1055-1082.
- Rowan, M.G., Jackson, M.P.A., and Trudgill, B.D., 1999, Salt-related fault families and fault welds in the northern Gulf of Mexico: *AAPG Bulletin*, v. 83, p. 1454–1484.
- Rowan, M.G., Lawton, T.F., Giles, K.A. and Ratliff, R.A., 2003, Near-salt deformation in La Popa basin, Mexico, and the northern Gulf of Mexico: A general model for passive diapirism: *AAPG Bulletin*, v.87 (5), 733-756.
- Rowan, M.G., Peel, F.J., and Vendeville, B.C., 2004, Gravity-driven fold belts on passive margins. In: McClay, K.R. (Ed.), *Thrust Tectonics and Hydrocarbon Systems: AAPG Memoir*, v. 82, p. 157–182.
- Rowan, M.G., Giles, K.A., Roca, E., Arbues, P., and Ferrer, O., 2012, Analysis of Growth Strata Adjacent to an Exposed Deepwater Salt Diapir, northern Spain: *American Association of Petroleum Geologists, Annual Convention, Long Beach, USA*.
- Rowan, M. G., Lawton, T. F., and Giles, K.A., 2012, Anatomy of an exposed vertical salt weld and flanking strata, La Popa Basin, Mexico, in: Alsop, G. I., Archer, S. G., Hartley, A. J., Grant, N. T., and Hodgkinson, R., eds., *Salt Tectonics, Sediments and Prospectivity*. Geological Society, London, Special Publications, v. 363, p. 33–57.
- Rowan, M.G., Giles, K.A., Hearon, T.E., and Fiduck, J.C., 2016, Megaflaps adjacent to salt diapirs: *AAPG Bulletin*, v. 100 (1), p. 1723-1747.
- Rowan, M.G., Urai, J.L., Fiduck, C.J., and Kukla, P.A., 2019, Deformation of intrasalt competent layers in different modes of salt tectonics: *Solid Earth*, v. 10, p. 987-1012.
- Sadler, P., 1981, Sediment Accumulation Rates and the completeness of Stratigraphic Sections: *The Journal of Geology*, v. 89 (5), p. 569-584.
- Sahoo, H., Gani, M.R., Gani, N.D., Hampson, G.J., Howell, J.A., Storms, J.E.A., Martinius, A.W., and Buckley, S.J., 2020, Predictable patterns in stacking and distribution of channelized fluvial sand bodies linked to channel mobility and avulsion processes: *Geology*, v. 48 (9), p. 903-907.
- Saidi, M.S., Rismanian, M., Monjezi, M., Zendehbad, M., and Fatehiboroujeni, S., 2014, Comparison between Lagrangian and Eulerian approaches in predicting motion of micron-sized particles in laminar flows: *Atmospheric Environment*, v. 89, p. 199-206.
- Saintot, A., Stephenson, R. A., Stovba, S., Brunet, M. F., Yegorova, T., and Starostenko, V., 2006, The evolution of the southern margin of Eastern Europe (Eastern European and Scythian platforms) from the latest Precambrian-Early Palaeozoic to the Early Cretaceous, in: Gee, D.G.,

and Stephenson, R.A., eds., *European Lithosphere Dynamics*: Geological Society, London, *Memoirs*, v. 32(1), 481–505.

Saller, A., Werner, K., Sugiaman, F., Cebastian, A., May, R., Glenn, D., and Barker, C., 2008, Characteristics of Pleistocene deep-water fan lobes and their application to an upper Miocene reservoir model, offshore East Kalimantan, Indonesia: *AAPG Bulletin*, v. 92 (7), p. 919–949.

Salles, L., Ford, M., and Joseph, P., 2014, Characteristics of axially-sourced turbidite sedimentation on an active wedge-top basin (Annot Sandstone, SE France): *Marine and Petroleum Geology*, v. 56, p. 305-323.

Sattar, N., Juhlin, C., Koyi, H. and Ahmad, N., 2017, Seismic stratigraphy and hydrocarbon prospectivity of the Lower Cretaceous Knurr Sandstone lobes along the southern margin of Loppa High, Hammerfest Basin, Barents Sea: *Marine and Petroleum Geology*, v. 85, p. 54-69.

Satterfield, W.M., and Behrens, E.W., 1990, A Late Quarternary canyon/channel system, north-west Gulf of Mexico continental slope: *Marine Geology*, v. 92 (1), p. 51-67.

Saura, E., Vergés, J. D., Martín-Martín, G., Messenger, M., Moragas, P., Razin, C., Grélaud, R., Joussiaume, M., Homke, S., and Hunt, D.W., 2014, Syn- to post-rift diapirism and minibasins of the Central High Atlas (Morocco): the changing face of a mountain belt: *Journal of the Geological Society*, London, v. 171, p. 97-105.

Saura, E., Ardèvol I Oró, L., Teixell, A. and Vergés, J., 2016, Rising and falling diapirs, shifting depocenters, and flap overturning in the Cretaceous Sopeira and Sant Gervàs subbasins (Ribagorça Basin, southern Pyrenees): *Tectonics*, v. 35, p. 638–662.

Sayer, Z., Edet, J., Gooder, R. and Love, A., The Machar Field, Block 23/26a, UK North Sea, in: Goffey, G., and Gluyas, J.G., eds., *United Kingdom Oil and Gas Fields: 50<sup>th</sup> Anniversary Commemorative Volume*, Geological Society, London, *Memoirs*, v. 52, p. 550-559.

Schmalz, R.F., 1969, Deep-water evaporite deposition: a genetic model. *AAPG Bulletin*, v. 53(4), p. 798-823.

Scholz, C. A., Rosendahl, B. R., and Scott, D. L., 1990, Development of coarse- grained facies in lacustrine rift basins: Examples from East Africa: *Geology*, v. 18, p. 140– 144.

Schorn, A., and Neubauer, F., 2014, The structure of the Hallstatt evaporite body (Northern Calcareous Alps, Austria): A compressive diapir superposed by strike-slip shear?: *Journal of Structural Geology*, v. 60, p. 70-84.

Schöpfer, M.P.J., Childs, C. and Walsh, J.J., 2006, Localisation of normal faults in multilayer sequences: *Journal of Structural Geology*, v. 28, p. 816-833.

Schultz-Ela, D., 2003, Origin of drag folds bordering salt diapirs: *AAPG Bulletin*, v. 87, p. 757–780.

Schultz-Ela, D. D., and Jackson, M.P.A., 1996, Relation of subsalt structures to suprasalt structures during extension: *AAPG Bulletin*, v. 80, p. 1896-1924.

- Schultz-Ela, D. D., and Walsh, P., 2002, Modeling of grabens extending above evaporites in Canyonlands National Park, Utah: *Journal of Structural Geology*, v. 24, p. 247–275.
- Schultz-Ela, D. D., Jackson, M.P.A., and Vendeville, B.C., 1993, Mechanics of active salt diapirism: *Tectonophysics*, v. 228, p. 275–312.
- Schwab, A.M., Cronin, B.T., and Ferreira, H., 2007, Seismic expression of channel outcrops: Offset stacked versus amalgamated channel systems: *Marine and Petroleum Geology*, v. 24, p. 504–514.
- Scott, E.D., Gelin, F., Jolley, S.J., Leenaarts, E., Sadler, S.P., and Elsinger, R.J., 2010, Sedimentological control of fluid flow in deep marine turbidite reservoirs: Pierce Field, UK Central North Sea, in: Jolley, S.J., Fisher, Q.J., Ainsworth, R.B., Vrolijk, P.J., and Delisle, S., eds., *Reservoir Compartmentalization*: Geological Society of London, Special Publication 347, p. 113–132.
- Sellier, N., and Vendeville, B.C., 2009, Gravitational Salt Tectonics Triggered by Deposition of Turbiditic Lobes: a New Experimental Modeling Approach with Applications to Salt Tongues in the U.S. Gulf of Mexico: *AAPG Search and Discovery Article #40478*.
- Seranne, M., and Anka, Z., 2005, South Atlantic continental margins of Africa: a comparison of the tectonic vs climate interplay on the evolution of equatorial west Africa and SW Africa margins: *Journal of African Earth Science*, v. 43, p. 283–300.
- Serié, C., Huuse, M., Schødt, N. H., Brooks, J. M., and Williams, A., 2017, Subsurface fluid flow in the deep-water Kwanza Basin, offshore Angola. *Basin Research*, v. 29, p. 149–179.
- Shanmugam, G., 1997, The Bouma Sequence and the turbidite mind set: *Earth-Science Reviews*, v. 42, p. 201–229.
- Shanmugam, G., 2017, Global case studies of soft-sediment deformation structures (SSDS): Definitions, classifications, advances, origins and problems: *Journal of Palaeogeography*, v. 6(4), p. 251–320.
- Shanmugam, G., and Moiola, R.J., 1988, Submarine fans: Characteristics, models, classification, and reservoir potential: *Earth-Science Reviews*, v. 24 (6), p. 383–428.
- Sharp, I.R., Gawthorpe, R.L., Underhill, J.R., and Gupta, S., 2002, Fault-propagation folding in extensional settings: Examples of structural style and synrift sedimentary response from the Suez rift, Sinai, Egypt: *GSA Bulletin* v. 112, p. 1877–1899.
- SHESHA (Euskadiko Hidrokarburoak), 2018, Oil and Gas in the Basque-Cantabrian Basin and Environments: Gaviota, available online <http://www.shesa.eus/en/oil-gas>.
- Shultz, M.R., and Hubbard, S.M., 2005, Sedimentology, stratigraphic architecture, and ichnology of gravity-flow deposits partially ponded in a growth-fault-controlled slope minibasin, Tres Pasos Formation (Cretaceous), southern Chile: *Journal of Sedimentary Research*, v. 75, p. 440–453.
- Sims, D. W., Morris, A.P., Wyrick, D.Y., Ferrill, D.A., Waiting, D.J., Franklin, N.M., Colton, S.L., Umezawa, Y.T., Takanashi, M., and Beverly, E. J., 2013, Analog modeling of normal faulting above Middle East domes during regional extension: *AAPG Bulletin*, v. 97, p. 877–898.

- Sinclair, H.D., 1994, The influence of lateral basin slopes on turbidite sedimentation in the Annot Sandstones of SE France: *Journal of Sedimentary Petrology*, v. B64, p. 42-54.
- Sinclair, H.D., and Tomasso, M., 2002, Depositional evolution of confined turbidite basins: *Journal of Sedimentary Research*, v. 72, p. 451-456.
- Sinclair, H.D. and Cowie, P.A., 2003. Basin-floor topography and the scaling of turbidites: *The Journal of Geology*, v. 111(3), p. 277-299.
- Smith, R., and Joseph, P., 2004, Onlap stratal architectures in the Gres d'Annot: geometric models and controlling factors, in: Joseph, P. and Lomas, S.A., eds., *Deep-Water Sedimentation in the Alpine Basin of SE France: New Perspectives on the Gres d'Annot and Related Systems*, Geological Society, London, Special Publications, v. 221, p. 389–399.
- Smith, R., 2004, Turbidite systems influenced by structurally induced topography in the multi-sourced Welsh Basin, in: Lomas, S.A., and Joseph, P., eds., *Confined Turbidite Systems*: Geological Society, London, Special Publication 222, p. 209-228.
- Snidero, M., Muñoz, J.A., Carrera, N., Butillé, M., Mencos, J., Motamedi, H., Piryaei, A., and Sàbat, F., 2019, Temporal evolution of the Darmadan salt diapir, eastern Fars region, Iran: *Tectonophysics*, v. 766, p. 115-130.
- Sobiesiak, M.S., Kneller, B., Alsop, G.I. and Milana, J.P., 2016, Inclusion of substrate blocks within a mass transport deposit: a case study from Cerro Bola, Argentina: *Submarine Mass Movements and Their Consequences*, Springer p. 487-496.
- Sobiesiak, M.S., Kneller, B., Alsop, G.I., and Milana, J.P., 2018, Styles of basal interaction beneath mass transport deposits: *Marine and Petroleum Geology*, v. 98, p. 629–639.
- Sohn, Y.K., 1997, On traction-carpet sedimentation: *Journal of Sedimentary Research*, v. 67, no. 3.
- Sohn, Y.K., 2000, Depositional processes of submarine debris flows in the Miocene fan deltas, Pohang Basin, SE Korea with special reference to flow transformation: *Journal of Sedimentary Research*, v. 70, p. 491–503.
- Sohn, Y.K., Choe, M.Y., and Jo, H.R., 2002, Transition from debris flow to hyperconcentrated flow in a submarine channel (the Cretaceous Cerro Toro Formation, southern Chile): *Terra Nova*, v. 14, p. 405-415.
- Sømme, T.O., Helland-Hansen, W., Martinsen, O.J., and Thurmond, J.B., 2009, Relationships between morphological and sedimentological parameters in source-to-sink systems: a basis for predicting semi-quantitative characteristics in subsurface systems: *Basin Research*, v. 21 (4) p. 361–387.
- Soto, R., Beamud, E., Roca, E., Carola, E., and Almar, Y., 2017, Distinguishing the effect of diapir growth on the magnetic fabrics of syn-diapiric overburden rocks: Basque Cantabrian Basin, Northern Spain: *Terra Nova*, v. 29, p. 191-201.
- Souche, L., Mahdavi, R., Mahmood, N.M, Alim, S., Masoudi, R. and Basu, D. 2015, Reservoir modelling of complex thin-bedded deep water deposits integrating well data, seismic inversion

and depositional model from Offshore Sabah, Malaysia: International Petroleum Technology Conference, Doha, Qatar.

Southern, S.J., Patacci, M., Felletti, F., and McCaffrey, W.D., 2015, Influence of flow containment and substrate entrainment upon sandy hybrid event beds containing a co-genetic mud-clast-rich division: *Sedimentary Geology*, v. 321, p. 105–122.

Southern, S.J., Kane, I.A., Warchol, M.J., Porten, K.W., and McCaffrey, W.D., 2017, Hybrid event beds dominated by transitional-flow facies: Character, distribution and significance in the Maastrichtian Springar Formation, north-west Vøring Basin, Norwegian Sea: *Sedimentology*, v. 64, no. 3, p. 747–776.

Soutter, E.L., Kane, I.A., and Huuse, M., 2018, Giant submarine landslide triggered by Paleocene mantle plume activity in the North Atlantic: *Geology*, v. 46, p. 511-514.

Soutter, E.L., Kane, I.A., Fuhrmann, A., Cumberpatch, Z.A., and Huuse, M., 2019, The stratigraphic evolution of onlap in clastic deep-water systems: Autogenic modulation of allogenic signals: *Journal of Sedimentary Research*, v. 89 (10), p. 890-917.

Soutter, E.L., Bell, D., Cumberpatch, Z.A., Ferguson, R.A., Kane, I.A., Spsychala, Y.T., and Eggenhuisen, J., 2021, The Influence of Confining Topography Orientation on Experimental Turbidity Currents and Geological Implications: *Frontiers in Earth Science*, v. 8.

Spence, G.H., and Finch, E., 2014, Influences of nodular chert rhythmites on natural fracture networks in carbonates: an outcrop and two-dimensional discrete element modelling study, in: Spence, G.H., Redfern, J., Aguilera, R., Bevan, T.G., Cosgrove, J.W., Couples, G.D., and Daniel, J.M., eds., *Advances in the Study of Fractured Reservoirs: Geological Society, London, Special Publications*, v. 374, p. 211-249.

Spiers, C. J., Schutjens, P. M. T. M., Brzesowsky, R. H., Peach, C. J., Liezenberg, J. L., and Zwart, H. J., 1990, Experimental determination of constitutive parameters governing creep of rocksalt by pressure solution, in: Knipe, R.J., and Rutter, E.H., eds., *Deformation Mechanisms, Rheology and Tectonics: Geological Society, London, Special Publications*, v. 54, 215–227

Sprague, A.R., Sullivan, M.D., Champion, K.M., Jensen, G.N., Goulding, F.J., Garfield, T.R., Sickafoose, D.K., Rossen, C., and Jeannette, D.C., 2002, The physical stratigraphy of deep-water strata: A hierarchical approach to the analysis of genetically-related stratigraphic elements for improved reservoir prediction, in National AAPG/SEPM meeting abstracts, Houston, Texas, p. 10–13.

Spsychala, Y.T., Hodgson, D.M., Flint, S.S., and Mountney, N.P., 2015, Constraining the sedimentology and stratigraphy of submarine intraslope lobe deposits using exhumed examples from the Karoo Basin, South Africa: *Sedimentary Geology*, v. 322, p. 67–81.

Spsychala, Y.T., Hodgson, D.M., and Lee, D.R., 2017a, Autogenic controls on hybrid bed distribution in submarine lobe complexes: *Marine and Petroleum Geology*, v. 88, p. 1078–1093.

Spsychala, Y.T., Hodgson, D.M., Prélat, A., Kane, I.A., Flint, S.S., and Mountney, N.P., 2017b, Frontal and lateral submarine lobe fringes: comparing sedimentary facies, architecture and flow processes: *Journal of Sedimentary Research*, v. 87, p. 75-96.

- Spychala, Y.T., Hodgson, D.M., and Stevenson, C.J., 2017c, Aggradational lobe fringes: The influence of subtle intrabasinal seabed topography on sediment gravity flow processes and lobe stacking patterns: *Sedimentology*, v. 64, p. 582–608.
- Spychala, Y., Eggenhuisen, J., Tilston, M., and Pohl, F., 2020, The influence of basin settings and flow properties on the dimensions of submarine lobe elements: *Sedimentology*, v. 67(7), p. 3471-3491.
- Stanbrook, D.A., Pringle, J.K., Elliot, T., Clark, J.D. and Gardiner, A., 2008, Resolving Deep-Water Stratigraphic Traps: Forward Seismic Modeling of a Turbidite Onlap; Montagne de Chalufy, Grès d'Annot Formation, Southeast France: in: Schofield, K., Rosen, N.C., Pfeiffer, D. and Johnson, S., eds., *Answering the Challenges of Production from Deep-Water Reservoirs: Analogues and Case Histories to Aid a New Generation*.
- Stevenson, C.J., and Peakall, J., 2010, Effects of topography on lofting gravity flows: Implications for the deposition of deep-water massive sands: *Marine and Petroleum Geology*, v. 27 (7), p. 1366-1378.
- Stevenson, C.J., Jackson, C.A.-L., Hodgson, D.M., Hubbard, S.M., and Eggenhuisen, J.T., 2015, Deep-water sediment bypass: *Journal of Sedimentary Research*, v. 85, p. 1058– 1081.
- Stevenson, C.J., Feldens, P., Georgiopoulou, A., Schönke, M., Krastel, S., Piper, D.J.W., Lindhorst, K., and Mosher, D., 2018, Reconstructing the sediment concentration of a giant submarine gravity flow: *Nature Communications*, v. 9, no. 1, p. 2616.
- Stevenson, C.J., Peakall, J., Hodgson, D.M., Bell, D., and Privat, A., 2020, Tb or not Tb: banding in turbidite sandstones: *Journal of Sedimentary Research*, v. 90 (8), p. 821-842.
- Stewart, S. A., 2006, Implications of passive salt diapir kinematics for reservoir segmentation by radial and concentric faults: *Marine and Petroleum Geology*, v. 23, p. 843–853.
- Stewart, S.A., 2017. Salt tectonics in the North Sea Basin: a structural style template for seismic interpreter, in: Ries, A.C., Butler, R.W.H., and Graham, R.H., eds., *Deformation of the Continental Crust: The Legacy of Mike Coward: Geological Society, London, Special Publications*, v. 272, p. 361-396.
- Stewart, S. A. and J.A. Clark, 1999, Impact of salt on the structure of the Central North Sea hydrocarbon fairways, in: Fleet, A.J., and Boldy, S.A.R., eds., *Petroleum Geology of Northwest Europe: Proceedings of the 5<sup>th</sup> Conference*, Geological Society, London, *Petroleum Geology Conference series*, v. 5, p. 179-200.
- Stow, D.A.V., Reading, H.G. and Collinson, J.D., 1996, Deep seas. In Reading, H.G., ed., *Sedimentary Environments: Processes, Facies and Stratigraphy* (3rd edition), Oxford, Blackwell Science, 395–453.
- Straub, K.M. and Pyles, D.R., 2012, Quantifying the hierarchical organisation of compensation in submarine fans using surface statistics: *Journal of Sedimentary Research*, v. 82, p. 889-898.
- Straub, K. M., Mohrig, D., McElroy, B., Buttles, J., and Pirmez, C., 2008, Interactions between turbidity currents and topography in aggradating sinuous submarine channels: A laboratory study. *GSA Bulletin*, v.120 (3), p. 368-385.

Straub, K.M., Paola, C., Mohrig, D., Wolinsky, M.A., and George, T., 2009, Compensational Stacking of Channelized Sedimentary Deposits: *Journal of Sedimentary Research*, v. 79 (9), p. 673-688.

Stricker, S., Jones, S.J., Meadows, N. and Bowen, L., 2018, Reservoir quality of fluvial sandstone reservoirs in salt-walled mini-basins: an example from the Seagull field, Central Graben, North Sea, UK: *Petroleum Science*, v. 15, p. 1–27.

Sullivan, M.D., Jensen, G.N., Goulding, F.J., Jennette, D.C., Foreman, J.L., and Stern, D., 2000, Architectural analysis of deep-water outcrops: Implications for exploration and development of the Diana sub-basin, western Gulf of Mexico, in: Weimer, P., Slatt, R.M., Bouma, A.H., and Lawrence, D.T. eds., *Deep-water reservoirs of the world*, Gulf Coast Section SEPM Foundation, Twentieth Annual Research Conference, p. 1010–1032.

Sumner, E., Amy, L., and Talling, P., 2008, Deposit structure and processes of sand deposition from decelerating sediment suspensions: *Journal of Sedimentary Research*, v. 78, p. 529–547.

Sumner, E.J., Talling, P.J., and Amy, L., 2009, Deposits of flows transitional between turbidity current and debris flow: *Geology*, v. 37, no. 11, p. 991–994.

Sumner, E.J., Peakall, J., Parsons, D.R., Wynn, R.B., Darby, S.E., Dorrell, R.M., McPhail, S.D., Perrett, J., Webb, A., and White, D., 2013, First direct measurements of hydraulic jumps in an active submarine density current: *Geophysical Research Letters*, v. 40, p. 5904-5908.

Suppe, J., 1985, *Principles of structural geology*: Englewood Cliffs, NJ, Prentice-Hall, 537 p.

Svendsen, J.B., Hansen, H.J., Størmosse, T., and Engkilde, M.K., 2010, Sand remobilization and injection above an active salt diapir: the Tyr sand of the Nini Field, Eastern North Sea: *Basin Research*, v. 22 (4) p. 548-561.

Sweet, M.L., Gaillot, G.T., Jouet, G., Rittenour, T.M., Toucanne, S., Marsset, T. and Blum, M.D., 2019, Sediment routing from shelf to basin floor in the Quaternary Golo System of Eastern Corsica, France, western Mediterranean Sea: *GSA Bulletin*, v. 132 (5-6), p. 1217-1234.

Sylvester, Z., and Lowe, D.R., 2004, Textural trends in turbidites and slurry beds from the Oligocene flysch of the East Carpathians, Romania: *Sedimentology*, v. 51, no. 5, p. 945–972.

Sylvester, Z., Pirmez, C. and Cantelli, A., 2011. A model of submarine channel-levee evolution based on channel trajectories: Implications for stratigraphic architecture. *Marine and Petroleum Geology*, v. 28, p. 716-727.

Sylvester, Z., Deptuck, M.E., Prather, B.E., Pirmez, C., and O’Byrne, C., 2012, *Seismic Stratigraphy of a Shelf-Edge Delta and Linked Submarine Channels in the Northeastern Gulf of Mexico*: SEPM Special Publication, v. 99, p. 31-59.

Sylvester, Z., Cantelli, A., and Pirmez, C., 2015, Stratigraphic evolution of intraslope minibasins: Insights from surface-based model: *AAPG Bulletin*, v. 99, p. 1099-1129.

Sztanó, O., Szafián, P., Magyar, I., Horányi, A., Bada, G., Hughes, D.W., Hoyer, D.L., and Wallis, R.J., 2013, Aggradation and progradation controlled clinothems and deep-water sand delivery



- model in the Neogene Lake Pannon, Makó Trough, Pannonian Basin, SE Hungary: *Global and Planetary Change*, v. 103, p. 149-167.
- Talbot, C.J., 1978, Halokinesis and thermal convection: *Nature* v. 273, p. 739–741.
- Talbot, C. J., 1981, Sliding and other deformation mechanisms in a glacier of salt in S. Iran, in: McClay, K.R., and Price, N.J., eds., *Thrust and nappe tectonics*: London, Geological Society, Special Publication 9, 173–183.
- Talbot, C. J., 1992, Quo vadis tectonophysics? With a pinch of salt!: *Journal of Geodynamics*, v. 16, p. 1–20.
- Talbot, C.J., 1993, Spreading of salt structures in the Gulf of Mexico, *Tectonophysics*, v, 228 (3-4), p. 151-166.
- Talbot, C.J., 1995. Molding of salt diapirs by stiff overburden, in: Jackson, M.P.A., Roberts, D.G., Snelson, S., eds., *Salt Tectonics: a Global Perspective*. AAPG Memoir, v. 65, p. 61–75.
- Talbot, C.J., and Pohjola, V., 2009, Subaerial salt extrusions in Iran as analogues of ice sheets, streams and glaciers: *Earth Science Reviews*, v. 97 (1-4), p. 155-183.
- Talling, P.J., 1998. How and where do incised valleys form if sea level remains above the shelf edge?: *Geology*, v. 26, p. 87-90.
- Talling, P.J., 2001, On the frequency distribution of turbidite thickness: *Sedimentology*, v. 48, p. 1297–1329.
- Talling, P., Amy, L., Wynn, R.B., Peakall, J., and Robinson, M., 2004, Beds comprising debrite sandwiched within co-genetic turbidite: Origin and widespread occurrence in distal depositional environments: *Sedimentology*, v. 51, p. 163–194.
- Talling, P.J., Amy, L.A., and Wynn, R.B., 2007, New insight into the evolution of large- volume turbidity currents: Comparison of turbidite shape and previous modelling results: *Sedimentology*, v. 54, no. 4, p. 737–769.
- Talling, P.J., Masson, D.G., Sumner, E.J., and Malgesini, G., 2012, Subaqueous sediment density flows: Depositional processes and deposit types: *Sedimentology*, v. 59, p. 1937–2003.
- Talling, P.J., Paull, C.K. and Piper, D.J., 2013, How are subaqueous sediment density flows triggered, what is their internal structure and how does it evolve? Direct observations from monitoring of active flows: *Earth-Science Reviews*, v. 125, p. 244-287.
- Talling, P.J., Clare, M., Urlaub, M., Pope, E., Hunt, J.E., and Watt, S.F.L., 2014, Large submarine landslides on continental slopes: *Oceanography*, v. 27, no. 2, p. 32–45.
- Talling, P.J., Allin, J., Armitage, D.A., Arnott, R.W., Cartigny, M.J., Clare, M.A., Felletti, F., Covault, J.A., Girardclos, S., Hansen, E. and Hill, P.R., 2015, Key future directions for research on turbidity currents and their deposits: *Journal of Sedimentary Research*, v. 85, p. 153-169.

- Tavani, S., and Granado, P., 2015, Along-strike evolution of folding, stretching and breaching of supra-salt strata in the Plataforma Burgalesa extensional forced fold system (northern Spain): *Basin Research*, v. 27 (4), p. 573-585.
- Taylor, J., 1990, Upper Permian—Zechstein: *Petroleum Geology of the North Sea: Basic Concepts and Recent Advances*, Fourth Edition, p. 174-211.
- Taylor, J.C.M. 1998. Upper Permian—Zechstein, in: Glennie, K.W., ed., *Petroleum Geology of the North Sea: Basic Concepts and Recent Advances*, Fourth Edition. Blackwell Science Ltd, Oxford, p. 174-211.
- Teixell, A., Barnalos, A., Rosales, I., and Arboleya, M-L., 2017, Structural and facies architecture of a diapir-related carbonate minibasin (lower and middle Jurassic, High Atlas, Morocco): *Marine and Petroleum Geology*, v. 81, p. 334-360.
- Teixell, A., Labaume, P., Ayarza, P., Espurt, N., de Saint Blanquat, M., and Lagabrielle, Y., 2018, Crustal structure and evolution of the Pyrenean-Cantabrian belt: A review and new interpretations from recent concepts and data: *Tectonophysics*, v. 724-725, p. 146-170.
- Teles, V., Chauveau, B., Joseph, P., Weill, P., and Maktouf, F., 2016, CATS- A process-based model for turbulent turbidite systems at reservoir scales: *Comptes Rendus Geoscience*, v. 384, p. 473-478.
- Tenzer, R., and Gladkikh, V., 2014, Assessment of Density Variations of Marine Sediments with Ocean and Sediment Depths: *The Scientific World Journal*. Article ID 823296.
- Terlaky, V., Rocheleau, J. and Arnott, R.W.C., 2016, Stratal composition and stratigraphic organization of stratal elements in an ancient deep-marine basin-floor succession, Neoproterozoic Windermere Supergroup, British Columbia, Canada: *Sedimentology*, v. 63, pp.136-175.
- Thielmann, M., and Kaus, B.J.P., 2012, Shear heating induced lithospheric-scale localization: Does it result in subduction?: *Earth and Planetary Science Letters*, v. 359-360, p. 1-13.
- Thoeni, K., Giacomini, A., Lambert, C., Sloan, S.W. and Carter, J.P., 2014, A 3D discrete element modelling approach for rockfall analysis with drapery systems: *International Journal of Rock Mechanics and Mining Sciences*, v. 68, p. 107-119.
- Tilhams, F., Gawthorpe, R.L., Jackson, C, A-L., and Rotevatn, A., 2021, Syn-rift sediment gravity flow deposition on a late Jurassic fault-terraced slope, northern north sea: *Basin Research*, online early.
- Tinterri, R. and Magalhaes, P.M., 2011, Synsedimentary structural control on foredeep turbidites: an example from Miocene Marnoso-arenacea Formation, Northern Apennines, Italy: *Marine and Petroleum Geology*, v. 28, p. 629-657.
- Tinterri, R., Drago, M., Consonni, A., Davoli, G., and Mutti, E., 2003, Modelling subaqueous bipartite sediment gravity flows on the basis of outcrop constraints: First results: *Marine and Petroleum Geology*, v. 20, (6-8) p. 911–933.
- Tinterri, R., Magalhaes, P.M., Tagliaferri, A., and Cunha, R.S., 2016, Convolute laminations and load structures in turbidites as indicators of flow reflections and decelerations against bounding

slopes. Examples from the Marnoso-arenacea Formation (northern Italy) and Annot Sandstones (south eastern France): *Sedimentary Geology*, v. 344, p. 382-407.

Toniolo, H., Lamb, M. and Parker, G., 2006. Depositional turbidity currents in diapiric mini-basins on the continental slope: formulation and theory: *Journal of Sedimentary Research*, v. 76, p. 783-797.

Trudgill, B., 2011, Evolution of salt structures in the northern Paradox Basin: controls on evaporite deposition, salt wall growth and supra-salt stratigraphic architecture: *Basin Research*, v. 23, pp. 208-238.

Trudgill, B.D. and Paz, M., 2009, Restoration of mountain front and salt structures in the northern Paradox Basin, SE Utah, in: Houston, W.S., Wray, L.L., and Moreland, P.G., eds., *The Paradox Basin Revisited – New Developments in Petroleum Systems and Basin Analysis* pp. 132–177. RMAG Special Publication, Denver, CO.

Trudgill, B., Banbury, N. and Underhill, J., 2004, Salt evolution as a control on structural and stratigraphic systems: northern Paradox foreland basin, southeast Utah, USA, in: Post, P., Olson, D., Lyons, K., Palmes, S., Harrison, P., and Rosen, N., eds., *Salt–Sediment Interactions and Hydrocarbon Prospectivity: Concepts, Applications, and Case Studies for the 21st century* pp. 669–700. 24th Annual GCSSEPM Bob F. Perkins Research Conference.

Trusheim, F., 1957, Über Halokinese und ihre Bedeutung für die strukturelle Entwicklung Norddeutschlands: *Zeitschrift der Deutschen Gesellschaft für Geowissenschaften*, v. 109, p.111-151.

Trusheim, F., 1960, Mechanism of Salt Migration in Northern Germany: *AAPG Bulletin*, v. 44 (9), p. 1519-1540.

Tvedt, A.B.M., Rotevatn, A., Jackson, C. A-L., Fossen, H., and Gawthorpe, R.L., 2013, Growth of normal faults in multilayer sequences: A 3D seismic case study from the Egersund Basin, Norwegian North Sea: *Journal of Structural Geology*, v. 55, p. 1-20.

Tvedt, A.B.M., Rotevatn, A., and Jackson, C.A-L., 2016, Supra-salt normal fault growth during the rise and fall of a diapir: Perspectives from 3D seismic reflection data, Norwegian North Sea: *Journal of Structural Geology*, v. 91, v. 1-26.

Ucgul, M., Saunders, C., and Fielke, J.M., 2018, Comparison of the discrete element and finite element methods to model the interaction of soil and tool cutting edge: *Biosystems Engineering*, v. 169, p. 199-208.

Urlaub, M., Geersen, J., Krastel, S. and Schwenk, T., 2018, Diatom ooze: Crucial for the generation of submarine mega-slides?: *Geology*, v. 46, p. 331-334.

Usiglio, J., 1849, Analyse de l'eau de la Mediterranee sur les cotes de France. *Annalen der Chemie*, v. 27, pp. 92-107.

Vail, P.R., Mitchumi, R.M., Jr., Todd, R.G., Widmier, J.M., Thompson, S., III, Sangree, J.B., Bubb, J.N., and Hatelid, W.G., 1977, Seismic stratigraphy and global changes of sea-level, in: Payton, C.E., ed., *Seismic Stratigraphy-Applications to Hydrocarbon Exploration: AAPG Memoir 26*, p. 49-212.

Valle, P. J., Gjelberg, J. G., and Helland-Hansen, W., 2001, Tectonostratigraphic development in the eastern lower Congo basin, offshore Angola, West Africa. *Marine and Petroleum Geology*, v. 18, p. 909–927.

Valyashko, M.G., 1956, Geochemistry of bromine in the processes of salt deposition and the use of the bromine content as a genetic and prospecting criterion: *Geochemistry*, v. 6, p. 570-589.

Vanoni, V.A., 1946, Transportation of suspended sediment by water: *Transactions of the American Society of Civil Engineers*, v. 111, p. 67-133.

Van Andel, T.H., and Komar, P.D., 1969, Ponded sediments of the Mid-Atlantic Ridge between 22 and 23 North latitude: *GSA Bulletin*, v. 80, p. 1163-1190.

Van Bergen, F., and De Leeuw, C.S., 2001, Salt Cementation of Reservoir Rocks near Salt Domes in the Netherlands North Sea Area – a new Mechanism: *Conference Proceedings, 63<sup>rd</sup> EAGE Conference and Exhibition, June 2001*.

Van Der Mewe, W.C., Hodgson, D.M., and Flint, S.S., Widespread syn-sedimentary deformation on a muddy deep-water basin-floor: the Vischkul Formation (Permian), Karoo Basin, South Africa: *Basin Research*, v. 21 (4), p. 389-406.

Van Der Voo, R., 1969, Paleomagnetic evidence for the rotation of the Iberian peninsula: *Tectonophysics*, v. 7, p. 5-56.

Vendeville, B. C., and Jackson, M.P.A., 1991, Deposition, extension, and the shape of down-building salt diapirs: *AAPG Bulletin*, v. 75, p. 687–688.

Vendeville, B.C., and Jackson, M.P.A., 1992a, The rise of diapirs during thin-skinned extension: *Marine and Petroleum Geology* v. 9, p. 331–353.

Vendeville, B.C., and Jackson, M.P.A., 1992b, The fall of diapirs during thin-skinned extension: *Marine and Petroleum Geology*, v. 9, p. 354–371.

Vendeville, B. C., and Nilsen, K.T., 1995, Episodic growth of salt diapirs driven by horizontal shortening, in: *Salt, sediment, and hydrocarbons: Society of Economic Paleontologists and Mineralogists Gulf Coast Section, 16th annual research conference program and extended abstracts*, p. 285–295.

Vendeville, B.C., Ge, H., and Jackson, M.P.A., 1995, Scale models of salt tectonics during basement-involved extension: *Petroleum Geoscience*, v. 1, p. 179-183.

Venus, J.H., Mountney, N.P., and McCaffrey, W.D., 2015, Syn-sedimentary salt diapirism as a control on fluvial- system evolution: an example from the proximal Permian Cutler Group, SE Utah, USA: *Basin Research*, v. 27, p. 152–182.

Vicente Bravo, J., and Robles, S., 1991a, Geometría y modelo deposicional de la secuencia Solube del Flysch Negro (Albiense medio, norte de Bizkaia): *Geogaceta*, v. 10, p. 69–72.

- Vicente Bravo, J., and Robles, S., 1991b, Caracterización de las facies de la transición canal-lóbulo en la secuencia Jata del Flysch Negro (Albiense Superior norte de Vizcaya): *Geogaceta*, v. 10, p. 72–75.
- Vicente Bravo, J.C., and Robles, S., 1995, Large-scale mesotopographic bedforms from the Albian Black Flysch, northern Spain: characterization, setting and comparisons with recent analogues, in: Pickering, K.T., Hiscott, R.N., Kenyon, N.H., Ricci Lucchi, F., and Smith, R.D.A., eds., *Atlas of Deep-water Environments: Architectural Style in Turbidites Systems*, p. 216-226.
- Vinnels, J.S., Butler, R.W., McCaffrey, W.D. and Paton, D.A., 2010, Depositional processes across the Sinú accretionary prism, offshore Colombia: *Marine and Petroleum Geology*, v. 27, p. 794-809.
- Von der Borch, C.C., Smit, R. and Grady, A.E., 1982, Late Precambrian submarine canyons of Adelaide Geosyncline, South Australia: *AAPG Bulletin*, v. 66, pp. 332–347.
- Walker, R.G., 1966, Deep channels in turbidite-bearing formations: *AAPG Bulletin*, v. 50 (9), p. 1899–1917.
- Walker, R.G., 1978, Deep-water sandstone facies and ancient submarine fans: Models for exploration for stratigraphic traps: *AAPG Bulletin*, v. 62 (6), p. 932–966.
- Walker, R.G., 1992, Turbidites and submarine fans, in: Walker, R.G. and James, N.P., eds., *Facies models: response to sea level change*, Geological Association of Canada Ontario, p. 239–263.
- Wang, Z.Y. and Larsen, P., 1994, Turbulence structure of flows of water and clay suspensions with bedload: *Journal of Hydraulic Engineering*, v. 120, p. 577–600.
- Wang, Z., and Plate, E.J., 1996, A preliminary study on the turbulence structure of flows on non-Newtonian fluid: *Journal of Hydraulic Research*, v. 34, p. 345–361.
- Wang, X., Luthi, S.M., Hodgson, D.M., Sokoutis, D., Willingshofer, E. and Groenenberg, R.M., 2017, Turbidite stacking patterns in salt-controlled minibasins: Insights from integrated analogue models and numerical fluid flow simulations: *Sedimentology*, v. 64, p. 530-552.
- Ward, S.N., 2001, Landslide tsunami: *Journal of Geophysical Research*, v. 106 (B6), p. 11201.
- Ward, N.I.P., Alves, T.M. and Blenkinsop, T.G., 2016, Reservoir leakage along concentric faults in the Southern North Sea: Implications for the deployment of CCS and EOR techniques: *Tectonophysics*, v. 690, p. 97-116.
- Ward, N.I.P., Alves, T. M., and Blenkinsop, T. G., 2018, Submarine sediment routing over a blocky mass-transport deposit in the Espírito Santo Basin, SE Brazil: *Basin Research*, v. 30, p. 816-834.
- Warren, J., 1999. *Evaporites: Their Evolution and Economics*. Blackwell Science, Oxford. 438 p.
- Warren, J.K., 2006, *Evaporites: Sediments, Resources and Hydrocarbons*. Springer Science and Business Media.

- Warren, J.K., 2010, Evaporites through time: Tectonic, climatic and eustatic controls in marine and nonmarine deposits: *Earth-Science Reviews*, v. 98, pp. 217-268.
- Warren, J., 2016, *Evaporites: A Geological Compendium*: New York, Springer, 1813 p.
- Warsitzka, M., Kley, J. and Kukowski, N., 2013, Salt diapirism driven by differential loading—some insights from analogue modelling: *Tectonophysics*, v. 591, p. 83-97.
- Weaver, P.P.E., and Kuijpers, A., 1983, Climatic control of turbidite deposition on the Madeira Abyssal Plain: *Nature*, v. 306, p. 360-363.
- Weijermars, R., Jackson, M.P.A., and Vendeville, B., 1993, Rheological and tectonic modeling of salt provinces: *Tectonophysics*, v. 217, p. 143–174.
- Weijermars, R., Hudec, M.R., Dooley, T.P. and Jackson, M.P.A. 2015, Downbuilding salt stocks and sheets quantified in 3-D analytical models: *Solid Earth*, v. 120, p. 4616-4644.
- Weimer, P., 1994, *Submarine Fans and Turbidite Systems*. Tulsa, OK: Gulf Coast Section-Society of Economic Paleontologists and Mineralogists.
- Weimer, P., and Link, M. H., 1991, *Seismic Facies and Sedimentary Processes of Submarine Fans and Turbidite Systems*. New York, NY: Springer-Verlag.
- Weinberg, R.F., and Schmeling, H., 1992, Polydiapirs: multiwave length gravity structures: *Journal of Structural Geology*, v. 14, p. 425-436.
- Weislogel, A., 2001 *The depositional system, stratigraphy, and petrology of the Maastrichtian Muerto Formation, La Popa Basin, Mexico: implications for diapirism and foreland evolution*. MS. Thesis. New Mexico State University, USA.
- Whitman, J.M., and Davies, T.A., 1979, Cenozoic oceanic sedimentation rates: how good are the data?: *Marine Geology*, v. 30, p. 269-284.
- Whyatt, M., Bowen, J. M., and Rhodes, D. N., 1991, Nelson – successful application of a development geo- seismic model in North Sea exploration. *First Break*, 9, 265–280.
- Wilkins, S., Mount, V., Davies, R., Butaud, T., Lindsey, B., Fenn, C., Syrek, J., Adiguna, H., and Matthews, I., 2019, Sub-seismic deformation in traps adjacent to salt stocks/walls: Observations from Green Canyon, Gulf of Mexico: *European Association of Geoscientists and Engineers, Conference Proceedings, Fifth International Conference on Fault and Top Seals* v. 2019, p. 1-5.
- Wilkinson, M., Haszeldine, S.R., Mackay, E., Smith, K. and Sargeant, S., 2013, A new stratigraphic trap for CO<sub>2</sub> in the UK North Sea: Appraisal using legacy information: *International Journal of Greenhouse Gas Control*, v. 12, p. 310-322.
- Willet, S.D., 1999, Rheological dependence of extension in wedge models of convergent orogens: *Tectonophysics*, v. 305, p. 419-435.
- Willet, S., Beaumont, C., and Fullsack, P., 1993, Mechanical model for the tectonics of doubly vergent compressional orogens: *Geology*, v. 21, p. 371–374.
- Wills, J. M., and Peattie, D. K. 1990. The Forties Sandstone Field and the evolution of a reservoir management strategy, in: Buller, A. T., Berg, E., Hjelmeland, O., Kleppe, J., Torsaeter, O.,

and Aasen, J. O., eds., North Sea Oil & Gas Reservoirs – II. Norwegian Institute of Technology. Graham and Trotman, London, 1–23.

Winker, C.D., 1996, High-resolution seismic stratigraphy of a late Pleistocene submarine fan ponded by salt-withdrawal mini-basins on the Gulf of Mexico continental slope. In Offshore Technology Conference. Offshore Technology Conference, p. 619-628.

Winker, C. D., and J. R. Booth, 2000, Sedimentary dynamics of the salt-dominated continental slope, Gulf of Mexico: Integration of observations from the seafloor, near-surface, and deep subsurface, in Deep-water reservoirs of the world: Society of Economic Paleontologists and Mineralogists Gulf Coast Section, 20th annual research conference, p. 1059–1086.

Winn, R.D., and Dott, R.H., 1979, Deep-water fan-channel conglomerates of Late Cretaceous age, southern Chile: *Sedimentology*, v. 26 (2), p. 203–228.

Withjack, M. O., and Callaway, S., 2000, Active normal faulting beneath a salt layer: An experimental study of deformation patterns in the cover sequence: *AAPG Bulletin*, v. 84, p. 627–651.

Withjack, M. O., and Scheiner, C., 1982, Fault patterns associated with domes—An experimental and analytical study: *AAPG*, v. 66, p. 302–316.

Woodall, L.C., Sanchez-Vidal, A., Canals, M., Paterson, G.L.J., Coppock, R., Sleight, V., Calafat, A., Rogers, A.D., Narayanaswamy, B.E., and Thompson, R.C., 2014, The deep sea is a major sink for microplastic debris: *Royal Society Open Science*, v. 1 (4).

Woods, P.J.E., 1979, The geology of Boulby Mine: *Economic Geology*, v. 74 (2), p. 409-418.

Wood, A., and Smith, J., 1958, The sedimentation and sedimentary history of the Aberystwyth Grits (Upper Llandoveryan): *Quarterly Journal of the Geological Society*, v. 114 (2) p. 163–195.

Wu, L., Trudgill, B. and Kluth, C.F., 2016, Salt diapir reactivation and normal faulting in an oblique extensional system, Vulcan Sub-basin, NW Australia: *Journal of the Geological Society*, v. 173, p. 783-799.

Wu, N., Jackson, C.A-L., Johnson, H.D., Hodgson, D.M., and Nugraha, H.D., 2020, Mass-transport complexes (MTCs) document subsidence patterns in a northern Gulf of Mexico salt minibasin: *Basin Research*, v. 32 (6), p. 1300-1327.

Wynn, R.B., Kenyon, N.H., Masson, D.G., Stow, D.A. V, and Weaver, P.P.E., 2002, Characterization and recognition of deep-water channel-lobe transition zones: *AAPG Bulletin*, v. 86 (8), p. 1441–1462.

Wynn, R.B. Cronin, B.T. and Peakall, J., 2007, Sinuous deep-water channels: Genesis, geometry and architecture: *Marine and Petroleum Geology*, v. 24, p.341–387.

Yamamoto, Y., 2014. Dewatering structure and soft-sediment deformation controlled by slope instability: examples from the late Miocene to Pliocene Miura-Boso accretionary prism and trench-slope basin, central Japan: *Marine Geology*, v. 356, p. 65-70.

Yin, H., and Groshong, R.H., Jr., 2007, A three-dimensional kinematic model for the deformation above an active diapir: *AAPG Bulletin*, v. 91, p. 343–363.

- Zamora, G., Fleming, M., and Gallastegui, J., 2017, Salt Tectonics within the offshore Asturian Basin: North Iberian Margin, in: Soto, J.I., Flinch, J.F., and Tari, G., eds., *Permo-Triassic Salt Provinces of Europe, North Africa and the Atlantic Margins*: Elsevier, p. 371-393.
- Zhang, J., Wu, S., Wang, X., Lin, Y., Fan, H., Jiang, L., Wan, Q., Yin, H., and Lu, Y., 2015, Reservoir quality variations within a sinuous deep water channel system in the Niger Delta Basin, offshore West Africa: *Marine and Petroleum Geology*, v. 63, p. 166–188.
- Zhang, X., and Scholz, C.A., 2015, Turbidite systems of lacustrine rift basins: Examples from the Lake Kivu and Lake Albert rifts, East Africa: *Sedimentary Geology*, v. 325, p. 177–191.
- Zhang, X., Scholz, C. A., Hecky, R. E., Wood, D. A., Zal, H. J., and Ebinger, C. J., 2014, Climatic control of the late Quaternary turbidite sedimentology of Lake Kivu, East Africa: Implications for deep mixing and geologic hazards: *Geology*, v. 42, p. 811– 814.
- Zhao, J.J., Xiao, J.G., Lee, M.L. and Ma, Y.T., 2016, Discrete element modelling of a mining-induced rock slide: *SpringerPlus*, v. 5, Article number 1633.
- Zhu, H.P., Zhou, Z.Y., Yang, R.Y., and Yu, A.B., 2008, Discrete Particle Simulation of Particulate Systems: A review of Major Applications and Findings: *Chemical Engineering Science*, v. 63, p. 5728-5770.
- Ziegler, P.A., 1992. North Sea rift system: *Tectonophysics* 208, 55-75.
- Zonenshain, L. P., and le Pichon, X., 1986, Deep basins of the black-sea and Caspian Sea as Remnants of Mesozoic Back-Arc basins: *Tectonophysics*, v. 123(1–4), p. 181–211.
- Zonneveld, J.P., Moslow, T.F., and Henderson, C.M., 1997, Lithofacies associations and depositional environments in a mixed siliciclastic-carbonate coastal depositional system, upper Liard Formation, Triassic, northeastern British Columbia: *Bulletin of Canadian Petroleum Geology*, v. 45 (4), p. 553-575.

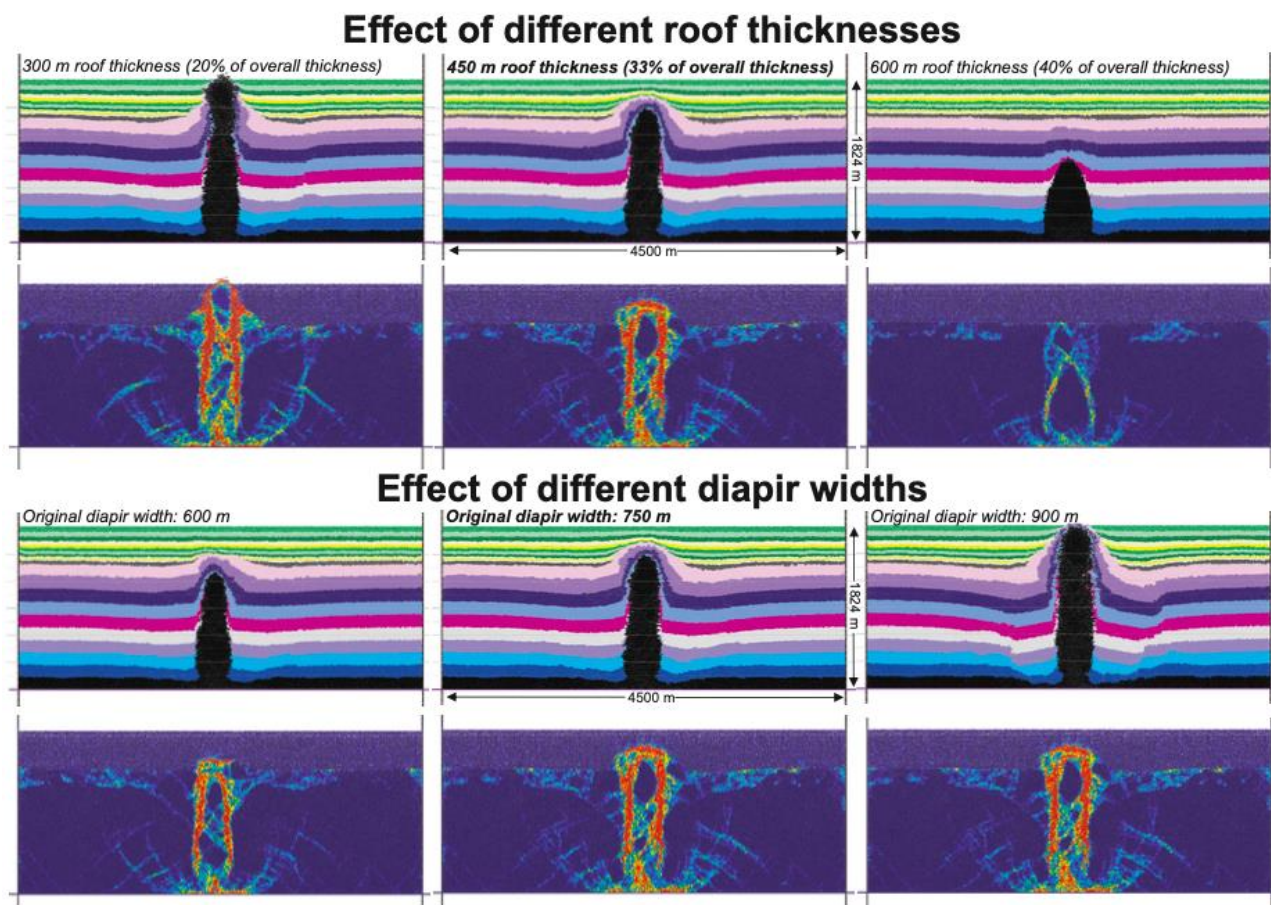


## **Appendix A: External signal preservation in halokinetic stratigraphy: A discrete element modelling approach**

*Cumberpatch, Z.A., Finch, E., and Kane, I. A., 2021, External signal preservation in halokinetic stratigraphy: A discrete element modelling approach: Geology, v. 49 (6), p.687-692.*

(Place holder page for paper)  
6 pages

## Supplementary Material



**Supplementary Figure 1:** Multiple modelling scenarios with various roof thicknesses and initial diapir widths used to refine initial parameters. The model described in this study, initially has a 450 m roof thickness and a 750 m wide diapir.

**Supplementary Table 1:** Summary of geological and mechanical parameter values used in the DEM in this study.

Property	Modelled value	Justification
<b>Salt</b>		
Young's modulus ( $E$ )	3.65 Gpa	Previous experiments (Liang et al. 2012; Pichel et al. 2017;2019) use similar values.
Poisson's ratio ( $\nu$ )	0.33	This value was used by Pichel et al. (2017; 2019), and corresponds to natural examples (Jackson and Hudec 2017).
Density ( $\rho$ )	2.22 gcm <sup>-3</sup>	Slightly higher density than pure halite (2.16 gcm <sup>-3</sup> ) to account for heterogeneity within the diapir. Similar value used by Fuchs et al. (2011) and Pichel et al. (2017;2019)
Viscosity ( $\mu$ )	1.1 x 10 <sup>9</sup> Pa.s	The same value used by Pichel et al. (2017;2019), lower than the real world viscosity (10 <sup>17-18</sup> Pa.s) but provides a reasonable approximation compared to physical models (10 <sup>4</sup> Pa.s)
Breaking separation (BS)	0.001	An approximation of the mechanical behaviour of rock-salt is achieved by reducing the breaking separation of particles representing salt to the point that they exhibit viscous plastic macroscopic behaviour during deformation. Biaxial compression tests conducted by Pichel et al. (2017) show that rocks with a breaking separation of 0.001 react with a non-localized and pervasive breaking of bonds, and generate a linear and horizontal response with insignificant elastic component, representative of ductile viscous-plastic materials that accumulate strain without significant variations in stress. Such characteristics are therefore capable of representing rock salt.
Source layer thickness	150 m	Layers below 100 m are thought to be insufficient for significant salt flow (Jackson and Hudec 2017).

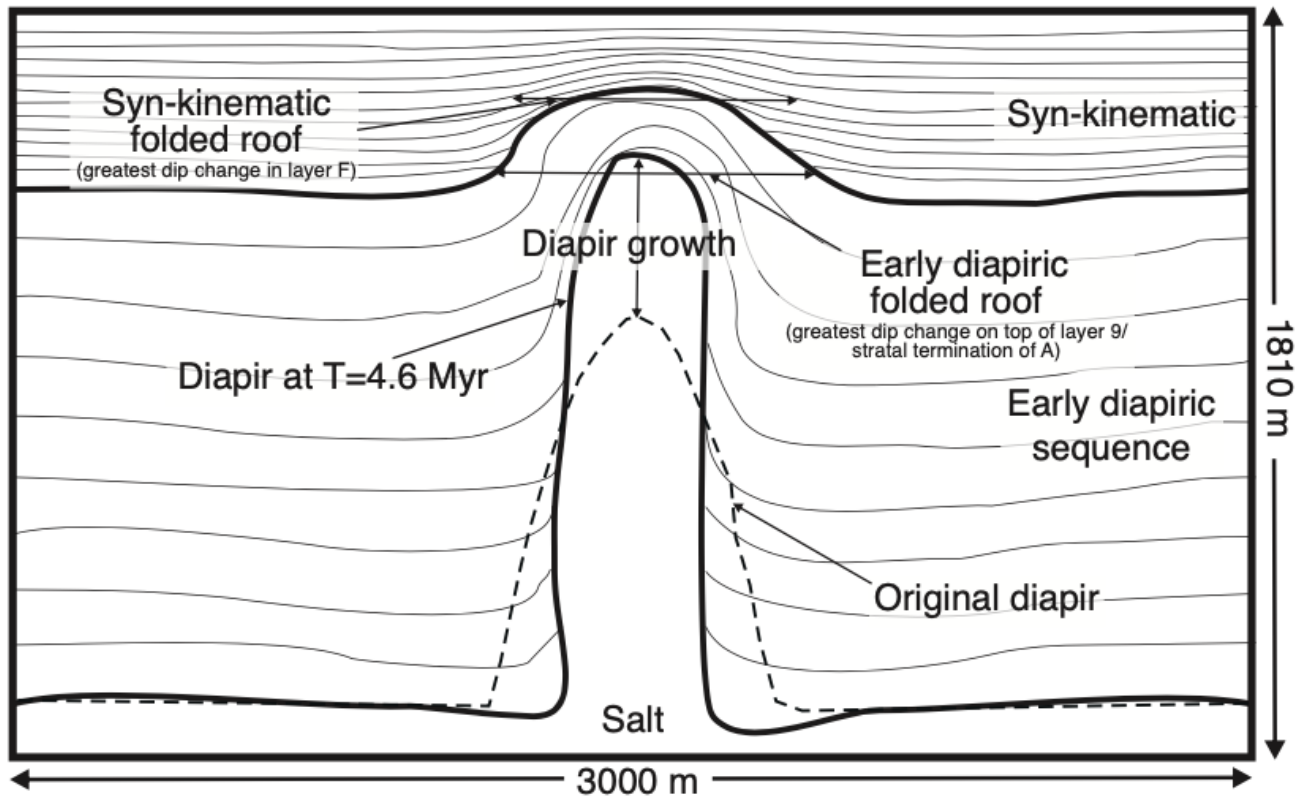
Original height	1050 m	A wide range of diapir heights are observed in nature, this value is 70% of the initial total overburden thickness (1500 m) and thus satisfies the simple force balance conditions for diapiric rise proposed by Schlutz-Ela et al. (1993)
Original width	750 m	A wide range of diapir width are observed in nature, width is similar to Pierce diapirs (Davison et al. 2000).
Rise rate	0.023 mm a <sup>-1</sup>	Dependent on diapir type and emergence rates can vary from 0.0008-3000 mm a <sup>-1</sup> (Jackson and Hudec 2017). 0.023 mm a <sup>-1</sup> is the rise rate of the buried crest of North Pierce (Davison et al. 2000).
<b>Early diapiric sequence (overburden)</b>		
Young's modulus ( <i>E</i> )	6.75 Gpa	Similar value used by Pichel et al. (2017;2019).
Poisson's ratio ( <i>ν</i> )	0.22	Similar value used by Hamilton-Wright et al. (2019).
Density ( <i>ρ</i> )	2.4 – 2.6 gcm <sup>-3</sup>	Density increases linearly with depth, to simulate natural conditions, values are typical for siliciclastic sedimentary rocks and those used in recent models (Pichel et al. 2017;2019).
Breaking separation (BS)	0.023-0.027	Breaking separation increases linearly with depth, to simulate an increase of strength due to compaction with depth. Similar values used as overburden in compression and extensional settings (Finch et al. 2003; 2004) and halokinetic settings (Pichel et al. 2017;2019). Finch et al. (2004) use biaxial compression tests showing the formation of well defines fault segments, typical for brittle materials at similar breaking separations.
Thickness	450 m	Very thick roof thicknesses may retard halokinesis (Jackson and Hudec 2017). This value accounts for 30% of the initial model thickness, thus satisfying the simple force balance conditions for diapiric rise proposed by Schlutz-Ela et al. (1993).
<b>Syn-kinematic sedimentation</b>		
Young's modulus ( <i>E</i> )	5 GPa	Similar value used by Pichel et al. (2017;2019).
Poisson's ratio ( <i>ν</i> )	0.20	Similar value used by Hamilton-Wright et al. (2019).
Density ( <i>ρ</i> )	2.3 gcm <sup>-3</sup>	Typical value for uncompacted sedimentary material, similar values used in recent numerical models (Pichel et al. 2017;2019; Hamilton-Wright et al. 2019).
Breaking separation (BS)	0.023	Similar values used by Pichel et al. (2017; 2019) to model syn-kinematic sedimentation in compressional salt tectonic settings.
Sedimentation rate	0.15 – 0.45 mm a <sup>-1</sup>	Sedimentation rates are wide ranging and can span 11 orders of magnitude, depending on depositional environment. Values chosen are similar to Cenozoic depositional rates in the North Sea (de Haas et al. 1996) and recent models (Fuchs et al. 2011; Hamilton-Wright et al. (2019).

## **Appendix B: Halokinetic modulation of sedimentary thickness and architecture: a numerical modelling approach**

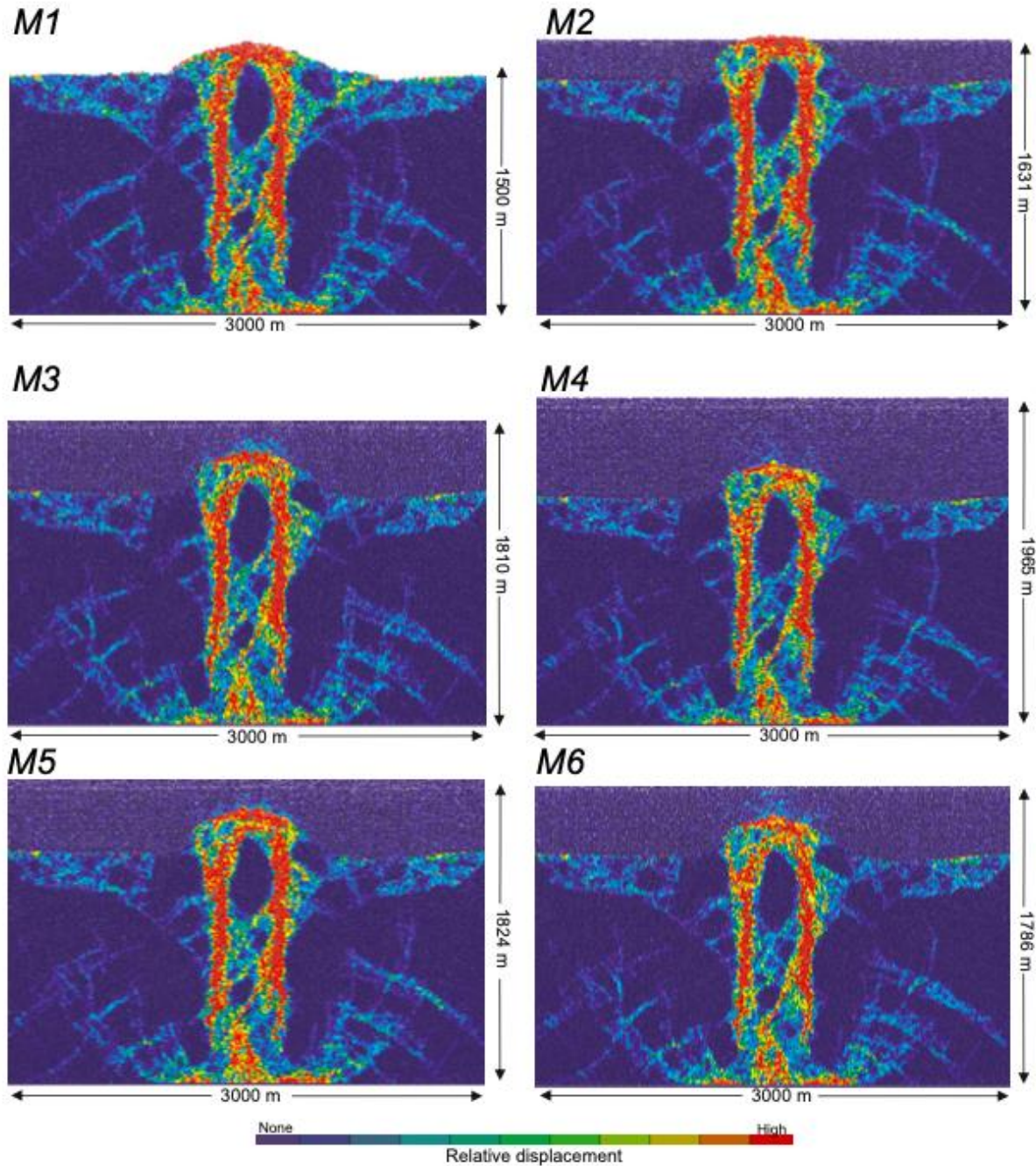
*Cumberpatch, Z A., Finch, E., Kane, I.A., Pichel, L.M., Jackson, C.A-L., Kilbams, B.A., Hodgson, D.M., and Huuse, M., accepted, Halokinetic modulation of sedimentary thickness and architecture: a numerical modelling approach: Basin Research, accepted, in press, available online.*

(Place holder page for paper)  
33 pages

## Supplementary Material

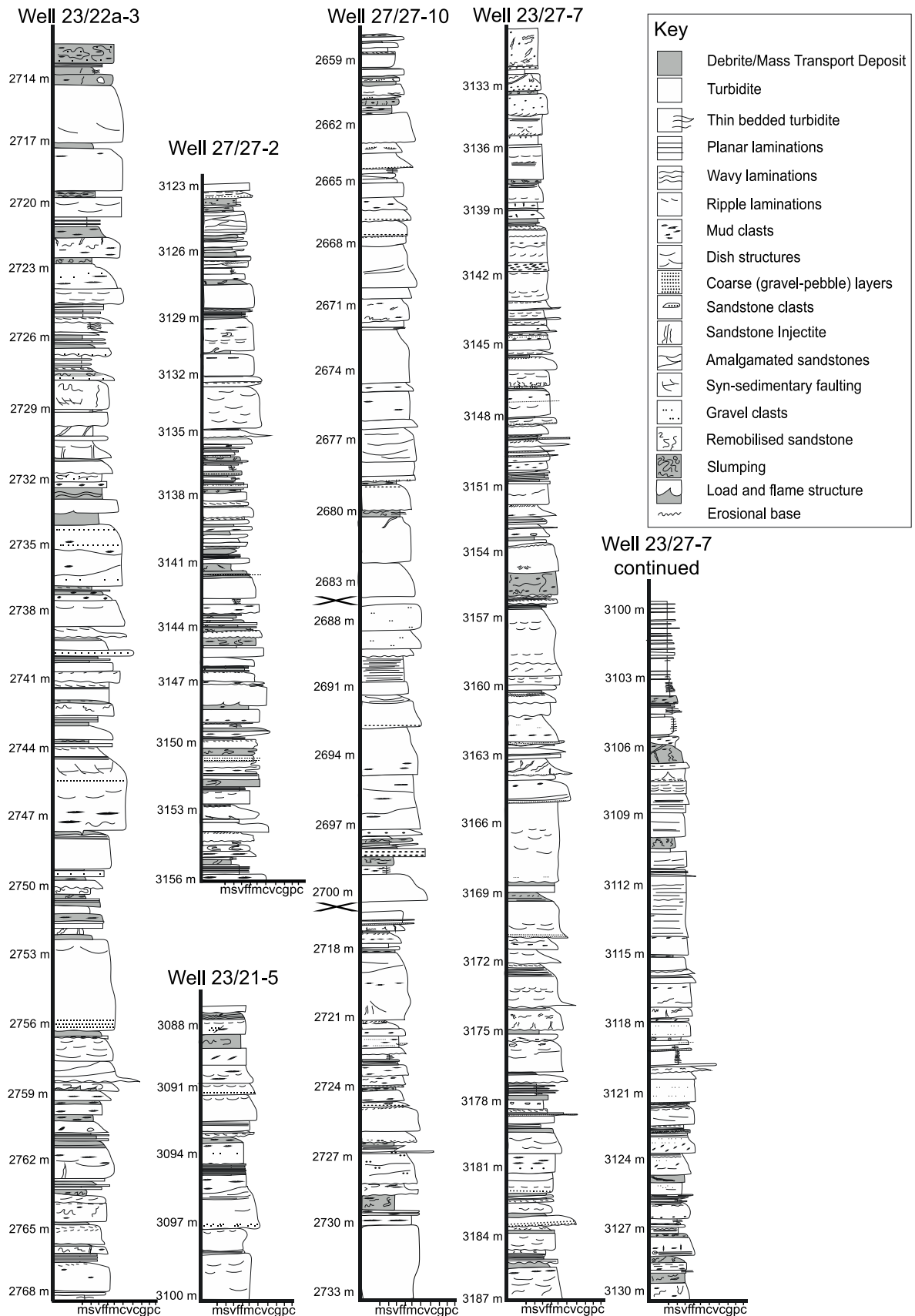


**Supplementary Figure 1:** Explanation of diapir growth, syn-kinematic folded roof and early diapiric folded roof measurements shown in Table 4.2, and described within the text. Diagram is based on M3, and terms are consistent across all models.



**Supplementary Figure 2:** Static image of element displacement relative to initial neighbours for all models at 4.6 Myr. Cold colours represent elements that are in contact with their original neighbour and hot colours suggest high displacement. This is used to show discontinuities and is a proxy for fault location. Note how the majority of the internal salt has remained in connection with its original neighbouring element, and the radial faults associated with salt withdrawal. The maximum displacement shows the relative movement of the salt to the neighbouring overburden and the high mobility of layers in close proximity to the diapir. An apparent lack of deformation is observed outside of the halokinetically deformed zone. Deformation in sediment is shown over the crest and in the flank region of each model (see Figure 4.7 for locations of these areas). Outside of these areas, less deformation is observed in the overburden, suggesting neighbours have remained in contact and overall packages have been rotated (consistent with bedding). Displacements relative to initial neighbour in the sedimentary sequence appear lower than the early diapiric overburden, because the overburden has been deforming for 4.6 Myr, while the sediment has only been deforming for 2.4 Myr. See Spence and Finch (2014) for further details on relative displacement from initial neighbour.





**Supplementary Figure 3:** Stratigraphic logs of the cored wells used in the Eastern Central Graben study. These logs were used to generate the pie charts in Figure 5.7. All cores were logged at the British Geological Survey.

**Supplementary Table 1:** Summary of geological and mechanical parameter values used in the DEM in this study and a justification for their use.

Property	Modelled value	Justification
<b>Salt</b>		
Young's modulus ( $E$ )	3.65 GPa	Previous experiments (Liang et al. 2012; Pichel et al. 2017; 2019) use similar values to represent rock salt (halite)
Poisson's ratio ( $\nu$ )	0.33	This value was used by Pichel et al. (2017; 2019), and agrees with examples (Jackson and Hudec 2017) for salt diapirs primarily composed of halite.
Density ( $\rho$ )	2.22 gcm <sup>-3</sup>	Slightly higher density than pure halite (2.16 gcm <sup>-3</sup> ) to account for heterogeneity within the diapir. Similar value used by Fuchs et al. (2011) and Pichel et al. (2017;2019)
Viscosity ( $\mu$ )	1.1 x 10 <sup>9</sup> Pa.s	The same value used by Pichel et al. (2017;2019), lower than the real world viscosity (10 <sup>17-18</sup> Pa.s) but provides a reasonable approximation compared to physical models (10 <sup>4</sup> Pa.s)
Breaking separation (BS)	0.001	An approximation of the mechanical behaviour of rock-salt is achieved by reducing the breaking separation of particles representing salt to the point that they exhibit viscous plastic macroscopic behaviour during deformation. Biaxial compression tests conducted by Pichel et al. (2017) show that rocks with a breaking separation of 0.001 react with a non-localized and pervasive breaking of bonds, and generate a linear and horizontal response with insignificant elastic component, representative of ductile viscous-plastic materials that accumulate strain without significant variations in stress. Such characteristics are therefore capable of representing rock salt.
Source layer thickness	150 m	Layers below 100 m are thought to be insufficient for significant salt flow (Jackson and Hudec 2017).
Original height	1050 m	A wide range of diapir heights are observed in nature, this value is 70% of the initial total overburden thickness (1500 m) and thus satisfies the simple force balance conditions for diapiric rise proposed by Schlutz-Ela et al. (1993)
Original width	750 m	A wide range of diapir width are observed in nature, width is similar to Pierce diapirs (Davison et al. 2000).
Rise rate	0.023-0.028 mm a <sup>-1</sup>	Dependent on diapir type and emergence rates can vary from 0.0008-3000 mm a <sup>-1</sup> (Jackson and Hudec 2017). 0.023 mm a <sup>-1</sup> is the rise rate of the buried crest of North Pierce (Davison et al. 2000).
Spacing of diapirs	1500m – 9000 m	Chosen for comparison to seismic data used within this study, and natural examples presented elsewhere (Mayall et al. 2006; Giles and Rowan 2012; Carruthers et al. 2013; Jackson and Hudec 2017).
<b>Early diapiric sequence (Pre-kinematic/ overburden stratigraphy).</b>		
Young's modulus ( $E$ )	6.75 GPa	Similar value used by Pichel et al. (2017; 2019) for moderately-deeply buried sedimentary rocks
Poisson's ratio ( $\nu$ )	0.22	Similar value used by Hamilton-Wright et al. (2019) to represent pre-kinematic siliciclastic layers.
Density ( $\rho$ )	2.4 – 2.6 gcm <sup>-3</sup>	Density increases linearly with depth, to simulate natural conditions, values are typical for siliciclastic sedimentary rocks and those used in recent models (Pichel et al. 2017;2019).
Breaking separation (BS)	0.023-0.027	Breaking separation increases linearly with depth, to simulate an increase of strength due to compaction with depth. Similar values used as overburden in compression and extensional settings (Finch et al. 2003; 2004) and halokinetic settings (Pichel et al. 2017;2019). Finch et al. (2004) use biaxial compression tests showing the formation of well defines fault segments, typical for brittle materials at similar breaking separations.
Thickness	450 m	Very thick roof thickness may be inappropriate for halokinesis to occur (Jackson and Hudec 2017). This value accounts for 30% of the initial model thickness, thus satisfying the simple force balance conditions for diapiric rise proposed by Schlutz-Ela et al. (1993).
<b>Syn-kinematic sedimentation</b>		

Young's modulus ( $E$ )	5 GPa	Similar value used by Pichel et al. (2017; 2019) to represent poorly-compacted sedimentary rocks.
Poisson's ratio ( $\nu$ )	0.20	Similar value used by Hamilton-Wright et al. (2019) to represent syn-kinematic layers.
Density ( $\rho$ )	2.3 gcm <sup>-3</sup>	Typical value for uncompacted sedimentary material, similar values used in recent numerical models (Pichel et al. 2017;2019; Hamilton-Wright et al. 2019).
Breaking separation (BS)	0.023	Similar values used by Pichel et al. (2017; 2019) to model syn-kinematic sedimentation in compressional salt tectonic settings, and by Finch et al. (2003; 2004) in extensional and compressional deformation zones.
Sedimentation rate	0.15 – 0.45 mm a <sup>-1</sup>	Sedimentation rates are wide ranging and can span 11 orders of magnitude, depending on depositional environment (Sadler 1981). Values chosen are similar to Cenozoic depositional rates in the North Sea (de Haas et al. 1996) and North Atlantic (Whitman and Davies 1979) and recent models (Fuchs et al. 2011; Hamilton-Wright et al. (2019).

**Supplementary Table 2:** Comparison of stratigraphic thinning across different stratigraphy approaching north Pierce diapir (Figure 4.14). Packages are compared to a specific sedimentation event in a specific model, e.g., the Mid-Miocene – Pleistocene is perhaps analogous to the final sedimentary sequence (S3) in the increasing sedimentation model. Percentage thinning and normalised thinning rates (%/m) are shown for U-C (Undeformed to Crest), U-F (Undeformed to Salt Flank) and F-C (Salt Flank to Crest). The positions of the U, F, and C stratigraphic profiles are spaced at the same distance as in modelled examples (Figure 4.7). In layers which do not extend across the entire model no results exist for U-C and F-C. An average seismic velocity of 2000 m/s was used for approximate depth conversion of the time-migrated seismic data for thinning rate calculations, we are aware this is an over simplification of seismic velocity, which varies with depth and lithology however it is suitable to give a comparison to modelled values. Colours subdivide different stratigraphy, and relate to Figure 4.14.

Stratigraphy	U-C (%)	U-C (%/m)	U-F (%)	U-F (%/m)	F-C (%)	F-C (%/m)
Top Cretaceous- Top Lista [M2, S1]	-	-	51.4	0.044	-	-
Top Lista – Tay [M2, S2]	-	-	35.2	0.031	-	-
Tay-Eocene [M2, S3]	-	-	21.3	0.019	-	-
Eocene – Oligo- cene [M3, S1]	-	-	16.3	0.014	-	-
Oligocene – Mid-Miocene [M3, S2]	65.4	0.044	9.5	0.008	55.9	0.16
Mid-Miocene – Pliocene [M3, S3]	48.9	0.033	27.9	0.024	21	0.06
Top Cretaceous – Eocene [M5, S1]	-	-	16.8	0.014	-	-
Eocene – Mid- Miocene [M5, S2]	88	0.059	18.4	0.016	70	0.20
Mid-Miocene – Pleistocene [M5, S3]	17.8	0.012	10	0.009	7.9	0.023

**Appendix C: Evolution of a mixed siliciclastic-carbonate deep-marine system on an unstable margin: the Cretaceous of the Eastern Greater Caucasus**

*Cumberpatch, Z.A., Soutter, E.L., Kane, I.A., Casson, M., and Vincent, S.J., 2020, Evolution of a mixed siliciclastic-carbonate deep-marine system on an unstable margin: the Cretaceous of the Eastern Greater Caucasus, Azerbaijan. Basin Research, v. 33 (1), p. 612-647.*

(Place holder page for paper)  
36 pages

## **Appendix D: The Influence of Confining Topography Orientation on Experimental Turbidity Currents and Geological Implications**

*Soutter, E.L., Bell, D., Cumberpatch, Z.A., Ferguson, R.A., Kane, I.A., Spychala, Y.T., and Eggenhuisen, J. 2021, The Influence of Confining Topography Orientation on Experimental Turbidity Currents and Geological Implications: Frontiers in Earth Science, v. 8.*

(Place holder page for paper)  
25 pages

